PB2007-108152

Impact of Aspect Ratio on Two-Column Bent Seismic Performance

Report No. CCEER 04-03

Khaled Mostafa

David Sanders

M. Saiid Saiidi

A Report for the
California Department of Transportation
Sacramento, California
under contract 59A0069

March 2004

UNIVERSITY OF NEVADA
•Reno

Center for Earthquake Engineering Research
Department of Civil and Environmental
Engineering/258
University of Nevada
Reno, Nevada 89557

ABSTRACT

The design of structural bridge elements like columns, beam-column joints, and cap beams has evolved in the past 20 years. Many experimental tests have been done in order to determine the behavior of bridge columns under seismic loading. Most of those tests were static performed with monotonic cyclic loading. Only a few of those tests were dynamically performed on shake tables to simulate the actual earthquakes. Based on the literature review, few studies were concerned about testing the seismic behavior of newly designed models; in particular, two-column bent models with hinged bases. Therefore, the objective of the present study was to test two-column bridge bents dynamically by subjecting them to actual time earthquakes. Three models with columns aspect ratios of 6.64, 4.5 and 2.5 and scale ratio of 0.3 were designed according to the updated Caltrans design criteria. The aspect ratio is the height of the column divided by the column diameter. The shake table was able to exert the record of the Sylmar earthquake, 1984 on the three specimens with various amplitudes. All deformations, rebar strains and mass accelerations were recorded during shaking. The three specimens behaved strongly and resisted high levels of the Sylmar earthquakes after experiencing high ductility levels. The two long specimens had a similar flexural behavior, whereas the short specimen had a hybrid between flexural and shear behavior. The data from these specimens will be used to understand joint, column and base hinge behavior to develop analytical models and to propose design recommendations.

ACKNOWLEDGEMENT

This study was funded by California Department of Transportation (CALTRANS). The findings in this study, however are those by the authors and do not necessarily represent the views of CALTRANS.

LIST OF CONTENTS

LIST OF TABLES

LIST OF FIGURES

CHAPTER 1

INTRODUCTION & LITERATURE REVIEW

1.1 Introduction

The 1971 San Fernando, 1989 Loma Prieta and 1994 Northridge Earthquakes caused severe economic losses. These earthquake effects helped to develop the capacity design method in which bridges are allowed to experience inelastic deformation and enough ductility is provided to protect bridges from failure. To achieve enough ductility, the bridge components such as the column plastic hinge zones, the beam-column joints and the column bases are seismically detailed for large deformation capacity. To verify the seismic details for the bridge components, CALTRANS has funded many experimental studies performed on large-scale specimens to test the critical parts of bridges. The current research study is to investigate the new design details[1] for two-column, box-superstructure, hinged-base bridge bents.

1.2 Literature Review

Many studies have investigated the behavior of individual R/C columns aiming to model small parts of the whole bridge whereas few studies have tested larger parts of bridges such as the multiple-column bents. This is because of the experimental and analytical simplicity of the single columns rather than the multiple-column bents. In most cases, the results from testing single columns can be useful not only for the single-column bridges but also for many other bridges.

Laplace, et al[2] examined the seismic behavior of two flexurally dominated 1/3-scale R/C circular bridge columns under El Centro Earthquake excitations. Both columns had an aspect ratio of 4.5. The two columns were identically constructed to investigate the load path and strain rate effect. The two columns were subjected to two different loading scenarios. The first column was subjected to increasing levels of the El Centro Earthquake until failure, whereas the second column was subjected to a large intensity earthquake followed by two aftershocks. In order to predict the columns response under earthquake excitations, a computer program called RC-Shake was developed. In this program, the Q-Hyst model was used to represent the strength degradation after large cyclic displacements. The developed program showed good correlation with the experimental results at small deflections but it showed discrepancy with experimental results at large deflections. The study concluded that columns subjected to sudden strong earthquake excitations, within the columns capacities, behaved stronger and less ductile than columns subjected to gradual earthquake intensities. This effect is called the load path effect, which is diminished after getting high damage levels from the first excitation. The reason of the load path effect is that steel and concrete can have higher strength under high strain rate resulted from dynamic excitation. Laplace, et al[3] also investigated the behavior of shear dominated columns. The CALTRANS shear equation including the strain rate effect predicted the peak shear capacity of the shear columns. The CALTRANS shear equation was used to predict the force-displacement envelope based on the displacement ductility. This calculated envelope had good correlation with the force-deformation envelope of the shear columns. The effect of load path was also investigated and was found to have no significant effect on the measured shear capacities of the columns. While the previous studies did a good job of documenting the single column behavior and showing that current details performed well, it did not investigate the system, joint or base-hinge behaviors.

For the multiple-column bents, a study by Sri Sritharan et al.[4] has investigated the seismic behavior of the CALTRANS 2001 based bridge bents. The main objectives of this study were to verify the recent proposed guidelines for the bridge bents and to examine the force transfer method for the joint design. Two 50 %-scale specimens were built to model part of the Santa Monica Viaduct in Los Angeles. Specimen columns were designed according to the ATC-32[5] specifications while the specimens T and knee joints were designed using the strut-and-tie method[6]. In both specimens, the bridge deck and soffit were not represented to simplify the test details. The expected inflection point in the prototype bridge column was modeled by R/C hinges at the base of each specimen column. The bridge gravity loading was simulated by tie-down system attached to the specimen beam while the seismic loading was quasistaticlly modeled by hydraulic actuators. Under the actuator pulling and pushing test, the R/C specimen reached a displacement ductility of 6, corresponding to a column drift of 8.7 %.

During cycling at this level of ductility, clear strength deterioration was observed as a result of the specimen T-joint failure. The specimen knee joint, however, continued to perform satisfactorily with limited damage forcing buckling in the exterior column longitudinal reinforcement. Despite the T-joint failure at the maximum ductility, the specimen continued to support the gravity loading throughout the test, which led to a conclusion that the joint details were sufficient to prevent collapse of the structure under severe earthquakes. Nonetheless, the reinforcement details of the T-joint failed to produce the desired seismic response. A subsequent analysis revealed the shortcomings in the strut-and-tie model for the T-joints, so another more realistic strut-and-tie model was suggested based on the existing joint reinforcement. The study concluded that a better understanding of the force-transfer through the specimen joints could reduce the steel congestion and make the construction much easier. The study also proved good performance of the 2001 designed specimens as they attained the maximum displacement ductility of 6 and 8. The study, however did not evaluate the following issues:

1- Behavior of the column base hinges since the column base sliding, as a function of the specimen response, was not experimentally measured.
2- Full dynamic response since the test was done under slow cyclic loading.
3- Impact of column aspect ratio on system behavior, or
4- Beam details that include the effective top and bottom slabs.

1.3 Research objectives

The study aimed to investigate the seismic behavior of the newly designed two-circular column, hinged base bridge bents with box superstructure type under dynamic loading. The specimens were designed to represent the newly designed prototype of the existing bridges in California. Based on the limited previous studies dealing with this topic, the research objectives can be summarized in the following points:

1- Test the specimens with more realistic dynamic loading using large shake tables that can exert real time-history earthquakes;

2- Model the bridge gravity loading accurately by placing an equivalent weight of lead blocks on the specimen cap. This creates a dynamic mass moving with the shake table excitation. It also simulates the actual effect of the P-δ;

3- Investigate the impact of the column aspect ratio on the seismic behavior of the two-column bridge bents. This was achieved by constructing three identical two-column specimens having their column height as the only variable;

4- Investigate the behavior and design of bridge joints;

5- Examine simple analytical models that can accurately predict the seismic behavior of two-column bents;

6- Evaluate the behavior of the two-way column hinges; and

7- Verify the importance of including the bridge soffit and deck to accurately model the superstructure configuration.

To perform this investigation, three specimens were designed based on the updated CALTRANS design criteria[1]. The three specimens were identical except for the column aspect ratios, which were 2.5, 4.5 and 6.64. Preliminary static and dynamic analyses were performed on the three specimens to predict the seismic behavior and to verify that the specimens will reach failure before reaching the shake table capacity. All analysis steps and details are illustrated in chapter 2. The specimen construction was the next step, which took three major stages: construction of footings, columns and cap beams. Before each stage, the specimen reinforcement was instrumented. In chapter 3, all construction stages are shown including the testing of the reinforcement and concrete cylinders. Each specimen was subjected to a series of increasing amplitudes the Sylmar record from the 1994 Northridge Earthquake. During loadings, the specimen displacements and accelerations as well as the reinforcement and concrete strains at critical sections were recorded. The full details of these results are documented in chapter 4. The experimental results in chapter 4 were used to evaluate the analytical models used to predict the seismic behavior. The analysis details are illustrated in chapter 5 in which two analytical models were recommended as a result of their simplicity and their good correlation with the experimental results. In chapter 6, the updated CALATRANS design criteria were evaluated based on the analytical and experimental results in chapters 4 and 5. Some of the CALTRANS details were supported by the research findings while others showed poor performance and required new details. Finally the main research findings are listed in chapter 7 and the design recommendations are outlined.

CHAPTER 2

EXPERIMENTAL PROGRAM

2.1 Introduction

This chapter illustrates the procedures used to develop the three test specimens. Based on the 0.3-scale as-built model developed from a previous research project[7], the specimens were designed to represent the configuration of the new bridges in California. The three specimens were designed according to the current CALTRANS specifications and recommendations[1].

The first specimen had an aspect ratio of 6.64, and it had the same geometrical configuration of the as-built model but with a new reinforcement design. The second and the third specimens were similar to the first one but with column aspect ratios of 4.5 and 2.5, respectively.

Several computer programs were used to predict the seismic behavior of the test specimens and to make sure that all specimens could reach total failure before exceeding the maximum shake table capacity. Based on the expected seismic behavior obtained from computer analysis, instrumentation layout was designed to measure the accelerations and displacements of each specimen and to record concrete and steel strains generated during testing.

2.2 Test Specimens

The as-built prototype bridge bent and the scaled down geometric configuration of the model were developed in a previous study[7]. The prototype was based on the average concrete dimensions of six bridges in Southern California having common design criteria (i.e. two circular-columns, hinged-bases, and box girder bridge bents). The three new specimens in this study had the same scale ratio used in the previous study[7] but with new details following the 2000 CALTRANS specifications[1]. To distinguish between specimens, they were labeled as B2CT, B2CM and B2CS, where “B” stood for bent, “2” for two columns, “C” for circular columns, “T” for tall columns, “M” for medium columns, and “S” for short columns. B2CT specimen had the same as-built model dimensions with a column aspect ratio of 6.64, where B2CM and B2CS had aspect ratios of 4.5 and 2.5, respectively. The dimensions and configurations of new specimens B2CT, B2CM, B2CS are shown in Figs. 2-1, 2-2, 2-3, respectively.

2.3 Specimen Design

The new design focused on the details of longitudinal and transverse reinforcement in both columns, cap beam and joints of each specimen. For the columns, the new design details were concerned about confining reinforcement and the development of both longitudinal and hinge dowel reinforcement. For the bent cap, the new design was mainly concerned about the developing of bottom and top longitudinal reinforcement as well as the development of the beam transverse reinforcement. For the beam-column joints, the new details were shown in the development and confinement of the column longitudinal reinforcement inside the joints.

2.3.1 Columns

Column longitudinal reinforcement ratio was taken as 2 % for all specimens. This steel ratio was the same as in the prototype columns. Column transverse reinforcement was, however, estimated based on shear capacity and confining requirements. In each specimen, the column longitudinal reinforcement was extended 16” (400 mm) into the cap beam and the developed length was confined with the same column confining steel as dictated by the CALTRANS new design[1]. This is shown in Figs. 2-4a, 2-5 and 2-6 for specimens B2CT, B2CM and B2CS, respectively. On the other hand, the old substandard design had a different configuration. As can be seen in Fig. 2-4b, the column longitudinal reinforcement is not well developed inside the bent cap and is not confined. The column confining reinforcement is also much less than in the new design. This is clearly shown in Table 2-1, in which the column confinement ratio, ρ_s in the old design is about as much as 0.20 the confinement in the new design.

2.3.2 Cap Beam

For the beam longitudinal reinforcement, no curtailment was made in either the top or bottom reinforcement. As shown in Fig. 2-7 (for specimens B2CT and B2CM) and Fig. 2-8 (for specimen B2CS), the top longitudinal reinforcement was hooked at the ends to have enough development length beyond the critical sections. The bottom longitudinal reinforcement was also sufficiently developed beyond the columns axes (Figs. 2-27 and 2-8). The beam hooks located in the beam mid-span (Figs. 2-7 and 2-8) were not dictated by the new design but they were used for stability considerations, which is discussed in Section 2.5.

For the beam transverse reinforcement, the shear demand required for design was calculated after increasing the column flexural capacity by 20 % as specified by CALTRANS. As a result of the higher lateral capacity of the short specimen B2CS than other specimens, the shear demand of the B2CS beam was much higher than in specimens B2CM and B2CT. This was translated into a higher number of stirrups in the B2CS beam (Fig. 2-8).

On the other hand, the beam old design had a different configuration[7]. As shown in Fig. 2-9, the beam longitudinal reinforcement is curtailed through the whole beam, which does not conform with the seismic-design requirements. The beam transverse reinforcement also consists of U-shaped stirrups, which provide no confinement to the beam cross-section.

2.3.3 Hinge Details

The hinge configuration at the column bases was taken similar to the substandard prototype but with increasing the hinge key depth to 0.5" and increasing the hinge bar development length to 17” (425 mm) according to the new design details. The hinge configuration details at the column bases of all specimens are shown in Fig. 2-10a. The old design details, however, had a different configuration. As shown in Fig. 2-10b, the hinge dowels are not well developed (development length = 7” (175 mm) only), and the hinge key depth is very small (1/12 in (2mm) only).

2.3.4 Footing

The footing of each specimen was designed to be totally fixed by neglecting the effect of soil-structure interaction. Each footing was clamped to the shake table by 16-tie down steel rods with the tensile force of 25 kips. The footing reinforcement and dimensions are shown in Figs. 2-11 and 2-12. The details of the footing reinforcement are also shown in Fig. 2-13. The plan footing dimensions were large enough to accommodate footing stability and lifting hooks (Figs. 2-11 and 2-12). The large footing dimensions also helped to reduce the effect of moment transmitted to the footing. Lifting the specimen from its lifting hooks was considered the first case of loading. The next load case was after leaving the loaded specimen resting on the shake table without any fixation to the shake table. The last and most critical load case was when the fully loaded specimen reached its failure mode.

2.4 Loading System

The actual bridge mass carried by each bent was replaced by a scaled mass of lead. Lead material was used in this study because it provided the most compact way to apply the extra mass, which made the columns and joints more visible to allow more accurate study of the cracks and spalling developed during testing. It also allowed the extra mass to be distributed close to the way in the prototype. The value of lead mass was calculated based on relating the model and prototype masses as follows:

$$M_m/M_p=W_m/W_p=F_m/F_p=\sigma_m*A_m/\ \sigma_p*A_p \quad (2.1)$$

Where,

M_m and M_p = the masses of model and prototype, respectively

W_m and W_p = the weights of model and prototype, respectively

F_m and F_p = the axial columns forces of model and prototype, respectively

A_m and A_p = the columns areas of model and prototype, respectively

σ_m and σ_p = the axial material stresses of model and prototype, respectively

Based on using equal material properties in both model and prototype, the cross-sectional stresses in both model and prototype should be the same, ($\sigma_m = \sigma_p$). Therefore, from equation 2.1, M_m/M_p equals the ratio between column cross-sectional areas A_m/A_p, which is equal to the square of the scale ratio (0.3^2=0.09). Based on that ratio, the required lead weight was estimated and translated into a group of lead blocks[7]. These blocks were contained in steel buckets to be easily loaded on the specimens. The steel buckets were designed to be rigidly attached to the cap beam body to minimize any relative motion between them. The configuration of the steel buckets carried on one of the three specimens is shown in Fig. 2-14. In this figure, the circled numbers indicate the weights of filled buckets including the weights of the steel buckets. The weights of the lower buckets include the buckets on both sides of the bent cap (Fig. 2-14, sec a-a). The weight of the steel tubes is not shown in Fig. 2-14. The weight of the small steel tubes is 0.14 k (0.62 kN) each and the weight of the large steel tubes located the bottom of the cap beam is 0.27 k (1.19 kN) each. There are additional lead blocks located in the middle cells of the cap beam. These blocks are also not shown in Fig. 2-14 for the clarity. These blocks in addition to the cap-beam and the side plates (Fig. 2-14, elevation) weigh 7.4 k (32.9 kN). From these numbers, the location of the center of mass can be calculated. The center of the dynamic mass was found 1.0 foot (12") above the bent-cap center. The centroid of the actual bridge would also be higher than the center due to the weight of topping surface and barrier rails. The total weight of lead buckets, steel tubes, side plates and bent cap is 74.8 k (333 kN). This load is carried by two columns. If f'_c is taken as 5.0 ksi (35 MPa), the load index of each column becomes 4.86 %.

2.5 Specimen Stability

The loading system allowed the mass on each bent to move freely back and forth during shaking. Thus, it was expected for the specimen to experience large displacements at failure. Therefore, a stability system was developed to limit large displacement after reaching the total failure.

For specimen B2CS, the stability system consisted of cables connected between the specimen cap beam and footing by means of hooks attached to specimen body and shake table (Fig. 2-14). The stability system was designed to restrain the excessive motion in the primary direction near failure (Fig. 2-14, elevation) and to support the specimen in the out-of-plane direction (Fig. 2-14, section A-A). For the middle and tall specimens, B2CM and B2CT, the stability system was different. In these relatively tall specimens, leaning toward the out-of-plane direction was more possible, so additional steel-bracing system was added. This bracing system shown in Figs. 2-15 and 2-16 worked as a support for the specimen mass in either in-plane or out-of-plane direction. This support helped to secure the area around the shake table and to protect the shake table from the damage that could follow the specimen failure. As shown in Fig. 2-15 section A-A, the specimen leaning in the out-of-plane direction can be controlled by the 6 x 6 steel tubes coming in contact with the top flange of the W10 x 49. The excessive large displacement in the in-plane direction can also be controlled by the steel cables connected between the cap beam and the steel frame (Fig. 2-15). In a worse case scenario, the 6 x 6 steel tubes would hit the support columns (W 14 x 99) stopping the excessive in-plane motion (Fig. 2-15, elevation).

2.6 Computer Analysis

Computer analysis was used to predict the behavior of each specimen before testing. Computer analysis was also needed to make sure that each specimen could reach failure before exceeding the maximum shake table capacity. It was also helpful in determining the effective and economical instrumentation.

Three computer programs were used to complete the analysis. First, the RCMC[8] program was used to determine the moment and curvature capacities for column and beam cross-sections in each specimen. Second, the Drain-3D[9] program was used to perform the push-over analysis for each specimen. Third, the RC-Shake[2] program was used to analyze specimens dynamically by subjecting them to earthquake records.

2.6.1 Moment-Curvature Analysis

The critical cross-sections of the columns and beam in each specimen were analyzed using the RCMC program. To perform the RCMC analysis, the properties of the reinforcement and the confined and unconfined concrete materials were needed. Kent and Park model was used to model the unconfined concrete properties, whereas modified Mander model was used to model the confined concrete properties[8]. To begin this preliminary analysis, appropriate concrete and steel properties were assumed based on previous tests. The unconfined concrete strength, f'_c was assumed 5.0 ksi (34.5 MPa) and the steel yield strength was assumed 60 ksi (414 MPa). The levels of axial forces in the specimen columns were initially taken to be equal. Then the equilibrium of the whole system was calculated and used to determine the actual axial force in each column. Based on the new levels of axial forces, new moment-curvature diagrams for each column were determined. This process is repeated till there is no significant difference between the successive values of the column axial forces. As a result of this process, the axial forces in the tall columns were determined as 63 k (280 kN) and 12 k (53.4 kN). The corresponding axial force in the cap beam was calculated as 15 k (67 kN). Based on that this analysis is a preliminary analysis, the previous levels of axial forces were used in analyzing the other two specimens. A more detailed analysis in this aspect is illustrated in chapter 5. The output results are shown in Figs. 2-17 to 2-21. The theoretical moment-curvature diagram for the beam section is shown in Fig. 2-17. The moment-curvature diagram for the two column sections are shown in Figs. 2-18 and 2-19. The moment curvature diagrams for the two column-base sections are shown in Fig. 2-20 and 2-21. On each diagram, the idealized moment-curvature curve was appended to determine the idealized yield moment and curvature for each section. The previous analysis was later refined in the final analysis after knowing the actual concrete and steel properties (chapter 5, section 5.3).

2.6.2 Pushover Analysis

Although pushover analysis was a static analysis, it was essential for predicting the change in structural stiffness during dynamic loading. The model used for performing this analysis was the Takeda model, which was developed from experimental studies[13]. The data required for this model were the plastic moments of the critical cross-sections (previously calculated from the RCMC analysis), the cracking moments for concrete sections calculated from transformed cross-section analysis, and the yield rotations for each plastic hinge calculated by the conjugate beam method. On each column, the moment diagram is transferred to a load by dividing the moment values by the average EI value of the column cross-section. The reaction due to this loading at each column end is equivalent to the end rotation.

The output results from DRAIN-3DX depicted in Figs. 2-22, 2-23 and 2-24 demonstrate the static load-displacement relationships for specimens B2CT, B2CM and B2CS, respectively. From these diagrams, maximum lateral load capacity and its corresponding yield displacement can be concluded of each specimen. The failure displacement, however, is not directly calculated by the DRAIN-3DX program, so it is calculated by hand. The ultimate displacement of each specimen can be calculated by adding the plastic displacement of each specimen, Δ_p to its corresponding yield displacement, Δ_y. The yield displacement, Δ_y of each column is calculated from the program whereas the plastic displacement, Δ_p is calculated by hand. These calculations are demonstrated as follows:

$$\Delta_m = \Delta_y + \Delta_p \tag{2.2}$$

$$\Delta_p = \theta_p *(H - L_p /2) \tag{2.3}$$

$$\theta_p = (\Phi_u - \Phi_y)*L_p \tag{2.4}$$

Where

Δ_m = maximum lateral displacement before failure directly

Δ_y = yield displacement, (obtained from Drain analysis)

Δ_p = plastic displacement

θ_p = plastic rotation

Φ_u=ultimate curvature of column section (obtained from RCMC analysis)

Φ_y = yield curvature of column section (obtained from RCMC analysis).

H = column clear height

L_p = plastic hinge length, (obtained from Paulay and Priestley empirical equations[10])

Based on the difference in the axial load level between the two columns, each column in each specimen has two different ultimate displacements. The ultimate specimen displacement was based on the column of the lower ductility.

2.6.3 Dynamic Analysis

The dynamic analysis was performed by the RC-Shake program, which was developed to solve nonlinear SDOF problems based on step-by-step integration procedure. The model used in this program was the Q-hyst model, which was developed by Saiidi, M.[11] to model the hysteretic loops of reinforced concrete members.

Before final analysis, the model was analyzed for four earthquake records to choose the most critical one. The comparison was based on maximum specimen response, so each specimen was subjected to several earthquakes adjusted to have the same maximum acceleration. The response to each earthquake for specimens B2CT, B2CM and B2CS are shown in Figs. 2-25, 2-26 and 2-27, respectively. It is shown in these figures that the 1994 Sylmar record from the Northridge Earthquake was the one that causes large excitations to the tall and middle specimens. The Sylmar earthquake was also used in the previous study[7], which was done on the substandard model.

To simulate the planned loading steps during testing, the Sylmar earthquake was modified to a group of successive earthquakes with increasing amplitudes. Fig. 2-28 shows the new ramped earthquake after scaling down the total time of actual earthquakes to match with the fundamental period of each specimen. The total time of each earthquake was scaled down by the square root of the scale ratio, $L_s^{0.5}$ (0.5477). This scaling-down ratio was obtained after relating the natural period of both model and prototype. The suggested ramped earthquake consisted of nine Sylmar records having maximum accelerations of 0.12g, 0.15g, 0.3g, 0.45g, 0.6g, 0.75g, 0.84g, 1.0g and 1.25g. This corresponds to a series of Sylmar records having factors of 0.2, 0.25, 0.5, 0.75, 1.0, 1.25, 1.40, 1.67, and 2.10 x Sylmar where the maximum acceleration of the Sylmar is 0.6 g. For the sake of comparison, the first set of seven loadings from 0.12g to 0.84g was the same as in the previous study[7]. In the actual test, a time gap existed after each earthquake, which was used for specimen observation and marking.

The ramped earthquake was used as input for the RC-Shake program to model the actual tests for the three specimens. The load-displacement output hysteresis are shown in Figs. 2-29, 2-30, and 2-31 for specimens B2CT, B2CM, and B2CS, respectively. Based on the difference in response, each specimen reached its maximum displacement under a specific ramped earthquake. The predicted failure of the middle specimen B2CM was at 0.84 x Sylmar while the predicted failure of the tall and short specimens was at 1.25 x Sylmar.

2.7 Instrumentation

Based on previous computer analyses, the instrumentation layout of each specimen was designed to record strains, displacements and accelerations generated at critical sections during testing. Each type of the instrumentation is individually discussed in the following subsections.

2.7.1 Strain Gages

Strain gages were used to record the strains generated in longitudinal and transverse steel at critical sections during testing. The critical sections were at the expected plastic hinge zones and at the zones of maximum shear stresses. It was decided to provide specimens B2CT and B2CM with the same instrumentation because it was expected for these specimens to experience similar responses. However, it was expected for specimen B2CS to experience higher shear demand because of its small column aspect ratio, so its instrumentation layout was slightly different. Figs. 2-32 and 2-33 show strain gage configuration of longitudinal and transverse reinforcement, respectively, in both specimens B2CT and B2CM. In these specimens, the distribution of strain gages was mainly concentrated in the plastic hinge zones. All gages in both specimens were labeled on the gage lead wires to recognize their positions after concrete casting. Figs. 2-34 and 2-35 show the gage labeling of longitudinal and transverse reinforcement, respectively.

Similarly, the strain gage configuration of longitudinal and transverse reinforcement in specimen B2CS was designed as shown in Figs. 2-36 and 2-37, respectively. The number of strain gages was reduced in the column plastic hinge zones due to the expected reduction in the plastic hinge length of each column. At beam critical sections, the number of strain gages was increased as a result of moment and shear increase at these sections. All gage labeling is shown in Figs. 2-38 and 2-39 for longitudinal and transverse reinforcement, respectively.

2.7.2 Novotechnik Transducers

The main purpose of the Novotechnick tranceducers was to determine curvatures and strains at the critical sections during testing. It was also used to measure the sliding and rotation at the column bases. The way of calculating curvature from the Novotechnick readings is shown schematically in Fig. 2-40. The calculated curvature was the average curvature of the cross section between the Novotechnik steel rods. The Novotechnick arrangement of specimens B2CT and B2CM are shown Fig. 2-41. Similarly, Fig. 2-42 shows the Novotechnik configuration for specimen B2CS. In this figure, the number of Novotechnik was slightly reduced at the column plastic hinge zones due to the expected reduction in flexural behavior in this specimen.

2.7.3 Accelerometers and Potentiometers

Accelerometers and potentiometers were used to record the specimen absolute accelerations and displacements, respectively. Fig. 2-43 shows the schematic configuration of these instruments for the short specimen B2CS. In this figure, the specimen top displacement in the main loading direction is measured by one potentiometer located on the west side of the bent-cap and directed in the E-W direction. The lateral displacement was measured by another potentiometer located at the center of bent cap and directed in the N-S direction.

To measure the specimen main and lateral accelerations, two accelerometers were located in one of the bent cap cells (Fig. 2-43) and directed in the E-W and N-S directions. An additional accelerometer was located at the top of a steel bucket to record the E-W accelerations of the steel buckets. Using the output of the steel buckets accelerometer, any relative motion between the steel buckets and the bent-cap could be determined.

The arrangement of accelerometers and potentiometers of specimens B2CT and B2CM were similar to specimen B2CS (Fig. 2-44). The only difference was in the arrangement of N-S potentiometers. Two potentiometers were attached to the bent-cap body to measure the out-of-plane displacements and rotations.

CHAPTER 3

SPECIMEN CONSTRUCTION

3.1 Introduction

This chapter describes the construction steps for the test specimens. Each specimen was constructed in three stages: footing, columns and cap beam. Each stage was performed using three steps: form building, reinforcement placement, and concrete casting and curing. Between reinforcement placement and concrete casting, strain gages were placed on the reinforcement. The three specimens were basically identical except in their column aspect ratios. Therefore, it was decided to build the three specimens simultaneously but due to construction difficulties, there was a time delay in construction between the short specimen and the other two specimens.

3.2 Construction of Footings

The footings of three specimens were identical, so it was decided to build and cast the three footings simultaneously. The forms were prepared with the required dimensions and details as shown in Fig. 3-1. In this figure, the 3.5” (88 mm) diameter PVC pipes were placed and fixed in their locations to create holes in each footing matching the shake table connection holes. These holes were used later in fixing each footing to the shake table.

The footing reinforcement was prepared and placed according to the required drawings (Fig. 2-11). The main reinforcement configuration consisted of bottom and top meshes of # 6 (19 M) bars (Figs. 3-2 to 3-4). The distance between the two meshes was maintained using the footing shear steel, which consisted of 32 one-leg chairs distributed through the whole footing. Footing hooks shown in Figs. 3-2 to 3-4 consisted of three different sets of hooks. The first set was 4 # 11 (36 M) hooks used for lifting the specimens. The distance between these hooks and their dimensions were designed according to the standard dimensions of the laboratory forklift. The second and third sets were 8 # 11 (36 M) and 4 # 7 (22 M) hooks, which were used for stability requirements during tests (Sec. 2.5). Footing dowels shown in Figs. 3-3 and 3-4 were the columns hinge reinforcement. They were 4 # 4 (13 M) bars, 4" (100 mm) apart in both directions to create the two-way hinges. They also extended 17" (425 mm) inside the column base to fully develop their yield strength. It was planned to place strain gages to these dowels at three levels. The first level was at the column-footing interface and the other two levels were at 4" (100 mm) above and 4" (100 mm) below the column-footing interface (Figs. 2-32 and 2-36). The strain gage lead wires coming from each level were collected at enough distance above the footing and covered to protect them from damage that might occur during concrete casting (Fig. 3-4).

After checking all reinforcement details, all footings were cast (Fig. 3-5). The concrete used in footing casting had the mix-design shown in Table 3-1.

During casting, concrete cylinders were taken to make sure of concrete quality and strength. Before the concrete surface was totally hardened, the footing surface area at each column-footing interface was roughened to 0.25” (6 mm) to create the construction joint between each footing and its columns. Fig. 3-6 shows the footing-column interface after roughening and before removing the resulting debris.

3.3 Construction of Columns

The construction process of all columns was standard. First, the steel cages of each column were constructed according to the required drawings (Figs. 2-4 to 2-6). Each cage consisted of 15 # 4 (13 M) longitudinal bars, uniformly distributed inside the gage 2 spiral of 12.5” (313 mm) external diameter and 2.25” (56 mm) pitch. The three sets of column cages were identical except for their longitudinal reinforcement lengths. The next step was placing strain gages at the required locations of each column cage. The strain gage locations were shown schematically in Figs. 2-32 and 2-33 for both tall B2CT and medium B2CM specimens and in Figs. 2-36 and 2-37 for the short specimen. To place strain gages, the rebar surface was marked and grinded at required locations as shown in Fig. 3-7. The strain gages were subsequently glued at grinded locations after cleaning all debris by a special solution. The gages were covered and insulated with a waterproof material to prevent any damage that could happen during and after concrete casting. The process of fixing strain ages was completely described in the Strain Gage Users' Guide[12].

Each strain gage was labeled at the end of its lead wire to recognize its location after concrete casting. To protect lead wires from damage, they were encased into plastic tubes as shown in Fig. 3-8. All plastic tubes were collected together to get out of each column as shown in Figs. 3-9 to 3-11. For short specimen columns (Fig. 3-9), all collected tubes exited from one outlet while in both medium B2CM and tall B2CT columns (Figs. 3-10 and 3-11, respectively), all tubes exited from two outlets. The locations of tube outlets were chosen at zones of minimum stresses where no concrete spalling was expected. Before starting the next construction step, it was found that the column longitudinal reinforcement hooks at the base of the column (Figs. 3-9 to 3-11) did not comply with the standard practice at CALTRANS as they use straight bars. As a result, these hooks were cut before placing the column cages in their appropriate forms.

The column forms were prepared with the required dimensions as shown in Figs. 3-12, 3-13 and 3-14 for short B2CS, medium B2CM and tall B2CT specimens, respectively. After covering each column cage with its form, all forms were supported and adjusted vertically (Figs. 3-12 to 3-14). The Novotechnik rods shown in Figs. 2-41 and 2-42 were also installed in their specified locations at the top and bottom of each column. The upper part of each column cage (16" (400 mm)) was left uncovered to be cast with bent cap beam. Before concrete casting, the gage lead wires of each column were collected and covered for protection. Figs. 3-15 and 3-16 show the casting process of the tall B2CT and medium B2CM columns, respectively. In these figures, all precautions were taken to prevent aggregate segregation during casting. The concrete used in casting of these columns had the mix design given in Table 3-1. During casting, concrete cylinders were taken from the same concrete mixture. The procedure and specifications for making concrete cylinders were described in ASTM C31/ C31M-98.

Some construction errors were made during column casting. The lack of the mechanical vibration during casting created a honeycomb appearance at the critical sections of both tall B2CT and medium B2CM columns. Fig. 3-17 shows a sample of damage occurred in tall-specimen columns. Based on this damage, it was decided to remove the tall B2CT and medium B2CM columns and rebuild them from the footings (Fig. 3-18). It was also decided to use another concrete mix-design in casting the new columns (Table 3-2). As a result of these construction difficulties in tall B2CT and medium B2CM specimens, the short specimen B2CS was constructed before the other two specimens.

3.4 Construction of Beams

Fig. 3-19 shows the first step in the beam construction in which part of the beam form is established to build the beam steel cage on it. Care was taken to make sure that each beam form was perfectly level. The clear height of each column was also checked. Secondly, the beam steel cages were constructed with the required details. As shown in Figs. 2-7 and 2-8, the main steel configuration of specimens beams consisted of top reinforcement of 6 # 5 (19 M) hooked ended bars and bottom reinforcement of 4 # 6 (19 M) bars. The spacing between top and bottom reinforcement was maintained constant after tied with No. 3 (10 M) hoops distributed along the beam length. The secondary reinforcement was for the cross beams and the top and bottom flanges. All details of cap beam reinforcement are shown in Figs. 3-20 and 3-21. The large U-shaped hooks shown in this figure were additional reinforcement for the stability system and not related to the beam design.

Thirdly, the strain gages were glued at the required locations of each beam. The strain gage locations were shown schematically in Figs. 2-32 and 2-33 for both tall and medium specimens and in Figs. 2-36 and 2-37 for short specimen B2CS. The gaging procedures previously mentioned for the columns were also used for the beams. The location of lead wire outlet was chosen at the beam mid-span where no concrete spalling was expected.

Based on the construction time delay between short specimen B2CS and the other two specimens, it was decided to cast the cap beam of short specimen B2CS and the columns of other two specimens, simultaneously. This made the short specimen B2CS ready for testing earlier than the others. Casting process is shown in Figs. 3-22, 3-23 and 3-24 for short B2CS, medium B2CM and tall B2CT specimen beams, respectively. The concrete used in casting the cap beams had the mix-design given in Table 3-2. The mechanical vibrator was continuously used to increase casting quality, especially in the narrow zones of cross beams (Fig. 3-22 b). During casting, concrete cylinders were taken from the same concrete mixture. After casting, all cap beams were covered to complete curing.

3.5 Materials Testing

Materials were tested before and after construction to make sure of material strength and quality. For steel, many tests were done on steel samples before construction to make sure that steel yield strength was near the target value. The results of steel testing were satisfactory for all steel except for the column transverse reinforcement. Therefore, it was decided to use a heat-treatment process for this reinforcement to adjust its yield strength. For concrete, standard cylinders were taken during casting to be able to determine their strength on the day when specimens were tested.

3.5.1 Testing of Steel Samples

The steel used in reinforcing the three specimens was identical. It consisted of several rebar diameters. The most critical rebars were size No. 4 (13 M) and Gage 2, because they constituted the longitudinal and transverse reinforcement of the specimen columns, respectively. No. 4 (13 M) rebar was also used as the hinge dowels of each column base. The other rebar sizes were No. 3 (10 M), No. 5 (16 M) and No. 6 (19 M). They were the transverse and longitudinal steel of the bent beams. No. 6 (19 M) rebar was used as the main reinforcement in the specimen footings.

The target yield strength was 60 ksi (414MPa). Three samples of each rebar diameter were tested and the average results of yield and ultimate strengths are shown in Table 3-3. The results were acceptable except for the samples of column spirals (gage 2). As shown in Fig. 3-25, Gage 2 did not experience any yield plateau, and its ultimate strain was too low (≈ 0.011). The gage yield strength was too high (107 ksi (738 MPa)). To modify these properties, the column spirals were heat-treated. Each column spiral was coiled to form one portable coil and to fit into the heat-treating oven. Before this step, the required heat-treatment ramp (Fig. 3-26) was determined. Six trials of heating ramps were applied the 10" (250 mm) Gage 2 samples with the maximum temperatures of 850 °C (1562 °F), 675 °C (1247 °F), 625 °C (1157 °F), 600 °C (1112 °F), 614 °C (1137 °F) and 615°C (1139 °F). The ramps stayed the same, only the maximum temperatures changed. Figs. 3-27 to 3-32 show the results of the heat-treatment trials on the stress-strain properties of the Gage 2 bar. The best result of the heat-treatment is shown in Fig. 3-32. The heating ramp of 615 ^{o}C (1139 ^{o}F) maximum temperature was chosen because it brought the gage to its target yield strength (60 ksi (414 MPa)) and produced a yield plateau (Fig. 3-32).

3.5.2 Testing of Concrete Cylinders

Concrete cylinders were taken from each concrete batch on the day of casting. For the three specimens, there were four days of casting. The first day was for casting the three footings of the three specimens. The second day was for casting the short specimen columns. The third day was for casting the short specimen cap beam and the columns of both medium B2CM and tall B2CT specimens. The fourth day was for casting the cap beams of medium B2CM and tall B2CT specimens. The number of concrete cylinders taken at each day of casting was twelve cylinders. Three of them were tested after seven days from casting to give a quick estimate of concrete strength. Three cylinders were tested after twenty-eight days from casting to give the standard strength. Three cylinders were tested on the day of specimen test. The last three cylinders were extra and were to be used in case of losing or damaging any other cylinders. After testing each set of cylinders, the concrete strength of footings, columns, and beams were calculated and listed in Table 3-4.

CHAPTER 4

EXPERIMENTAL RESULTS

4.1 Introduction

This chapter shows the experimental procedures and results of the specimens B2CS, B2CM, and B2CT. The experimental testing was performed using a 14 feet (4.30 m) x 14.50 (4.40 m) feet-shake table. The loading sequence was taken as a series of successive Sylmar records from the Northridge Earthquake, 1994 with increasing amplitudes. The specimen accelerations (in-plane and out-of-plane accelerations) generated after each loading were measured by two accelerometers attached to the specimen mass (Figs. 2-43 and 2-44). The accelerometers had a high measuring sensitivity, so it was decided to filter their output in a way to smooth the acceleration history. Care was taken in choosing the smoothing-filtering frequency to avoid loosing some of the original data. For the tall and medium specimens, the soothing-filtering frequency was taken as 30 Hz while for the short specimen the filtering frequency was taken as 10 Hz.

The specimen displacements generated during each loading were also measured by two displacement transducers attached to the specimen mass to measure the in-plane and out-of-plane displacements (Figs. 2-43 and 2-44). The curvatures at critical sections were measured using Novotechnick instruments installed at the specimen critical locations (Figs. 2-41 and 2-42). Inside the specimen, the reinforcement strains generated during each loading were also measured by gages attached to the reinforcement surface (Figs. 2-32 to 2-39). All results of reinforcement strains, specimen displacements, and accelerations and section curvatures were collected during loading at the time step of 1/160 sec (160 Hz). This frequency created a large data, so in order to reduce the volume of results without affecting the extreme values, the output data were resampled at lower frequencies suitable for each specimen (80 Hz for short specimen B2CS, 30 HZ for medium specimen B2CM and 50 Hz for tall specimen B2CT). The resampled results for each specimen were plotted in a way to verify instrument performance and to investigate the specimen behavior.

4.2 Loading Sequence

It was decided to test each specimen with a ramped earthquake, which consisted of a group of Sylmar records (from the Northridge earthquake, 1994) with increasing amplitudes. To have a valid comparison between the new design in this study and the old design in a previous study done on an as-built specimen[7], the initial loading runs of each specimen were close to the loading runs of the previous study[7]. For higher-amplitude loading runs, the level of loading was selected based on specimen response. There was a difference between the target and achieved earthquakes. Tables 4-1, 4-2 and 4-3 show the sequence of loading runs for specimens B2CS, B2CM and B2CT, respectively. These tables also show a comparison between the maximum achieved and target accelerations at each loading run. The maximum difference between the achieved and target accelerations after 1.0 x Sylmar were 16 %, 28 % and 9 % for specimens B2CS, B2CM and B2CT, respectively. Despite this difference in acceleration maximum values, the frequency content of the target and achieved records were close. This is shown in Figs. 4-1, 4-2 and 4-3 for the short, medium and tall specimens, respectively, during the records of 1.0, 1.75 and 2.5 x Sylmar for each specimen.

4.3 Observed Response

The response of each specimen was observed during testing by marking the cracks developed after each loading and recording the first loadings causing concrete spalling. The response of medium and tall specimens was close to each other while the response of short specimen was different. The dominant direction for the Sylmar record was to the west (See Figs. 2-43 and 2-44 for the location of the specimen with respect to the main direction).

4.3.1 Observed Response of Short Specimen, B2CS

Short specimen B2CS was subjected to seventeen Sylmar Earthquakes with increasing amplitudes (Table 4-1). From 0.20 x Sylmar to 1.0 x Sylmar, no cracks were observed. After the loading of 1.0 x Sylmar, the first flexural cracks were observed in the west and east columns at the plastic hinge zones (Figs. 4-4 and 4-5). The cracks were getting wider and larger as the loading increased. The first shear cracks were observed at the loading of 1.40 x Sylmar where diagonal cracks appeared in the west column and in the east beam-column joint (Figs. 4-6 and 4-7). At the loading of 2.0 x Sylmar, shear cracks appeared in the west beam-column joint and in the east and west columns through the whole column length (Figs. 4-8 and 4-9). The first concrete spalling occurred on the east side of the east column at the loading of 2.5 x Sylmar (Fig. 4-10). Spalling started to expose the confinement reinforcement on the east side of the west column at the loading of 3.0 x Sylmar (Fig. 4-11). Severe damage happened on the west side of the west column base after the loading of 3.25 x Sylmar where a large piece of concrete spalled out leaving the column longitudinal and transverse reinforcement exposed (Fig. 4-12). The east column base also experienced a significant slippage. The maximum slippage at this base was 0.56” (14 mm) toward the west direction. After 3.25 x Sylmar, the residual slippage at the east column base was as shown in Fig. 4-13 in which the column base slipped leaving a part of the expansion-joint filler exposed. As a result of this damage, it was decided to stop the test at this level of loading (3.25 x Sylmar). The general condition of east and west column after the maximum loading is shown in Figs. 4-14 and 4-15, respectively. In these figures, shear cracks are extended along the whole length of each column and the dominant direction of these cracks are with the dominant direction of the seismic force (west direction). Shear cracks are also more concentrated at the top of each column. The flexural behavior at the maximum loading is shown in Figs. 4-16 and 4-17 for the east and west columns, respectively. As can be seen from these figures, the concrete spalling is well contained where the transverse reinforcement only is partially exposed. This is an indication that the columns could sustain loading higher than the 3.25 x Sylmar. During the whole test of this specimen, the cap-beam was considered intact. In the beam-column joints, the cracks were minimal and no additional cracks were observed after the loading of 2.0 x Sylmar. All of the previous observations for this specimen are summarized in Table 4-4.

4.3.2 Observed Response of Medium Specimen, B2CM

Medium specimen B2CM was subjected to fifteen Sylmar Earthquakes with increasing amplitudes (Table 4-2). At the first loading of 0.10 x Sylmar, no cracks were observed while after the loading of 0.2 x Sylmar, minor flexural cracks were observed in east and west columns at the plastic hinge zones (Figs. 4-18 and 4-19). The cracks were getting wider and larger as the loading increased; the number of cracks also increased and distributed over longer portions of the columns. The first shear cracks were observed at the loading of 1.25 x Sylmar where diagonal cracks appeared along the plastic hinge zones in both columns, (Figs. 4-20 and 4-21). Minor shear cracks started in the west and east beam-column joints after the loadings of 1.50 x Sylmar (Figs. 4-22 and 4-23, respectively). The first concrete spalling occurred on the east side of both columns at the top of the columns after the loading of 1.25 x Sylmar (Figs. 4-24 and 4-25); at this level of loading, minor concrete spalling started also on the west side of both column bases (Figs. 4-26 and 4-27). After the loading of 1.50 x Sylmar, spalling increased till exposing the transverse and longitudinal reinforcement on the east side of the west column (Fig. 4-28). After the loading of 2.0 x Sylmar, spalling started to expose the transverse reinforcement on the east side of the east column (Fig. 4-29); at this level of loading, the longitudinal and transverse reinforcement on the east side of the west column were fully exposed (Fig. 4-30). At the loading of 2.25 x Sylmar, a vertical cracking appeared on the west side of the west column base (Fig. 4-31); at the same loading, spalling increased on the east side of the east column till exposing longitudinal reinforcement (Fig. 4-32). During 2.25 x Sylmar, minor cracking started at the bottom of the cap-beam on the west side of the west column (Fig. 4-33). After 2.5 x Sylmar, spalling started at the same region of the cap-beam (Fig. 4-34). After the loading of 2.75 x Sylmar, the specimen leaned toward the north direction (Fig. 4-35). At this loading, concrete spalling increased at the plastic hinge zones of the east and west columns. This made the columns transverse and longitudinal reinforcement more visible (Figs. 4-36 and 4-37). After the loading of 3.0 x Sylmar, concrete spalling deeply increased on the east side of the west column at the plastic hinge region. As shown in Fig. 4-38, some of the confined concrete core spalled leaving the transverse and longitudinal reinforcement unsupported. This allows some bucking in the column longitudinal reinforcement. The west column base was also damaged after 3.0 x Sylmar. As shown in Fig. 4-39, concrete spalled out from the west column base on the west side. Based on this damage, it was decided to stop the test at this level of loading. All of the previous observations for this specimen are summarized in Table 4-5.

4.3.3 Observed Response of Tall Specimen B2CT

Tall specimen B2CT was subjected to fourteen of Sylmar records (from the Northridge earthquake) with increasing amplitudes (Table 4-3). At the first loading of 0.10 x Sylmar, no significant cracks were observed while after the loading of 0.2 x Sylmar, minor flexural cracks started in east and west columns at plastic hinge zones (Figs. 4-40 and 4-41, respectively). The cracks were getting wider and larger as the loading increased; the number of cracks also increased and distributed over longer portions of the columns. The first shear cracks were observed at the loading of 1.25 x Sylmar where diagonal cracks appeared at the plastic hinge zones of both columns (Figs. 4-42 and 4-43, respectively). Minor shear cracks started in west and east beam-column joints after the loadings of 1.00 and 1.50 x Sylmar, respectively (Figs. 4-44 and 4-45, respectively). After the loading of 1.5 x Sylmar, the first concrete spalling occurred on the west and east sides of the east column and on the east side of the west column at the plastic hinge zones (Figs. 4-46 and 4-47, respectively). At this level of loading, no spalling was observed on the west side of the west column. The spalling on this side started after the loading of 2.0 x Sylmar (Fig. 4-48); at this level of loading, the column bases were considered intact (Fig. 4-49). After the loading of 2.0 x Sylmar, spalling increased on the west side of the east column till exposing the transverse reinforcement (Fig. 4-50). After the loading of 2.25 x Sylmar, spalling started to expose transverse reinforcement on the east side of the west column

(Fig. 4-51); at this level of loading, vertical cracks appeared on the west side of the west column base (Fig. 4-52). After the loading of 2.5 x Sylmar, the specimen leaned toward the north direction (Fig. 4-53). Spalling also increased till exposing the longitudinal reinforcement on all sides of columns except the west side of the west column (Figs. 4-54 and 4-55). The west column base was also damaged on the west side of the column. As shown in Fig. 4-56, concrete spalled out exposing one of the column transverse reinforcement. During the loading of 2.5 x Sylmar, minor spalling was observed at the bottom of the specimen cap-beam on the west side of the west column (Fig. 4-57). After the loading of 2.75 x Sylmar, concrete spalling increased in all previous zones without damaging the concrete core in the plastic hinge zones and without exposing any reinforcement on the west side of the west column (Figs. 4-58 and 4-59). Spalling also increased at the west column base exposing parts of the column longitudinal reinforcement while at the east column base, no spalling was observed (Figs. 4-60 and 4-61). After the loading of 2.75 x Sylmar, the specimen was leaning on the steel frame, so it was decided to stop the test at this level of loading. All of the previous observations for this specimen are summarized in Table 4-6.

4.4 Measured Response

The instrumentation layout was discussed in chapter 2. The majority of the instruments were for measuring reinforcement strains at critical locations while the rest of instruments were for measuring section curvatures and specimen accelerations and displacements. Following are the details of the measured data from each instrument.

4.4.1 Measured Strains

The numbers and positions of strain gages on longitudinal and transverse reinforcement for the three specimens are shown in Figs. 2-29 to 2-36. At each loading run, the strain history of each gage was recorded with the maximum reading limit of 0.04 strains. The maximum measured strains generated at each loading were tabulated and classified into four groups according to the position of the strain gages. The first and second groups were for the gages on the column longitudinal and transverse reinforcement, respectively. The third and fourth groups were for the gages on beam longitudinal and transverse reinforcement, respectively. All of these groups are shown in Tables 4-7 to 4-12 for specimens B2CS, in Tables 4-13 to 4-18 for specimen B2CM and in Tables 4-19 to 4-24 for specimen B2CT, respectively. From these tables, the bad gages of unreasonable maximum response could be easily discovered. The response of each gage to each loading could also be shown.

Another way to examine the strain gages response was as a function of time. For each gage in each specimen, the strain history was plotted versus the accumulated time of all loadings. The strain-time histories figures of all gages are shown in appendices A, B and C for short, medium and tall specimens, respectively. Using these figures, the behavior of each gage with loading could be examined. After studying B2CS figures, it was found that gages 9, 48 and 56 malfunctioned. Gages 9 and 48 were damaged during the last two loadings (Figs. A-3, A-15) while gage 56 was damaged during the last eight loadings (Fig. A-17). For B2CM, all the gages provided a good response throughout the loading history (Appendix B) except gages 7 and 33. Gage 7 became bad during the last two loadings (Fig. B-79) while gage 33 became bad during the last loading (Fig. B-87). The strains from gages 62 and 63 are not reliable because their response at specific loadings mismatched the seismic loading history (Fig. B-96). After studying B2CT figures, it was found that all gages responded to the loadings properly (Appendix C) expect gages 5, 7 and 51 which were damaged during the last two loadings (Figs. C-2, C-3 and Fig. C-16, respectively) and gage 98 which was not responding to the loading properly (Fig. C-31).

4.4.1.1 Measured Strains in Short Specimen, B2CS

Studying Tables 4-9 and 4-10 showed that column transverse reinforcement did not yield except at gages 65, 70, 75, and 83 where yielding started at the loadings of 2.75, 3.25, 2.50, and 2.125 x Sylmar, respectively. Gages 65 and 70 are located on the east side of the east column base and on the west side of the west column base, respectively (Fig. 2-39). Gages 75 and 83 are located on the east and west sides, respectively, of the east column at its plastic hinge zone (Fig. 2-39).

For column longitudinal reinforcement, yielding was mainly concentrated in the plastic hinge regions and in particular on the west side of the columns. This is shown in Tables 4-7 and 4-8 in which gages 18, 20, 26, 34, 42, and 44 (Fig. 2-38) in east column and gages 22, 24, 29, 30, 31, 32, 37, 38, and 39 (Fig. 2-38) in west column yielded at intermediate levels of loadings. The maximum-recorded tensile and compressive strains of longitudinal reinforcement were +0.0309 and -0.0192, respectively in gages 32 and 29 (Fig. 2-38) on the west and east sides of the west column, respectively. These levels of strains were almost 14 and 8.5 times the yield strain, respectively. At these levels of strains, the confined concrete was considered intact which indicated that the vertical ultimate strain of the confined concrete has not reached yet. The strain-time history of gages 29 and 32 is shown in Figs 4-62.

For the hinge dowels at the column-footing interface surface, yielding started during 1.40 x Sylmar on the east side of each column base at gages 5 and 7 (Fig. 2-38). At this level of loading, no spalling or significant cracking was noticed at this region. After the loading of 2.75 x Sylmar, the hinge dowels at gages 5 and 7 reached the maximum strains of + 0.02653 and + 0.03266. These strains were almost 12 and 13.5 times the yield strain, respectively. The strain-time history of these gages is also shown in Fig. 4-63. The strain profile along the hinge dowels in east and west column bases is shown in Fig. 4-64. It was decided to draw only the development of strains for the more critical dowels located on the west side of each column base since their tension increases with the dominant direction of the earthquake. As can be seen in Fig. 4-64, the hinge dowels in east and west column bases were well developed inside the specimen footing because the strain dropped dramatically and abruptly as the hinge dowels entered the footing. The maximum strains of hinge dowels at column-footing interface dropped by almost 91% and 92 % in east and west column bases, respectively after the distance of 0.3 times the development length inside the footing. Similarly, the hinge dowels inside the column bases were also developed. Fig. 4-64 also shows a drop in the dowel strain at the column-footing interface as the hinge dowel entered the column. At the maximum loading (3.25 x Sylmar), however, the hinge dowel in east column base showed poor development. This is shown in the dowels strain increase at 3.25 x Sylmar as the dowel enters the column base. This result could be useful for investigating the behavior of column bases.

For the beam longitudinal, no yielding was recorded. The maximum strain was +0.0019 in gage 57 on the bottom reinforcement close to the east beam-column joint (Fig. 2-38). For beam transverse reinforcement, no yielding was also recorded where the maximum strain was +0.00087 in gage 110 close to the west beam-column joint (Fig. 2-39). The strain-time history of gages 57 and 110 is shown in Fig. 4-65.

In beam-column joints, the transverse reinforcement did not show any yielding where the maximum strains were 0.00106 and 0.000686 in east and west beam-column joints, respectively (Tables 4-9 and 4-10). The strain profile of beam-column transverse reinforcement is also shown in Fig. 4-66. As can be seen in this figure, the maximum strain was almost at mid-height of the beam-column joints. This result helps to imagine the flow of forces inside the beam-column joints (Sec. 5-7). Similar to the transverse reinforcement, the strain profile of longitudinal reinforcement inside the beam-column joints is shown in Fig. 4-67. The column longitudinal reinforcement was well developed inside the beam-column joints because the beam-column interface strains dropped dramatically and abruptly after a distance of 0.20 times the total development length as the reinforcement entered the beam-column joint.

4.4.1.2 Measured Strains in Medium Specimen, B2CM

Studying Tables 4-15 and 4-16 showed that column transverse reinforcement did not yield during the loading runs. The maximum-recorded strain of transverse reinforcement was +0.0014 in gage 91 on the east side of the east column in the plastic hinge zone, and was +0.00084 in gage 90 on the west side of the west column in the plastic hinge zone (Fig. 2-35). The strain-time history of these gages is also shown in Fig. 4-68. For column longitudinal reinforcement, yielding was mainly concentrated at the plastic hinge zones and on both sides of each column. This is shown in Tables 4-13 and 4-14. In the east column, the maximum-recorded tensile and compressive strains were +0.04048 and –0.04023 in gages 40 and 37 on west and east sides, respectively. The strain-time history of these gages is also shown in Fig. 4-69. In the west column, the maximum-recorded tensile and compressive strains were +0.0403 and -0.0403 in gages 50 and 33 on west and east sides, respectively. The strain-time history of these gages is also shown in Fig. 4-70. At the location of gage 33, the column longitudinal reinforcement started to buckle after 3.0 x Sylmar (Fig. 4-38) leaving a little gap in front of the confined core. This is an indication that the confined concrete strength started to degrade at this level of strain and loading.

For the hinge dowels at the column-footing interface, yielding started at an early loading of 0.50 x Sylmar at gage 7 (Table 4-14a) on the east side of the west column base (the gages at the east column base were bad gages). At this level of loading, no spalling or significant cracking was noticed at this region. The strain profile along the hinge dowel on the west side of the west column base is shown in Fig. 4-71. As can be seen, the hinge dowel is well developed inside the column base. The maximum interface strain at 3.0 x Sylmar dropped by 88 % at the distance of 0.24 x the dowel development length.

For beam reinforcement, the longitudinal rebar yielded after 3.0 x Sylmar with the maximum strain of 0.00226 in gage 4 on the top reinforcement close to the west beam-column joint (Fig. 2-34), while the transverse reinforcement did not yield (Tables 4-17 and 4-18).

For beam-column joints, the transverse reinforcement did not yield where the maximum strain was 0.00052 in gage 97 in the east beam-column joint (Fig. 2-

35). The strain profile of transverse reinforcement inside the beam-column joints is shown in Fig. 4-72. The strain profile of longitudinal reinforcement through the beam-column joints is also shown in Fig. 4-73. As can be seen, although the longitudinal reinforcement reached high levels of strain at the beam-column interface, these strains dropped significantly as the reinforcement entered the beam-column joints. This is an indication that column longitudinal reinforcement was well developed inside the beam-column joints.

4.4.1.3 Measured Strains in Tall Specimen, B2CT

Studying Tables 4-21 and 4-22 showed that columns transverse reinforcement did not yield during the loading runs. The maximum-recorded strain for transverse reinforcement was +0.00135 in gage 94 on the east side of the west column in plastic hinge zone (Fig. 2-35). For column longitudinal reinforcement, yielding was mainly concentrated at plastic hinge zones and on both sides of each column. This is shown in Tables 4-19 and 4-20. In the east column, the maximum-recorded tensile and compressive strains were +0.04043 and –0.02461 in gages 38 and 29 on the west and east sides, respectively; these strains are almost 18 and 11 times the yield strain, respectively. The strain-time history of these gages is shown in Fig. 4-74. In the west column, the maximum-recorded tensile and compressive strains were +0.0404 and -0.0426 in gages 34 and 41 on west and east sides, respectively (Fig. 2-34). These strains are almost 18 and 19 times the yield strain, respectively. The strain-time history of these gages is shown in Fig. 4-75. In both columns, the maximum compressive strain in longitudinal reinforcement indicated the maximum vertical compressive strain at the periphery of the confined concrete core. This shows that the maximum vertical compressive strain in the confined concrete core in both columns was almost -0.0426 (gage 41 on east side of west column). It is important to note that at the maximum loading of 2.75 x Sylmar, the confined concrete was considered intact (Figs. 4-58 and 4-59) which indicated that the concrete ultimate vertical compressive strain has not reached. This confirms that the ultimate vertical strain of the confined concrete core could be more than –0.0426 strains.

For the hinge dowels (Fig. 2-34) at the column-footing interface, yielding started at an early loading of 0.25 x Sylmar at gage 8 (Table 4-20a) on the west side of the west column base. At this level of loading, no spalling or significant cracking was observed at this region. The maximum strains of hinge dowels at column-footing interface were 0.04409 and 0.04327 after 3.0 x Sylmar in gages 5 and 7 on the east sides of the east and west column bases, respectively. These strains are almost 20 and 19 times the yield strain, respectively. The strain-time history of these gages is also shown in Fig. 4-76. The strain profile along the hinge dowels on the east side of both column bases is shown in Fig. 4-77. As can be seen, the hinge dowels are well developed inside the column base because the strain dropped abruptly and dramatically as the hinge dowels entered the column base. The maximum interface strain at the maximum loading dropped by almost

96 % in both column bases after the distance of 0.24 x the dowels development length.

For the beam reinforcement (Tables 4-23 and 4-24), the longitudinal reinforcement yielded at three locations. The first yielding occurred after 1.0 x Sylmar in gage 65 on the bottom reinforcement in the east beam-column joint and the maximum strain in this gage was 0.0052 after 2.75 x Sylmar. The second yielding occurred after 1.25 x Sylmar in gage 67 on the bottom reinforcement in the west beam-column joint and the maximum strain in this gage was 0.00314 after 2.0 x Sylmar. The third yielding occurred after 2.0 x Sylmar in gage 61 on the bottom reinforcement near the east beam-column joint and the maximum strain in this gage was 0.00321 after 2.75 x Sylmar. For the beam transverse reinforcement, however, no yielding was measured where the maximum-recorded strain was 0.000767 after 2.25 x Sylmar in gage 111 on the west beam-column joint (Table 4-24).

For beam-column joints, the transverse reinforcement did not yield where the maximum strain was 0.00045 in gage 101 in the east beam-column joint (Fig. 2-35). The strain profile of transverse reinforcement inside the beam-column joints is shown in Fig. 4-78. As can bean seen, the location of extreme strains in transverse reinforcement is close to the quarter depth of the beam-column joint from the bottom. This result could be useful in knowing the flow of forces inside the beam-column joints (Sec. 5-7). The strain profile of longitudinal reinforcement through the beam-column joints is also shown in Fig. 4-79. (The west beam-column joint is not shown because all longitudinal reinforcement gages in this joint malfunctioned). As can be seen, although the longitudinal reinforcement reached high levels of strains at the beam-column interface, these strains dropped significantly as the reinforcement entered the beam-column joint. The maximum strain on longitudinal reinforcement at beam-column interface dropped by 56 % at the distance of 0.20 x the development length. This is an indication that column longitudinal reinforcement was well developed inside the beam-column joints.

4.4.2 Strain-Displacement Profile

The strain-displacement profile at a specific location of reinforcement is the relationship between the maximum strain generated at a specific loading and the maximum displacement that the specimen reached at the same loading. It is expected to generally have a direct increase in strain as the loading increases. If the reinforcement strain in not responding directly to the loading as the specimen displacement increases, the gage could be damaged or the bar where this gage at could experience some slippage. To investigate reinforcement slippage, strain-displacement profiles are plotted for the longitudinal reinforcement at beam-column and at column-footing interfaces.

4.4.2.1 Strain-Displacement Profile in B2CS

Figs. 4-80 and 4-81 show the strain-displacement profiles for the column longitudinal reinforcement at the beam-column interfaces (see Fig. 2-38).

Although the strains in this reinforcement at these locations were relatively high (maximum strain is almost 12 times the yield strain), no slippage was shown because the gages were responding properly to the loading as the specimen displacement increased (represented as a drift ratio). Figs. 4-82 and 4-83 show the strain-displacement profiles for the hinge dowels at the column-footing interfaces (see Fig. 2-38). For east column-footing interface, slippage started in gage 5 on the east side after 2.625 x Sylmar and at the drift level of 4.4 % (Fig. 4-82). At this slippage, the reinforcement strain reached almost 12 times its yield strain. For gage 6 on the west side of east column base, slippage started after 2.5 x Sylmar and at the drift level of 3.9 % (Fig. 4-82). At this slippage, the reinforcement strain reached almost 6 times its yield strain (Fig. 4-82). For west column-footing interface, slippage started at gage 7 on the east side after 2.625 x Sylmar and drift level of 4.4 % (Fig. 4-83). At this slippage, the reinforcement strain reached almost 15 times its yield strain. For gage 8 on the west side, slippage started after 2.375x Sylmar and drift ratio of 3.4 % (Fig. 4-83). At this slippage, the reinforcement strain reached almost 5 times its yield strain. It is important to note that slippage at hinge dowels were completely yielded.

4.4.2.2 Strain-Displacement Profile in B2CM

Figs. 4-84 to 4-86 show the strain-displacement profiles for the column longitudinal reinforcement at the beam-column interfaces (see Fig. 2-34). For the west beam-column interface, slippage started at gage 52 (Fig. 4-86) on the west side after 2.5 x Sylmar. At this slippage, the specimen reached the drift level of 6.6 % and the reinforcement strain at this gage reached almost 13 times its yield strain. For the east beam-column interface, slippage started at gage 47 (Fig. 4-85) on the east side of the column after 2.75 x Sylmar. At this slippage, the specimen reached the drift ratio of 8 % and the reinforcement strain at this gage reached almost 5 times its yield strain. Fig. 4-87 shows the strain-displacement profiles of the hinge dowels at west column base (Fig. 2-34). As can be seen in Fig. 4-87, slippage started at gage 8 on the west side after 2.75 x Sylmar and after the specimen reached the drift ratio of 8 %. At this slippage, the reinforcement strain at this gage reached almost 18 times the yield strain. For dowels on the east side of the west column base (gage 7), no slippage was recorded. For east column-footing interface, the two gages at this location were bad, so no behavior was concluded on this side.

4.4.2.3 Strain-Displacement Profile in B2CT

Figs. 4-88 to 4-90 show the strain-displacement profiles for the column longitudinal reinforcement at the beam-column interfaces (see Fig. 2-34). As shown in these figures, no slippage was seen at the east and west beam-column interfaces. Figs. 4-91 to 4-92 show the strain-displacement profiles of hinge dowels. For east column-footing interface, no slippage was recorded at the hinge dowels. However, for west column-footing interface, the hinge dowel at gage 8 experienced slippage after 1.25 x Sylmar. At this slippage, the specimen reached the drift ratio of 2.25 % and the hinge dowel reached almost 15 times its yield strain (Fig. 4-92).

4.4.3 Measured Accelerations and Displacements

Each specimen was provided with instruments for measuring displacements and accelerations in both in-plane and out-of-plane directions (Fig. 2-43 and 2-44). Displacements and accelerations are indirectly used to plot the load-displacement hystereses. In the load-displacement plot, the x-axis represents the specimen relative displacement, which is calculated by deducting the shake-table displacement from the specimen total displacement. The y-axis represents the specimen total resisting force, which is calculated by multiplying the specimen total acceleration by the dynamic mass. The equivalent dynamic mass of the specimen is the mass of the superstructure represented by the specimen cap-beam loaded with the attached lead buckets (Fig. 2-14) in addition to half of the weight of the specimen columns. The total weight of these loads is 74.5 k (332.7 kN) (section 2.4). The main purpose of load-displacement plots is to determine the strength and stiffness degradation of the specimen after successive loadings and to show the levels of ductility and damping that the specimen reached.

4.4.3.1 Short Specimen, B2CS

Figs. 4-93 to 4-109 show the load-displacement hystereses curves at each loading run for the short specimen B2CS. From these figures, the maximum resisting force and the corresponding lateral displacement at each loading run were determined as shown in Table 4-25. At 3.25 x Sylmar, the maximum lateral displacement was 2.27” (57 mm) and the corresponding resisting force was 65 kips (289 kN) while the maximum resisting force was 92 kips (409 kN) and the corresponding lateral displacement was 1.125” (28 mm). Table 4-26 was also developed from the load-displacement hystereses. Each hysetersis curve at each loading run was represented by an equivalent line using the linear curve fitting, then the chord stiffness is calculated as the slope of this line. From the specimen chord stiffness at each loading, the specimen corresponding frequencies were calculated. Table 4-26 shows a clear stiffness degradation after 1.75 x Sylmar.

The envelope of the maximum load and the corresponding displacement is shown in Fig. 4-110. This envelope is idealized by a bilinear curve (Fig. 4-111). The areas under both idealized and actual curves are the same. From the idealized curve, the points of yield and maximum displacements are determined as shown in Table 4-31. In this table, the specimen reached the displacement ductility of 4.0. At this point, the load degraded to 85 % of the maximum load.

In addition to the previous plots, the history of specimen displacement and the generated forces were plotted to show the change in lateral displacement and resisting force with time and to determine the increase in the residual displacement as the loading increased. Figs. 4-112 and 4-113 show the history of lateral displacement and resisting force, respectively under the seventeen loading runs. The residual displacement shown in Fig. 4-112 reached its maximum value of

0.745 inches toward the west direction, after the 3.25 x Sylmar loading. It is also shown in Fig. 4-113 that in most earthquake loadings, the resisting force did not increase as the loading level increased. This was caused by plastic hinging of the columns and by shifting of the specimen natural frequency within the content of the earthquake.

4.4.3.2 Medium Specimen, B2CM

For medium specimen B2CM, the load-displacement hysterses curves at each loading run are shown in Figs. 4-114 to 4-128. From these figures, the points of peak displacements and peak forces were calculated as shown in Table 4-27. At 3.0 x Sylmar, the maximum lateral displacement was 6.34” (159 mm) and the corresponding resisting force was 45 kips (200 KN) while the maximum resisting force was 49 kips (218 mm) and the corresponding lateral displacement was 5.5” (138 mm). Table 4-28 developed from the load-displacement hystereses shows the specimen chord stiffness and the corresponding frequency at each loading. Table 4-28 also shows a clear stiffness degradation after 0.5 x Sylmar.

The envelope of the maximum load and the corresponding displacement is shown in Fig. 4-129. This envelope is idealized by a bilinear curve (Fig. 4-130). The areas under both idealized and actual curves are the same. From the idealized curve, the points of yield and maximum displacements are determined as shown in Table 4-31. In this table, the specimen reached the displacement ductility of 6.0. At this point, the load had degraded to 85 % of the maximum.

In addition to the plots of load-displacement hystereses, the history of displacement and lateral forces were plotted to show the change in lateral displacement and resisting force with time and to determine the increase in the residual displacement as the loading increased. Figs. 4-131 and 4-132 show the history of lateral displacement and resisting force, respectively under the fifteen loading runs. The residual displacement reached a maximum value of 1.7” (43 mm), toward the west direction, after 3.0 x Sylmar.

4.4.3.3 Tall Specimen, B2CT

For tall specimen B2CT, the load-displacement hystereses curves at each loading are shown in Figs. 4-133 to 4-146. From these figures, the points of peak displacements and peak forces at each loading were calculated as shown in Table 4-29. At 2.75 x Sylmar, the maximum lateral displacement was 10.0” (250 mm) and the corresponding resisting force was 27.5 kips (122 KN) while the maximum resisting force was 33.23 kips (148 KN) and the corresponding lateral displacement was 7.5” (188 mm). Table 4-30 developed from the load-displacement hystereses shows the specimen chord stiffness and the corresponding frequency at each loading. Table 4-30 also shows a clear stiffness degradation after the loading of 0.2 x Sylmar.

The envelope of the maximum load and the corresponding displacement is shown in Fig. 4-147. This envelope is idealized by a bilinear curve (Fig. 4-148). The areas under both idealized and actual curves are the same. From the idealized curve, the points of yield and maximum displacements are determined as shown in Table 4-31. In this table, the tall specimen reached the displacement ductility of 8.0. At this point, the load had degraded to 85 % of the maximum.

In addition to the plots of load-displacement hystereses, the history of displacement and lateral forces were plotted to show the change in lateral displacement and resisting force with time and to determine the increase in the residual displacement as the loading increased. Figs. 4-149 and 4-150 show the history of lateral displacement and resisting force, respectively under the fourteen loading runs. The residual displacement reached its maximum value of 2.7 inches toward the west direction, after 3.0 x Sylmar.

4.4.4 Measured Curvature

For each specimen, the curvature instruments were installed in three locations: at the expected plastic hinge zones of each column, at each column base, and at each cap-beam maximum moment location. The way of calculating curvature using these instruments is shown in Fig. 2-40. From these measurements, the concrete surface strains can also be calculated. The level of curvature at each section is related to the yield curvature at the same section. For sections where yield curvature can not be easily calculated experimentally, the yield curvature is calculated analytically and added to each figure in the form of dashed lines.

4.4.4.1 Measured Curvatures in Specimen B2CS

For curvature in plastic hinge regions, Figs. 4-151 and 4-152 show the maximum curvatures at each loading for east and west columns, respectively. In these figures, a special sign convention was taken; the positive curvature was measured when the specimen reached its maximum displacement toward the west direction and vice versa. For the purpose of clarity, each figure was divided into two parts: one for the first eight loadings and the second part for the last loadings. It is shown in these figures that positive curvatures are relatively larger than the negative ones. This was because the major tendency of the Sylmar record was toward the west direction. The curvature profiles were also as predicted. This was shown in the direct relation between curvatures and both of maximum moments. For the east column (Fig. 4-151), yielding started in plastic hinge zone at 2” (50 mm) down the beam-column interface after 0.50 x Sylmar while after 1.75 x Sylmar, yielding covered a larger distance of 14” (350 mm) from the beam-column interface. For the west column (Fig. 4-152), yielding started in plastic hinge zone after 1.0 x Sylmar, at 2” (50 mm) down the beam-column interface while after 2.75 x Sylmar, the yielding covered a larger distance of 14” (350 mm) down the beam-column interface. This distance is the same as the column diameter and is called the plastic hinge region.

For column bases, Figs. 4-153 and 4-154 show the maximum curvatures generated at the seventeen seismic loadings for the east and west columns, respectively. At the east column base (Fig. 4-153), the maximum curvature was almost 1.5 times the maximum curvature at the column plastic hinge zone (Fig. 4-151). Similarly, the maximum curvature at the west column base (Fig. 4-154) was almost 2.0 times the maximum curvature at the column plastic hinge zone (Fig. 4-152). The high curvature values at column bases were an indication of the cross-section weakness, which allowed more rotation at the column bases. The yield curvature of the column-base section can be calculated experimentally. It is the curvature value corresponded to the loading at which the first yielding in the hinge dowels started. In Tables 4-7a and 4-8a, the hinge dowels on the east side of both column bases at column-footing interface (gages 5 and 7) started yielding at the loading of 1.40 x Sylmar. At this loading, the measured curvature at both east and west column bases was almost 0.002 rad/in. (0.08 rad/m). After this value of yield curvature, the plastic rotations started to form at each column base. At each loading, the plastic curvature can be calculated by subtracting the yield curvature value from the total curvature. Based on this, the column base rotations after yielding can be calculated by multiplying the plastic curvature with the measured-curvature depth at the column-footing interface (almost 4"(100 mm)). This ends up with the maximum rotations of 0.034 and 0.044 rad at the east and west column bases, respectively. It is important to note that these rotations are much less than the rotations required to close the hinge gap at the column bases (≈ 0.07 rad as a minimum). This assures that the hinge gap at each column base did not close during testing. This means that the failure on the west side of the west column base (Fig. 4-12) is referred to another mechanism. The high compression at the west column base in addition to the lack of confinement at the hinge gap could be the reason of the hinge failure on the west side of the west column. The detailed analysis interpreting this failure is discussed in chapter 5 (section 5.5.3.1).

For the cap-beam, Figs. 4-155 and 4-156 show the maximum curvatures as a function of the seventeen seismic loadings for the beam critical-sections on the east and west sides, respectively. The yield curvature of the beam cross-section is determined analytically (since it is hard to be determined experimentally) and is represented as a dashed line in the same plot. The beams were expected to experience curvatures lower than the yielding curvature. This is because the beam longitudinal reinforcement did not yield (Table 4-11). The beam curvatures at critical cross-sections on the west side, however, became higher than the analytically calculated yield curvature after 1.25 x Sylmar (Fig. 4-156). This does not mean yielding in the beam cross-section as it appears because the curvature after the yield limit does not increase as the loading increases. The reason of this disagreement between analytical and experimental curvatures could be because of the approximation in calculating the yield curvature.

4.4.4.2 Measured Curvatures in Specimen B2CM

For curvatures in plastic hinge zones, Figs. 4-157 and 4-158 show the maximum curvatures at each loading for east and west columns, respectively. For the purpose of clarity, each figure was divided into two parts: one for the first seven loadings and the second part for the last loadings. Unlike the short specimen, the tendency of the curvature toward the west side only occurred at high levels of loadings. The maximum curvature values were also higher than that in the short specimen. For example, after 3.0 x Sylmar, the maximum curvature of the west column was almost 2.25 times that in the short specimen. In east column, after 3.0 x Sylmar, the maximum curvature was almost 2.70 times that in the short specimen. Relating to the yield curvature (dashed lines in Figs. 4-157 and 4-158), the yielding covered the 14”(350 mm)-distance near to the column top (this distance is called the plastic hinge zone) in the east and west columns after 1.25 and 1.0 x Sylmar, respectively.

For columns bases, Figs. 4-159 and 4-160 show the maximum curvatures for the east and west columns, respectively. Compared with the short specimen, the values of the maximum curvature were much higher because of the higher specimen flexibility. For example, at east column base (Fig. 4-159), the maximum curvature after 3.0 x Sylmar was almost 2.0 times that in short specimen (Fig. 4-153). At west column base (Fig. 4-160), the maximum curvature after 3.0 x Sylmar was almost 2.4 times that in the short specimen (Fig. 4-154). Compared with curvatures in the plastic hinge zones of both medium columns, the base curvatures were also higher. For instance, after 3.0 x Sylmar, the maximum curvature at east column base was almost 1.50 times that at the plastic hinge zone of the same column (Fig. 4-157). For west column base (Fig. 4-160) and after 3.0 x Sylmar, the maximum curvature was almost 1.5 times that at plastic hinge zone of the same column (Fig. 4-158). The high curvature values at column bases were an indication of the gap and cross-section weakness, which allowed more rotation at the bases. The yield curvature of the column-base section can be calculated experimentally. It is the curvature corresponding to the loading at which the first yielding of the hinge dowel started. In Table 4-14a, the hinge dowel on the east side of the west column base at column footing interface (gage 7) started yielding at 0.5 x Sylmar. At this loading, the measure curvature at both east and west column bases was almost 0.00165 rad/in. (0.067 rad/m). After this value, plastic rotations started to form at each column base. At each loading, the plastic curvature can be calculated by subtracting the yield curvature value from the total curvature. Based on this, the base rotations after yielding can be easily calculated by multiplying the plastic curvature with the measured-curvature depth at the column bases (almost 4”(100 mm)). This ends up with the maximum rotations of 0.09 and 0.098 rad at the east and west column bases, respectively. It is important to note that these rotations are around the rotation required to close the hinge gap at the column bases (≈ 0.07 rad as a minimum). This shows a possibility of closing the hinge gap in east and west column bases during specimen testing.

For the cap beam, Figs. 4-161 and 4-162 show the maximum curvatures at each loading. The beam curvatures shown in these figures became smaller than that in the short specimen. For example, the maximum curvature on west side of the cap beam was almost 0.06 times that in the short specimen. This reduction in curvature was due to the reduction in columns to beam stiffness ratio as the column heights increased in the medium specimen. The yield curvature of the beam cross-section is determined analytically (since it is hard to be determined experimentally) and is represented as a dashed line in the same plot. As seen in Figs. 4-161 and 4-162, the beam curvatures at east and west sides are much less than the yield curvature. This is also shown in the beam longitudinal reinforcement, which did not yield during the maximum excitation (Table 4-17).

4.4.4.3 Measured Curvatures in Specimen B2CT

For curvatures in plastic hinge regions, Figs. 4-163 and 4-164 show the maximum curvatures at each loading for east and west columns, respectively. The curvatures on the west side of each column were relatively larger than that on the east side. Unlike the short columns, the tendency of the curvature toward the west side only occured at the higher levels of loadings (after 2.5 x Sylmar).

For columns bases, Figs. 4-165 and 4-166 show the maximum curvatures at east and west column bases, respectively. The values of the maximum curvatures were fairly close to that in the medium specimen. The yield curvature of the column-base section can be calculated experimentally. It is the curvature corresponding to the loading at which the first yielding of the hinge dowel started. In Tables 4-19a and 4-20a, the hinge dowels on the east side of east and west column bases at column footing interface (gages 5 and 7) started yielding at 0.5 x Sylmar. At this loading, the measured curvature was almost 0.0025 rad/in. (0.10 rad/m). After this value of yield curvature, plastic rotations started to form at each column base. At each loading, the plastic curvature can be calculated by subtracting the yield curvature value from the total curvature. Based on this, the base rotations after yielding can be calculated by multiplying the plastic curvature with the measured-curvature depth at the column bases (almost 4”(100 mm)). This ends up with the maximum plastic rotations of 0.088 and 0.096 rad at the east and west column bases, respectively. It is important to note that these rotations are around the rotation required to close the hinge gap at the column bases (≈ 0.07 rad as a minimum). This shows a possibility of closing the hinge gap in east and west column bases during specimen testing.

For cap beam, Figs. 4-167 and 4-168 show the maximum curvatures at beam critical sections on east and west sides, respectively. Similar to the medium specimen, the beam curvatures were far below the yield curvatures due to the reduction in column stiffness relative to the cap beam stiffness as the column height increases.

4.4.5 Out-Of-Plane Behavior

Each specimen was tested dynamically by shaking in its in-plane direction, which was considered the transverse direction of the overall bridge. In addition to the specimen in-plane response, some out-of-plane responses were expected, especially in the medium and tall specimens whose out-of-plane stability was highly critical. Additional accelerometers and potentiometers were installed to measure the out-of-plane resisting forces and displacements, respectively. Figs. 2-43 to 2-44 show the instrumentation layout for the three specimens For the short specimen B2CS, the average out-of-plane displacement was determined using one instrument attached to the bent-cap concrete (Fig. 2-43) while for specimens B2CM and B2CT (Fig. 2-44), the average out-of-plane displacement and rotation were determined using two instruments attached to the bent cap at 10' (3048 mm) apart. The out-of-plane acceleration was also measured using an additional accelerometer directed toward the north-south direction and fixed to the bent-cap concrete in each specimen.

4.4.5.1 Specimen B2CS

In this specimen, the out-of-plane displacement and resisting force histories were plotted to show the change in lateral responses as the loading increased and to determine the time and loadings at which the specimen leaned or became laterally unstable. Figs. 4-169 and 4-170 show the history of displacement and resisting forces, respectively. The lateral displacement was measured directly as the total out-of-plane displacements. The total resisting force was calculated indirectly after multiplying the specimen out-of-plane total acceleration by the specimen dynamic mass (section 4.4.3). From these figures, the maximum residual displacement was 0.08 inches toward the north direction and the maximum resisting force was 10 kips (44.5 kN) after the loading of 3.25 x Sylmar. These results are useful in determining the maximum out-of-plane moments on column bases. They can be calculated as the maximum resisting force times the distance from the dynamic mass center to column-footing interface. This ends up with 280 k.in (31 kN.m) maximum out-of-plane moment on each column base. The out-of-plane P-delta effect can also be added by multiplying the maximum out-of-plane displacement times the specimen weight after adding a reasonable impact factor (25 %). This ends up with an additional out-of-plane moment of 7.45 k.in (0.825 kN.m) on each column base. It is important to note that these out-of-plane moments on each column base were significant since they are very close to the column-base flexural capacity. It is also important to note that this out-of-plane moment works in the phase with the maximum in-plane actions.

4.4.5.2 Specimen B2CM

Similar to the short specimen, Figs. 4-171 and 4-172 show the history of out-of-plane displacements and resisting forces, respectively. From these figures, the maximum residual displacements were 1.18” (30 mm) and 3.27” (82 mm) toward the north direction after the loadings of 2.5 and 2.75 times Sylmar, respectively. The maximum recorded resisting force was 4.0 kips (17.8 kN) at the loading of 3.0 x Sylmar. These results are useful in determining the maximum out-of-plane moments on column bases. The method used in short specimen for calculating out-of-plane base moments can also be used in this specimen but not after the loading of 2.75 x Sylmar since after this loading the specimen leaned out-of-plane and rested on the steel frame (Fig. 4-35). During 2.75 x Sylmar, the out-of-plane displacement, corresponding to the maximum in-plane accelerations, was 0.375” (9 mm) and the corresponding out-of-plane resisting force was 0.75 kips (3.35 kN). This caused a total out-of plane moment of 49 k.in (5.45 kN.m) on each column base. This moment works in the same phase with the in-plane moments acting at the specimen bases.

4.4.5.3 Specimen B2CT

Figs. 4-173 and 4-174 show the history of out-of-plane displacements and resisting forces, respectively. From these figures, the maximum residual displacements were 1.45” (36 mm) and 7.8” (195 mm) toward the north direction at the loadings of 2.25 and 2.5 x Sylmar, respectively. The maximum recorded resisting force was 5 kips (22.25 kN) at the loading of 2.75 x Sylmar. These results are useful in determining the maximum out-of-plane moments on column bases. The method used in short specimen for calculating out-of-plane base moments can also be used in this specimen but not after the loading of 2.5 x Sylmar since after this loading the specimen leaned out-of-plane and rested on the steel frame (Fig. 4-53). During 2.5 x Sylmar, the out-of-plane displacement corresponding to the specimen maximum in-plane accelerations was 0.75” (19 mm) and the corresponding out-of-plane resisting force was 2.4 kips (10.8 kN). This caused a total out-of plane moment of 172 k.in (19 kN.m) on each column base. This moment is significant compared with the flexural capacity of the column bases, so it should be considered when analyzing the column bases.

4.4.6 Measured Behavior of Column Bases

The details of hinge keys in column bases for the three specimens were discussed in chapter 2. At each column base, the hinge key was formed by reducing the column cross-section by 29 % to 10” (250 mm). This reduced cross-section had a thickness of 0.5” (13 mm), and is called the hinge gap. Closing this hinge gap during specimen testing is not desirable since it can create complicated modes of failure. To investigate whether the hinge gap closed during testing, the readings of the vertical instruments (Novotechnicks instruments, Figs. 2-41 and 2-42) at the column bases were checked as the loading increased. Using these readings, the value of gap compression at each column base was calculated. It was decided to investigate the hinge gap closure on the west side of the west column base since damage in this region for each specimen (as shown in Figs. 4-12, 4-39 and 4-60, for short, medium, and tall specimens, respectively) could be the result of the hinge gap closure. Fig. 4-175 shows the compression of the gap end on the west side of the west column base in each specimen as a function of the increase in loading (represented by the increases in specimen displacement). Fig. 4-175 shows a direct relation between the two variables, which indicated that there was enough room for the vertical instrument to get compressed freely. This result confirms that hinge gap did not close during the testing of the three specimens. The failure occurred on the west side of the west column base in each specimen could be referred to the lack of the hinge confinement in addition to the high compression in the west column base (section 5.5.3.1).

4.4.7 Sliding at Column Bases

As observed in the tall and medium specimens, the column base sliding was not significant whereas in the short specimen the column base sliding was evident at the east column base (Fig. 4-13) where the level of axial force was reduced as a result of the seismic overturning moment. The measured relationships between the shear forces transferred at the specimen column bases and the corresponding sliding displacements can show the actual shear-friction mechanism at column bases. This can help in modeling this kind of behavior. Sliding at each column base was measured by a Novotechnick instrument attached at each column base (Figs. 2-41 and 2-42), whereas the shear force carried by each column was not directly calculated. Since the specimen structure is indeterminate, the total seismic force is approximately distributed between the two columns from the structural equilibrium after forming the column plastic hinges. The flexural capacity of the column top and bottom sections were calculated analytically, and the corresponding shear and axial forces carried by each column were calculated from equilibrium (Table 5-4). Figs. 4-176, 4-177 and 4-178 show the shear-slippage envelopes calculated for the short, medium and tall specimens, respectively. Since the flexural behavior was dominant in the tall and medium specimens, the column base sliding was too small (0.2" (5 mm) for medium specimen and 0.1" (3 mm) for tall specimen). The shear-sliding hysteretic loops were also stable (no strength degradation). For the short specimen (Fig. 4-176), however, the shear demand was so high that it caused noticeable sliding at the east column base (0.55" (14 mm)). The residual displacement of this sliding is also shown in Fig. 4-13. As shown in Fig. 4-176a, the shear-sliding resistance was increasing at the east column base till the sliding displacement reaches 0.25" (6 mm). After this displacement, the shear strength started to degrade. The strength degradation after exceeding this displacement could be the result of destroying the aggregate interlocking at the column-footing interface (see section 5.5.3.1 for more analysis details). At the west column base (Fig. 4-176b), the behavior was different. Although the base sliding was small (0.1" (3 mm)), there was clear strength degradation. This reduction in shear strength could be due to the concrete failure on the west side of the west column base after the last loading run (Fig. 4-12) as a result of the confinement shortage at the column base. The analytical details interpreting this failure are shown in chapter 5, section 5.5.3.1.

CHAPTER 5

SPECIMEN MODELING AND ANALYTICAL RESULTS

5.1 Introduction

This chapter shows how experimental results can be predicted analytically. Two analytical models were used to analyze the three specimens statically and dynamically. The first model was the lumped plasticity model in which concentrated flexural and shear springs were used to model the inelastic behavior at the critical column cross-sections. This model was used to perform the push-over analysis for each specimen to predict the specimen force and displacement capacities. It was also used for dynamic analysis. In the dynamic analysis, each specimen was subjected to seismic loadings and the seismic hysteretic loops were predicted using stiffness and strength degradation factors.

The second analytical model was a strut-and-tie model in which the flow of forces inside each specimen body was simulated as a combination of concrete struts and steel ties. This model helped to understand the experimental results, especially in the D-regions (discontinuity region) of each specimen (beam-column joints, column plastic hinges and column hinge bases). It also helped to determine the maximum lateral capacity of each specimen.

In both analytical models, material properties for both concrete and steel were modified to account for the dynamic loading effect.

5.2 Strain Rate Effect

To analyze column and beam cross-sections, the actual concrete and steel properties had to be determined. To get these properties, concrete cylinders and steel samples were taken from each specimen. The concrete cylinders were tested at 7 days and 28 days, and on the day of test (Sec. 3-5). The results shown in Tables 3-1 and 3-2 were from static-loadings tests (low strain-rate loadings), whereas, in reality each specimen was tested dynamically causing high rates of strains for both concrete and steel. The way of calculating the effect of dynamic loading on the concrete and steel properties was investigated in a study by Shrikrishna and Shah[13]. Three logarithmic equations were adopted for determining the effect of strain rate. Equations 5.1 and 5.2 were used to determine the increase in steel yield strength (α_{Steel}) as a result of the strain rate effect.

$$\alpha_{Steel}=0.0124\ \ln(\dot{\varepsilon})+0.9632 \qquad \text{for fy = 45 ksi} \qquad (5.1)$$

and

$$\alpha_{Steel}=0.0328\ \ln(\dot{\varepsilon})+0.9873 \qquad \text{for fy = 75 ksi} \qquad (5.2)$$

where $\dot{\varepsilon}$ is the maximum strain rate in the reinforcement.

Equation 5.3 was for determining the increase in concrete compressive strength ($\alpha_{Concrete}$) as a result of the strain rate effect.

$$\alpha_{Concrete}=0.0222\ \ln(\dot{\varepsilon})+0.9973 \qquad (5.3)$$

where $\varepsilon^{\bullet}$ is the maximum strain rate in the concrete. The strain rate was determined by Shrikrishna and Shah from the curvature rate of critical sections by multiplying the curvature rate times the distance from the section neutral axis to the each cross-section layer[13]. In the current research, the strain rate was determined directly from the gage strain history generated in the steel bars of the column and beam critical sections. Figs. 5-1 and 5-2 show the locations of the strain gages chosen to determine the strain rate effect on steel and concrete strengths in the three specimens. Since the seismic loading had a dominant direction, there were sides in the specimen where either tension or compression was dominant. On the side where tension was dominant, the strain gages were chosen to calculate the strain rate effect of the steel, while on the sides where compression is dominant the strain gages were chosen to calculate the strain rate effect on concrete strength. For example, in the short specimen B2CS (Fig. 5-1), gages 26 and 28, and gages 30 and 32 were chosen to determine the strain rate effect on the yield strength of column longitudinal reinforcement at critical sections of east and west columns, respectively. Similarly, gages 25 and 27, and gages 29 and 31 were chosen to determine the strain rate effect on the concrete compressive strengths at critical sections of east and west columns, respectively. For column bases, gages 5 and 7 were chosen to determine the strain rate effect on the yield strength of hinge dowels at east and west column bases, respectively. Gages 6 and 8 were chosen to determine the strain rate effect on the concrete compressive strength at east and west column bases, respectively. For the cap beam, gage 57 was chosen to determine the strain rate effect on the yield strength of the beam longitudinal reinforcement while gage 58 was used for the compression strength factor at the beam critical section. For the medium and tall specimens, the strain gages for calculating the strain rate effect were chosen in the same manner (Fig. 5-2).

The process of calculating the strain rate effect at critical locations is summarized in Tables 5-1, 5-2 and 5-3 for short, medium and tall specimens, respectively. The maximum strain of each gage at critical locations was taken just before yielding since the effect of strain rate diminishes after yielding[2]. To get the strain-rate upper bound effect, the maximum value of the strain rate history of each gage was taken. Perfect bond was assumed between the compression bars and the concrete. Therefore, the concrete strain rate was taken as equal to the reinforcement strain rate. The increase in steel yield and concrete strengths was calculated in the last column of each table. These values were used for updating the moment-curvature analyses for the critical sections in the three specimens as shown in the next section.

5.3 Moment-Curvature (M-φ) Relationships

For each specimen, there are three critical sections: beam-joint interface, column-joint interface and column-footing interface. To analyze the critical sections, a computer program, RCMC was used that had the ability to model the realistic properties of concrete and steel in each section. The strain profile through the cross sections was assumed linear in this program (Bernoulli hypothesis).

5.3.1 Tall Specimen, B2CT

Material properties of tall-specimen columns and beam were shown in Sec. 3-5. These properties with the effect of strain rate (Sec. 5-2) are used as an input for the RCMC program. The values shown in the last columns of Tables 5-3a and 5-3b were used to account for the strain rate effect on the steel and concrete strengths, respectively for the column and beam cross-sections. The analysis results of this program are shown in Figs. 5-3 to 5-6. The S.R.E. in the figures stands for the Strain Rate Effect and indicates that the analysis included the effect on the material properties. The idealized curves represented by dashed lines were determined by choosing the best bilinear curve that can represent the actual M-φ curve without any significant difference in the area under both curves. The idealized curves for beam section (Fig. 5-3) are approximately taken as elastic-fully plastic since the accuracy in modeling the post-yielding stage for this section was not needed. This was because yielding is only expected at the column sections. For the column sections (Figs. 5-4 –5-6), however, the idealized curves were taken as elastic-linearly plastic for representing the actual post-yielding stage.

For the tall-specimen beam (Fig. 5-3), the preliminary analysis indicated that the level of axial force on the beam section increased from 0.0 (0.0 KN) to 20 k (89 KN) as the specimen lateral seismic demand increased from 0.0 to the level of yielding for the specimen columns. As can be seen in Figs. 5-3-a and 5-3-b, the effect of changing the beam axial load on either the section capacity or the ductility is insignificant whereas the strain rate effect has a large impact (about 25% increase) on the section capacity for both levels of axial forces. For the tall-specimen columns (Fig. 5-4), the preliminary analysis shows a difference in the level of axial forces between the left and right columns (from 4.5k (20 KN) to 70k (311 KN)) as the specimen columns reach their yielding capacity. This difference creates a significant increase in the section yielding capacity (almost 17 %) between the left and right column sections (Figs. 5-4-a and 5-4-b). It also creates a significant decrease in the section ductility (about 15 % decrease in the ultimate curvature). The effect of strain rate also creates an increase in the column yielding moment by about 17 % and 20 % for the left and right columns, respectively. For the tall-column bases (Figs. 5-5-a and 5-5-b), the same change in column axial forces also creates an increase of about 50 % in the bases yielding moment. The strain rate effect also added about 15 % and 25 % to the original yielding moment of the left and right column bases, respectively.

For simpler and easier analysis, the level of axial forces in right and left columns was taken as the average of the two column axial load levels. This reduces the analysis effort where two sections only are to be analyzed: the column top and base hinge cross sections. Figs. 5-6a and 5-6b show the new M-φ diagrams for the column top and base-hinge, respectively after using the average axial load of 37.25 k (166 KN).

5.3.2 Medium Specimen, B2CM

The analysis results of RCMC program are shown in Figs. 5-7 to 5-10. For middle-specimen beam (Fig. 5-7), the preliminary analysis shows that the level of axial force for the beam section increased from 0.0 to 28 k (125 KN) as the specimen lateral seismic demand increased from 0.0 to the level of yielding for the specimen columns. As can be seen in Figs. 5-7a and 5-7b, the effect of changing the beam axial load on the either the section capacity and ductility is insignificant whereas the strain rate effect has a large impact (about 21% increase) on the section capacity for both levels of axial forces. For the middle-specimen columns (Fig. 5-8), the preliminary analysis shows a difference in the level of axial forces between the left and right columns (from 2.5k (11 KN) to 72k (320 KN)) as the specimen columns reach their yielding capacity. This difference creates a significant increase in the moment capacity (almost 17 %) between the left and right column sections (Figs. 5-8-a and 5-8-b). It also creates a significant decrease in the section ductility (about 13 % decrease in the ultimate curvature). The effect of strain rate also creates an increase in the column yielding moment by almost 17 % and 20 % for the left and right columns, respectively. For the middle-column bases (Figs. 5-9-a and 5-9-b), the same change in the column axial forces also creates an increase of about 60 % in the base yielding moment. The strain rate effect also added about 14 % and 23 % to the original yielding moment of the left and right column bases, respectively.

For simpler and easier analysis, the level of axial forces in right and left columns was taken as the average of the two column axial load levels. This reduces the analysis effort where two sections only are to be analyzed: the column top and base hinge cross sections. Figs. 5-10a and 5-10b show the new M-φ diagrams for the column top and base-hinge, respectively after using the average axial load of 37.25 k (166 KN).

5.3.3 Short Specimen, B2CS

The analysis results of the RCMC program are shown in Figs. 5-11 to 5-14. For short-specimen beam (Fig. 5-11), the preliminary analysis shows that the level of axial force on the beam section increased from 0.0 to 50 k (222 KN) as the specimen lateral seismic force increased from 0.0 to the level of yielding for the specimen columns. As can be seen in Figs. 5-11a and 5-11b, the effect of changing the beam axial load on either the section capacity or the ductility is insignificant whereas the strain rate effect has a large impact (about 24% increase) on the section capacity. For the short-specimen columns (Fig. 5-12), the preliminary analysis shows a difference in the level of axial forces between the left and right columns (from -1k (-4.45 KN) to 76k (338 KN)) as the specimen columns reach their yielding capacity. This difference creates a significant increase in the column yielding moment (about 18 %) between the left and right column sections (Figs. 5-

12a and 5-12b). It also creates a significant decrease in the section ductility (about 12 % decrease in the ultimate curvature). The effect of strain rate also creates an increase in the moment capacity by about 18 % and 23 % for the left and right columns, respectively. For the short-column bases (Figs. 5-13a and 5-13b), the same change in the column axial forces also creates an increase of about 70 % in the bases yielding moment. The strain rate effect also added about 14 % and 23 % to the original yielding moment of the left and right column bases, respectively.

For simpler and easier analysis, the level of axial forces in right and left columns was taken as the average of the two column axial load levels. This reduces the analysis effort where two sections only are to be analyzed: the column top and base hinge cross sections. Figs. 5-14a and 5-14b show the new M-φ diagrams for the column top and base-hinge, respectively after using the average axial load of 37.25 k (166 KN).

5.4 Lumped Plasticity Model

Although this model is relatively simple, it is powerful and reliable for predicting the seismic responses for the specimens with flexural-dominated failure[11, 14]. In this model, the plastic hinge properties distributed through the plastic hinge regions of each column are concentrated in zero-length plastic hinges (Fig. 5-15). The required properties of these hinges are the moment-rotation relationships, which can be approximately calculated using the beam theory (e.g., the conjugate beam method).

Fig. 5-16 schematically shows the steps of calculating the hinge properties at the column top and base. The first step (Fig. 5-16a) shows the formation of the first hinge at the column base since it has the lowest capacity (moment capacity is intentionally reduced at each column base to create the two-way hinge). At this step, the moments at the column top and base are assumed to be equal for the sake of simplicity. The column base can be initially assumed fixed. The experimental results also supported this assumption. As mentioned in section 4.4.4, the curvatures and the corresponding rotations measured at the column hinges before reaching the yielding capacity were negligible. Based on this, the rotation from this step is only for the column top ($\Delta\theta_1$). The second step (Fig. 5-16b) shows the formation of the second plastic hinge at the column top. The additional moment required for forming this hinge is ΔM at the column top and the corresponding additional rotation is $\Delta\theta_2$. At this step, the total rotation at the column top is $\Delta\theta_1 + \Delta\theta_2$. In Fig. 5-16, the EI used for the column top and bottom sections is taken as the initial slope (neglecting the uncracked stiffness) of the M-φ diagrams of these sections.

Fig. 5-17 shows the moment-rotation relationships for the plastic hinges at top and bottom of each column. As shown in this figure, the column base is modeled as a fixed support that rotates only when it reaches its yielding capacity and the column top is modeled as a rigid joint that rotates elastically and plastically according to its moment demand. The ultimate rotation shown in this figure is obtained after determining the plastic rotation for each plastic hinge, $\Delta\theta_p$ (Sec. 2.6.2).

5.4.1 Reinforcement-Slippage Deformations

Reinforcement slippage occurs at connections interface (joint-column and column-footing connections) due to the tensile strains generated in the reinforcement development length. The way of calculating slippage rotation at connections interface at yield and ultimate moments is illustrated in reference 15. The method used in this reference was followed except that the rotational slippage at the column base (Fig. 5-17a) was doubled. The reason for this is that the reinforcement subjected to slippage at the column base (the hinge dowels) is surrounded by a large piece of uncracked concrete. This makes the column base and footing as two parts pushing away from each other, which indicates that the concentration of strain at the interface can occur from both column base and footings sides. However, at the column plastic hinge region (Fig. 5-17b) after reinforcement yielding, cracks are distributed widely through this region, which makes the strain distributed throughout the column instead of just at the interface.

Reinforcement slippage can be modeled by adding the slippage rotation at yield and ultimate moments to the yield and ultimate rotations of each plastic hinge. This is shown in Fig. 5-18 in which the new M-θ diagram after reinforcement slippage is represented by dashed lines. The plastic hinge at the column top (Fig. 5-18 a) experiences some elastic rotation (θ_y) before it reaches its yielding capacity. This is because the column top joint can rotate. The plastic hinge at column bottom (Fig. 5-18 b) is assumed to only rotate after the base hinge reaches its yielding capacity. This is because the column-footing connection is essentially fixed (θ_y= 0) for the purpose of the analysis.

5.4.2 Shear Deformations

Shear deformations are significant in short, deep concrete members whereas for slender members, the effect of shear on deflection can be neglected. Shear deformations can be calculated for uncracked concrete members by using the theory of elasticity. For cracked members, however, calculating shear deformations is complicated and needs another mechanism to be formulated. For cracked concrete members under high shear forces, the truss mechanism (strut-and-tie-model) is the most reliable model that can predict the shear behavior. Using the truss mechanism, the equivalent shear stiffness for cracked members with rectangular cross-sections was derived by Park and Paulay[16]. For concrete members with circular cross-sections (specimen columns), the same methodology used in the previous study[16] can be followed to derive new shear stiffness. Fig. 5-19a shows a part of a circular column with height d and diameter d. The column is subjected to shear force V_s and the resulting shear deformation is Δ_V. The shear force, V_s is assumed equal to the total shear force as the concrete shear capacity, V_c is neglected. From the geometry shown in Fig. 5-19a, the total shear deformation, Δ_V, is equation 5.4.

$$\Delta_V = \Delta_s + \sqrt{2}\,\Delta_c \tag{5.4}$$

where Δ_s is the steel deformation and Δ_c is the inclined concrete strut deformation. Assume the column hoops or spirals take an elliptical shape after deformation (Fig. 5-19b). The new ellipse perimeter can be taken as π times the average ellipse diameter= $\pi\,(d + (d + \Delta_s))/2$ and the original (before deformation) ellipse perimeter is $\pi\,(d)$. The change of transverse reinforcement shape creates a reinforcement strain, ε_s, of $\{\pi\,(d + (d + \Delta_s))/2 - \pi\,(d)\}/\,\pi\,(d)$, that simplifies to equation 5.5.

$$\varepsilon_s = f_s / E_s = \Delta_s / 2d \tag{5.5}$$

Since the column part at plastic hinge zone is subjected to shear and moment, the crack length required to mobilizing the column spirals stops in the column compression zone (Fig. 5-19c). The relation between the shear force, Vs and the stress in transverse reinforcement can be represented by equation 5.6[17]

$$V_s = \pi\, A_{sp}\, f_s\, (D\text{-}c\text{-}cover) / 2 \times S \tag{5.6}$$ [17]

where c is the neutral axis depth to the extreme compression fiber, S is the transverse reinforcement spacing, D is the total column diameter, A_{sp} is the cross-sectional area of the transverse reinforcement and f_s is the tensile stress generated in the transverse reinforcement. This equation is simplified to equation 5.7 if $d \approx$ D-cover, $c \approx 0.25\, d$.

$$V_s = 1.178\, A_{sp}\, f_s\, d / S \tag{5.7}$$

Using equations 5.5 and 5.7, the transverse reinforcement deformation is simplified to equation 5.8.

$$\Delta_s = 1.698\ V_s \text{ x } S / A_{sp} \text{ x } E_S \quad (5.8)$$

For the 45º inclined compressive strut of length of d √2 and axial deformation of Δ_c (Fig. 5-19a), the axial strain can be described by equation 5.9.

$$\varepsilon_c = \Delta_c / d\sqrt{2} \quad (5.9)$$

This strain is also equal to σ_c / E_C where σ_c is the stress in the inclined strut (strut force, C/strut area, A) and E_C is the concrete young's modulus. Based on this, equation 5.9 can be written as in equation 5.10.

$$\varepsilon_c = \Delta_c / d\sqrt{2} = \sigma_c / E_C = C/A_{st}\ E_C \quad (5.10)$$

Fig. 5-19d shows how the inclined strut cross-sectional area, A_{st} is calculated. It is very difficult to determine the A_{st} directly. To calculate A_{st}, it is necessary to determine a portion of the strut volume (the hatched part) with a known length. Since the length of this volume is known (d /√2) as shown in Fig. 5-19d, the cross-sectional area of the strut can be determined. This is valid for a strut angle of 45˚. The total volume of the column portion being considered is $\pi\ d^3 /4$. From this volume, the 4 volumes outside the strut-hatched part are subtracted. Each part of the 4 volumes has 1/8 of the total volume. Therefore, the remaining strut volume is $\pi\ d^3 /8$. Since the length of the volume is d/√2, the cross-sectional area is $(\pi\ d^3 /8)/ (d\sqrt{2}/2) = \sqrt{2}\ d^2 /8$. Substituting in (5.10),

$$\Delta_c = 8\sqrt{2}\ V_s / \pi\ d \text{ x } E_c \quad (5.11)$$

Substituting equations 5.7 and 5.10 in 5.4 results in

$$V_s = (E_s\ \pi\ d\ \rho_s) \text{ x } \Delta_v\ / (6.8\ \pi\ + 16\ n\ \rho_s) \quad (5.12)$$

Based on the previous equation, the shear stiffness of the part of the column with the length of d and the diameter of d is calculated as

$$E_s \pi d \rho_s / (6.8 \pi + 16 n \rho_s) \tag{5.13}$$

From the shear stiffness, the effective shear area, A_{sh} of this part of column is calculated as

$$2.5 \pi n d^2 \rho_s / (6.8 \pi + 16 n \rho_s) \tag{5.14}$$

To apply this result on the actual columns, the calculated shear area by truss mechanism is only for the parts of the columns where shear cracks are intense (e.g., the plastic hinge zones). For other parts of columns where shear cracks are minimal, it is advisable to use the shear area calculated by the elasticity theory, which is 0.9 the cross-sectional area for the circular members (this is because flexural spalling in circular cross sections does not represent a significant area). From experimental results for the three specimens, it was found that in the specimen columns, shear cracks were mainly concentrated at the column top through a distance of 2 times the column diameter (Figs. 5-20a and 5-20b). Using these results, the equivalent shear area of the entire column can be calculated (Figs. 5-20a and 5-20b). The total shear deformation of the entire column is the summation of the shear deformations of each column part. For the tall and middle specimen columns (Fig. 5-20a) and short specimen columns (Fig. 5-20b), the total shear deformation is given in equations 5.15 and 5.16.

$$\Delta_{sh} = V_s L_1/GA_1 + V_s L_2/GA_2 = Vs (L_1 A_2 + L_2 A_1)/GA_1A_2 \tag{5.15}$$

$$\Delta_{sh} = V_s L_{total} / GA_{equivalent.} \quad (5.16)$$

where $A_{equivalent} = L_{total} A_1 A_2 / (L_1 A_2 + L_2 A_1)$ (5.17)

It is important to note the shear area, $A_{equivalent}$ is used to calculate the maximum shear deformation at the maximum column response shown by intensive flexural and shear cracks at the plastic hinge regions. Computer programs such as SAP2000[18] and RAM Perform[19] use this shear area, $A_{equivalent}$ as an input for calculating the maximum shear deformations. To verify the previous method for calculating the shear deformation, additional instruments were to be installed on the test specimens to measure the shear deformations. Since these instruments were not provided in this study as a result of the limited number of channels, the shear deformations using the derived shear area, $A_{equivalent}$ were calculated for other columns (9S1 and 9S2) in the previous study[3]. These columns, 9S1 and 9S2 have the aspect ratio of 1.5. Both columns have the diameter and height of 16" (400 mm) and 48" (1200 mm), respectively. Based on these proportions, the $A_{equivalent}$ was assumed to be for the whole column height. The strain rate effect was assumed 25% to account for the increase in concrete strength, f'_c, during the seismic loading. This increased the concrete shear modulus, G, by 12 %. Substituting in the derived shear area formula, the shear area was calculated as 4.8 in^2 (3000 mm^2) for both columns. Under the maximum shear forces of 85 k (348 kN) and 94 k (418 kN) for columns 9S1 and 9S2, respectively, the corresponding shear deformations were calculated as 0.438" (11 mm) and 0.483" (12 mm), respectively. These values for are 0.99 and 1.09 the corresponding experimental shear deformations for columns 9S1 and 9S2 respectively[3]. This assures that the use of the derived shear area in predicting the seismic shear deformations is reliable.

5.5 Push-Over Analysis

The push-over analysis is a nonlinear static analysis in which the specimen is pushed laterally by incremental lateral forces till the specimen fails. This analysis can predict the peak seismic demands (peak seismic forces and displacements) for each specimen; and it can show the type of failure and the locations where failure starts. This helps to identify the critical elements and joints in each specimen, which in turn helps to determine the cause of failure and the how to control it. To perform this analysis on the three specimens, three computer programs (SAP2000, RAM Perform and W-Frame[20]) were used. The analytical model used in these programs was the Lumped Plasticity Model (see Section 5-4). A comparison between these programs was made to evaluate each program and adopt the best one for this type of analysis.

5.5.1 Push-Over Analysis using SAP2000 Program

In this program, the inelastic behavior is modeled by M-θ plastic hinges at critical sections. The M-θ relationship for each plastic hinge was calculated as in Sec. 5-4. The effects of shear and slippage deformations (Sec. 5-4.1 and Sec. 5.4.2) were also included. The analysis results of this program are shown in Figs.

5-21, 5-22 and 5-23 for the tall, middle and short specimens, respectively. Despite the simplicity in specimen modeling, the predicted results showed good correlation with the experimental results. For the tall specimen B2CT (Fig. 5-21), the push-over analysis predicted about 0.94 of the seismic peak capacity and about 1.0 of the peak seismic displacement that the specimen reached before it leaned in the transverse direction (section 4.3.3). After specimen leaning (section 4.3.3), the deterioration at the specimen bases created some stiffness degradation causing larger displacement (Fig. 5-21). This specimen situation could not be modeled in the SAP2000 Program. This caused the predicted displacement to be about 12% less than the actual maximum displacement after the specimen leaned (Fig. 5-21). A good correlation between the analytical and experimental results was achieved after including the effect of column geometrical non-linearity (P-δ effect, which is calculated internally by SAP2000).

For the middle specimen B2CM (Fig. 5-22), the push-over analysis predicted the entire peak seismic capacity and displacement that the specimen reached before it leaned in the transverse direction (section 4.3.2). After specimen leaning (section 4.3.2), the specimen experienced larger displacement as a result of the strength deterioration at the specimen bases (Fig. 5-22). For the short specimen B2CS (Fig. 5-23), the push-over analysis overestimated the maximum seismic response. The predicted displacement was 57.5 % higher than the actual displacement and the predicted maximum force was 6 % higher than the actual maximum force (at the same displacement). This disagreement showed some shortcomings in modeling the behavior of short specimen B2CS since it underwent significant slippage at its column bases in addition to the overall flexural behavior. To be more realistic, a suitable representation for the column base slippage is to be modeled which will be discussed in the following sections.

5.5.2 Push-Over Analysis using RAM Perform Program

In this program, the inelastic behavior is modeled by M-φ plastic hinges at critical sections. This model is much simpler than the previous model used in SAP2000 program in which the plastic hinge rotations had to be calculated. The M-φ relationship for each plastic hinge is calculated as in Sec. 5-3. Figs. 5-6, 5-10 and 5-14 show the M-φ relationships used as input for the tall, middle and short specimens, respectively. The effects of shear deformations are included as in Sec. 5.4.2. The effect of slippage on curvature was also considered by changing the curvature, ($\varphi_{\text{Before Slippage}}$) in the previous M-φ diagrams by a new curvature ($\varphi_{\text{After Slippage}}$) coming from equation 5.18:

$$\varphi_{\text{After Slippage}} = \varphi_{\text{Before Slippage}} + \theta_s / L_p \qquad (5.18)$$

where θ_s is the rotational slippage calculated as in Sec. 5.4.1 and L_p is the plastic hinge length which was developed from the previous experimental data[10]. In RAM-Perform program, the length L_p is used as curvature multiplier to calculate the ultimate plastic rotation in the expected plastic hinges. Based on this, the ultimate rotational slippage was included in this program by dividing the rotational slippage over the plastic hinge length (θ_s /L_p). The push-over analysis results by RAM Perform program are shown in Figs. 5-24 and 5-25 and 5-26 for the tall, middle and short specimens, respectively. Despite the simplicity of the analytical model, the predicted results had good correlation with the experimental results. For the tall specimen B2CT (Fig. 5-24), the push-over analysis predicted about 0.96 of the peak seismic capacity and about 1.0 of the peak seismic displacement before specimen leaning. For the middle specimen B2CM (Fig. 5-25), the push-over analysis almost predicted the peak seismic capacity and 0.90 of the peak seismic displacement before leaning. For the short specimen B2CS (Fig. 5-26), the push-over analysis overestimated the maximum seismic response. The predicted displacement was almost 15 % higher than the actual displacement and the predicted maximum force was 11 % higher than the actual maximum force. This poor correlation shows some shortcomings in modeling the behavior of the short specimen. The behavior of the short specimen was not only controlled by the flexural yielding in the column plastic hinges but it was also affected by the sliding at the column bases (Sec. 4.3.1). To include this sliding in the analytical model, additional nonlinear springs (Fig. 5-15) are added at each column base. The properties of these springs are calculated in the following section.

5.5.3 Shear-Friction Springs

For the short specimen, the shear-sliding mechanism was shown in the significant base sliding at the east column base and the severe spalling on the west side of the west column base (Figs. 4-9 and 4-10). For the middle and tall specimens, however, the shear-sliding mechanism was not evident since the flexural behavior was more dominant due to the higher column aspect ratios (section 4.4.7). The shear-friction mechanism at the column bases of each specimen was not a case of pure shear. This is shown in Fig. 5-27 in which the column bases are subjected to a combination of shear, axial and flexural actions. The values of shear force, Q and axial forces, N carried by each column, and the location of the inflection points at east and west columns are functions of the moment capacities of the column top and bottom sections (Fig. 5.27). For the three specimens, the ratio between the column bottom and top section capacities is almost 0.25. This makes the length of the lower part of the column to the inflection point about 0.2 the column height, H. Table 5-4 shows the calculated moment capacity of the specimen columns at the top and bottom sections as well as the shear and axial forces. It can be concluded from this table that the level of axial force in the east column of the three specimens is negligible compared with the level of axial force carried by the west column. This is because the dominant direction of the seismic loading (Sylmar record) was toward the west direction according to the location of the specimen. This difference in axial forces (Fig. 5-27b, c) created significantly different shear-friction capacities in the east and west column bases. This is shown in Fig. 4-170 in which there is significant difference in the shear-sliding envelopes between the east and west column bases in the short specimen, B2CS. In Fig. 4-170a, the east column base experienced large sliding toward the dominant direction of the seismic loading. This sliding is governed by equation 5.19.

$$Q = \mu C \tag{5.19}$$

where Q is the shear–friction capacity, μ is the shear friction coefficient and C, the flexural compression force, is the axial force acting at the friction interface surface (Fig. 5-27b, c). The compression force C can be calculated from the hinge cross-section analysis (using the RCMC Program) at the level of cross-section yielding. The value of C at the east column base was calculated as 65.5 kips (291 KN) and the value of Q was calculated as 45 kips (200 KN) after yielding the column top and bottom sections (Table 5-4). By substituting these values in equation 5.19, the value of μ is determined as 0.7. It is worth noting that the value of μ recommended by the ACI code[21] for the specimen column bases is 1.0. To start analyzing the west column base, the value of axial force, N and shear force, Q acting on the west column as the column top and bottom section reached their yielding capacities are 74.5 k (349 KN), 56.6 k (252 KN), respectively (considering zero axial force carried by the east column). From the sectional analysis using the RCMC program, the values of C and T were calculated as 106.5 k (474 KN) and 32.0 k (142 KN), respectively. Using the coefficient of friction, μ of 0.70 (calculated from the east column base-sliding mechanism) and the compression force, C acting on the sliding surface, the shear-sliding capacity, μC is 82.6 k (367 KN), which is 32 %

higher than the maximum shear demand, Q acting on the west column base. This prevents the shear-friction mechanism from forming at the west column base.

Equation 5.19 assumes no participation for the dowels in the shear-friction mechanism either by the clamping or the dowel action. This is because the hinge dowels were expected to yield due to the low moment capacity at the column base before the shear-friction mechanism starts. This assumption was confirmed experimentally (section 4.4.1.1) where the hinge dowels of the east column base started yielding at the shear-friction interface under early loadings. Under 1.4 x Sylmar, the hinge dowels on the east side of the east column base started yielding and the maximum sliding displacement was 0.035" (0.9 mm) at the same hinge base. Under 2.0 x Sylmar, the hinge dowels on the west side of the east column base started yielding and the maximum sliding displacement at the same base was 0.04" (1.0 mm). This also agrees with the analytical results where all the hinge dowels were in tension as the cross-section reaches its yielding capacity. The early flexural yielding of the hinge dowels means that the dowels do not have shear capacity, dowel action. This is shown by von Mises' criterion that provides the interaction between the steel shear and tensile strength ($\sigma^2_x + 3\ \tau^2_{xy} = \sigma_y$).

Although equation 5.19 can predict the peak shear-friction capacity, it does not reveal the shear-sliding envelope. Based on the experimental results from this study and another related study[22], the analytical model of the shear-sliding envelopes can be developed. Fig. 5-28a shows the analytical model of the shear-sliding mechanism, represented by three major segments. Segment 1 represents the peak shear-sliding capacity (neglecting the slight ascending tendency in the experimental envelope (Fig. 4-140a) caused by the steel strain hardening). Segment 1 is only valid from the start of hinge flexural yielding up to a sliding displacement of δ. Referring to the experimental results, the displacement δ was about 0.25” (6 mm) which was equal to the roughed depth at the shear-sliding surface. After exceeding this displacement, strength degradation started from displacement δ to 2δ as shown in Fig. 4-170. This is modeled by segment 2. This degradation in strength is referred to the destruction of the aggregate interlocking after exceeding the displacement δ (Fig. 5-28). The slope of segment 2, K2 is experimentally taken as –35 k/in (-6.25 KN/mm). The rest of the envelope could not be developed from the experimental results in this study since the loading level stopped at the sliding displacement of 2δ. Based on this, a survey was done on the related experimental works to develop the rest of the shear-sliding envelope. In a previous related study by Silva, P. F. et al[22], the shear-friction behavior of the sacrificial interior shear keys was investigated. The shear keys were designed with different aspect ratios and different reinforcement ratios. The shear keys were tested with no axial load, which makes this similar to the east column base in the current study in which the axial load is reduced due to the large tendency of the seismic loading toward the west direction. The shear keys in the previous study[22] were tested till failure under different types of loadings such as monotonic, quasistatic cyclic and dynamic loadings. Fig. 5-28b shows the shear load-displacement envelopes for three specimens. The result from the specimen 2A was taken since its failure was mainly governed by shear-friction (no compression failure was observed in the specimen). This is the same failure mode as the east column base in the current study. As shown in Fig. 5-28b, the slope of the last part of the envelope, K3 can be taken as 40 k / in (7 kN / mm). Fig. 5-28a shows the three-segment model of the shear-friction mechanism for the east column base in the short specimen. This model can be used to represent the properties of the shear springs at the column base (Fig. 5-15).

At the west column base in the short specimen, the shear sliding capacity was increased by the large axial force, N and its corresponding value of C (Fig. 5-27b). Therefore limited base sliding occurred (Fig. 4-170). As shown in Fig. 5-27b, the capacity of the base hinge was controlled by the capacity of the inclined struts and their node on the west side of the west column base. The degradation in the strength of these struts and the corresponding node can affect the overall shear-sliding capacity of the west column base. Referring to the experimental observation, clear damage was observed close to the location of the struts node (the hatched triangular part shown in Fig. 5-27b) on the west side of the west column base under the last seismic loading (Fig. 4-9). At this loading, the shear-sliding capacity started to drop by almost 15 % as shown in Fig. 4-170b. This experimental data agrees with the analytical model concept mentioned earlier.

Another mechanism called the Strut-and-Tie-Model became dominant at the west column base. This model was used in the previous study[22] to interpret the failure of some shear-friction specimens. This model is also used in detail in this study (section 5.7) to interpret the failure of the three specimens. In this model, the forces are imagined to flow through a stable strut-and-tie combination (Fig. 5-29b). The node represented by the hatched area in Fig. 5.29b is considered critical for two reasons: First, this node is located in unconfined concrete zone caused by the lack of transverse reinforcement at the column base (section 6.2.1). Second, this node is only surrounded by compression forces from two sides (the horizontal and the inclined side) whereas the vertical side is free from supporting forces. The resultant of the two struts, R (Fig. 5.29b) is compared with the strut capacity (equation 5.21) close to the hatched node. To calculate the strut capacity (equation 5.22), the f'_c was taken as 5.86 ksi (41 MPa), which is the same concrete strength on the day of the test. The concrete strength was 25% increased to account for strain rate effect (section 5.2). The strut spreading factor, βs is taken as 0.75 (section 5.3.1) and the strut area was calculated as 21.4 in^2 (13806 mm^2). The strut capacity was determined to be 100 k (445 kN), whereas the strut demand, R was calculated as 122.6 k (545 kN). Therefore, this strut is critical and limited the capacity of the system.

Fig. 5.29a shows the suitable analytical model for the west column base. In this model, the shear-sliding capacity is calculated either by equation 5.19 or by the STM, whichever is lower. In the case of the west column base, the strut capacity from the STM model controls. The two mechanisms of the east and west column bases were modeled in the SAP2000 program since it was not possible to model the shear-friction spring in the east column base (Fig 5-28a) in the RAM Perform program. The result of the SAP2000 push-over analysis after including the base-slippage model is shown in Fig. 5-30. As can be seen in this figure, the predicted results are better correlated with the experimental results from the strength and displacement perspectives. For tall and middle specimens, however, the sliding model did not change the response shown in Figs. 5-21 and 5-22 since the column shear demands in these specimens are much less than sliding model shear capacity.

5.5.4 Push-Over Analysis using wFRAME Program

The wFRAME program is used by CALTRANS to perform push-over analysis on bridge frames and bents. It can represent the soil-structure interaction by modeling the foundation piles and the nonlinear soil behavior. It can also model the in-phase and out-of-phase modes for double-deck bridges. Despite the advantages of wFRAME program, it has limitations. For example, the rotational capacity of each plastic hinge is not included in the program, which precludes the ability to model the slippage rotations. Shear deformations, however can be included in this program by using the reduced shear area. Furthermore, the program stops at the start of the structure collapse mechanism and it does not calculate the structure peak displacement. The program does not calculate the effect of P-δ.

To check the range of applicability of wFRAME program, it was used to perform the push-over analysis on the three specimens. For the tall specimen B2CT (Fig. 5-31), the predicted yield displacement by the program is satisfactory whereas the predicted capacity is 10 % higher the actual capacity. This is because the wFRAME program does not account for the P-δ effect, which is significant in the tall specimen. The plastic deformation, Δ_p shown in Fig. 5-31 is calculated using equations 2.3 and 2.4 in section 2.6.2 and added to the program output. For middle specimen B2CM (Fig. 5-32), the specimen stiffness before yielding is a little bit stiffer than the actual stiffness. This could be enhanced if the P-δ effect is included. Adding the deformation due to reinforcement slippage to the specimen yield displacement could also enhance the correlation. The plastic deformation, Δ_p is calculated separately (section 2.6.2) and added in the same diagram (Fig. 5-32). For the short specimen B2CS (Fig. 5-33), the predicted results by wFRAME do not correlate with the experimental results. The use of actual shear area for specimen columns and adding the P-δ effect could enhance this correlation. The plastic deformation, Δ_p is calculated separately (section 2.6.2) and added to the same diagram. In line with the above, wFRAME program lacks the ability to model some crucial issues, which cannot be overlooked in R/C structures. For example, reinforcement slippage adds more rotations at critical sections of R/C structures, which can impact the overall structural behavior. In addition, the geometrical non-linearity (P-δ effect) can impact the overall structural response at large lateral displacements.

5.6 Dynamic Analysis

Although nonlinear static analysis can predict the maximum structure response (maximum seismic displacement and capacity), it cannot predict the structure response to the increasing excitation. To predict these effects analytically, a dynamic analysis by DRAIN-3DX program was performed on the three specimens. The model used by DRAIN-3DX is the lumped plasticity model shown in Fig. 5-15. As discussed before, the shear and slippage deformations can be predicted using this model. The nonlinear behavior was represented by the Takeda model (Fig. 5-34), which was found successful in predicting the dynamic response of R/C members[11]. The Takeda model shown in Fig. 5-34 consists of hysteretic rules operating on a trilinear primary curve. The Takeda hysteretic rules do not cover the "pinching" effects, which occur due to the closing of concrete cracks[14]. Two main points are to be determined on the primary curve: the point of cracking load and displacement, and the point of yield load and displacement. After yielding point, the model has the ability to represent the strain hardening effect. The input earthquake loading for each specimen was taken as the earthquake record achieved by the shake table. Fig. 5-35 shows the achieved acceleration history records used in testing the three specimens. Each loading consists of a series of Sylmar records of the Northridge Earthquake (peak acceleration of 0.61g) with increasing amplitudes. Each loading was recorded every 0.00625 sec. This time increment is so small that it caused some numerical errors in the dynamic analysis output. To avoid this problem, the time step was increased to 0.02 sec by resampling the earthquake history for each specimen. Care was taken in calculating the new time increment since it can affect the numerical solution accuracy. Thus, the new time step was conservatively taken as 1/10 the lowest fundamental period of the three specimens (assuming that the numerical solution in the DRAIN-3DX Program is conditionally stable). Since the lowest fundamental period was 0.21 sec for the short, the incremental time step was taken as 0.02 sec. The new earthquakes after resampling process are shown in Fig. 5-35b. The peak accelerations of the resampled earthquakes, especially at the last runs, are a little bit lower than the actual peak values (Fig. 5-35a) as the resampling process cut some of the original data. This difference should be taken into consideration as it could cause some difference between the analytical and experimental results.

Before performing the dynamic analysis, the classical damping matrix for each specimen had to be determined. Damping matrix, C can be taken as a combination of stiffness (K) and mass (M) proportional matrices, i.e., $C = \alpha M + \beta K$. The values of α and β are frequency and damping dependent. The natural frequencies for each specimen are calculated from the free vibration analysis while the damping ratios for each specimen (just before specimen yielding) are assumed 5 % and 10 % for the first and second modes of vibration, respectively[23]. From this assumption, the calculated β values for each specimen were almost zeros while the calculated α values were 0.9, 2.2 and 2.70 for the tall, medium and short specimens, respectively.

The output results for tall specimen B2CT are summarized in Fig. 5-36 to Fig. 5-38. Fig. 5-36a shows the load-displacement hysteretic curves for both analytical and experimental results. A good correlation between the predicted and experimental results is achieved. The maximum predicted displacement is 87.5 % the maximum actual displacement. A better correlation can be achieved by including the P-δ effect. This effect was not an option in the Takeda model, so it was approximately calculated by changing the Takeda input data according to the effect of P-δ on the push-over diagram. As shown in Figs. 5-21 and 5-24, including the P-δ effect is reducing the total frame capacity at the yield and ultimate conditions. According to this reduction, the yield and ultimate moment capacities of the column top and bottom sections (Fig. 5-6) were also reduced. A better correlation in the shape of hysteretic loops was also achieved by changing the unloading coefficient from 0.5 to 0.75. Fig. 5-36b shows better agreement between the predicted and measured hysteretic loops after including the P-δ effect and after using the new unloading coefficient. Fig. 5-37 also shows a comparison between the predicted and measured history of the specimen relative displacement.

The analytical model predicted 100 % of the specimen maximum displacement in both west (- sign) and east (+ sign) directions. To have a clearer evaluation of displacement history calculated analytically, it was put in the same diagram (Fig. 5-38) with the actual displacement time history. As shown in Fig. 5-38, there is a shift in the residual displacement between analytical and experimental displacement histories. This shift becomes clear during the loading that is before the last loading. This is because the specimen leaned toward the out-of-plane direction during this loading decreasing the specimen residual displacement.

For the medium specimen B2CM, the analytical results are summarized in Fig. 5-39 to Fig. 5-41. Fig. 5-39a shows the load-displacement hysteretic curves for both analytical and experimental results. The maximum predicted displacement is 88 % the maximum actual displacement in west direction (- sign) and 45% the maximum actual displacement in the east direction (+ sign). A better correlation in the predicted strength can be achieved by including the P-δ effect. The correlation in the shape of hysteretic loops can also be improved by changing the unloading coefficient from 0.5 to 0.7. Fig. 5-39b slightly shows better agreement between the predicted and measured hysteretic loops after calculating the P-δ effect and after using the new unloading coefficient. Fig. 5-40 shows a comparison between the predicted and measured history of the specimen relative displacement. The analytical model predicted 88 % of the specimen maximum displacement in the west direction (- sign) and 50 % of the maximum displacement in the east direction (+ sign). The large difference in maximum displacement on east side is accompanied with a shift in the residual displacement (about 1.0” (25 mm) maximum) between the predicted and measured displacement history (Fig. 5-41). The difference in residual displacement between the predicted and analytical results could be due to the strength deterioration at the column bases at the last loadings due to the out-of-plane effects. This impact could not be modeled in the DRAIN-3DX program.

For the short specimen B2CS, the analytical results are summarized in Fig. 5-42 to Fig. 5-44. Although shear demand was significant in this specimen, the analytical model (Takeda’s Model) used in the dynamic analysis for this specimen was mainly flexural. Fig. 5-42a shows the load-displacement hysteretic curves for both analytical and experimental results. A good agreement between analytical and experimental results is achieved except that the impact of P- δ is not included. A better correlation in the predicted strength can be achieved by including the P-δ effect. After changing the unloading coefficient from 0.5 to 0.70, the shape of the hysteretic loops became closer to the experimental ones despite the increase in the maximum displacement (Fig. 5-42b). Fig. 5-43 shows a comparison between the predicted and measured history of the specimen relative displacement. The analytical model predicted 133 % of the specimen maximum displacement in the west direction (- sign) and 200 % of the maximum displacement in the east direction (+ sign). The large difference in maximum displacement is accompanied with a shift in the residual displacement (about 0.375” (9 mm) maximum) between the predicted and measured history (Fig. 5-44). The disagreement in the hystereses loops between the analytical and the experimental results is referred to the difference between the actual behavior and the behavior that the Takeda’s model can predict. This is because the Takeda’s Model was mainly developed for the R/C members with flexurally dominated failure whereas the behavior of the short specimen included slippage at the column bases in addition to the shear and the flexural behavior of the columns. The resampling process (Figs. 5-33a and 5-33b) could be also the second reason of having different disagreement between analytical and experimental results.

5.7 Strut-and-Tie Model

The strut-and-tie model, “STM” is a powerful design tool for concrete structures. It was mainly developed for designing the structural D-regions (where beam theory is not applicable), and it could be conservatively used for designing the structural B-regions (where flexural beam and shear theories are applicable). Research about STM and its applications in concrete design has been developed in the past 20 years[24, 25]. Recently, design with STM was added to the ACI 318 code[21]. To design a structure using STM the external forces applied on such a structure are transferred in the structural body through a combination of struts and ties. The joints connecting struts and ties are called nodes. At these nodes, equilibrium is to be maintained for calculating forces in struts and ties. Once the forces in the STM are calculated, the design and detailing can be done.

5.7.1 Specimen Design

The first step of design is to calculate the external loadings carried by each specimen. Since all specimen mass is placed on its cap beam, the lateral seismic loading can be modeled as a lateral static force distributed along the cap beam body. Fig. 5-45 shows the vertical and lateral loads on each specimen. As a result of the lateral loading, the plastic hinges will form at the column sections and hinge bases. To make the problem determinate, the moment capacity of column sections, M_{C1}, M_{C2} and base hinges M_{B1} and M_{B2} (Fig. 5-45) were calculated using the RCMC program. The level of axial force in each column was based on overall equilibrium.

The second step in design is to define and determine the dimensions of D-regions. According to St. Venant's principle, D-regions are assumed to extend approximately a distance equal to the member depth from the point of disturbance. Fig. 5-46 shows the locations of B and D regions in the three specimens after assuming a uniformly distributed dead load on the specimen cap-beam. As can be seen in this figure, the configuration of D, B-regions is almost identical in the three specimens except that the size of B-regions in the columns decrease as the column aspect ratio decreases. The third step is to calculate the internal forces at the boundaries of the D-regions.

5.7.1.1 Columns

After calculating the yield moment for column sections using the RCMC program (assuming initial axial load values), the shear forces carried by each column are calculated from the equilibrium of each column individually. The total lateral loading simulating the maximum seismic loading is taken as the summation of the shear forces of the specimen columns. The resulting level of axial force carried by each column is calculated from the overall structure equilibrium. Another trial was done to have the exact moment capacity of each column section according to the new level of column axial force. In RCMC modeling, the effect of strain rate (Section 5-2) on concrete and steel properties was taken into consideration to account for the dynamic loading effect. The results for the three specimens are shown in Table 5-1. The impact of changing the column axial force on the yield moment is also shown in the same table. It is worth noting that despite the reduction in axial force level in east column of short specimen, the moment capacity of this column is still higher than that in other two specimens. This is because the concrete strength of the short specimen columns is higher than the strength of the other two specimen columns. This is shown in Table 3-4 in which the concrete strength of the short columns is 5.86 ksi (40.4 MPa) while the concrete strength of the tall and medium columns is 4.1 ksi (28.3 MPa).

5.7.1.1.1 Tall Specimen Columns

From the RCMC analysis (Table 5-1), the internal forces in east and west column boundaries are transferred to tensile and compression forces (Fig. 5-47). Shear forces calculated from external equilibrium and carried by each column are assumed to act through the compression zone of each section. The flow of forces in each column takes the equivalent truss shown in Fig. 5-47. The tie created at each column base (4-12, 11-6 at east and west column bases, respectively) is located at the centroid of the transverse reinforcement and to simulate the specimen detail in which there is no enough transverse reinforcement at the column base near the hinge key (see section 6.2.1 and Fig. 6-4a). The locations of the ties 4-12 and 11-6 are far enough into the column for the column longitudinal reinforcement to be developed. Development does not control because the required development length of the column longitudinal reinforcement at joints 6 and 12 is small as a result of the low forces generated in the longitudinal reinforcement close to the column bases. The bearing areas of critical struts (Fig. 5-47) are calculated from cross-sectional analysis assuming that plane sections remain plane (one of the RCMC program assumptions), which gives some approximation in this model. Forces are calculated in the D-regions of each column after satisfying equilibrium at each joint. Struts 1-2, 2-5, and 3-4 in the east column, and struts 7-8, 7-9, and 10-11 (Fig. 5-48) in the west column are considered critical because their dimensions are controlled by the bearing areas at the top and bottom sections of each column (Fig. 5-47). Ties 5-1 and 4-12 in east column, and ties 9-8 and 11-6 in west column are considered critical because of their high tensile forces. Stresses in these struts and ties are checked by comparing the demand carried by each member to its capacity determined from equations 5.20, 5.21 and 5.22[26].

For Struts, $Fu = \phi\,(0.85\, f'_c\, \beta_s\, A_c)$ 5.20

For Ties, $Fu = \phi\,(A_s\, f_y)$ 5.21

For nodes, $Fu = \phi\,(0.85\, f'_c\, \beta_n\, A_n)$ 5.22

The strength reduction factor, ϕ is taken as 1.0 since the STM is used to check the existing design. β_s and β_n are the strut and node strength factors, respectively. β_s is taken as 0.75 for the critical struts to account for the spreading effect that starts at the strut bearing area. β_n is taken as 1.0 for all nodes since no ties are being anchored through the critical nodes (nodes 2 and 7). Other nodes where ties are being anchored are considered not critical since their dimensions are not limited. A_c is the strut bearing area, measured perpendicular to the line of axis of the strut. In calculating the strut area, A_c (Figs. 5-47, 5-49 and 5-51), the unconfined concrete is deducted from the total bearing area to account for the unconfined concrete spalling that is expected when columns reach their yielding capacity. A_s is the steel area tributary to each tie. f'_c is the concrete strength of the concrete struts and is taken as the actual concrete strength on the day of testing after adding the confinement and strain rate effects. The confinement effect was added by increasing the unconfined concrete strength by 35 % (assuming Mander's model[27] of confinement) and the strain rate effect was added by increasing the unconfined concrete strength by 25 % (Section 5-2). Similarly, the steel yield strength, f_y is taken as the spiral yield strength after adding the strain rate effect (25% increase in steel yield strength as concluded in Section 5-2). Equations 5.20, 5.21 and 5.22 are used to calculate the capacity of the critical struts, ties and nodes. These capacities are compared (Table 5-5) with the demand forces calculated when the system reaches its yielding capacity.

In Table 5-5, failure is controlled by struts 1-2 and 7-8 (at the plastic hinge zone of east and west columns, respectively) since they have the lowest strength/ demand ratio. The experimental results however showed no failure at these struts where spalling in the strut regions did not extend to the confined core (Figs. 4-52 and 4-53). This disagreement gives some doubt about the strut spreading factor, β_s that makes the strut strength satisfactory if its value is changed to unity instead of 0.75. This finding is also supported by other experiments[26] that showed greater value of β_s.

At the bases of east and west columns, respectively, struts 3-4 and 10-11 also fail since their calculated strength is lower than their calculated demand. The concrete strength used in these struts was assumed confined regardless the strength of nodes 10 and 3. Failure of strut 10-11 agrees with the experimental results in which a large piece of concrete spalled on the west side of the west column base

(Fig. 4-54) after high levels of loadings. Failure of strut 3-4, however does not agree with the experimental results in which no apparent failure was noticed at region of this strut (Fig. 4-54). This disagreement could be due to the approximation in calculating the strut bearing area at the column-footing interface, which requires a linear strain profile. This is not true, especially at the column-footing interface where there is a flexural-shear interaction.

To compare between the system shear capacity predicted by STM and the shear capacity calculated experimentally, the shear force carried by each column is reduced based on the lowest member capacity (members 1-2 and 7-8 in east and west columns, respectively, Table 5-5). Using STM, the specimen shear capacity is predicted to be 28.9 k (129 kN), which is 13 % lower the maximum shear capacity calculated experimentally (Table 4-26). This means that the STM prediction is conservative.

5.7.1.1.2 Medium Specimen Columns

Similar to the tall specimen, the flow of forces in east and west columns are represented by the truss model shown in Fig. 5-49. The strut-and-tie-model configuration is adjusted at the column bases so that the ties at the bottom of each column are located in the centroid of the existing lateral reinforcement. The location of these ties also allowed enough development length for the column longitudinal reinforcement since the stress in the column longitudinal reinforcement at the column bases is minimal. As mentioned in the previous section, the critical struts and ties are chosen based on their locations and their force levels. The forces generated in the critical struts and ties in the column D-regions are shown in Fig. 5-50. Equations 5.20 to 5.22 are used to calculate the capacity of the critical members. These capacities are compared (Table 5-6) with the demand forces calculated when the system reaches its yielding capacity.

In Table 5-6, failure is controlled by strut 1-2 and tie 9-8 in the east and west columns, respectively since they have the lowest strength/demand ratio. The experimental results however showed no failure at the region of this strut and no yielding in the column transverse reinforcement represented by this tie. A β_s factor of 0.75 was used in the calculations based on the ACI code[21]. Since the tests showed no failure, the β_s factor can be increased more than 0.75. Using the experimental results the β_s factor can be back calculated to be 0.90. This finding is also supported by other experiments[26] that showed greater value of β_s.

At the bases of east and west columns, respectively, struts 3-4 and 10-11 also fail since their calculated strength is lower than their calculated demand. The concrete strength used in these struts was assumed confined regardless the strength of nodes 10 and 3. Failure of strut 10-11 agrees with the experimental results in which a large piece of concrete spalled on the west side of the west column base (Fig. 4-34) after high levels of loadings. Failure of strut 3-4, however does not agree with the experimental results in which no apparent failure was noticed in this region. This disagreement could be due to the approximation in calculating the strut bearing area at the column-footing interface, which requires a linear strain profile. This assumption is questionable, especially at the column-footing interface where there is a flexural-shear interaction.

To compare between the system shear capacity predicted by STM and the shear capacity calculated experimentally, the shear force carried by each column is reduced based on the lowest member capacity (strut 1-2 and tie 9-8 in east and west columns, respectively, Table 5-6). Using STM, the specimen shear capacity is predicted to be 41.0 k (182 kN), which is 18 % lower the maximum shear capacity calculated experimentally (Table 4-24). When the concrete shear resistance, V_c taken as $2\sqrt{f'_c}\ A_c$ is added to the tie capacity, the shear capacity in the west column was increased to 23.9 k (106 KN). This increased the total specimen capacity to 44.5 k (198 KN), which is 9.0 % lower than the total specimen capacity calculated experimentally. This was not done for the tall specimen model because the forces in the ties were not critical.

5.7.1.1.3 Short Specimen Columns

Similar to the tall and middle specimens, the truss model transferring the boundary forces in each column is shown in Fig. 5-51. The configuration of the STM at the east column base is different as the inclination of the strut 3-4 and the location of base tension forces makes it difficult to locate a tie close to the column base. Critical struts and ties are numbered in Figure 5-52. The forces generated in the critical members are also shown in Fig. 5-52. The design process of these members is summarized in Table 5-7. As shown in this table, the failure is controlled by ties 5-1 and 6-12 in the east and west columns, respectively as they have the lowest capacity/demand ratio. Based on this, the specimen shear capacity predicted by the STM is 40.7 k (181 kN), which is 56 % lower that the actual capacity measured experimentally. This large difference is caused by neglecting the concrete shear capacity, V_c taken as $2\sqrt{f'c}\ Ac$, which in reality works with steel shear capacity, V_s to constitute the total tie resistance. Table 5-7 shows that after adding the concrete shear resistance, V_c to the tie capacity, the specimen overall shear capacity becomes 75.5 k (336 kN), which is only 18 % lower than the actual capacity.

5.7.1.2 Beams

The truss model in Fig. 5-53 represents the flow of forces in each specimen beam. This model is basically for connecting the forces generated at the adjoining column sections. The model carries the gravity loadings and the equivalent static lateral loading. The gravity loading represents the weight of the beam body and the weight of the lead buckets. The lateral loading is in equilibrium with the specimen column shear forces, which are calculated based on the flexural capacity of the column top and bottom sections (Table 5-4). The vertical and horizontal loads carried by the beam are distributed over the truss joints (Fig. 5-53). Member forces in the STM of each specimen beam are shown in Fig. 5-54. These forces are very similar in the three specimens, so there is no need to repeat the design process for each specimen. Table 5-8 shows the design details for the short specimen beam, which has the most critical forces of the three beams (Fig. 5-54c). For the other two specimens, the beam design will be the same.

In Table 5-8, Tie 1-2 does not fail. This complies with the experimental results in which the beam longitudinal reinforcement did not yield when the specimen reached its yielding capacity. Tie 1-3, however fails, which doesn't agree with the experimental results in which the beam transverse reinforcement did not yield. This is because the concrete participation for shear resistance, V_c taken as $2\sqrt{f'c}\ b_w d$ is not included in the STM. This in turn reduces the actual system shear capacity by about 12 %, which makes the STM conservative. When the concrete shear resistance, V_c is included; the tie capacity becomes higher than its demand. This makes the STM predict the whole system capacity. Strut 8-11 does not fail. This agrees with the experimental results in which no significant cracks were observed at the region of this strut. The resultant of struts 2-7 & 2-8 and the resultant of struts 8-9 & 8-10, at the east and west beam-column joints, respectively do not fail since their demand is far below their capacity. This agrees with the experimental results in which no significant cracks were observed at the regions of theses struts (beam-column regions) as discussed in Chapter 4, section 4.3.

Since the specimen beam and columns are parts of the same system, the capacity of the system will be controlled by the most critical part. Comparing the capacity/demand values for columns and beam in Tables 5-7 and 5-8, respectively, it is found that the specimen columns are more critical since they predict a lower capacity. The predicted STM capacity of each specimen based on the column capacity (the controlling part of the specimen) are shown in Table 5-9. To evaluate the STM, the predicted capacity of each specimen is compared with the actual capacity calculated experimentally. As shown in Table 5-9, the STM proves to be a conservative model as it underestimates the actual system capacity.

CHAPTER 6

DESIGN RECOMMENDATIONS

6.1 Introduction

In this chapter, the current CALTRANS design criteria is evaluated. New design details at critical locations are also recommended. The observed and measured performance for the specimens in this study and in a similar study[28] are examined to determine the design advantages and shortcomings. At specific locations in each specimen, the observed and measured performance was satisfactory which indicated that these locations were well designed. At other locations, however, the design details caused undesirable performance. In each specimen, the critical locations are those affecting the behavior such as the beam-column joints, the base hinges and the column plastic hinge zones. Based on the observed and measured experimental results at these locations, new design details are suggested.

6.2 Behavior of Beam-Column Joints in Current Study

Beam-column joint is one of the most critical locations in the bent. It is responsible for creating the frame action, so any degradation in its strength can decrease the total capacity of the frame dramatically. In the three specimens, the details of the beam-column joints were simple and constructible. In Fig. 6-1, the column longitudinal reinforcement is extended to the beam top reinforcement without additional end hooks. Inside the beam-column joint, the column reinforcement is confined with confinement steel that is the same as the column. No additional shear reinforcement (either vertical or horizontal) is added in the beam-column joint. This reduced the steel congestion in this region and facilitated the joint construction. Despite the simplicity of the beam-column joint details, the performance at these regions was very satisfactory. Table 6-1 summarizes the main experimental results at the beam-column joints in the three specimens. The first cracks in the east and west beam-column joints in the three specimens were hair line cracks and started at high levels of seismic loadings (at 2, 2 and 1.5 x Sylmar for short, medium and tall specimens, respectively). At these levels of seismic loadings, the columns, however, experienced significant levels of flexural and shear cracks (Figs. 4-6, 4-27 and 4-44 for short, medium and tall specimens, respectively). During the maximum loadings for each specimen (3.25, 3 and 2.75 x Sylmar for short, medium and tall specimens, respectively), additional cracks did develop in the beam-column joints but were narrow and minimal. At maximum loadings, the columns, however, experienced high levels of cracks and spalling (Figs. 4-13, 4-35 and 4-55 for short, medium and tall specimens, respectively). The columns also reached their maximum capacity. This is an indication that the strength of the beam-column joints was much higher than that of the columns. The measured results also proved a good performance. Column longitudinal reinforcement was well developed inside the beam-column joints (Figs. 4-64, 4-70 and 4-76 for short, medium and tall specimens, respectively). Maximum strains of the column transverse reinforcement inside the beam column joints (the joint shear reinforcement) were also far below the yield strains (0.387, 0.135 and 0.25 the yield strain in short, medium and tall specimens, respectively) as shown in Figs 4-63, 4-69 and 4-75 for short, medium and tall specimen, respectively. Based on this performance, the current details of the beam-column joints (Fig. 6-2) were sufficient to protect the joints from failure. As shown in Fig. 6-2, the effective width of bridge soffit and deck including their reinforcement is modeled. This caused an increase in the beam flexural capacity compared with its demand. The maximum actual flexural demand/capacity ratio for the beam critical section was found in the short specimen and it was 0.27. The cap-beam moment demand was calculated after the columns reached their yielding capacity and the cap-beam flexural strength was calculated using the actual material properties on the test day (Table 3-4). This low ratio indicates the high flexural capacity for the cap-beam section in the three specimens. For the beam shear capacity, based on its shear reinforcement details (Fig. 6-2), the maximum shear demand/capacity at critical section was found in the short specimen and it was 0.6. This value indicates the high shear capacity for the cap-beam section in the three specimens.

6.3 Behavior of Beam-Column Joints in Similar Study

The results in this study were compared with a previous study done on similar specimens but with architecturally flared columns[28]. In the previous study, the behavior of cap beam and beam-column joints were different. At low levels of seismic loadings (0.5 x Sylmar) cracks were observed at the joint region and at high levels of loadings (3.25 x Sylmar) the cap beam and the joint regions were extensively damaged. During testing, the gap between column flares and beam closed creating higher shear and flexural demands on the cap beam. After gap closure, the calculated flexural demand/capacity ratio for the cap beam was almost 0.85 while the calculated shear demand/capacity ratio was almost 1.40. The high shear and flexural demands in the cap beam were observed in extensive shear and flexural cracks at beam critical sections.

6.4 CALTRANS Joint Design

To evaluate the CALTRANS method for the joint shear design[1], the principal stresses at the joint region were calculated based on the actual concrete and steel properties in both columns and cap beam (Chapter 3). Strain rate effect was also included to account for the dynamic loading effect. The maximum principal stresses were found in the short specimen joints. The extreme tensile and compression principal stresses were +0.52 ksi (3.60 MPa) and –0.81 ksi (5.70 MPa), at east and west beam-column joints, respectively. In the CALTRANS specifications, the principal tensile and compressive stresses in the joint region are limited to 12 $\sqrt{f'_c}$ ksi ($\sqrt{f'_c}$ MPa) and 0.25 f'_c, respectively. These limits are equivalent to 0.76 ksi (5.3 MPa) and 1.0 ksi (7.0 MPa), respectively for the short specimen joints. The calculated tensile and compressive stresses at critical joints were approximately 50 % and 25 % less than the CALTRANS tensile and compressive stress limits, respectively.

In the previous study[28], the calculated principal tensile and compressive stresses at the joint region after the gap closure of the column flares were +0.80 ksi (5.6 MPa) and –1.06 ksi (7.40 MPa) and the CALTRANS tensile and compressive stress limits were +0.90 ksi (6.3 MPa) and –1.50 ksi (10.5 MPa), respectively. The calculated stresses were approximately 15 % and 45 % less than the CALTRANS tensile and compressive stress limits, respectively. The beam-column joints in the previous study, however, were severely damaged during seismic loadings. Therefore, adjustments are needed in either the stress limits or the methodology. For the joints in the current study, the maximum principal tensile stress was +0.52 ksi (3.60 MPa), which was higher than the CALTRANS tensile stress limit, $3.5\sqrt{f'_c}$ ksi ($0.29\sqrt{f'_c}$ MPa) for requiring additional shear reinforcement (0.22 ksi (1.54 MPa)), whereas the behavior in the joint regions (Section 6.2) did not require any shear reinforcement. In the previous study[28], however, the principal tensile stress criterion required additional shear reinforcement in the joint region. Despite that this reinforcement was added, the joint behavior was not satisfactory. This indicates that the CALTRANS criterion for determining the additional shear reinforcement is not reliable. As an alternative for the principal stress method, the Strut-and-Tie method can be implemented since it was successful in predicting the behavior of the beam-column joints in the current study (Section 5.7) and in the previous study as well.

6.5 Two-Way Hinge Details

The two-way base hinges are provided at the column-footing connection to eliminate moments transmitted to the foundation in both directions. This in turn reduces the footing actions and makes footing design simpler and more economical[29]. Practically, the base hinges are detailed to make the flexural capacity at the hinge key as small as possible in a way that maintains the bearing and shear transfer capacity at this region. The base hinge region is subjected to three different modes of failure, which can occur individually or together. The first mode is the bearing failure, which is not likely in most cases since the section is confined by the column and the footing[30]. The second mode is the flexural failure, which can occur due to the pull out of the hinge bars because of the lack of development length or the concrete crushing at the edge of the hinge caused by gap closure in case of small hinge gap depth. The third mode is the shear failure, which is the most critical and complicated one. The shear capacity stems from the concrete friction at the column-footing interface caused by the column axial force and increased by the dowel clamping force activated by tension. When there is an interaction between the second and third mode (the flexural and shear friction modes), the hinge base can reach its flexural capacity before reaching the shear-friction capacity. This is because the shear corresponding to the base flexural capacity is much lower than the shear-friction resistance. This causes the hinge dowels at the hinge base to yield in flexural and in turn diminishes their effectiveness in the shear-friction mechanism. A good arrangement of hinge dowels at the hinge base could delay the flexural yielding of some of the dowels. This in turn makes these dowels share in the shear-friction resistance. One of the aims of this study is to investigate this effect.

6.5.1 Two-Way Hinge Behavior in Current Study

For the three specimens, the main configuration of the column base hinges was derived from CALTRANS details and recommendations[1]. As shown in Fig. 6-3, the hinge key is formed by reducing the column cross-sectional area by almost 30 % and by terminating the column longitudinal reinforcement at the column-footing interface. Dowels are not collected in the hinge center but they are distributed as shown in Fig. 6-3a. This arrangement allows half of the hinge dowels to be located close to the neutral axis where the flexural tension is small. This could allow half of the dowels to work effectively in the shear-friction mechanism under moderate seismic loadings while the other half only works in the flexural tension mechanism. The dowels are also well developed to prevent flexural pull out. The hinge key depth was taken as 0.5” (13 mm) to provide enough room for the column base rotation before the hinge gap closes. The behavior of the hinge base in the three specimens was satisfactory at moderate levels of loadings (Tables 4-4 to 4-6). After high levels of loadings (3.25, 3.0 and

2.75 x Sylmar for short medium and tall specimens, respectively), however, damage was observed at the hinge bases. As shown in Figs. 4-9, 4-36 and 4-57 for short, medium and tall specimens, respectively, a large piece of concrete spalled out on the west side of the west column base in each specimen. This result indicated a shortcoming in the hinge base details for the three specimens. More confinement is needed at the location of spalling at the very bottom of the column. As shown in Fig. 6-3b, the column longitudinal reinforcement should be kept straight allowing the column transverse reinforcement to cover the region at the very bottom of the column. It is worth noting that removing the hooks from the column longitudinal reinforcement will not affect the behavior of the region since the tensile forces in these bars at the column base are minimal (see Figs. 5-48, 5-50 and 5-52 for the tall, medium and short specimens, respectively).

The measured curvatures at the hinge base location showed possible hinge gap closure in the medium and tall specimens (Sec. 4.4.4). This requires some enlargement in the hinge gap depth (more than 0.5” (13 mm)) to accommodate the maximum column base rotation. Based on the maximum measured curvature at the base hinges in medium and tall specimens (Figs. 4-154 and 4-160), the gap hinge can be conservatively taken as 1.0” (25 mm) assuming that the center of rotation at the base hinge is the center of gravity of the hinge cross-section. In the prototype bridge, the hinge gap can be taken as 3.5” (88 mm) based on the scale ratio.

The column bases in each specimen experienced some shear sliding (section 4.4.7). For the short specimen, the maximum base sliding was 0.56” (14 mm) and it occurred in the east column base, whereas in the west column base, the sliding was minimal (0.1” (3 mm)). It is important to note that the sliding at the east column base will be very difficult to retrofit in the prototype. The maximum base sliding in this specimen is considered significant since it represents 23 % of the specimen maximum displacement. For the medium and tall specimens, however, sliding was insignificant. For these two specimens, base sliding at east and west column bases was very close (section 4.4.7). The average sliding displacements of the two column bases in the medium and tall specimens were 0.18” (5 mm) and 0.125” (3 mm), respectively. These sliding displacements represent 2.8 % and 1.25 % of the maximum displacement of the medium and tall specimens, respectively. This indicates that as the column aspect ratio increases, the shear-sliding mechanism becomes insignificant as a result of decreasing the column shear demand. To determine the other factors that could reduce the shear sliding, the behavior at the column bases in this study is compared with a previous study having a different hinge configuration.

6.5.2 Behavior of Two-Way Hinges in Previous Study[28]

To evaluate the behavior of the base hinges in this study, the observed and measured results from this study are compared with others from the previous study done on two-column specimens with architectural flares[28]. To have a valid comparison, the results from the previous study are only taken before the gap closure at the column flares. The results of specimens LFCD1 and LFCD2 from the previous study are compared with the medium specimen B2CM results in the current study since they have approximately the same aspect ratio (≈ 4.50). The results from specimen SFCD2 from the previous study are also compared with the short specimen B2CS in the current study since the two specimens almost have the same aspect ratio (≈ 2.5).

For the shear-sliding behavior, the specimens in the current study behaved much better than the previous study[28]. The base slippage in the previous study specimens was much higher than the current study specimens at the same normalized loading (Fig. 6-4). The values of loadings and the corresponding displacements in this figure were taken at 0.5, 0.75, 1.0 and 1.25 x Sylmar in both current and previous studies. As can be seen in Fig. 6-4a, the average base slippage in the previous study specimens (LFCD1 & LFCD2) is 2.5 times as the average base slippage in the current study specimen (B2CM) at 90 % of the yielding capacity. In Fig. 6-5b the average base slippage in the previous study specimen (SFCDS) reaches about 1.5 times the base slippage in the current study specimen (B2CS) at 60 % of their yielding capacity. The previous normalized comparison (Fig. 6-4) was only before specimen yielding since the gap closure in the previous study specimens started at the yielding limit.

The reduction of the base slippage in the current study specimens stems from the enhancement of the shear friction mechanism. The shear-friction equation 5.19 ($Q = \mu C$) developed in chapter 5, section 5.5.3.1 is applicable at high seismic demands (3.25 x Sylmar) by which all the hinge dowels at the column base surface reach their yielding strength. At moderate seismic loading (which existed in the comparison case in Fig. 6-4), however, half of the hinge dowels reach their yielding strength while the other half is stressed below the yield stress (could be close to the flexural neutral axis). Since the tensile stress in half of dowels is small, they could resist some of the shear force by dowel action. This is shown in the von Mises yielding criterion, which allows the steel to resist shear as long as its tensile stress is below yielding ($\sigma^2_x + 3\,\tau^2_{xy} = \sigma^2_y$). In addition, the low stressed half of the hinge dowels can add some clamping force as the shear sliding starts. This helps enhance the shear-friction resistance by changing equation 5.19 to equation 6.1.

$$Q = \mu(C_1 + \sigma_{xs} A_s/2) + \tau_{xy} A_s/2 \qquad 6.1$$

Where Q is the total shear-friction resistance, μ is the coefficient of friction at the column base, σ_{xs} is the portion of the bar tension capacity that is provided to the shear-friction mechanism, $A_s/2$ is half of the hinge-dowel area, τ is the shear resistance remaining after the effect of σ_{xs} of the half of the hinge dowels and C_1 is the flexural concrete compression force at the east column base (section 5.5.3.1) that can be taken as $f_y A_s/2$ since axial force in the east column is essentially zero.

After flexural yielding, it is required to know how much of the bar capacity should be allocated to the shear-friction mechanism and how much to the dowel action.

In the current study, the $D_{dowel} / D_{hinge\ base}$ is 0.57 (Fig. 6-4a) whereas in the previous study[28] (Fig. 6-4c), the hinge dowels were concentrated at the centroid of the column base ($D_{dowel} / D_{hinge\ base} = 0.18$). This makes all the hinge dowels in the previous study yield at the same time. In this case, the shear-friction is only resisted by equation 5.19 ($Q = \mu C_2$). Where C_2 is the flexural compression force (section 5.5.3.1) and in this case is the total hinge-dowel area, A_s, times the dowel yield stress, f_y, as a result of the low axial force in the east column. To compare between equations 5.19 and 6.1, a reasonable value of σ_{xs} should be assumed and the corresponding value of τ_{xy} can be determined. Assuming σ_{xs} is $0.8\sigma_y$, the remaining shear strength (by the von Mises yield criterion) is calculated as $0.35\sigma_y$. This makes the shear resistance, Q equal $0.803\sigma_y A_s$ after substituting μ by 0.70 (section 5.5.3). In equation 5.19, however, the shear resistance is calculated as $0.7\sigma_y A_s$. Based on this, the shear resistance in the current study (equation 6.1) is 14.7 % higher than in the previous study (equation 5.19). This is the reason of the limited shear sliding at the column bases in the current study under the moderate loadings (from 0.50 to 1.25 x Sylmar) as shown in Fig. 6-4. Based on the previous result, it is advisable to increase the number of hinge dowels and to compensate the corresponding increase in the hinge flexural capacity by reducing the hinge cross section (Fig. 6-3b). The increase in the hinge dowel number increases the tensile force in the hinge cross-section and in turn adds more compression force. This enhances the shear-friction resistance, μC. As a result of the new dowel configuration (Fig. 6-3b), more shear resistance (dowel action) for the dowels located close to the hinge neutral axis should be included. This analytical finding for the hinge configuration should be also experimentally verified.

In addition to the suggested hinge configuration, the minimum shear and bearing strengths at the hinge cross-section should also be satisfied.

6.6 Shear Capacity

Extensive experimental tests have been performed on single columns to develop equations to predict the column shear capacity[17]. The CALTRANS shear design method[1] has also been examined for a wide range of single columns[17]. It has been found that this method for shear strength is conservative as it predicted the lower bound strength of the test columns. However, for the multi-column systems the CALTRANS shear design method has not been as extensively evaluated. The results from this study will be used to examine the updated CALTRANS shear equations. The new UCSD shear equation[17] will also be used. In both methods, the angle of shear cracks is taken as 45°. In both methods, the shear capacity of each column is calculated based on the level of ductility measured experimentally (see Table 4-31). The yield displacement of each column is taken as the average yield displacement of the whole specimen after idealizing the experimental load-displacement curve. The level of axial force in each column at each loading is calculated analytically since the specimen is statically indeterminate. The change of axial load between the specimen columns is also included. For each column, the shear capacity is calculated after determining the level of axial force and ductility at each loading. In the CALTRANS and the new UCSD shear equations, the effect of strain rate (section 5.2) on the concrete and transverse reinforcement properties is included. The total shear capacity of the specimen is taken as the sum of the shear capacities for each column. Figs. 6-5, 6-6 and 6-7 show the shear capacities of tall, medium and short specimens, respectively compared with the actual shear demand calculated at each loading. In the three specimens, the point of shear failure does not exist as there is no intersection between the shear demand and capacity envelopes. This complies with the experimental results in which the three specimens did not fail in a shear mode. In the tall B2CT and middle B2CM specimens (Figs. 6-5 and 6-6), the new UCSD is more conservative than the CALTRANS shear equation while in the short specimen B2CS (Fig. 6-7), the CALTRANS shear equation becomes more conservative after the ductility level of 0.90. This finding agrees with the previous tests performed on single columns[17].

CHAPTER 7

SUMMARY, CONCLUSIONS AND RECOMMENDATIONS

7.1 Summary

To investigate the CALTRANS design criteria for two-column bridge bents, three 0.3-scale models were designed according to the updated CATRANS specifications[1]. The focus was on the column confinement, the hinge bar development length, the beam-column joint configuration and the cap-beam reinforcement details. The three specimens were identical except in their column aspect ratios. The three specimens were classified as tall, medium and short specimens. The tall and medium specimens had the column aspect ratios of 6.64 and 4.5, respectively while the short specimen had the column aspect ratio of 2.5. A preliminary dynamic analysis was performed using the RC-Shake program to choose the earthquake record that can be used in testing the three specimens. The Sylmar record from the 1994 Northridge Earthquake, was chosen as the most critical one. The three specimens were subjected to increasing amplitudes of the Sylmar record 1994. Each specimen was connected to approximately 140 channels of the data acquisition to record reinforcement strains, specimen accelerations and displacements generated during loading. The observed behavior was also recorded by marking the cracks generated after each loading. To analyze the experimental results, the three specimens were modeled using a 2D-beam model. For the tall and medium specimens, the flexural behavior at critical locations was represented by lumped flexural springs. For short specimen, additional shear springs were added to model the shear-friction mechanism at the column bases. Another model (the Strut-and-Tie-Model) was used to understand the behavior at the specimen joints and column bases.

7.2 Conclusions

The main conclusions of this study are based on the research findings detailed in chapters 4, 5 and 6. Some of these findings are based on the experimental observations while others are based on the analytical results. The experimental findings can be summarized as follows:

- The tall and medium specimens behaved satisfactorily as their behavior was controlled by flexure. They experienced large levels of ductility and drift before failure. The tall specimen (with aspect ratio of 6.64) reached the ductility and drift levels of 7.7 and 10.8 %, respectively. The medium specimen (with aspect ratio of 4.5) reached the ductility and drift levels of 5.8 and 10.2 %, respectively.
- The short specimen (with aspect ratio of 2.5), however, behaved with a combined flexural/shear mode. Before failure, the short specimen reached the ductility and drift levels of 4.3 and 4.9 %, respectively.
- As a result of the small aspect ratio of the short specimen columns, they had high shear demands at the column bases. Sliding failure at the base of

the short specimen columns precluded the columns from reaching their maximum flexural capacity.

- In all specimens, the column flexural concrete spalling was well contained and the column-confined core was almost intact at high levels of loadings.
- The cap beam in the three specimens experienced only limited cracking. Modeling the effective width of the bridge soffit and deck in the specimen caps added significant flexural capacity to the cap beam. This in turn reduced the impact of the flexural demands on the cap beam.
- Despite the simplicity of the beam-column joint details, they were sufficient to protect the joints from failure. In the three specimens, the measured and observed results assured that the joint strength was significantly higher the adjoining columns.
- During peak seismic loading levels (3.25, 3.0 and 2.5 x Sylmar for the short, medium and tall specimens), the lack of confinement close to the column hinges was translated into significant spalling at the column bases in three specimens.
- The two-way hinge details in this study were more successful than other details in a previous study in controlling the slippage at the column bases under moderate seismic loadings (from 0.5 to 1.25 x Sylmar) because the hinge steel was more distributed.

In addition to the experimental conclusions, the following conclusions from the analytical work were made.

- Using the simple analytical models (2D-beam with the lumped plasticity model) in SAP2000 and RAM Perform programs predicted the behavior of the three specimens with good correlation with the experimental results.
- Using the Takeda model in DRAIN-3DX accurately predicted the nonlinear seismic response of the flexurally dominated specimens. For the last specimen where shear was significant, the predicted response became slightly different than the actual response.
- The behavior of the column bases in the short specimen was well defined. In the east column base, the shear-friction mechanism was dominant as a result of the low axial force in the east column. A three-segment model of load versus displacement was developed from the experimental results in this study and in another study. The three-segment model can be used to interpret the shear-friction mechanism. To model this mechanism, a lumped spring carries the properties of the three-segment model can be added at the column base. In the west column base, however, the large axial force controlled the base slippage and precluded the shear-friction mechanism to form. The compression failure at the west column base was well recognized by the strut-and-tie model.

- The use of the strut-and-tie-model was useful in understanding the behavior of the beam-column joints.
- The strut-and-tie model was successful in predicting the specimen capacity. It predicted 92%, 83% and 88.5% of the short, medium and tall specimen capacities, respectively.

7.3 Recommendations

- Using the SAP2000 and RAM Perform programs is recommended for performing the nonlinear static analysis (push-over analysis). The use of RAM Perform program is considered easier than SAP2000 since it requires the moment-curvature relationships directly instead of calculating the plastic hinge rotations. Despite this advantage, care must taken in modeling the reinforcement slippage effect.
- Using the Takeda model in Drian-3DX program is recommended for predicting the nonlinear dynamic response of flexurally dominated structures. Shear models should be included in the DRAIN-3DX to work in parallel with the flexure Takeda model to accurately predict the behavior of shear/flexure structures.
- Strut-and-tie-model (STM) is a powerful and conservative design tool. It is strongly recommended to use STM to predict stresses at the beam-column joints and at the hinge bases.

- The CALTRANS shear equation is more conservative than the new UCSD shear equation. It is recommended to use this equation in the column design.
- To control slippage at the hinge bases, care must be taken in distributing the hinge dowels in the hinge cross-section. The well-distributed dowels can enhance the shear-friction resistance, which can limit the shear sliding. Increasing the column aspect ratio more than 2.5 is another alternative, if it is practical, for reducing the base shear demand and in turn can reduce the base sliding.

REFERENCES

1. CALTRANS Code, July –1999

2. Patrick N. Laplace, David H. Sanders, M. Saiid Saiidi, and Bruce Douglas, "Shake Table Testing of Flexure Dominated Reinforced Concrete Bridge Columns", Civil Engineering Department, University of Nevada, Reno, Report No. CCEER-99-13, August 1999.

3. Patrick N. Laplace, David H. Sanders, M. Saiid Saiidi, and Bruce Douglas, "Experimental Study and Analysis of Refrofitted Flexure and Shear Dominated circular Reinforced Concrete Bridge Columns Subjected to Shake Table Excitation", Civil Engineering Department, University of Nevada, Reno, Report No. CCEER-01-6, June 2001.

4. Sritharan Sri, M. J. Priestley and Seible F., "Seismic Design and Experimental Verification of Concrete Multiple Column Bridge Bents", ACI Structural Journal, Vol. 98, No. 3, May-June 2001.

5. "Improved Seismic Design Criteria for California Bridges: Provisional Recommendations", ATC-32, Applied Rechnology Council, Calif., 1996.

6. Sritharan, S., Analysis of Concrete Bridge Joints Subjected to Seismic Excitation, Doctoral Dissertation, Division of Structural Engineering, University of California at San Diego, California.

7. Jennifer L. Moore, David H. Sanders, M. Saiid Saiidi, "Shake Table Testing of two Column Bent with Hinged Bases", Civil Engineering Department, University of Nevada, Reno, Report No. CCEER 00.09, Dec.- 2000.

8. Wehbe, N., and M. Saiidi, "User's Manual for RCMC v1.2-A computer Program for Moment-Curvature Analysis of confined and Unconfined Concrete Sections", Civil Engineering Department, University of Nevada, Reno, Report No. CCEER-99-6, May 1999.

9. Prakash, V., Powell, G. H., and Cambell, S., 1993, "DRAIN-3DX: Base Program User Guide, V1.1", Structural Engineering Mechanics and Materials, Department of Civil Engineering, University of California, Berkely, November 1993.

10. Seismic Design of reinforced Concrete and Masonry Buildings, 1992, by T. Paulauy and M. J. N. Priestley, Wiley Interscience.

11. M. Saiidi, “Hysteresis Models for Reinforced Concrete”, Journal of Structural Division, ASCE, Vol. 108, No. ST5, May, 1982.

12. Strain Gage Users’ Guide, Tokyo Sokki Kenkyujo Co., Ltd.

13. M. Kulkarni, S. and P. Shah, S., “Response of Reinforced Concrete Beams at High Strain Rates”, ACI Structural Journal, Col. 95, No. 6, Nov.-Dec., 1998.

14. Mehdi Saiid and Mete A. Sozen, “Simple and complex Models for Nonlinear Seismic Response of Reinforced Concrete Structures”, University of Illinois at Urbana-Champaign, Report No PFR-78-16318, Aug. 1979.

15. Nadim I. Wehbi, M. Saiid Saiidi and David H. Sanders, “Effect of Confinement and Flares on the Seismic Performance of Reinforced Concrete Bridge Columns”, civil Engineering Department, University of Nevada, Reno, Report No. CCEER-97-1.

16. Reinforced Concrete Structures, 1975, by Park and Paulay, Wiley Interscience.

17. Kowalsky, M. J., Priestley, M. J. N., “Improved Analytical Model for Shear Strength of Circular Reinforced Concrete columns in seismic Regions”, ACI structural Journal, May-June, 2000.

18. SAP2000, Integrated Structural Analysis and design Software.

19. RAM Perform-2D, version 1.2, 1998-2000.

20. User's Manual for "wFrame", 2-D Pushover Analysis Program, 1994-1999 Mark Seyed.

21. ACI 318 (2002): Building Code Requirements for Structural Concrete and Commentary. American Concrete Institute, Farmington Hills.

22. Silva, P. F., Megally, S. and Seible, F., "Seismic Performance of Sacrificial Interior Shear Keys", ACI structural Journal, March-April 2003.

23. Dynamics of Structures: Theory and Applications to Earthquake engineering, Anil K. Chopra, 1995, Prentice-Hall, Inc.

24. Schlaich, J., Schafer, K. and Jennewein, M., "Toward a Consistent Design of Structural Concrete", PCI Journal, May-June, 1987.

25. Schlaich, J. and Anagnostou, G., Stress Field for Nodes of Strut-and –Tie Models", Journal of Structural Engineering, Vol. 116, No. 1, Jan., 1990.

26. Karl-Heinz Reineck, “Examples for the Design of Structural Concrete with Strut-and-Tie Models”, ACI international, SP-208, 2002.

27. J. B. Mander, M. J. N. Priestley and R. Park, “Theoretical Stress-Strain Model for Confined Concrete”, Journal of Structural Engineering, Vol. 114, No. 8, august, 1988.

28. Hisham Nada, David Sanders and M. Saiid Saiidi, “Seismic Performance of R/C Bridge Frames with Architectural Flared Columns”, Civil Engineering Department, University of Nevada, Reno, Report No. CCEER-03-01, January 2003.

29. M. J. N. Priestley, Frieder Seible and Gian Michele Calvi, “Seismic Design and Retrofit of Bridges”, Wiley, 1996.

30. Adrew Griezic, William D. Cook and Denis Mitchell, “Stress-Strain Characteristics of Confined Concrete in column “Hinges””, ACI structural Journal, July-August 1998.

Table 2-1: Main Differences Between Old and New Design

View of Comparison	Substandard Specimen	New Design		
		B2CT	B2CM	B2CS
Column aspect ratio	6.64	6.64	4.5	2.5
Columns confinement ratio, ρ_s	0.0017	0.00784		
Beam confinement ratio, $\rho_{s}= \rho_{x}+ \rho_y$	0.00237	0.00835	0.00835	0.00974
Column longitudinal reinf. ratio, ρ_l	1.95 %	1.95 %		
Beam longitudinal reinf. ratio	0.39 %	0.45 %		
Development length of hinge bars into the columns bases	7”	17”		
Development length of column longitudinal reinf. into the beam-column joint	14”	16”		
Confinement of column long. reinf. inside the beam-column joint	0	0.00784		

Table 3-1: Concrete Mix Design for Footings and Short Columns

Criterion	Value For one cubic yard
Cement-Nevada Type II	611 lbs (277 kg)
Water	301 lbs (137 kg)
No. 67 Stone	1425 lbs (646 kg)
Sand	1193 lbs (541 kg)
Daracem 55	1.94 lbs (0.88 kg)
Daracem 19	1.94 lbs (0.88 kg)
Concrete Design Properties	
Unit Weight	130.5 pcf (2090 kg /m^3)
Water-Cement Ratio by weight	0.50
Maximum Aggregate Size	1 / 2” (13 mm)
Air Content	1.4 %
28-Day Compressive Strength	5000 psi (35 MPa)
Slump	3” (75 mm) after Daracen 55 6.5” (163 mm) after Daracem 19

Table 3-2: Concrete Mix Design for Tall, Middle Columns and all Beams

Criterion	Value For one cubic yard
Cement-Nevada Type II	705 lbs (277 kg)
Water	305 lbs (137 kg)
No. 8 Stone	1103 lbs (646 kg)
Sand	1614 lbs (541 kg)
Master Building Micro Air	7.1 lbs (3.2 kg)
Master Building 344N	42 lbs (19 kg)
Concrete Design Properties	
Water-Cement Ratio by weight	0.43
28-Day Compressive Strength	4500 psi (31 MPa)
Slump	3.5 in. (88 mm)
Air Content	6 %
Unit Weight	138.1 pcf (2212 kg /m^3)
Maximum Aggregate Size	3/8” (9 mm)

Table 3-3: Measured Properties of Steel Samples

Bar #	Average Results	
	Yield Strength	Ultimate Strength
# 3	68.4 ksi 471 MPa	107.7 ksi 742 MPa
# 4	65.0 ksi 448 MPa	100.3 ksi 691 MPa
# 5	65.9 ksi 454 MPa	100.8 ksi 695 MPa
# 6	63.6 ksi 438 MPa	102.0 ksi 703 MPa
Gage 2 (Before Heat-Treatment)	107.0 ksi 738 MPa	117.0 ksi 807 MPa
Gage 2 (After Heat-Treatment	60.0 ksi 414 MPa	82.5 ksi 569 MPa

Table 3-4: Measured Compressive Strength of Concrete Cylinders

Structural Member of each Specimen		Test Results				
		At 7 Days	At 28 Days	At the Test Day		
				Short	Middle	Tall
All footings		3.50 ksi 24.0 MPa	4.80 ksi 33.0 MPa	5.44 ksi 37.5 MPa	5.44 ksi 37.5 MPa	5.44 ksi 37.5 MPa
Columns	**Short**	3.83 ksi 26.4 MPa	5.3 ksi 36.5 MPa	5.86 ksi 40.4 MPa	------	-------
	Middle & Tall	2.83 ksi 19.5 MPa	3.95 ksi 27.0 MPa	------	4.10 ksi 28.3 MPa	4.11 ksi 28.3 MPa
Beams	**Short**	2.83 ksi 19.5 MPa	3.95 ksi 27.0 MPa	4.00 ksi 27.6 MPa	-------- --------	------- --------
	Middle & Tall	3.01 ksi 20.8 MPa	4.77 ksi 33.0 MPa	-------- --------	4.84 ksi 33.4 MPa	4.84 ksi 33.4 MPa

Table 4-1: Testing Sequence for Specimen B2CS

Run No.	Motion	Maximum Target Shake Table Acceleration	Maximum Achieved Shake Table Acceleration	Achieved to Target
1	Snap before compensation			
2	0.20 x Sylmar	0.12g	0.14g	1.17
3	Snap after 0.20x Sylmar			
4	0.25 x Sylmar	0.15g	0.17g	1.13
5	0.50 x Sylmar	0.30g	0.26g	0.87
6	0.75 x Sylmar	0.45g	0.39g	0.87
7	1.00 x Sylmar	0.60g	0.57g	0.95
8	Snap after 1.00x Sylmar			
9	1.25 x Sylmar	0.75g	0.75g	1.00
10	1.40 x Sylmar	0.84g	0.82g	0.98
11	1.75 x Sylmar	1.05g	1.04g	0.99
12	2.00x Sylmar	1.20g	1.31g	1.09
13	Snap after 2.0 x Sylmar			
14	2.125 x Sylmar	1.28g	1.48g	1.16
15	2.25 x Sylmar	1.36g	1.53g	1.13
16	2.375 x Sylmar	1.43g	1.60g	1.12
17	2.50 x Sylmar	1.50g	1.65g	1.10
18	2.625 x Sylmar	1.58g	1.59g	1.01
19	2.75 x Sylmar	1.66g	1.60g	0.96
20	3.00 x Sylmar	1.81g	1.76g	0.97
21	3.25 x Sylmar	1.96g	1.95g	0.99

Table 4-2: Testing Sequence for Specimen B2CM

Run No.	Motion	Maximum Target Shake Table Acceleration	Maximum Achieved Shake Table Acceleration	Achieved to Target
1	Snap before compensation			
2	0.10 x Sylmar	0.06g	0.09g	1.50
3	0.20 x Sylmar	0.12g	0.15g	1.25
4	0.25 x Sylmar	0.15g	0.18g	1.20
5	0.50 x Sylmar	0.30g	0.33g	1.10
6	0.75 x Sylmar	0.45g	0.40g	0.89
7	1.00 x Sylmar	0.60g	0.51g	0.85
8	Snap after 1.00x Sylmar			
9	1.25 x Sylmar	0.75g	0.54g	0.72
10	1.40 x Sylmar	0.84g	0.66g	0.79
11	1.50 x Sylmar	0.90g	0.87g	0.97
12	1.75 x Sylmar	1.05g	1.09g	1.04
13	2.00x Sylmar	1.20g	1.27g	1.06
14	Snap after 2.0 x Sylmar			
15	2.25 x Sylmar	1.36g	1.47g	1.08
16	2.50 x Sylmar	1.51g	1.64g	1.09
17	2.75 x Sylmar	1.66g	1.71g	1.03
18	3.00 x Sylmar	1.81g	1.90g	1.05

Table 4-3: Testing Sequence for Specimen B2CT

Run No.	Motion	Maximum Target Shake Table Acceleration	Maximum Achieved Shake Table Acceleration	Achieved to Target
1	Snap after Tuning			
2	0.10 x Sylmar	0.06g	0.05g	0.83
3	0.20 x Sylmar	0.12g	0.09g	0.75
4	0.25 x Sylmar	0.15g	0.15g	1.00
5	0.50 x Sylmar	0.30g	0.23g	0.77
6	0.75 x Sylmar	0.45g	0.36g	0.80
7	0.85 x Sylmar	0.51g	0.50g	0.98
8	1.00 x Sylmar	0.60g	0.60g	1.00
9	1.25 x Sylmar	0.75g	0.80g	1.07
10	Snap after 1.25 x Sylmar			
11	1.50 x Sylmar	0.90g	0.98g	1.09
12	1.75 x Sylmar	1.05g	1.07g	1.02
13	2.00x Sylmar	1.20g	1.21g	1.01
14	Snap after 2.0 x Sylmar			
15	2.25 x Sylmar	1.36g	1.35g	0.99
16	2.50 x Sylmar	1.51g	1.55g	1.03
17	2.75 x Sylmar	1.66g	1.66g	1.00
18	Snap after 2.75 x Sylmar			

Table 4-4a: Test Summary for Short Specimen, B2CS

<table>
<tr><th rowspan="2">Loading Times Sylmar</th><th colspan="2">Columns</th><th rowspan="2">Beam-Column Joint</th><th rowspan="2">Cap Beam</th><th rowspan="2">Hinge Base</th></tr>
<tr><th>East Column</th><th>West Column</th></tr>
<tr><td>0.20</td><td colspan="5" rowspan="4">No observed cracks</td></tr>
<tr><td>0.25</td></tr>
<tr><td>0.50</td></tr>
<tr><td>0.75</td></tr>
<tr><td>1.00</td><td colspan="2">First flexural cracks appeared at plastic hinge zones</td><td></td><td rowspan="9">Considered intact</td><td></td></tr>
<tr><td>1.25</td><td></td><td></td><td></td><td></td></tr>
<tr><td>1.40</td><td></td><td>First shear cracks appeared at plastic hinge zone</td><td>First shear cracks appeared in east joint</td><td></td></tr>
<tr><td>1.75</td><td colspan="2"></td><td></td><td></td></tr>
<tr><td>2.00</td><td colspan="2">Shear cracks largely distributed along the whole column length</td><td>First shear cracks appeared in west joint</td><td></td></tr>
<tr><td>2.125</td><td></td><td></td><td></td><td></td></tr>
<tr><td>2.25</td><td></td><td></td><td></td><td></td></tr>
<tr><td>2.375</td><td></td><td></td><td></td><td></td></tr>
<tr><td>2.50</td><td>First concrete spalling occurred on the east side at plastic hinge zone</td><td></td><td></td><td></td></tr>
</table>

Table 4-4b: Test Summary for Short Specimen, B2CS

Loading Times Sylmar	Columns		Beam-Column Joint	Cap Beam	Hinge Base
	East Column	West Column			
2.625					
2.75					
3.00		Spalling started to expose the confinement reinforcement on the east side at plastic hinge zone			
3.25				Considered intact	A large piece of concrete spalled out on the west side of the west column base leaving the column longitudinal and transverse reinforcement exposed. A significant slippage 0.6" (14mm) toward the west direction occurred at the east column base
General Condition after the last loading	Shear cracks are distributed along the whole length of each column. Concrete spalling at plastic hinge zones was well contained where the transverse reinforcement only is partially exposed				

Table 4-5a: Test Summary for Middle Specimen, B2CM

Loading Times Sylmar	Columns		Beam-Column Joint	Cap Beam	Hinge Base
	East Column	West Column			
0.10	No significant cracks				
0.20	Minor flexural cracks at plastic hinge zones				
0.25	Increase of length and number of flexural cracks and distribution of cracks over larger areas				
0.50					
0.75					
1.00					
1.25	Shear cracks appeared in plastic hinge Spalling started on the east sides at plastic hinge zones		Minor shear cracks started in east and west joints		Minor concrete spalling started on the
1.40					
1.50		Spalling increased till exposing the transverse			
1.75					
2.00	Spalling increased till exposing the transverse reinforcement on the east side at plastic hinge zone	Spalling increased till exposing longitudinal reinforcement on the east side at plastic hinge zone			
2.25	Spalling increased till exposing longitudinal reinforcement on the east side at plastic hinge zone			Minor cracking occurred at the bent cap bottom close to the west side of the west column	Vertical cracking appeared on the west side of the west column base

Table 4-5b: Test Summary for Middle Specimen, B2CM

<table>
<tr><th rowspan="2">Loading Times Sylmar</th><th colspan="2">Columns</th><th rowspan="2">Beam-Column Joint</th><th rowspan="2">Cap Beam</th><th rowspan="2">Hinge Base</th></tr>
<tr><th>East Column</th><th>West Column</th></tr>
<tr><td>2.50</td><td></td><td></td><td></td><td></td><td></td></tr>
<tr><td>2.75 (Specimen leaned toward the north direction)</td><td colspan="2">Spalling increased to make the longitudinal and transverse reinforcement more visible</td><td></td><td>Cracking increased at the same location without exposing any reinforcement</td><td></td></tr>
<tr><td>3.00</td><td></td><td>Spalling deeply increased on the east side at plastic hinge zone leaving a part of longitudinal reinforcement unsupported causing buckling in this reinforcement</td><td></td><td></td><td>Concrete spalled out on the west side of the west column base</td></tr>
<tr><td>General condition after the last loading</td><td colspan="5">The flexural behavior was clearly shown in the specimen column. Concrete spalling was concentrated at plastic hinge zones of each column. Clear damage was shown on the west side of the west column base. The specimen cap beam is considered intact. The specimen leaned out-of-plane toward the north direction.</td></tr>
</table>

Table 4-6a: Test Summary for Tall Specimen, B2CT

<table>
<tr><th rowspan="2">Loading Times Sylmar</th><th colspan="2">Columns</th><th rowspan="2">Beam-Column Joint</th><th rowspan="2">Cap Beam</th><th rowspan="2">Hinge Base</th></tr>
<tr><th>East Column</th><th>West Column</th></tr>
<tr><td>0.1</td><td colspan="5">No Significant Cracks</td></tr>
<tr><td>0.2</td><td colspan="2">Minor flexural cracks at plastic hinge zones</td><td></td><td rowspan="9">Beam is considered intact</td><td rowspan="9">No significant cracks</td></tr>
<tr><td>0.25</td><td colspan="2" rowspan="5">Increase of length and number of flexural cracks and distribution of cracks over larger areas</td><td></td></tr>
<tr><td>0.50</td><td></td></tr>
<tr><td>0.75</td><td></td></tr>
<tr><td>0.85</td><td></td></tr>
<tr><td>1.0</td><td>Minor shear cracks in</td></tr>
<tr><td>1.25</td><td colspan="2">Shear cracks at plastic hinge zones of each column</td><td></td></tr>
<tr><td>1.50</td><td>First concrete spalling occurred on the west and east sides at plastic hinge zone</td><td>First concrete spalling on the east side at plastic hinge zone</td><td>Minor shear cracks in east and west joints</td></tr>
<tr><td>1.75</td><td></td><td></td><td></td></tr>
<tr><td>24.00</td><td>Spalling exposed the transverse reinforcement on the west side</td><td>First spalling occurred on the west side at plastic hinge zone</td><td></td></tr>
<tr><td>2.25</td><td></td><td>Spalling exposed the transverse reinforcement on the east side</td><td></td><td></td><td>Vertical cracks appeared on the west side of the of the west column base</td></tr>
</table>

Table 4-6b: Test Summary for Tall Specimen, B2CT

Loading Times Sylmar	Columns		Beam-Column Joint	Cap Beam	Hinge Base
	East Column	West Column			
2.50 (After this loading, the specimen leaned toward the north direction)	Spalling increased till exposing the longitudinal reinforcement on the east and west sides at plastic hinge zones	Spalling increased till exposing the longitudinal reinforcement on the east side at plastic hinge zone		Minor cracking occurred at the bent cap bottom close to the west side of the west column	Concrete spalled out the west side of the west column base till exposing the column transverse reinforcement
2.75	Spalling increased without affecting the column concrete core and without exposing any reinforcement on the west side of the west column				Concrete spalling increased on the west side of the west column base till exposing parts of the column Longitudinal reinforcement while the east column base was considered intact
General condition after the last loading	The flexural behavior was clearly shown in the specimen column. Concrete spalling was concentrated at plastic hinge zones of each column. Clear damage was shown on the west side of the west column base. The specimen cap beam is considered intact. The specimen leaned out-of-plane toward the north direction.				

Table 4-7a: Maximum Strain (micro strain) of Longitudinal Reinforcement in East Column, Specimen B2CS

Gage No		Loading = X Sylmar																
		0.2	0.25	0.5	0.75	1.0	1.25	1.4	1.75	2.0	2.125	2.25	2.375	2.5	2.625	2.75	3.0	3.25
1	+	N/A	N/A	156	513	823	1143	1466	1458	1658	1839	1974	2078	2185	2284	2407	2493	2900
	-	224	236	241	219	233	198	504	586	1167	1365	1452	1596	1711	1772	1805	1897	2117
2	+	5	20	78	144	225	300	357	501	925	1161	1282	1325	1374	1392	1413	1418	1422
	-	38	36	36	52	62	79	52	111	96	240	418	580	705	789	847	929	949
5	+	135	224	920	1424	1712	2048	2672	2639	14418	17617	19936	22401	24815	26516	26533	26062	2606
	-	118	122	137	203	258	178	472	441	328	N/A	N/A	N/A	N/A	N/A	N/A	N/A	1024
6	+	N/A	N/A	86	391	770	928	1682	1605	2823	2932	2991	3726	13842	18202	4980	5175	4285
	-	208	206	223	218	254	230	234	271	487	942	1242	1389	1268	N/A	1794	4035	534
9	+	42	71	319	693	987	1599	2205	2189	2480	2561	12790	13222	15470	17911	20074	23596	2718
	-	131	142	171	207	273	266	392	511	1231	1578	1549	N/A	N/A	N/A	N/A	47500	4615
10	+	N/A	N/A	N/A	113	326	570	734	1034	1318	1626	1695	1762	1792	1895	2010	2164	2824
	-	193	199	189	196	185	136	101	144	125	175	300	446	480	558	618	752	984
13	+	N/A	N/A	36	49	52	73	65	87	92	91	121	115	110	110	112	121	260
	-	115	114	161	187	233	273	304	273	291	220	210	223	180	141	97	43	38
14	+	3	12	38	57	68	80	69	76	351	508	598	619	645	664	671	705	684
	-	61	60	67	76	89	81	53	82	58	N/A	N/A	18	33	42	50	57	83
17	+	7	15	30	50	67	99	124	133	379	457	521	596	670	685	681	703	724
	-	11	14	17	10	4	N/A	N/A	N/A	N/A	N/A	N/A	N/A	N/A	N/A	N/A	N/A	N/A
18	+	N/A	39	287	702	944	1221	1702	1764	2711	2776	6821	12243	13696	15902	17779	20041	2203
	-	228	242	339	413	483	581	610	719	966	1337	1531	1738	N/A	N/A	N/A	N/A	N/A
19	+	66	73	162	296	456	648	751	951	1073	1208	1468	1689	1789	1892	2114	2271	2390
	-	48	71	161	194	176	120	52	57	N/A	N/A	N/A	N/A	N/A	N/A	N/A	N/A	N/A
20	+	53	110	472	976	1266	1627	2173	2210	2791	9661	13234	15142	17012	19231	21542	24467	2681
	-	251	265	391	492	578	703	759	928	1322	1455	294	N/A	N/A	N/A	N/A	N/A	N/A
25	+	147	180	375	567	791	1054	1162	1440	1589	1744	2012	2373	2453	2479	2699	4293	5652
	-	135	171	392	577	705	837	1144	1132	1637	1848	2005	2136	2174	2314	4176	6236	6615
26	+	N/A	21	276	587	793	1098	1616	1665	2357	2350	2531	11937	14109	17118	19438	21872	2413
	-	248	269	366	441	526	615	644	751	1327	1754	1917	2333	1274	N/A	N/A	N/A	N/A

Table 4-7b: Maximum Strain (micro strain) of Longitudinal Reinforcement in East Column, Specimen B2CS

Gage No		Loading= X Sylmar																
		0.2	0.25	0.5	0.75	1.0	1.25	1.4	1.75	2.0	2.125	2.25	2.375	2.5	2.625	2.75	3.0	3.25
33	+	N/A	N/A	N/A	19	42	58	29	44	19	N/A	51	175	101	122	136	176	335
	-	42	41	45	55	60	46	49	66	92	109	82	115	158	156	176	135	132
34	+	N/A	34	398	750	969	1336	1897	1961	11686	14180	16122	17457	17796	19863	21584	23645	25514
	-	279	300	393	465	539	577	665	783	829	N/A	N/A	N/A	N/A	N/A	N/A	N/A	N/A
35	+	9	9	35	46	54	70	73	123	114	94	82	83	57	57	53	50	1178
	-	18	25	24	21	21	13	5	13	N/A	N/A	N/A	9	16	11	9	N/A	4
41	+	65	78	149	279	433	702	858	1133	1321	1472	1692	1984	2061	2106	2292	2342	2381
	-	50	63	166	244	286	348	496	505	784	899	1008	1143	1242	1296	1342	1399	1451
42	+	N/A	N/A	300	699	977	1449	2139	2171	4213	8021	10921	12477	12982	14240	15268	16534	17778
	-	179	190	220	263	282	282	335	393	426	174	N/A	N/A	N/A	N/A	N/A	N/A	N/A
43	+	38	50	103	185	287	466	663	832	1029	1334	1646	1677	1725	1816	2009	2166	2251
	-	28	29	66	63	18	N/A	N/A	N/A	N/A	N/A	N/A	N/A	N/A	N/A	N/A	N/A	N/A
44	+	34	81	458	827	1103	1498	2169	2185	2986	3060	7591	11856	13757	15753	17592	19659	21589
	-	191	204	276	342	388	441	464	532	1014	1256	1276	301	N/A	N/A	N/A	N/A	N/A
49	+	N/A	N/A	N/A	8	20	52	58	59	56	58	55	57	54	57	53	58	60
	-	37	27	23	24	25	11	7	1	17	16	24	30	22	34	47	60	69
50	+	N/A	13	41	71	185	254	341	399	643	745	825	878	900	904	914	930	941
	-	26	17	26	17	N/A	N/A	N/A	N/A	N/A	N/A	N/A	N/A	N/A	N/A	N/A	N/A	N/A
51	+	N/A	N/A	N/A	N/A	N/A	22	13	30	31	19	23	9	32	54	71	69	75
	-	48	58	43	39	37	7	16	3	N/A	15	8	25	4	N/A	N/A	N/A	N/A
52	+	21	10	25	32	37	53	58	57	65	68	71	70	71	68	61	60	57
	-	N/A	N/A	N/A	N/A	N/A	N/A	N/A	N/A	N/A	N/A	N/A	N/A	N/A	N/A	N/A	N/A	11

See Figs. 2-35 and 2-36 for checking the location of each gage
(+) Tension (-) Compression

Table 4-8a: Maximum Strain (micro strain) of Longitudinal Reinforcement in West Column, Specimen B2CS

Gage No		Loading = X Sylmar																
		0.2	0.25	0.5	0.75	1.0	1.25	1.4	1.75	2.0	2.125	2.25	2.375	2.5	2.625	2.75	3.0	3.25
3	+	N/A	N/A	130	289	506	790	1105	1056	1284	1439	1580	1683	1788	1908	1985	2077	2179
	-	108	120	133	190	254	273	406	459	927	1099	1206	1295	1371	1416	1435	1440	1409
4	+	N/A	N/A	25	121	276	430	486	758	853	816	949	970	991	969	1018	1012	1056
	-	189	196	215	234	274	328	305	346	329	292	302	494	554	590	621	662	871
7	+	35	89	611	1099	1422	1815	2556	2240	14218	17220	20456	23859	28127	32533	32662	31860	24642
	-	125	130	132	214	280	293	361	355	230	N/A	N/A	N/A	N/A	N/A	N/A	N/A	N/A
8	+	N/A	N/A	173	706	1136	1463	1453	1945	2101	2210	5795	11141	11355	11038	11263	11475	10343
	-	358	363	376	405	484	496	454	500	409	285	221	N/A	N/A	N/A	N/A	N/A	N/A
11	+	N/A	N/A	101	317	583	962	1617	1555	1897	2141	2348	2491	2684	2979	9110	13618	16443
	-	123	124	134	128	80	78	253	320	705	1018	1238	1392	1514	1614	1587	956	N/A
12	+	N/A	N/A	N/A	138	393	609	682	1114	1303	1271	1510	1560	2035	2512	3100	3219	4878
	-	302	299	354	372	342	284	267	297	280	240	294	531	528	507	437	404	561
15	+	7	16	39	61	79	75	66	55	71	89	127	213	219	229	215	210	210
	-	76	79	94	106	119	135	112	140	131	86	N/A	19	N/A	N/A	N/A	N/A	N/A
16	+	N/A	N/A	N/A	N/A	N/A	N/A	N/A	N/A	14	33	11	26	17	33	48	N/A	N/A
	-	174	199	299	368	396	460	524	483	580	551	529	452	162	129	200	349	333
22	+	12	22	206	400	622	952	1502	1370	2212	2424	2466	2431	2542	10696	12317	14853	18057
	-	121	132	187	227	263	248	240	246	230	592	846	1120	1292	1325	N/A	N/A	N/A
23	+	N/A	4	159	343	597	816	929	1246	1314	1297	1344	1625	1659	1527	1567	1531	1466
	-	259	288	475	611	713	826	1094	982	1351	1441	1506	1617	1738	1748	1831	1940	2042
24	+	164	195	536	837	1082	1520	2268	2051	2857	4560	9420	11997	15408	18364	21006	25014	30190
	-	62	84	211	311	419	461	503	577	856	971	939	N/A	N/A	N/A	N/A	N/A	N/A
29	+	6	42	223	447	732	938	1028	1370	1521	1531	437	791	516	0	194	N/A	N/A
	-	285	321	604	860	1032	1247	1785	1624	2366	6891	9607	11292	12472	13444	14161	16106	19173
30	+	39	46	285	633	902	1185	1716	1518	2538	9073	11548	13111	15582	18144	20375	23714	28150
	-	114	122	181	221	258	239	262	272	269	275	N/A	N/A	N/A	N/A	N/A	N/A	N/A
31	+	25	57	215	402	649	844	898	1216	1305	1323	1402	1779	1909	1771	1975	964	N/A
	-	233	258	459	620	761	900	1249	1173	1703	1882	2203	2475	4447	7468	10689	12651	14486

Table 4-8b: Maximum Strain (micro strain) of Longitudinal Reinforcement in West Column, Specimen B2CS

Gage No		Loading= X Sylmar																
		0.2	0.25	0.5	0.75	1.0	1.25	1.4	1.75	2.0	2.125	2.25	2.375	2.5	2.625	2.75	3.0	3.25
32	+	145	162	477	832	1086	1427	2143	1930	2788	14141	13916	14083	16247	19246	21873	25723	30893
	-	168	219	401	527	680	783	885	955	1200	1607	1068	N/A	N/A	N/A	N/A	N/A	N/A
37	+	N/A	36	298	607	929	1082	1104	1436	1532	1518	1788	2079	2705	3874	5168	5220	5168
	-	366	399	631	827	1005	1212	1662	1538	2344	2528	2327	2367	4016	6945	8164	9872	13725
38	+	2	21	231	510	810	1168	1680	1472	2530	11225	12400	13246	15234	17556	19513	22517	26623
	-	158	178	247	316	378	382	430	430	432	432	N/A	N/A	N/A	N/A	N/A	N/A	N/A
39	+	N/A	12	201	514	837	1038	1039	1394	1458	1414	1499	1889	2029	2149	2321	2521	3019
	-	279	300	470	592	693	784	1053	978	1361	1628	1857	2095	2305	2451	2841	3414	4578
45	+	N/A	N/A	8	237	580	873	999	1288	1467	1475	1714	2007	2087	2112	2215	2214	2258
	-	274	288	377	450	501	595	773	765	1003	1144	1216	1280	1360	1371	1445	1505	1604
47	+	N/A	N/A	49	281	618	875	925	1206	1349	1425	1547	1858	1983	1983	2125	2158	2193
	-	172	193	282	296	327	367	472	431	574	481	536	604	693	741	828	923	990
48	+	103	119	203	279	710	1048	1677	1582	2389	2482	2542	2618	2812	2884	7060	43099	43574
	-	N/A	N/A	39	80	102	152	208	234	343	641	809	984	1147	1226	1297	1653	1607
53	+	N/A	N/A	N/A	N/A	7	7	18	22	31	26	38	23	22	24	20	26	32
	-	43	58	80	83	43	31	27	35	22	32	45	50	66	68	70	66	74
54	+	N/A	N/A	N/A	N/A	N/A	N/A	25	42	724	858	933	932	968	977	990	1028	1046
	-	25	22	22	25	22	18	15	4	N/A	N/A	N/A	N/A	N/A	N/A	N/A	N/A	N/A
55	+	24	24	23	60	62	89	93	174	266	298	366	456	546	586	642	650	692
	-	11	9	9	10	N/A	N/A	N/A	N/A	N/A	6	8	27	33	50	60	77	137
56	+	13	42	43	50	51	166	172	171	164	43052	45566	42983	43933	44765	45225	43144	42906
	-	N/A	N/A	N/A	N/A	N/A	N/A	N/A	N/A	N/A	317	3476	1267	1523	1676	995	1828	2471

See Figs. 2-35 and 2-36 for Getting the Locations of Strain Gages
(+) Tension (-) Compression

Table 4-9a: Maximum Strain (micro strain) of Transverse Reinforcement in East Column, Specimen B2CS

Gage No		Loading = X Sylmar																
		0.2	0.25	0.5	0.75	1.0	1.25	1.4	1.75	2.0	2.125	2.25	2.375	2.5	2.625	2.75	3.0	3.25
65	+	97	118	224	401	661	880	981	1217	1313	1471	1685	1992	2072	2161	2422	2694	7382
	-	45	55	153	172	169	149	82	108	44	51	9	N/A	N/A	N/A	N/A	N/A	N/A
67	+	37	45	54	57	65	80	66	74	67	76	83	89	91	87	104	99	408
	-	N/A	N/A	N/A	N/A	N/A	N/A	N/A	N/A	N/A	N/A	N/A	N/A	N/A	N/A	N/A	N/A	N/A
71	+	N/A	N/A	9	28	36	44	38	38	63	98	141	150	161	171	179	188	191
	-	40	51	49	33	N/A	N/A	N/A	N/A	N/A	N/A	N/A	N/A	N/A	N/A	N/A	N/A	N/A
72	+	5	10	17	21	27	43	37	39	45	63	82	92	85	67	53	48	50
	-	1	N/A	N/A	N/A	N/A	N/A	N/A	N/A	N/A	N/A	N/A	N/A	N/A	N/A	N/A	1	6
75	+	117	141	299	473	664	946	1078	1356	1514	1673	1846	2151	2279	2338	2425	2415	2443
	-	109	135	328	470	546	654	920	900	1287	1363	1481	1603	1600	1612	1606	1641	1697
76	+	54	59	71	81	85	108	181	278	796	935	992	1060	1122	1152	1168	1208	1304
	-	N/A	N/A	N/A	N/A	3	N/A	N/A	N/A	N/A	N/A	N/A	N/A	N/A	N/A	N/A	N/A	N/A
77	+	24	36	46	57	68	115	147	158	216	210	235	275	313	366	300	227	212
	-	N/A	N/A	N/A	N/A	N/A	N/A	N/A	N/A	N/A	N/A	N/A	N/A	N/A	N/A	N/A	N/A	N/A
81	+	6	16	42	53	57	68	74	68	222	321	384	536	646	715	802	909	996
	-	12	9	13	19	13	2	14	26	48	40	18	N/A	N/A	N/A	N/A	N/A	N/A
82	+	5	2	4	4	3	44	42	44	44	3	46	116	194	236	274	340	390
	-	47	40	42	43	42	5	7	6	43	82	84	111	122	125	162	162	191

Table 4-9b: Maximum Strain (micro strain) of Transverse Reinforcement in East Column, Specimen B2CS

Gage No		Loading = X Sylmar																
		0.2	0.25	0.5	0.75	1.0	1.25	1.4	1.75	2.0	2.125	2.25	2.375	2.5	2.625	2.75	3.0	3.25
83	+	154	188	357	535	868	1204	1332	1635	1781	1929	2174	2936	4445	4095	4942	4759	5615
	-	127	159	391	596	746	910	1270	1280	1943	2366	3315	7493	8561	9071	9344	10060	11079
84	+	7	10	15	23	31	47	52	44	54	75	109	167	270	367	446	520	587
	-	2	1	5	30	25	N/A	N/A	N/A	1	50	54	67	71	71	60	52	35
90	+	N/A	N/A	24	52	89	124	132	117	160	108	107	133	198	232	261	316	347
	-	26	29	31	14	16	N/A	N/A	N/A	N/A	17	N/A	N/A	N/A	N/A	N/A	N/A	N/A
91	+	N/A	N/A	1	3	N/A	6	6	14	72	113	75	18	N/A	42	87	149	167
	-	32	29	31	38	53	59	72	79	99	105	104	121	120	53	70	85	130
92	+	16	27	47	129	208	279	268	230	306	314	348	374	389	382	385	379	384
	-	3	N/A	3	5	N/A	N/A	N/A	N/A	N/A	N/A	N/A	N/A	N/A	1	8	34	56
97	+	8	16	52	79	86	114	368	401	718	862	949	963	955	917	930	929	955
	-	17	16	26	45	59	54	60	43	33	23	7	23	17	39	38	50	51
98	+	2	9	31	55	134	275	603	567	930	1041	1057	964	842	802	837	816	846
	-	18	15	25	36	37	20	17	N/A	N/A	N/A	10	14	34	141	181	199	224
102	+	N/A	N/A	6	21	25	38	16	5	36	73	108	147	193	216	234	260	278
	-	12	15	21	24	25	21	44	80	61	49	34	10	N/A	N/A	N/A	N/A	N/A

- See Fig. 2-35 and 2-36 for Getting the Locations of Strain Gage
- (+) Tension (-) Compression

Table 4-10a: Maximum Strain (micro strain) of Transverse Reinforcement in West Column, Specimen B2CS

Gage No		Loading= X Sylmar																
		0.2	0.25	0.5	0.75	1.0	1.25	1.4	1.75	2.0	2.125	2.25	2.375	2.5	2.625	2.75	3.0	3.25
70	+	N/A	N/A	10	31	62	89	101	97	153	204	286	956	1187	1285	1405	1702	3541
	-	37	36	46	49	40	16	23	17	3	5	N/A	N/A	N/A	N/A	N/A	N/A	N/A
73	+	N/A	N/A	N/A	N/A	N/A	6	6	8	13	8	19	344	526	573	600	654	723
	-	29	28	28	30	29	24	31	31	34	45	39	36	50	65	80	97	146
74	+	3	6	13	17	19	31	27	24	24	25	30	529	692	732	771	815	837
	-	3	N/A	N/A	N/A	N/A	N/A	N/A	N/A	N/A	N/A	N/A	74	96	105	110	110	118
78	+	4	N/A	24	43	61	78	86	89	99	76	111	146	169	202	243	291	349
	-	9	18	19	15	N/A	N/A	N/A	N/A	N/A	43	54	67	72	68	71	72	69
80	+	26	34	34	34	62	63	35	35	68	191	275	288	305	324	339	455	746
	-	1	N/A	1	1	0	0	81	100	140	132	136	139	155	162	160	164	178
86	+	N/A	N/A	N/A	N/A	N/A	N/A	N/A	N/A	N/A	N/A	N/A	N/A	N/A	N/A	N/A	N/A	N/A
	-	904	868	857	867	866	824	852	1101	890	925	939	943	1006	1147	1182	1279	1383
87	+	N/A	8	87	125	146	157	165	150	255	467	431	359	454	535	585	683	757
	-	14	3	3	N/A	N/A	N/A	N/A	N/A	N/A	N/A	N/A	N/A	N/A	N/A	N/A	N/A	N/A
88	+	49	45	53	59	71	92	104	96	118	173	221	228	265	334	409	444	409
	-	N/A	N/A	N/A	N/A	N/A	N/A	N/A	N/A	N/A	50	105	127	122	119	149	184	191
93	+	0	3	4	4	5	26	32	93	118	162	188	190	193	196	200	225	227
	-	37	28	30	52	65	43	25	30	44	44	39	38	12	9	12	12	13

Table 4-10b: Maximum Strain (micro strain) of Transverse Reinforcement in West Column, Specimen B2CS

Gage No		Loading = X Sylmar																
		0.2	0.25	0.5	0.75	1.0	1.25	1.4	1.75	2.0	2.125	2.25	2.375	2.5	2.625	2.75	3.0	3.25
94	+	N/A	N/A	N/A	N/A	19	86	80	79	131	195	219	230	269	323	353	466	626
	-	103	106	100	93	62	N/A	5	25	48	35	30	13	N/A	N/A	2	24	15
95	+	23	26	49	58	84	100	99	76	112	219	297	317	320	336	330	325	330
	-	N/A	N/A	N/A	N/A	N/A	N/A	5	N/A	25	18	8	N/A	N/A	N/A	N/A	3	18
100	+	N/A	8	16	20	57	98	123	137	403	403	437	445	479	507	521	551	579
	-	25	24	25	27	10	N/A	N/A	N/A	N/A	N/A	N/A	N/A	N/A	N/A	N/A	N/A	N/A
103	+	17	25	38	45	61	78	98	151	577	653	663	613	642	663	647	648	686
	-	N/A	N/A	N/A	4	1	N/A	8	N/A	N/A	N/A	N/A	N/A	N/A	N/A	N/A	N/A	N/A
104	+	N/A	N/A	N/A	N/A	N/A	12	2	14	223	232	246	196	214	258	257	260	297
	-	44	42	47	50	41	18	29	47	34	60	34	42	34	15	9	7	6

* See Figs. 2-35 and 2-36 for Getting the Strain Gage Locations

(+) Tension (-) Compression

Table 4-11: Maximum Strain (micro strain) of Longitudinal Reinforcement in Cap-Beam, Specimen B2CS

Gage No		Loading= X Sylmar																
		0.2	0.25	0.5	0.75	1.0	1.25	1.4	1.75	2.0	2.125	2.25	2.375	2.5	2.625	2.75	3.0	3.25
57	+	N/A	N/A	54	101	243	406	656	674	1191	1381	1496	1644	1728	1774	1818	1895	1924
	-	69	79	100	115	101	56	26	N/A	N/A	N/A	N/A	N/A	N/A	N/A	N/A	N/A	N/A
58	+	53	59	121	345	534	705	821	920	1032	1093	1087	1210	1214	1224	1236	1203	1255
	-	10	19	74	94	73	55	139	83	169	175	185	190	191	181	171	183	175
59	+	10	15	43	69	111	188	267	427	646	726	803	930	1015	1058	1106	1119	1135
	-	34	39	73	105	114	72	38	N/A	N/A	N/A	N/A	N/A	N/A	N/A	N/A	N/A	N/A
60	+	58	63	140	253	439	624	830	915	1194	1368	1437	1412	1504	1552	1529	1530	1601
	-	N/A	7	22	35	17	N/A	N/A	N/A	N/A	N/A	N/A	22	28	N/A	4	N/A	N/A
61	+	6	15	60	110	216	337	702	721	1195	1317	1375	1393	1429	1444	1477	1517	1534
	-	40	41	58	68	62	41	30	N/A	1	2	9	24	38	32	N/A	N/A	N/A
62	+	77	78	93	101	116	137	142	215	290	389	456	548	629	692	816	824	857
	-	N/A	N/A	N/A	N/A	2	0	7	N/A	7	17	28	29	22	15	N/A	N/A	N/A
64	+	84	87	102	117	170	253	453	617	1130	1266	1306	1245	1315	1391	1342	1323	1422
	-	N/A	N/A	N/A	N/A	N/A	N/A	N/A	N/A	N/A	N/A	N/A	N/A	N/A	N/A	N/A	N/A	N/A

Table 4-12: Maximum Strain (micro strain) of Transverse Reinforcement in Cap-Beam, Specimen B2CS

Gage No		Loading= X Sylmar																
		0.2	0.25	0.5	0.75	1.0	1.25	1.4	1.75	2.0	2.125	2.25	2.375	2.5	2.625	2.75	3.0	3.25
105	+	N/A	N/A	N/A	N/A	N/A	N/A	N/A	N/A	N/A	N/A	N/A	N/A	N/A	31	49	54	76
	-	25	33	53	64	68	68	89	95	127	141	153	180	189	208	237	194	196
106	+	5	4	20	25	38	52	61	59	79	65	68	67	73	80	85	93	104
	-	17	23	33	41	45	43	51	59	95	109	109	107	110	120	110	97	110
107	+	N/A	N/A	N/A	7	35	68	117	182	223	203	199	201	219	268	308	356	388
	-	28	37	43	48	55	22	14	N/A	N/A	N/A	N/A	N/A	N/A	N/A	N/A	N/A	N/A
108	+	N/A	N/A	N/A	N/A	N/A	N/A	N/A	N/A	N/A	N/A	N/A	N/A	N/A	N/A	5	8	15
	-	54	61	70	86	91	68	105	97	112	98	84	80	76	51	58	39	39
109	+	N/A	N/A	N/A	N/A	N/A	N/A	N/A	N/A	N/A	N/A	N/A	N/A	N/A	N/A	N/A	N/A	N/A
	-	45	48	48	61	67	53	71	100	86	91	85	88	86	84	93	90	97
110	+	N/A	N/A	N/A	N/A	N/A	20	68	102	134	153	153	212	360	512	682	752	871
	-	31	40	43	46	43	23	5	N/A	N/A	N/A	N/A	N/A	N/A	N/A	N/A	N/A	N/A
111	+	N/A	N/A	N/A	N/A	N/A	N/A	N/A	N/A	N/A	3	7	13	19	21	20	22	32
	-	44	46	45	49	52	43	59	56	50	63	63	70	67	64	72	71	61

See Figs. 2-35 and 2-36 for Getting the Strain Gage Locations

(+) Tension (-) Compression

Table 4-13a: Maximum Strain (micro strain) of Longitudinal Reinforcement in East Column, Specimen B2CM

Gage No.		Loading =X Sylmar														
		0.10	0.20	0.25	0.50	0.75	1.00	1.25	1.40	1.50	1.75	2.00	2.25	2.50	2.75	3.00
SG 9	+	N/A	25	130	680	888	1146	1528	1380	1672	1737	1791	1849	1909	2022	2257
	-	160	169	156	364	515	619	739	694	785	825	858	921	988	1076	1264
SG10	+	N/A	N/A	N/A	148	301	683	946	842	1019	1149	1215	1296	1353	1375	1407
	-	270	254	292	347	360	461	408	473	493	541	583	637	666	666	667
SG13	+	52	73	85	109	98	98	107	104	113	123	127	127	132	131	123
	-	117	158	188	305	363	446	440	475	430	417	427	438	391	321	83
SG17	+	196	326	424	989	1298	1967	2391	2477	2461	2600	2778	2873	2960	3059	3249
	-	112	188	256	505	785	1041	1292	1242	1339	1384	1422	1481	1540	1650	1921
SG18	+	53	291	452	1161	1946	2660	4364	3173	7840	8957	9580	10774	12167	14080	17064
	-	496	596	668	963	1145	1568	1816	1865	2038	1837	1313	1009	600	245	558
SG21	+	235	355	441	1020	1361	2104	2550	2636	2639	2854	3399	7848	8984	10450	12042
	-	217	349	435	743	1076	1526	1866	1839	1914	1968	2074	2613	3700	3980	4935
SG22	+	N/A	77	250	857	1502	2180	2871	2574	4538	6808	8386	10733	13400	17188	22684
	-	620	700	729	988	1138	1464	1969	1830	2487	3009	3221	3285	2951	2289	343
SG23	+	N/A	61	106	485	711	1116	1468	1455	1614	2155	2574	2877	3021	3122	3323
	-	136	148	166	174	145	169	209	169	277	251	355	600	816	1046	1083
SG24	+	122	365	523	1185	1835	2464	7640	4732	9711	11412	13498	16260	19161	23116	28463
	-	526	644	744	1180	1487	2115	3770	3228	4163	4077	3823	3727	3652	4446	6320
SG31	+	18	79	121	429	705	1314	1988	1897	2192	2662	2998	3418	5996	7679	8314
	-	165	189	212	237	260	264	334	263	409	520	702	1037	1300	877	681
SG32	+	121	353	508	1182	1893	2600	10553	7892	12177	14009	16495	19986	24166	30299	39025
	-	565	672	764	1143	1399	1930	3225	2713	2999	2921	4247	6261	8356	11426	15432

Table 4-13b: Maximum Strain (micro strain) of Longitudinal Reinforcement in East Column, Specimen B2CM

Gage No.		Loading =X Sylmar														
		0.10	0.20	0.25	0.50	0.75	1.00	1.25	1.40	1.50	1.75	2.00	2.25	2.50	2.75	3.00
SG37	+	507	703	831	1440	1874	2796	7273	7753	7875	8494	11508	13572	14432	13349	6662
	-	444	686	830	1296	1717	2337	9228	7687	11054	12760	15369	17531	20264	26450	40229
SG38	+	210	525	727	1483	2143	8052	13916	12174	15338	17234	19795	23088	26732	33070	40221
	-	564	656	716	936	1092	1411	140	864	322	503	710	476	86	389	2438
SG40	+	273	660	907	1788	2533	9490	16846	14393	18913	21639	25332	29270	33420	40473	40481
	-	695	842	938	1342	1631	2622	2637	4407	2371	2412	3382	4493	3175	498	10262
SG45	+	350	493	614	1370	1859	2763	4361	3865	5558	9385	13134	15889	17580	18792	20146
	-	210	347	441	841	1199	1700	2850	2353	3530	4076	4264	4964	6524	9433	12914
SG46	+	121	350	512	1215	1845	2613	10247	8594	11669	13395	15836	19913	25126	31704	40103
	-	467	541	583	742	858	1249	915	1478	649	391	83	749	2179	4617	8161
SG47	+	46	133	191	671	951	1451	1900	1874	2047	2642	9721	10620	11450	11849	12446
	-	142	137	151	140	133	149	34	82	21	6	89	3578	3712	3779	3371
SG53	+	109	208	305	858	1266	2072	2745	2682	2823	3008	6486	10282	12063	13891	15190
	-	110	160	211	394	598	922	1186	1115	1256	1316	1401	1492	1003	1180	2023
SG54	+	88	299	472	1225	1933	2653	10096	8084	11155	12501	14249	17186	21310	26793	35167
	-	346	379	410	530	613	936	576	1046	1138	1470	1831	2345	3244	4811	7215
SG57	+	6.1	10	11	17	21	142	381	310	412	463	517	552	589	642	679
	-	0.40	0.74	1.16	8.8	24	24.6	71	1.2	76	74	78	74	77	86	88
SG58	+	2.86	36	43	356	532	792	1049	1014	1070	1097	1106	1141	1189	1255	1273
	-	27	28	28	29	76	88	159	131	143	131	120	120	119	130	120

See Fig. 2-31 for Checking the Strain Gage Locations
(+) Tensile (-) Compressive

Table 4-14a: Maximum Strain (micro strain) of Longitudinal Reinforcement in West Column, Specimen B2CM

Gage No.		Loading =X* Sylmar														
		0.10	0.20	0.25	0.50	0.75	1.00	1.25	1.40	1.50	1.75	2.00	2.25	2.50	2.75	3.00
SG7	+	367	909	1288	3208	9896	16326	28460	24653	31812	35711	40166	40202	40356	43328	43328
	-	-141	-142	-139	-133	273	1883	4152	2787	5482	6997	8374	9755	13331	20482	26342
SG 8	+	N/A	143	246	1385	2801	12894	18273	17331	19923	25593	32411	38628	39915	39906	36835
	-	-707	-704	-722	-752	-759	-601	3063	2329	3894	4664	5553	6677	7787	8002	10879
SG 11	+	N/A	26	73	613	938	1385	1792	1635	1902	2041	2156	2283	2417	2628	4408
	-	-78	-77	-75	-122	-305	-377	-555	-483	-643	-738	-844	-936	-1012	-1081	-665
SG 12	+	N/A	N/A	N/A	138	322	558	800	709	860	959	1036	1132	1190	1334	1819
	-	-304	-328	-345	-378	-418	-472	-546	-524	-566	-603	-639	-664	-689	-750	-1414
SG 16	+	30	39	53	77	77	108	466	244	583	632	665	663	645	594	200
	-	-177	-258	-296	-455	-584	-607	-504	-675	-451	-419	-380	-398	-463	-1065	-2173
SG 19	+	159	306	394	893	1228	1915	2481	2440	2564	2890	3716	6032	7395	7869	7483
	-	-470	-656	-776	-1187	-1528	-1906	-2251	-2140	-2361	-2538	-2865	-3857	-5493	-5830	-5867
SG 20	+	186	437	594	1282	1968	2683	3115	2959	3734	5718	7965	9694	10878	12832	15649
	-	-344	-396	-448	-630	-756	-1003	-1174	-1156	-1205	-1221	-995	-441	-133	200	847
SG 25	+	241	406	508	1040	1327	2132	2831	2714	3145	4941	7821	8553	9738	11517	13394
	-	-428	-604	-730	-1190	-1739	-2275	-2940	-2607	-3506	-4478	-5739	-5707	-5907	-7626	-7153
SG 26	+	200	408	541	1190	1810	2597	3131	2963	3407	5282	9227	10906	14351	18979	25911
	-	-188	-224	-266	-472	-682	-919	-1216	-1156	-1323	-1732	-1641	-1191	-402	937	3703

Table 4-14b: Maximum Strain (micro strain) of Longitudinal Reinforcement in West Column, Specimen B2CM

Gage No.		Loading =X* Sylmar														
		0.10	0.20	0.25	0.50	0.75	1.00	1.25	1.40	1.50	1.75	2.00	2.25	2.50	2.75	3.00
SG 27	+	166	303	413	991	1325	2069	2553	2595	2623	2980	8626	11735	14182	16589	18565
	-	-243	-329	-410	-769	-1104	-1430	-1710	-1649	-1742	-1765	-1849	-1993	-1424	-1191	-275
SG 28	+	169	377	514	1136	1836	2592	7591	3102	9025	9927	11667	14644	18466	23790	30933
	-	-286	-354	-415	-727	-960	-1344	-1597	-1583	-1727	-1260	-1113	-971	-21	2279	5433
SG 33	+	298	485	602	1206	1559	2345	5447	7113	5824	6138	8375	8981	7293	1285	-12804
	-	-597	-842	-1001	-1604	-2100	-7840	-10853	-9004	-12443	-14312	-17342	-22554	-30924	-40306	-43307
SG 34	+	170	364	506	1258	2093	3075	11596	10985	13024	14714	16848	19938	23768	29510	38437
	-	-289	-361	-419	-631	-751	-1055	-119	-1377	221	495	1055	1961	3644	5632	9349
SG 35	+	118	233	296	737	1036	1700	2942	2447	3752	6474	8386	10231	11942	13471	15860
	-	-405	-540	-643	-1003	-1314	-1791	-3247	-2446	-5328	-6129	-6062	-5540	-5795	-7337	-11728
SG 36	+	244	508	685	1394	2286	3205	12584	11077	14256	16207	18905	23086	27756	19130	15549
	-	-385	-476	-547	-802	-950	-1367	-1288	-1652	-972	-675	-195	427	2622	4859	5503
SG 42	+	378	740	963	1781	2484	8906	15243	13689	16813	18858	21775	25823	19813	12655	10406
	-	-323	-379	-435	-619	-756	-1069	328	-351	735	1174	1932	3001	4532	4013	3180
SG 43	+	265	453	584	1199	1540	2359	4376	2981	6149	9841	13287	16354	18659	20695	22341
	-	-462	-648	-792	-1406	-1916	-2472	-4185	-3131	-5860	-6146	-6251	-6472	-6834	-7801	-5938
SG 44	+	392	775	980	1817	2465	6955	14335	12029	16359	18773	21950	25732	24316	17111	11293
	-	-425	-499	-588	-898	-1158	-1555	-1229	-2222	-630	-33	855	2190	4489	4481	4244

Table 4-14c: Maximum Strain (micro strain) of Longitudinal Reinforcement in West Column, Specimen B2CM

Gage No.		Loading =X* Sylmar														
		0.10	0.20	0.25	0.50	0.75	1.00	1.25	1.40	1.50	1.75	2.00	2.25	2.50	2.75	3.00
SG 49	+	155	289	391	986	1382	2110	4274	2989	5634	8045	11341	14174	15932	16458	18572
	-	-392	-534	-631	-1011	-1405	-1968	-4381	-3144	-5887	-6256	-6685	-7341	-8993	-12609	-19227
SG 50	+	349	653	849	1852	2571	10299	15608	13894	16715	18552	21382	25267	30085	37590	40294
	-	-333	-427	-502	-800	-994	-1438	-468	-886	-179	148	831	1889	3922	6852	10376
SG 51	+	53	94	124	311	791	1208	1349	1322	1365	1382	1435	1487	1526	1571	1602
	-	-15	-13	-8	-36	-13	-36	-45	-72	-41	-21	-10	21	60	91	119
SG 52	+	323	627	844	1868	2623	9773	13882	12153	15173	16994	19623	23710	28792	29759	20663
	-	-394	-495	-582	-995	-1290	-1950	-2387	-3240	-2243	-2043	-1997	-1650	-111	1617	2528
SG 55	+	72	167	230	661	946	1642	2352	2240	2375	2537	2919	3340	3921	5162	7087
	-	-365	-496	-587	-889	-1168	-1565	-2158	-2059	-2232	-2291	-2420	-2620	-3025	-4090	-6019
SG 56	+	105	228	340	1209	1956	2787	11309	9422	13248	15168	17442	20957	25233	31378	37317
	-	-106	-135	-167	-313	-446	-676	909	-824	1113	1347	1700	2100	2978	4336	7358
SG 59	+	18	34	40	40	14	23	30	28	30	31	44	53	52	56	55
	-	12	20	24	24	6	15	18	16	14	18	24	30	30	30	31
SG 60	+	0	10	15	15	4	7	13	13	12	24	27	29	33	35	36
	-	-5	4	7	6	-8	-9	-3	-8	-4	9	9	10	15	15	17

See Fig. 2-31 for Checking the Strain Gage Locations
(+) Tension (-) Compression

Table 4-15a: Maximum Strain (micro strain) of Transverse Reinforcement in East Column, Specimen B2CM

Gage No.		Loading =X Sylmar														
		0.10	0.20	0.25	0.50	0.75	1.00	1.25	1.40	1.50	1.75	2.00	2.25	2.50	2.75	3.00
SG69	+	N/A	N/A	N/A	N/A	N/A	N/A	N/A	N/A	N/A	N/A	N/A	N/A	N/A	N/A	N/A
	-	-41	-34	-36	-44	-65	-85	-68	-73	-63	-48	-52	-54	-55	-47	-46
SG70	+	N/A	2	8	7	4	17	22	19	17	22	26	33	27	21	6
	-	-14	-5	0	-2	-6	6	10	8	6	9	10	12	11	0	-19
SG73	+	N/A	11	14	63	48	51	47	64	38	28	16	N/A	N/A	N/A	N/A
	-	-14	-8	-10	-26	-67	-65	-49	-48	-50	-98	-154	-188	-213	-229	-253
SG74	+	20	20	20	17	13	3	N/A	N/A	N/A	N/A	N/A	N/A	N/A	N/A	N/A
	-	-11	-10	-9	-19	-34	-86	-149	-123	-161	-180	-190	-216	-231	-236	-271
SG75	+	25	43	29	51	42	25	6	20	8	4	N/A	N/A	N/A	N/A	N/A
	-	14	17	17	11	-26	-44	-103	-66	-103	-105	-121	-164	-186	-204	-220
SG79	+	N/A	N/A	9	26	15	6	N/A	N/A	N/A	N/A	N/A	N/A	N/A	N/A	N/A
	-	-51	-53	-52	-62	-73	-123	-184	-168	-222	-251	-271	-282	-297	-335	-436
SG80	+	N/A	N/A	N/A	9	5	N/A	N/A	N/A	N/A	N/A	N/A	N/A	N/A	N/A	N/A
	-	-31	-34	-29	-29	-56	-163	-279	-222	-333	-362	-416	-466	-542	-658	-734
SG81	+	29	26	28	56	27	26	26	20	106	216	314	427	562	716	919
	-	4	12	14	-2	-43	-64	-64	-63	-64	-63	-62	-93	-107	-131	-99
SG85	+	N/A	N/A	16	43	39	33	4	17	60	112	155	233	305	413	541
	-	-28	-26	-27	-42	-48	-57	-145	-110	-159	-166	-173	-187	-207	-194	-276
SG86	+	13	27	27	25	3	15	N/A	N/A	N/A	N/A	N/A	N/A	N/A	N/A	N/A
	-	-5	-4	-3	-6	-28	-85	-139	-105	-204	-303	-417	-553	-721	-1017	-1474

Table 4-15b: Maximum Strain (micro strain) of Transverse Reinforcement in East Column, Specimen B2CM

Gage No.		Loading =X Sylmar														
		0.10	0.20	0.25	0.50	0.75	1.00	1.25	1.40	1.50	1.75	2.00	2.25	2.50	2.75	3.00
SG87	+	2	18	26	41	39	15	N/A	N/A	N/A	N/A	N/A	N/A	2	78	198
	-	-35	-33	-33	-44	-63	-107	-320	-215	-384	-437	-506	-532	-510	-513	-481
SG91	+	15	17	13	18	13	25	110	123	43	66	99	300	581	1414	1250
	-	6	7	5	1	-13	-41	-152	-120	-176	-212	-233	-252	-287	-241	-585
SG92	+	0	8	12	22	N/A	N/A	N/A	N/A	N/A	N/A	N/A	N/A	N/A	N/A	139
	-	-9	-5	-7	-18	-53	-153	-344	-318	-362	-381	-382	-405	-424	-453	-406
SG93	+	N/A	N/A	N/A	N/A	N/A	N/A	N/A	N/A	N/A	N/A	N/A	196	226	N/A	N/A
	-	-259	-249	-215	-211	-174	-247	-339	-334	-420	-471	-417	-368	-450	-621	-1011
SG97	+	30	46	53	75	34	6	84	16	153	220	291	358	392	488	520
	-	-3	1	-2	-10	-39	-86	-169	-155	-179	-190	-212	-232	-239	-296	-396
SG98	+	12	17	26	61	38	125	131	120	143	149	139	158	202	232	194
	-	-9	-15	-12	-22	-17	-26	-62	-58	-67	-75	-93	-92	-68	-80	-87
SG101	+	N/A	8	9	13	12	179	155	231	120	114	119	116	102	142	283
	-	-24	-2	-7	-10	-22	-167	-178	-189	-160	-165	-173	-198	-211	-214	-175
SG102	+	23	26	29	23	33	81	N/A	22	N/A	N/A	15	30	56	62	26
	-	-7	1	0	-10	-21	-46	-119	-97	-138	-134	-135	-134	-145	-174	-226
SG105	+	0	15	13	16	58	66	50	62	32	39	41	46	40	25	51
	-	-5	8	7	8	34	28	-1	23	-23	-22	-21	-24	-41	-58	-69

See Fig. 2-32 for Checking the Strain Gage Locations
(+) Tension (-) Compression

Table 4-16a: Maximum Strain (micro strain) of Transverse Reinforcement in West Column, Specimen B2CM

Gage No.		Loading =X Sylmar														
		0.10	0.20	0.25	0.50	0.75	1.00	1.25	1.40	1.50	1.75	2.00	2.25	2.50	2.75	3.00
SG71	+	19	23	28	25	14	28	34	31	35	44	50	53	46	48	136
	-	7	8	11	-1	-18	-4	-1	-3	4	10	11	11	11	14	-25
SG72	+	82	93	86	81	24	82	266	130	309	330	335	348	358	341	105
	-	50	57	53	48	13	49	69	50	105	118	118	112	95	-46	-224
SG76	+	32	70	71	94	107	142	175	160	183	206	223	257	302	353	433
	-	19	42	42	42	42	62	70	80	58	55	49	39	36	25	16
SG77	+	2	42	35	32	54	71	102	60	141	184	242	268	298	332	328
	-	-4	27	21	17	-26	-26	-77	-53	-82	-92	-95	-121	-125	-129	-152
SG78	+	10	34	42	69	64	66	62	57	66	68	72	84	89	130	118
	-	0	17	17	14	-11	-14	-37	-13	-63	-79	-98	-99	-119	-133	-132
SG82	+	21	40	42	49	27	22	N/A	N/A	15	72	111	135	248	499	600
	-	-18	-16	-22	-34	-56	-58	-168	-112	-183	-197	-199	-213	-213	-213	-232
SG83	+	N/A	17	26	44	59	47	N/A	N/A	N/A	N/A	51	153	222	278	347
	-	-8	9	15	11	8	-214	-385	-317	-440	-490	-522	-592	-661	-859	-1016
SG84	+	21	32	34	39	26	38	N/A	29	N/A	N/A	26	128	230	275	280
	-	2	3	-2	-18	-46	-31	-126	-28	-166	-197	-225	-261	-323	-355	-454
SG88	+	52	129	150	270	353	1077	1077	1117	1131	1302	1812	3514	3112	1543	1905
	-	-15	20	15	-45	-53	324	289	280	294	231	158	206	227	234	242
SG89	+	N/A	N/A	N/A	N/A	N/A	N/A	N/A	N/A	N/A	N/A	N/A	N/A	N/A	N/A	N/A
	-	-178	-210	-189	-198	-213	-243	-277	-267	-316	-349	-374	-358	-385	-488	-593

Table 4-16b: Maximum Strains (micro strain) of Transverse Reinforcement in West Column, Specimen B2CM

Gage No.		Loading =X Sylmar														
		0.10	0.20	0.25	0.50	0.75	1.00	1.25	1.40	1.50	1.75	2.00	2.25	2.50	2.75	3.00
SG90	+	22	40	40	49	N/A	N/A	N/A	N/A	4	36	90	134	206	357	840
	-	-1	3	-3	-11	-97	-180	-179	-194	-177	-174	-192	-220	-246	-308	-441
SG94	+	10	45	57	100	119	342	476	480	495	551	337	325	357	309	397
	-	-27	-11	-9	-16	-61	-51	-32	-44	-33	-15	6	19	-18	-25	-175
SG95	+	37	65	87	126	137	181	63	93	65	148	270	331	399	388	361
	-	-15	-6	-4	1	-33	-81	-79	-91	-73	-69	-41	-9	33	1	17
SG96	+	3	26	29	28	N/A	N/A	N/A	N/A	N/A	N/A	20	58	113	179	403
	-	-20	-5	-7	-55	-109	-156	-210	-196	-224	-235	-227	-240	-195	-179	-199
SG99	+	12	31	32	33	7	44	29	36	25	27	23	1	N/A	N/A	5
	-	4	16	17	12	-9	-76	-111	-137	-114	-111	-117	-139	-148	-159	-144
SG100	+	2	4	6	15	24	62	100	104	100	105	108	184	130	136	142
	-	-10	-15	-16	-20	-21	0	30	23	24	20	16	-17	-38	-37	-20
SG103	+	N/A	N/A	N/A	N/A	N/A	N/A	48	97	N/A	1	6	17	4	N/A	N/A
	-	-71	-54	-22	-23	-44	-39	-123	-112	-156	-159	-175	-182	-221	-276	-315
SG104	+	5	53	45	44	23	49	83	93	110	131	141	156	164	201	230
	-	0	32	26	24	3	-2	-11	-20	7	23	22	4	2	9	2
SG106	+	21	49	32	43	49	74	49	66	40	33	41	59	61	69	59
	-	9	26	14	12	4	-1	-16	-19	-20	-28	-20	-15	-33	-43	-54

See Fig. 2-32 for Strain Gage Locations
(+) Tension (-) Compression

Table 4-17: Maximum Strain (micro strain) of Longitudinal Reinforcement in Cap-Beam, Specimen B2CM

Gage No.		Loading =X Sylmar														
		0.10	0.20	0.25	0.50	0.75	1.00	1.25	1.40	1.50	1.75	2.00	2.25	2.50	2.75	3.00
SG1	+	75	112	151	275	393	623	861	806	892	944	968	1002	1035	1094	1191
	-	-4	-8	-6	-30	-44	-12	28	5	48	65	77	86	98	101	102
SG2	+	-170	-176	-152	-129	-89	-74	-76	-92	-97	-120	-116	-91	-107	-124	-152
	-	-278	-287	-249	-216	-150	-125	-129	-155	-158	-198	-192	-148	-177	-211	-251
SG3	+	-1	6	11	24	-8	-29	5	-2	27	42	56	78	95	100	115
	-	-7	0	5	10	-29	-57	-16	-42	-3	15	21	32	39	47	48
SG4	+	25	52	69	181	441	1090	1545	1459	1607	1673	1730	1816	1918	2104	2260
	-	-14	-10	-10	-22	8	71	111	101	133	144	143	141	128	122	120
SG61	+	89	126	153	366	599	1039	1191	1204	1238	1294	1352	1426	1495	1592	1738
	-	26	27	29	17	47	96	132	104	155	185	209	233	260	274	296
SG62	+	378	400	427	525	682	796	927	931	1181	1251	2173	1977	3002	1930	3401
	-	225	227	230	83	147	75	239	195	242	162	306	433	412	309	-20
SG63	+	52	129	150	270	353	1077	1077	1117	1131	1302	1812	3514	3112	1543	1905
	-	-15	20	15	-45	-53	324	289	280	294	231	158	206	227	234	242
SG64	+	81	82	118	275	501	733	866	849	892	888	928	967	1007	1006	1047
	-	-3	-4	-4	-5	-5	-42	-42	-77	-42	-25	-36	-42	-38	-28	-3
SG66	+	41	54	56	56	88	-165	500	154	582	676	780	929	997	983	1227
	-	11	10	4	-32	-36	-361	-218	-322	-189	-145	-87	22	79	64	169
SG67	+	20	40	53	123	269	702	1183	1064	1274	1367	1489	1606	1710	1745	1723
	-	-28	-31	-36	-39	-15	57	188	123	202	179	181	154	144	117	42
SG68		36	59	74	102	232	505	783	742	804	811	833	872	906	941	978
		3	8	12	7	-18	-15	19	-29	27	49	56	76	122	145	165

Table 4-18: Maximum Strain (micro strain) of Transverse Reinforcement in Cap-Beam, Specimen B2CM

Gage No.		Loading =X Sylmar														
		0.10	0.20	0.25	0.50	0.75	1.00	1.25	1.40	1.50	1.75	2.00	2.25	2.50	2.75	3.00
SG107	+	-3	1	3	4	-5	-4	36	0	38	57	67	52	72	67	71
	-	-24	-29	-36	-56	-82	-91	-117	-116	-117	-114	-103	-112	-89	-88	-93
SG108	+	-4	-3	-2	-44	-66	-64	-38	-47	-18	341	702	1440	1579	1642	1602
	-	-17	-22	-23	-100	-136	-142	-96	-105	-84	-45	191	367	735	984	208
SG109	+	21	30	32	50	55	147	258	220	349	411	434	480	566	552	565
	-	10	18	19	24	-12	45	104	83	135	158	165	196	187	213	192
SG111	+	8	16	20	27	5	83	277	211	310	344	385	425	464	514	538
	-	3	9	11	15	-10	-5	66	35	73	89	95	100	106	108	112
SG112	+	-34	-26	-28	-26	-52	-37	-69	-70	-61	-47	-4	18	38	75	94
	-	-56	-48	-53	-66	-102	-159	-193	-186	-168	-148	-108	-88	-70	-33	-32
SG113	+	-54	-50	-47	-49	-78	-72	-83	-79	-87	-88	-91	-63	-68	-70	-61
	-	-93	-93	-95	-117	-165	-186	-215	-200	-204	-182	-191	-159	-178	-168	-169
SG114	+	63	84	81	83	60	75	374	280	433	480	527	576	651	723	808
	-	36	47	43	40	0	-23	60	-30	97	116	125	126	152	172	212

See Figs. 2-32 and 2-32 for Strain Gage Locations
(+) Tension (-) Compression

Table 4-19a: Maximum Strain (micro strain) of Longitudinal Reinforcement in East Column, Specimen B2CT

Gage No.		Loading =X Sylmar													
		0.10	0.20	0.25	0.50	0.75	0.85	1.00	1.25	1.50	1.75	2.00	2.25	2.50	2.75
5	+	218	939	2194	14103	10371	14987	18294	28623	39666	40881	40981	44089	44089	44089
	-	-239	-244	-380	-317	1956	2144	2478	2449	3244	5260	7609	10311	26805	26805
6	+	-125	507	1278	4550	4618	11567	13456	20852	27695	30140	33044	35504	36310	37183
	-	-440	-432	-495	-571	-9	198	2007	2108	2854	3392	3993	4817	6039	9656
9	+	20	49	237	565	587	725	901	1111	1361	1544	1650	1797	2118	2199
	-	-72	-111	-144	-64	-91	-130	-153	-229	-322	-309	-337	-405	-463	-723
10	+	21	57	125	637	717	882	979	1189	1379	1543	1632	1713	1770	1783
	-	-41	-53	-100	-68	-70	-116	-175	-244	-331	-341	-389	-422	-477	-464
13	+	72	100	79	74	88	115	107	145	228	325	368	382	385	382
	-	-121	-276	-420	-537	-529	-553	-565	-616	-513	-312	-197	-114	-25	-11
14	+	70	143	221	307	303	334	342	343	344	378	366	344	305	284
	-	-146	-214	-334	-349	-308	-330	-326	-375	-418	-368	-372	-382	-433	-420
17	+	120	361	765	1638	1615	2073	2538	3016	3417	4026	5653	6644	7143	6644
	-	-209	-378	-685	-1115	-913	-1145	-1384	-1806	-2087	-2182	-2679	-3632	-4029	-4870
18	+	77	286	719	1700	1336	1813	2314	2730	3011	3258	5834	10229	16919	22915
	-	-303	-494	-750	-1157	-1144	-1352	-1549	-1746	-1872	-2040	-2585	-2135	-1690	-942
21	+	142	438	871	1805	1770	2270	2747	5400	10621	12783	14820	15904	16091	14539
	-	-262	-470	-822	-1233	-1039	-1261	-1519	-2123	-4184	-3073	-2720	-2871	-4869	-8620
22	+	3	163	551	1326	1033	1421	1877	3195	7543	7858	9983	14092	19655	26320
	-	-267	-415	-586	-796	-797	-911	-1037	-1450	-1218	-1147	-1058	-763	-497	123

Table 4-19b: Maximum Strain (micro strain) of Longitudinal Reinforcement in East Column, Specimen B2CT

Gage No.		Loading =X Sylmar													
		0.10	0.20	0.25	0.50	0.75	0.85	1.00	1.25	1.50	1.75	2.00	2.25	2.50	2.75
23	+	4	157	577	1234	1229	1578	1999	2653	3023	4394	7723	8890	9720	8667
	-	-183	-278	-351	-572	-500	-609	-705	-963	-1425	-1729	-2000	-2154	-1965	-2468
24	+	46	262	868	1879	1446	1970	2581	7100	10439	11231	14135	19463	26534	33839
	-	-325	-568	-895	-1449	-1442	-1714	-1984	-2870	-2687	-2332	-1923	-1259	-657	502
29	+	194	585	1061	2022	1964	2519	3259	8409	13029	14955	16857	17513	16256	14808
	-	-358	-591	-963	-1425	-1177	-1433	-1711	-5283	-5464	-4583	-5308	-9133	-15602	-24607
30	+	8	249	598	1357	1074	1496	1991	3704	8546	9119	11727	16484	22874	31183
	-	-417	-602	-779	-984	-965	-1078	-1194	-1750	-2014	-1951	-1901	-1622	-1228	-156
31	+	130	396	791	1564	1529	1975	2468	4816	9898	11277	12521	13267	13909	12194
	-	-218	-364	-550	-738	-609	-691	-802	-1082	-1457	-697	-344	-482	-1564	-3530
32	+	147	540	1156	2247	1776	2407	3754	9822	14644	14991	17871	23895	33049	40249
	-	-634	-989	-1307	-1860	-1806	-2121	-3059	-4186	-5701	-6690	-7767	-7660	-5597	-3826
37	+	204	597	1066	2011	1956	2487	3143	8849	13398	15555	17938	19201	19103	17676
	-	-343	-581	-952	-1519	-1261	-1567	-1936	-6022	-8810	-8297	-9269	-12045	-17131	-24130
38	+	3	262	783	1620	1253	1733	2266	10177	14310	14633	17628	22962	31078	40433
	-	-337	-485	-676	-886	-869	-969	-1095	-1040	132	163	266	516	834	2068
39	+	217	532	975	1748	1686	2118	2677	8512	12101	13492	15127	16024	16388	14077
	-	-150	-290	-469	-681	-579	-682	-805	-1069	-453	-374	-122	-64	-507	-3242
40	+	97	517	1181	2184	1678	2285	3616	10929	16207	16563	20259	26794	37445	40261
	-	-555	-846	-1174	-1779	-1742	-2077	-2901	-4516	-7083	-7849	-8167	-7828	-7090	-5749

Table 4-19c: Maximum Strains (micro strain) of Longitudinal Reinforcement in East Column, Specimen B2CT

Gage No.		Loading =X Sylmar													
		0.10	0.20	0.25	0.50	0.75	0.85	1.00	1.25	1.50	1.75	2.00	2.25	2.50	2.75
45	+	155	437	1083	2310	2245	2934	5845	11323	15636	17538	19605	20834	21672	19986
	-	-143	-262	-491	-859	-691	-834	-1060	-1594	-1051	-894	-1056	-1693	-3172	-4621
46	+	-54	182	690	1580	1218	1710	2230	8081	12994	13559	16483	21518	28743	37722
	-	-399	-535	-661	-837	-816	-897	-991	-937	586	1036	1399	1918	2409	3696
47	+	162	394	850	1669	1613	2066	2569	6906	11358	12833	14468	15453	16013	14180
	-	-100	-201	-327	-476	-401	-457	-535	-607	535	860	1211	1676	2243	1683
48	+	24	336	1026	2084	1585	2200	2971	9459	15722	16195	19835	26179	35546	40166
	-	-450	-653	-886	-1358	-1326	-1564	-1862	-2035	-2259	-2003	-1544	-190	1388	3384
53	+	116	186	382	1280	1287	1753	2272	2714	3269	4554	7873	8838	9707	9272
	-	-5	-74	-211	-346	-281	-378	-494	-735	-1019	-1156	-1263	-967	-856	-812
54	+	21	84	413	1295	1057	1493	2031	2382	3177	3722	6793	9572	12979	16982
	-	-88	-166	-255	-378	-363	-419	-509	-692	-914	-950	-800	-57	356	753
57	+	-84	-88	-89	-85	-34	33	37	69	65	37	34	35	72	64
	-	-146	-152	-160	-156	-144	-115	-96	-56	-82	-67	-94	-118	-57	-8
58	+	-34	-44	-55	-52	-45	-33	-26	-33	-59	-24	-62	-31	-1	18
	-	-69	-85	-94	-93	-111	-93	-83	-101	-139	-110	-116	-110	-105	-60

See Fig. 2-31 for Strain Gage Locations
(+) Tensile (-) Compressive

Table 4-20a: Maximum Strains (micro strain) of Longitudinal Reinforcement in West Column, Specimen B2CT

Gage No.		Loading =X Sylmar													
		0.10	0.20	0.25	0.50	0.75	0.85	1.00	1.25	1.50	1.75	2.00	2.25	2.50	2.75
7	+	149	750	1824	14691	10811	15088	17922	24862	34370	35989	40144	40177	40328	43270
	-	-201	-218	-315	-295	3658	3814	4143	3901	4120	6002	7723	10007	13788	124
8	+	64	1175	2378	14803	13550	17306	21947	34001	28370	16683	13358	13454	13868	10261
	-	-398	-427	-631	-603	2191	2509	2489	2822	1508	-4014	-6936	-3647	-11397	-15776
11	+	-6	9	110	283	282	376	481	613	839	1036	1165	1315	1801	1612
	-	-54	-63	-37	-7	7	15	31	-16	-62	-32	-57	-81	-67	-162
15	+	20	44	29	73	94	150	196	162	185	219	207	216	215	207
	-	-131	-232	-350	-369	-319	-283	-270	-312	-299	-261	-248	-213	-137	-143
16	+	92	115	92	124	126	140	160	267	459	606	719	799	845	535
	-	-58	-134	-268	-320	-248	-278	-286	-278	-93	276	303	330	228	-303
19	+	34	316	774	1682	1638	2101	2594	3663	5631	6619	7589	8382	9144	8676
	-	-392	-609	-958	-1439	-1180	-1424	-1744	-2144	-2604	-2364	-2270	-2388	-2758	-3488
20	+	-7	234	627	1703	1326	1857	2455	3362	5912	6329	7379	10102	14355	18267
	-	-359	-569	-778	-932	-891	-1014	-1172	-1475	-1348	-1090	-776	-473	-125	304
25	+	-4	-7	-7	12	18	36	36	39	44	45	39	35	41	22
	-	-10	-15	-17	-15	-30	-1	6	-5	-1	13	-15	-10	16	-10

Table 4-20b: Maximum Strains (micro strain) of Longitudinal Reinforcement in West Column, Specimen B2CT

Gage No.		Loading =X Sylmar													
		0.10	0.20	0.25	0.50	0.75	0.85	1.00	1.25	1.50	1.75	2.00	2.25	2.50	2.75
26	+	52	245	713	1551	1252	1700	2205	2942	6902	7396	8946	12505	19384	25935
	-	-280	-434	-550	-724	-648	-717	-822	-1160	-1026	-962	-872	-891	-576	159
27	+	-114	171	516	1142	1079	1437	1807	2582	3342	6261	7561	8168	8621	8164
	-	-500	-640	-901	-1100	-984	-1110	-1283	-1604	-1916	-1932	-2171	-2226	-2581	-2556
28	+	135	381	882	1795	1423	1924	2455	3345	7560	8547	11471	15954	21543	27681
	-	-264	-475	-720	-1053	-1037	-1191	-1383	-1793	-1923	-1760	-1393	-709	-100	822
33	+	47	396	793	1540	1497	1967	3230	6302	8800	10368	12010	12323	11408	10120
	-	-539	-834	-1330	-2079	-1738	-2124	-3963	-7623	-8212	-8051	-10150	-16448	-27679	-40397
34	+	175	458	908	1752	1385	1881	2519	6640	12519	12711	16391	24568	35825	40383
	-	-287	-498	-672	-850	-845	-936	-1072	-1665	-1070	-989	-581	274	2097	6530
35	+	-106	108	444	1258	1259	1618	2020	3109	8098	8592	9645	10297	10560	9940
	-	-438	-572	-807	-993	-851	-984	-1175	-1589	-2034	-2590	-2571	-2929	-3699	-3985
36	+	114	367	826	1740	1410	1908	2523	6609	11086	11586	14482	19941	28580	39333
	-	-340	-628	-903	-1259	-1222	-1425	-1684	-3616	-3196	-3187	-3036	-2216	-1191	1080
41	+	120	591	1064	1926	1862	2370	2887	8717	11753	13522	15667	16587	17395	15823
	-	-498	-728	-1145	-1710	-1432	-1695	-2192	-5659	-8762	-8494	-10362	-14658	-21462	-42581

Table 4-20c: Maximum Strains (micro strain) of Longitudinal RFMT in West Column, Specimen B2CT

Gage No.		Loading =X Sylmar													
		0.10	0.20	0.25	0.50	0.75	0.85	1.00	1.25	1.50	1.75	2.00	2.25	2.50	2.75
42	+	185	484	1164	2206	1802	2416	3380	11332	15651	15595	18361	23655	32413	40001
	-	-245	-436	-595	-811	-750	-841	-962	-863	219	33	341	1399	1896	3524
43	+	-5	342	819	1586	1553	1916	2359	10894	12294	14024	15766	16544	16312	15015
	-	-490	-685	-976	-1348	-1196	-1365	-1666	-2411	-4007	-2955	-3313	-5023	-9230	-13115
44	+	210	537	1071	1993	1596	2216	2907	9434	14097	14693	17957	24028	33427	40302
	-	-324	-563	-856	-1263	-1193	-1361	-1618	-2529	-3408	-4212	-4861	-4572	-3733	-2568
51	+	21	229	638	1352	1324	1680	2077	4040	13171	14562	16312	17321	584	645
	-	-222	-334	-551	-832	-737	-889	-1124	-1853	-2630	-1207	-705	-502	-335	-362
52	+	230	536	1139	2141	1706	2280	3166	11561	16362	16481	19728	25911	35524	40230
	-	-166	-359	-573	-910	-895	-1083	-1300	-1283	-1824	-1812	-1571	-322	1074	3522
55	+	61	296	682	1494	1459	1956	2530	4422	10175	12173	14022	15352	17159	16392
	-	-137	-223	-393	-557	-454	-531	-628	-769	-495	1286	1773	2191	2649	3241
56	+	-33	-31	-42	-28	8	23	35	30	78	69	142	215	146	69
	-	-89	-79	-101	-101	-93	-47	-31	-21	-119	-167	-212	-290	-475	-617
60	+	-34	-43	-22	10	-1	68	116	148	172	154	107	89	111	146
	-	-65	-76	-46	-62	-59	-38	1	9	76	76	-7	-46	-39	8

See Fig. 2-32 for Strain Gage Locations
(+) Tensile (-) Compressive

Table 4-21a: Maximum Strain (micro strain) of Transverse Reinforcement in West Column, Specimen B2CT

Gage No.		Loading =X Sylmar													
		0.10	0.20	0.25	0.50	0.75	0.85	1.00	1.25	1.50	1.75	2.00	2.25	2.50	2.75
71	+	13	14	13	33	31	36	46	28	19	55	44	49	52	57
	-	-19	-39	-65	-58	-65	-60	-55	-77	-92	-56	-75	-67	-67	-45
72	+	26	25	N/A	10	12	23	50	157	211	255	275	268	134	10
	-	12	5	-35	-33	-15	-16	3	1	11	58	57	28	-47	-111
76	+	N/A	N/A	N/A	3	22	30	21	1	N/A	26	20	34	60	91
	-	-23	-27	-44	-39	-30	-5	-34	-67	-93	-90	-100	-110	-92	-88
77	+	41	37	42	53	66	72	88	143	200	112	88	64	88	111
	-	-29	-108	-128	-47	-33	-12	15	2	-45	-68	-99	-93	-91	-93
78	+	N/A	N/A	N/A	N/A	N/A	20	24	14	7	4	-8	-6	24	255
	-	-91	-91	-126	-112	-101	-44	-77	-111	-152	-169	-124	-106	-133	-140
82	+	N/A	N/A	N/A	N/A	N/A	11	5	N/A	N/A	N/A	N/A	N/A	57	190
	-	-177	-225	-309	-321	-327	-279	-300	-375	-345	-286	-265	-281	-292	-264
83	+	N/A	N/A	N/A	N/A	58	56	108	102	50	118	131	206	411	677
	-	-120	-137	-174	-167	-169	-107	-66	-26	-147	-65	-78	-140	-156	-219

Table 4-21b: Maximum Strain (micro strain) of Transverse Reinforcement in West Column, Specimen B2CT

Gage No.		Loading =X Sylmar													
		0.10	0.20	0.25	0.50	0.75	0.85	1.00	1.25	1.50	1.75	2.00	2.25	2.50	2.75
84	+	58	60	27	59	72	118	112	79	42	116	167	191	284	415
	-	36	33	7	13	24	45	48	24	-8	10	37	42	24	19
88	+	N/A	N/A	N/A	N/A	41	70	56	202	571	264	295	374	507	737
	-	-44	-66	-55	-80	-70	-28	-12	-76	-96	-111	-135	-145	-121	-163
90	+	19	33	27	74	64	89	95	83	51	175	388	637	784	906
	-	10	9	-17	-9	-8	9	2	-37	-105	-104	-160	-200	-203	-183
94	+	10	19	24	67	72	99	91	151	254	390	602	1106	1348	279
	-	-34	-75	-68	-81	-52	34	33	-78	-163	-31	-48	-88	-72	-181
95	+	7	21	45	35	N/A	11	0	N/A	N/A	N/A	N/A	N/A	N/A	N/A
	-	0	-3	-23	-38	-36	-25	-67	-207	-303	-304	-342	-388	-458	-615
96	+	44	51	54	56	42	66	63	35	N/A	N/A	N/A	18	186	142
	-	-3	-22	-41	-44	-48	-28	-50	-239	-221	-210	-256	-242	-192	-240
104	+	N/A	N/A	N/A	19	23	45	57	64	51	39	18	21	20	7
	-	-42	-51	-135	-122	-92	-5	24	17	11	-11	-58	-93	-104	-140

See Fig. 2-32 for Strain Gage Locations
(+) Tension (-) Compression

Table 4-22a: Maximum Strain (micro strain) of Transverse Reinforcement in East Column, Specimen B2CT

Gage No.		Loading =X Sylmar													
		0.10	0.20	0.25	0.50	0.75	0.85	1.00	1.25	1.50	1.75	2.00	2.25	2.50	2.75
69	+	42	47	42	58	52	82	77	107	149	227	261	257	241	242
	-	17	9	-11	-2	2	25	11	-3	4	34	54	71	81	96
70	+	6	11	2	1	11	13	39	22	11	52	49	50	51	49
	-	-2	-3	-33	-42	-33	-33	-17	-46	-19	3	-7	-10	-17	-17
73	+	N/A	N/A	N/A	N/A	N/A	N/A	N/A	N/A	N/A	N/A	N/A	N/A	N/A	N/A
	-	-138	-161	-166	-193	-183	-198	-202	-224	-233	-207	-261	-220	-195	-136
74	+	117	117	120	128	114	117	120	99	85	109	108	130	206	465
	-	71	70	67	72	69	71	73	58	30	58	49	51	42	7
75	+	51	56	34	44	46	50	48	27	13	38	27	21	6	62
	-	13	-14	-56	-73	-61	-63	-70	-94	-116	-99	-126	-171	-258	-337
79	+	172	173	77	121	114	134	105	51	N/A	N/A	42	78	90	97
	-	103	103	43	61	70	81	59	28	-29	-42	17	44	50	52
80	+	23	31	39	78	77	98	89	56	36	60	66	47	167	340
	-	12	10	-11	-4	14	30	17	-13	-45	-75	-99	-105	-109	-101
81	+	N/A	N/A	N/A	N/A	N/A	N/A	N/A	N/A	N/A	N/A	N/A	18	41	241
	-	-76	-108	-154	-183	-178	-183	-187	-218	-231	-194	-225	-236	-314	-352
85	+	52	69	51	53	53	75	73	48	-20	50	86	82	142	246
	-	-2	-30	-58	-56	-41	-32	-26	-147	-149	-119	-120	-105	-85	-115
86	+	22	22	1	18	13	24	22	75	189	228	256	287	369	421
	-	13	12	-16	-8	-12	-5	-2	-50	-119	-127	-132	-112	-84	-68

Table 4-22b: Maximum Strain (micro strain) of Transverse Reinforcement in East Column, Specimen B2CT

Gage No.		Loading =X Sylmar													
		0.10	0.20	0.25	0.50	0.75	0.85	1.00	1.25	1.50	1.75	2.00	2.25	2.50	2.75
87	+	37	37	48	24	N/A	N/A	N/A	N/A	164	424	594	691	596	483
	-	-38	-82	-90	-108	-119	-131	-154	-190	-225	-160	-129	-109	-88	-210
91	+	53	57	26	N/A	N/A	N/A	N/A	68	273	321	414	591	925	1206
	-	31	31	-83	-121	-102	-90	-99	-122	-224	-216	-201	-192	-187	-179
92	+	5	19	11	19	13	26	33	23	N/A	N/A	N/A	N/A	10	42
	-	-29	-42	-50	-41	-19	-8	-5	-95	-149	-160	-189	-210	-250	-247
93	+	N/A	N/A	N/A	N/A	N/A	9	N/A	5	406	748	1026	1138	1210	983
	-	-98	-112	-144	-125	-73	-45	-67	-82	-106	-99	-104	-76	-132	-168
97	+	3	13	9	53	79	149	196	212	209	172	194	232	282	399
	-	-24	-30	-41	-107	-77	-40	0	-11	-57	-40	-76	-79	-83	-82
98	+	N/A	N/A	25	99	52	72	116	175	232	1109	177	152	145	131
	-	-97	-103	-5	-15	-6	3	33	52	84	-141	38	2	-19	-22
101	+	1	6	12	21	22	49	195	288	347	324	341	383	434	448
	-	-6	-10	-10	-8	4	24	22	7	17	14	4	3	2	10
102	+	16	18	19	90	56	83	113	119	117	135	157	149	167	155
	-	7	8	-12	-11	17	14	-12	-35	-65	-63	-73	-76	-64	-50
105	+	N/A	N/A	N/A	N/A	N/A	7	43	158	177	187	168	167	173	169
	-	-28	-35	-60	-54	-52	-45	-50	-30	-33	-28	-52	-72	-62	-71

See Fig. 2-32 for Strain Gage Locations
(+) Tension (-) Compression

Table 4-23: Maximum Strain (micro strain) of Longitudinal Reinforcement in Cap-Beam, Specimen B2CT

Gage No.		Loading =X Sylmar													
		0.10	0.20	0.25	0.50	0.75	0.85	1.00	1.25	1.50	1.75	2.00	2.25	2.50	2.75
1	+	14	74	193	507	444	588	653	791	898	882	896	912	912	869
	-	-52	-77	-124	-110	-6	14	29	8	22	54	53	54	40	-11
2	+	102	163	338	734	754	905	1049	1230	1283	1325	1337	1347	1343	1290
	-	46	20	37	-14	79	57	14	16	19	84	65	46	39	21
3	+	104	149	226	535	525	574	555	641	744	772	763	737	711	786
	-	54	54	11	28	99	102	90	75	86	111	108	104	98	65
4	+	N/A	N/A	3	36	N/A	18	44	31	14	N/A	N/A	N/A	N/A	N/A
	-	-126	-173	-358	-719	-644	-773	-916	-1121	-1214	-1221	-1265	-1316	-1369	-1392
61	+	168	210	242	639	593	786	1354	1815	2116	2155	2295	2606	2919	3210
	-	82	38	-35	-59	63	61	101	86	224	297	284	327	349	408
62	+	114	168	259	460	475	591	689	801	855	894	904	933	913	884
	-	55	27	-12	-76	4	-3	-56	-96	-104	-58	-65	-62	-82	-77
63	+	65	106	119	397	420	658	933	1263	1506	1588	1654	1659	1668	1600
	-	9	-12	-97	-66	39	25	35	64	151	199	221	231	256	255
64	+	151	185	155	406	366	486	681	932	1043	1070	1152	1265	1306	1334
	-	74	32	-86	-126	-81	-111	-153	-209	-230	-135	-99	-42	-34	-29
65	+	87	91	91	873	780	1129	2243	3209	3765	3646	3812	4249	4856	5199
	-	-5	-94	-181	-179	-5	77	76	161	247	248	164	158	249	160
66	+	128	141	128	235	264	355	458	859	918	968	943	960	965	907
	-	75	77	46	26	81	77	54	70	171	236	195	177	199	151
67	+	76	115	141	621	683	1000	1393	2230	2895	3053	3139	3081	3087	2853
	-	19	-3	-49	-19	103	95	102	-4	60	62	61	31	-46	-176
68	+	105	113	154	287	292	341	372	830	938	960	1026	1100	1181	1238
	-	63	66	83	90	116	107	80	76	179	266	286	296	311	319

Table 4-24: Maximum Strain (micro strain) of Transverse Reinforcement in cap-Beam, Specimen B2CT

Gage No.		Loading =X Sylmar													
		0.10	0.20	0.25	0.50	0.75	0.85	1.00	1.25	1.50	1.75	2.00	2.25	2.50	2.75
107	+	36	46	5	21	19	13	25	88	129	133	142	127	132	126
	-	20	20	-35	-42	-34	-124	-60	-60	-35	-25	-41	-60	-60	-68
108	+	N/A	N/A	N/A	N/A	N/A	N/A	N/A	N/A	5	8	21	40	146	406
	-	-46	-60	-91	-117	-120	-117	-114	-129	-113	-113	-121	-122	-109	-96
109	+	48	42	10	11	0	1	N/A	N/A	N/A	29	45	64	87	108
	-	29	23	-18	-32	-33	-37	-47	-55	-60	-28	-18	-6	10	-33
111	+	39	42	18	61	75	123	251	502	611	669	690	767	734	742
	-	23	22	-3	-3	24	49	60	84	91	121	107	150	129	195
112	+	N/A	N/A	N/A	N/A	N/A	N/A	N/A	N/A	N/A	N/A	16	41	64	75
	-	-41	-45	-40	-79	-80	-88	-118	-167	-175	-207	-174	-188	-144	-176
113	+	N/A	8	N/A	N/A	N/A	N/A	N/A	N/A	0	47	83	105	128	127
	-	-25	-42	-126	-141	-122	-124	-145	-164	-169	-145	-135	-133	-136	-119
114	+	N/a	14	N/a	N/A	N/A	60	69	173	203	250	250	273	319	598
	-	-34	-54	-161	-193	-168	-119	-147	-193	-189	-88	-98	-79	-64	-55

See Figs. 2-31 and 2-32 for Strain Gage Locations
(+) Tension (-) Compression

Table 4-25: Measured Peak Forces and Peak Displacements for Specimen B2CS

Loading	Point of Peak Force				Point of Peak Displacement			
	Max. Force		Corresponding Displacement		Max. Displacement		Corresponding Force	
0.2 x Sylmar	13.00 57.80	(kips) (kN)	0.09 2.16	(in.) (mm.)	0.11 2.80	(in.) (mm.)	5.00 22.00	(kips) (kN)
0.25 x Sylmar	15.60 69.40	(kips) (kN)	0.09 2.29	(in.) (mm.)	0.12 2.90	(in.) (mm.)	6.25 27.80	(kips) (kN)
0.50x Sylmar	30.45 135.60	(kips) (kN)	0.13 3.30	(in.) (mm.)	0.14 3.60	(in.) (mm.)	15.00 66.70	(kips) (kN)
0.75 x Sylmar	42.25 187.90	(kips) (kN)	0.18 4.45	(in.) (mm.)	0.18 4.06	(in.) (mm.)	40.00 178.00	(kips) (kN)
1.0 x Sylmar	48.30 214.85	(kips) (kN)	0.21 5.40	(in.) (mm.)	0.24 6.10	(in.) (mm.)	40.00 178.00	(kips) (kN)
1.25 x Sylmar	54.60 242.90	(kips) (kN)	0.25 6.35	(in.) (mm.)	0.26 6.60	(in.) (mm.)	35.00 156.00	(kips) (kN)
1.4x Sylmar	64.00 285.00	(kips) (kN)	0.43 10.80	(in.) (mm.)	0.44 11.20	(in.) (mm.)	60.00 267.00	(kips) (kN)
1.75 x Sylmar	56.00 249.00	(kips) (kN)	0.42 10.70	(in.) (mm.)	0.42 10.70	(in.) (mm.)	56.00 249.00	(kips) (kN)
2.00 x Sylmar	75.00 334.00	(kips) (kN)	0.55 14.00	(in.) (mm.)	0.72 18.30	(in.) (mm.)	55.00 245.00	(kips) (kN)
2.125 x Sylmar	75.30 337.00	(kips) (kN)	0.74 18.80	(in.) (mm.)	0.90 22.90	(in.) (mm.)	52.50 234.00	(kips) (kN)
2.25 x Sylmar	79.00 351.00	(kips) (kN)	0.55 14.00	(in.) (mm.)	1.03 26.20	(in.) (mm.)	50.00 222.00	(kips) (kN)
2.375 x Sylmar	84.00 374.00	(kips) (kN)	0.75 19.00	(in.) (mm.)	1.17 29.70	(in.) (mm.)	50.00 222.00	(kips) (kN)
2.50 x Sylmar	79.75 355.00	(kips) (kN)	1.05 26.70	(in.) (mm.)	1.34 34.00	(in.) (mm.)	62.50 278.00	(kips) (kN)
2.625 x Sylmar	80.00 356.00	(kips) (kN)	1.20 30.50	(in.) (mm.)	1.53 38.90	(in.) (mm.)	65.00 289.00	(kips) (kN)
2.75 x Sylmar	81.76 364.00	(kips) (kN)	1.20 30.50	(in.) (mm.)	1.70 43.20	(in.) (mm.)	65.00 289.00	(kips) (kN)
3.0 x Sylmar	87.73 390.00	(kips) (kN)	1.00 25.40	(in.) (mm.)	1.94 49.40	(in.) (mm.)	62.50 279.00	(kips) (kN)
3.25 x Sylmar	92.00 409.00	(kips) (kN)	1.13 28.60	(in.) (mm.)	2.27 57.70	(in.) (mm.)	65.00 289.00	(kips) (kN)

Table 4-26: Average Dynamic Properties from Measured Data of Specimen B2CS

Loading	Stiffness		Fundamental Modal Characteristics		
			Circular Frequency, ω (rad/sec)	Cyclic Frequency, f (Hz)	Natural Period, T (sec.)
0.2 x Sylmar	17.00 2.98	(K/in) (KN/mm)	9.39	1.50	0.67
0.25 x Sylmar	24.00 4.20	(K/in) (KN/mm)	11.15	1.77	0.56
0.50x Sylmar	63.00 11.00	(K/in) (KN/mm)	18.07	2.87	0.35
0.75 x Sylmar	100.00 17.51	(K/in) (KN/mm)	22.80	3.62	0.28
1.0 x Sylmar	120.00 21.00	(K/in) (KN/mm)	24.93	3.97	0.25
1.25 x Sylmar	140.00 24.52	(K/in) (KN/mm)	26.93	4.29	0.23
1.4x Sylmar	120.00 24.52	(K/in) (KN/mm)	24.93	3.97	0.25
1.75 x Sylmar	140.00 24.52	(K/in) (KN/mm)	26.93	4.29	0.23
2.00 x Sylmar	110.00 19.26	(K/in) (KN/mm)	23.87	3.80	0.26
2.125 x Sylmar	100.00 17.51	(K/in) (KN/mm)	22.80	3.62	0.28
2.25 x Sylmar	92.00 16.11	(K/in) (KN/mm)	21.83	3.47	0.29
2.375 x Sylmar	83.00 14.53	(K/in) (KN/mm)	20.74	3.30	0.30
2.50 x Sylmar	71.00 12.43	(K/in) (KN/mm)	19.18	3.05	0.33
2.625 x Sylmar	63.00 11.00	(K/in) (KN/mm)	18.07	2.87	0.35
2.75 x Sylmar	58.00 10.16	(K/in) (KN/mm)	17.34	2.76	0.36
3.0 x Sylmar	52.00 9.11	(K/in) (KN/mm)	16.14	2.61	0.38
3.25 x Sylmar	44.00 7.71	(K/in) (KN/mm)	15.10	2.41	0.42

Table 4-27: Measured Peak Forces and Peak Displacements for Specimen B2CM

Loading	Point of Peak Force				Point of Peak Displacement			
	Max. Force		Corresponding Displacement		Max. Displacement		Corresponding Force	
0.1 x Sylmar	9.87	(kips)	0.05	(in.)	0.13	(in.)	8.25	(kips)
	43.90	(kN)	1.14	(mm.)	3.30	(mm.)	36.70	(kN)
0.2 x Sylmar	14.45	(kips)	0.15	(in.)	0.17	(in.)	12.50	(kips)
	64.00	(kN)	3.08	(mm.)	4.30	(mm.)	55.60	(kN)
0.25 x Sylmar	17.70	(kips)	0.20	(in.)	0.23	(in.)	16.00	(kips)
	79.00	(kN)	5.10	(mm.)	5.80	(mm.)	71.20	(kN)
0.50x Sylmar	28.60	(kips)	0.46	(in.)	0.46	(in.)	28.60	(kips)
	127.00	(kN)	11.70	(mm.)	11.70	(mm.)	127.00	(kN)
0.75 x Sylmar	36.20	(kips)	0.65	(in.)	0.72	(in.)	35.00	(kips)
	161.00	(kN)	16.50	(mm.)	18.30	(mm.)	156.00	(kN)
1.0 x Sylmar	43.70	(kips)	1.05	(in.)	1.12	(in.)	41.50	(kips)
	194.00	(kN)	26.70	(mm.)	28.40	(mm.)	185.00	(kN)
1.25 x Sylmar	49.50	(kips)	2.00	(in.)	2.15	(in.)	46.00	(kips)
	220.00	(kN)	50.80	(mm.)	54.60	(mm.)	205.00	(kN)
1.4x Sylmar	49.25	(kips)	1.60	(in.)	1.83	(in.)	45.00	(kips)
	219.00	(kN)	40.60	(mm.)	46.50	(mm.)	200.00	(kN)
1.50 x Sylmar	49.72	(kips)	2.15	(in.)	2.40	(in.)	45.00	(kips)
	221.00	(kN)	54.60	(mm.)	61.00	(mm.)	200.00	(kN)
1.75 x Sylmar	48.40	(kips)	2.40	(in.)	2.65	(in.)	45.00	(kips)
	215.00	(kN)	61.00	(mm.)	67.00	(mm.)	200.00	(kN)
2.00 x Sylmar	47.70	(kips)	3.00	(in.)	3.00	(in.)	46.25	(kips)
	212.00	(kN)	76.00	(mm.)	76.00	(mm.)	206.00	(kN)
2.25 x Sylmar	48.62	(kips)	2.88	(in.)	3.50	(in.)	47.50	(kips)
	216.00	(kN)	73.00	(mm.)	89.00	(mm.)	211.00	(kN)
2.50 x Sylmar	49.70	(kips)	4.00	(in.)	4.10	(in.)	47.50	(kips)
	221.00	(kN)	102.00	(mm.)	104.00	(mm.)	211.00	(kN)
2.75 x Sylmar	50.20	(kips)	4.50	(in.)	5.00	(in.)	47.50	(kips)
	223.00	(kN)	114.00	(mm.)	127.00	(mm.)	211.00	(kN)
3.0 x Sylmar	49.00	(kips)	5.50	(in.)	6.34	(in.)	45.00	(kips)
	218.00	(kN)	140.00	(mm.)	161.00	(mm.)	200.00	(kN)

Table 4-28: Average Dynamic Properties from Measured Data of Specimen B2CM

Loading	Stiffness		Fundamental Modal Characteristics		
			Circular Frequency, ω (rad/sec)	Cyclic Frequency, f (Hz)	Natural Period, T (sec.)
0.1 x Sylmar	54.00 9.46	(K/in) (KN/mm)	16.73	2.66	0.38
0.2 x Sylmar	58.00 10.16	(K/in) (KN/mm)	17.34	2.76	0.36
0.25 x Sylmar	62.00 10.86	(K/in) (KN/mm)	17.90	2.85	0.35
0.50x Sylmar	66.00 11.56	(K/in) (KN/mm)	18.49	2.94	0.34
0.75 x Sylmar	54.00 9.46	(K/in) (KN/mm)	16.73	2.66	0.38
1.0 x Sylmar	44.00 7.70	(K/in) (KN/mm)	15.10	2.40	0.42
1.25 x Sylmar	32.00 5.60	(K/in) (KN/mm)	12.88	2.05	0.49
1.4x Sylmar	27.00 4.73	(K/in) (KN/mm)	11.83	1.88	0.53
1.50 x Sylmar	24.00 4.20	(K/in) (KN/mm)	11.15	1.77	0.56
1.75 x Sylmar	22.00 3.85	(K/in) (KN/mm)	10.68	1.04	0.59
2.00 x Sylmar	19.00 3.33	(K/in) (KN/mm)	9.92	1.58	0.63
2.25 x Sylmar	16.00 2.80	(K/in) (KN/mm)	9.10	1.45	0.69
2.50 x Sylmar	14.00 2.45	(K/in) (KN/mm)	8.52	1.36	0.74
2.75 x Sylmar	11.00 1.93	(K/in) (KN/mm)	7.55	1.20	0.83
3.0 x Sylmar	8.30 1.45	(K/in) (KN/mm)	6.56	1.04	0.96

Table 4-29: Measured Peak Forces and Peak Displacements for Specimen B2CT

Loading	Point of Peak Force				Point of Peak Displacement			
	Max. Force		Corresponding Displacement		Max. Displacement		Corresponding Force	
0.1 x Sylmar	5.80	(kips)	0.12	(in.)	0.13	(in.)	4.50	(kips)
	25.80	(kN)	2.90	(mm.)	3.28	(mm.)	20.00	(kN)
0.2 x Sylmar	10.83	(kips)	0.15	(in.)	0.30	(in.)	9.00	(kips)
	48.20	(kN)	3.80	(mm.)	7.60	(mm.)	40.00	(kN)
0.25 x Sylmar	16.00	(kips)	0.50	(in.)	0.52	(in.)	15.00	(kips)
	71.20	(kN)	12.70	(mm.)	13.20	(mm.)	67.00	(kN)
0.50x Sylmar	22.80	(kips)	1.00	(in.)	1.09	(in.)	22.50	(kips)
	101.40	(kN)	25.40	(mm.)	27.50	(mm.)	100.00	(kN)
0.75 x Sylmar	20.92	(kips)	0.75	(in.)	0.90	(in.)	17.50	(kips)
	93.00	(kN)	19.10	(mm.)	22.90	(mm.)	78.00	(kN)
0.85 x Sylmar	24.60	(kips)	1.00	(in.)	1.20	(in.)	21.25	(kips)
	109.40	(kN)	25.40	(mm.)	30.50	(mm.)	95.00	(kN)
1.0 x Sylmar	27.80	(kips)	1.25	(in.)	1.60	(in.)	25.00	(kips)
	124.00	(kN)	32.00	(mm.)	40.60	(mm.)	111.00	(kN)
1.25 x Sylmar	30.70	(kips)	1.88	(in.)	2.50	(in.)	30.00	(kips)
	136.50	(kN)	48.00	(mm.)	63.50	(mm.)	133.00	(kN)
1.50 x Sylmar	32.60	(kips)	2.75	(in.)	3.51	(in.)	30.00	(kips)
	145.00	(kN)	70.00	(mm.)	89.00	(mm.)	133.00	(kN)
1.75 x Sylmar	31.10	(kips)	3.00	(in.)	3.60	(in.)	28.00	(kips)
	138.00	(kN)	76.00	(mm.)	91.00	(mm.)	125.00	(kN)
2.00 x Sylmar	31.00	(kips)	3.50	(in.)	4.20	(in.)	30.00	(kips)
	138.00	(kN)	89.00	(mm.)	107.00	(mm.)	133.00	(kN)
2.25 x Sylmar	32.10	(kips)	5.25	(in.)	5.50	(in.)	30.00	(kips)
	143.00	(kN)	133.00	(mm.)	140.00	(mm.)	133.00	(kN)
2.50 x Sylmar	33.00	(kips)	5.50	(in.)	7.50	(in.)	30.00	(kips)
	147.00	(kN)	140.00	(mm.)	190.50	(mm.)	133.00	(kN)
2.75 x Sylmar	33.23	(kips)	7.50	(in.)	10.00	(in.)	27.50	(kips)
	148.00	(kN)	190.00	(mm.)	254.00	(mm.)	122.00	(kN)

Table 4-30: Average Dynamic Properties from Measured Data of Specimen B2CT

Loading	Stiffness		Fundamental Modal Characteristics		
			Circular Frequency, ω (rad/sec)	Cyclic Frequency, f (Hz)	Natural Period, T (sec.)
0.1 x Sylmar	41.00 7.18	(K/in) (KN/mm)	14.60	2.32	0.43
0.2 x Sylmar	44.00 7.71	(K/in) (KN/mm)	15.10	2.40	0.42
0.25 x Sylmar	38.00 6.65	(K/in) (KN/mm)	14.00	2.23	0.45
0.50x Sylmar	25.00 4.38	(K/in) (KN/mm)	11.40	1.82	0.55
0.75 x Sylmar	22.00 3.85	(K/in) (KN/mm)	10.70	1.70	0.59
0.85 x Sylmar	21.00 3.68	(K/in) (KN/mm)	10.40	1.66	0.60
1.0 x Sylmar	18.00 3.15	(K/in) (KN/mm)	9.66	1.54	0.65
1.25 x Sylmar	14.00 2.45	(K/in) (KN/mm)	8.52	1.36	0.74
1.50 x Sylmar	9.40 1.65	(K/in) (KN/mm)	7.00	1.11	0.90
1.75 x Sylmar	8.30 1.45	(K/in) (KN/mm)	6.56	1.04	0.96
2.00 x Sylmar	7.20 1.26	(K/in) (KN/mm)	6.11	0.97	1.03
2.25 x Sylmar	6.20 1.09	(K/in) (KN/mm)	5.67	0.90	1.11
2.50 x Sylmar	4.80 0.84	(K/in) (KN/mm)	5.00	0.79	1.26
2.750 x Sylmar	3.30 0.58	(K/in) (KN/mm)	4.13	0.66	1.52

Table 4-31: Bilinear Representation of Dynamic Force-Displacement Relations

Specimen	P_y		Δ_y		P_{max}		Δ_{max}		μ_Δ
	kips	kN	in.	mm.	kips	kN	in.	mm.	
Short Specimen, B2CS	80.0	356.0	0.4	10.8	87.0	387.0	1.7	43.4	4.3
Middle Specimen, B2CM	48.0	214.0	1.1	26.7	50.4	224.0	6.4	161.0	5.8
Tall Specimen, B2CT	30.8	137.0	1.3	31.8	33.4	148.0	10.0	254.0	7.7

Table 5-1a: Strain Rate Effect on Rebar Yield Strength in Specimen B2CS

Location		SG #	Record (x Sylmar)	Max. Strain (με)	Max. Strain Rate (με /sec.)	Average Cross-Section Strain Rate	Yield Strength increase (%)
West Column	Plastic Hinge Zone	30	1.75	+1518	+24400	+32200	24.90
		32	1.75	+1930	+40000		
	Base	7	1.25	+1815	+38000	+38000	25.30
East Column	Plastic Hinge Zone	26	1.75	+1665	+27900	+27900	24.50
		28 (bad)	---------	---------	---------		
	Base	5	1.25	+2048	+37500	+37500	25.30
Beam Cross-Section	East Section	57	3.25	+1924	+19100	+19100	23.60

Table 5-1b: Strain Rate Effect on Concrete Strength in Specimen B2CS

Location		SG #	Record (x Sylmar)	Max. Strain (με)	Max. Strain Rate (με /sec.)	Average Cross-Section Strain Rate	Compressive Strength increase (%)
West Column	Plastic Hinge Zone	29	1.75	-1624	-40000	-37500	23.00
		31	2.25	-2203	-35000		
	Base	8	1.75	-500	-33500	-33500	23.00
East Column	Plastic Hinge Zone	25	2.5	-2174	-50000	-50000	23.75
		27 (bad)	---------	---------	---------		
	Base	6	2.75	-1794	-50000	-50000	23.75
Beam Cross-Section	East Section	58	2.50	-191	-15000	-15000	21.10

Table 5-2a: Strain Rate Effect on Rebar Yield Strength in Specimen B2CM

Location		SG #	Record (x Sylmar)	Max. Strain (με)	Max. Strain Rate (με /sec.)	Average Cross-Section Strain Rate	Yield Strength increase (%)
West Column	Plastic Hinge Zone	34	0.75	+2093	+21000	+21500	24
		36	0.75	+2286	+22000		
	Base	7	0.25	+1288	+14500	+14500	22.6
East Column	Plastic Hinge Zone	30	0.75	+1820	+20800	+20900	23.8
		32	0.75	+1893	+21000		
	Base	5 (bad gage)	----------	----------	----------	----------	----------
Beam Cross-Section	East Section	61	2.50	+1495	+7700	+7700	21.2

Table 5-2b: Strain Rate Effect on Concrete Strength in Specimen B2CM

Location		SG #	Record (x Sylmar)	Max. Strain (με)	Max. Strain Rate (με /sec.)	Average Cross-Section Strain Rate	Compressive Strength increase (%)
West Column	Plastic Hinge Zone	33	0.75	-2100	-20900	-20950	21.8
		35	1.0	-1791	-21000		
	Base	8	0.50	-752	-18000	-18000	21.5
East Column	Plastic Hinge Zone	29	1.0	-692	-23000	-18300	21.5
		31	2.50	-1300	-13600		
	Base	6 (Bad gage)	----------	----------	----------	----------	----------
Beam Cross-Section	West Section	64	1.40	-77	-3800	-3800	18

Table 5-3a: Strain Rate Effect on Rebar Yield Strength in Specimen B2CT

Location		SG #	Record (x Sylmar)	Max. Strain (με)	Max. Strain Rate (με /sec.)	Average Cross-Section Strain Rate	Yield Strength increase (%)
West Column	Plastic Hinge Zone	34	0.85	+1881	+18000	+18000	23
		36	0.85	+1908	+18000		
	Base	7	0.25	+1824	+26000	+26000	24
East Column	Plastic Hinge Zone	30	1.00	+1991	+20000	17500	23
		32	0.75	+1776	+15000		
	Base	5	0.25	+2194	+30000	+30000	25
Beam Cross-Section	East Section	61	1.75	+2155	+12900	+12900	22.5

Table 5-3b: Strain Rate Effect on Concrete Strength in Specimen B2CT

Location		SG #	Record (x Sylmar)	Max. Strain (με)	Max. Strain Rate (με /sec.)	Average Cross-Section Strain Rate	Compressive Strength increase (%)
West Column	Plastic Hinge Zone	33	0.85	-2124	-18400	-24200	22
		35	1.50	-2034	-30000		
	Base	8	0.25	-631	-30000	-30000	23
East Column	Plastic Hinge Zone	29	1.00	-1711	-25000	-42500	23.4
		31	2.50	-1564	-60000		
	Base	6	0.50	-571	-35000	-35000	23
Beam Cross-Section	East Section	62	1.50	-104	-4000	-4000	18

Table 5-4: Forces Generated at each Column Boundary at the Maximum Lateral Force, k (kN) & k.in (kN.m)

Location Of Cross-Section		Specimen Columns								
		Tall Specimen			Middle Specimen			Short Specimen		
		Yield Moment	Axial Force	Shear Force	Yield Moment	Axial Force	Shear Force	Yield Moment	Axial Force	Shear Force
East Column	Top	1286 (143)	3.0 (13)	16.5 (73)	1250 (141)	1.7 (7.6)	24.15 (107)	1305 (145)	-4.0 (-18)	45 (200)
	Bottom	250 (28)	3.0 (13)	16.5 (73)	250 (28)	1.7 (7.6)	24.15 (107)	275 (30.5)	-4.0 (-18)	45 (200)
West Column	Top	1450 (161)	71.5 (318)	19.84 (88)	1450 (161)	72.8 (324)	29.5 (131)	1525 (169)	78.5 (349)	56.6 (252)
	Bottom	395 (44)	71.5 (318)	19.84 (88)	410 (46)	72.8 (324)	29.5 (131)	455 (50.5)	78.5 (349)	56.6 (252)

Table 5-5: Design Procedures of Strut-and-Tie Model for Tall Specimen Columns

Location	Type	Member ID	Demand k (kN)	Capacity k (kN)	Capacity / Demand	Column Shear Capacity, k (kN)	System Shear Capacity, k (kN)
East Column	Struts	1-2	154 (685)	115 (512)	0.75	12.4 (55.1)	28.9 (129)
		2-5	22.8 (101)	111 (494)	4.87		
		3-4	69.5 (309)	62 (276)	0.89		
	Ties	5-1	16.5 (73.4)	21.5 (96)	1.31		
	Nodes	Node 2	170 (756)	214 (952)	1.26		
West Column	Struts	7-8	202 (898)	167 (742)	0.83	16.5 (73.4)	
		7-9	28.1 (125)	137 (609)	4.88		
		10-11	105 (467)	94 (420)	0.90		
	Ties	11-6	9.8 (43.6)	16.8 (74.7)	1.71		
	Nodes	Node 7	222 (987)	258 (1142)	1.16		

Table 5-6: Design Procedures of Strut-and-Tie Model in Medium Specimen Columns

Location	Type	Member ID	Demand k (kN)	Capacity k (kN)	Capacity/ Demand	Column Shear Capacity, k (kN)	System Shear Capacity, k (kN)
East Column	Struts	1-2	145 (645)	123.5 (549)	0.86	20.6 (91.8)	41 (182) at $V_c = 0$
		2-5	33.4 (149)	155 (688)	4.64		
		3-4	67 (298)	58 (257)	0.87		
	Ties	5-1	24.0 (107)	22.2 (98.7)	0.93		
	Nodes	Node 2	168 (747)	206 (916)	1.23		
West Column	Struts	7-8	194 (863)	174 (774)	0.90	20.4 (90.5) at $V_c=0$ 23.9 (106) at $V_c \neq 0$	44.5 (198) at $V_c \neq 0$
		7-9	41 (182)	155 (688)	3.78		
		10-11	110 (489)	89 (396)	0.81		
	Ties	9-8	29.5 (131)	20.4 (90.7) at $V_c=0$ 44.0 (196) at $V_c \neq 0$	0.69 1.49		
	Nodes	Node 7	222 (987)	259 (1152)	1.17		

Table 5-7: Design Procedures of Strut-and-Tie Model in Short Specimen B2CS

Location	Type	Member ID	Demand k (kN)	Capacity k (kN)	Capacity / Demand	Column Shear Capacity, k (kN)	System Shear Capacity, k (kN)
East Column	Struts	1-2	135 (600)	142 (632)	1.05	20.3 (90.0) at V_c=0	40.7 (181) at V_c=0
		2-5	64 (285)	156 (694)	2.44		
		3-4	80 (356)	58 (260)	0.73		
	Ties	5-1	45 (200)	20.4 (90.6) at V_c=0	0.45	33 (146) at $V_c \neq 0$	
				44 (196) at $V_c \neq 0$	0.98		
	Nodes	Node 2	180 (800)	244 (1086)	1.36		
West Column	Struts	7-8	174 (774)	264 (1174)	1.52	20.4 (90.6) at V_c=0	75.5 (336) at $V_c \neq 0$
		7-9	80 (356)	256 (1140)	3.2		
		10-11	128 (569)	102 (454)	0.80		
	Ties	6-12	60.4(269)	21.5 (96) at V_c=0	0.36	42.5 (189) at $V_c \neq 0$	
				45 (200) at $V_c \neq 0$	0.75		
	Nodes	Node 7	230 (1023)	325 (1446)	1.41		

Table 5-8: Design of Strut-and-Tie Model in Short Specimen Beam

Location	Type	Member ID	Demand k (kN)	Capacity k (kN)	Capacity / Demand
East Beam-Column Joint	Struts	2-7 & 2-6	245 (1090)	365 (1624)	1.50
	Ties	1-2	215 (956)	273 (1214)	1.17
		1-3	71 (316)	56.4 (251) at $V_c = 0$	0.79
				90.0 (400) at $V_c \neq 0$	1.27
West Beam-Column Joint	Struts	8-9 & 8-10	222 (987)	327 (1454)	1.47
		8-11	81 (360)	100 (447)	1.23
	Ties	4-5	54 (240)	56 (251)	1.04

Table 5-9: Strut-and-Tie Model Evaluation in Three Specimens

Specimen	STM Predicted Capacity, k (kN)	Experimental Capacity, k (kN)	Experimental / Predicted
Short Specimen, B2CS	75.5 (336)	82 (365)	1.09
Medium Specimen, B2CM	41 (182)	49 (218)	1.20
Tall Specimen, B2CT	28.9 (129)	32.5 (145)	1.13

Table 6-1a: Observed Performance at the East Beam-Column Joint

Specimen	At the First Joint Cracking				At the Maximum Loading			
	Loading	Displacement Ductility	Crack Direction	Crack Type	Loading (X Sylmar)	Displacement Ductility	Total No. Of Cracks	Type of Cracks
B2CS	1.40	1.0	To Open the Joint	Diagonal, Short and Hair	3.25	4.0	3	Narrow, Short and Diagonal
B2CM	1.25	1.90			3.0	6.0	5	
B2CT	1.0	1.0			2.75	8.0	3	

Table 6-1b: Observed Performance at the West Beam-Column Joint

Specimen	At the First Joint Cracking				At the Maximum Loading			
	Loading (X Sylmar)	Displacement Ductility	Crack Direction	Crack Type	Loading (X Sylmar)	Displacement Ductility	No. Of Cracks	Type of Cracks
B2CS	2.0	1.30	To Close the Joint	Diagonal, Short and Hair	3.25	4.0	3	Narrow, Short and Diagonal
B2CM	2.0	2.8			3.0	6.0	2	
B2CT	1.50	2.2	To Open the Joint		2.75	8.0	3	

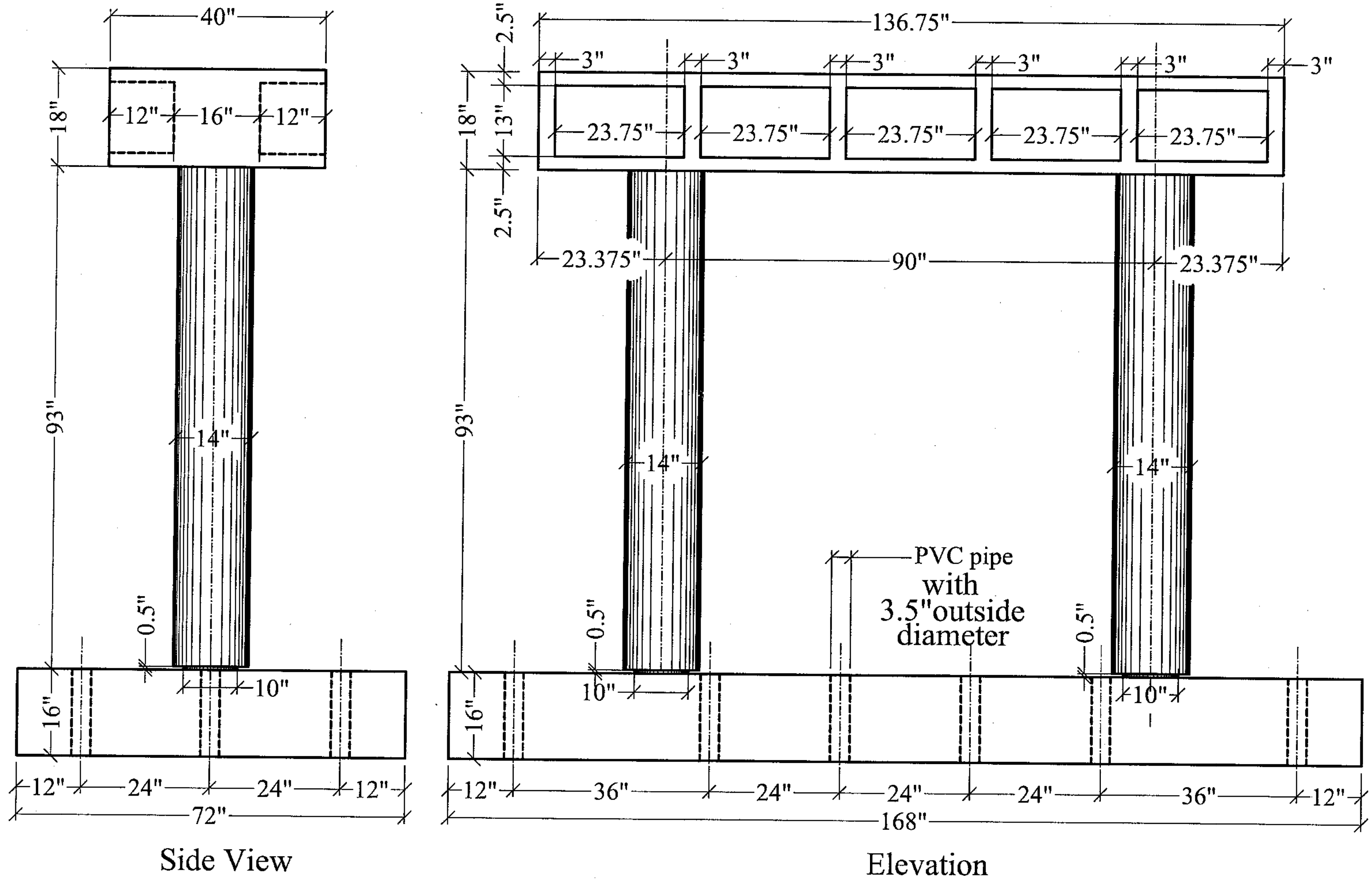

Fig. 2-1a : Concrete Dimensions of Specimen B2CT, (English Units)

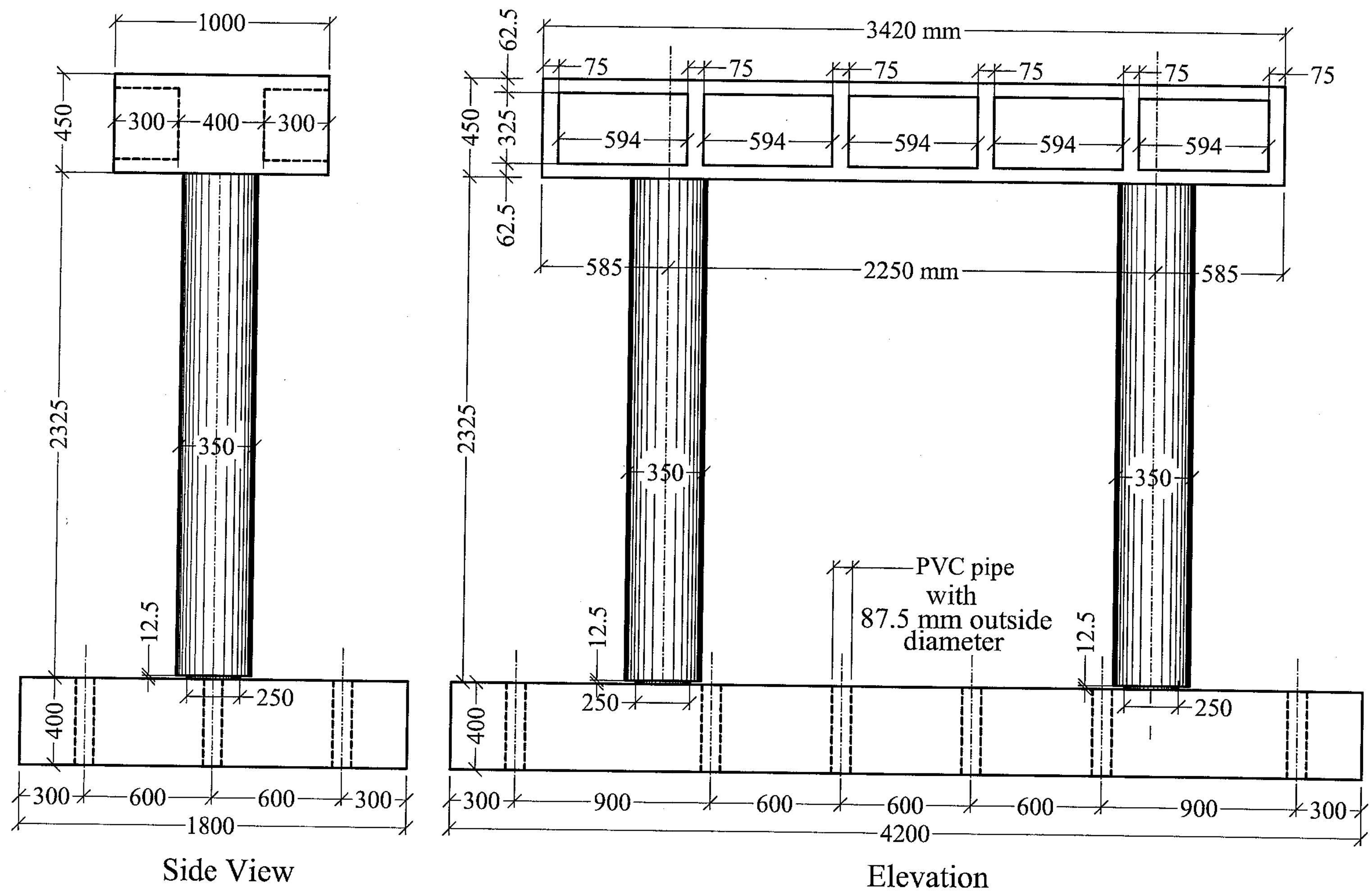

Fig. 2-1b : Concrete Dimensions of Specimen B2CT, (SI Units)

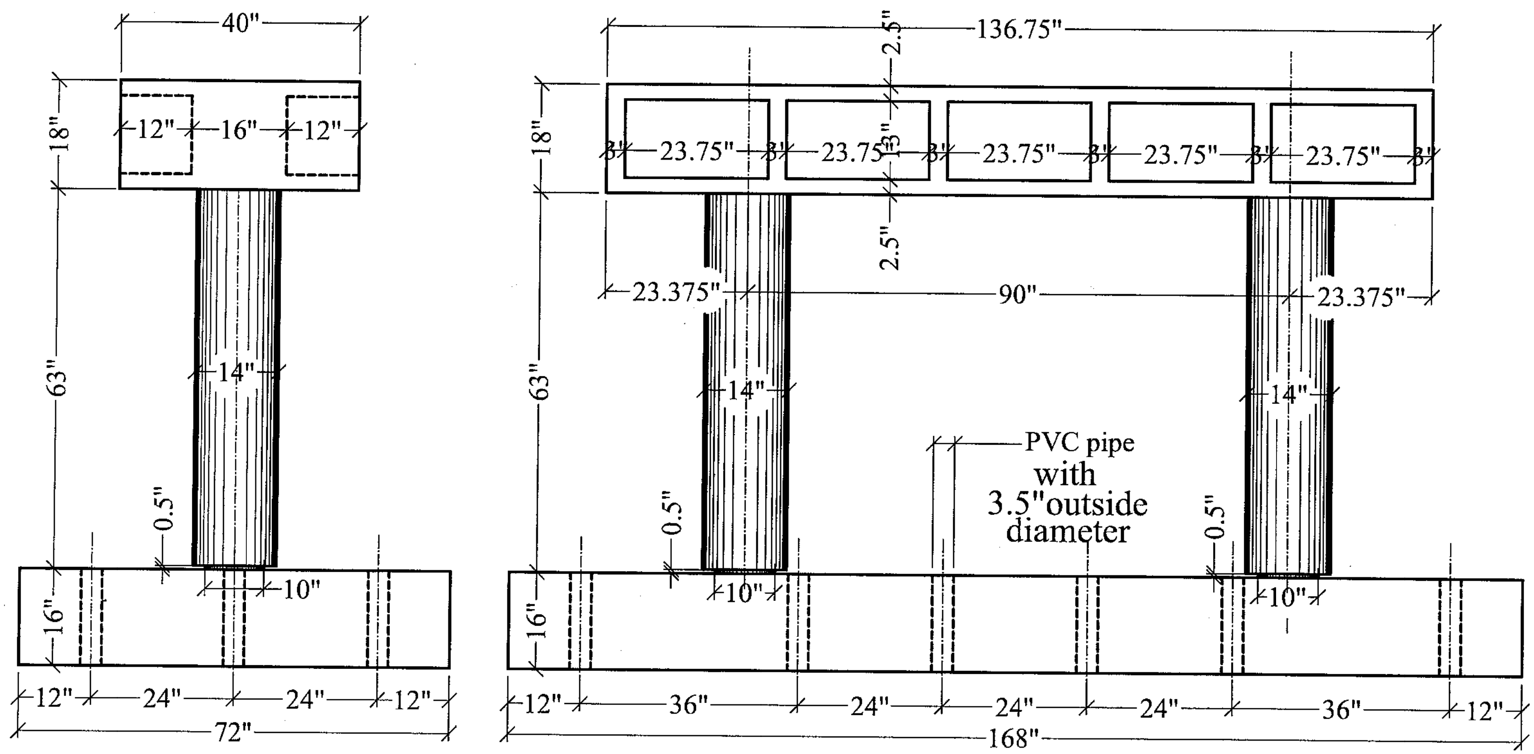

Fig. 2-2a : Concrete Dimensions of Specimen B2CM, (English Units)

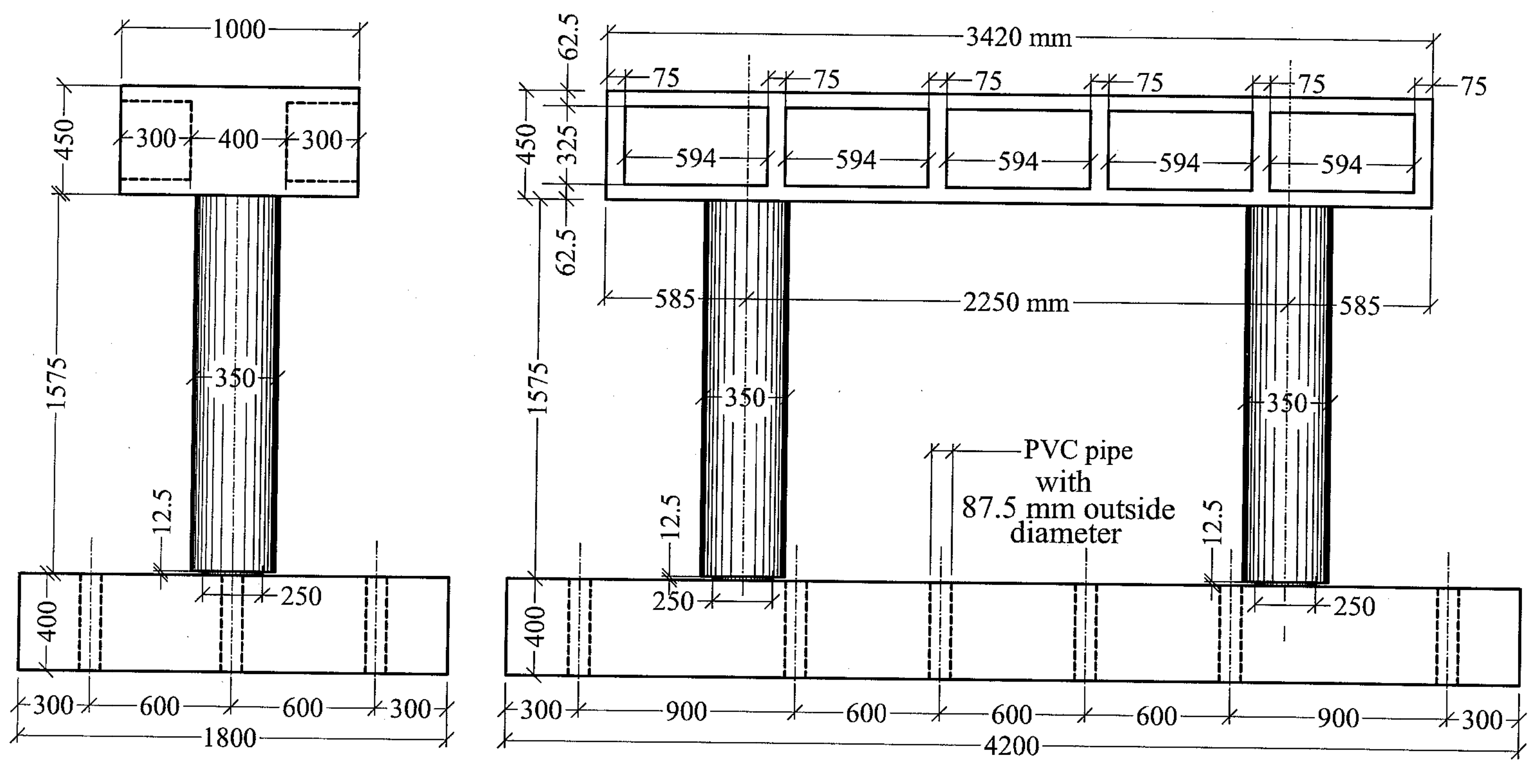

Fig. 2-2b : Concrete Dimensions of Specimen B2CM, (SI Units)

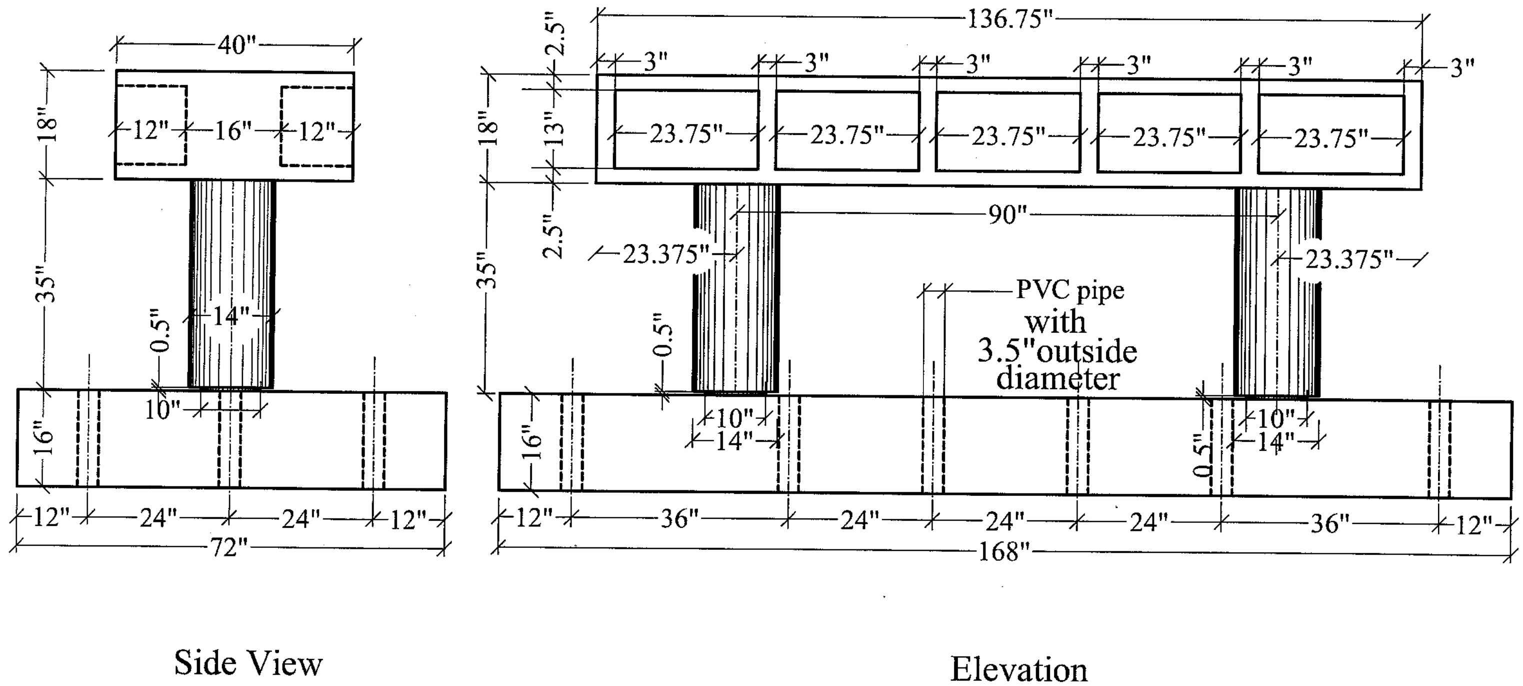

Fig. 2-3a : Concrete Dimensions of Specimen B2CS, (English Units)

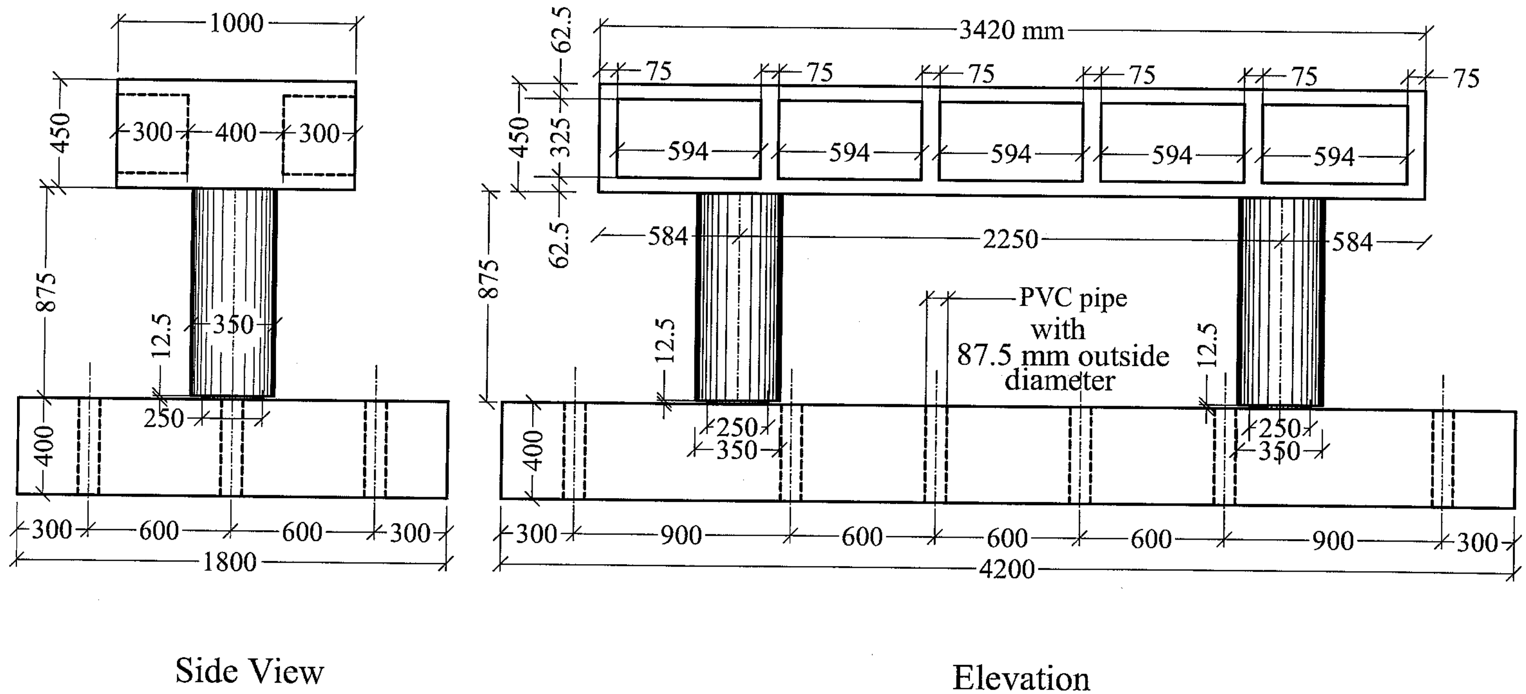

Fig. 2-3b: Concrete Dimensions of Specimen B2CS, (SI Units)

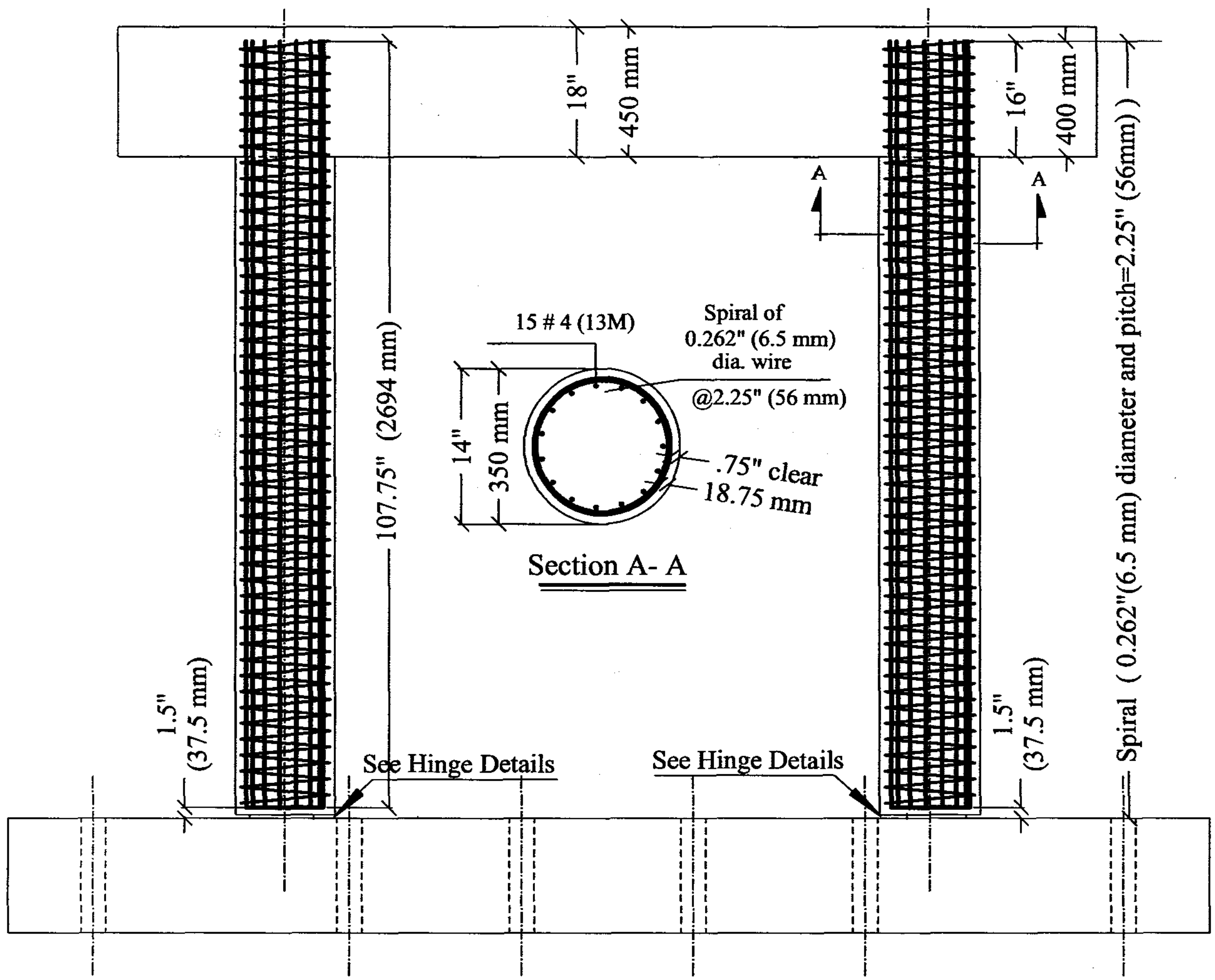

Fig. 2-4a: Columns Longitudinal and Transverse Reinf. of Specimen B2CT

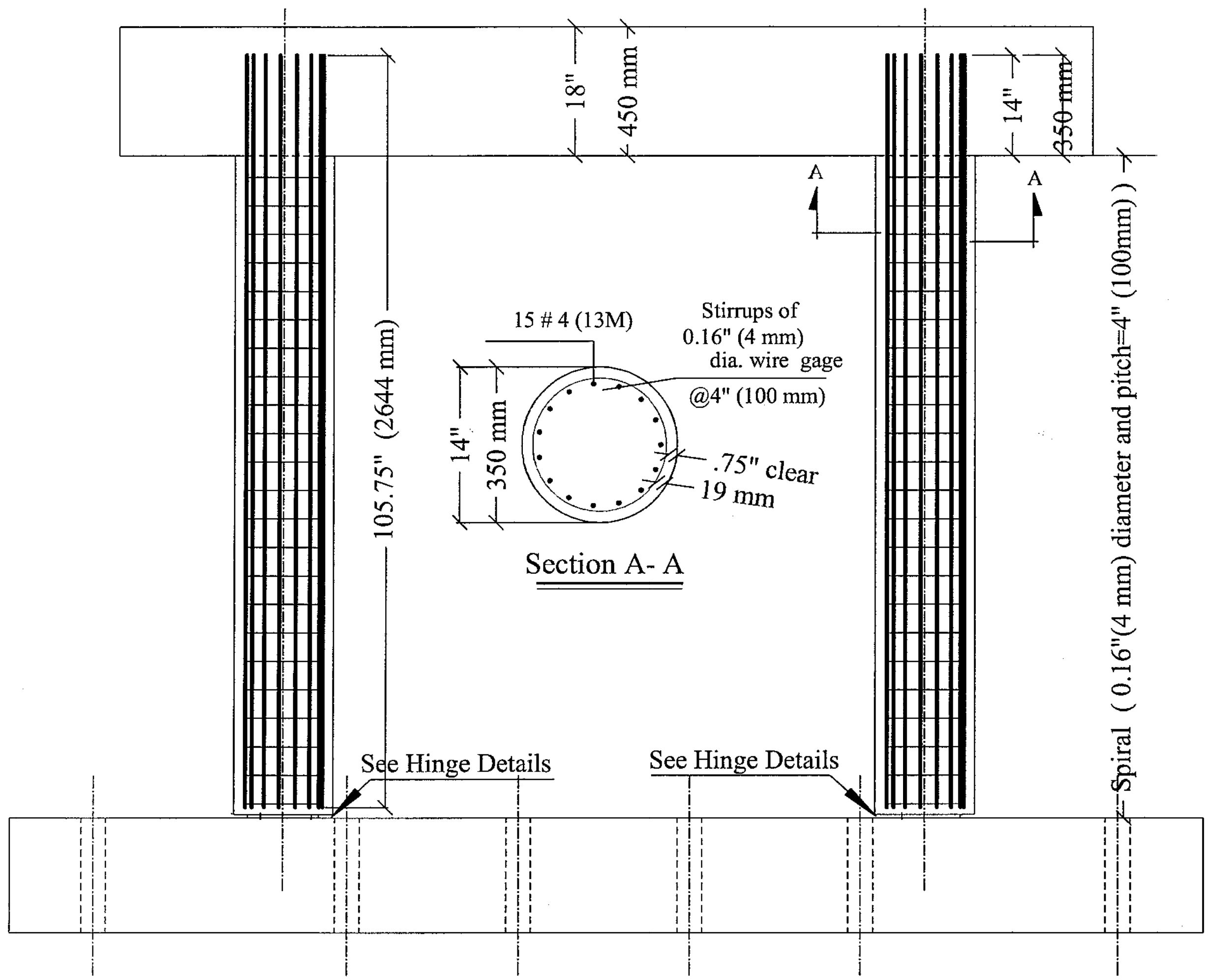

Fig. 2-4b: Columns Longitudinal and Transverse Reinf. of As-Built Specimen

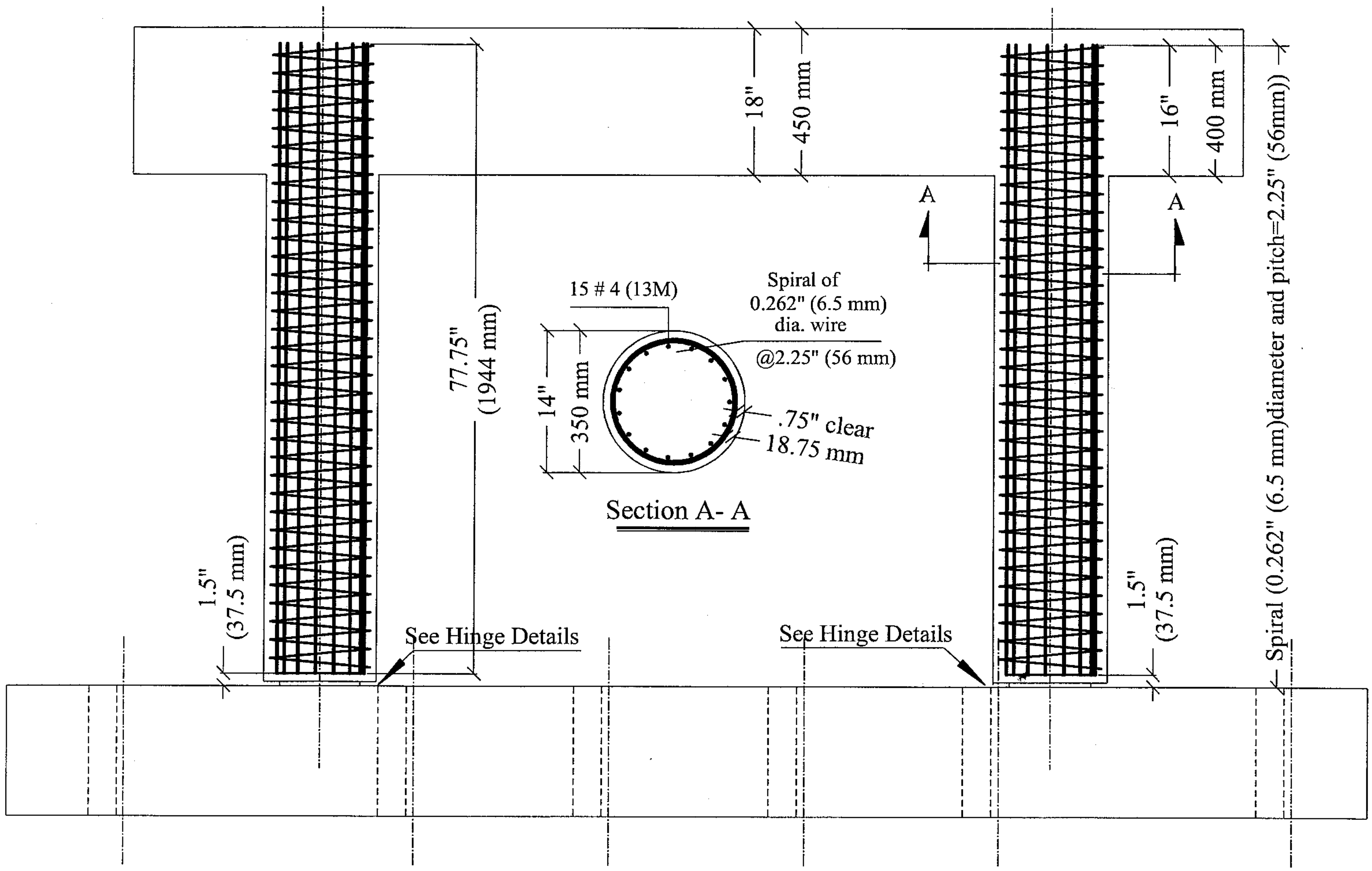

Fig. 2-5: Columns Longitudinal and Transverse Reinf. of Specimen B2CM

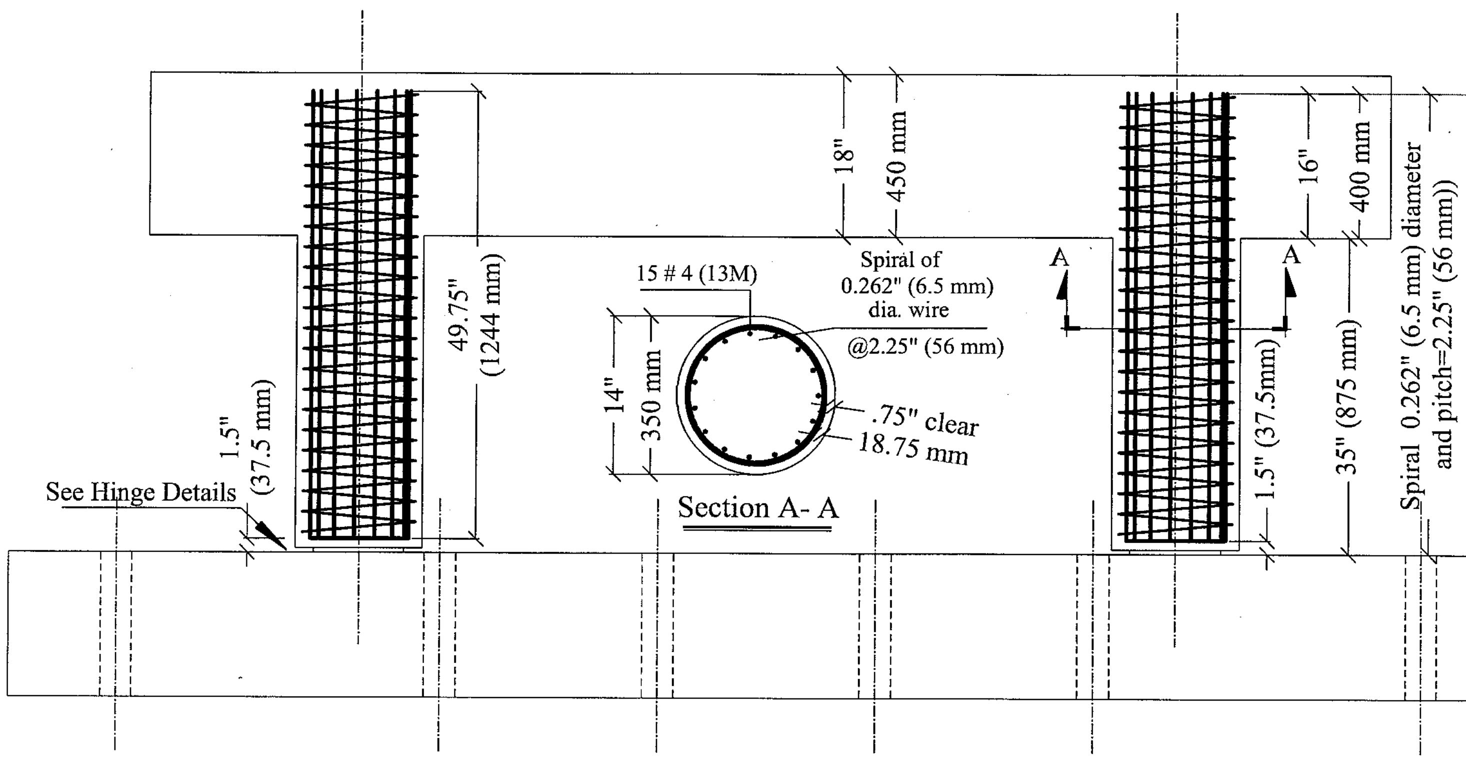

Fig. 2-6: Columns Longitudinal and Transverse Reinf. of Specimen B2CS

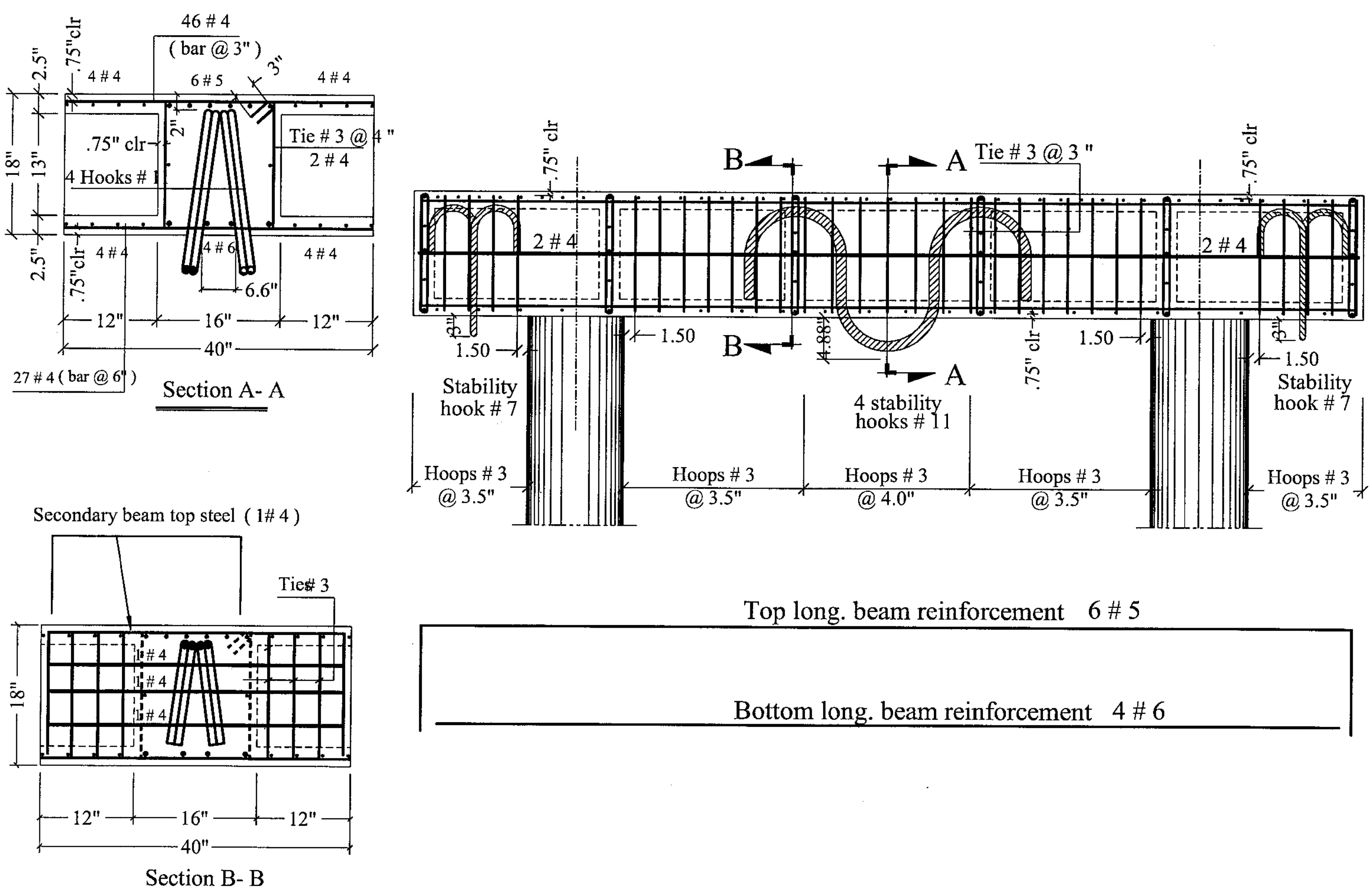

Fig. 2-7a: Details of Beam Reinforcement of both Specimens B2CT and B2CM, (English Units)

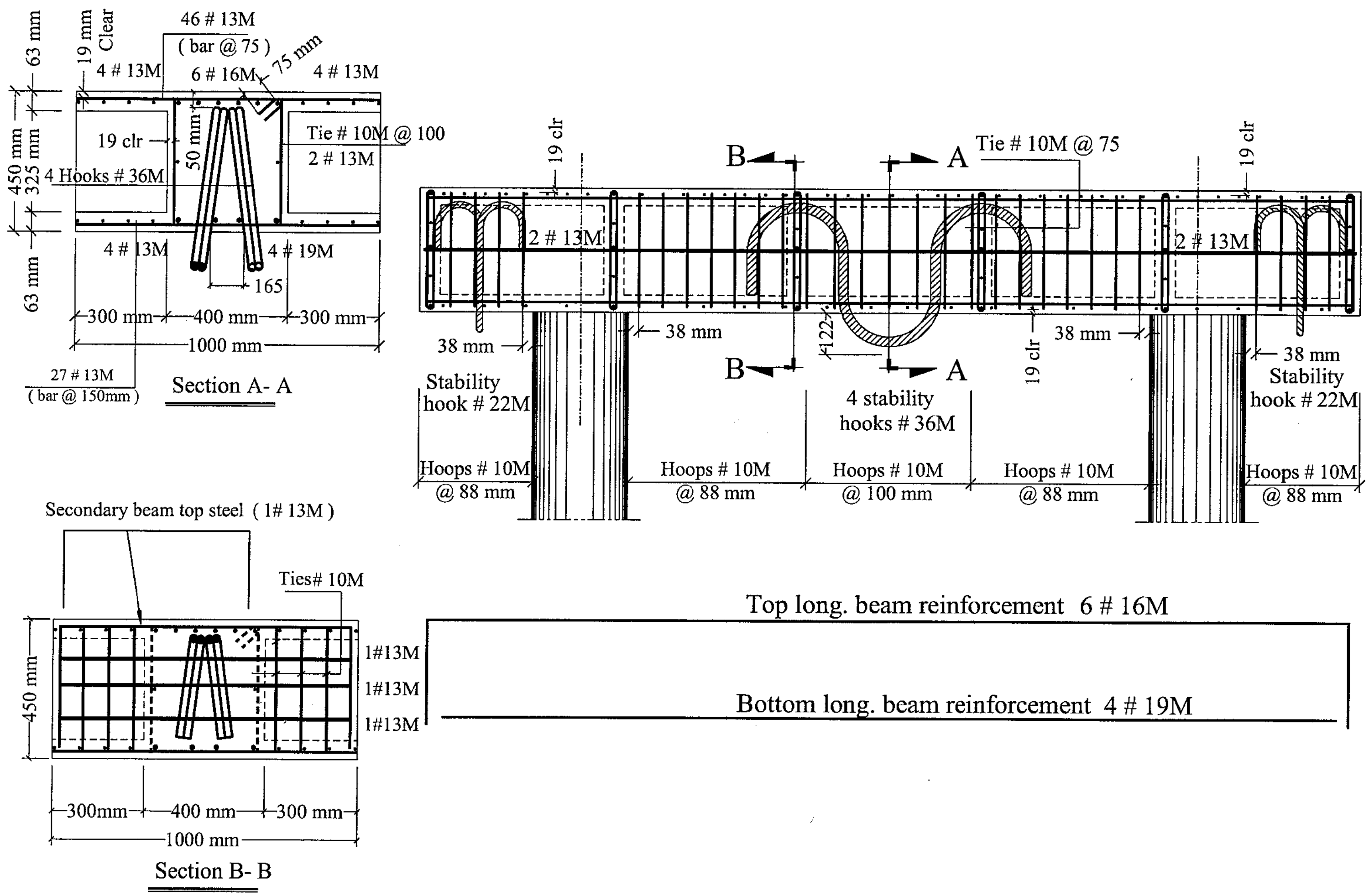

Fig. 2-7b: Details of Beam Reinforcement of both Specimens B2CT and B2CM, (SI Units)

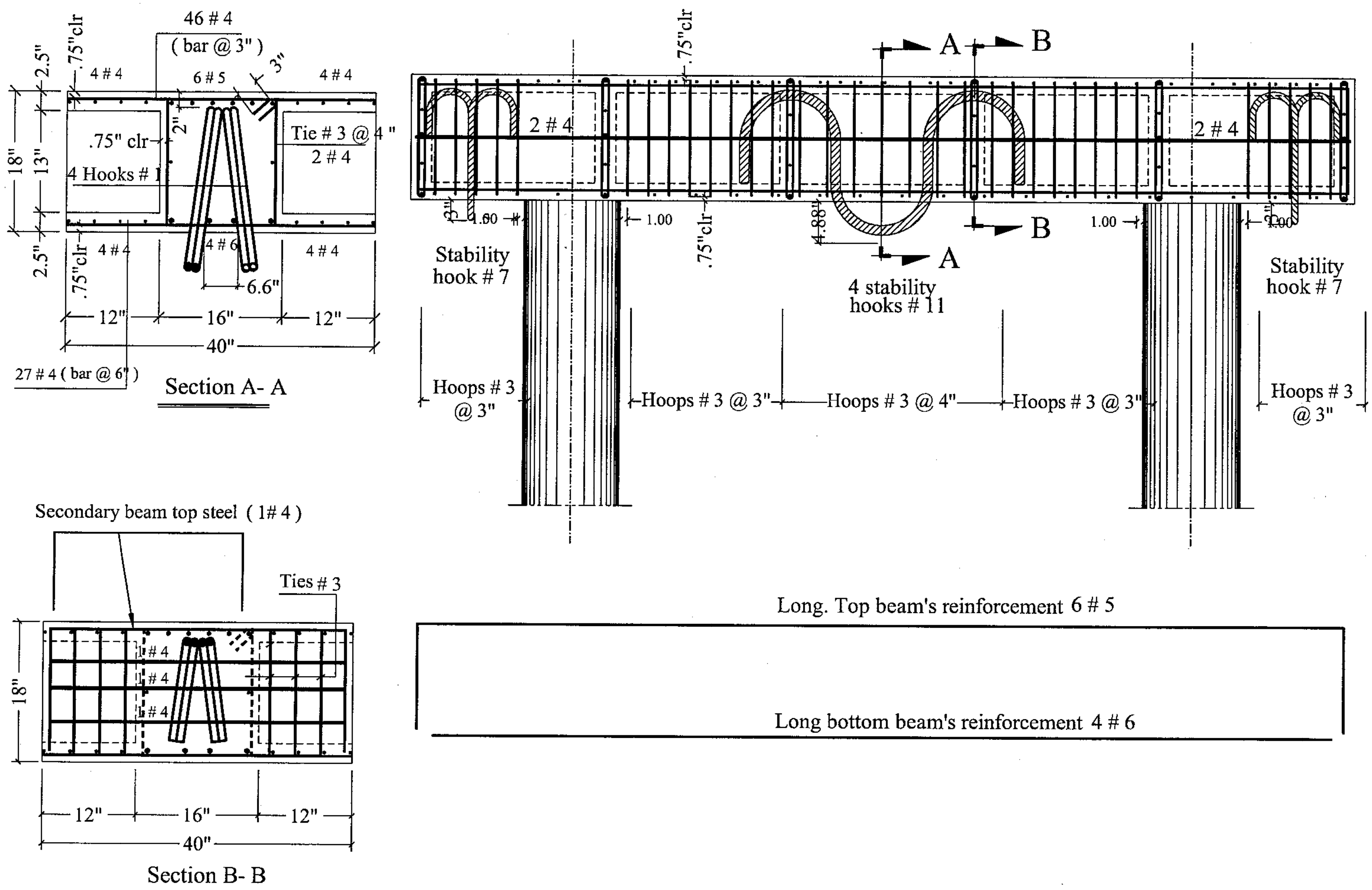

Fig. 2-8a: Details of Beam Reinforcement of Specimen B2CS, (English Units)

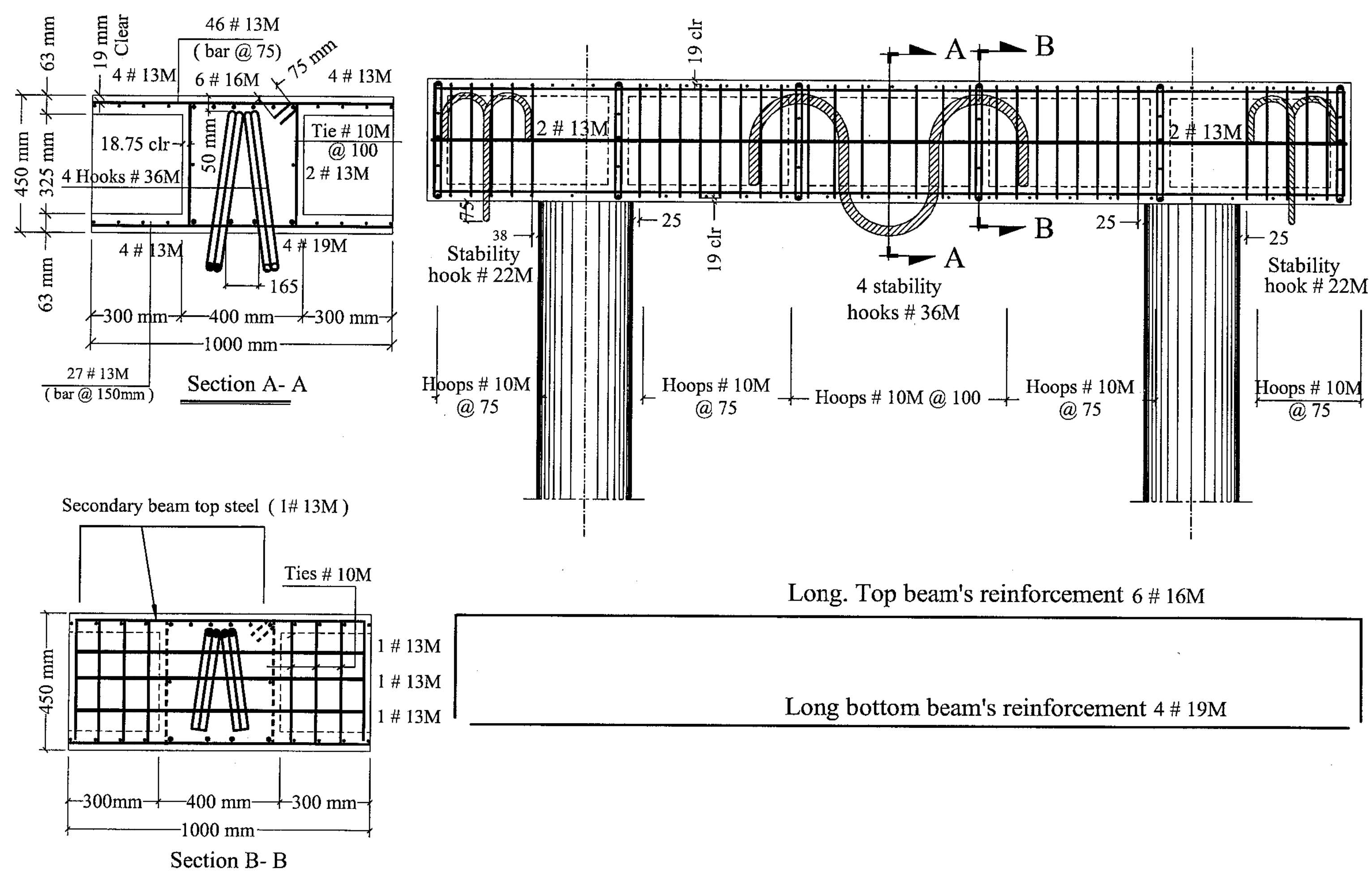

Fig. 2-8b: Details of Beam Reinforcement of Specimen B2CS, (SI Units)

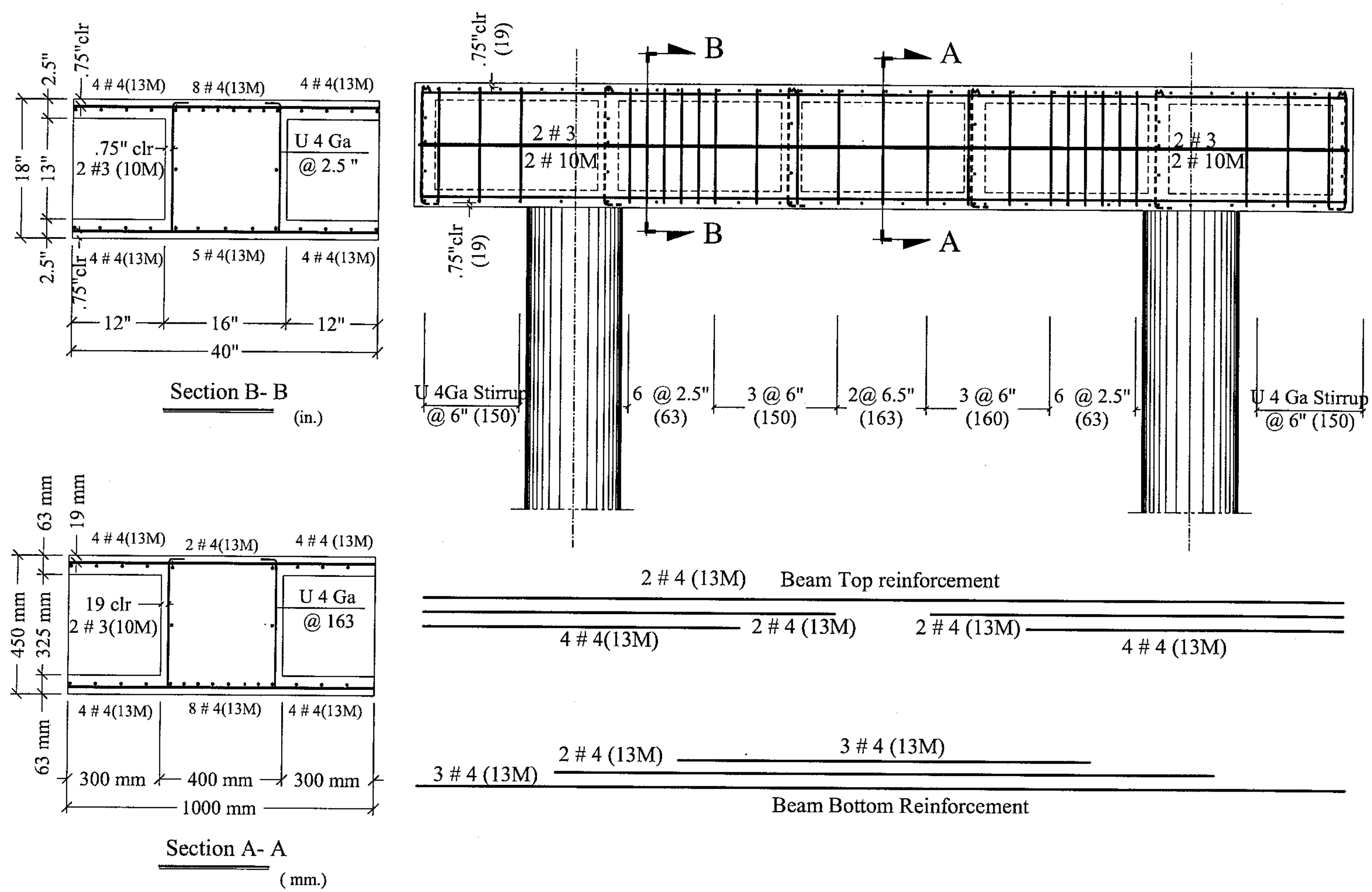

Fig. 2-9: Details of Beam Reinforcement of As-Built Specimen (SI & English Units)

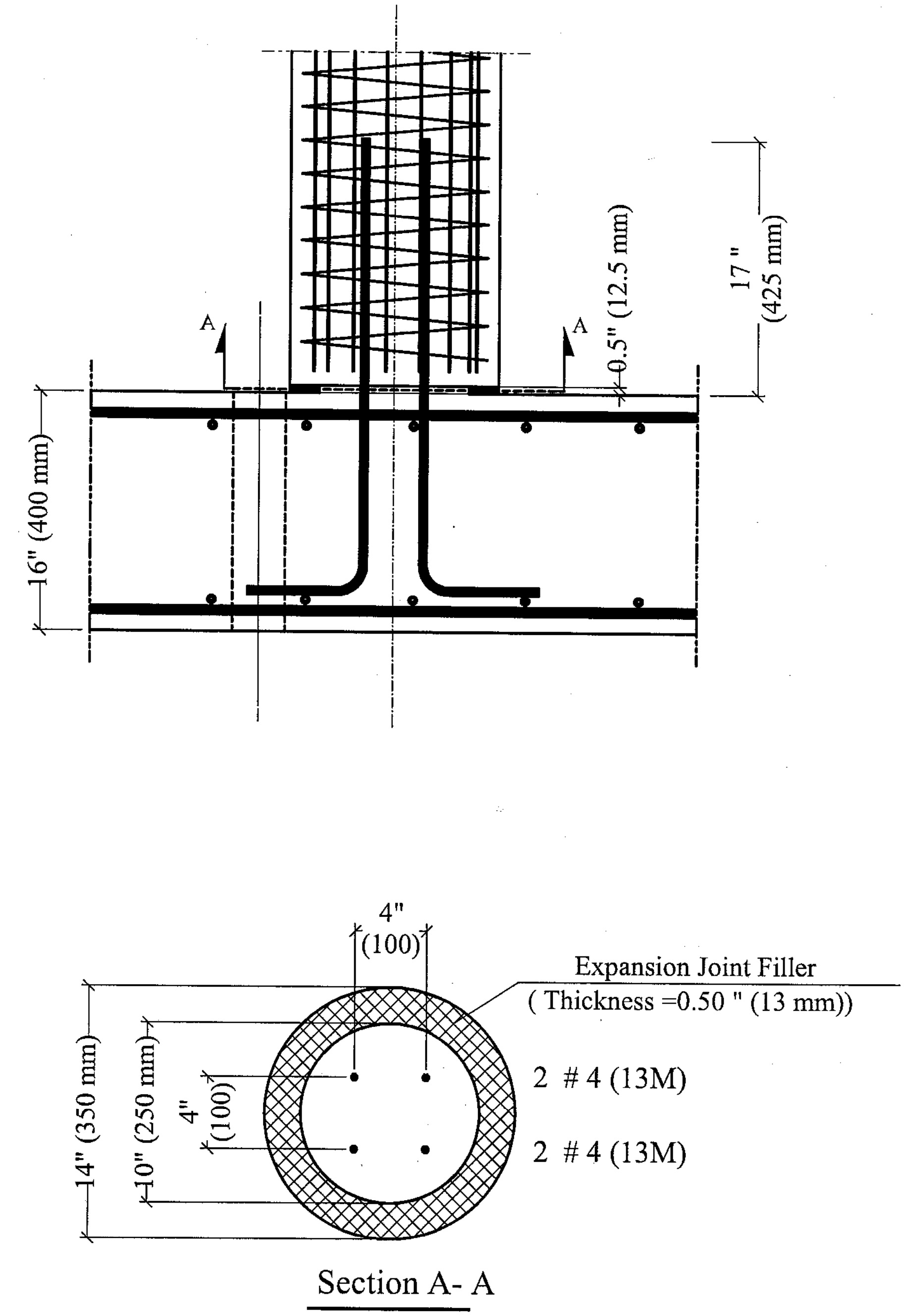

Fig. 2-10a: Details of the Hinge Key of All Specimens

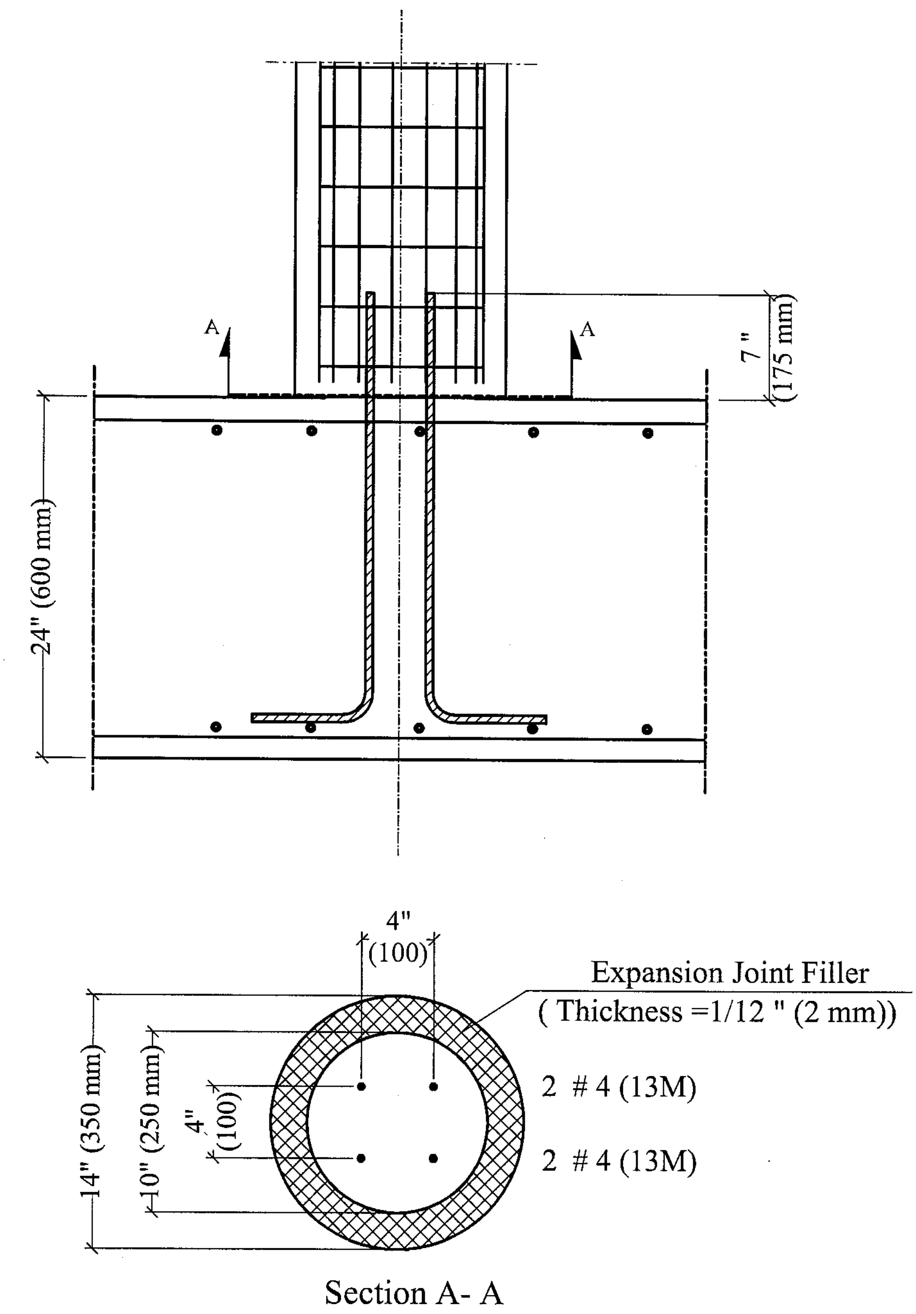

Fig. 2-10b: Details of the Hinge Key of the As-built Specimen

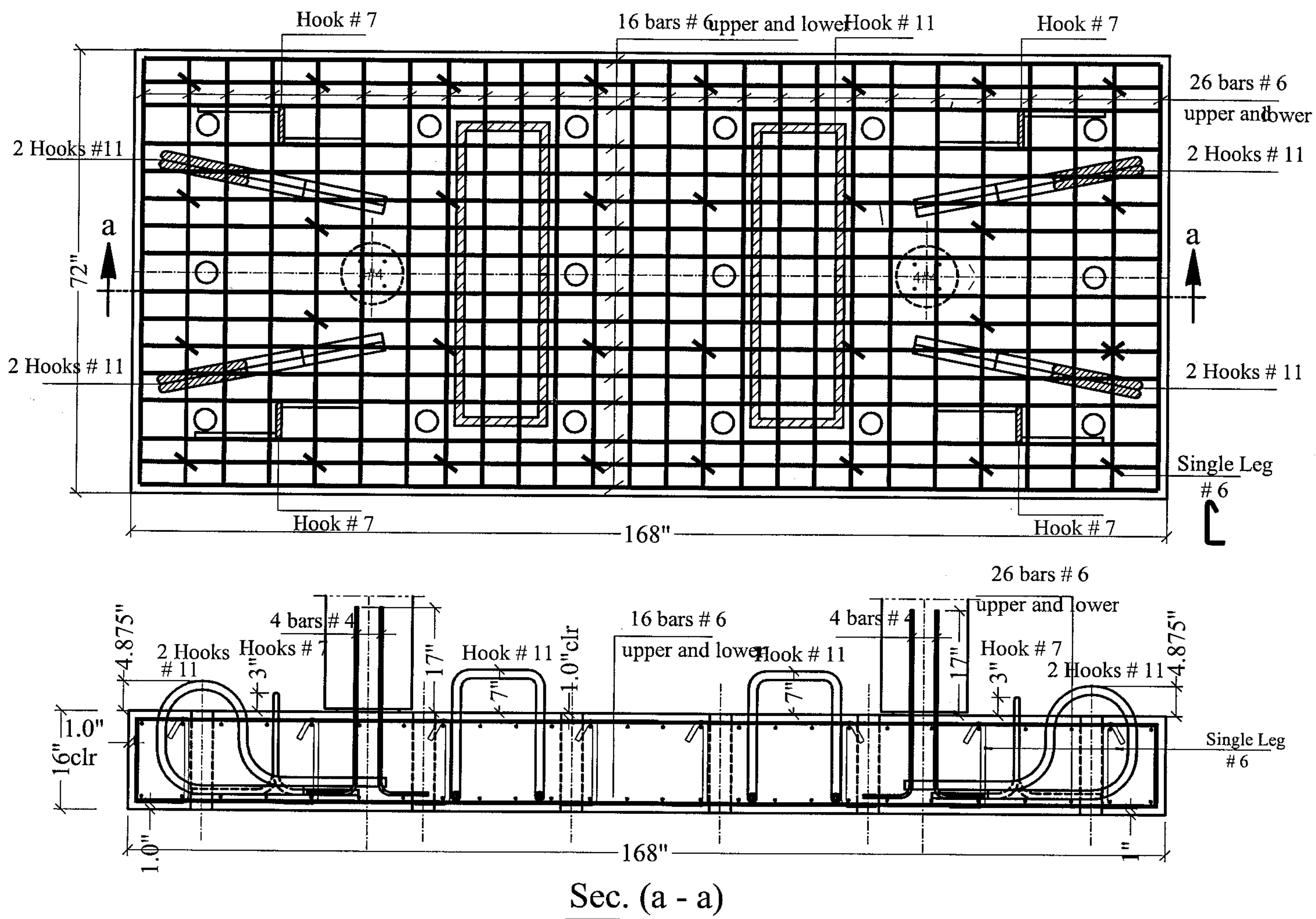

Sec. (a - a)

Fig. 2-11a: Footing Dimensions and Reinf. of All Specimens (English Units)

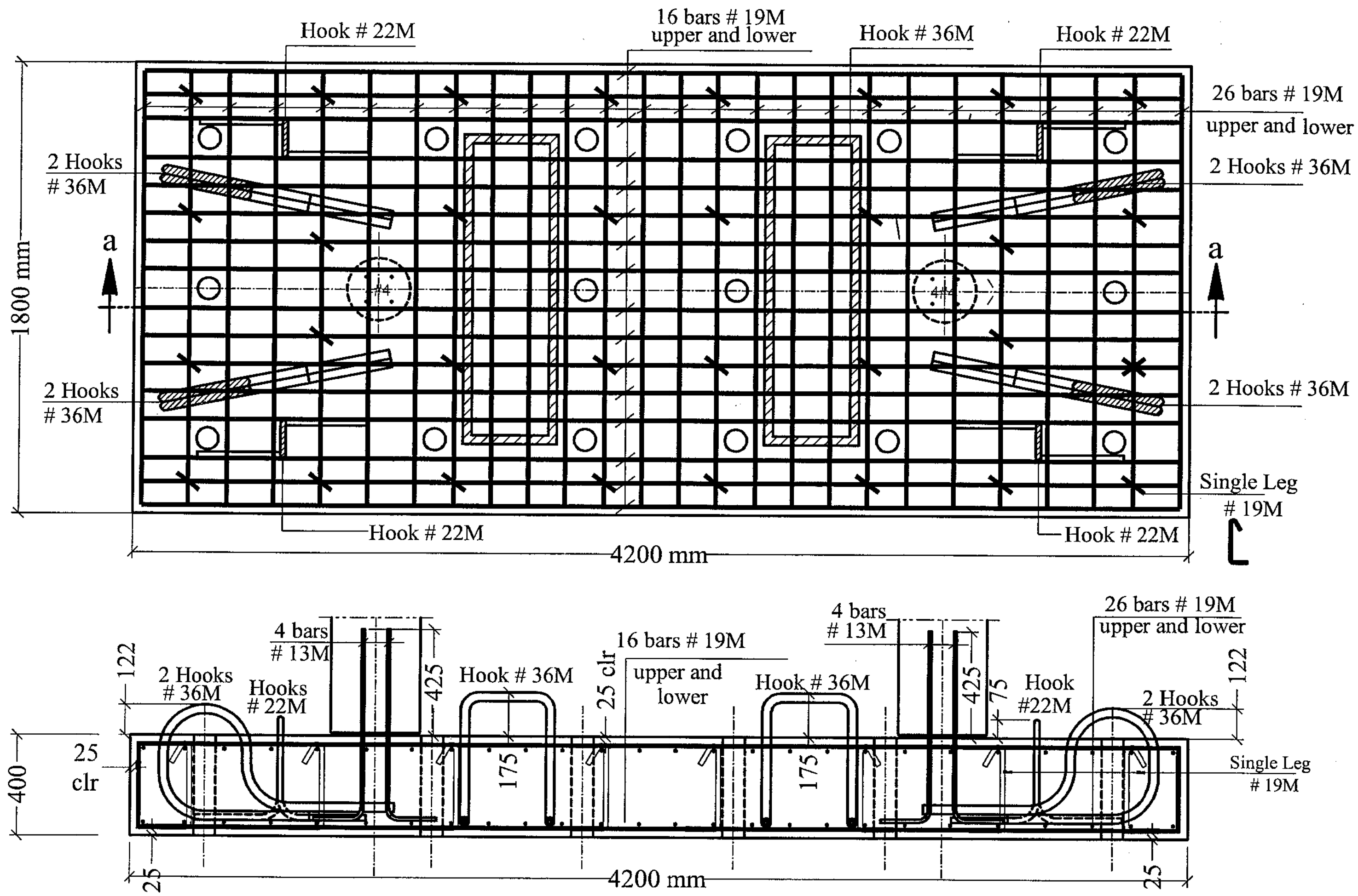

Sec. (a - a)

Fig. 2-11b: Footing Dimensions and Reinf. of All Specimens (SI Units)

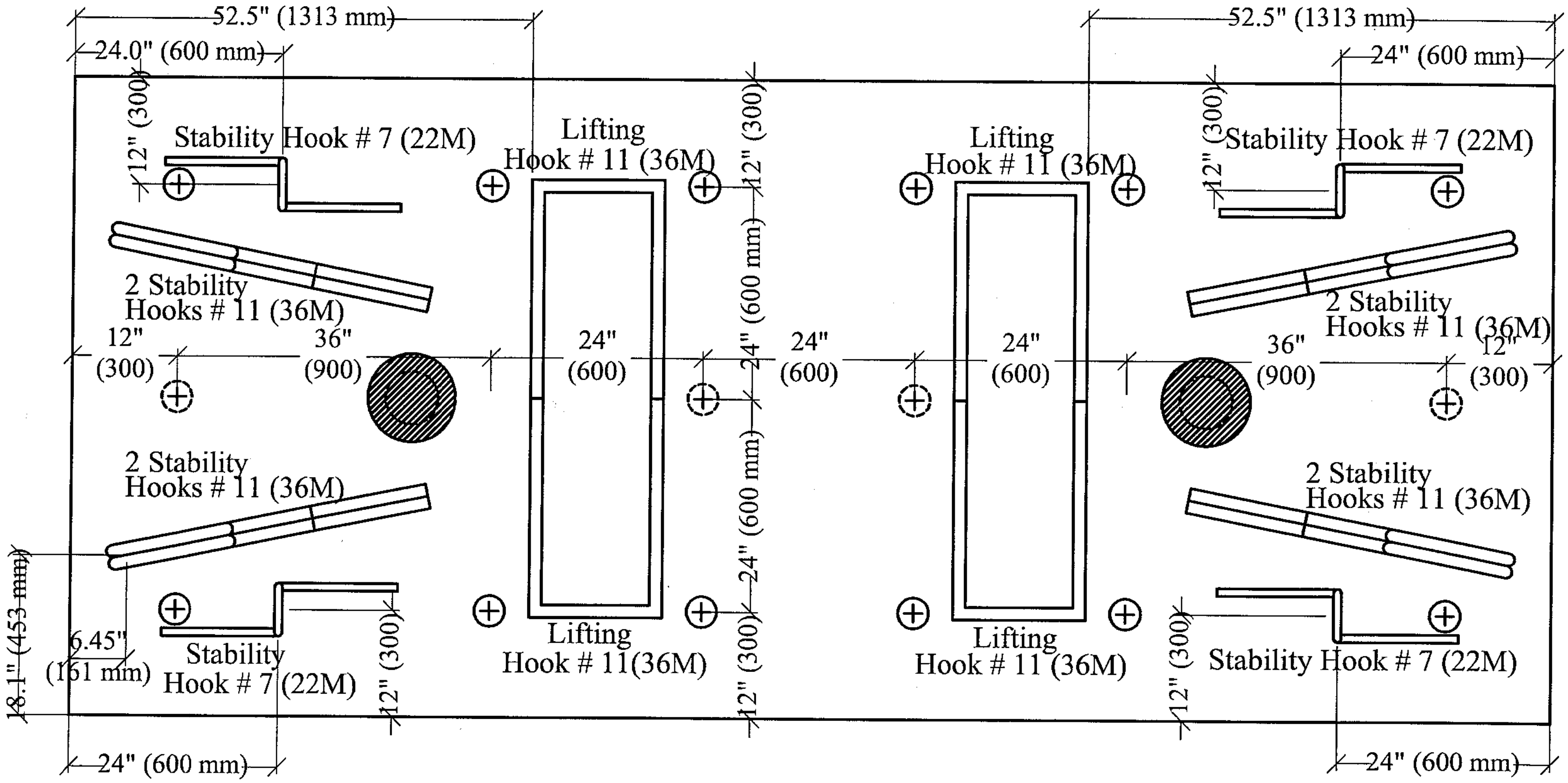

Fig. 2-12: Positions of Footing Hooks and Holes for All Specimens (SI & English Units)

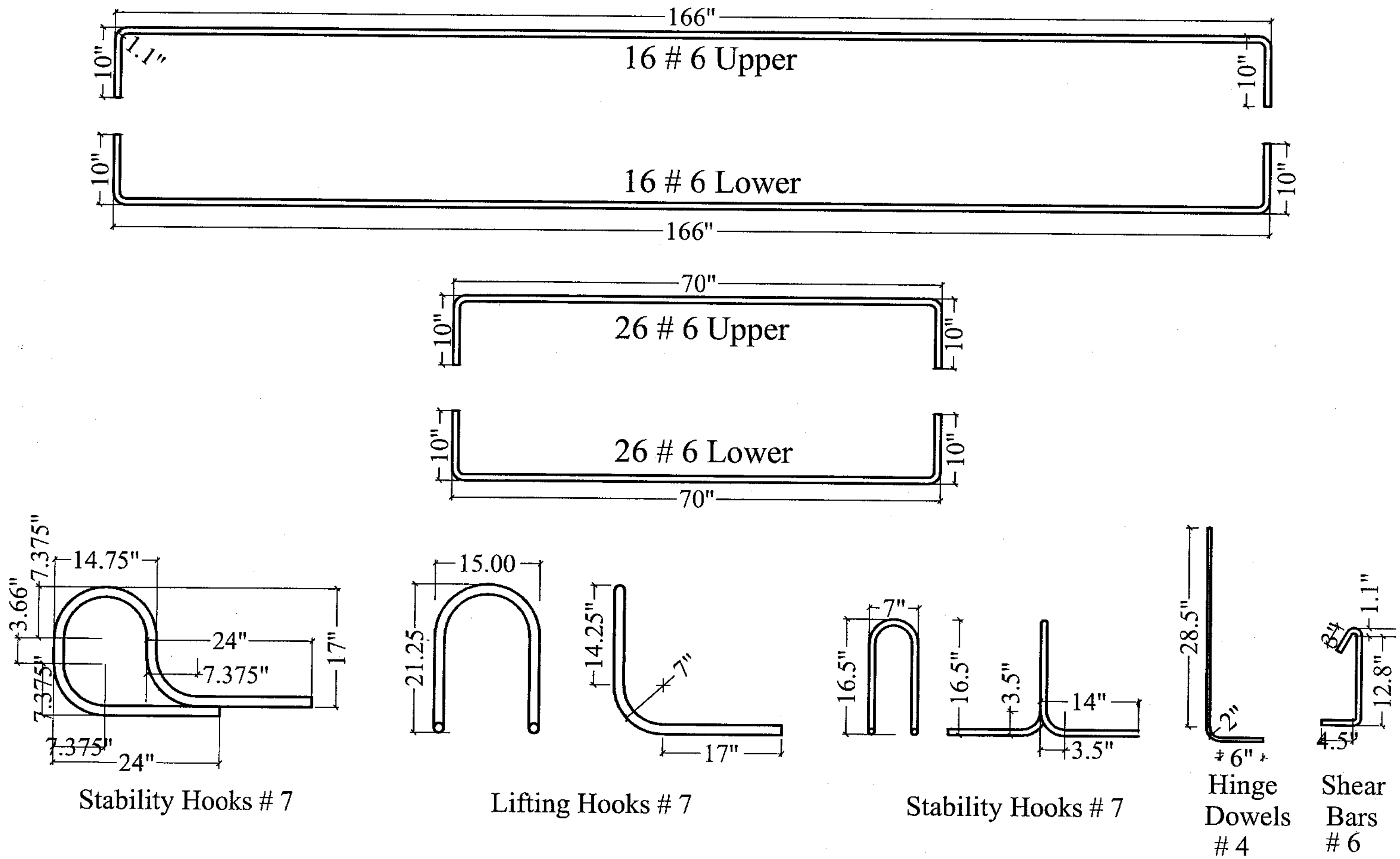

Fig. 2-13a: Details of Footing Reinforcement for All Specimens (English Units)

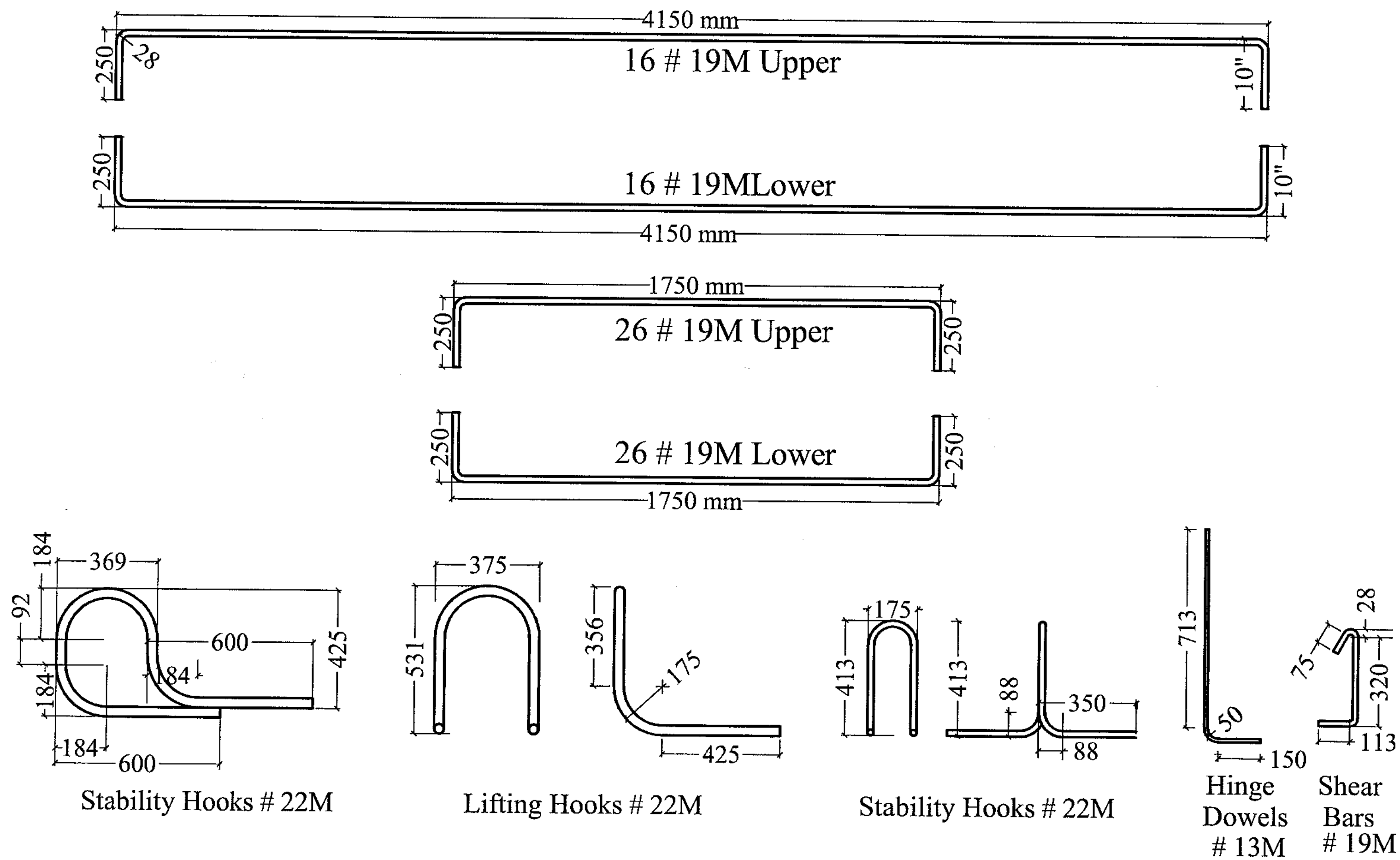

Fig. 2-13b: Details of Footing Reinforcement for All Specimens (SI Units)

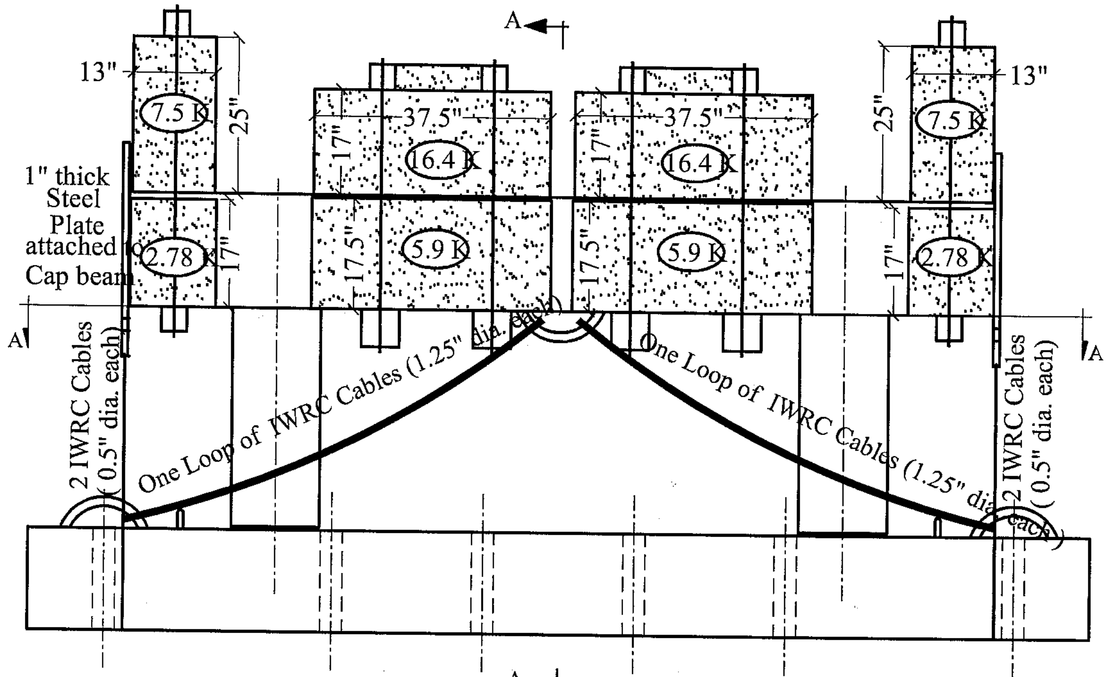

Elevation

6 Square Tubes of 4 * 4 * 3/8 and 8.0 feet long

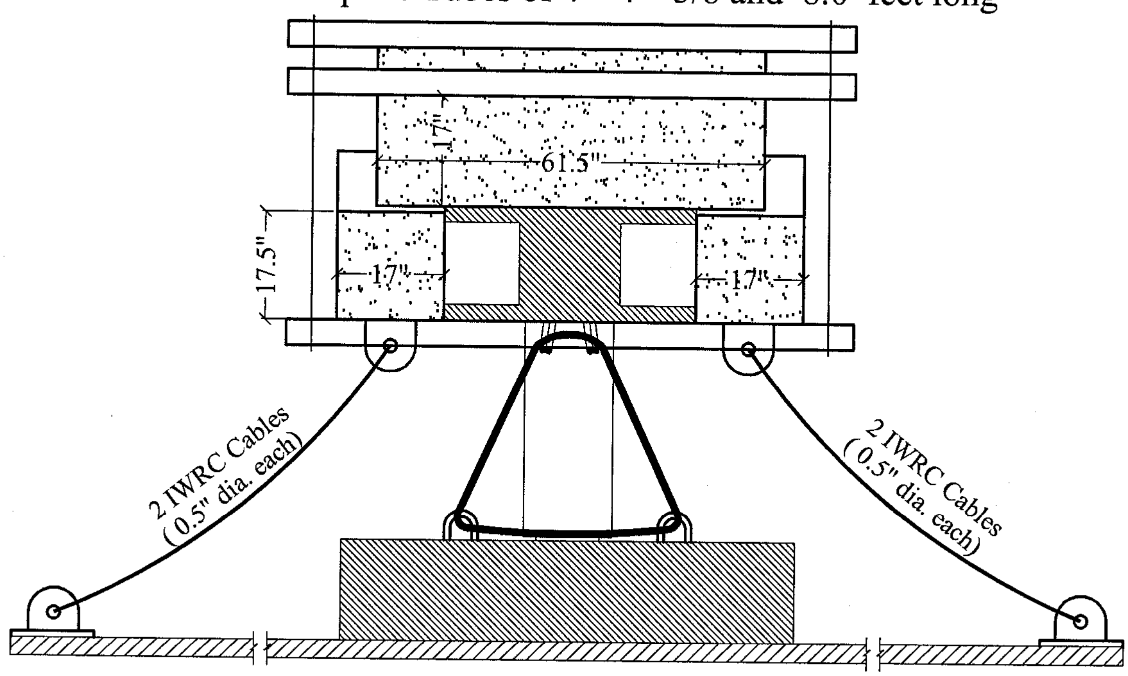

Section A- A

Fig. 2-13-a : Stability System Configuration for Specimen B2CS (English Units)

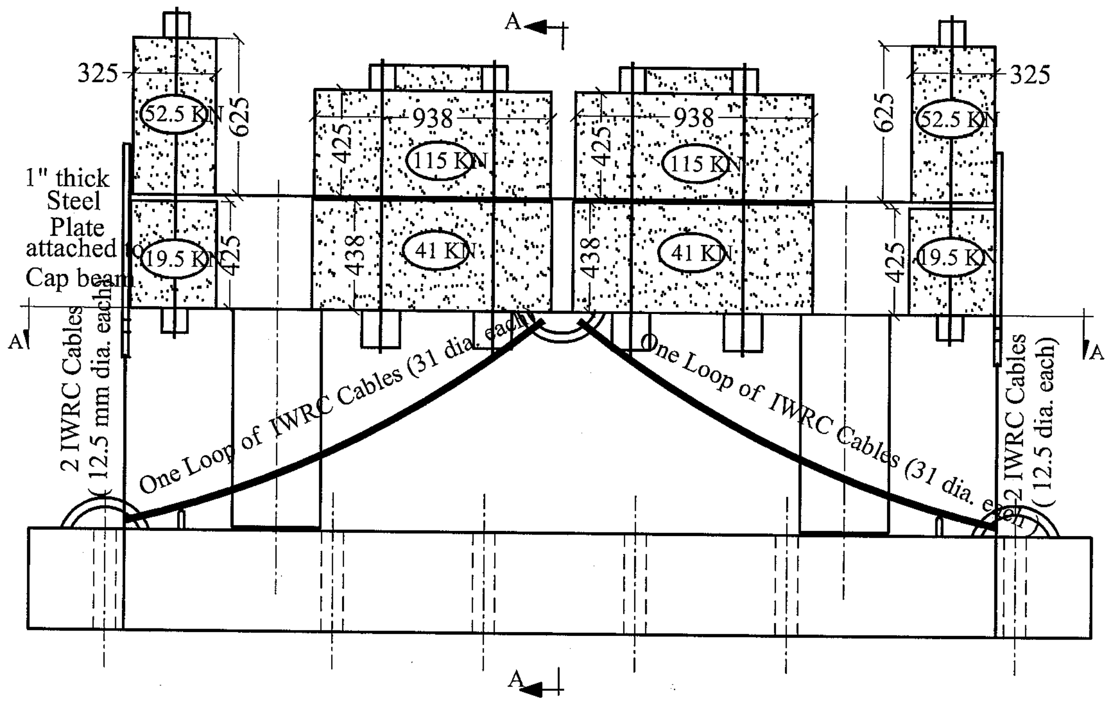

Elevation

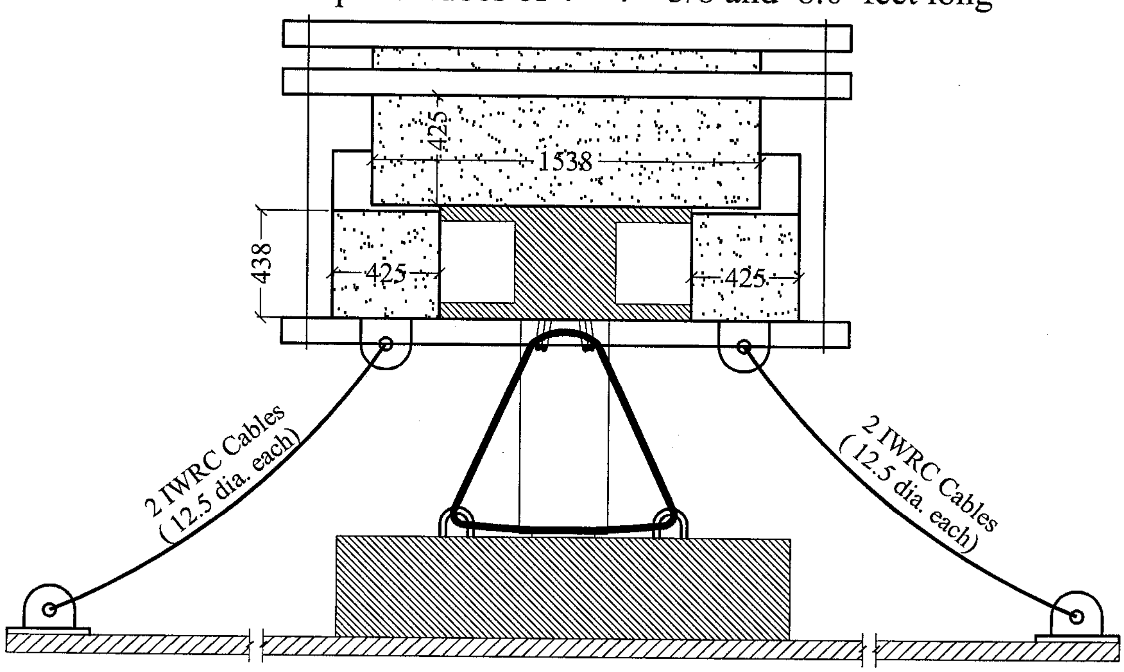

Section A- A

Fig. 2-13-b : Stability System Configuration for Specimen B2CS (SI Units)

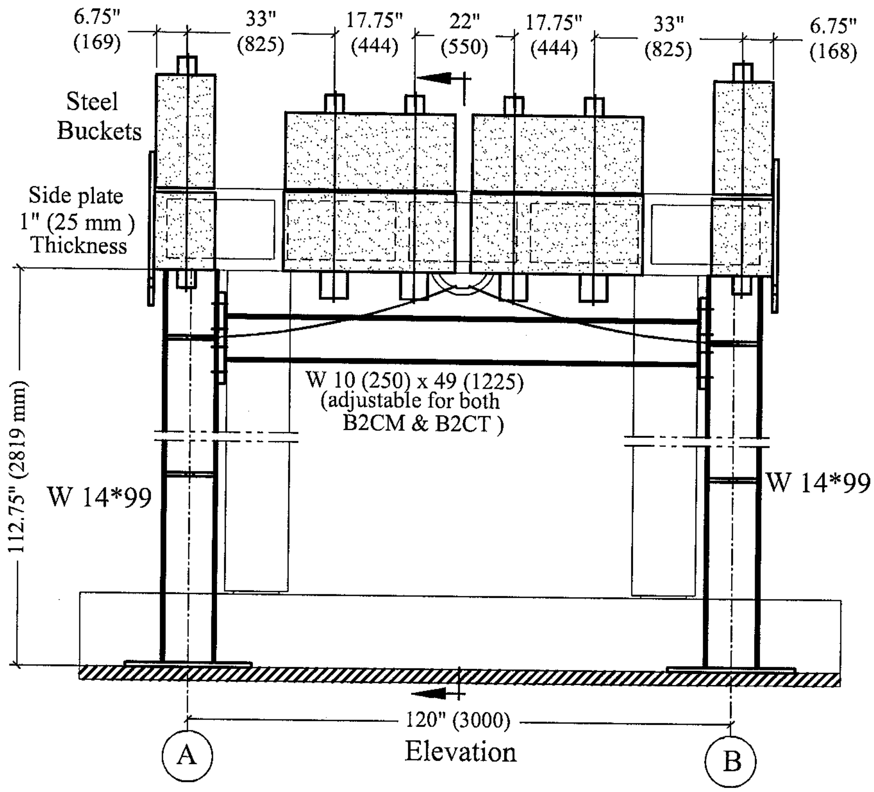

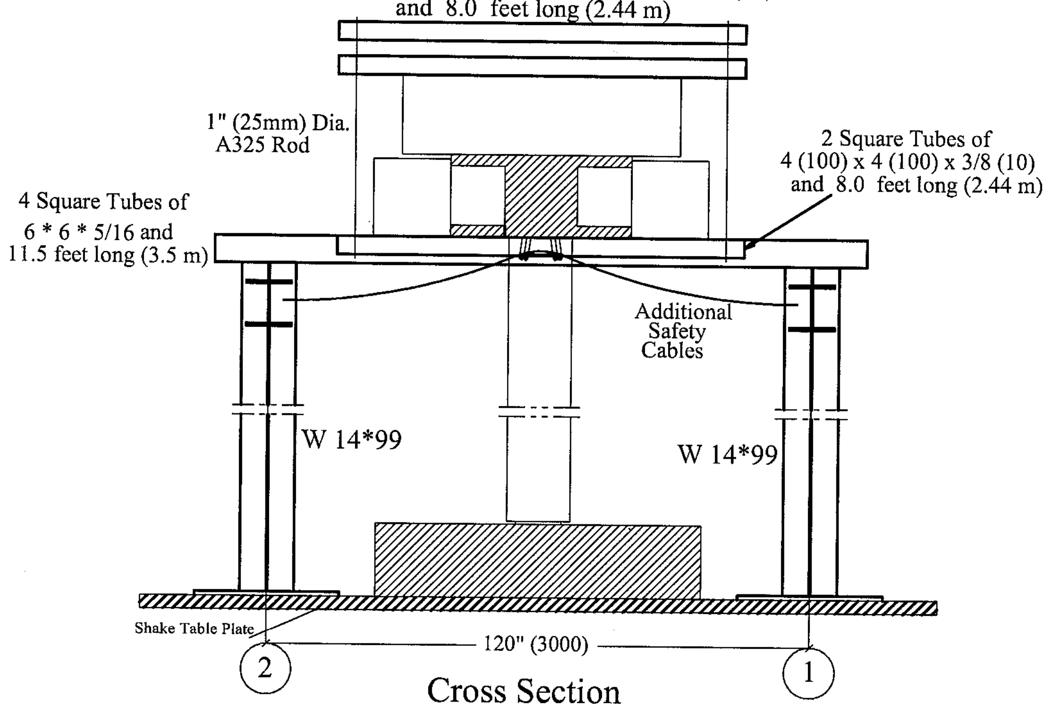

Fig. 2-15: Stability System for B2CM & B2CT

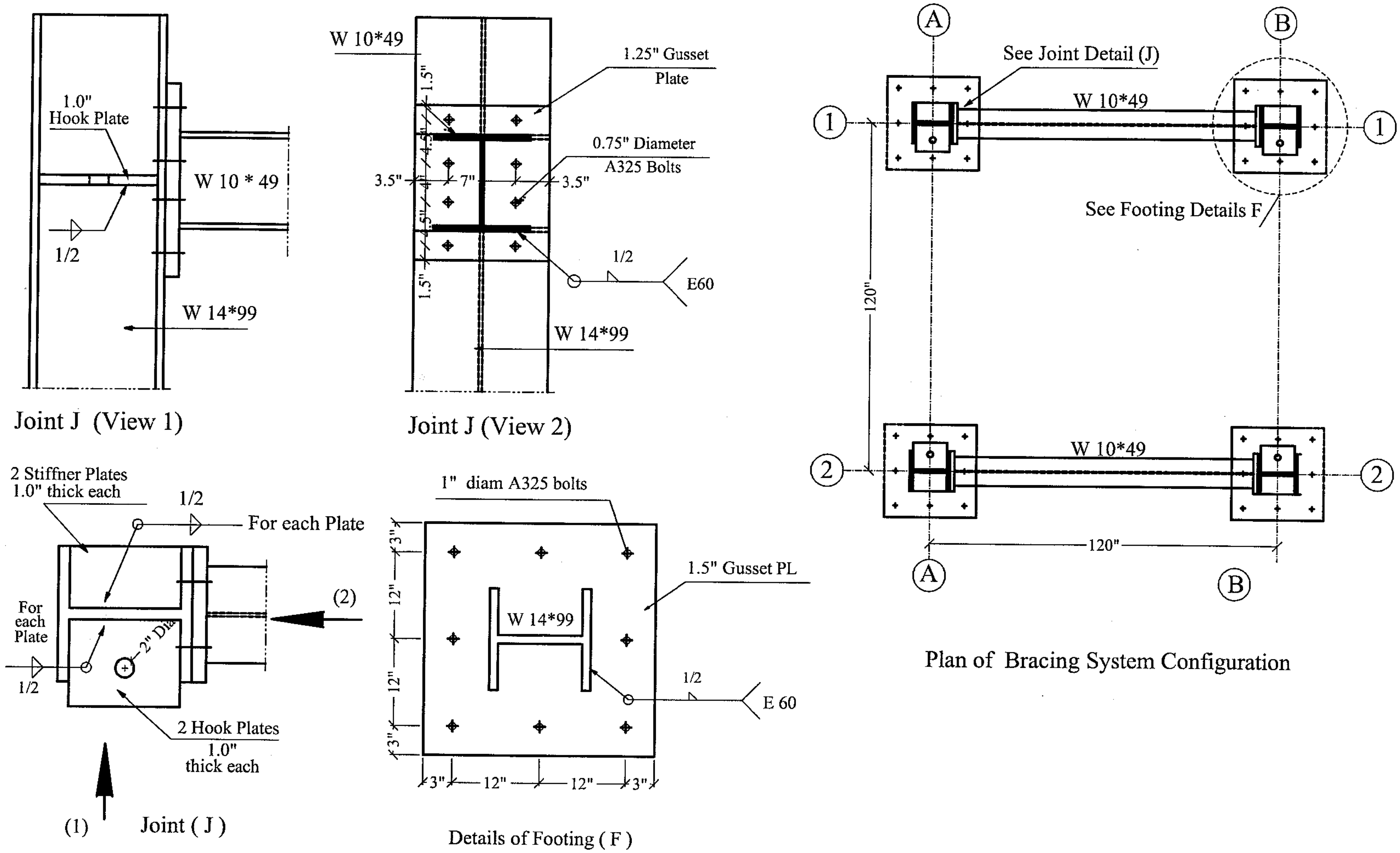

Fig. 2-16a: Section Details of Steel Stability System (Enlish Units)

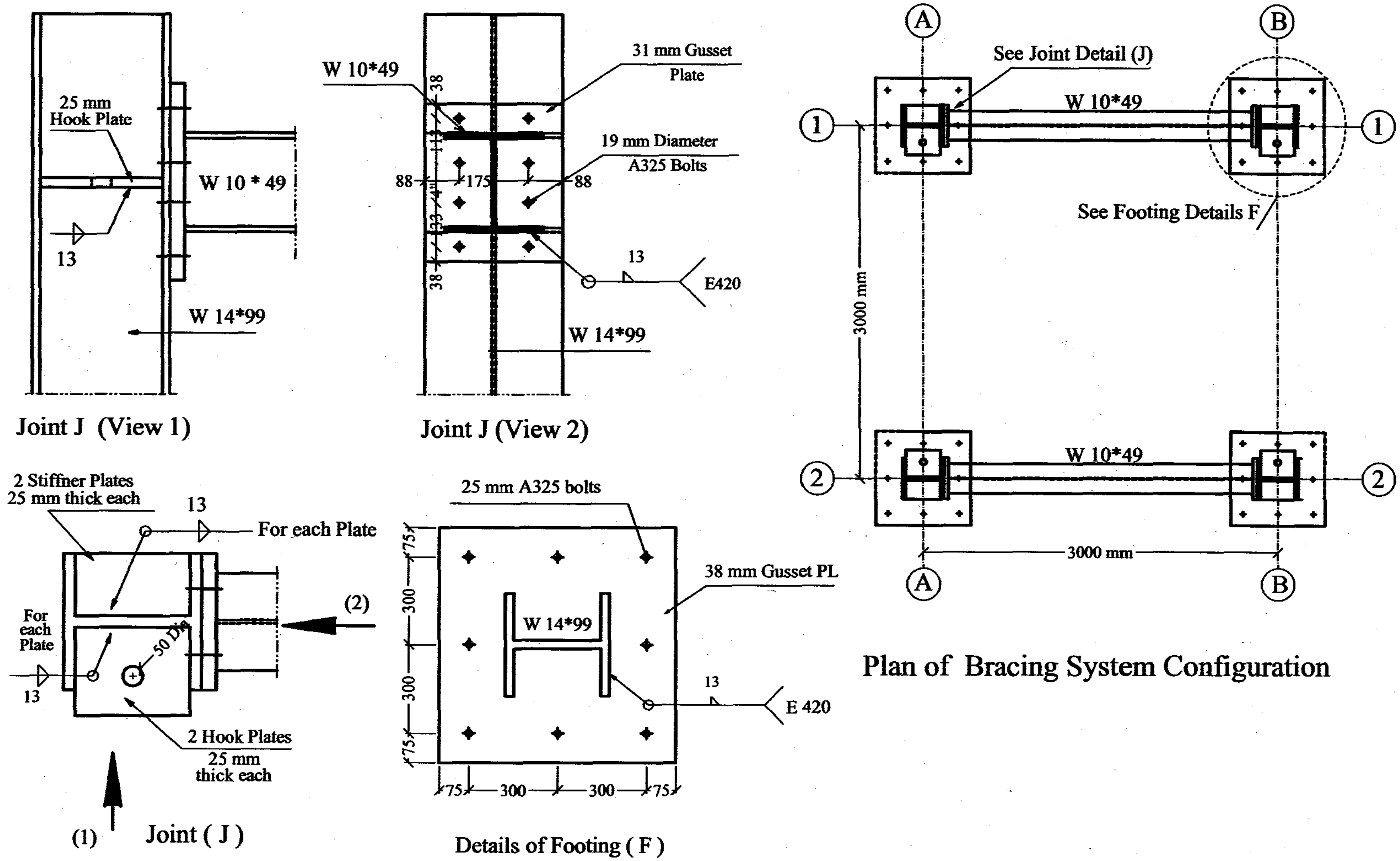

Fig. 2-16b: Section Details of Steel Stability System (Metric Units)

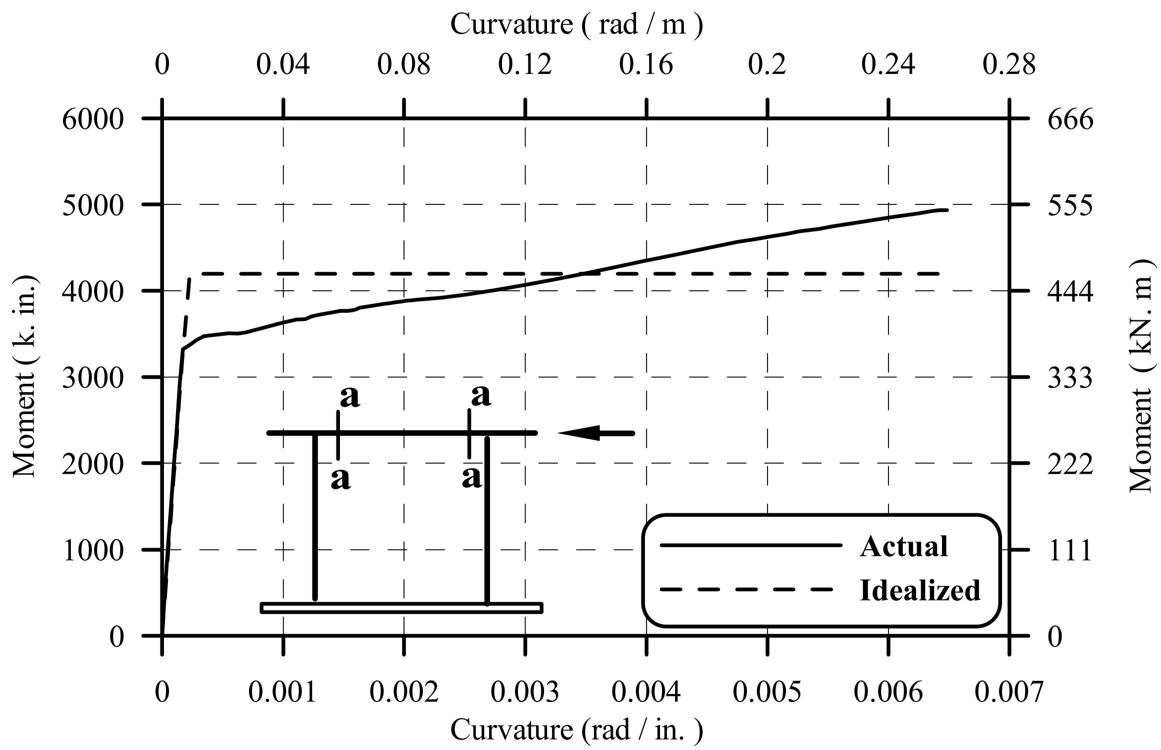

Fig. 2-17: Moment-Curvature Diagram at Section a-a of Bent Beam

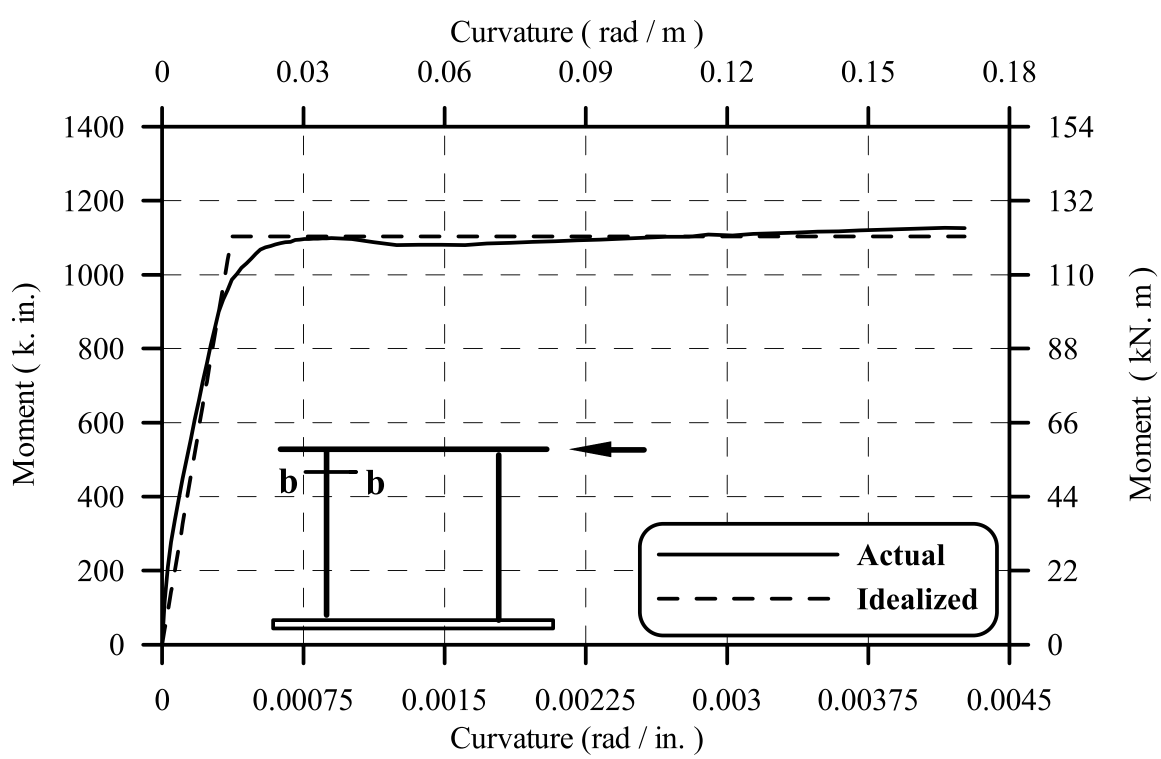

Fig. 2-18: Moment-Curvature Diagram at Sec. b-b of Bent Column

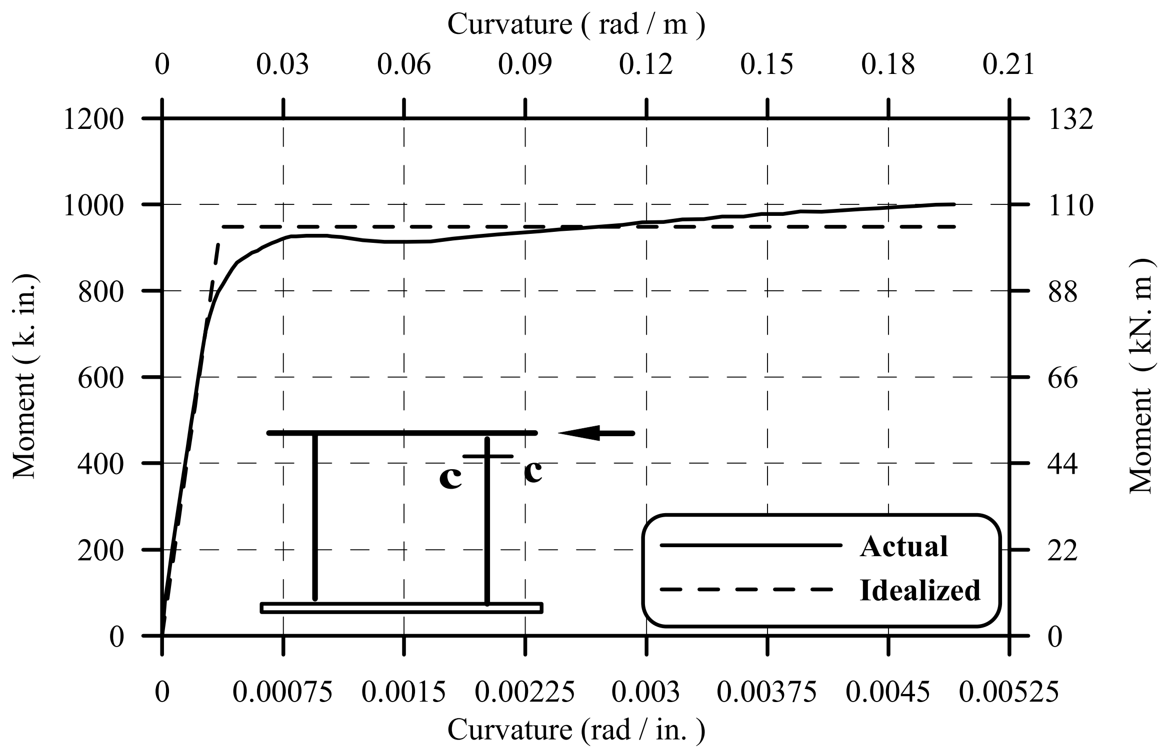

Fig. 2-19: Moment-Curvature Diagram at Sec. c-c at of Bent Column

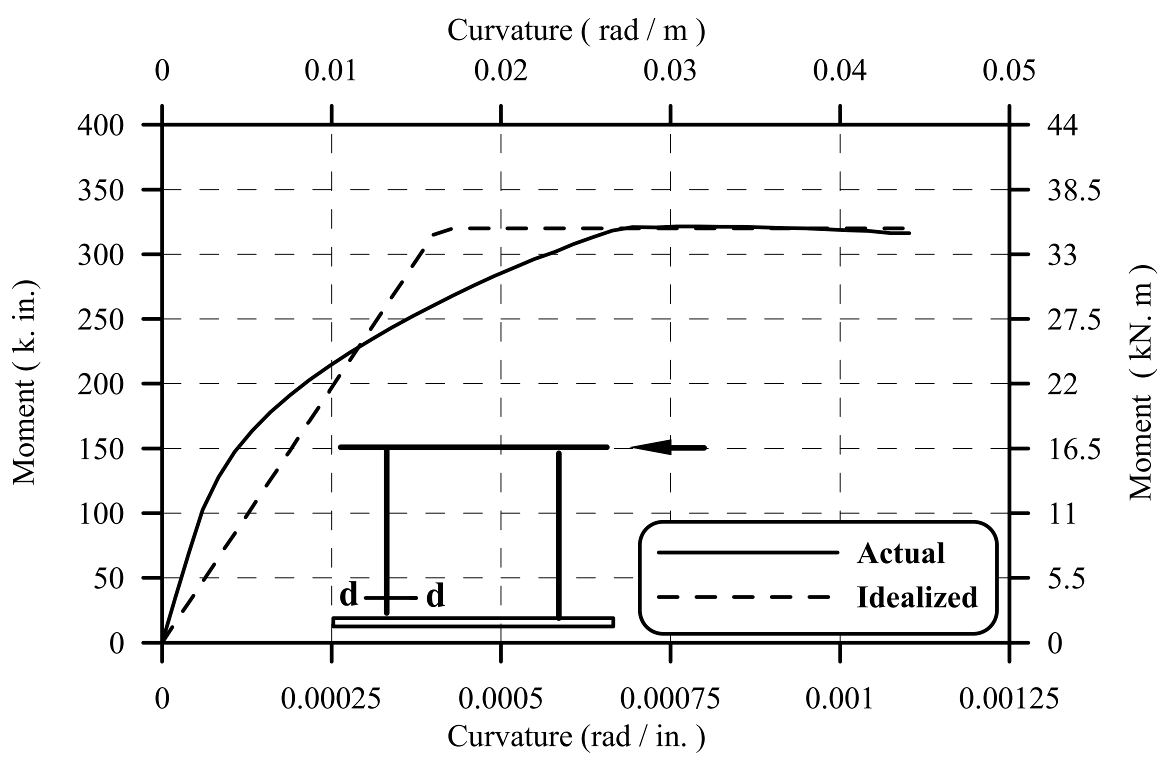

Fig. 2-20: Moment-Curvature Diagram at Sec. d-d of Bent Column Base

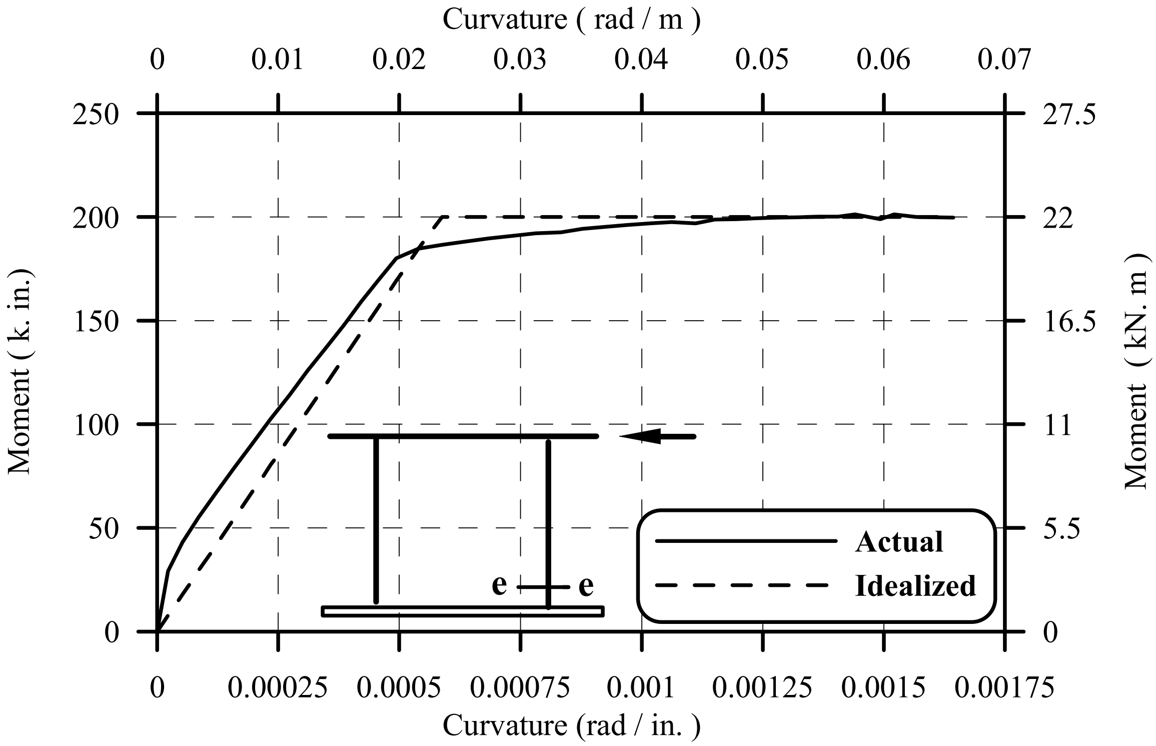

Fig. 2-21: Moment-Curvature Diagram at Sec. e-e of Bent Column Base

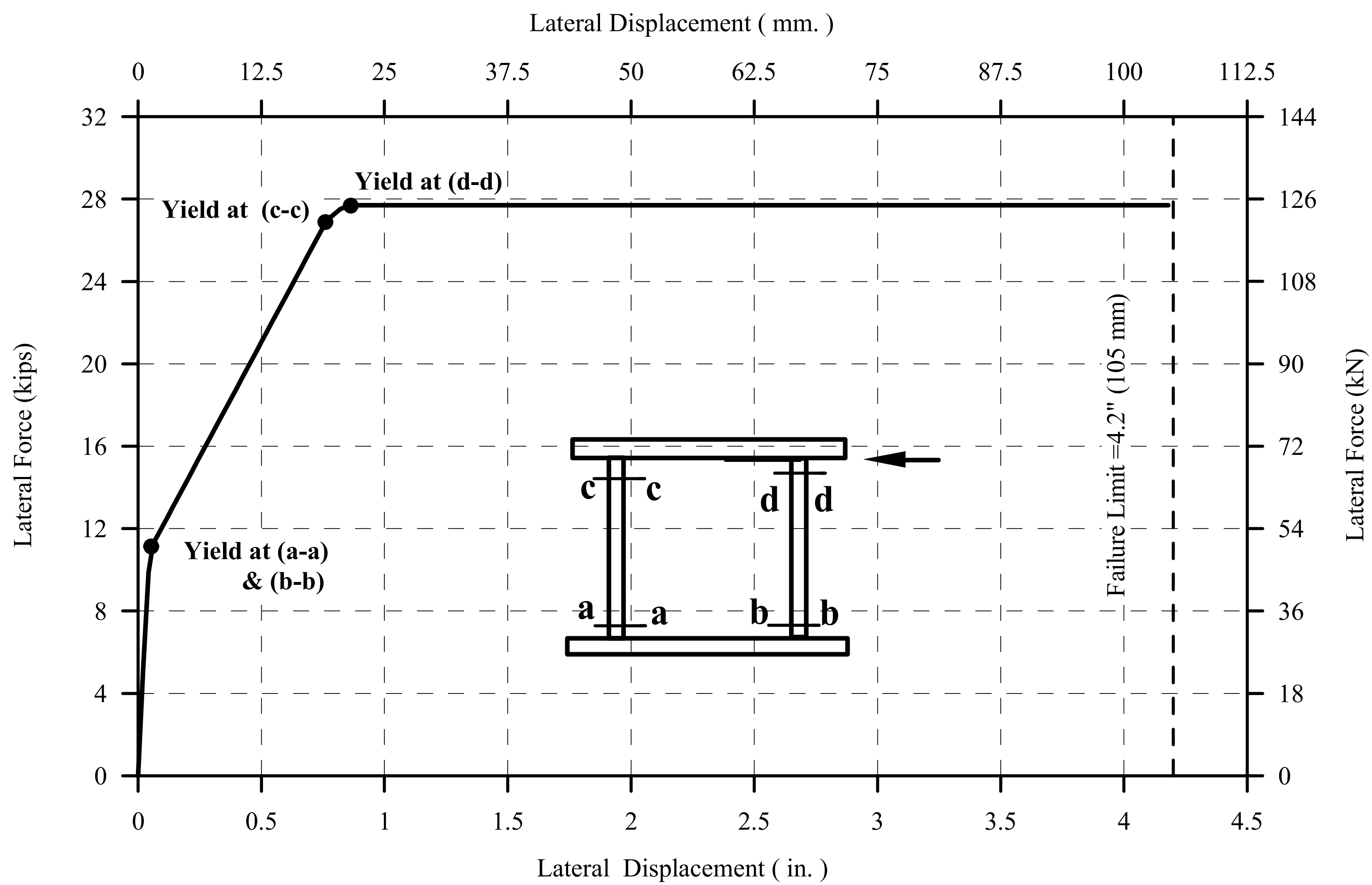

Fig. 2-22: Pushover Diagram for Tall Specimen B2CT

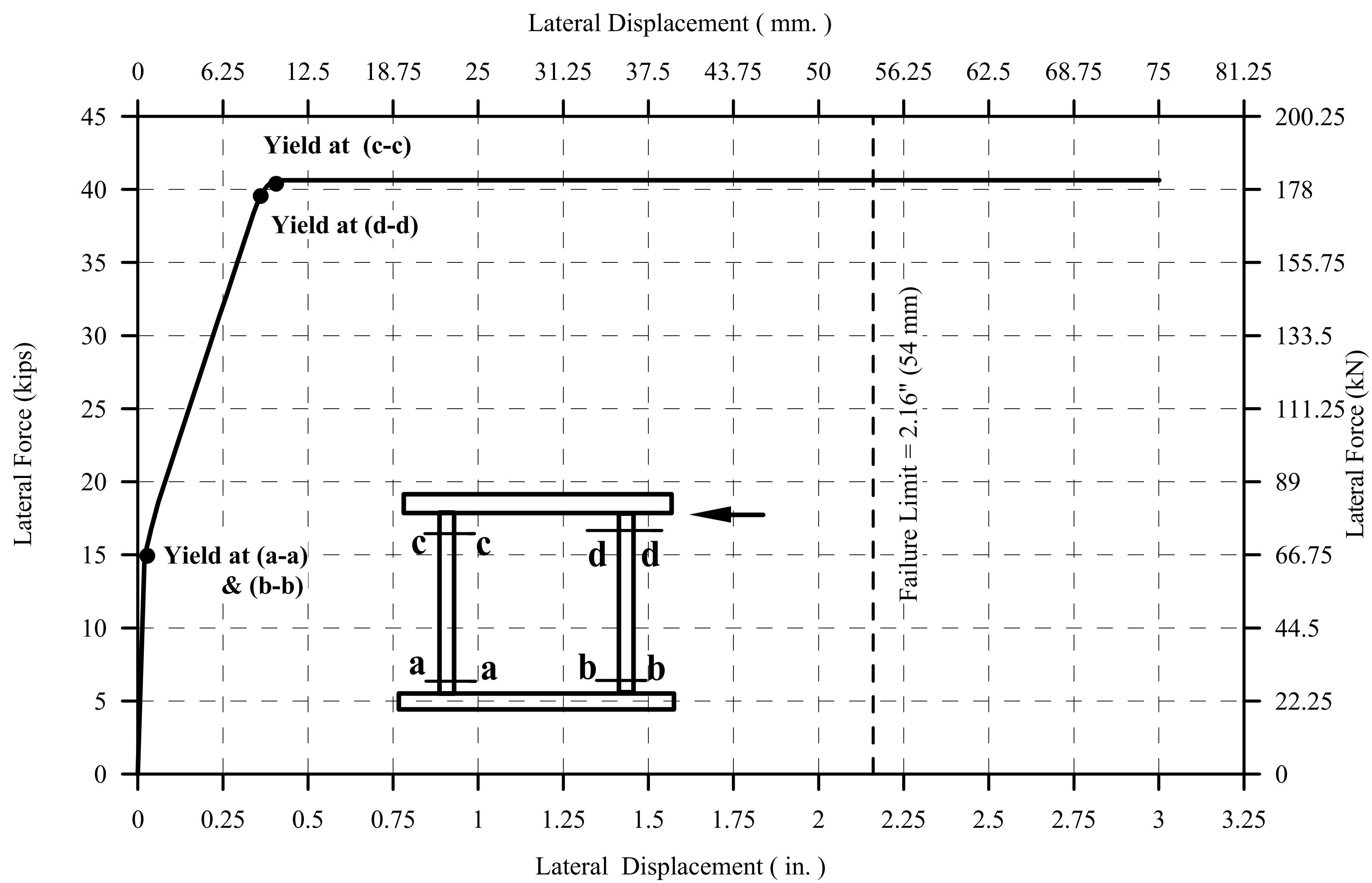

Fig. 2-23: Pushover Diagram for Middle Specimen B2CM

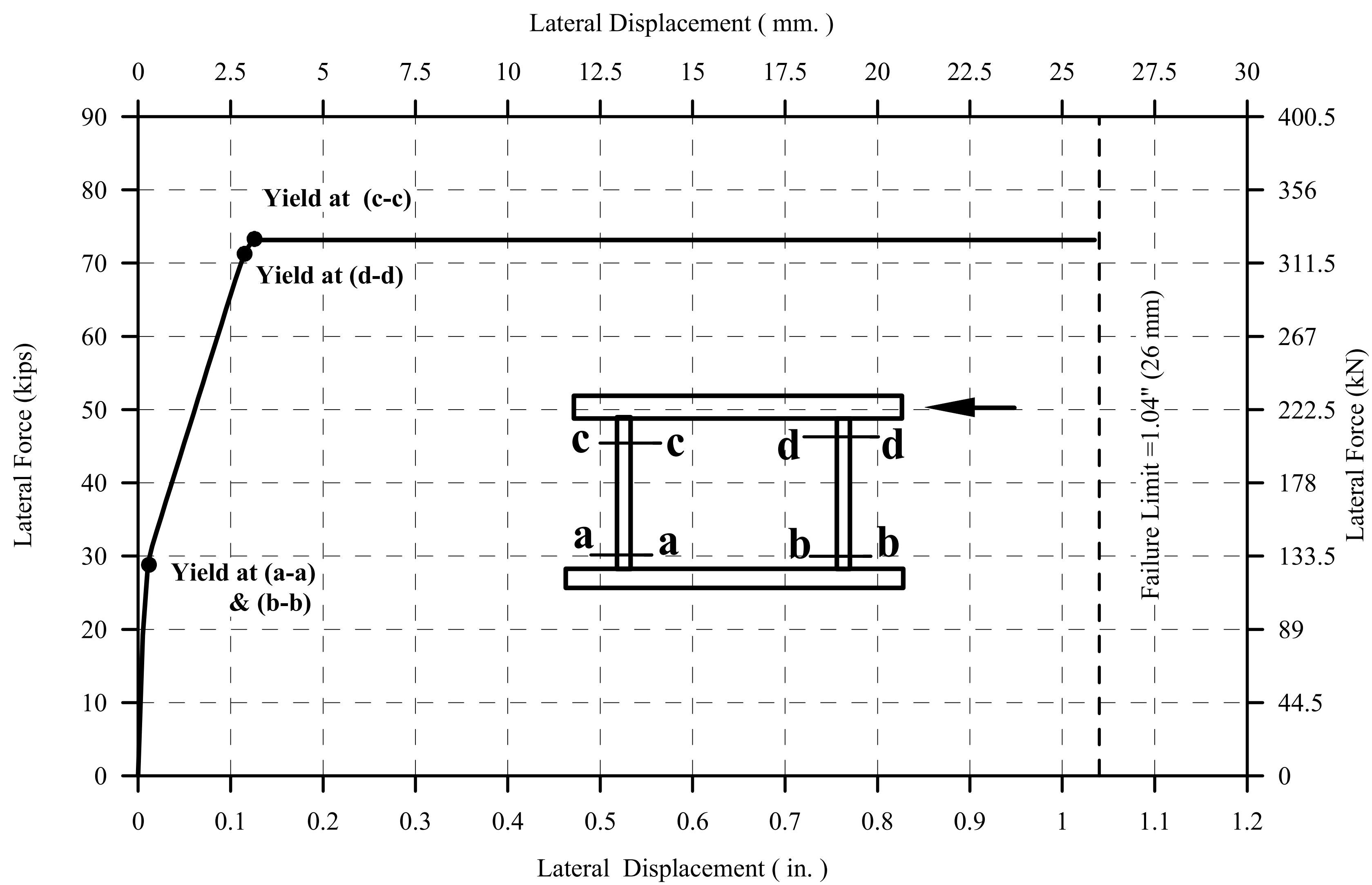

Fig. 2-24: Pushover Diagram for Short Specimen B2CS

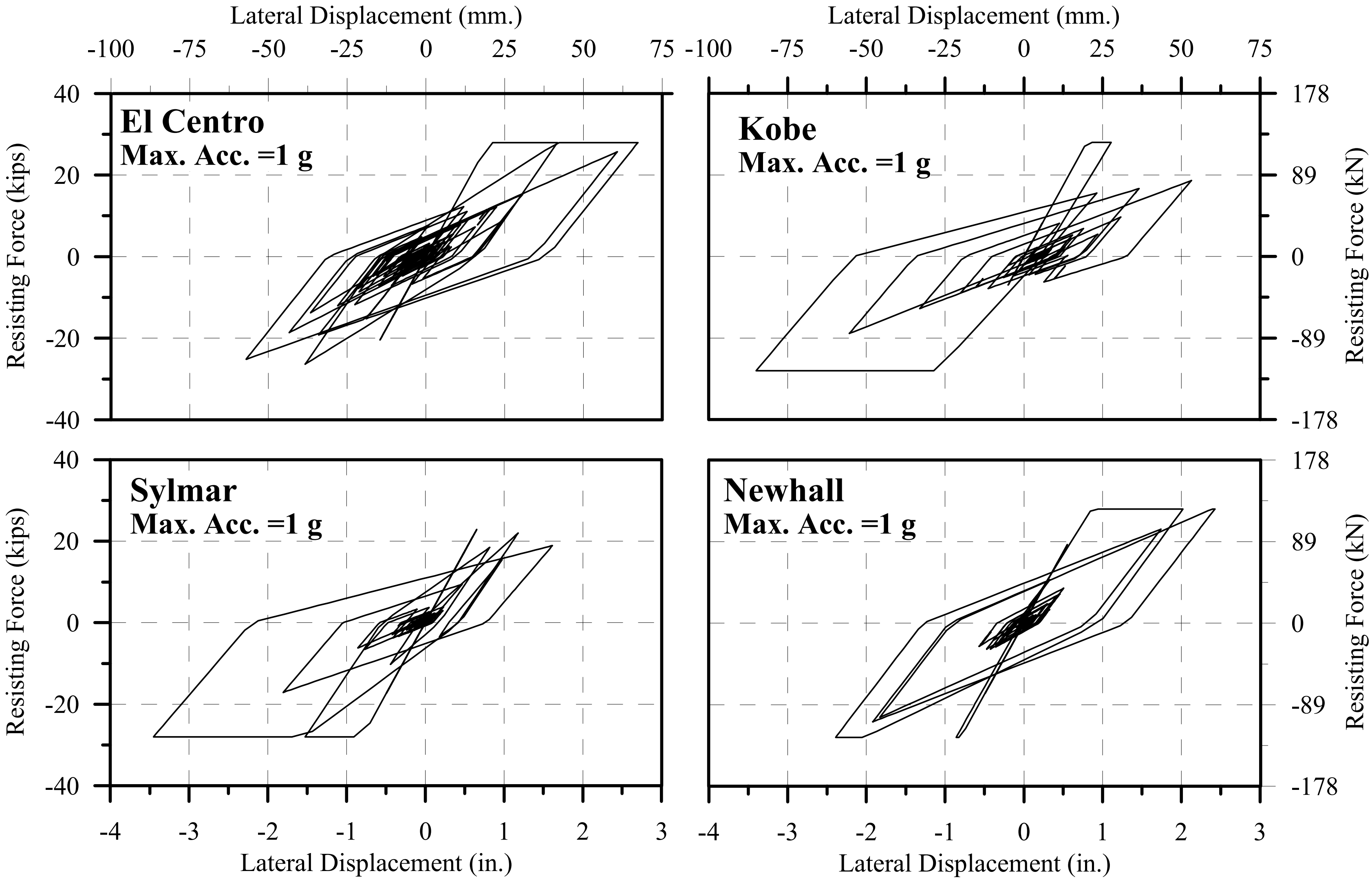

Fig. 2-25: Load-Displacement Hystereses for Specimen B2CT Subjected to Four Different Earhquakes

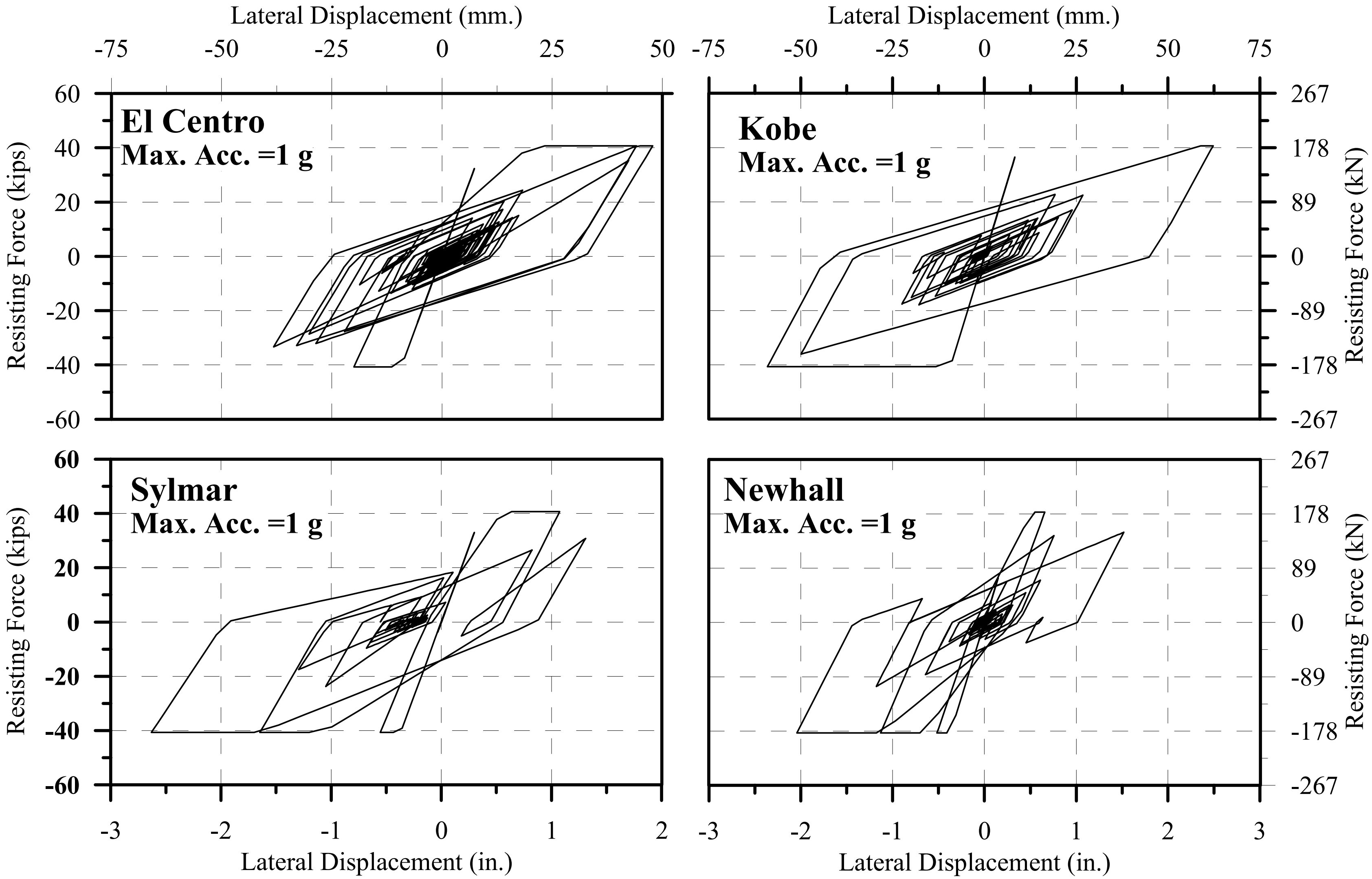

Fig. 2-26: Load-Displacement Hystereses of Specimen B2CM Subjected to Four Different Earhquakes

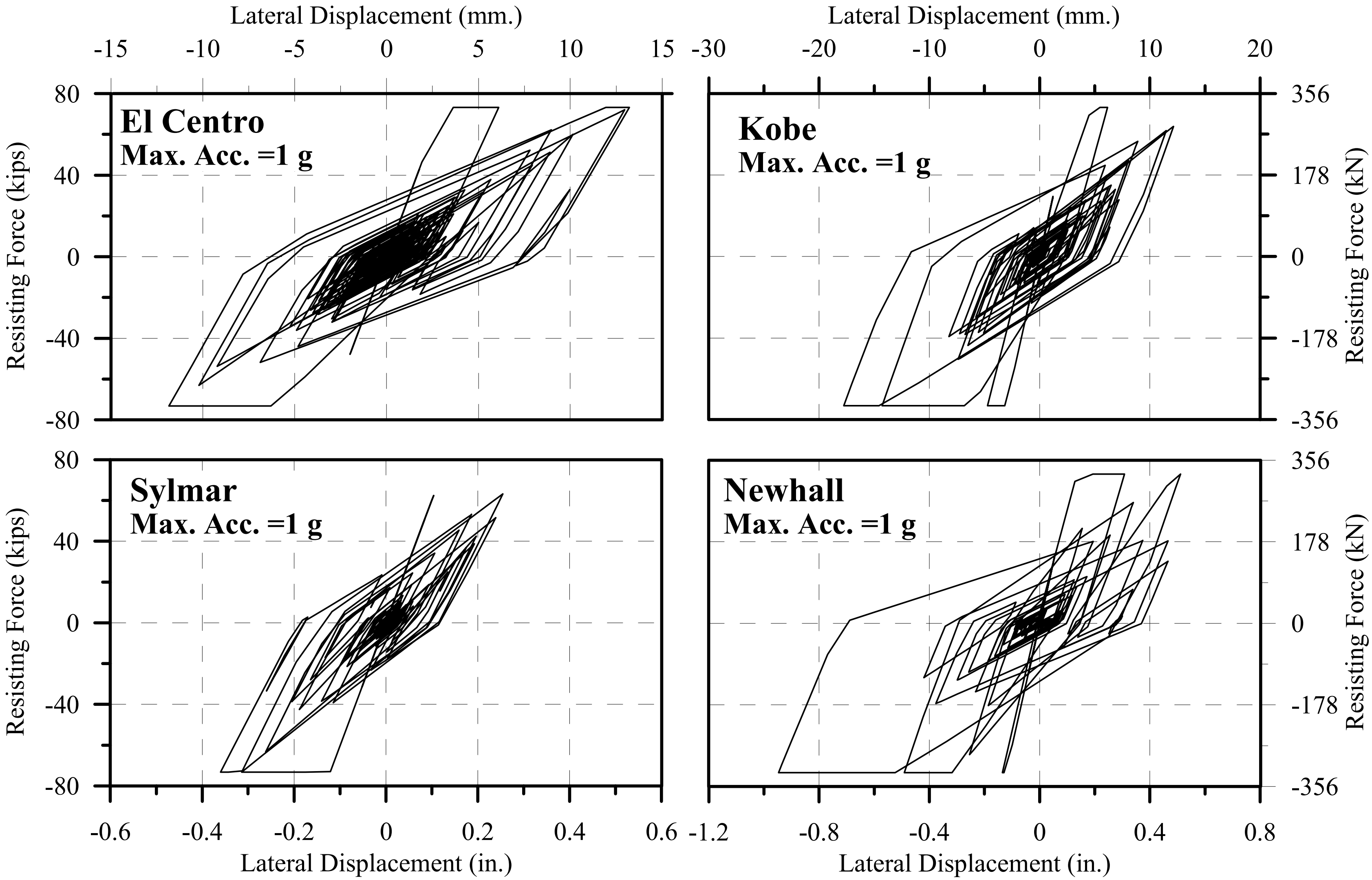

Fig. 2-27: Load-Displacement Hystereses of Specimen B2CS Subjected to Four Different Earhquakes

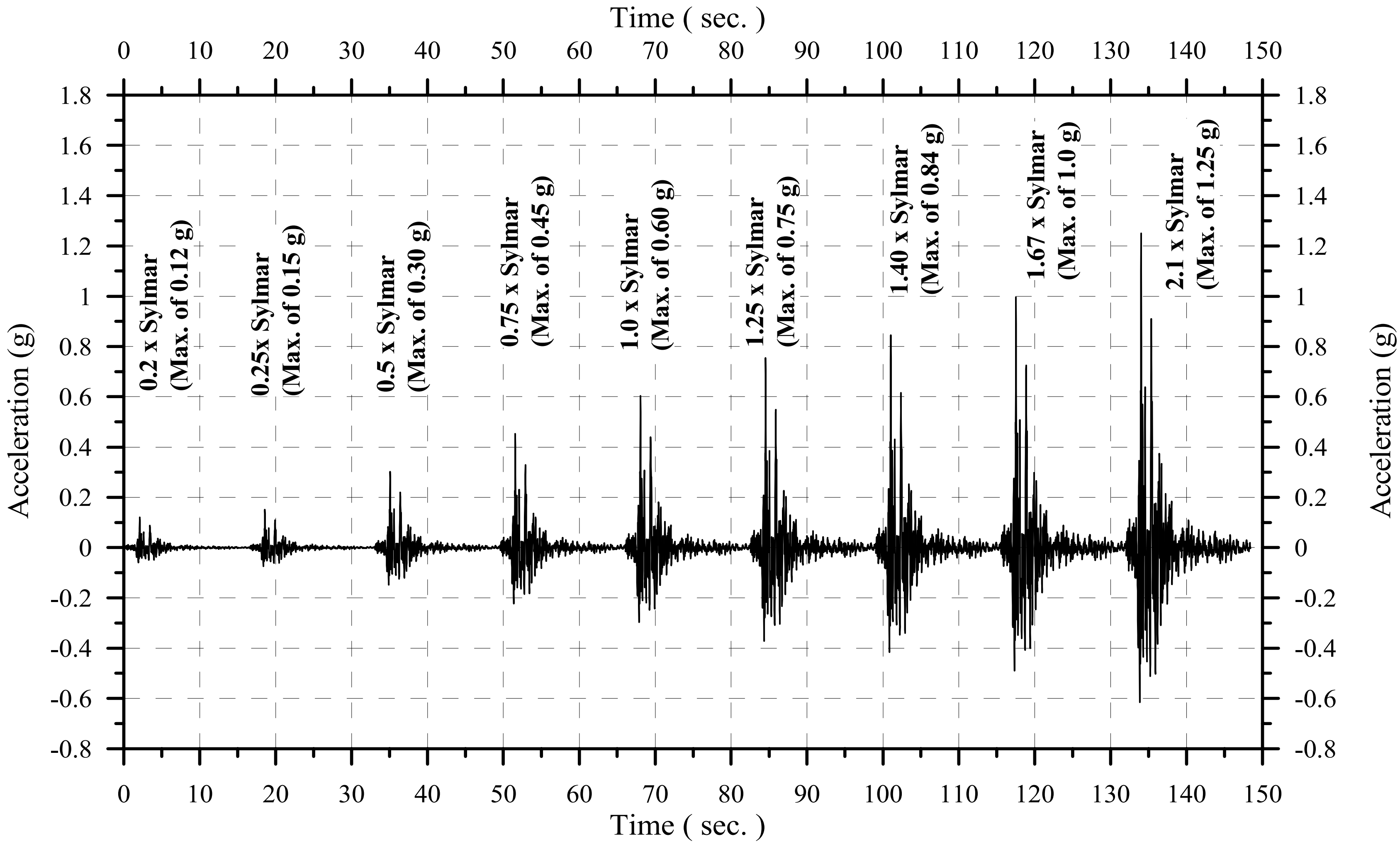

Fig. 2-28: Suggested Ramped Earthquake

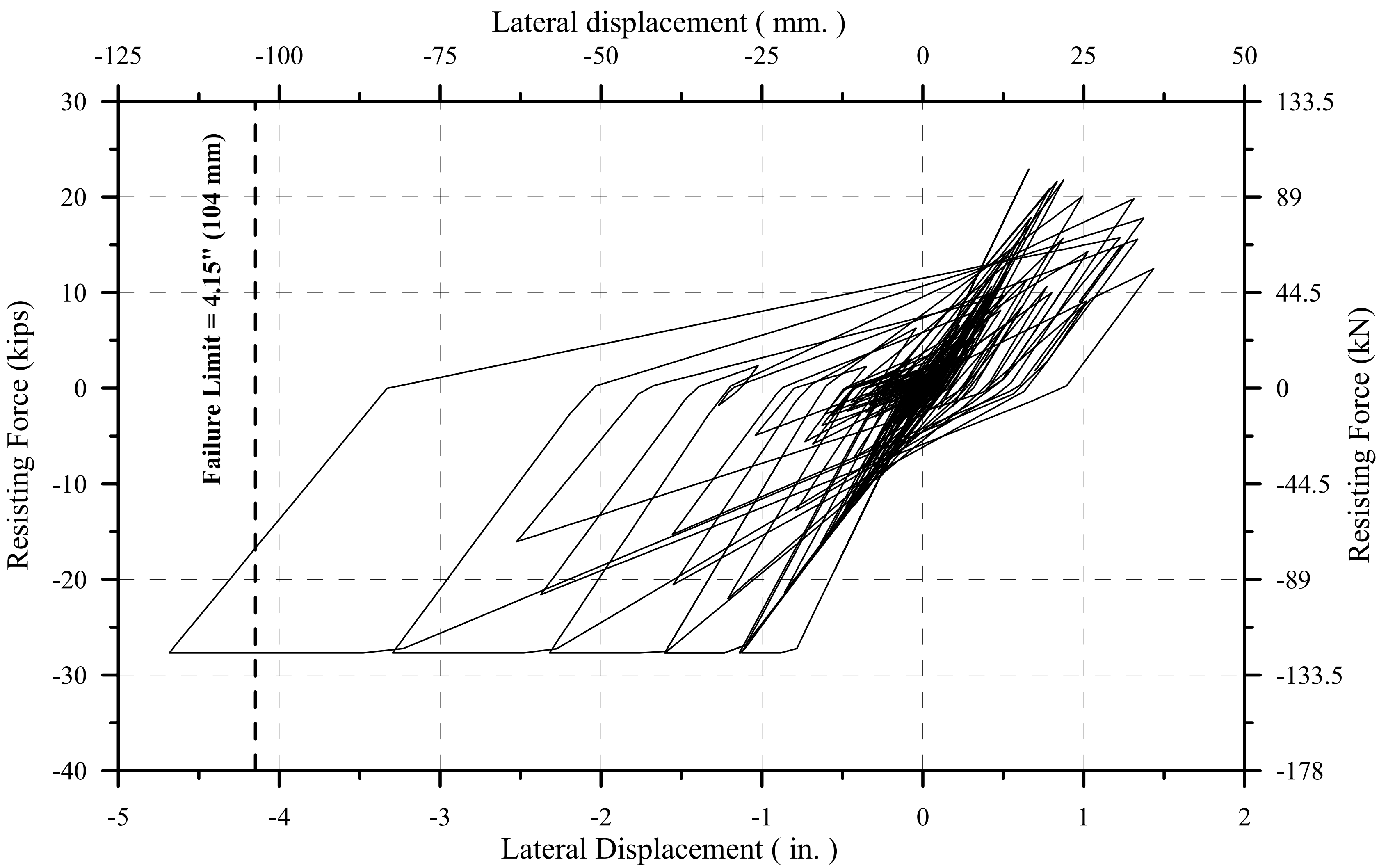

Fig. 2-29: Predicted Load-Displacement Hystereses of Specimen B2CT Subjected to Ramped Earthquake

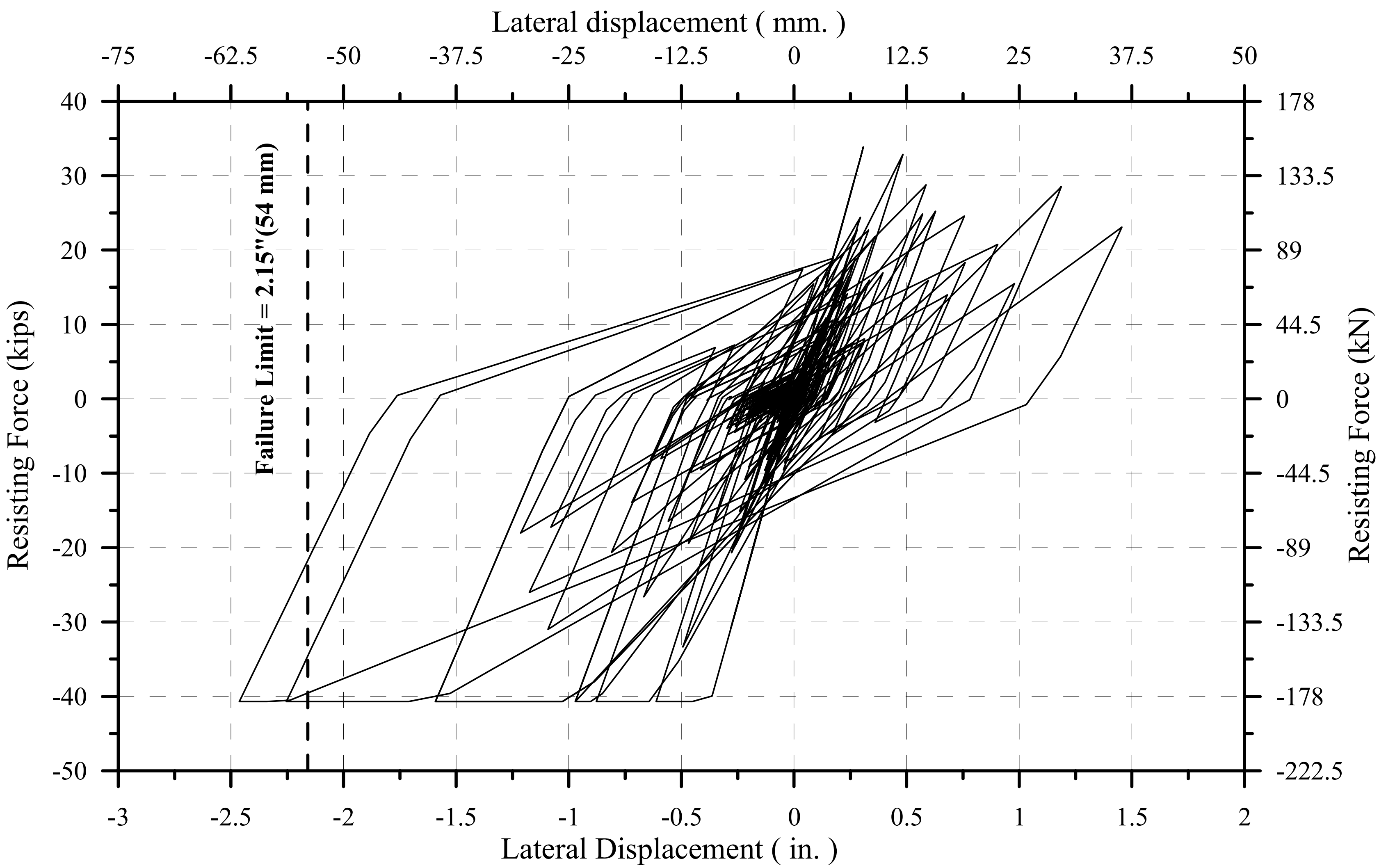

Fig. 2-30: Predicted Load-Displacement Hystereses of Specimen B2CM Subjected to Ramped Earthquake

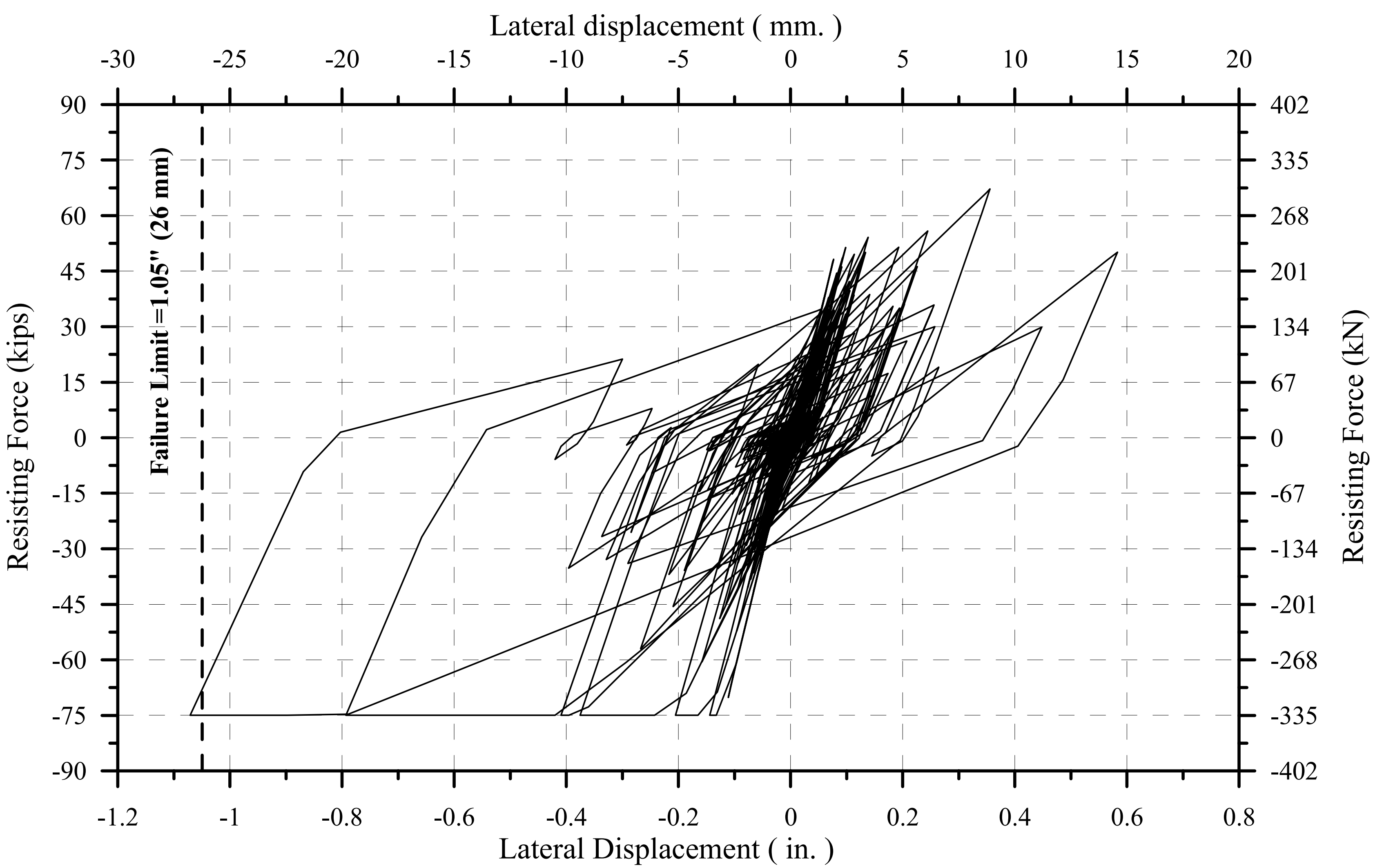

Fig. 2-31: Predicted Load-Displacement Hystereses of Specimen B2CS Subjected to the Ramped Earthquake

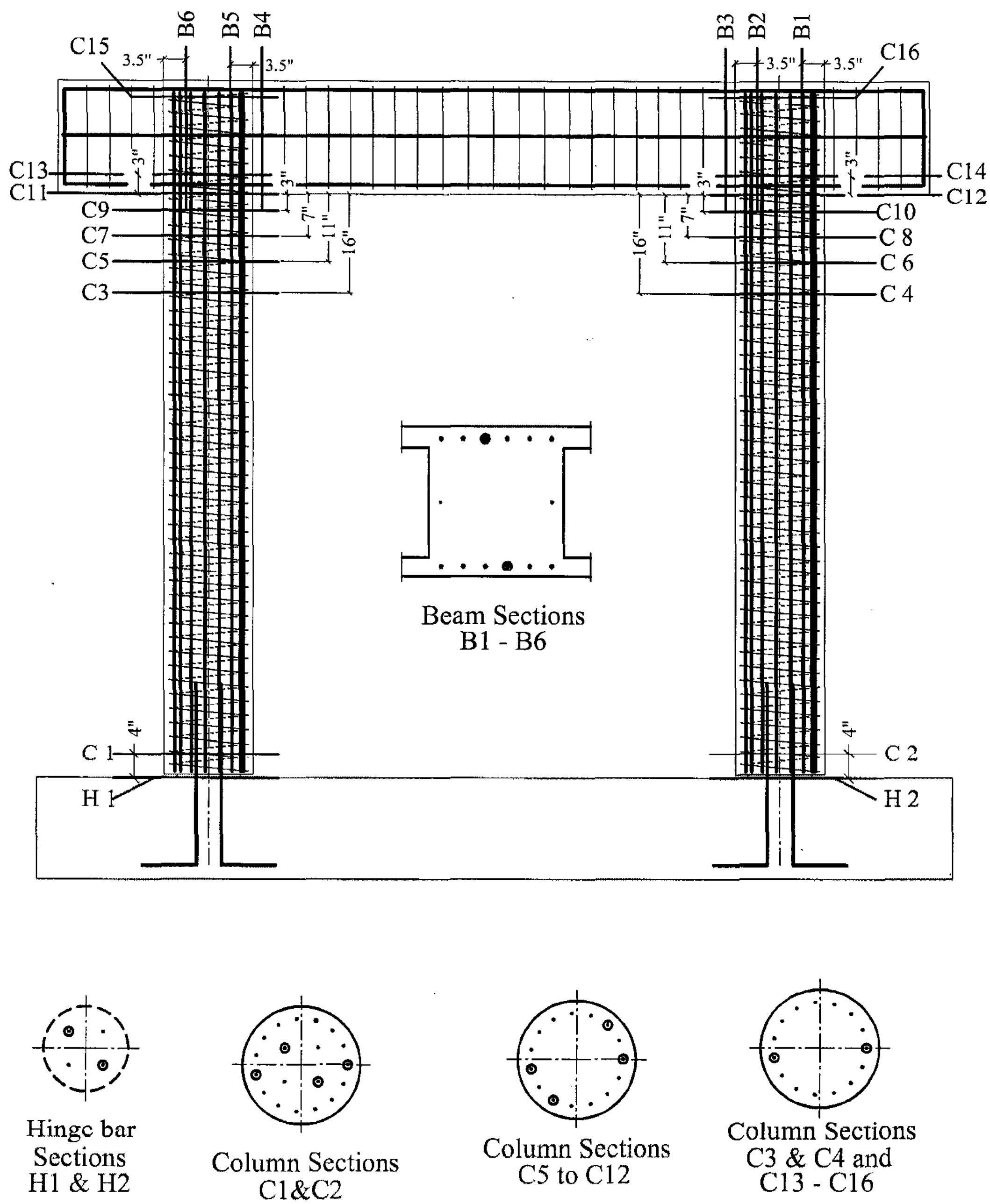

Fig. 2-32a: Strain Gages of Longitudinal Reinf. in both Specimens B2CT and B2CM (dimensions in inches)

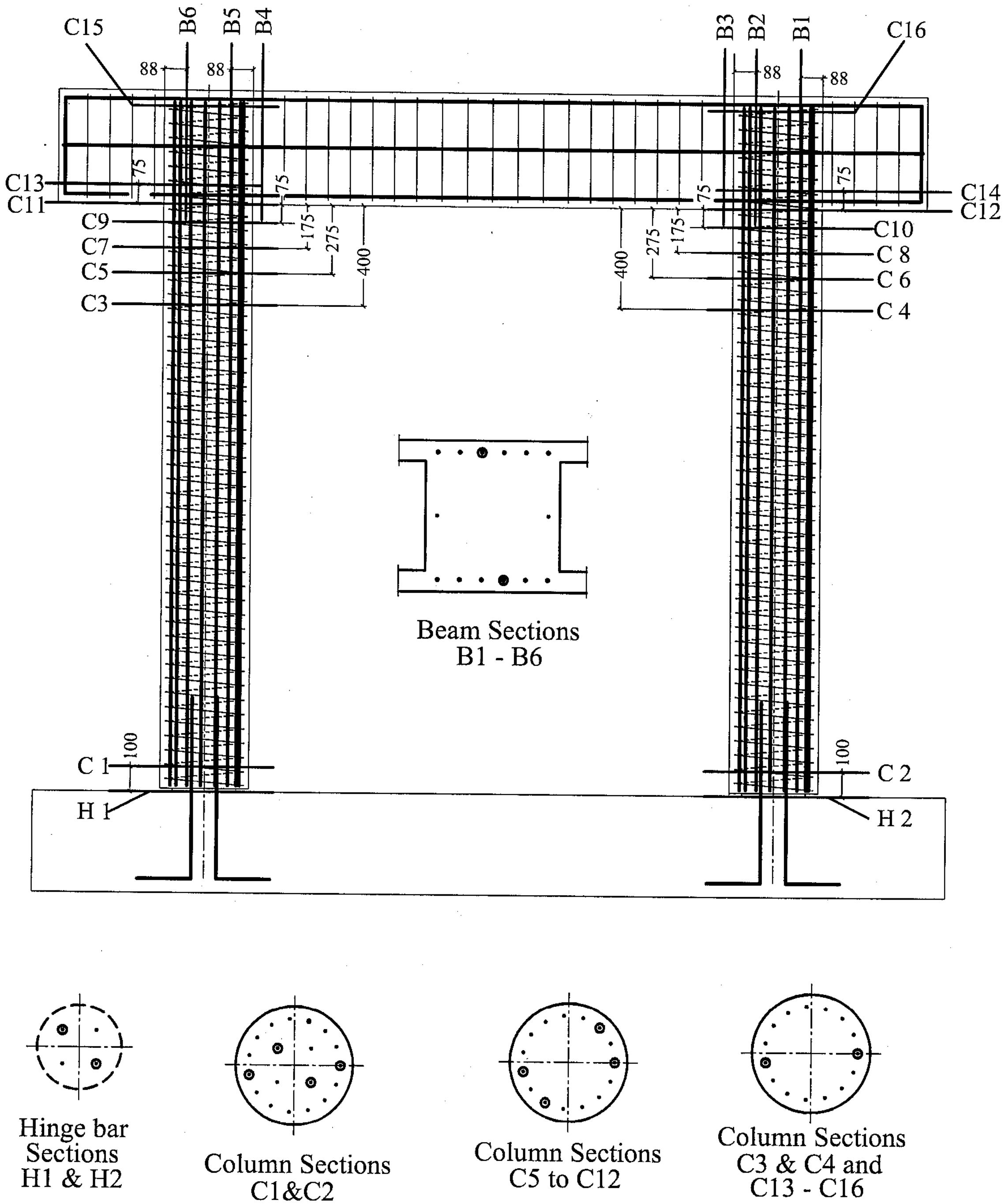

Fig. 2-32b: Strain Gages of Longitudinal Reinf. in both of Specimens B2CT and B2CM (dimensions in mm.)

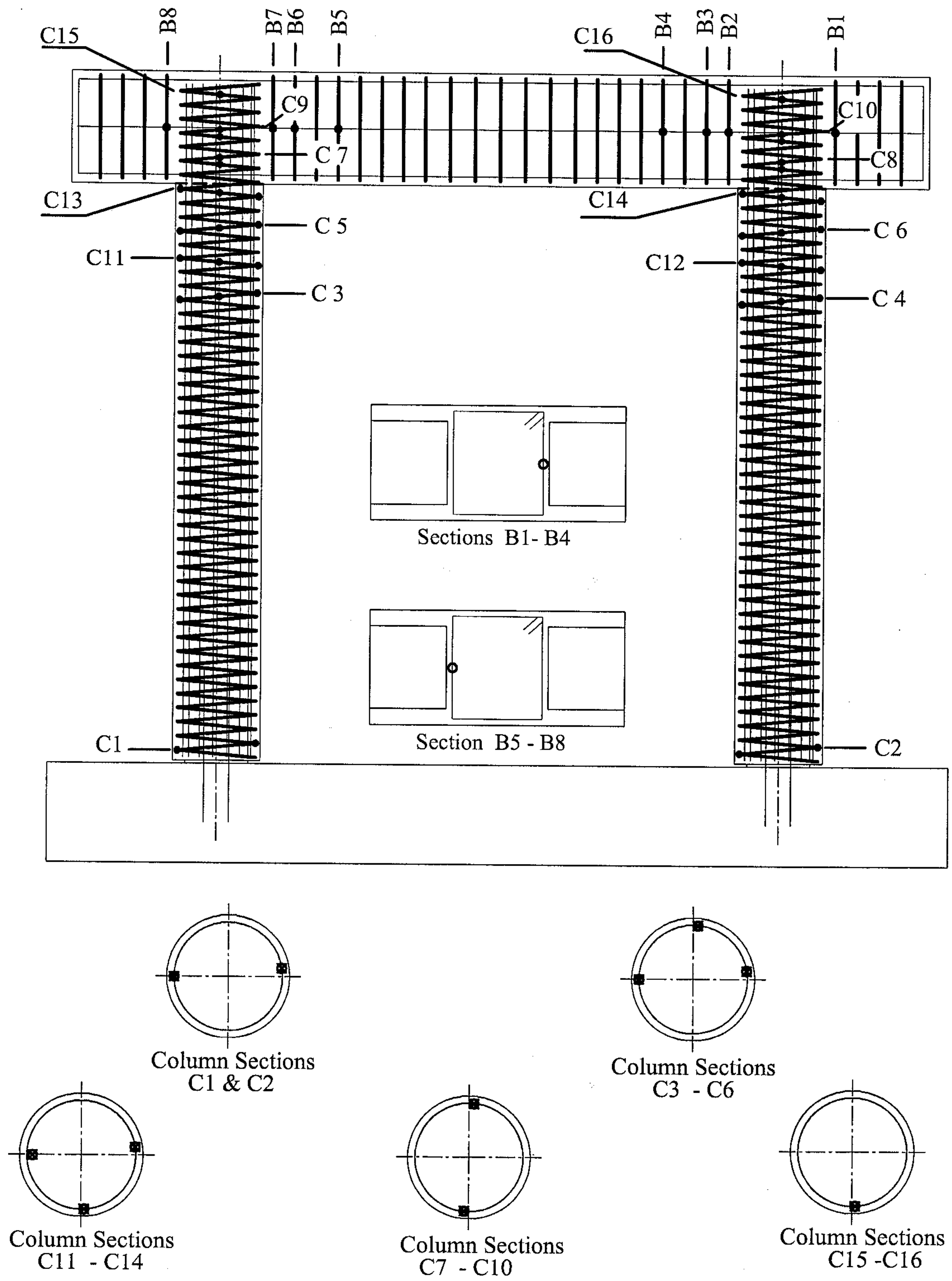

Fig. 2-33: Strain Gages of Transverse Reinf. in both Specimens B2CM and B2CT

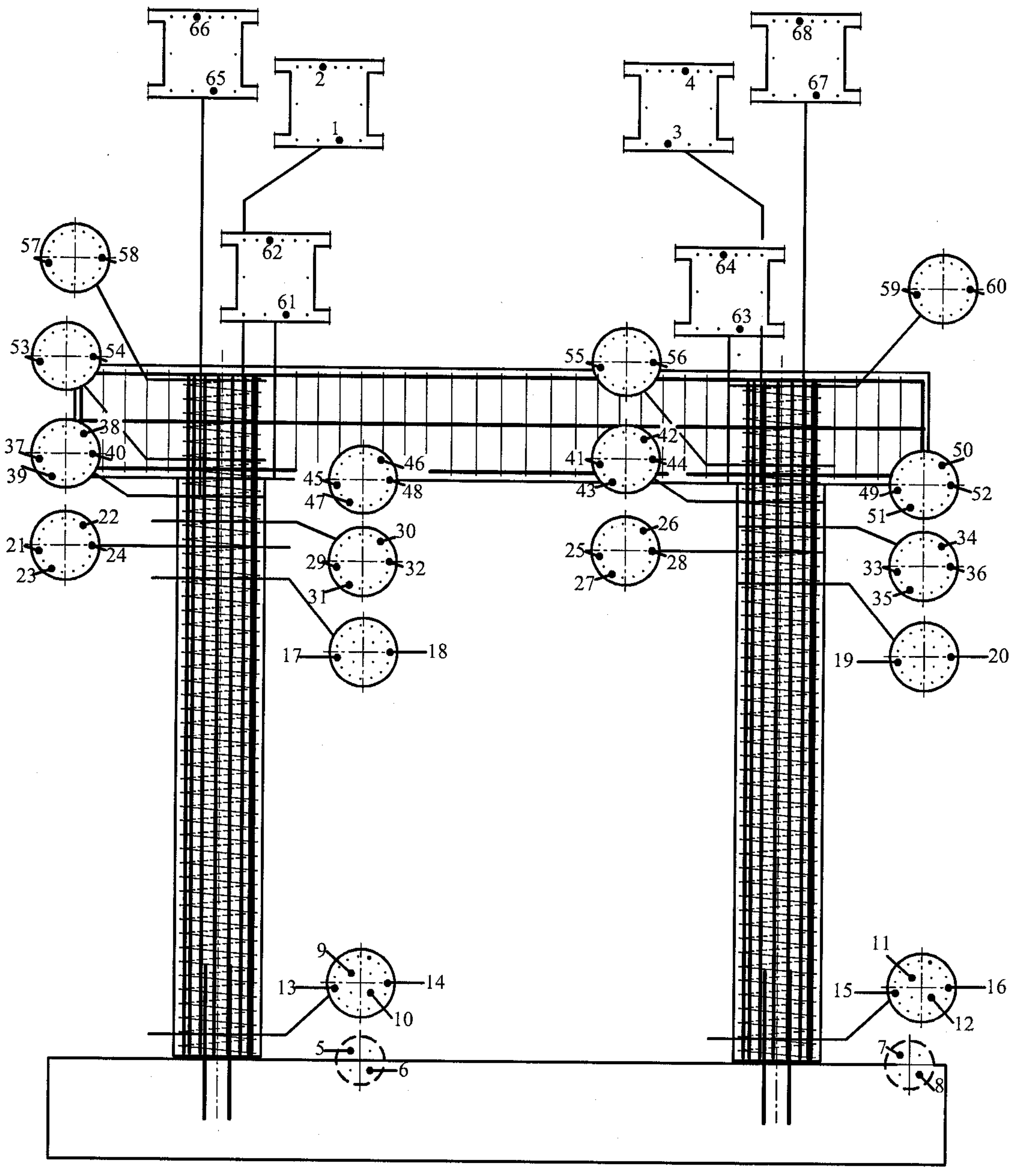

Fig. 2-34: Strain Gage Numbering of Longitudinal Reinf. in Both Specimens B2CM and B2CT

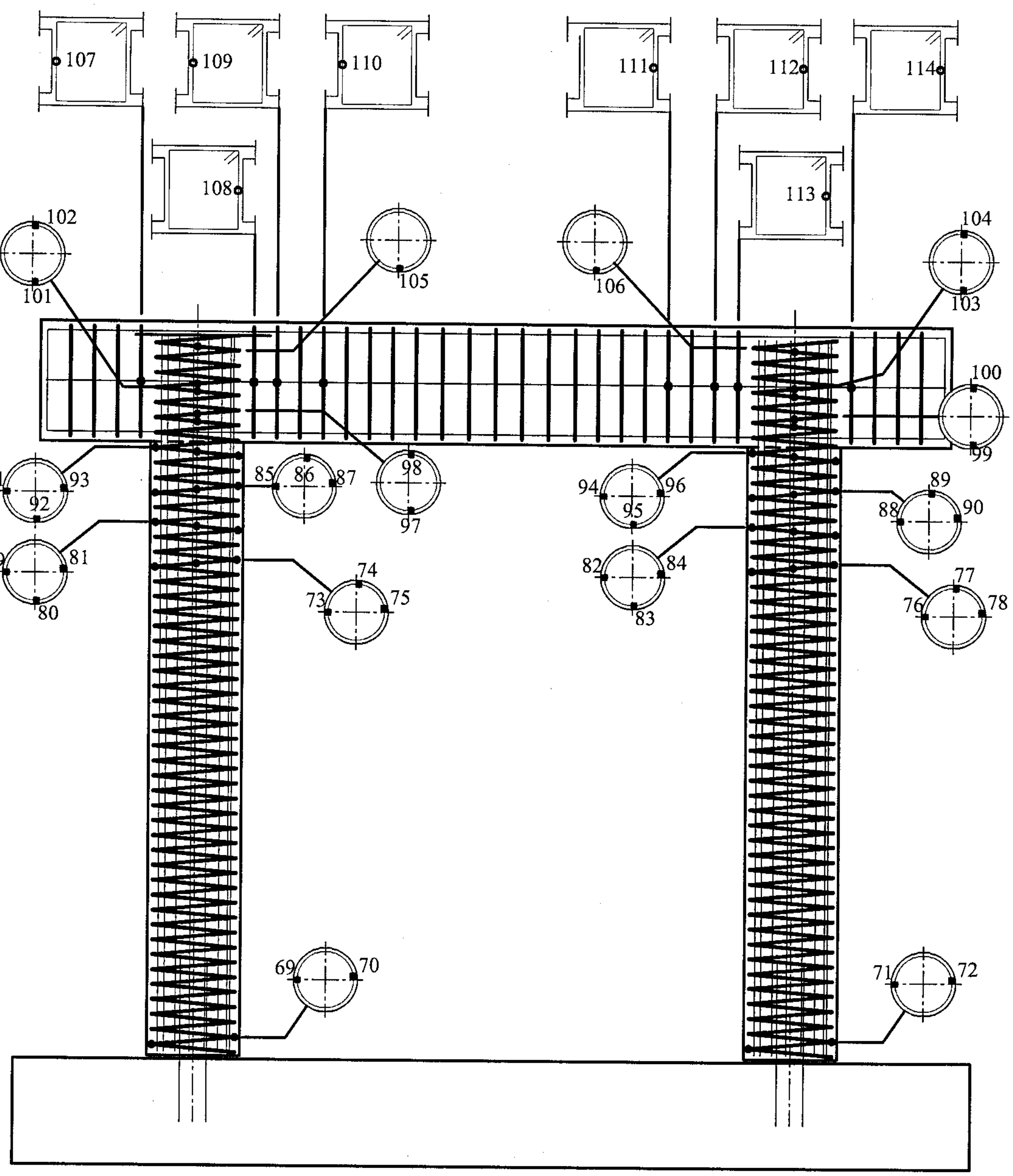

Fig.2-35: Straing Gage Numbering of Transverse Reinf. in both Specimens B2CM and B2CT

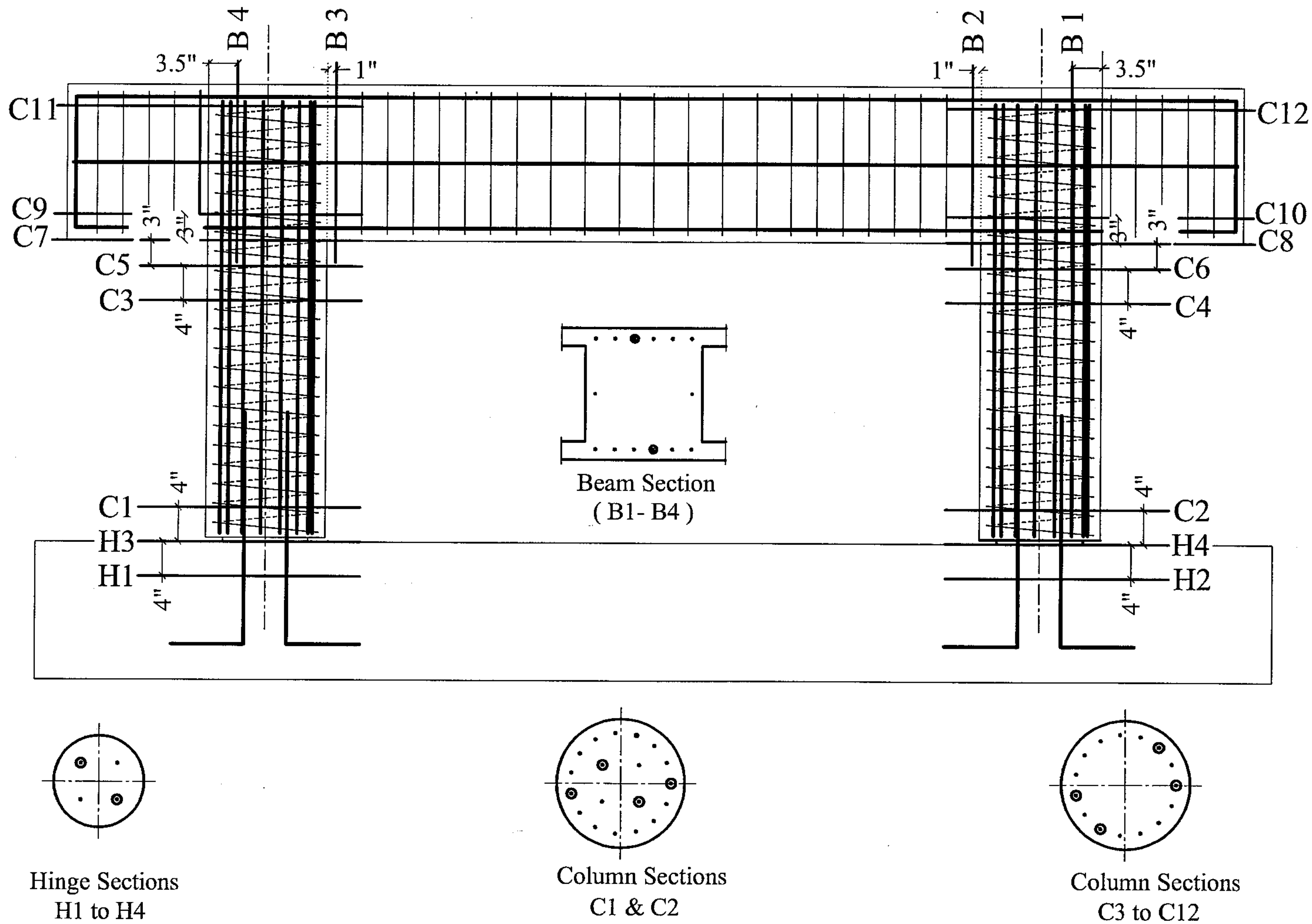

Fig.2-36a: Strain Gages of Longitudinal Reinf. in Specimen B2CS (dimensions in inches)

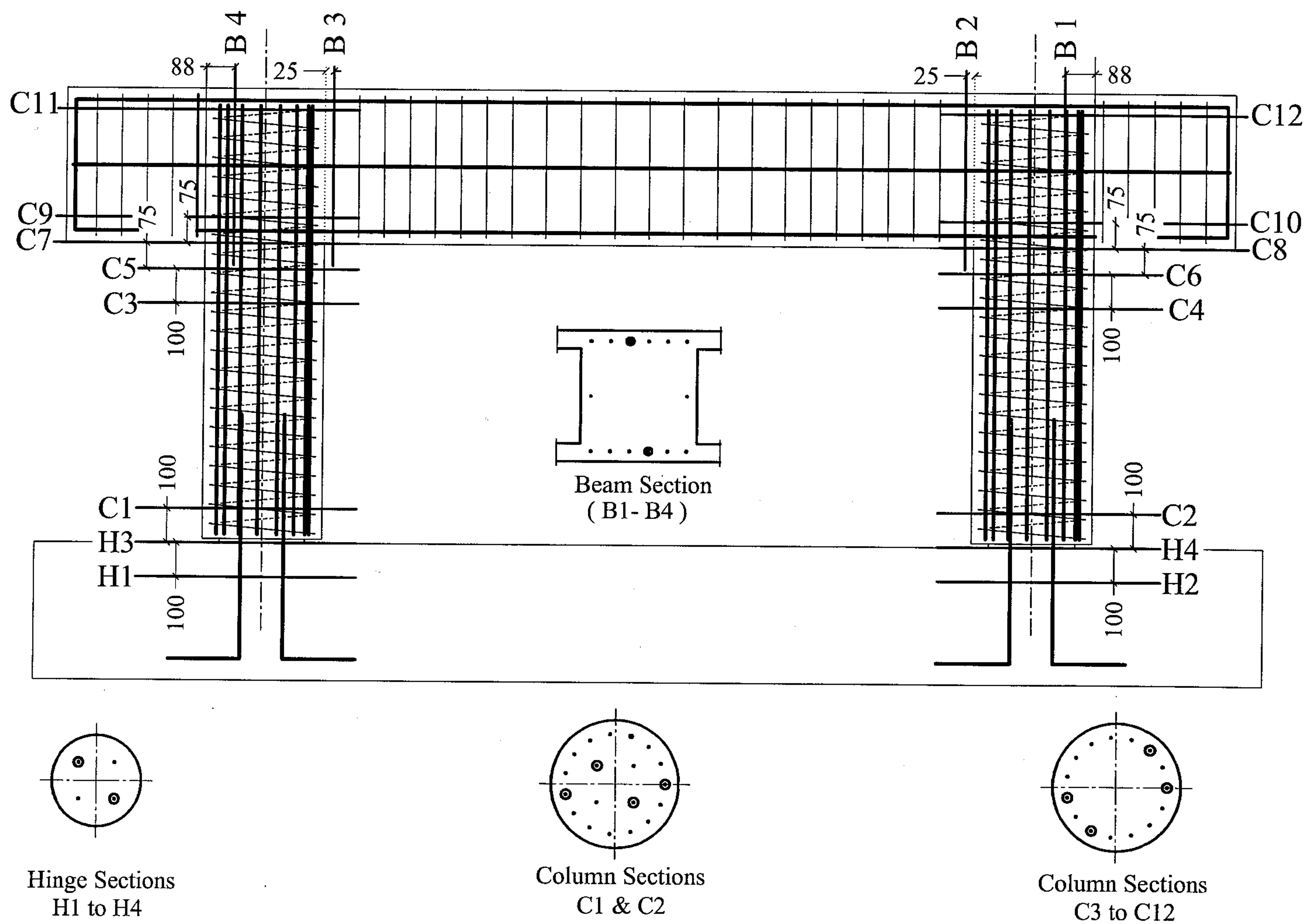

Fig.2-36b: Strain Gages of Longitudinal Reinf. in Specimen B2CS (dimensions in mm.)

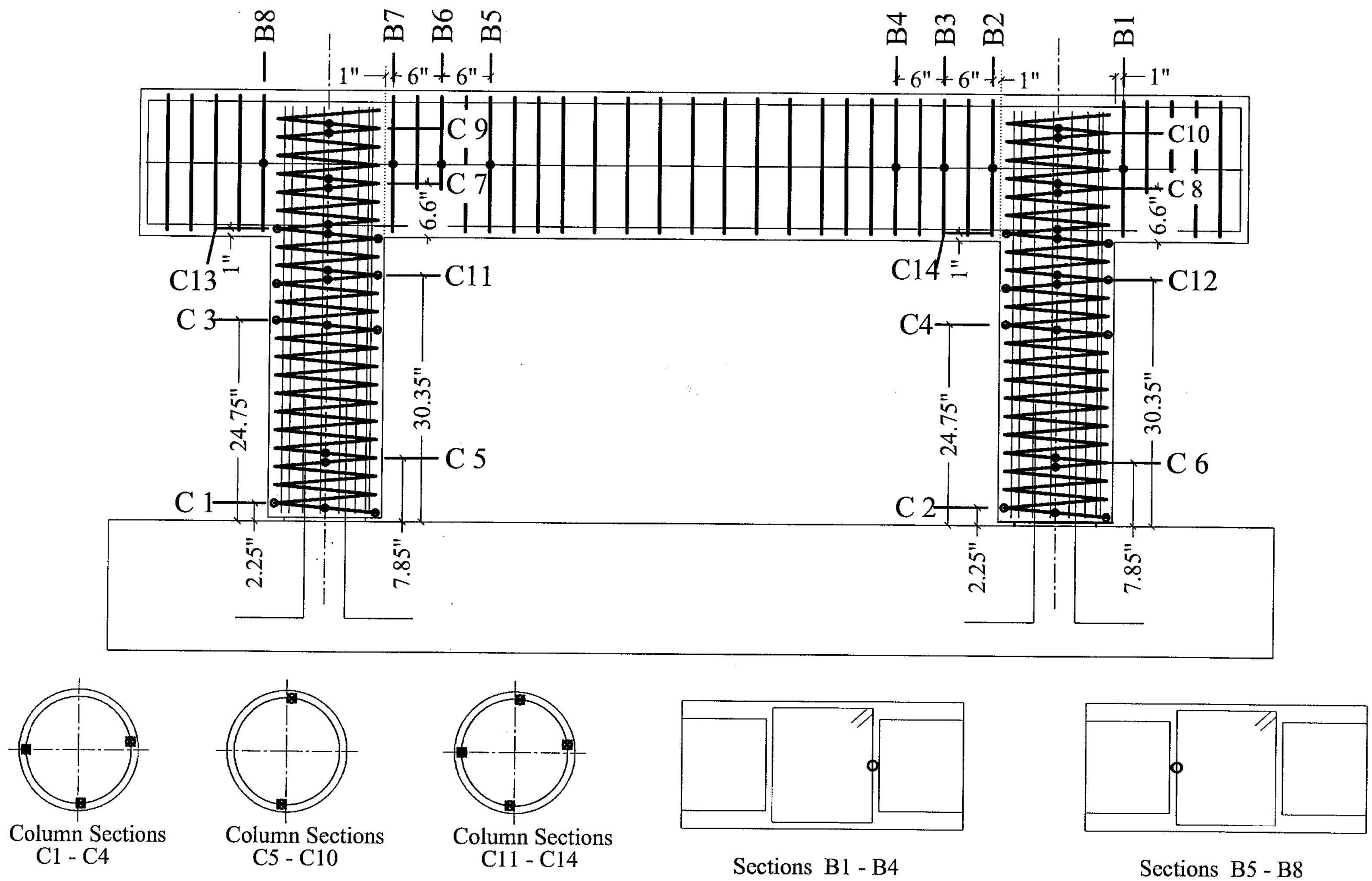

Fig.2-37a: Strain Gages of Transverse Reinf. in Specimen B2CS (dimensions in inches)

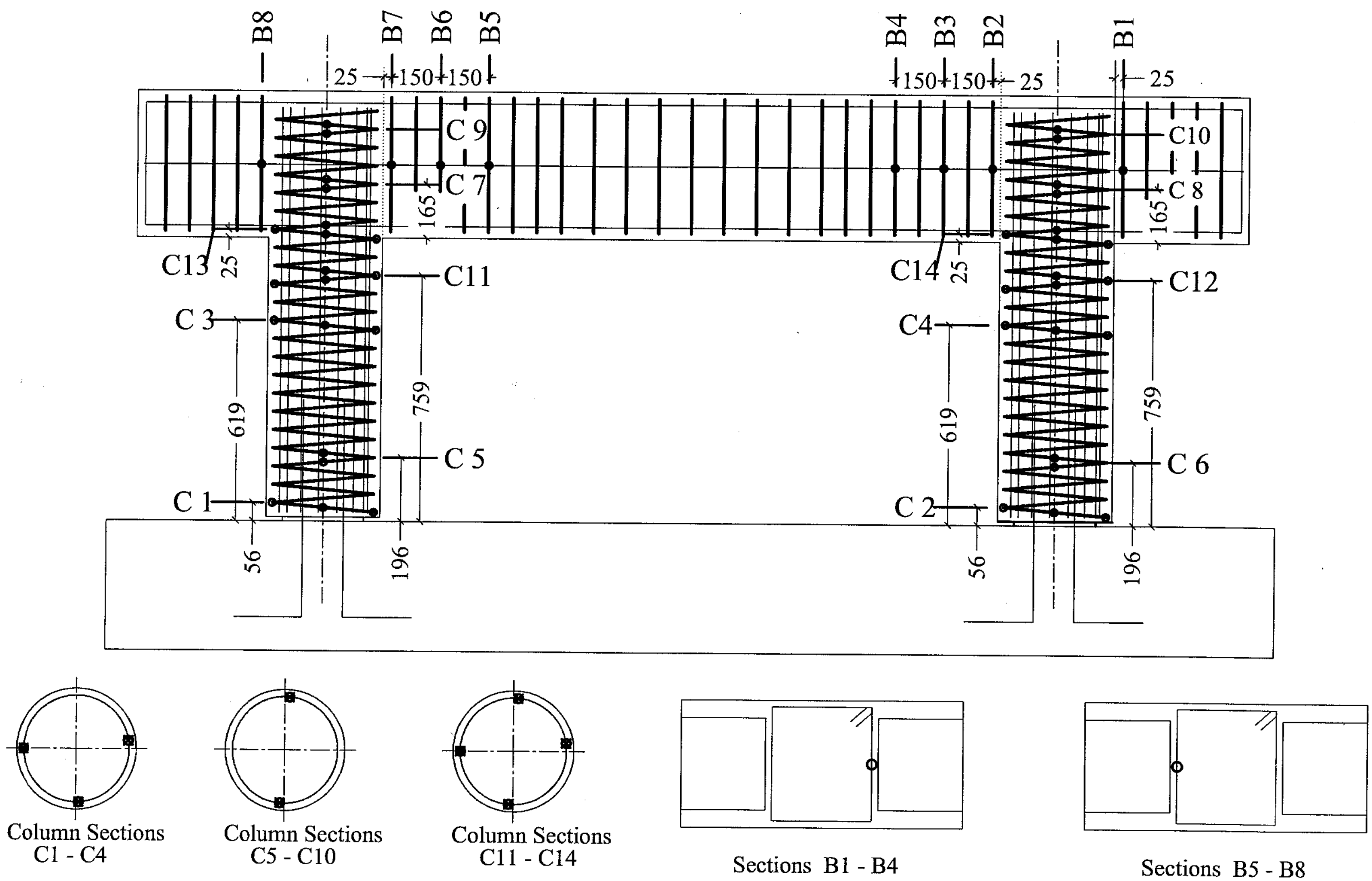

Fig.2-37b: Strain Gages of Transverse Reinf. in Specimen B2CS (dimensions in mm.)

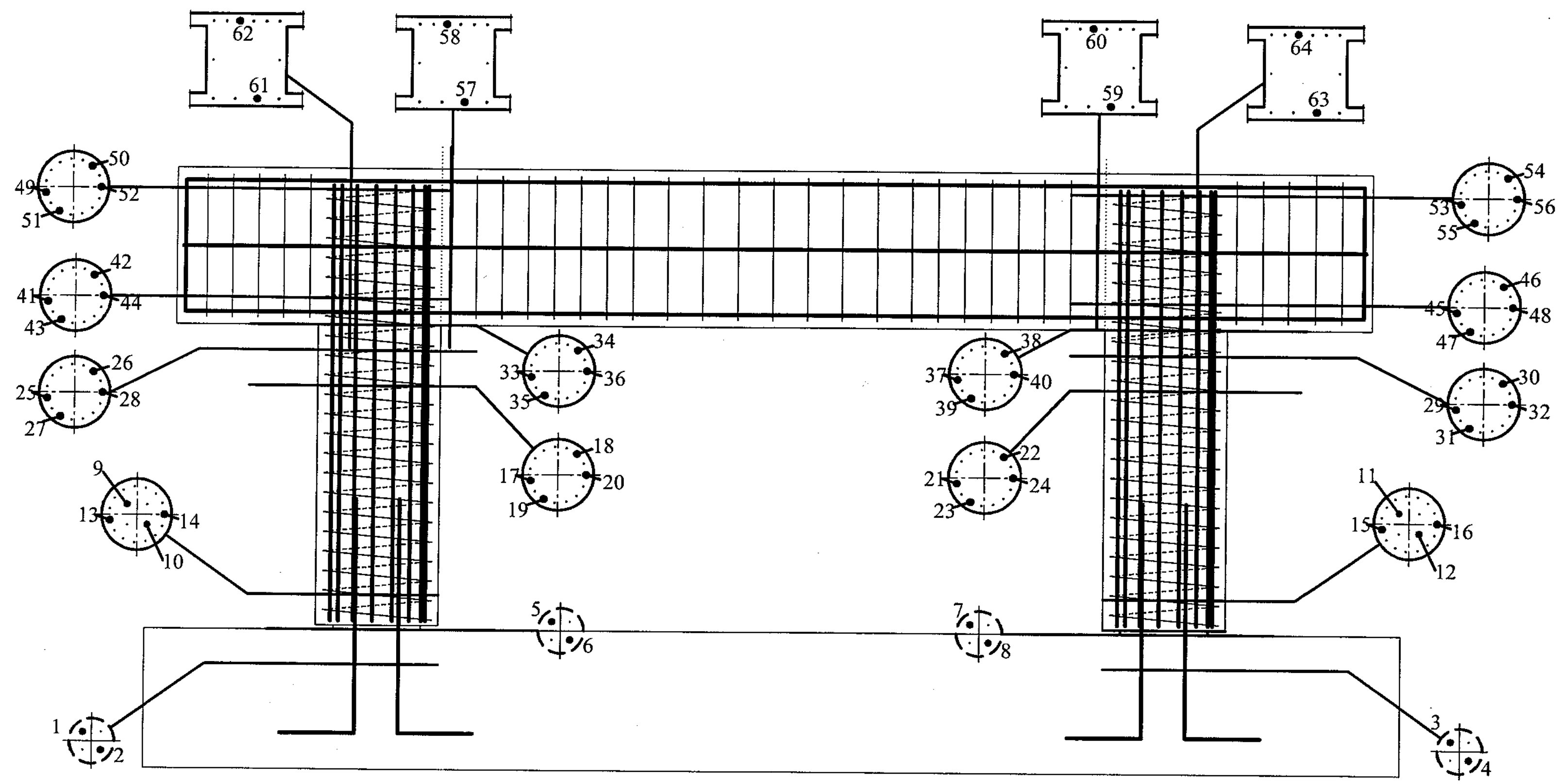

Fig. 2-38: Strain Gage Numbering of Longitudinal Reinf. in Specimen B2CS

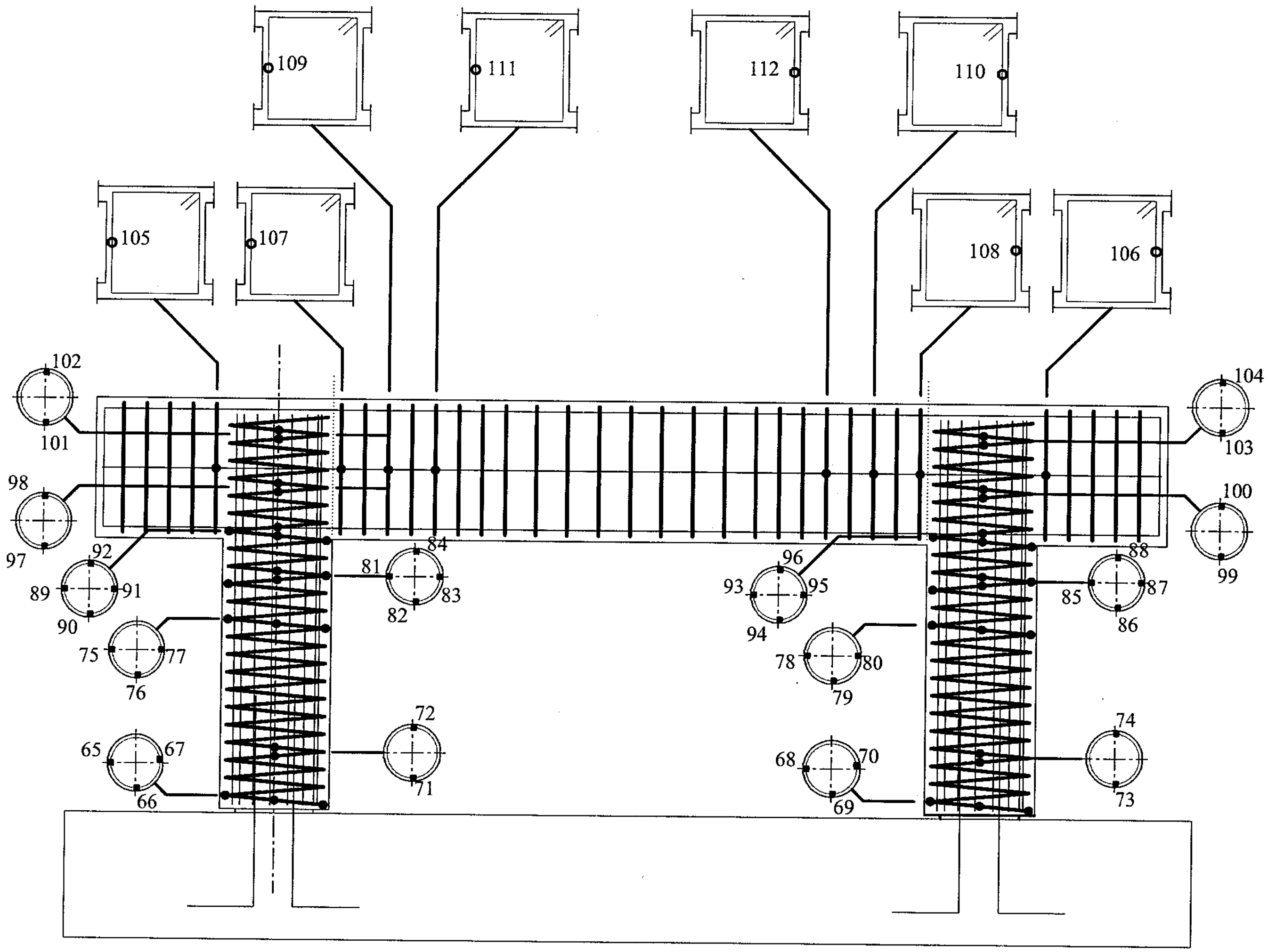

Fig. 2-39: Strain Gage Numbering of Transverse Reinf. in Specimen B2CS

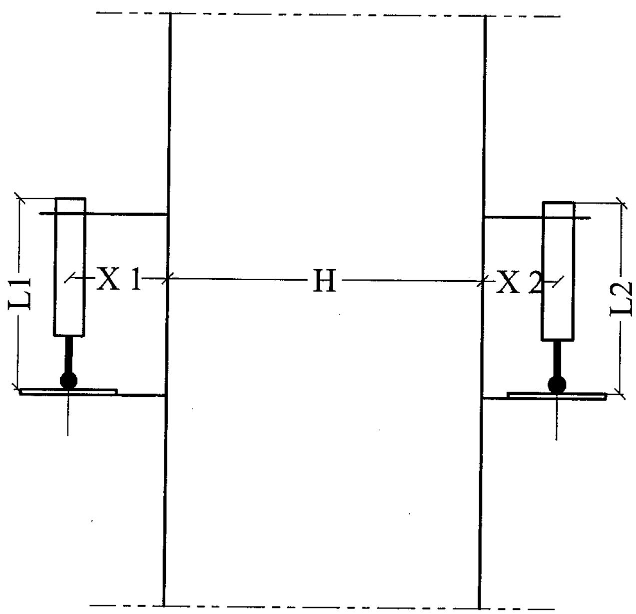

H Section Before Deformation

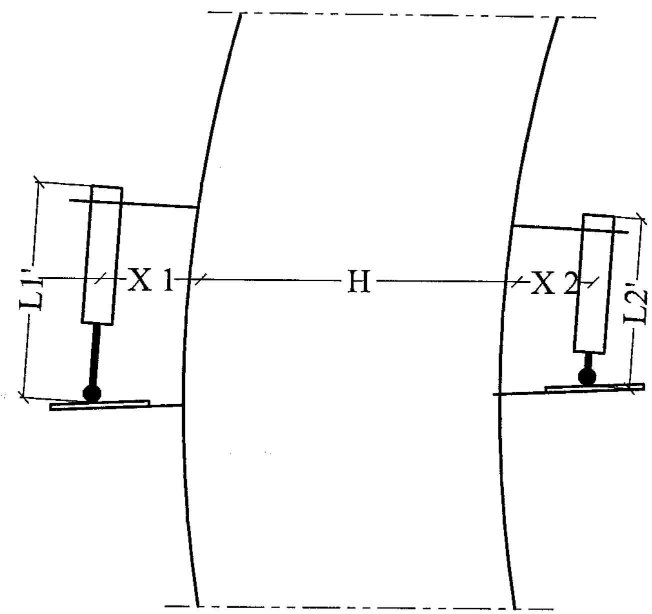

H Section After Deformation

- Reading in Novotechnik 1 = L1' - L1
- Reading in Novotechnik 1 = L2 - L2'
- Strain at Novotechnik 1 (Strain 1)= (L1'-L1) / L1
- Strain at Novotechnik 2 (Strain 2)= (L2 - L2) / L2
- Section Curvature (between the Novotechnik Bars) =
  (Strain 1 - Strain 2) / (H + X 1 + X 2)

Fig. 2-40: Method of Curvature Calculation

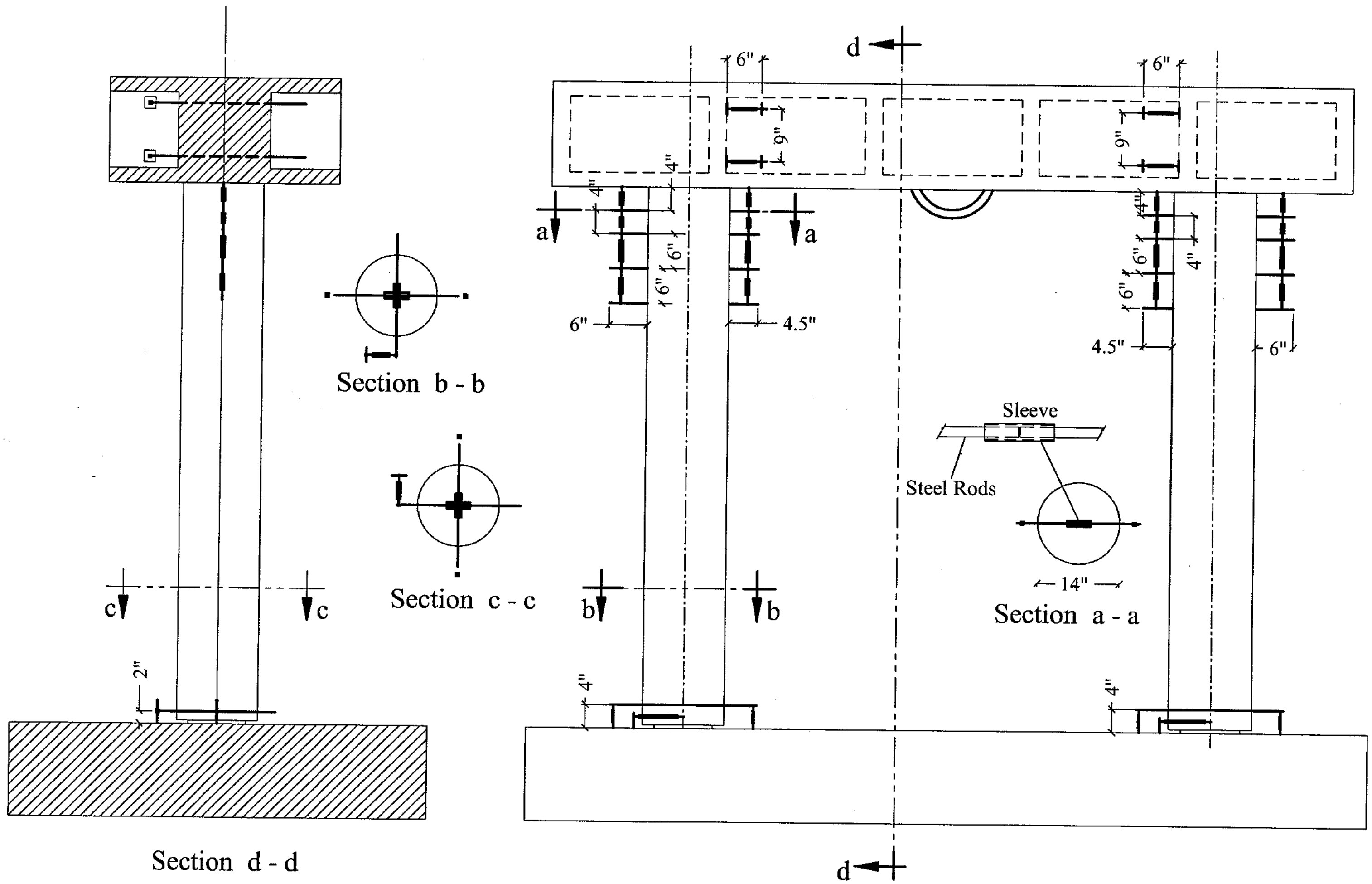

Fig.2-41a: Novotechnicks Configuration of Both Specimens B2CM and B2CT (Dimensions in Inches)

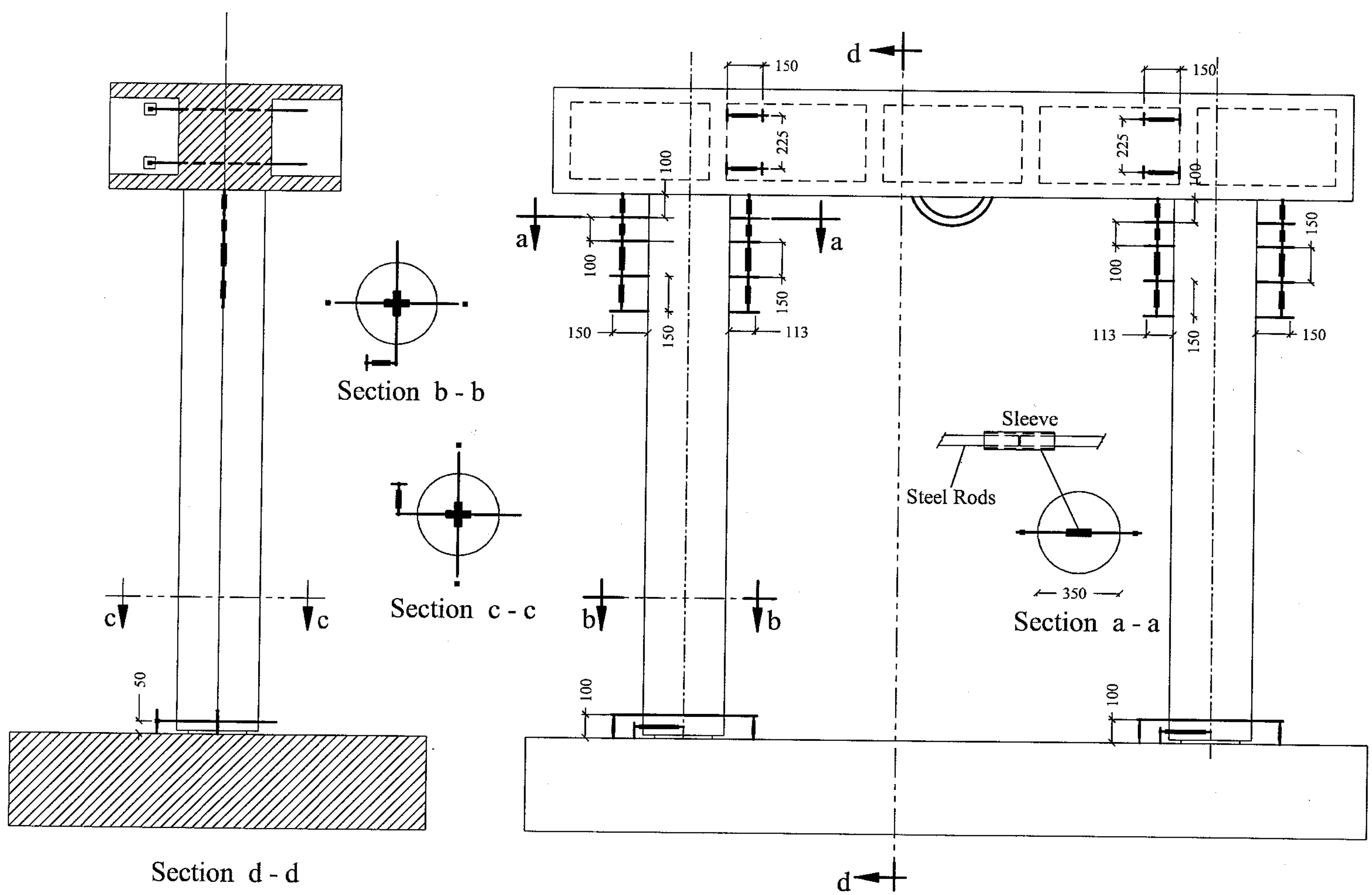

Fig.2-41b: Novotechnicks Configuration of Both Specimens B2CM and B2CT (Dimensions in mm)

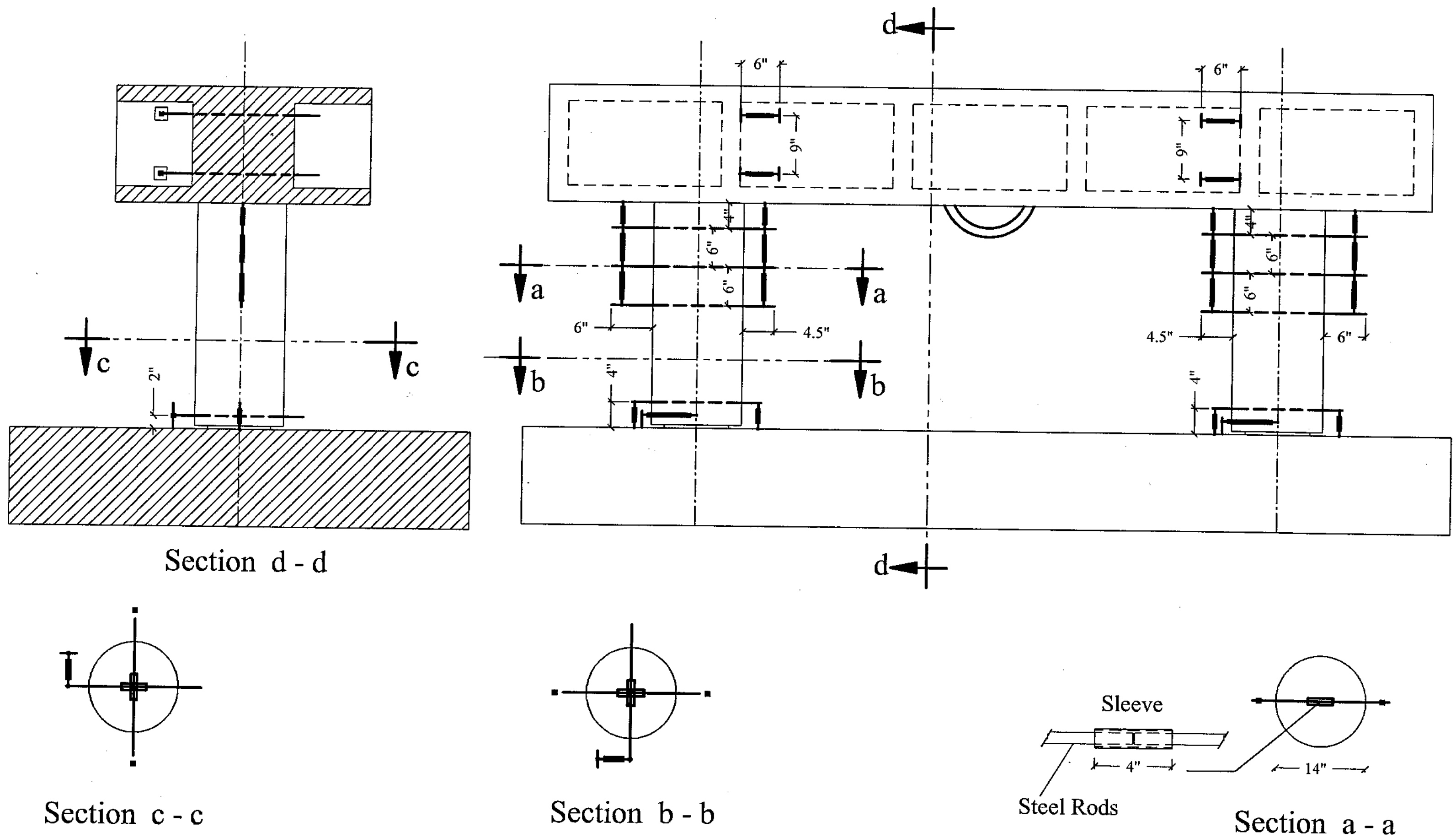

Fig.2-42a: Novotechniks Configuration of Specimen B2CS (Dimensions in Inches)

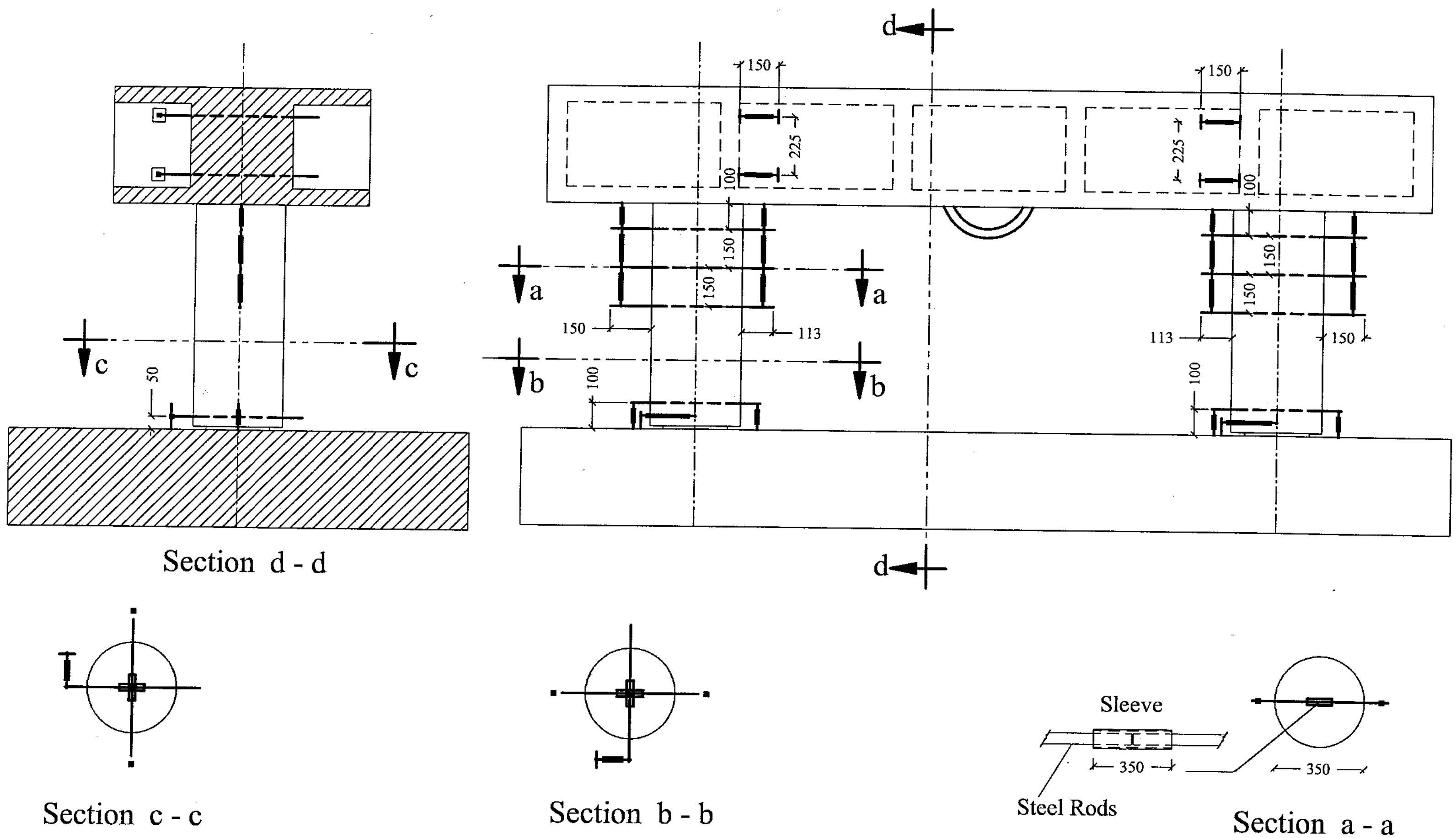

Fig.2-42b: Novotechnik Configuration of Specimen B2CS (Dimensions in mm)

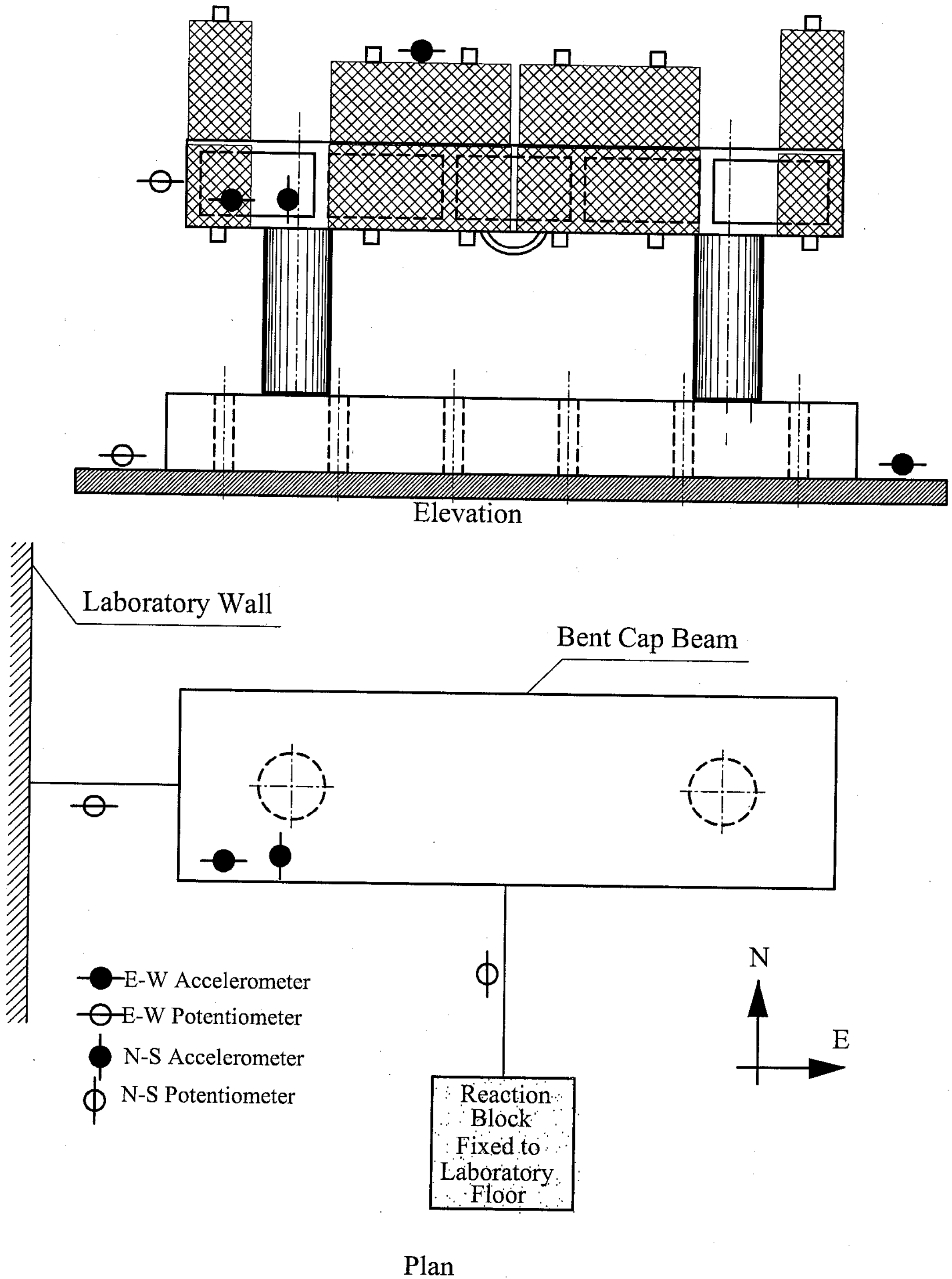

Fig.2-43: Displacement and Acceleration Instruments of Specimen B2CS

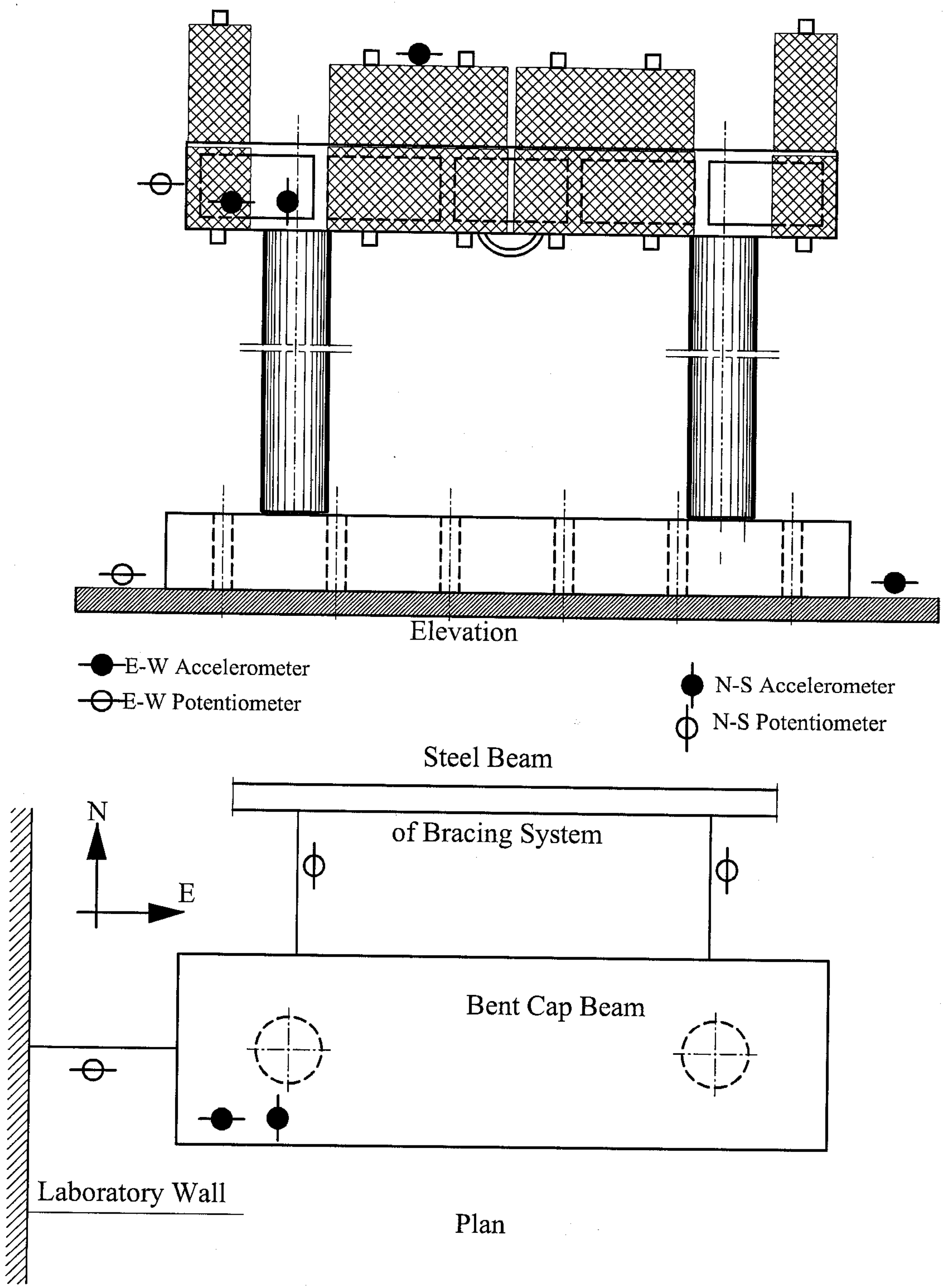

Fig.2-44: Displacement and Acceleration Instruments of both Specimens B2CM and B2CT

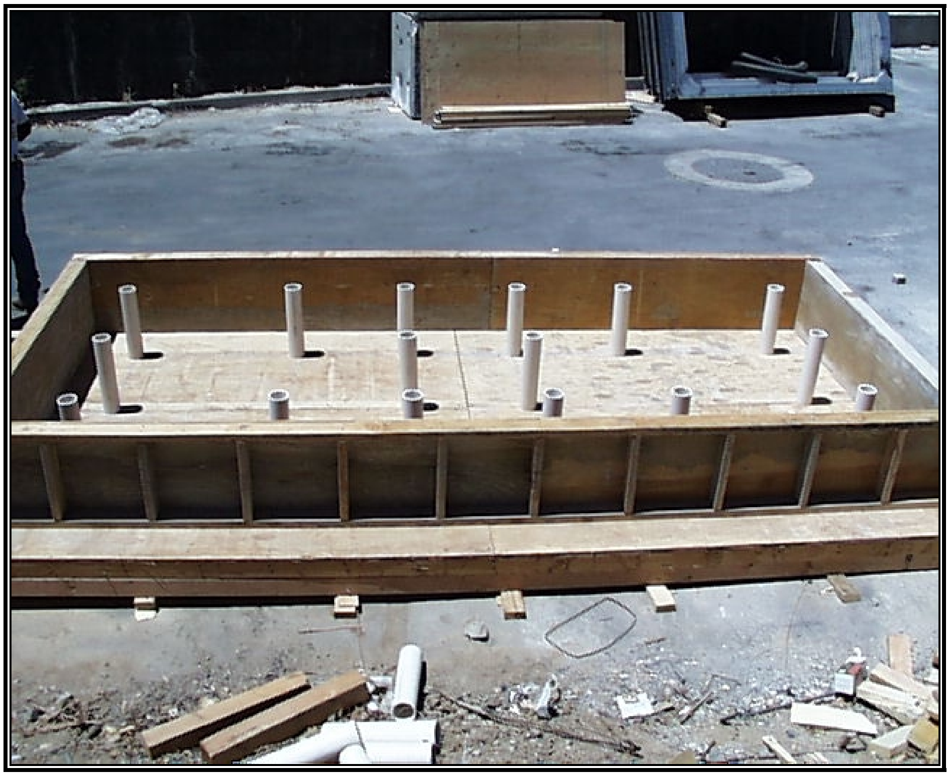

Fig. 3-1: Footing Formwork

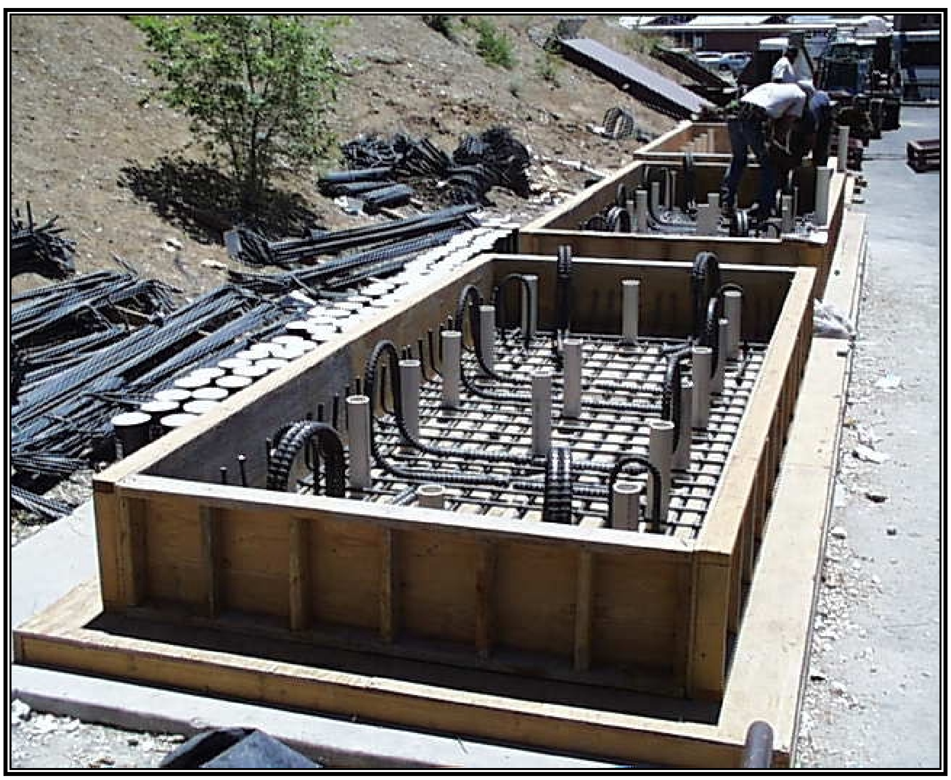

Fig. 3-2: Footing Bottom Reinforcement

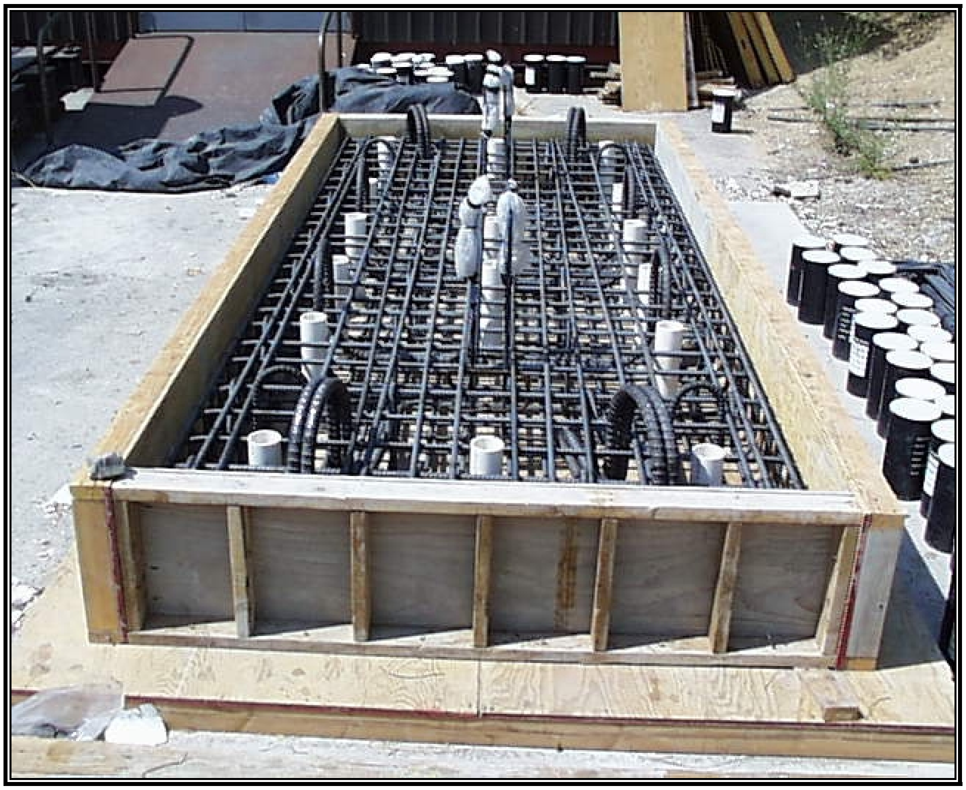

Fig. 3-3: Footing Bottom and Top Reinforcement

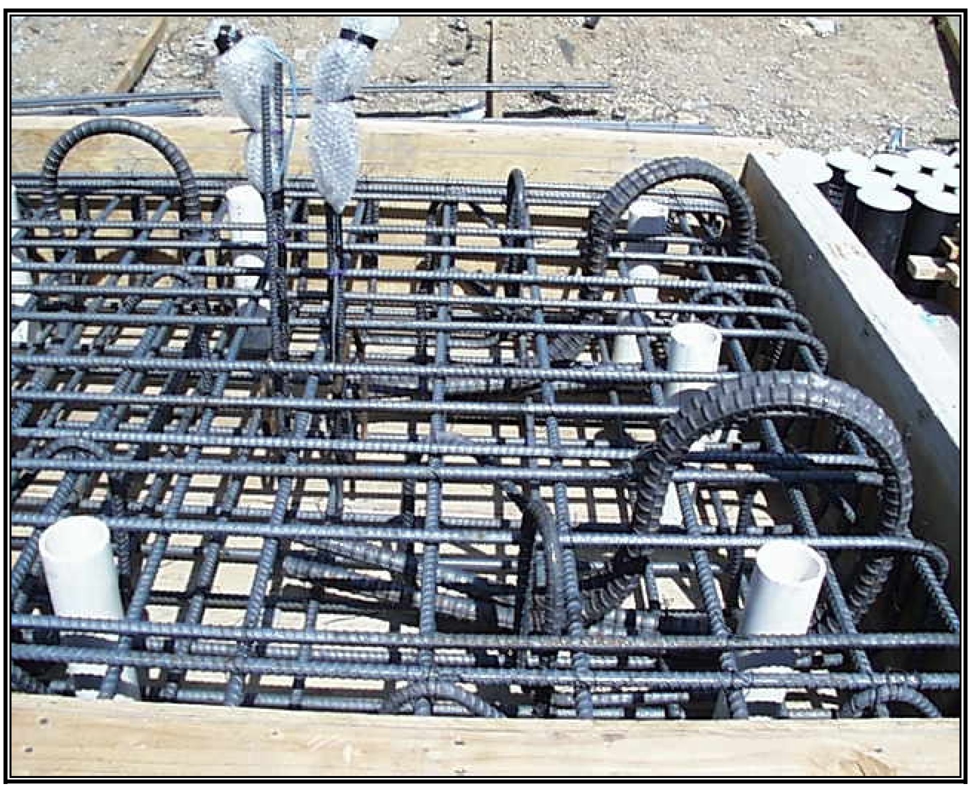

Fig. 3-4: Footing Hooks and Dowels

Fig. 3-5: Concrete casting of all Footings

Fig. 3-6: Roughing the Column-Footing Interface Surface

Fig. 3-7: Rebar Surface Preparation

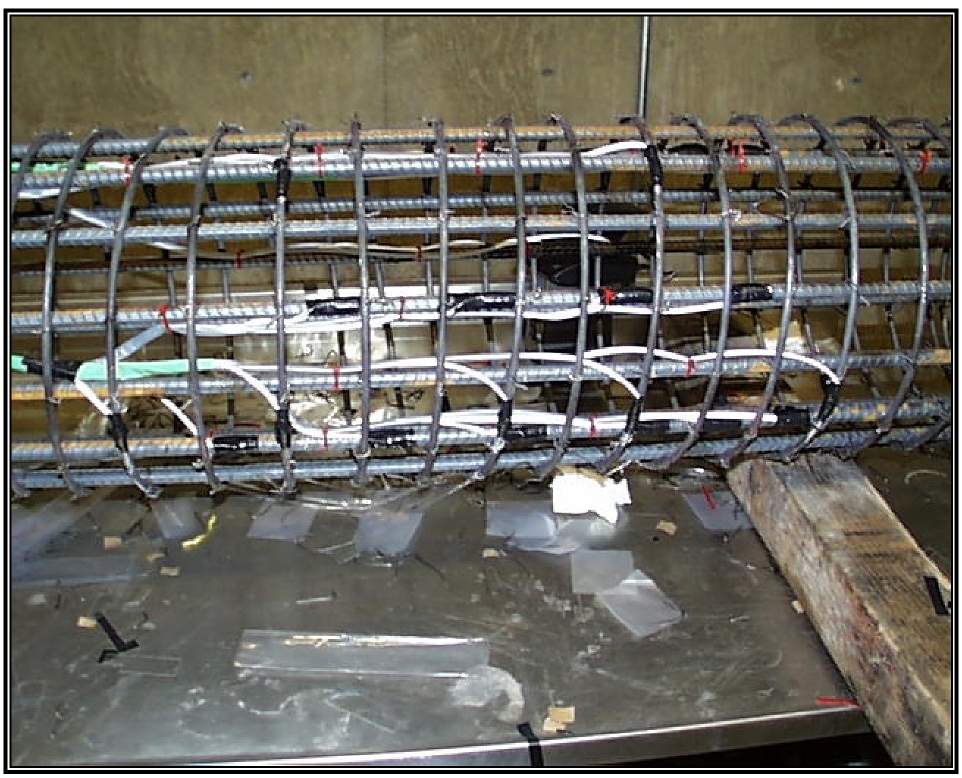

Fig. 3-8: Strain Gage Placement to Column Rebar

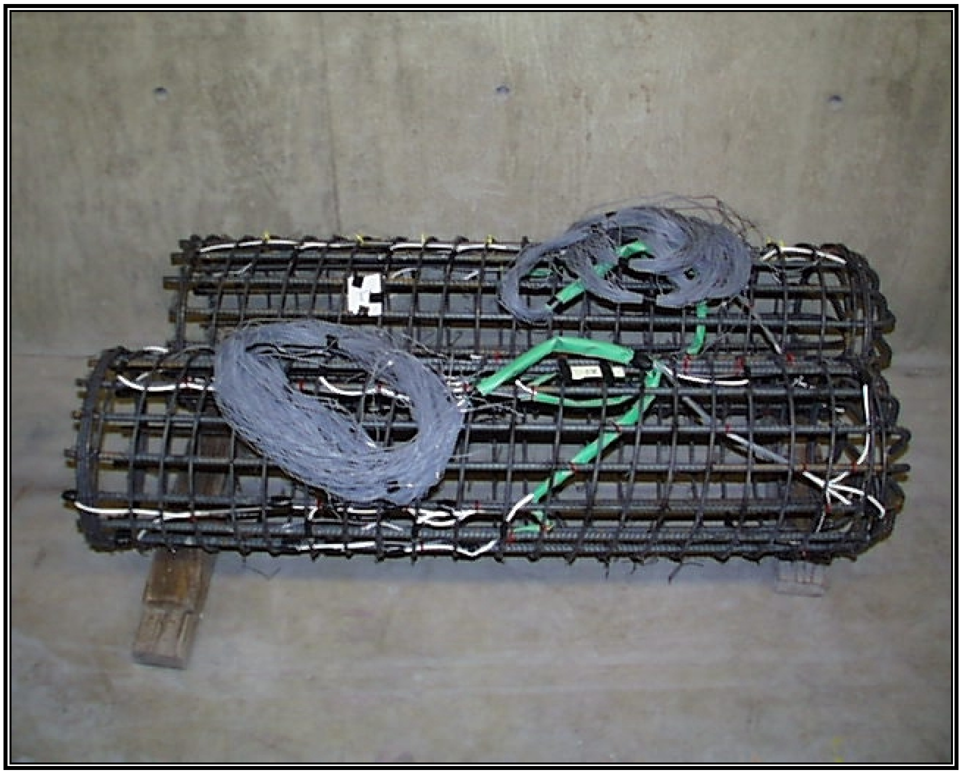
Fig. 3-9: Gaging Process of Short Specimen Columns


Fig. 3-10: Gaging Process of Medium Specimen Columns

Fig. 3-11: Gaging Process of Tall Specimen Columns

Fig. 3-12: Formwork of Short Specimen Columns

Fig. 3-13: Formwork of Medium Specimen Columns

Fig. 3-14: Formwork of Tall Specimen Columns

Fig. 3-15: Concrete Casting of Tall-Specimen Columns

Fig. 3-16: Concrete Casting of Medium-Specimen Columns

Fig. 3-17a: Casting Errors at Column Top in East-West Direction

Fig. 3-17b: Casting Errors at Column Top in North-South Direction


Fig. 3-17c: Casting Errors at Column Bottom in North-South Direction


Fig. 3-17d: Casting Errors at Column Middle in East-West Direction

Fig. 3-18a:Removing of both Tall and Medium Columns

Fig. 3-18b: Removing Damaged Parts

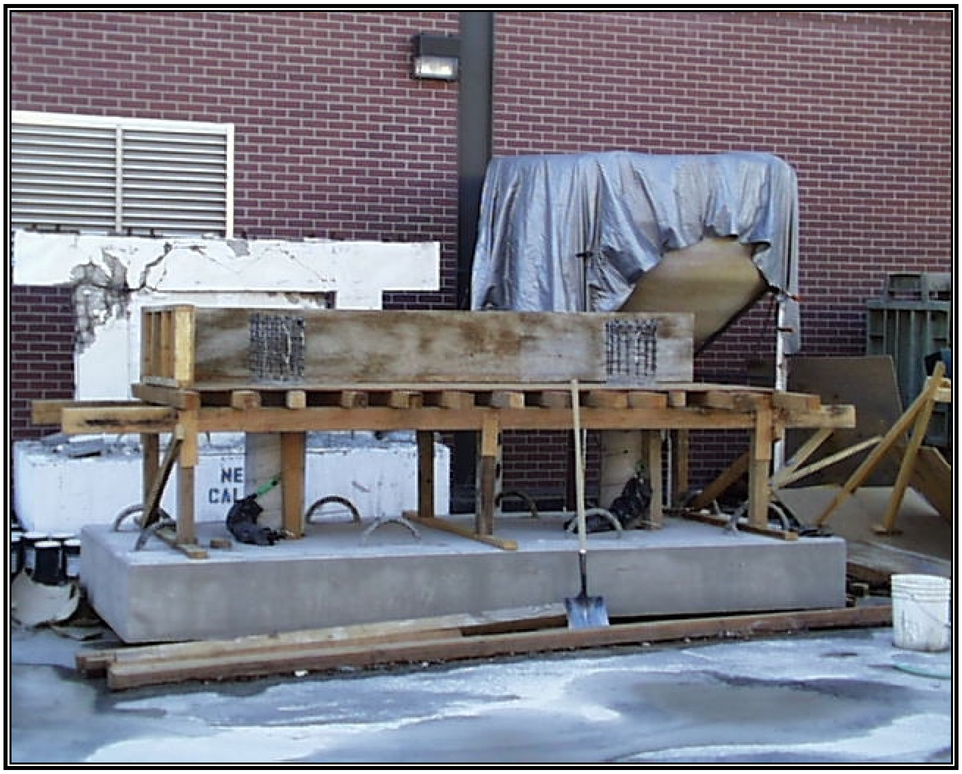

Fig. 3-19: Formwork of Bent Cap Beam

Fig. 3-20: Bent Cap Reinforcement

Fig. 3-21: Bent-Cap Reinforcement Details

Fig. 3-22.a: Concrete Casting for Short Specimen Beam

Fig. 3-22.b: Concrete Casting for Short Specimen Beam

Fig. 3-23: Concrete Casting for Middle Specimen Beam

Fig. 3-24: Concrete Casting for Tall Specimen Beam

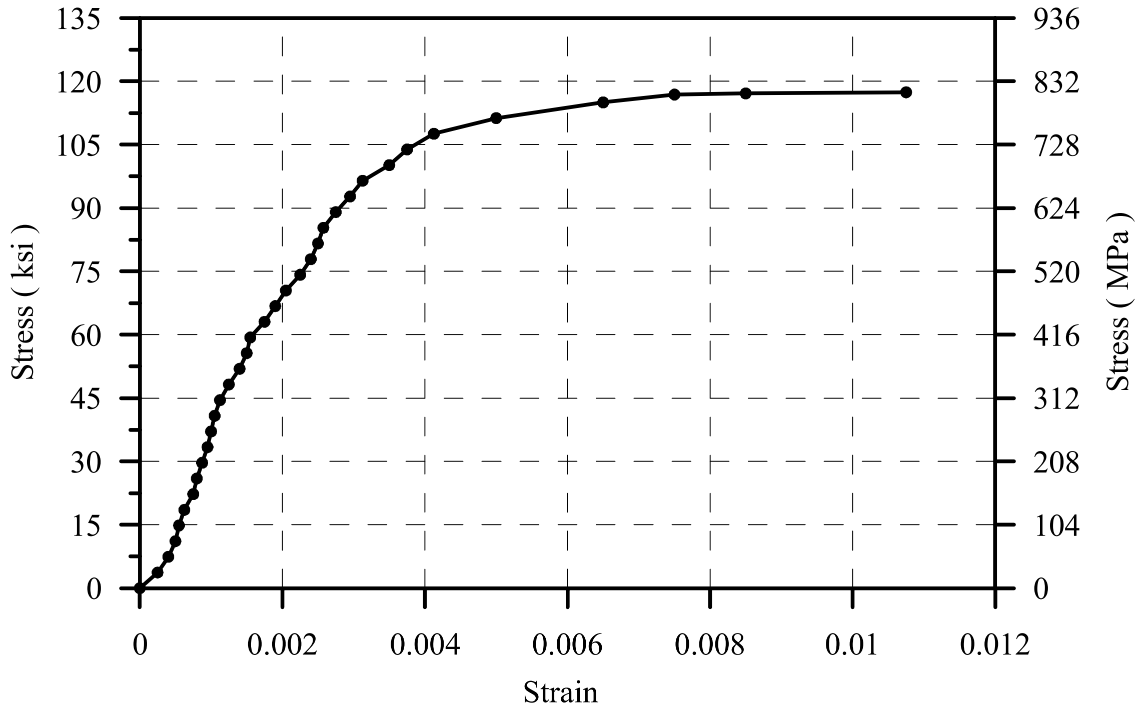

Fig. 3-25: Stress-Strain Profile of Gage 2 Sample before Heat Treatment

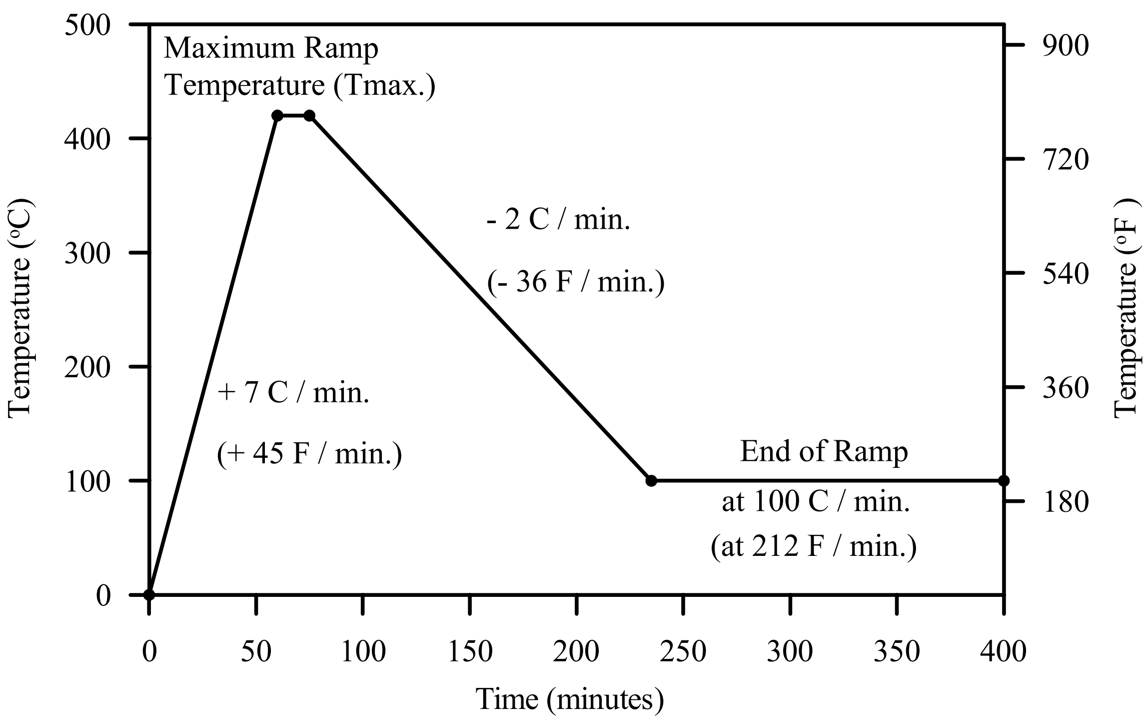

Fig. 3-26: Schematic Diagram of Heat-Treating Ramp

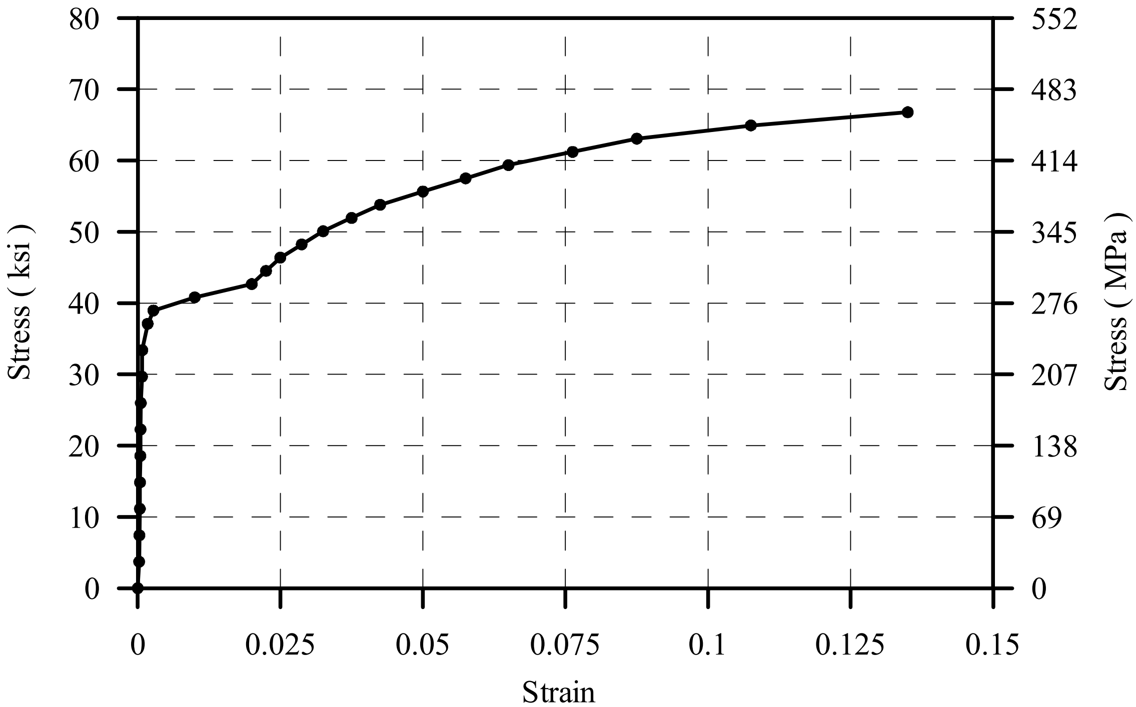

Fig. 3-27: Stress-Strain Profile of Gage 2 after 850^{O} C Heat Treatment

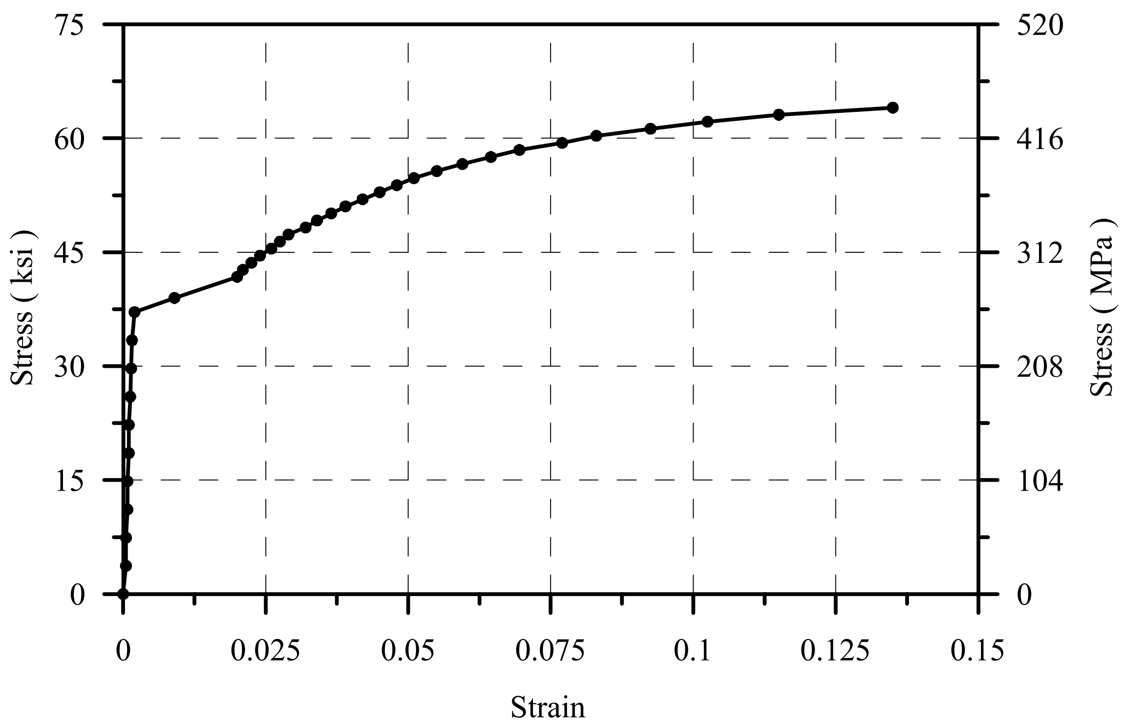

Fig. 3-28: Stress-Strain Profile of Gage 2 after 675^{O} C Heat Treatment

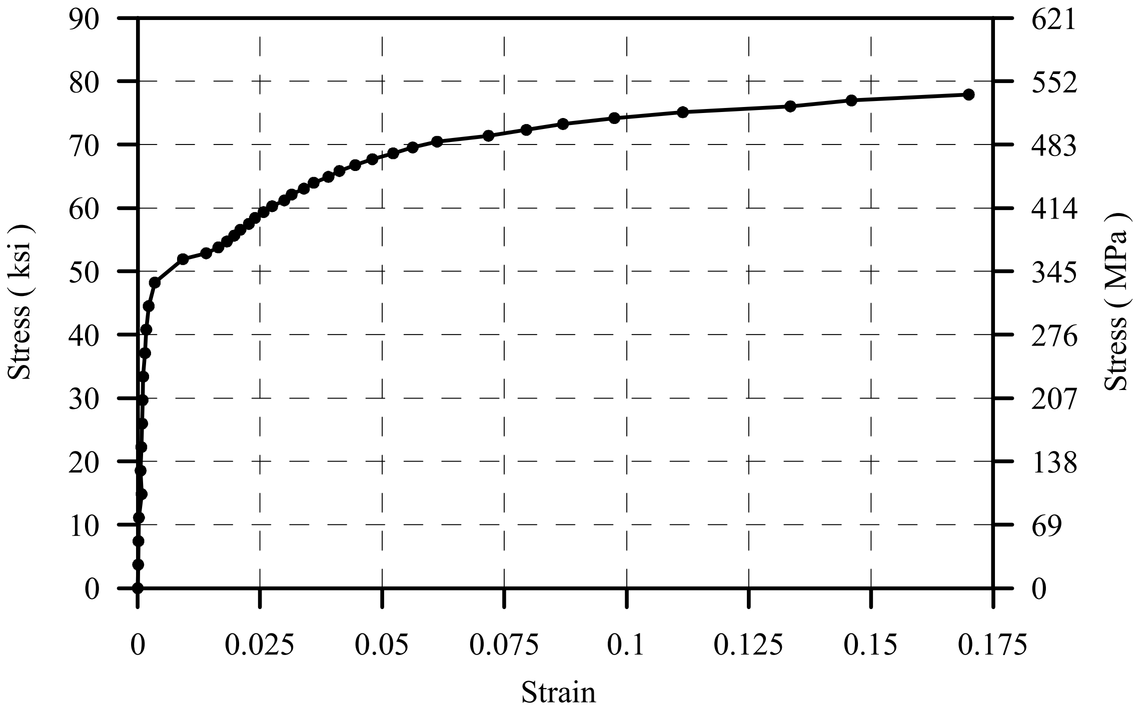

Fig. 3-29: Stress-Strain Profile of Gage 2 after 625^{O} C Heat Treatment

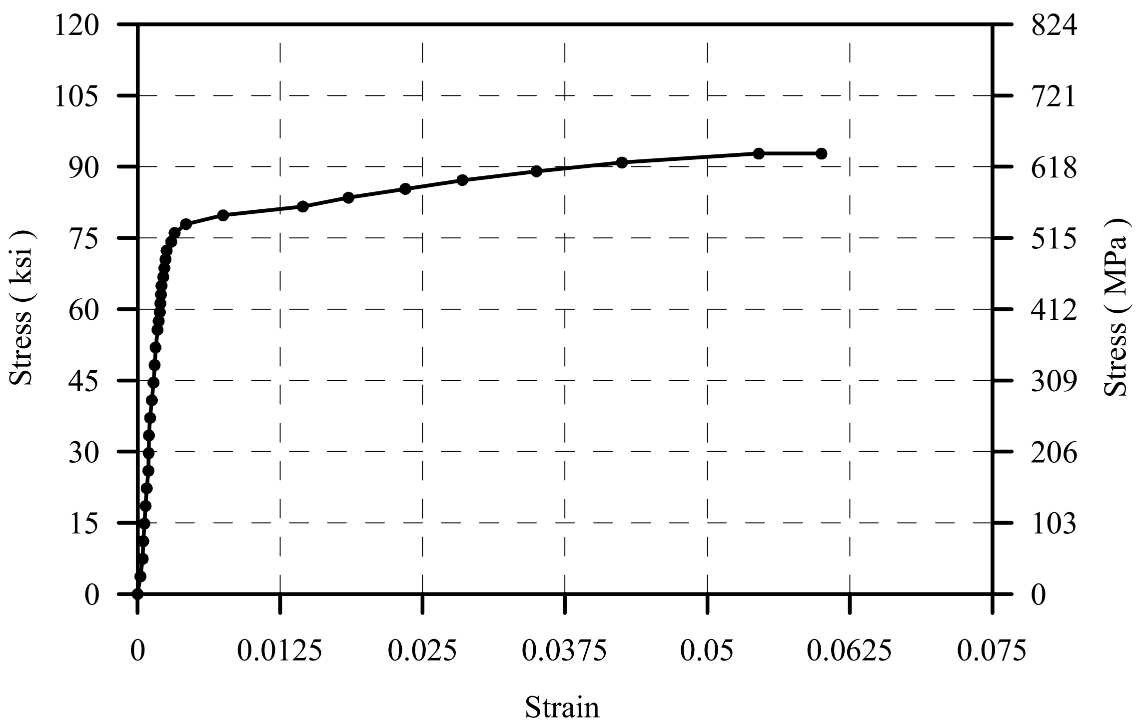

Fig. 3-30: Stress-Strain Profile of Gage 2 after 600^{O} C Heat Treatment

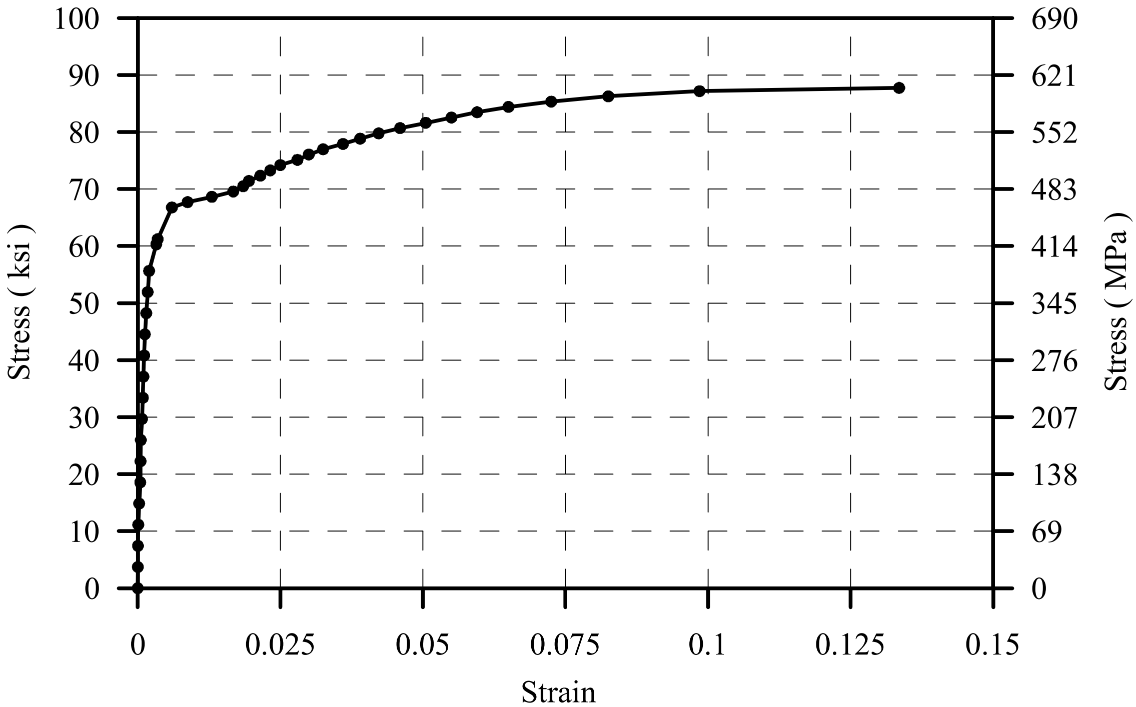

Fig. 3-31: Stress-Strain Profile of Gage 2 after 614^{O} C Heat Treatment

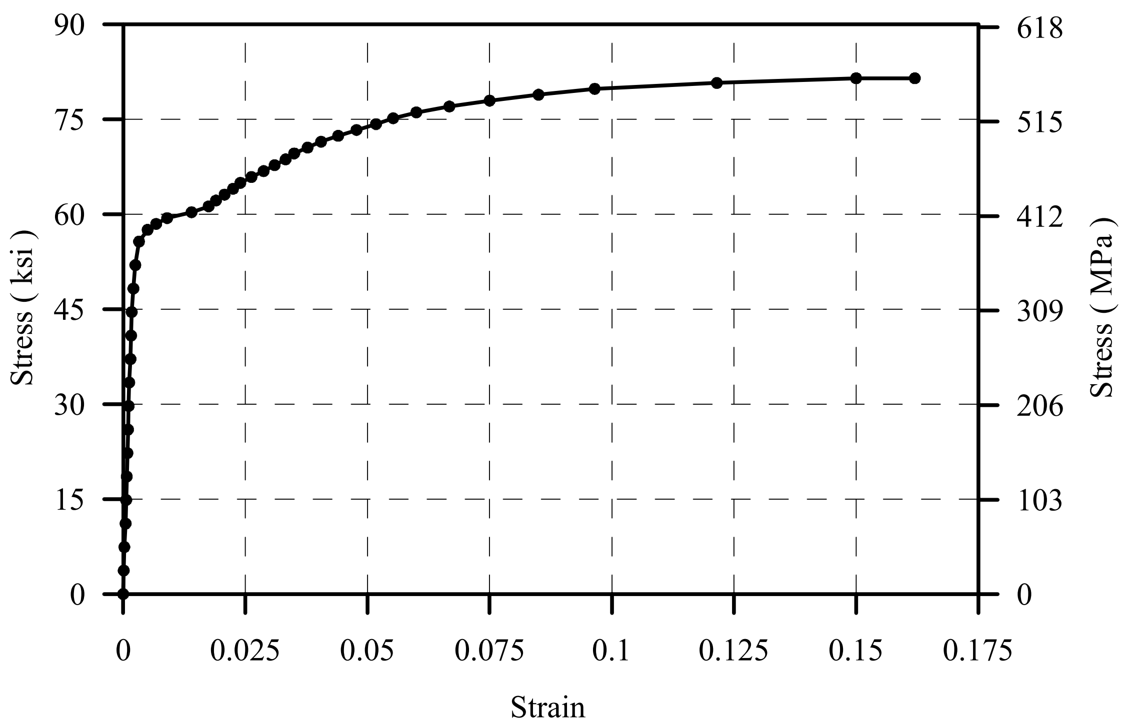

Fig. 3-32: Stress-Strain Profile of Gage 2 after 615^{O} C Heat Treatment

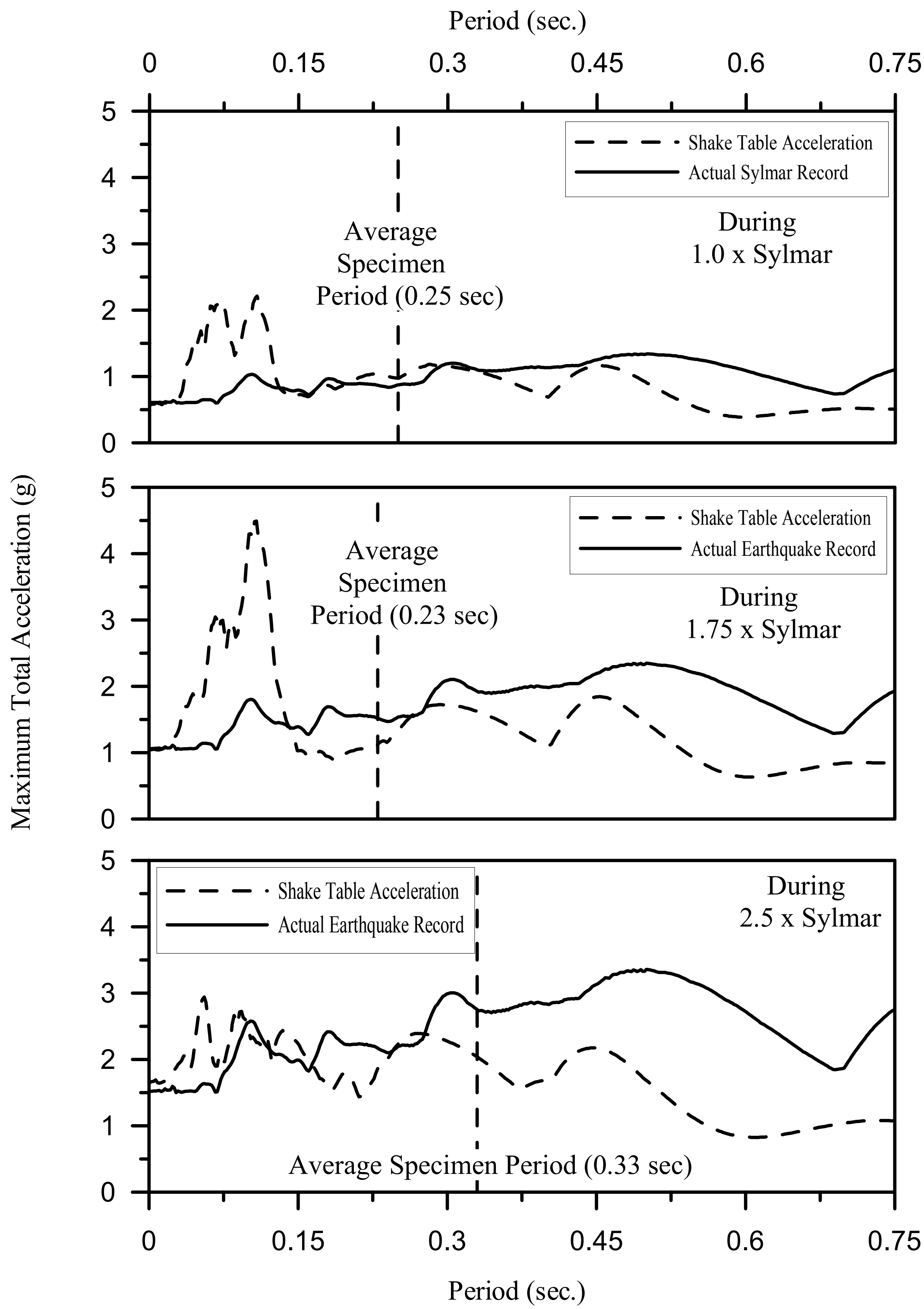

Fig. 4-1: Acceleration Response Spectrum of Achieved and Target Records for Short Specimen B2CS

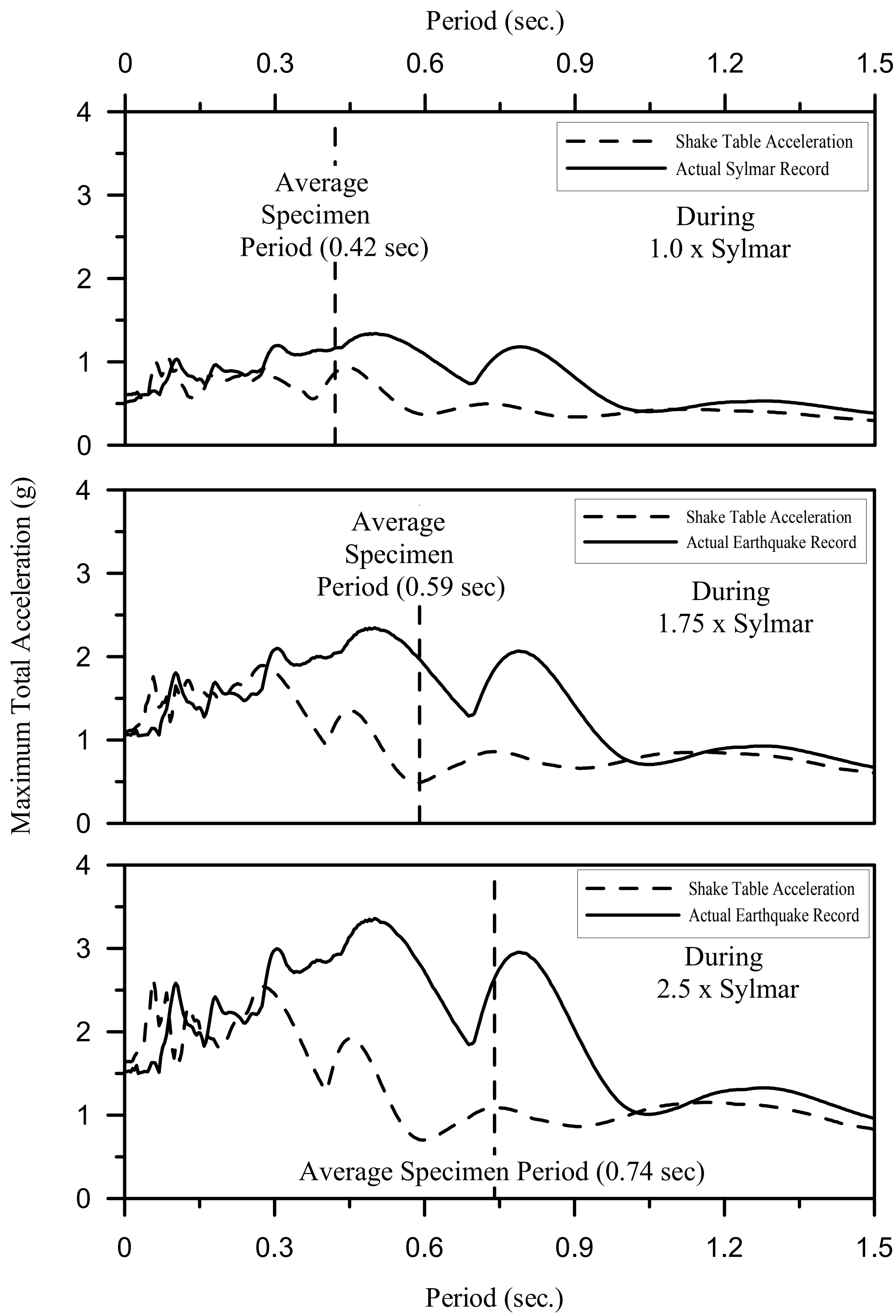

Fig. 4-2: Acceleration Response Spectrum of Achieved and Target Records for Middle Specimen B2CM

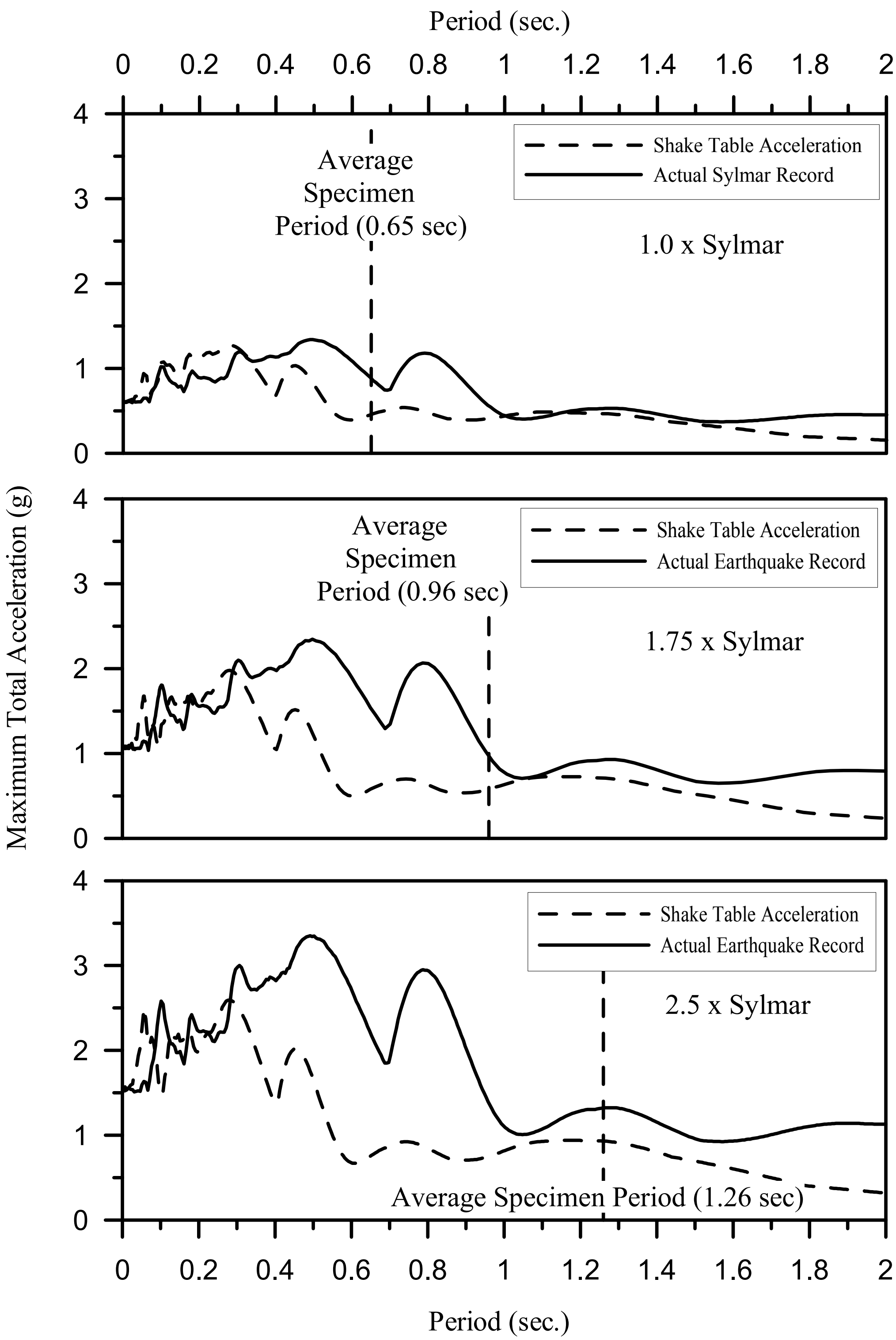

Fig. 4-3: Response Spectrum of Achieved and Target Records
for Tall Specimen B2CT

Fig. 4-4: Flexural Cracks in East Column

Fig. 4-5: Flexural Cracks in West Column

Fig. 4-6: Shear Cracks in West Column

Fig. 4-7: Shear Cracks in East Beam-Column Joint

Fig. 4-8: Shear Cracks in West Beam-Column-Joint

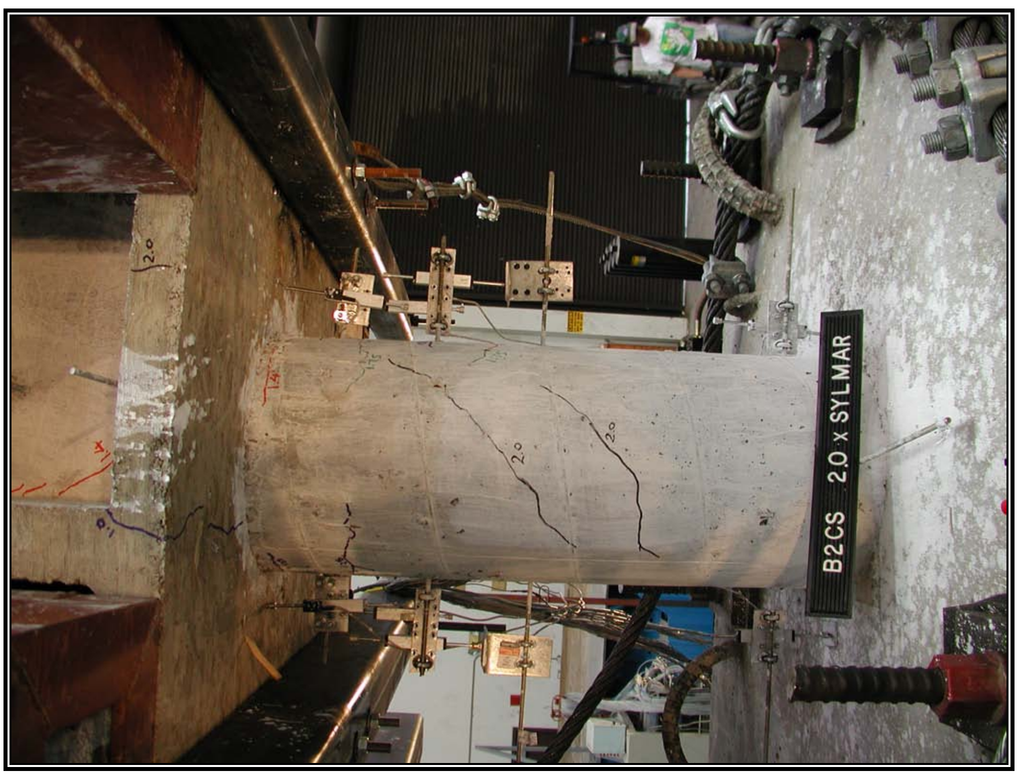

Fig. 4-9: Shear Cracks in East Column

Fig. 4-10: Concrete Spalling in East Column at 2.5x Sylmar

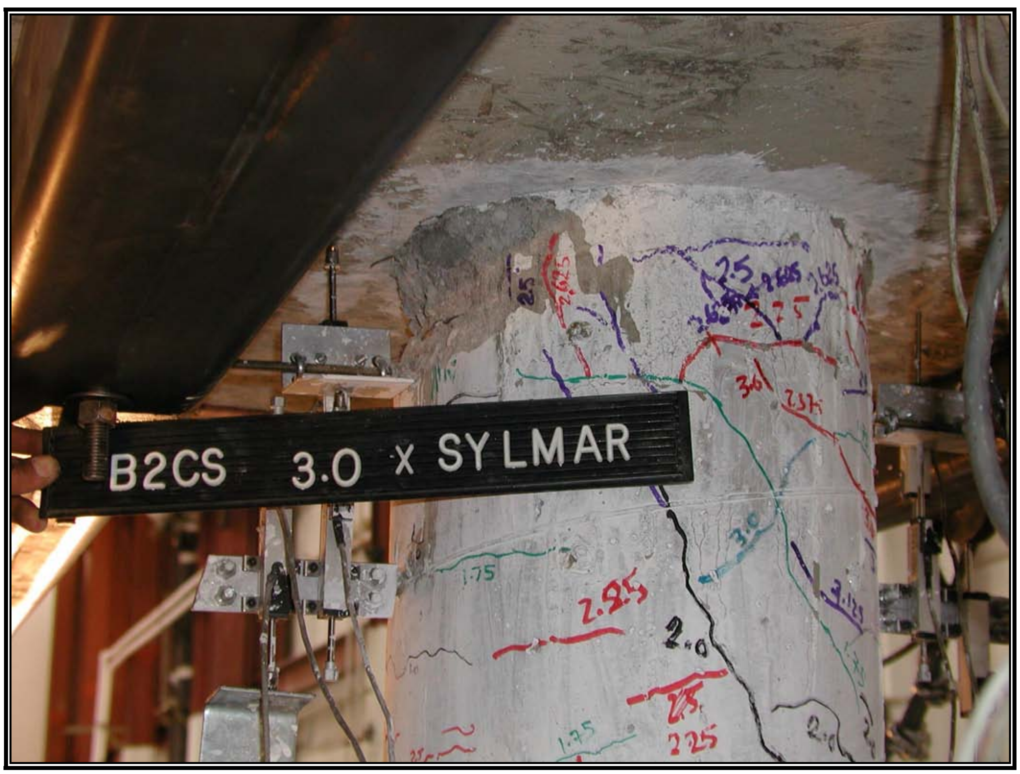

Fig. 4-11: Lateral Reinf. Exposure in West Column

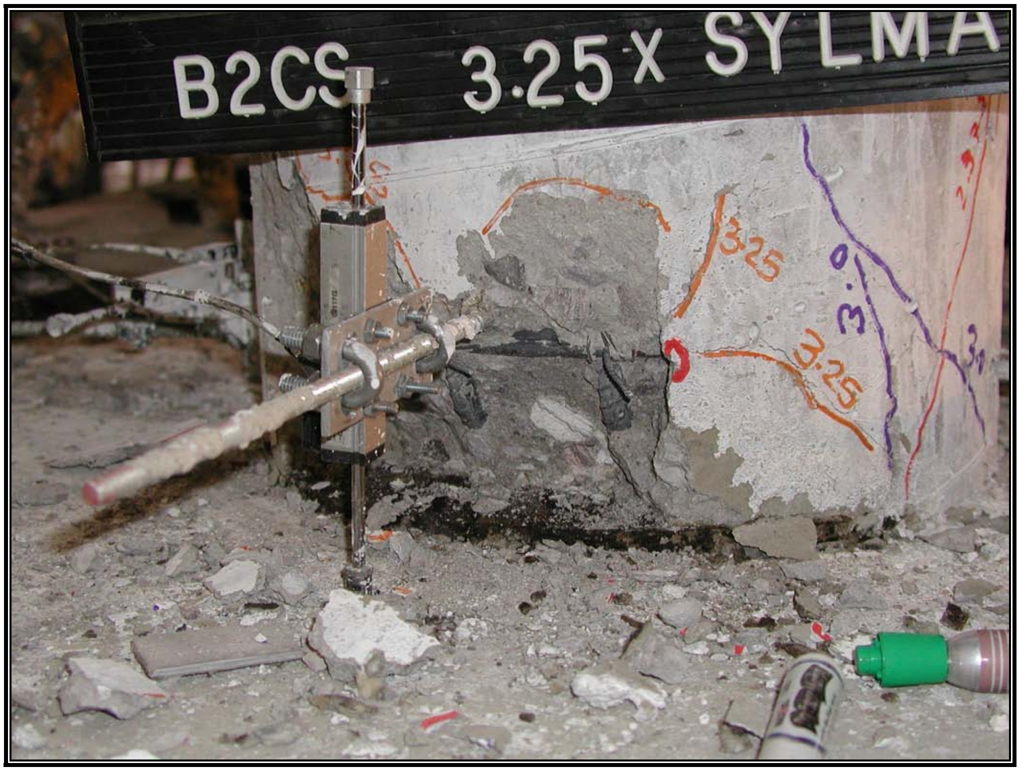

Fig. 4-12: Base Damage in West Column

Fig. 4-13: Base Slippage in East Column

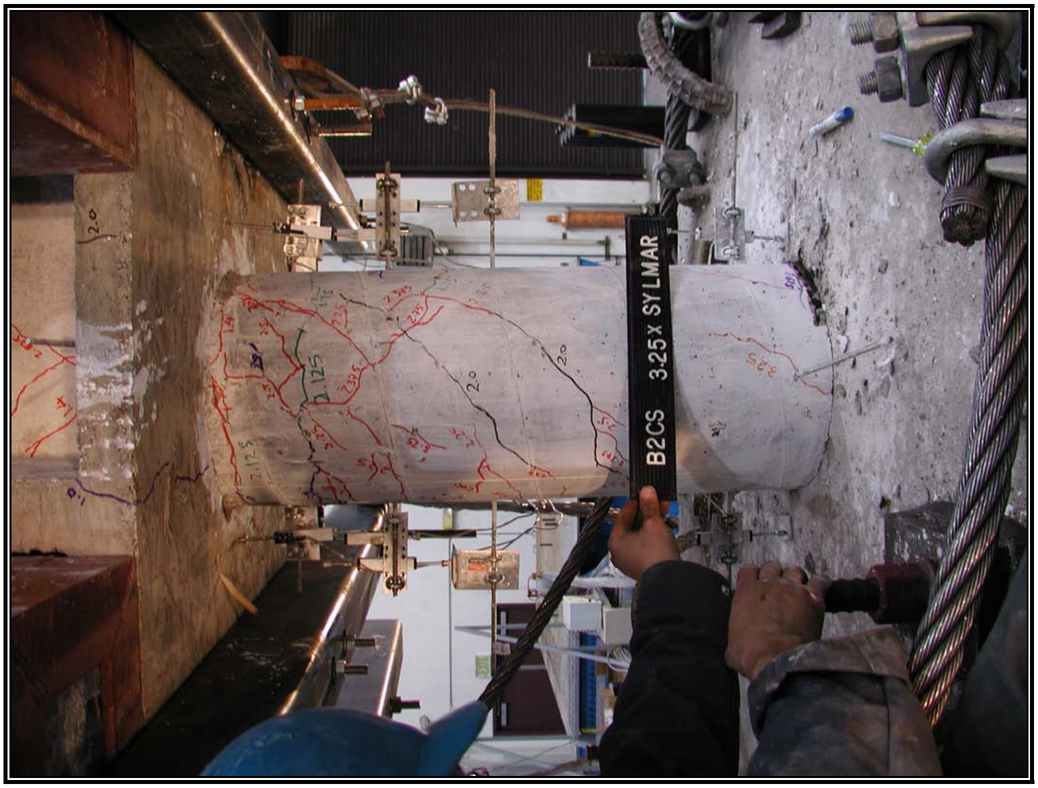

Fig. 4-14: Condition of East Column after Max. Loading

Fig. 4-15: Condition of West Column after Max. Loading

Fig. 4-16: Lateral Reinf. Exposure in East Column

Fig. 4-17: Level of Spalling in West Column

Fig. 4-18: Flexural Cracks in East Column

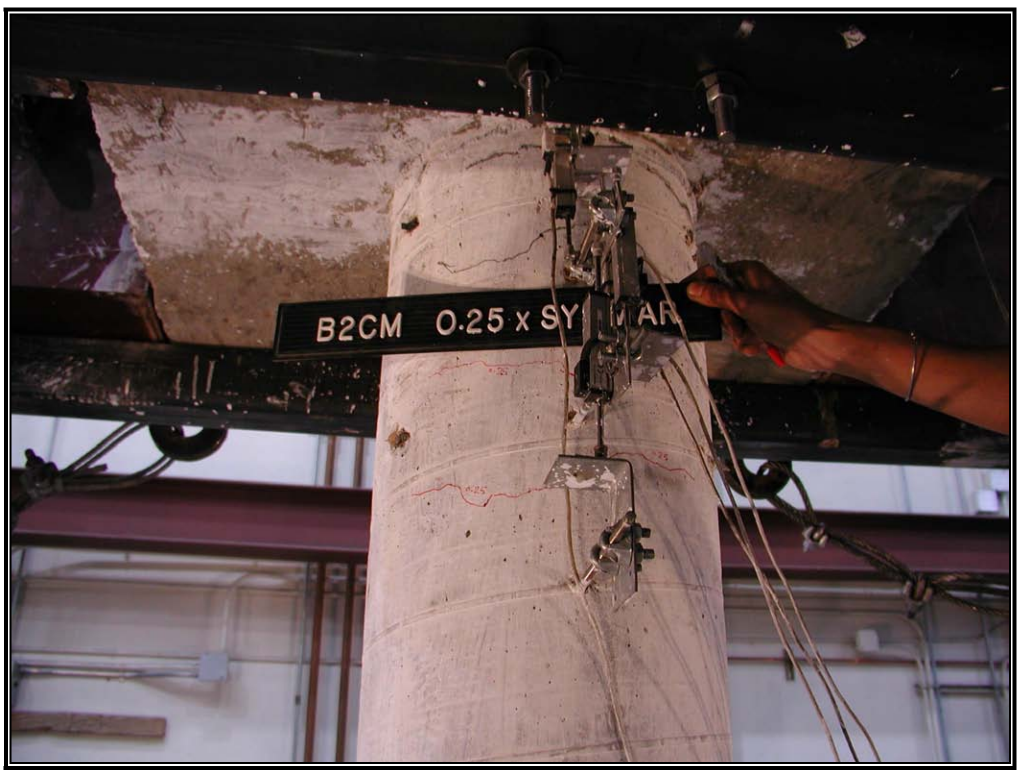

Fig. 4-18: Flexural Cracks in West Column

Fig. 4-20: Shear Cracks on South Side of East Column

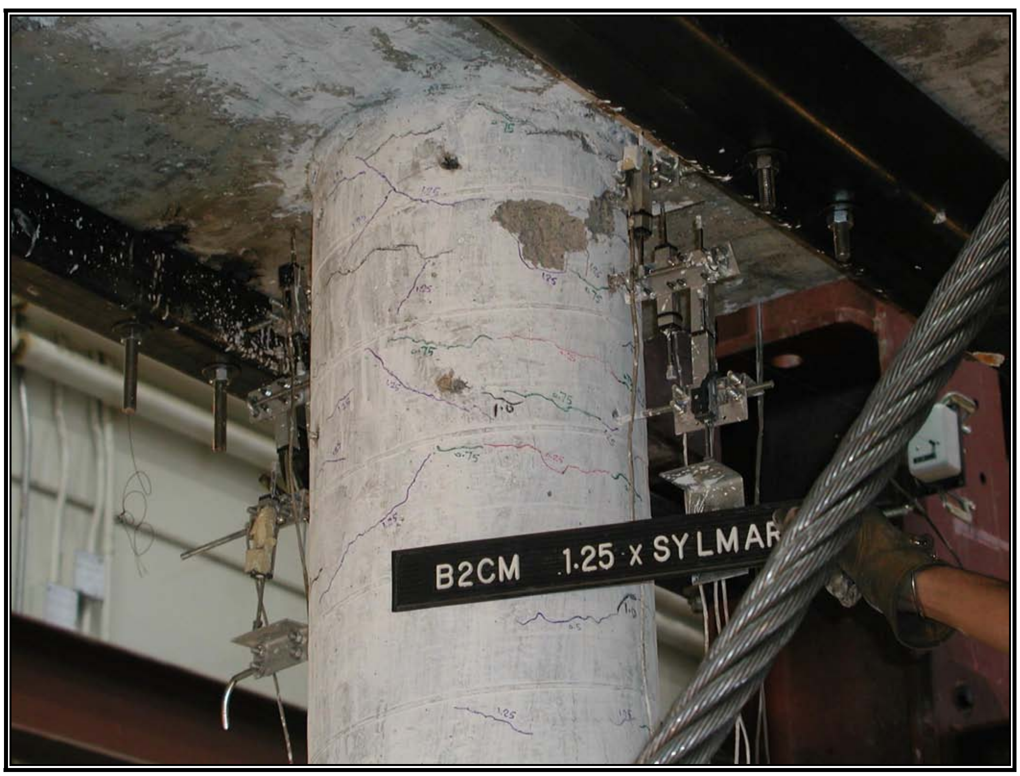

Fig. 4-21: Shear cracks on South Side of West Column

Fig. 4-22: Shear Cracks in West Beam-Column Joint

Fig. 4-23: Shear Cracks in East Beam-Column Joint

Fig. 4-24: Spalling on East Side of East Column

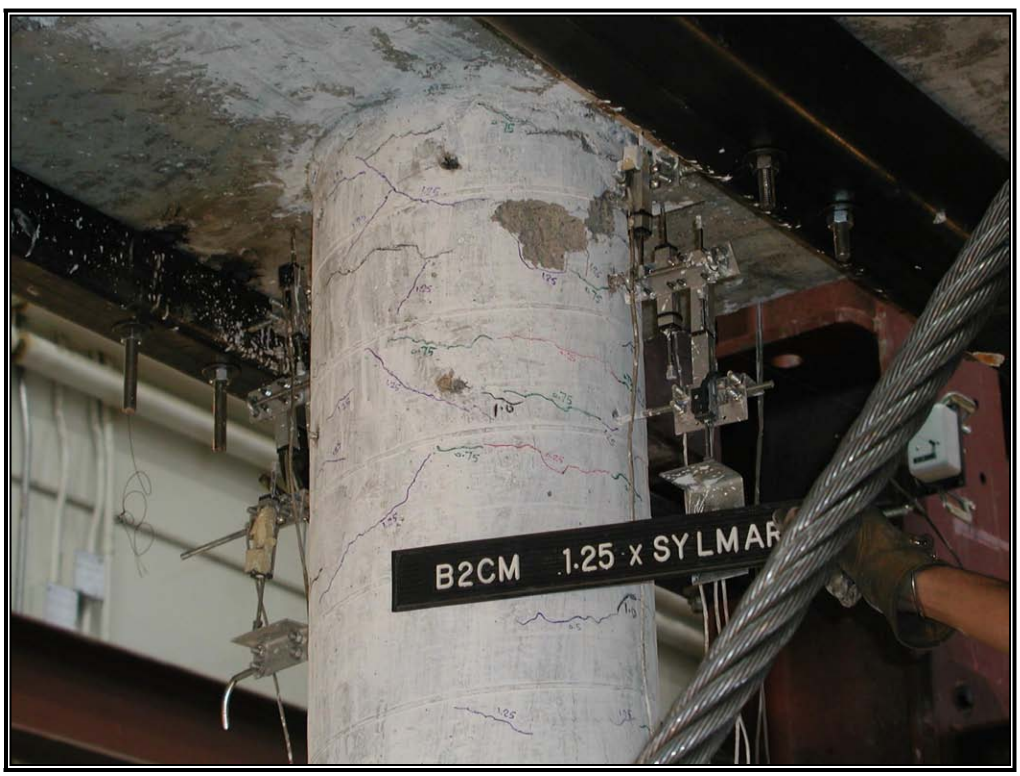

Fig. 4-25: Spalling on East Side of West Column

Fig. 4-26: Spalling on West Side of East Column Base

Fig. 4-27: Spalling on West Side of West Column Base

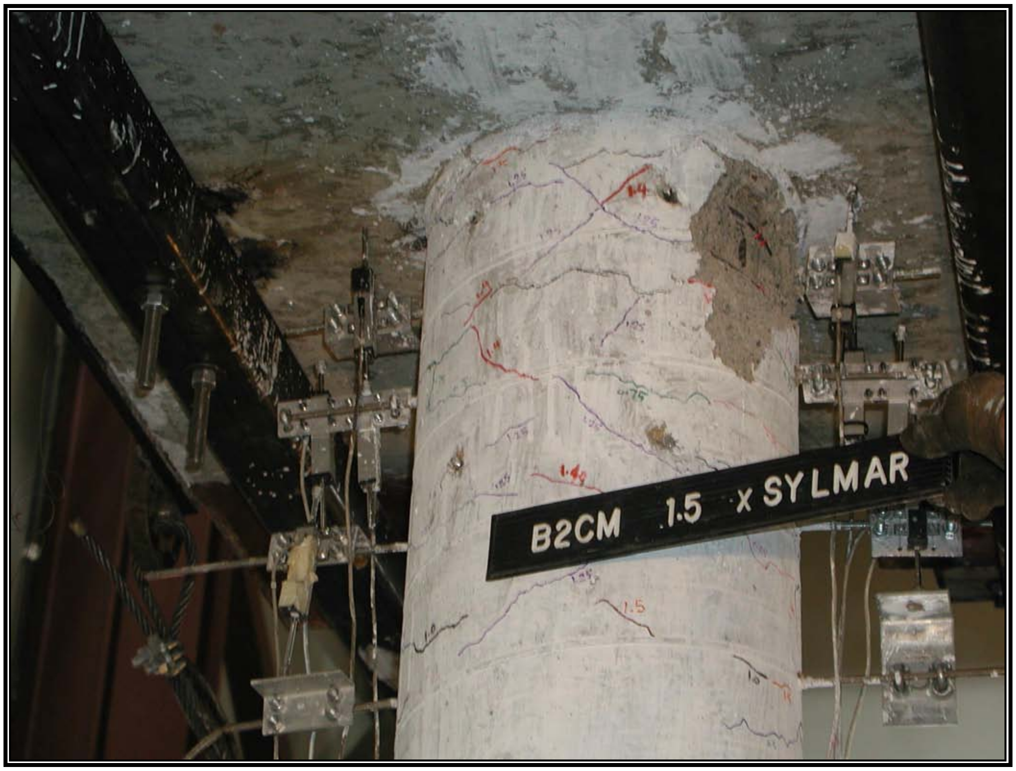

Fig. 4-28: Transverse and Longitudinal Reinf. Exposure in West Column

Fig. 4-29: Transverse Reinf. Exposure in East Column

Fig. 4-30: Transverse and Long. Reinf. Exposure in West Column

Fig. 4-31: Vertical Cracking in West Column Base

Fig. 4-32: Transverse and Longitudinal Reinf. Exposure in East Column

Fig. 4-33: Minor Cracking in the Cap-Beam

Fig. 4-34: Minor Spalling in the Cap-Beam

Fig. 4-35: Middle Specimen Leaning after 2.75 x Sylmar

Fig. 4-36: Concrete Spalling on East Side of West Column

Fig. 4-37: Concrete Spalling on East Side of East Column

Fig. 4-38: Concrete Spalling on East Side of West Column

Fig. 4-39: Base Damage in West Column

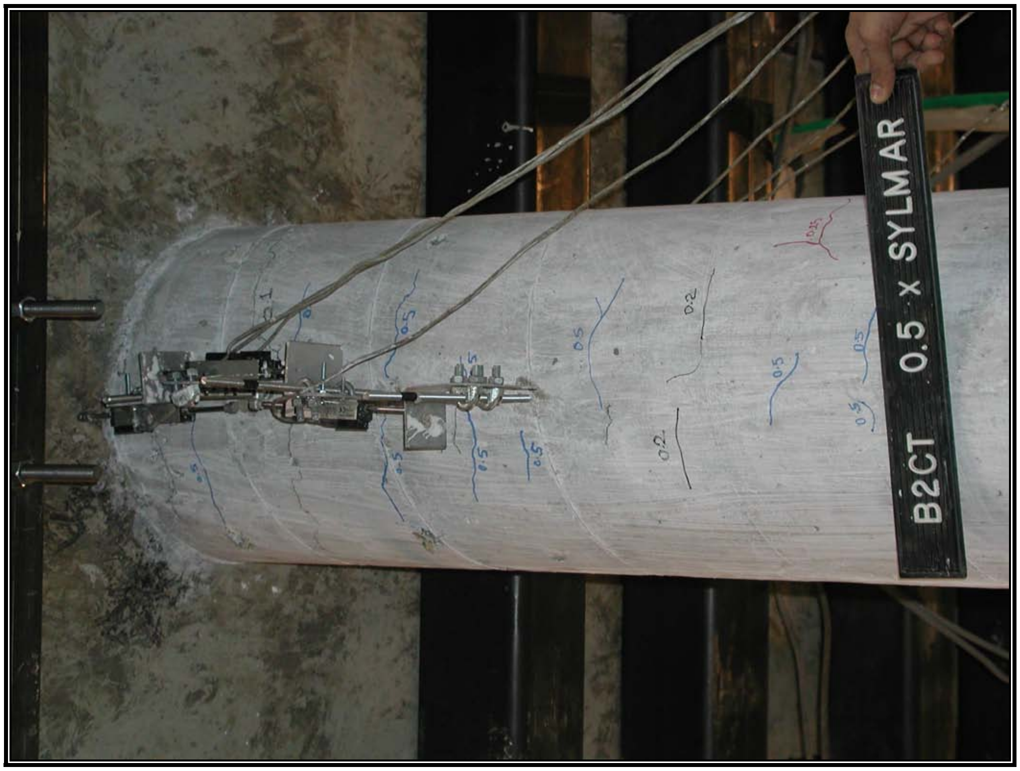

Fig. 4-40: Flexural Cracks in East Column

Fig. 4-41: Flexural Cracks in West Column

Fig. 4-42: Shear Cracks in East column

Fig. 4-43: Shear Cracks in West Column

Fig. 4-44: Shear Cracks in West Beam-Column-Joint

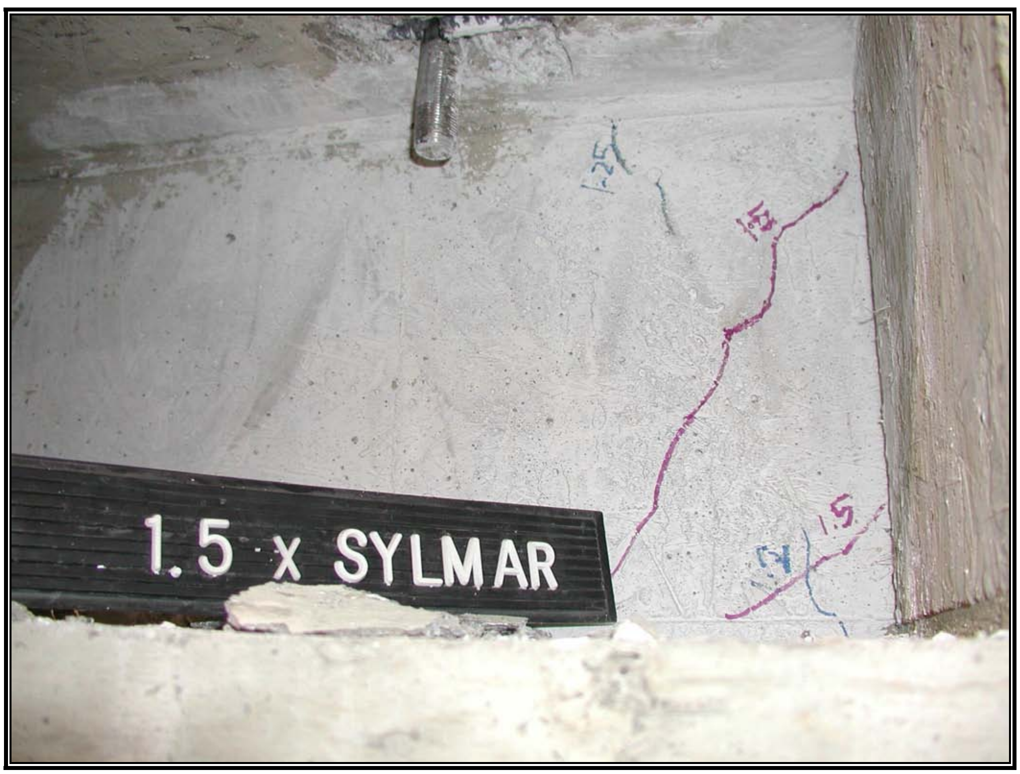

Fig. 4-45: Shear Cracks in East Beam-Column-Joint

Fig. 4-46: Concrete Spalling on West Side of East Column

Fig. 4-47: Concrete Spalling on East Side of West Column

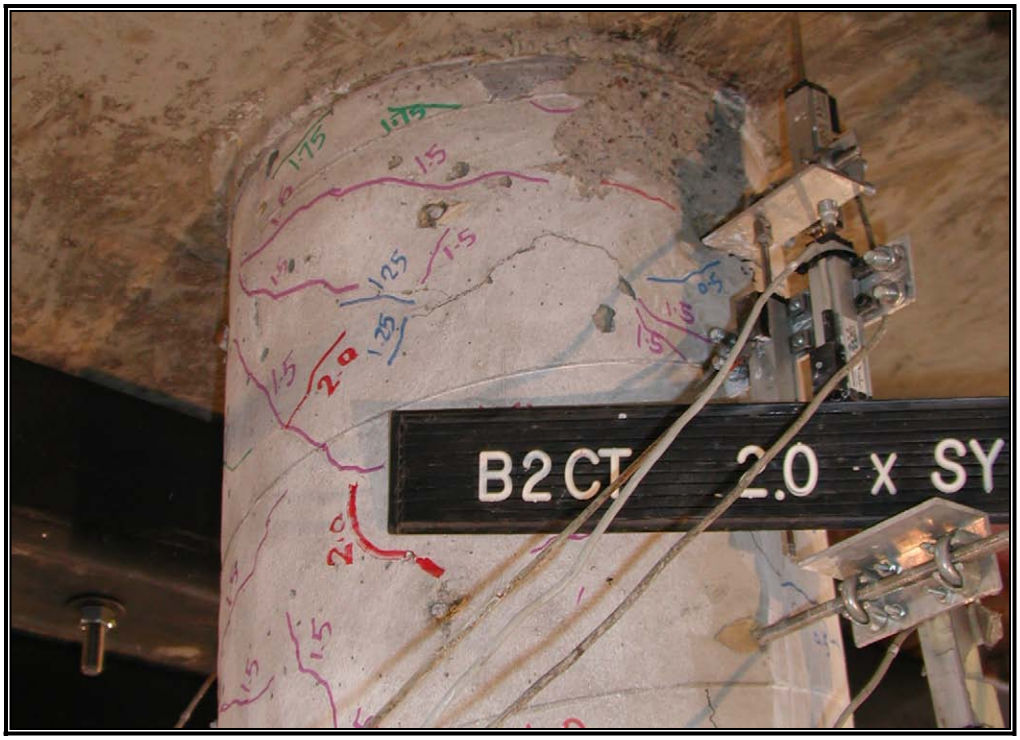

Fig. 4-48: Concrete Spalling on West Side of West Column

Fig. 4-49: West Side of East Column Base after 2.0 x Sylmar

Fig. 4-50: Concrete Spalling on West Side of East Column

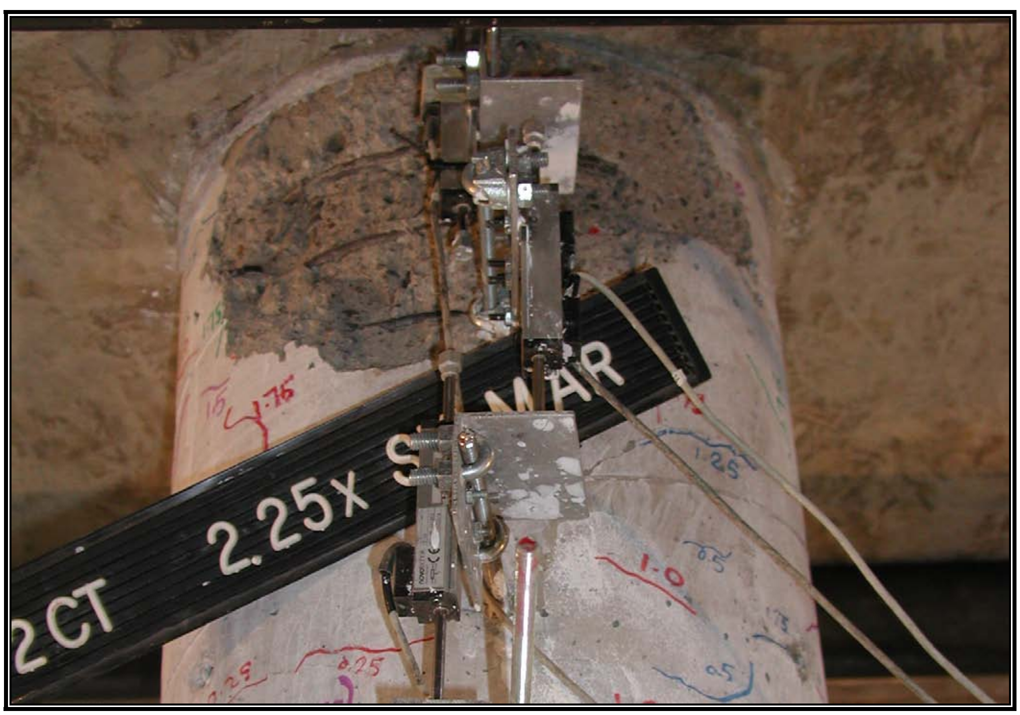

Fig. 4-51: Concrete Spalling on East Side of West Column

Fig. 4-52: Concrete Cracking on West Side of West Column Base

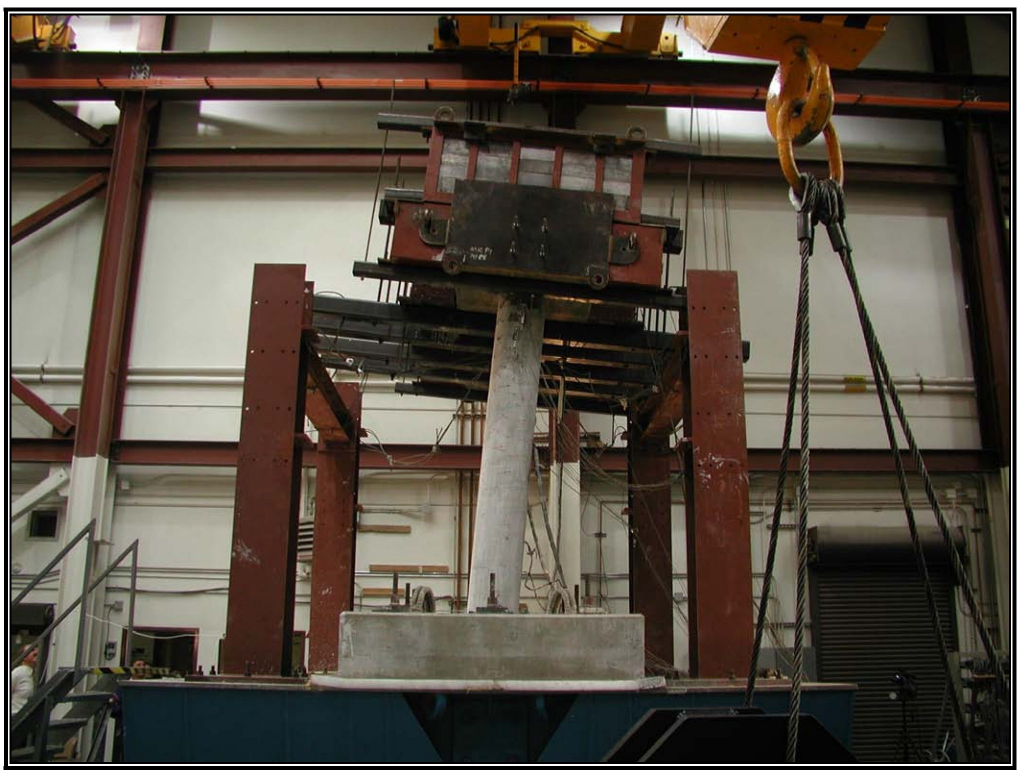
Fig. 4-53: Tall Specimen Leaning after 2.5 X Sylmar

Fig. 4-54: Concrete Spalling on West Side of East Column

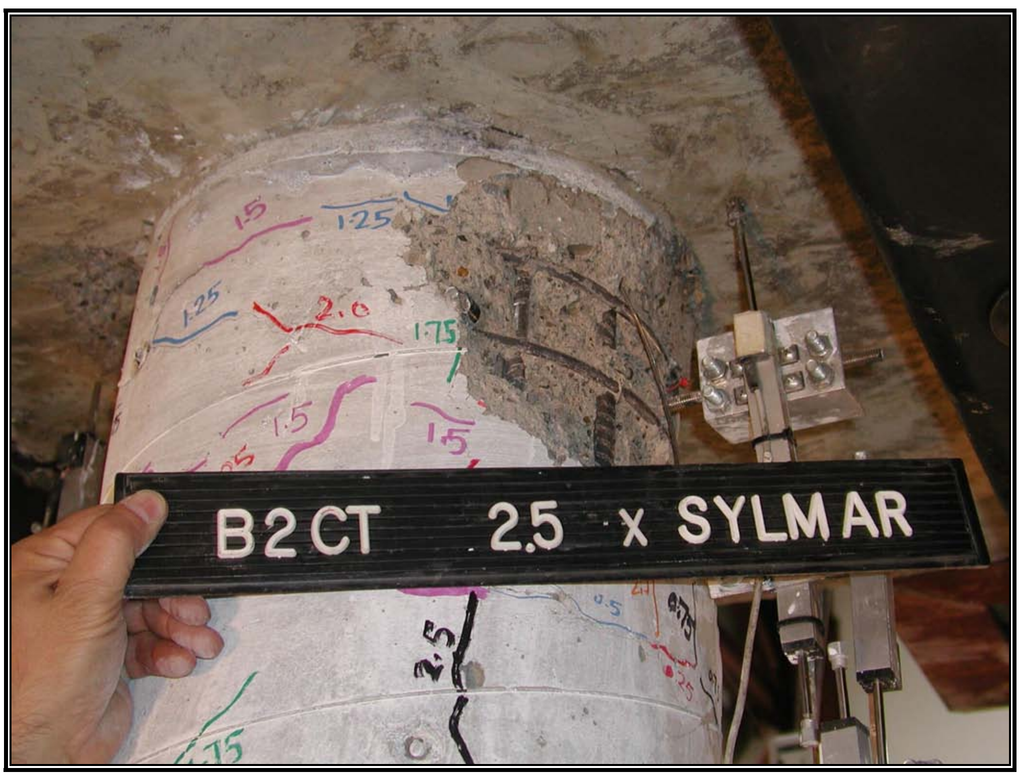

Fig. 4-55: Concrete Spalling on East Side of West Column

Fig. 4-56: Base Damage in West Column

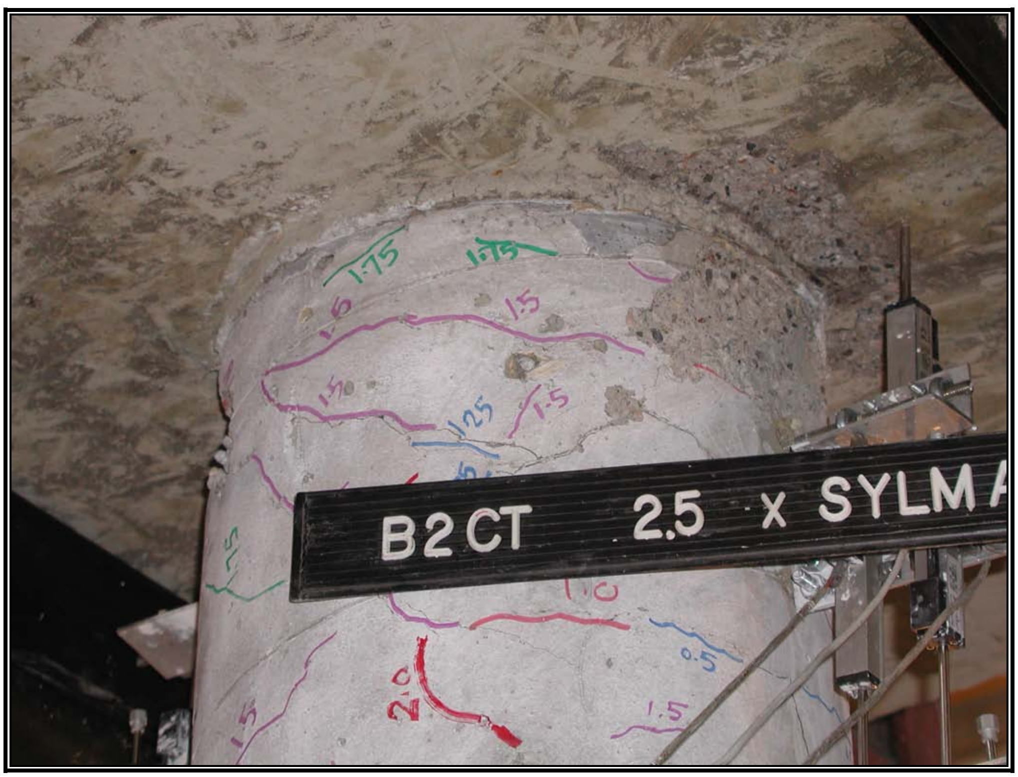

Fig. 4-57: Minor Spalling in Cap-Beam

Fig. 4-58: Deep Concrete Spalling on West Side of East Column

Fig. 4-59: Spalling on West Side of West Column

Fig. 4-60: Concrete Spalling on West side of West Column Base

Fig. 4-61: West Side of East Column Base

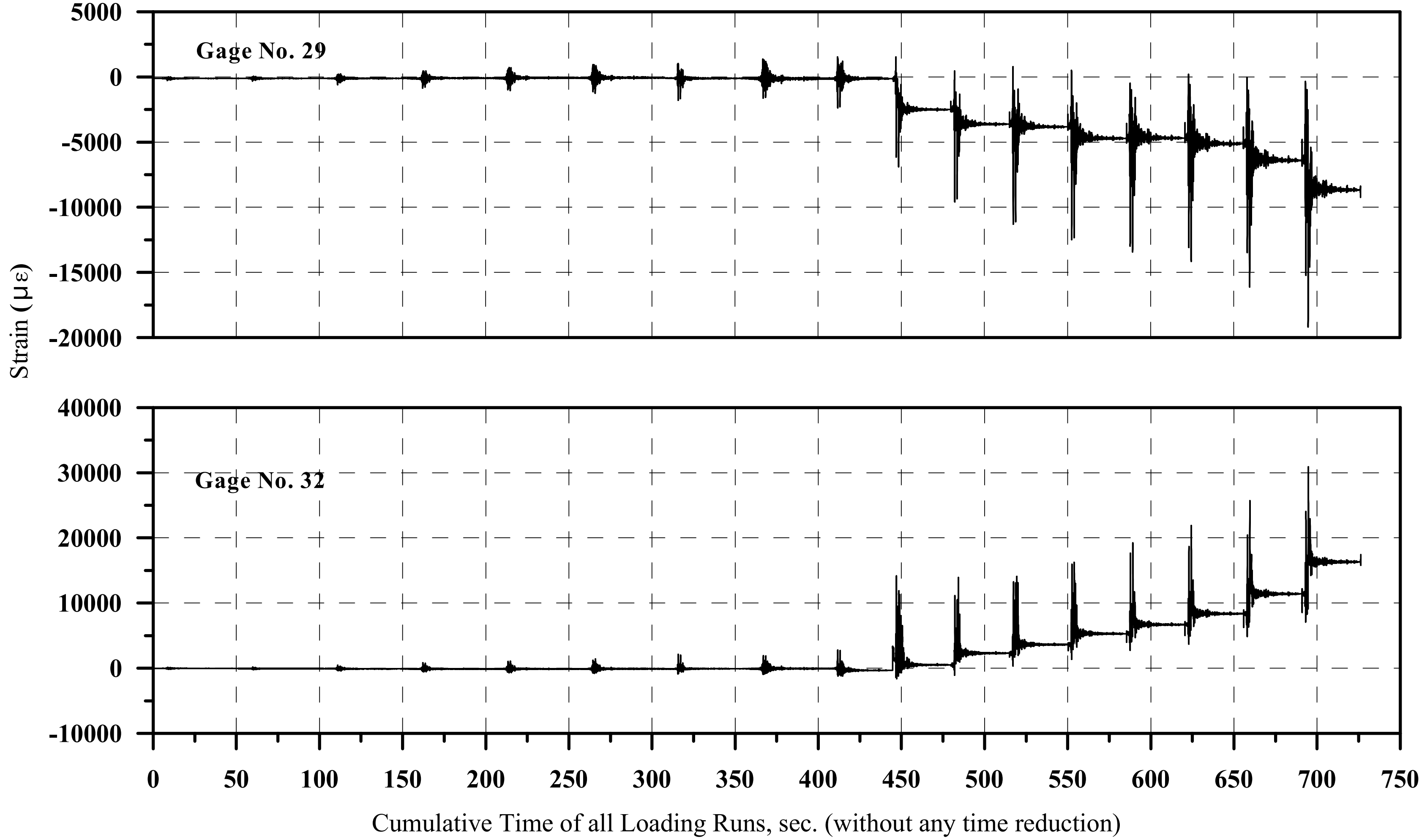

Fig. 4-62: Strain History of Gages 29 and 32 in Specimen B2CS

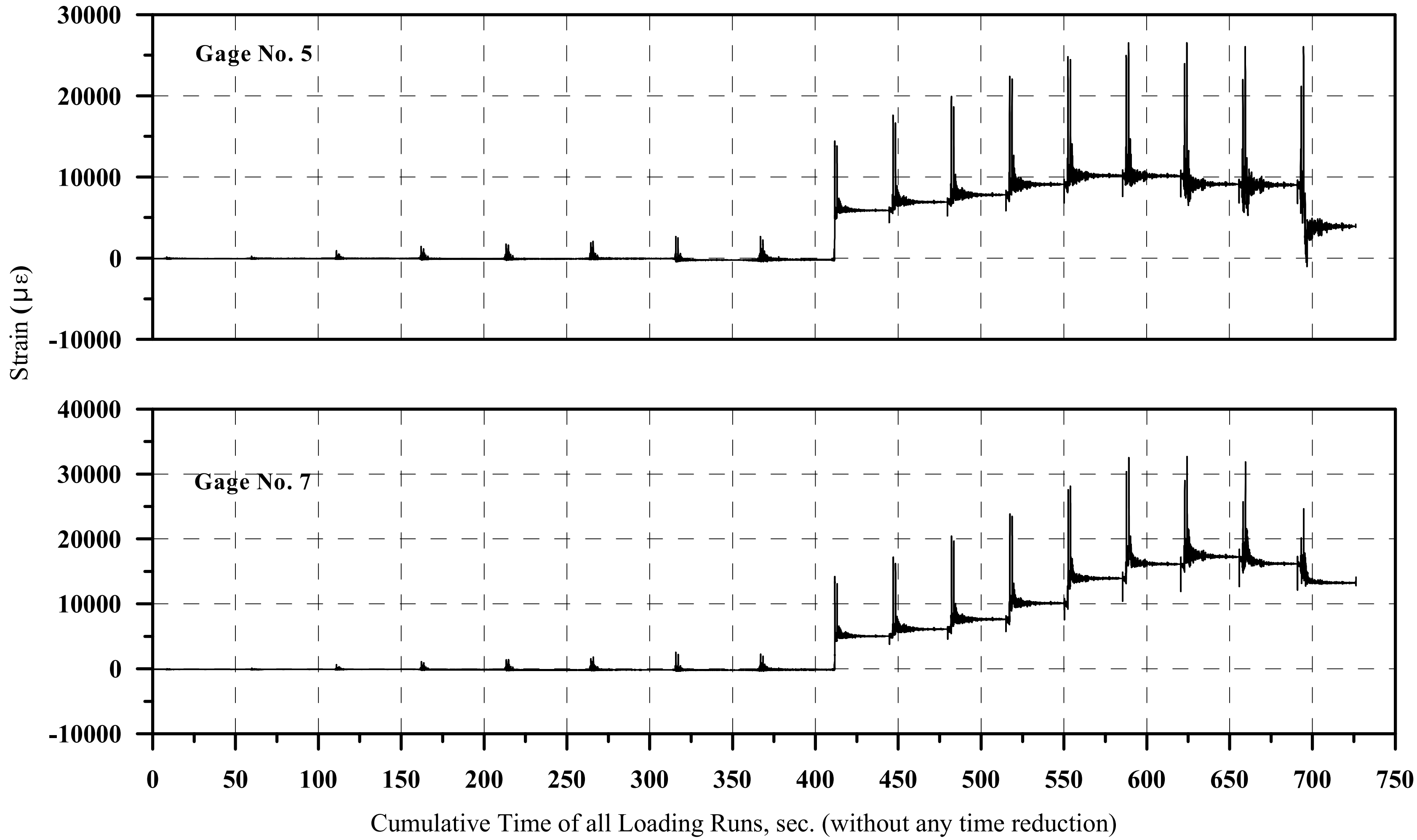

Fig. 4-63: Strain History of Gages 5 and 7 in Specimen B2CS

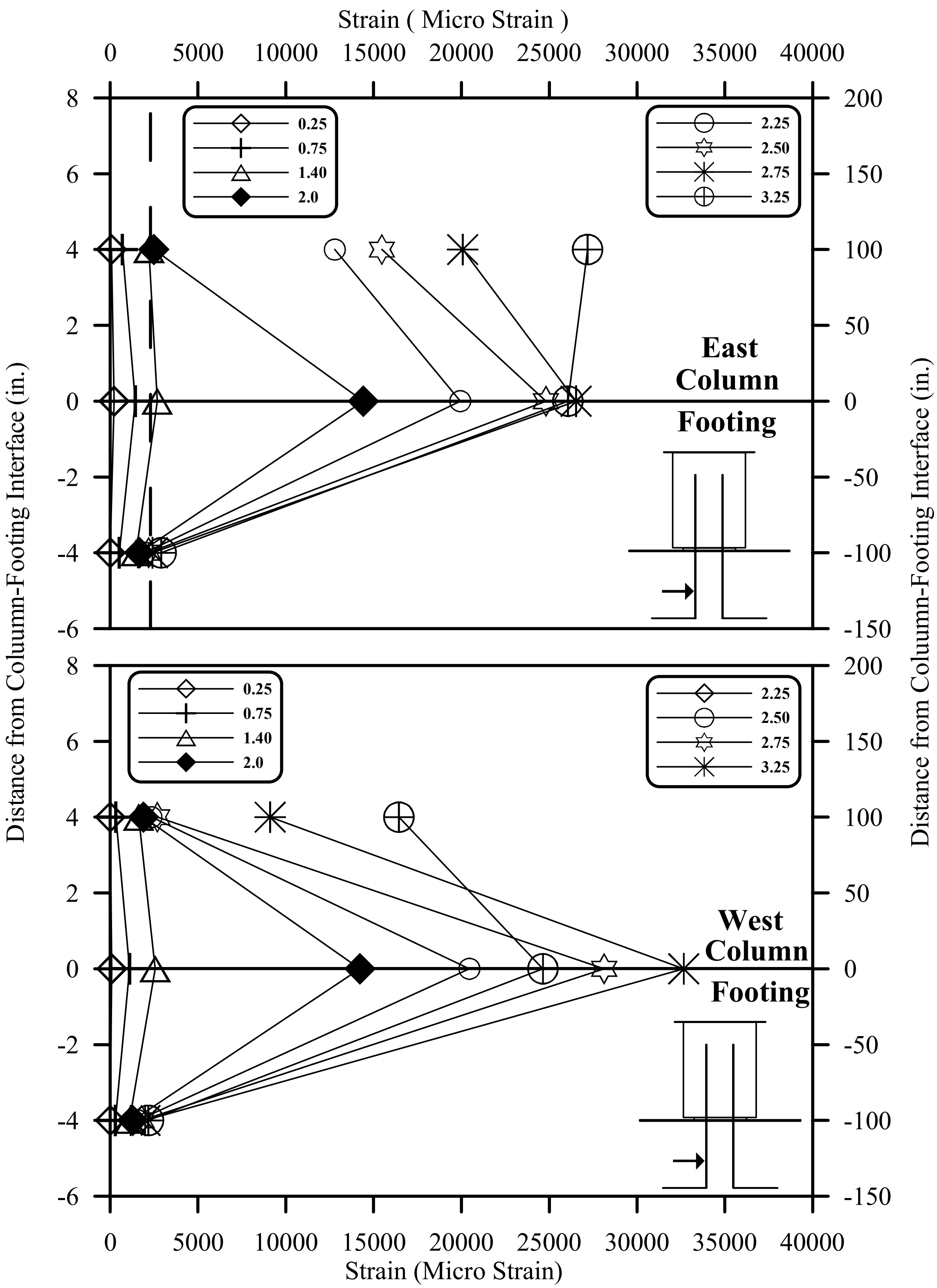

Fig. 4-64: Strain Profile Along the Hinge Dowels on West Side of Each Column Base in Short Specimen B2CS

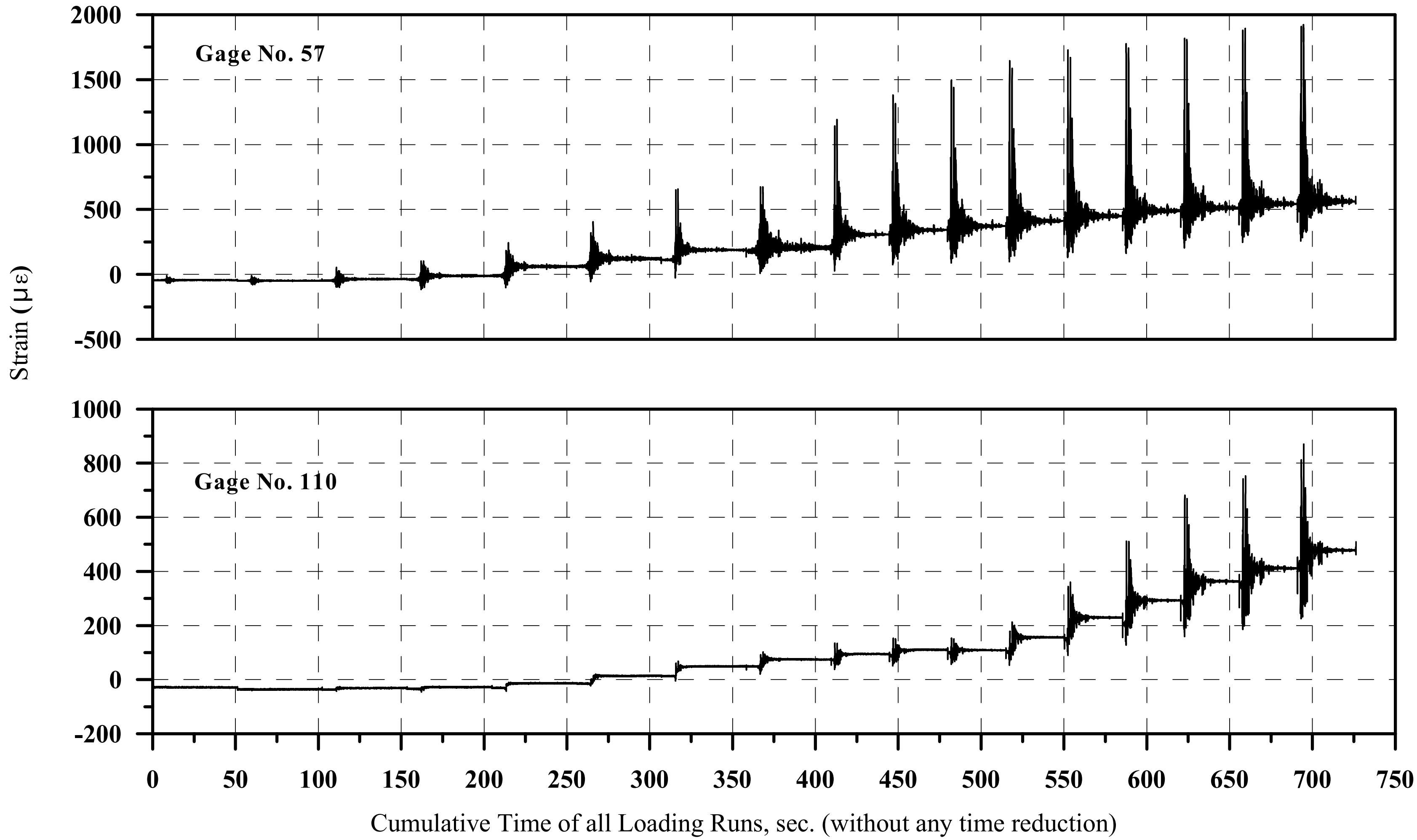

Fig. 4-65: Strain History of Gages 57 and 110 in Specimen B2CS

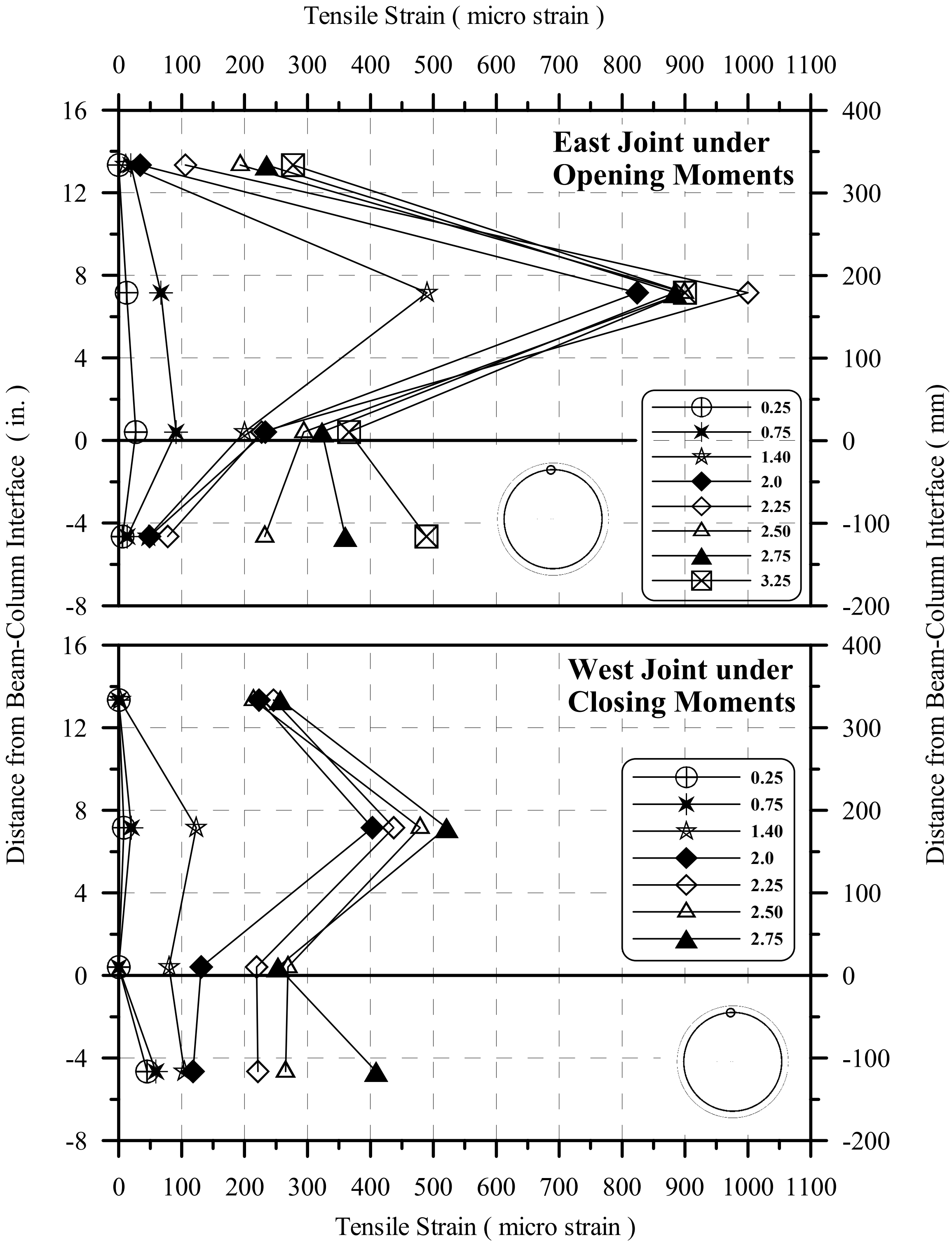

Fig. 4-66: Strain Profile of Column Transverse Reinforcement at Beam-Column Joints in Specimen B2CS

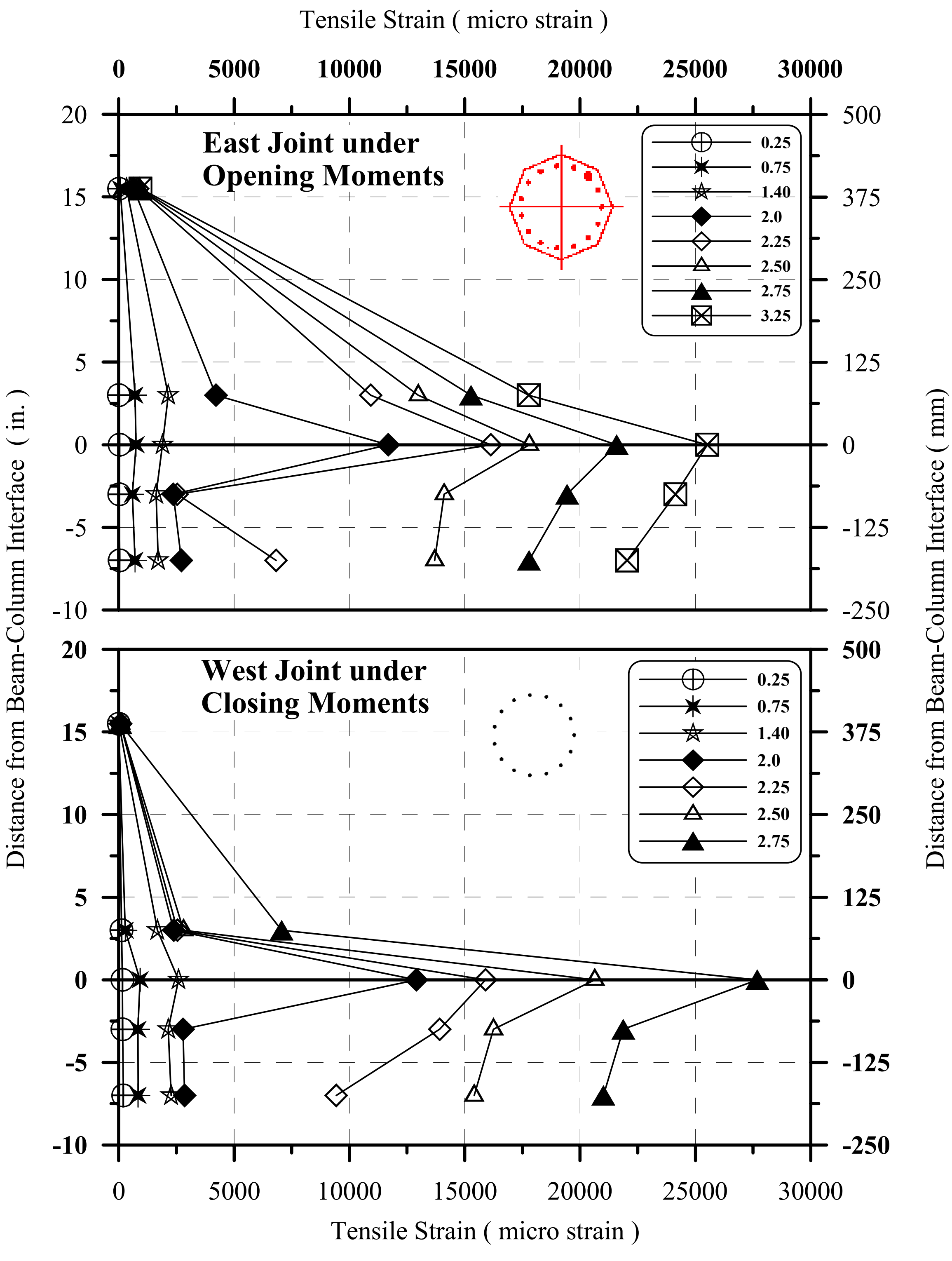

Fig. 4-67: Strain Profile of Column Longitudinal Reinforcement at Beam-Column Joints in Short Specimen B2CS

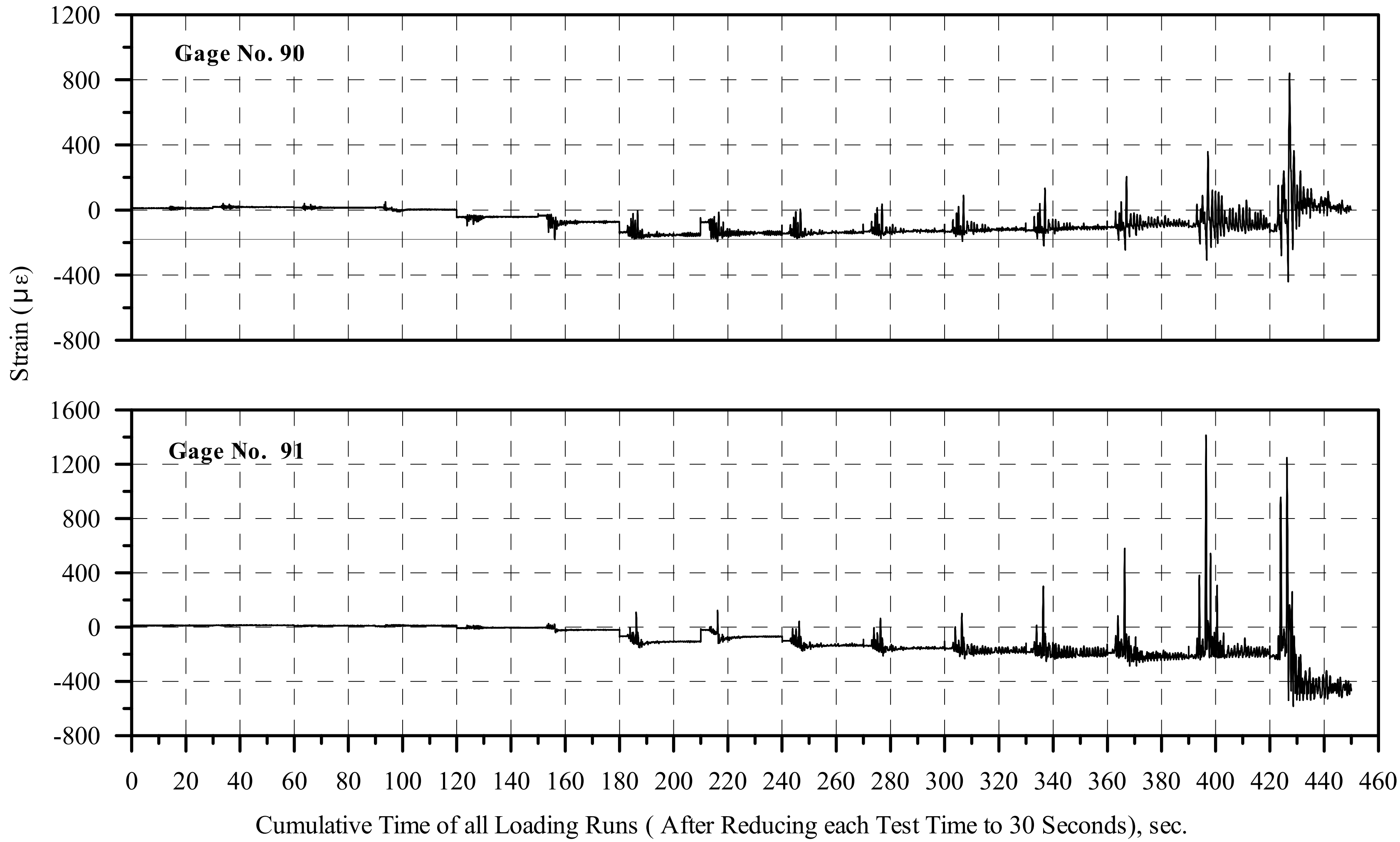

Fig. 4-68: Strain History of Gages 90 and 91 in Specimen B2CM

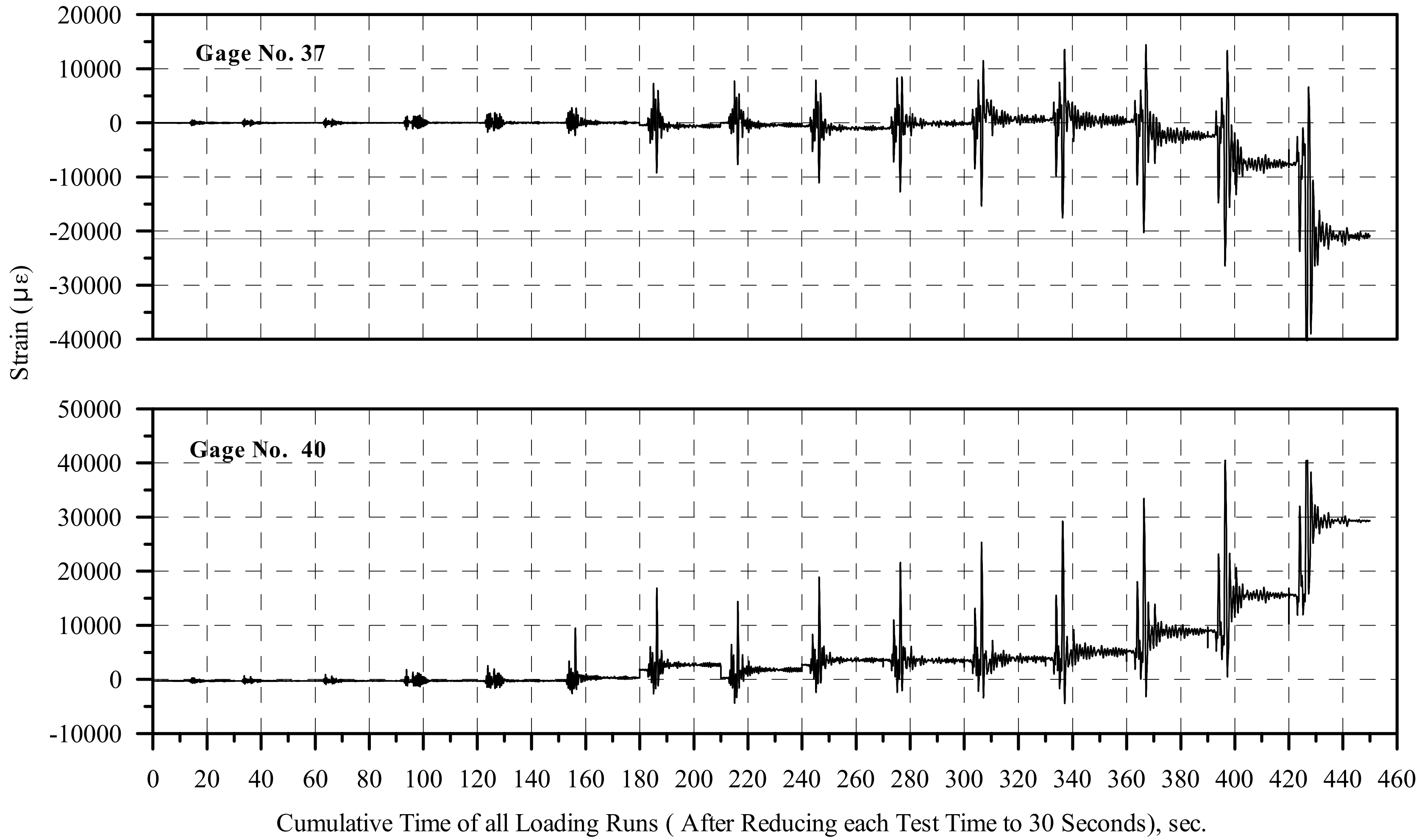

Fig. 4-69: Strain History of Gages 37 and 40 in Specimen B2CM

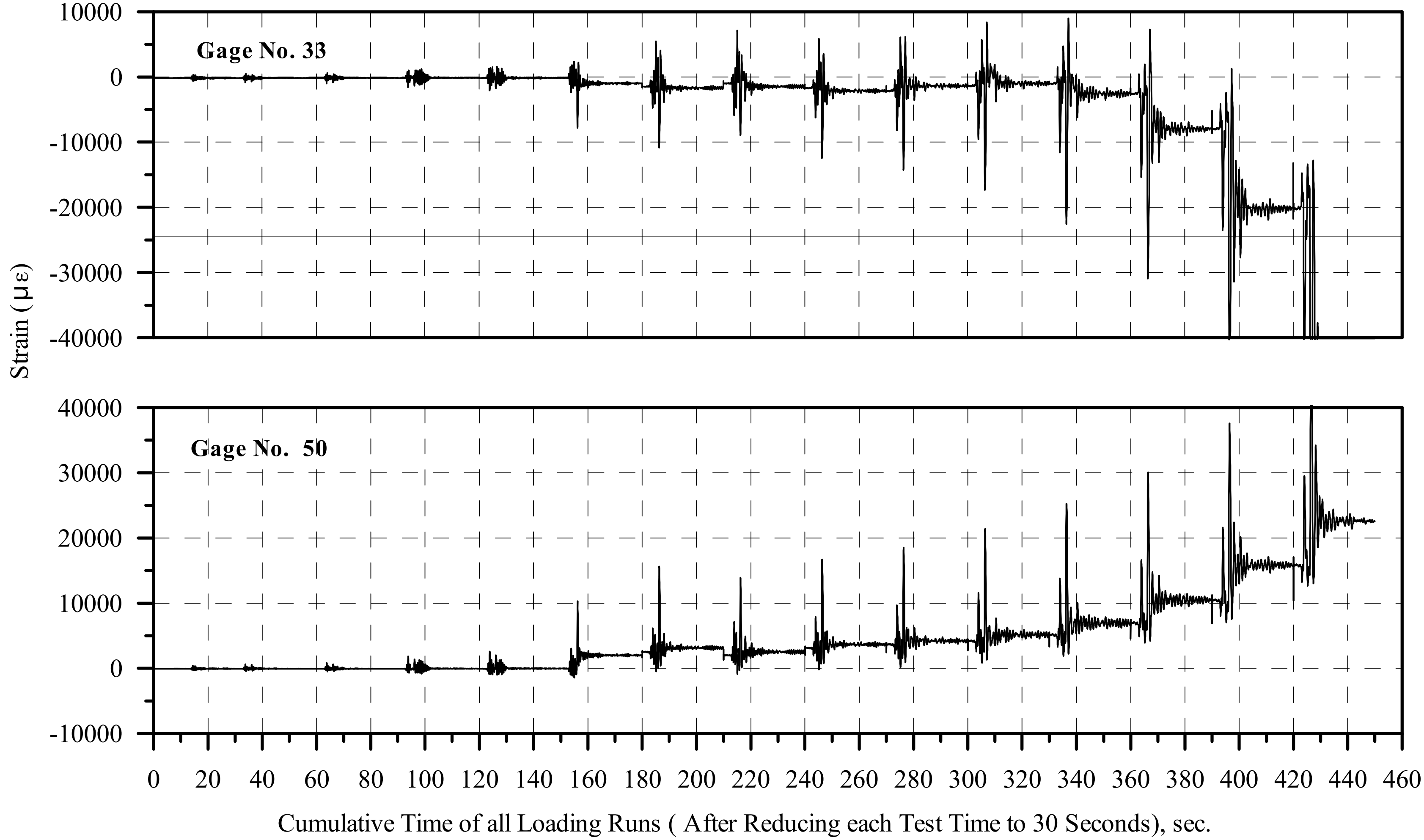

Fig. 4-70: Strain History of Gages 33 and 50 in Specimen B2CM

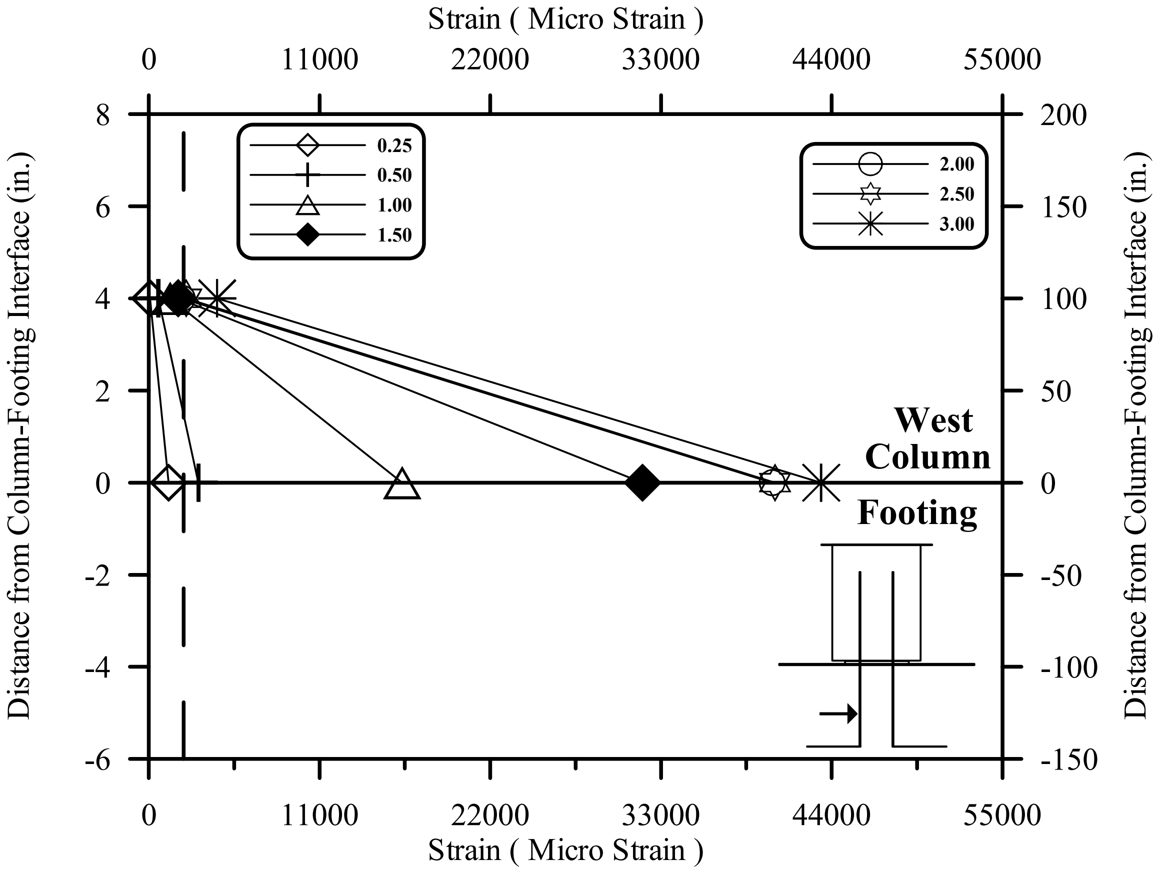

Fig. 4-71: Strain Profile Along the Hinge Dowel on East Side of West Column Base in Middle Specimen B2CM

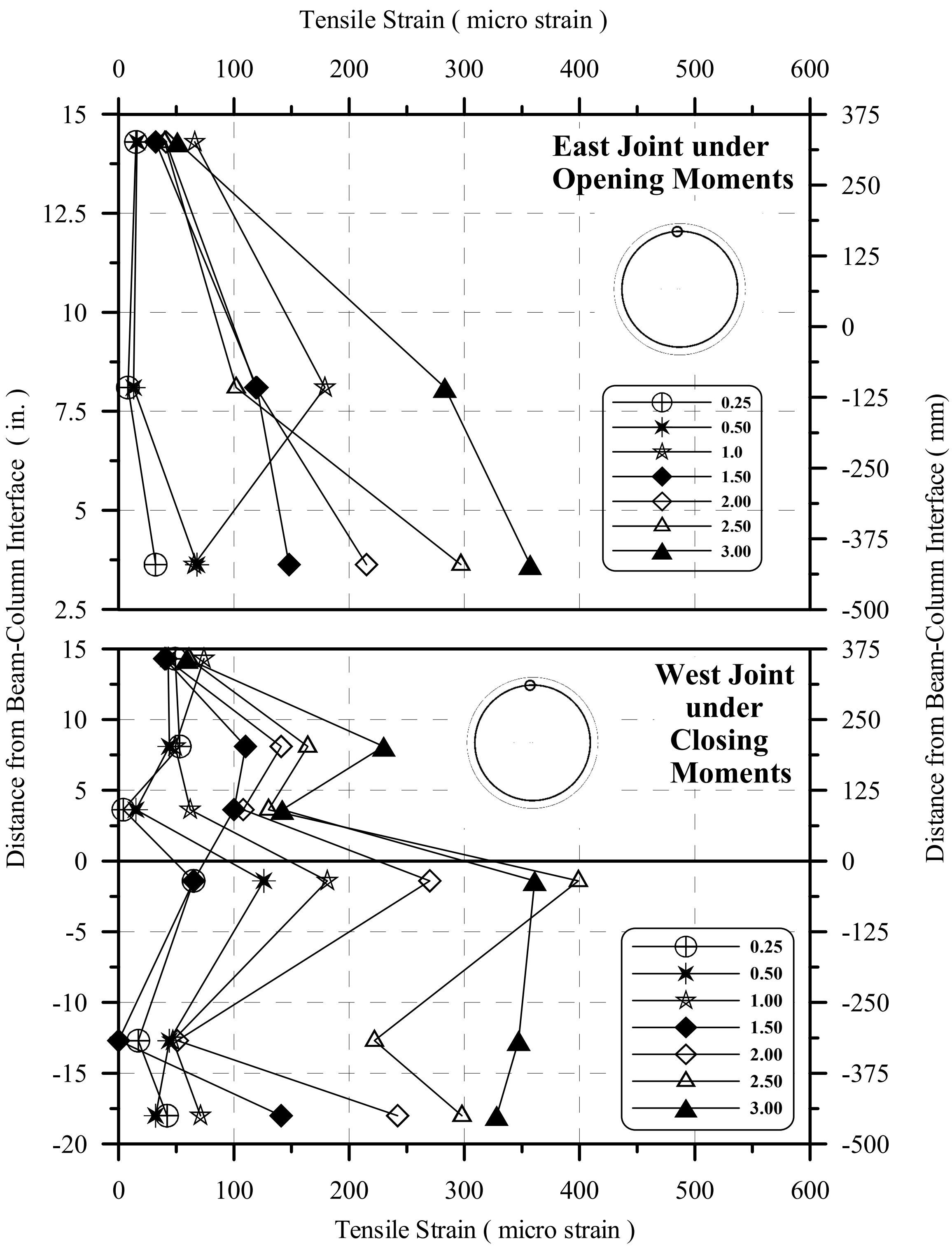

Fig. 4-72: Strain Profile of Column Transverse Reinforcement at Beam-Column Joints in Middle Specimen B2CM

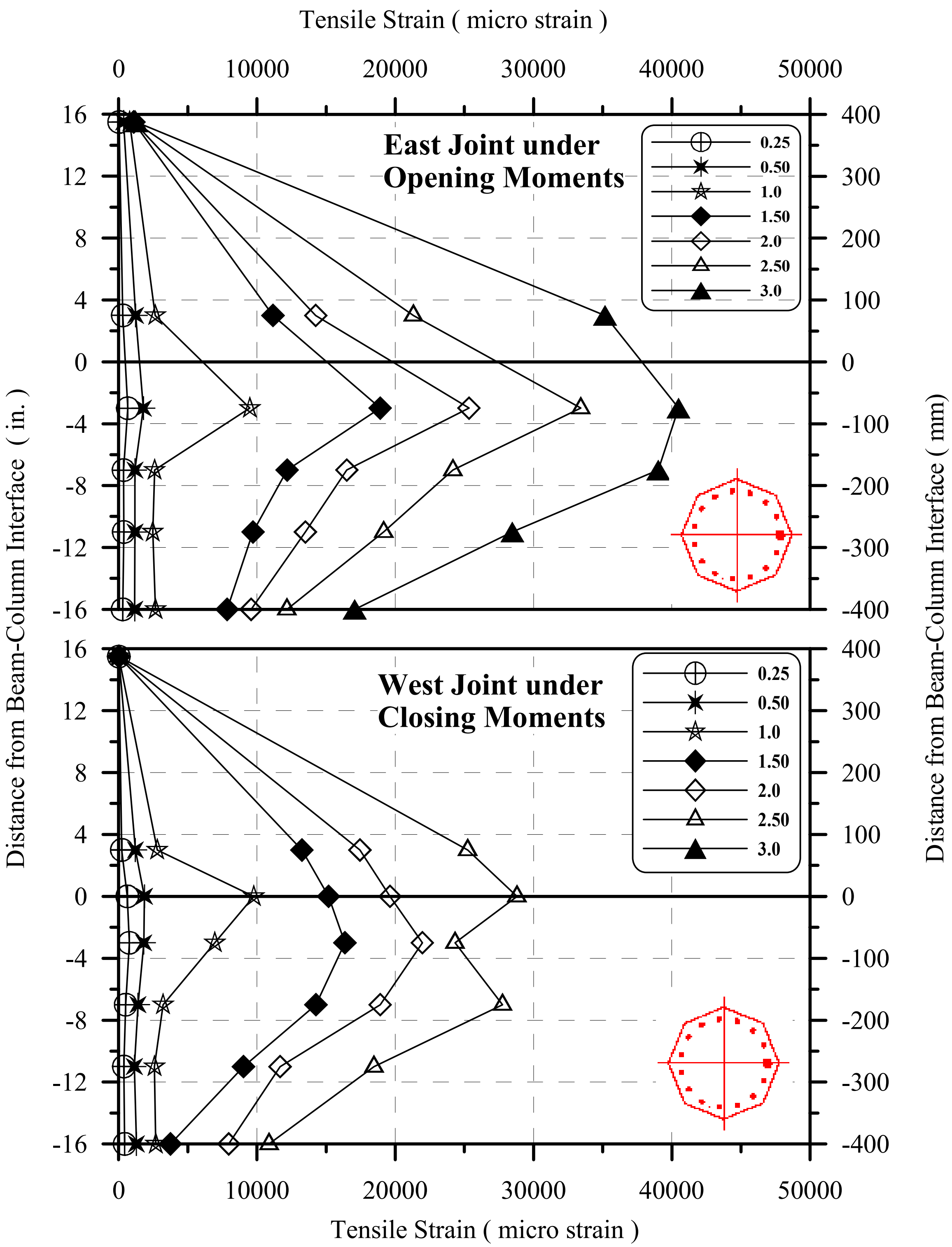

Fig. 4-73: Strain Profile of Column Longitudinal Reinforcement at Beam-Column Joints in Middle Specimen B2CM

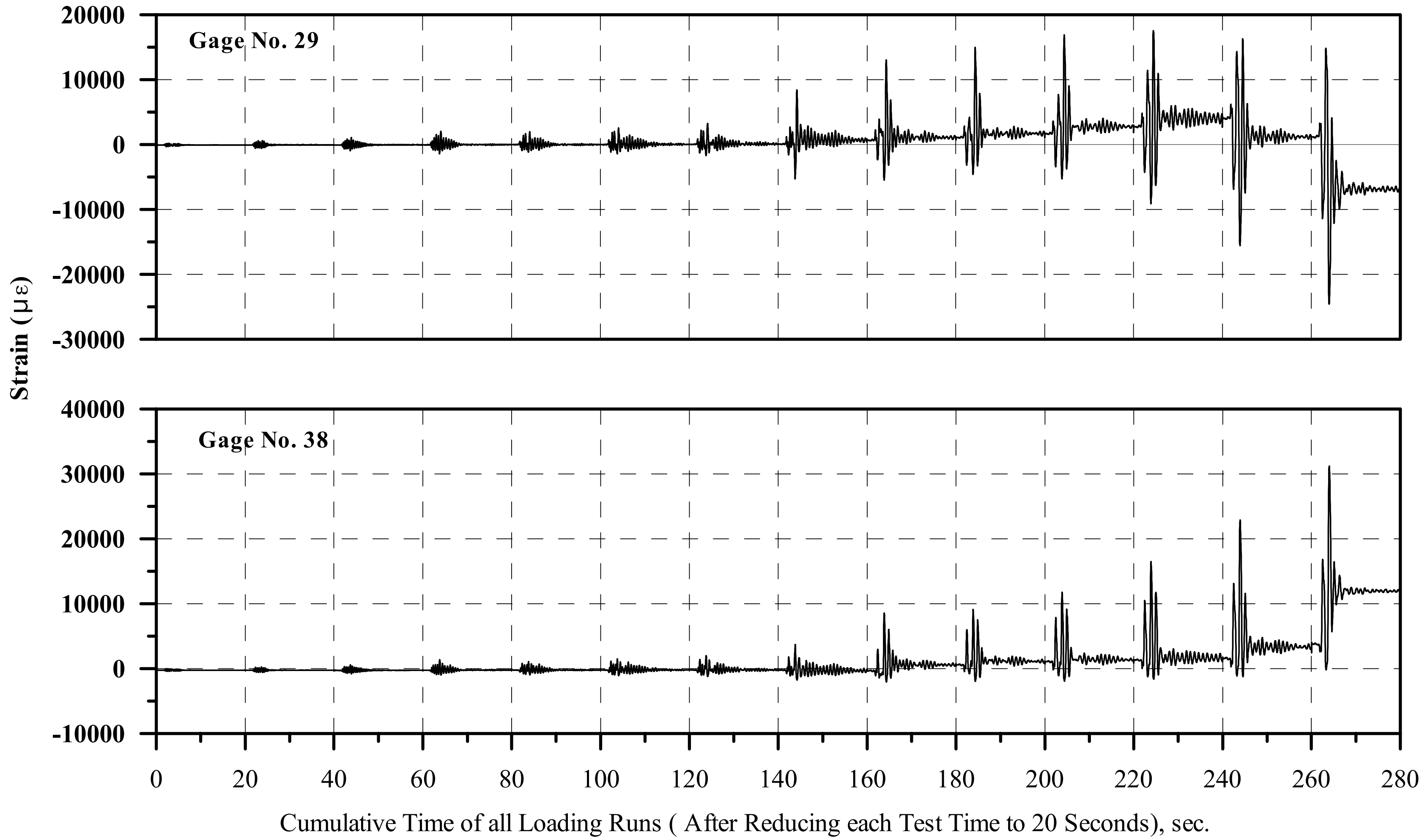

Fig. 4-74: Strain History of Gages 29 and 38 in Specimen B2CT

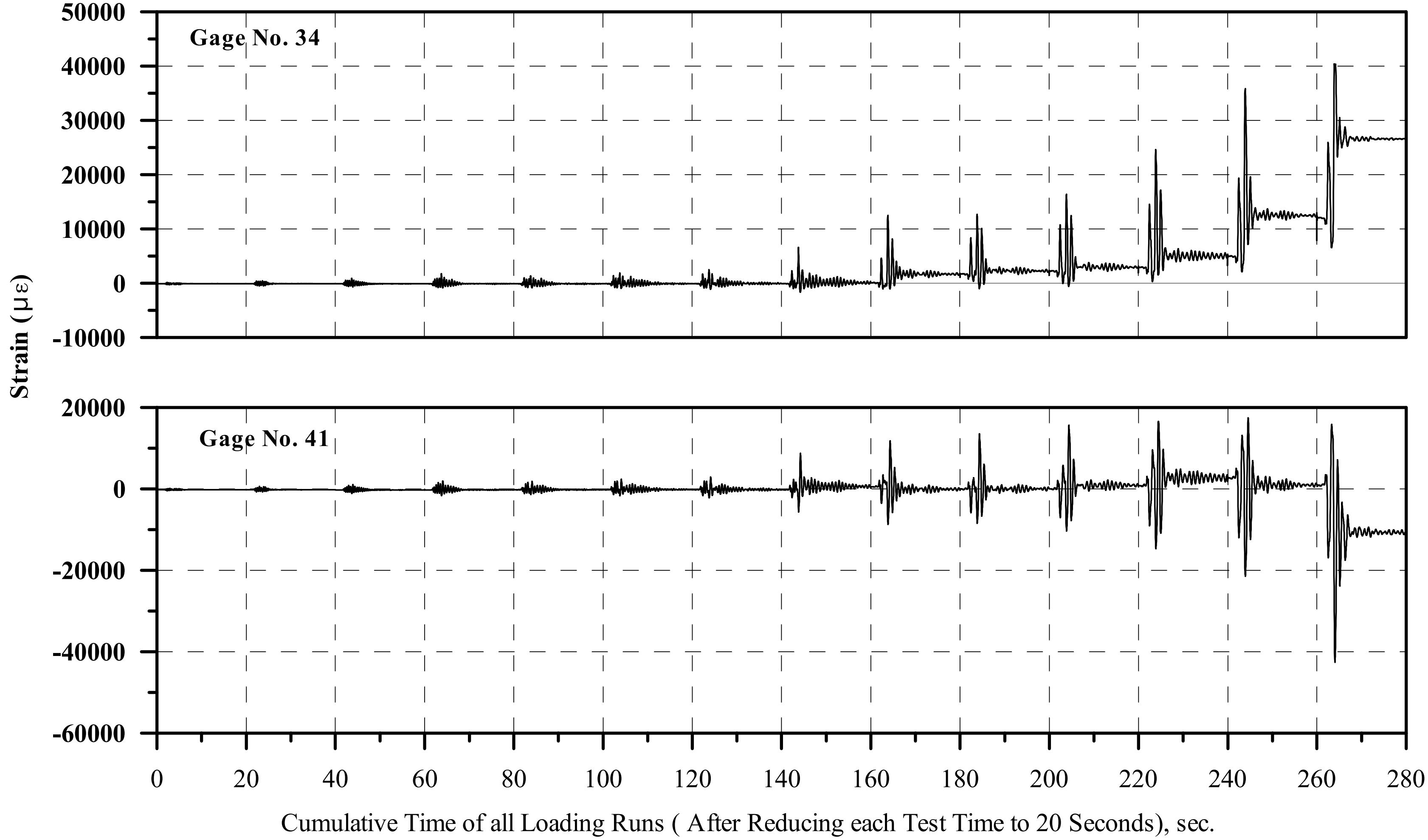

Fig. 4-75: Strain History of Gages 34 and 41 in Specimen B2CT

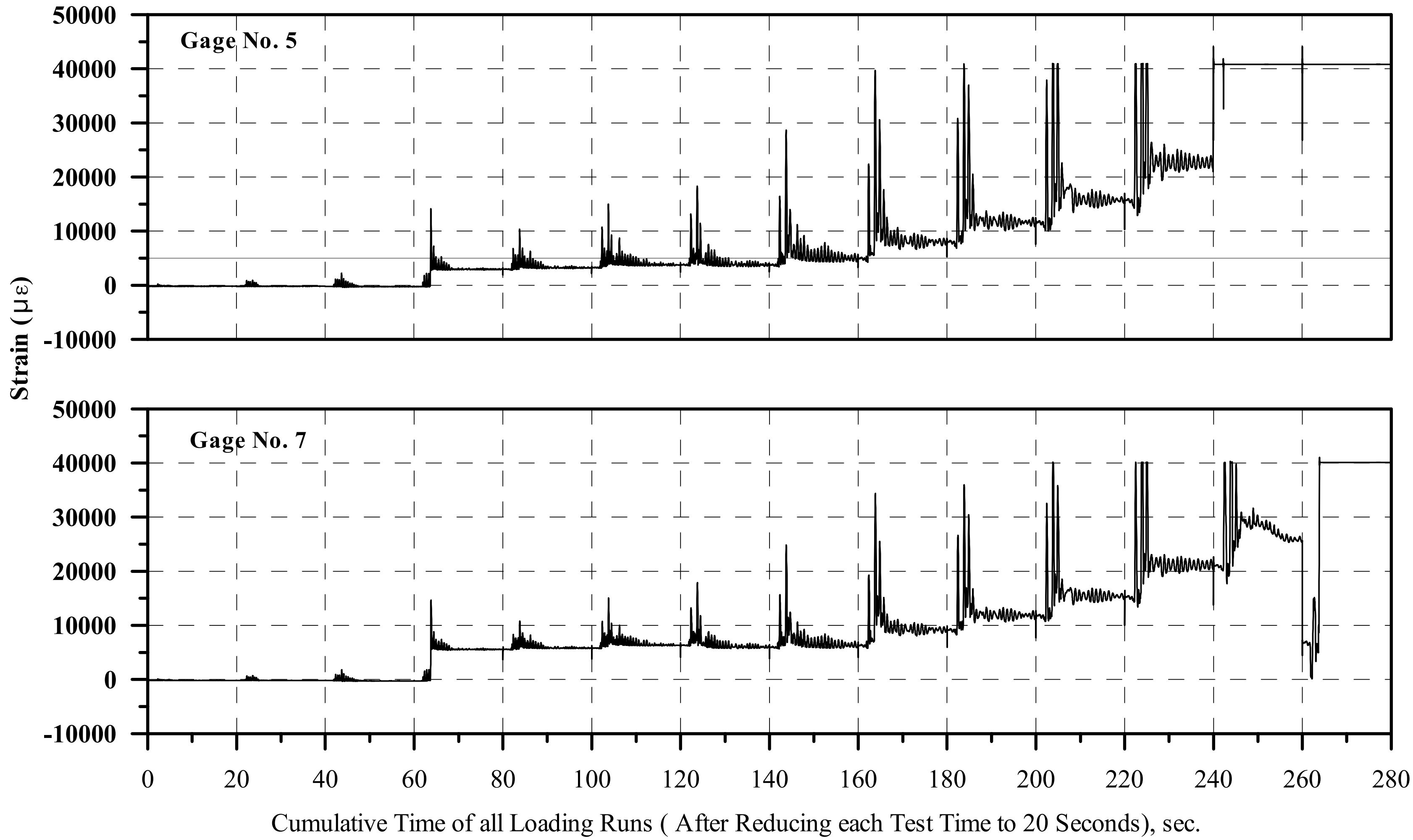

Fig. 4-76: Strain History of Gages 5 and 7 in Specimen B2CT

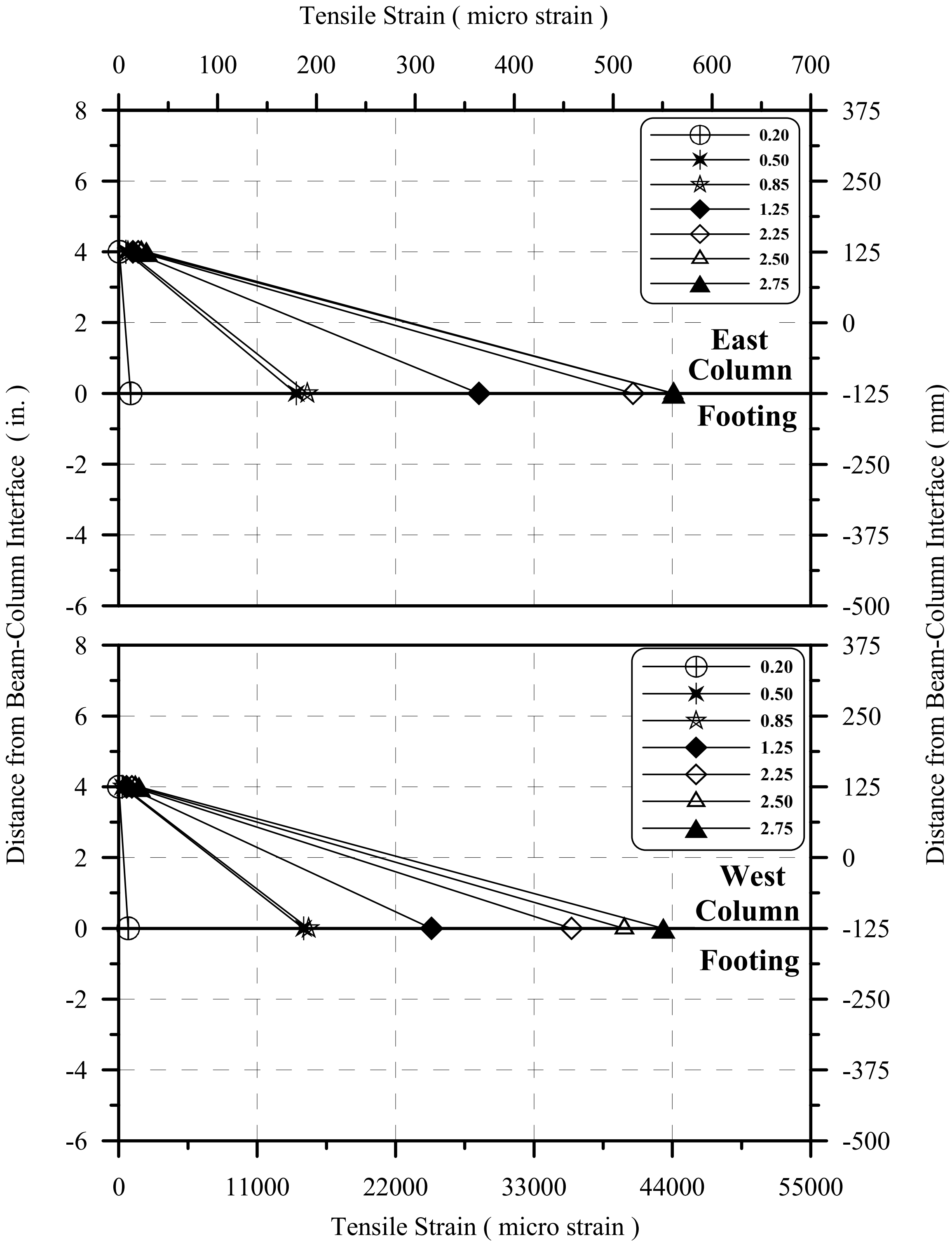

Fig. 4-77: Strain Profile along the Hinge Dowels on East Side of Each Column Base in Tall Specimen B2CT

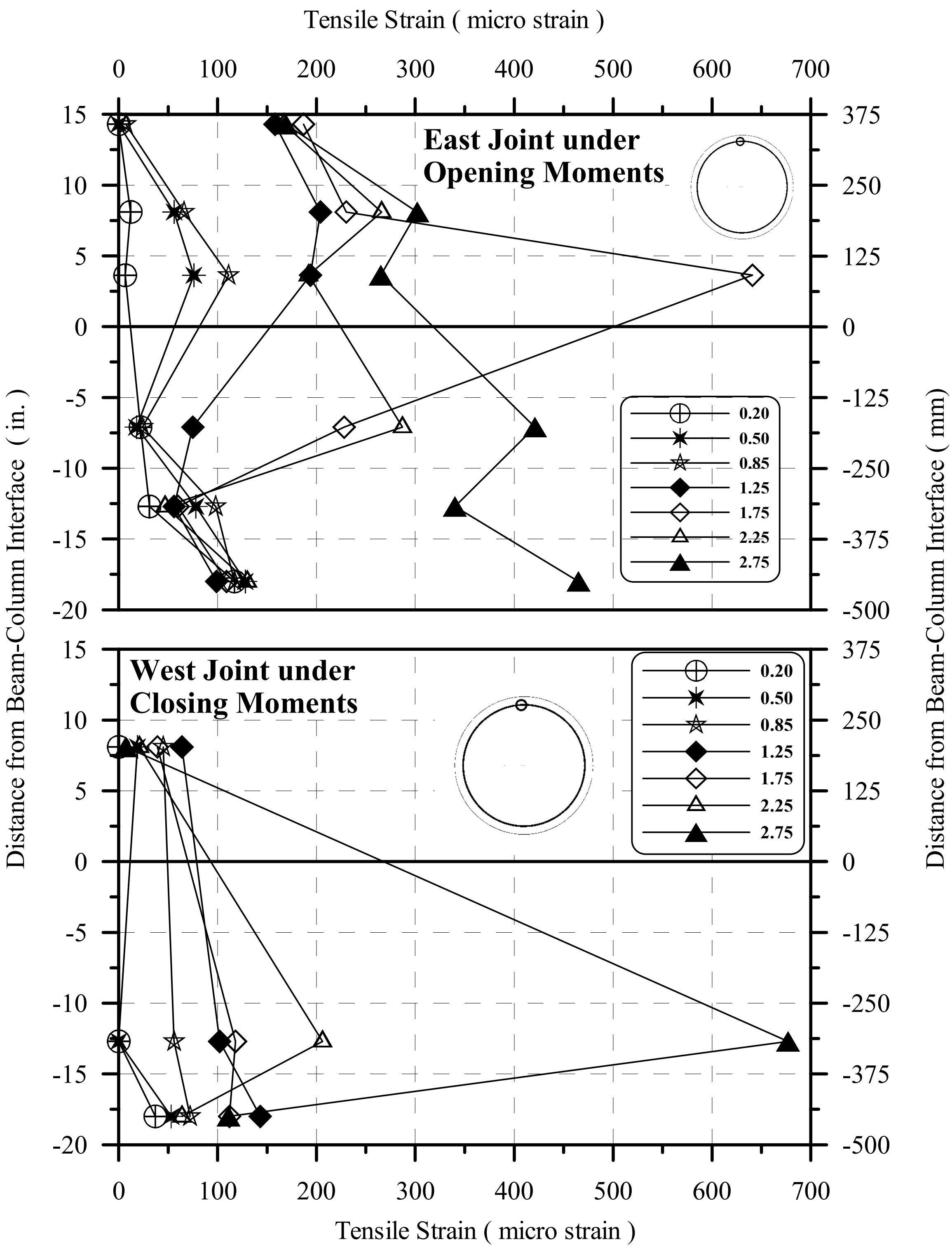

Fig. 4-78: Strain Profile of Column Transverse Reinforcement at Beam-Column Joints in Tall Specimen B2CT

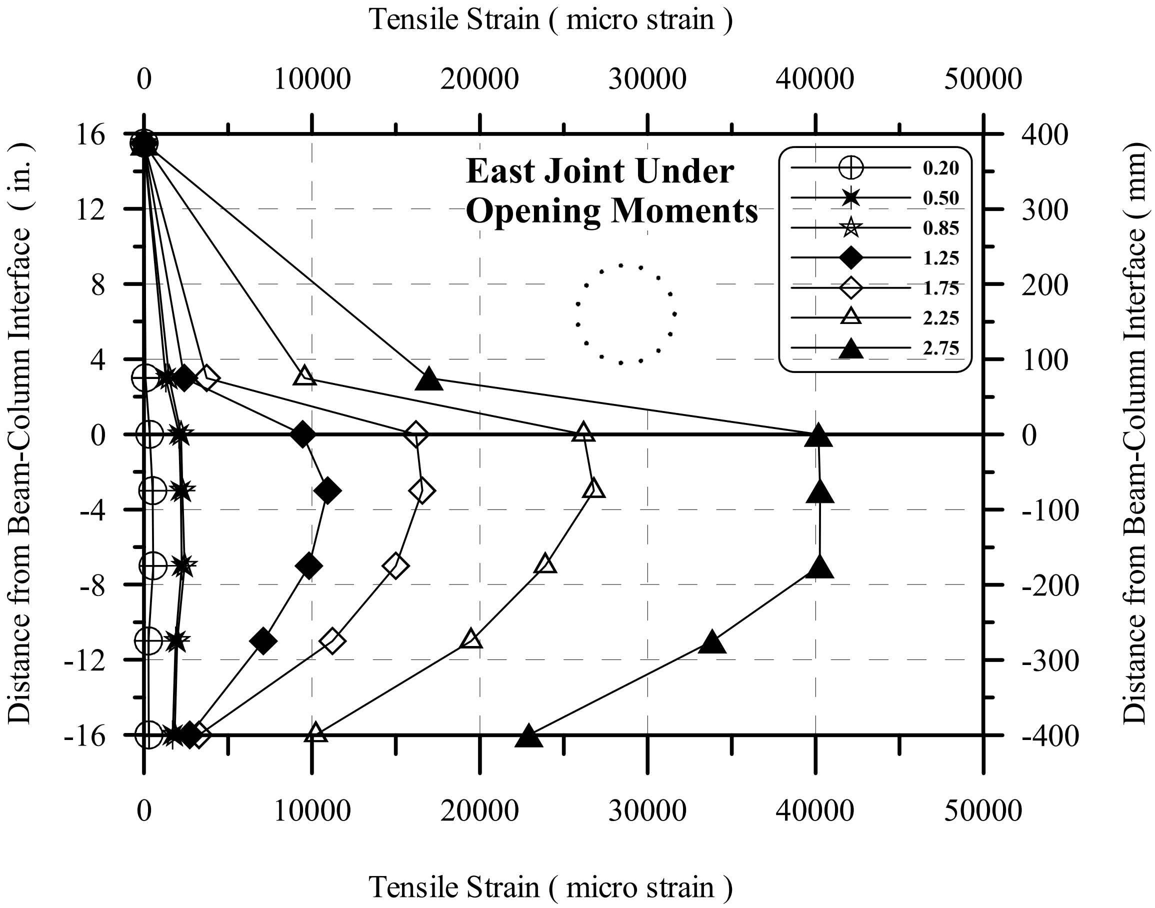

Fig. 4-79: Strain Profile of Column Longitudinal Reinforcement at East Beam-Column Joint in Tall Specimen B2CT

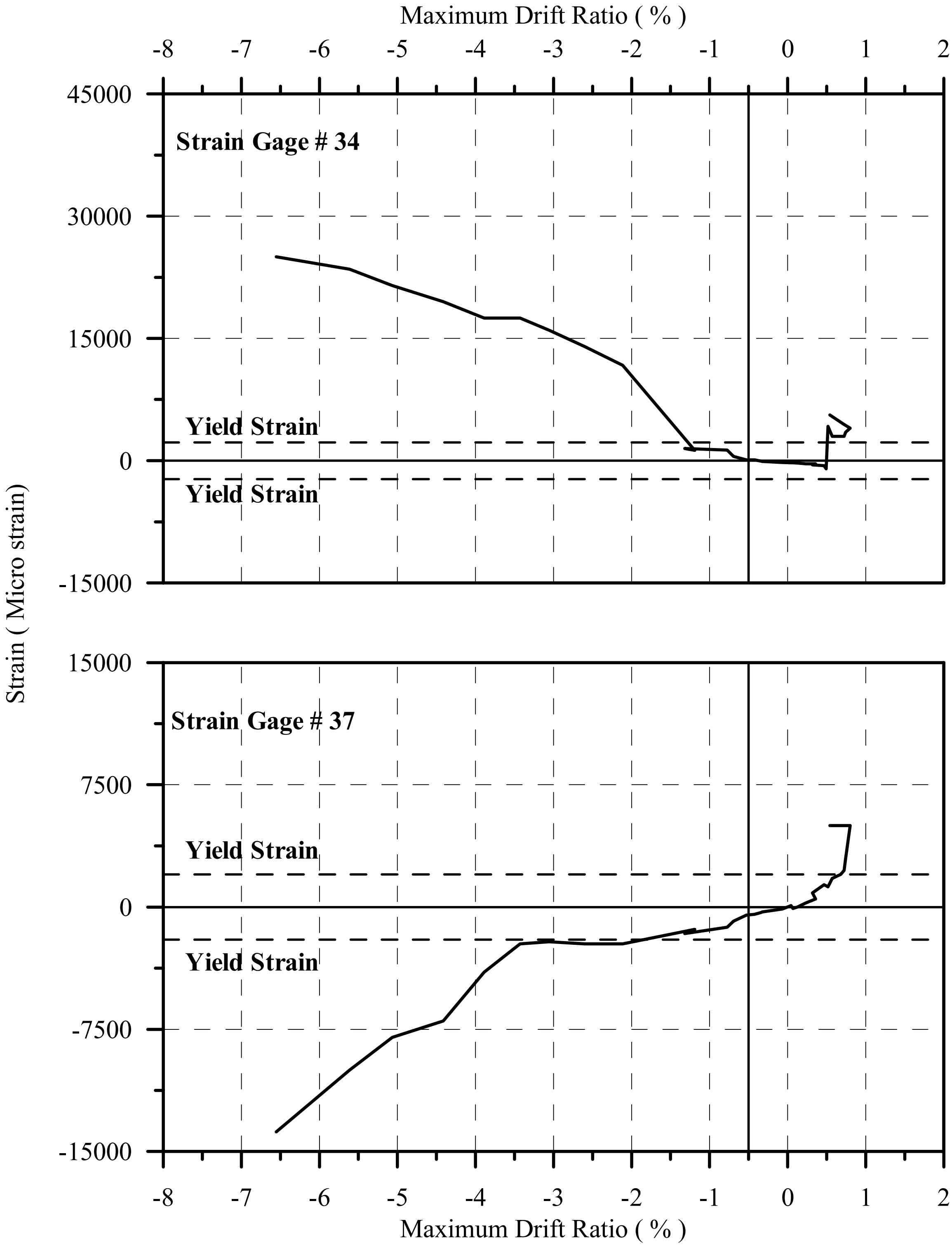

Fig. 4-80: Envelope of Strain-Displacement Hysteresis of Gages 34 and 37 in Specimen B2CS.

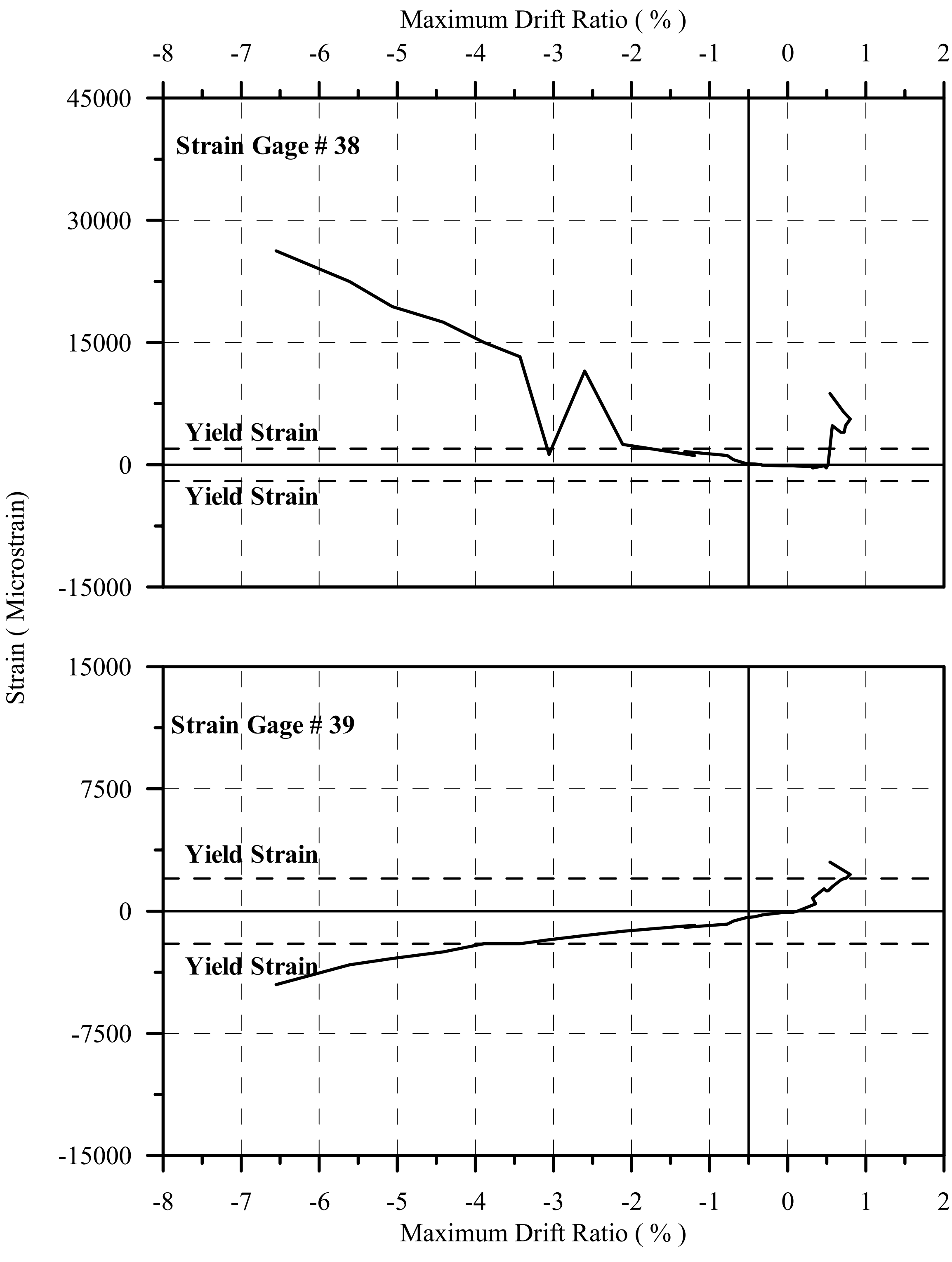

Fig 4-81: Envelope of Strain-Displacement Hysteresis of Gages 38 and 39 in Short Specimen B2CS.

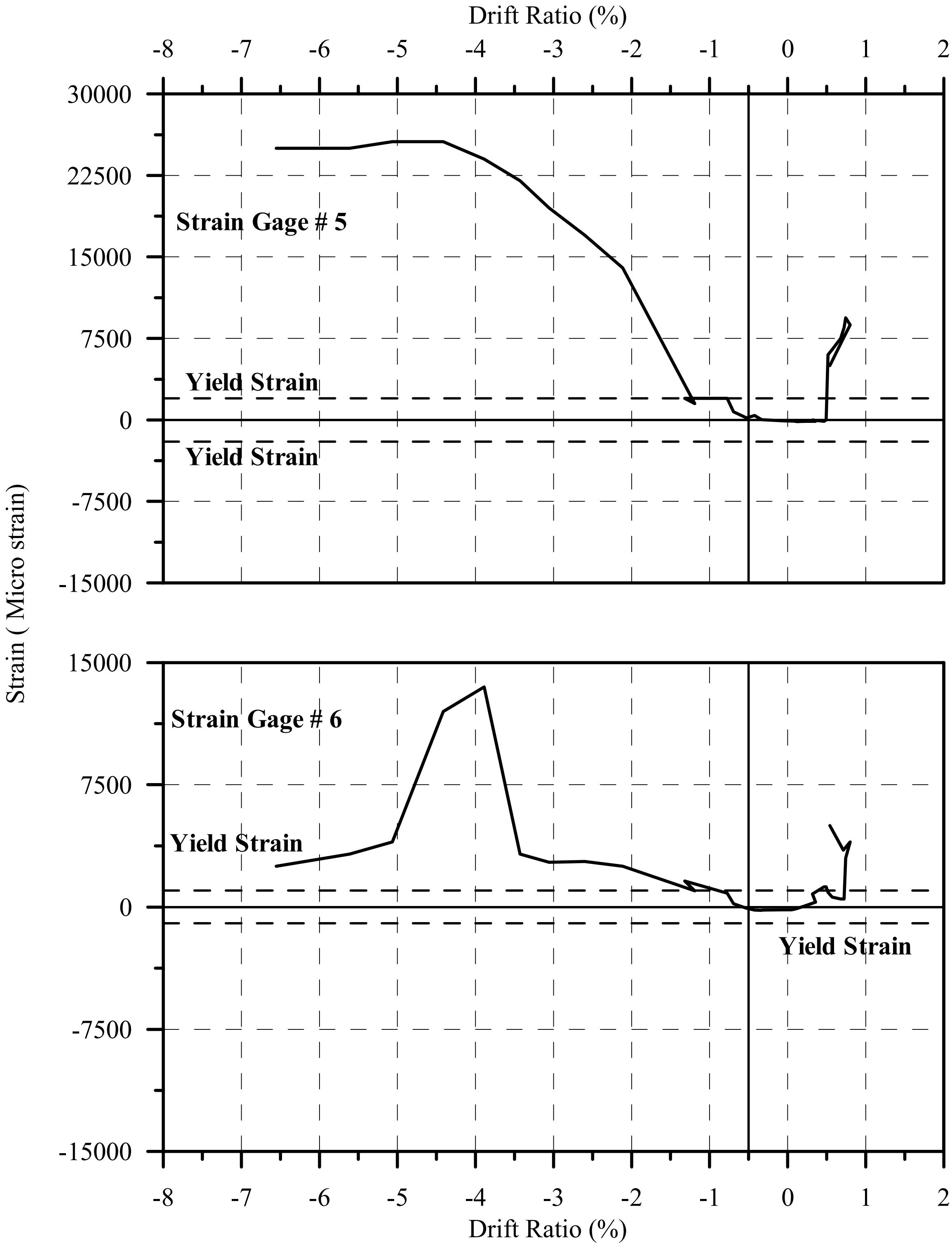

Fig. 4-82: Envelope of Strain-Displacement Hysteresis of Gages 5 and 6 in Short Specimen B2CS.

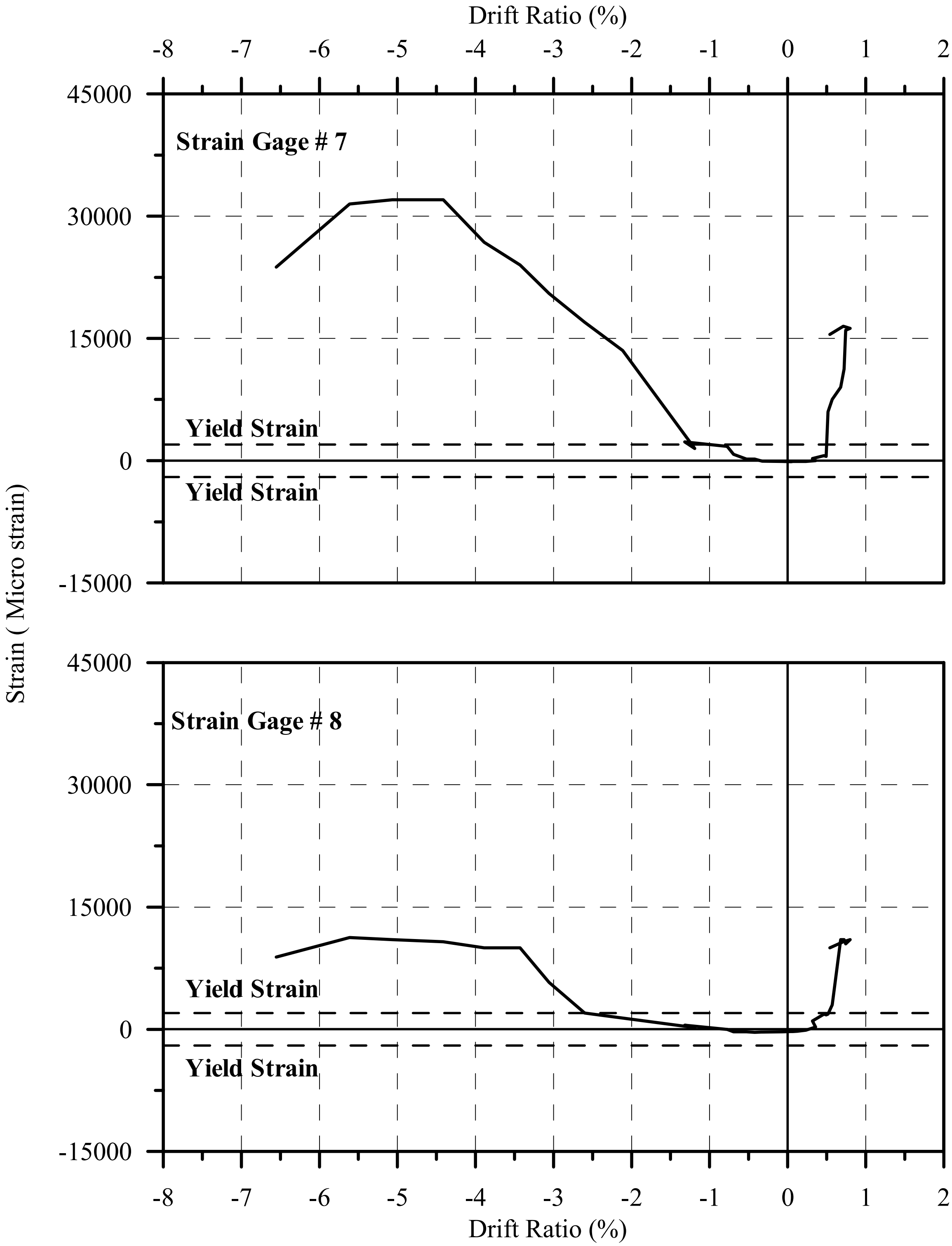

Fig. 4-83: Envelope of Strain-Displacement Hysteresis of Gages 7 and 8 in Short Specimen B2CS.

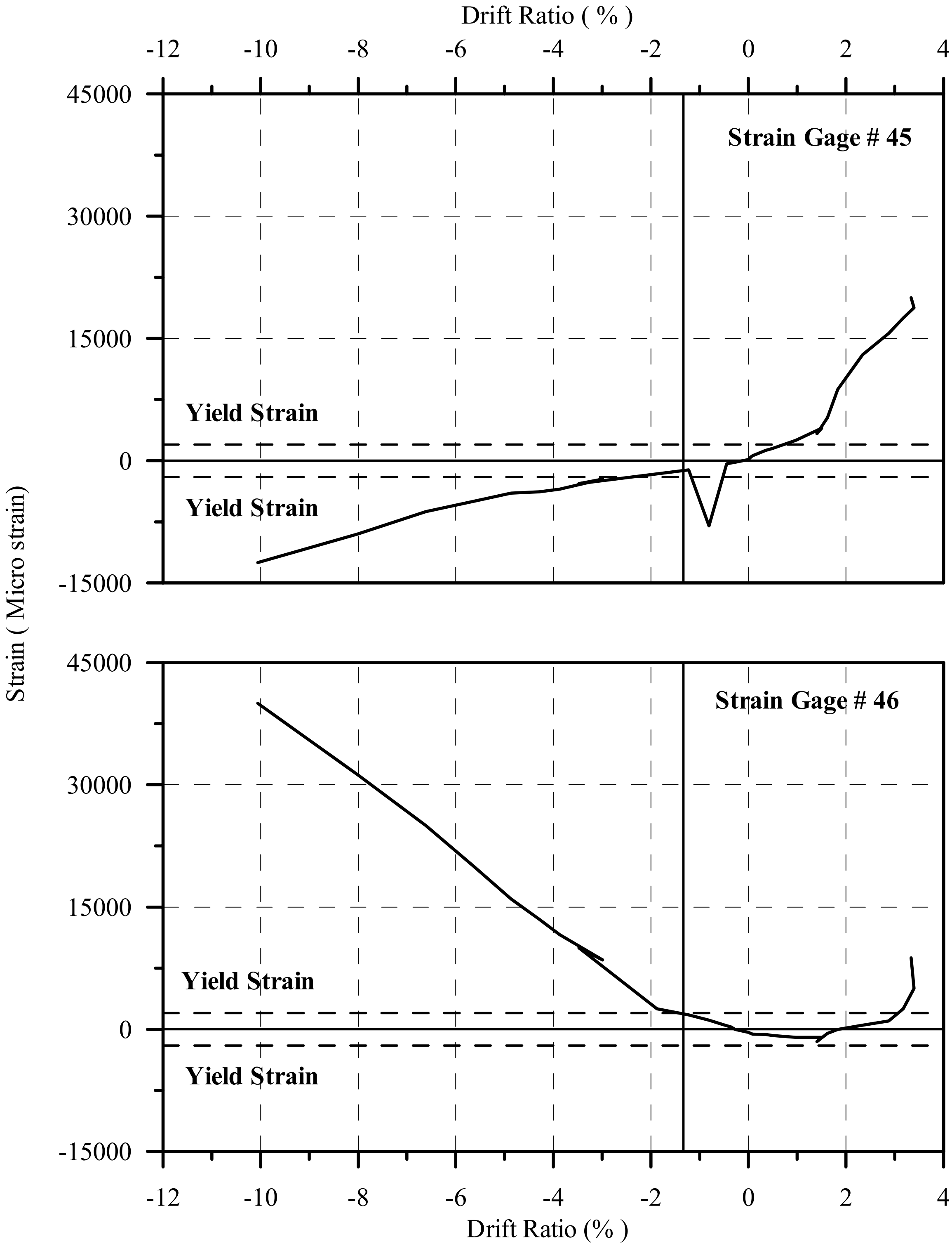

Fig 4-84: Envelope of Strain-Displacement Hysteresis of Gages 45 and 46 in Middle Specimen B2CM

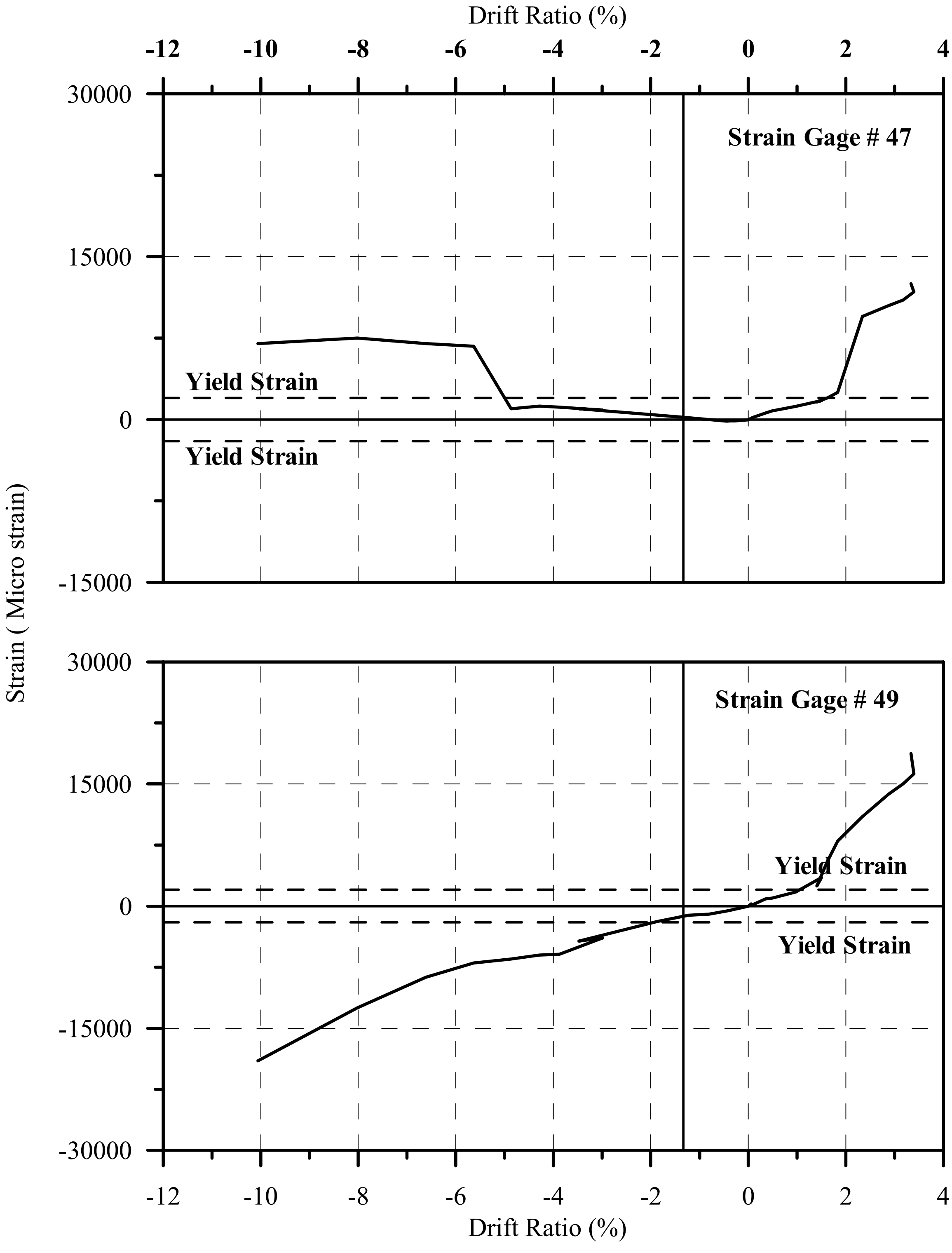

Fig 4-85: Envelope of Strain-Displacement Hysteresis of Gages 47 and 49 in Middle Specimen B2CM

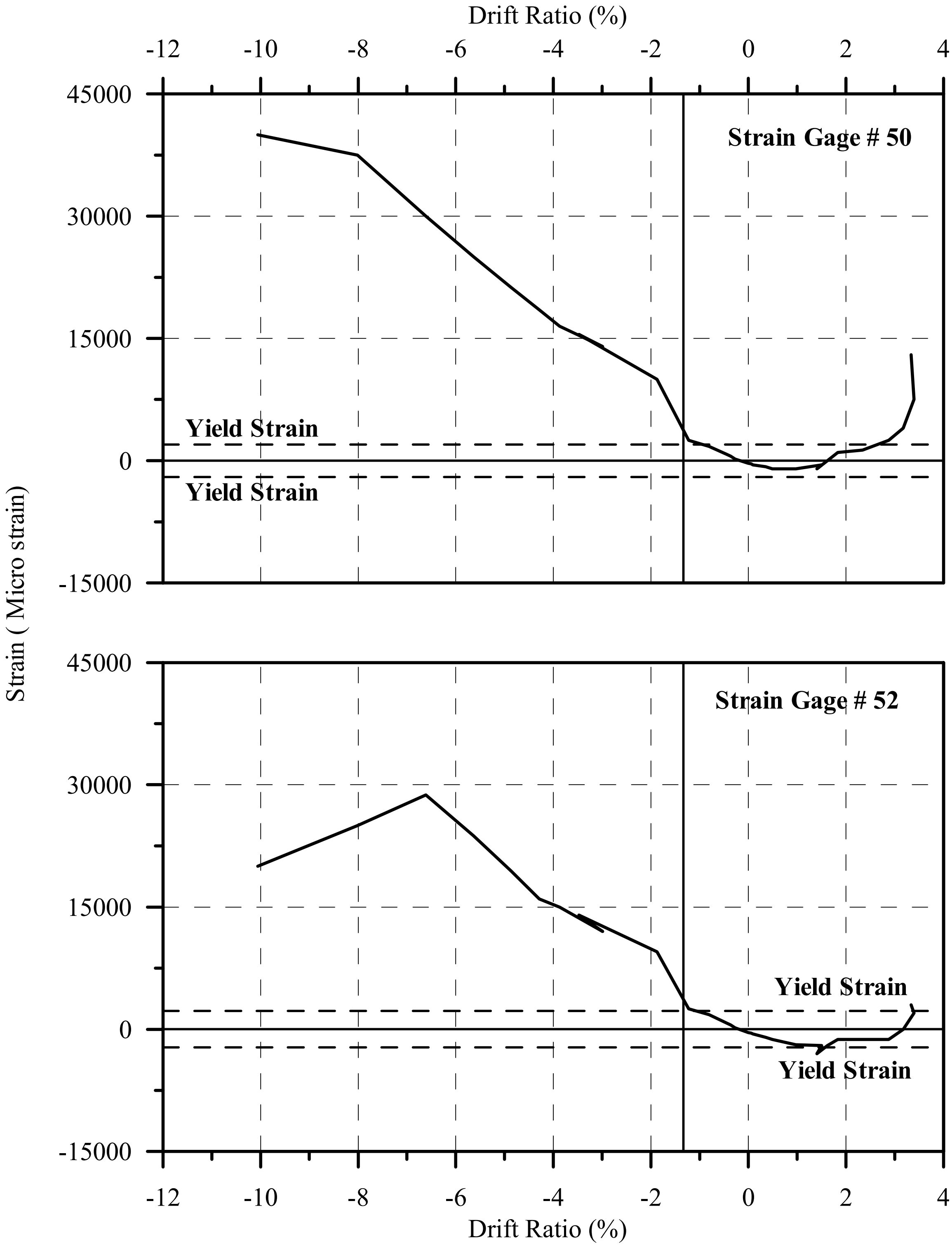

Fig. 4-86: Envelope of Strain-Displacement Hysteresis of gages 50 and 52 in Middle Specimen B2CM

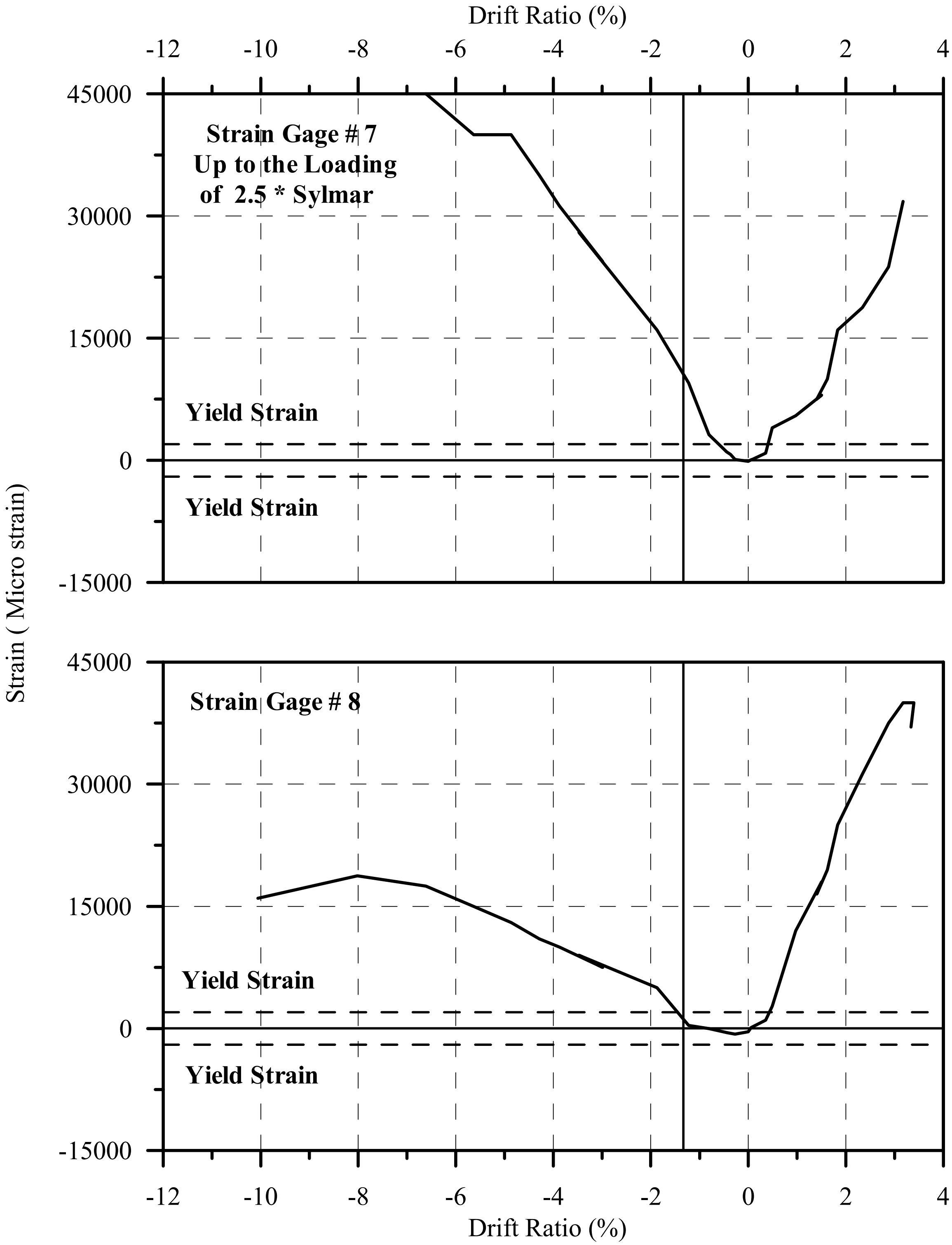

Fig.4-87: Envelope of Strain-Displacement Hysteresis of Gages 7 and 8 in Middle Specimen B2CM

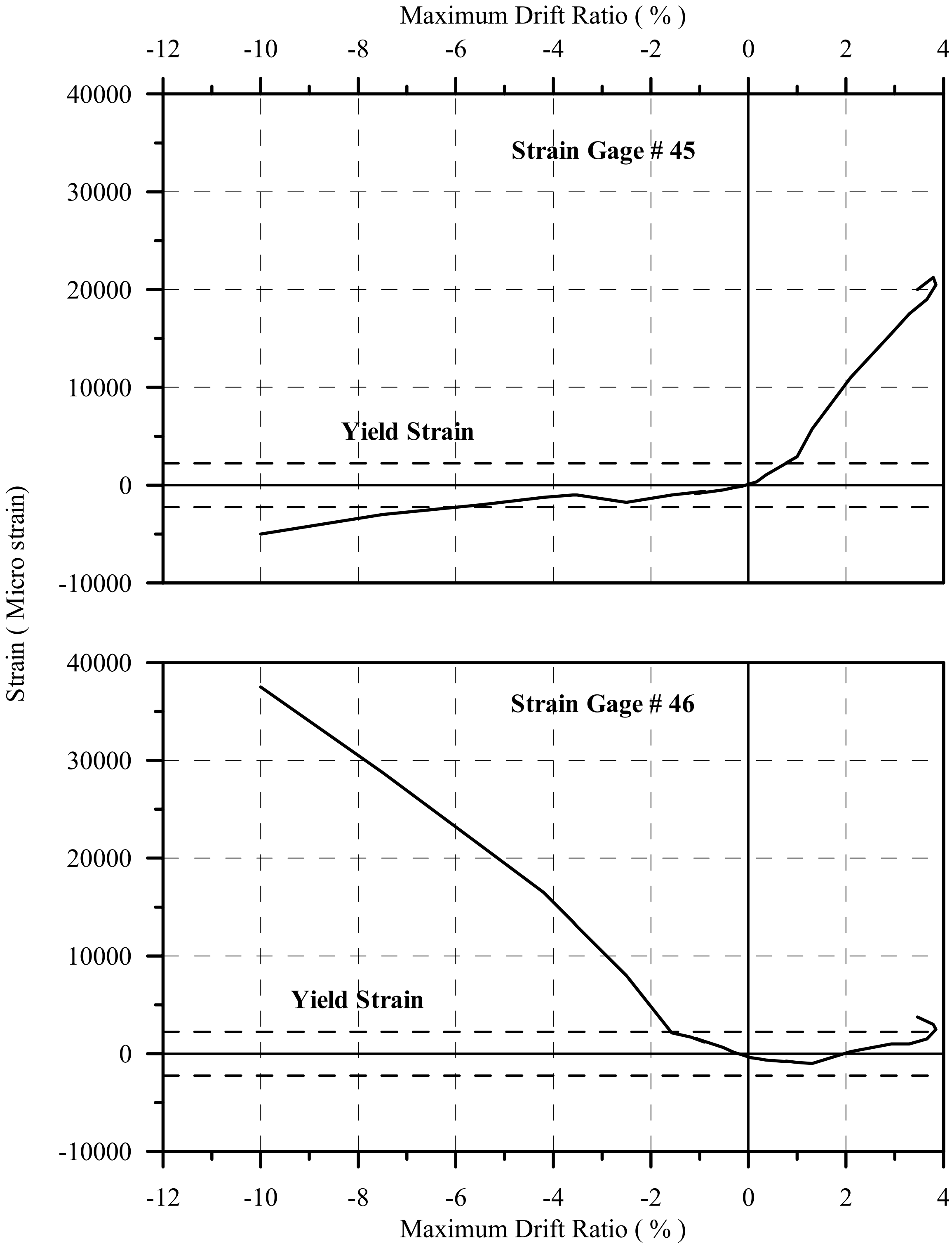

Fig. 4-88:Envelope of Strain-Displacement Hysteresis for Gages 45 and 46 in Tall Specimen B2CT

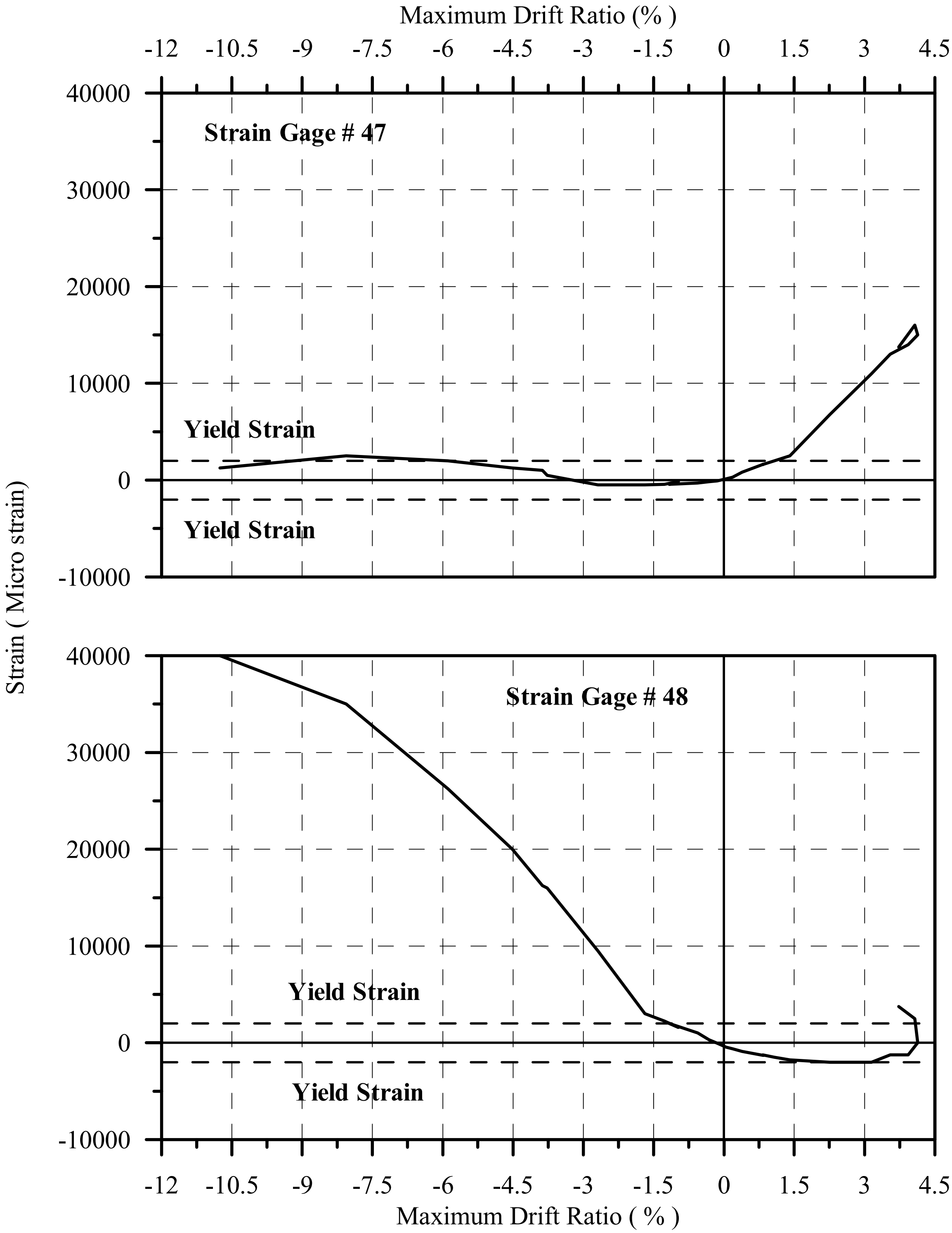

Fig. 4-89: Envelope of Strain-Displacement Hysteresis for Gages 47 and 48 in Tall Specimen B2CT

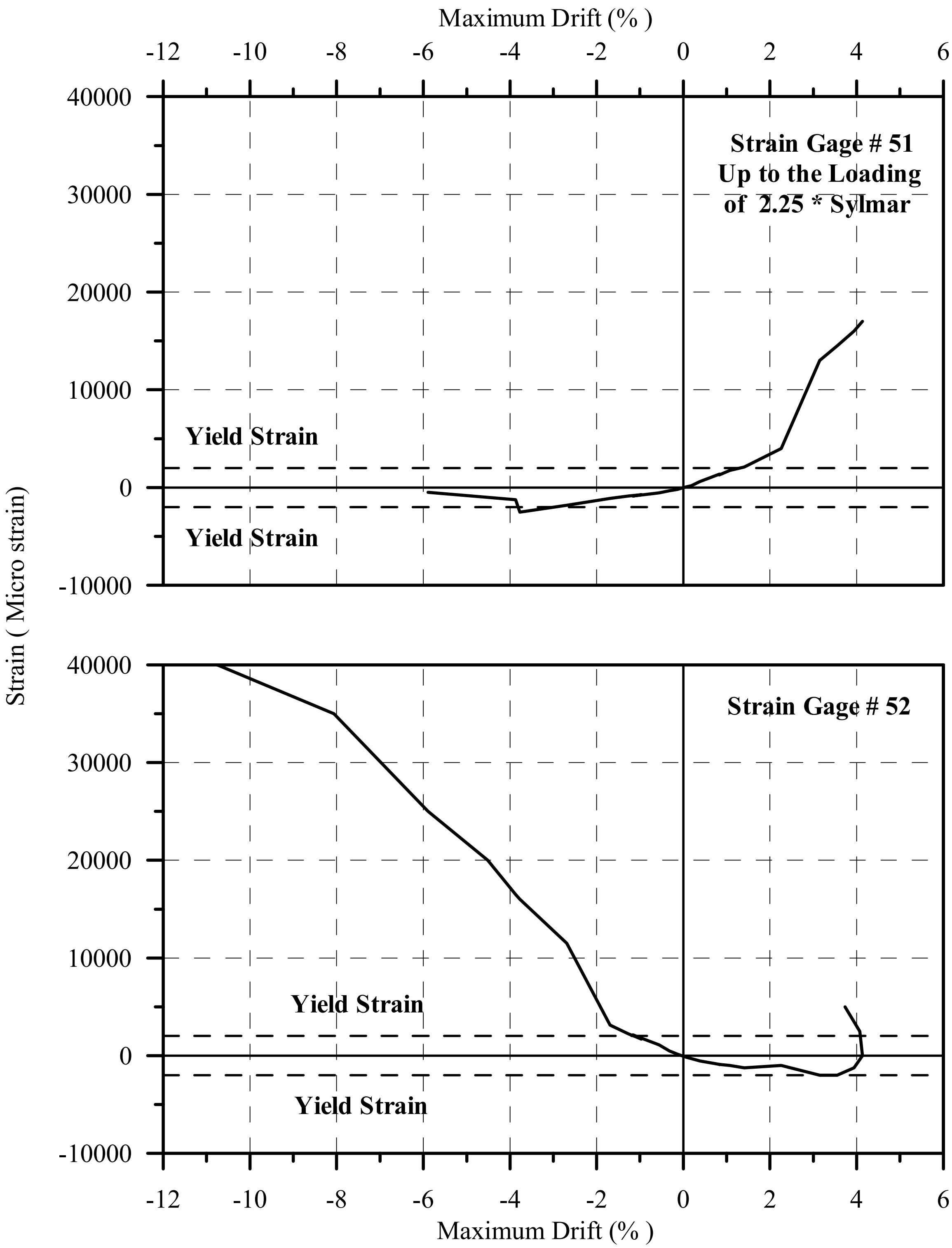

Fig. 4-90: Envelope of Strain-Displacement Hysteresis for Gages 51 and 52 in Tall Specimen B2CT

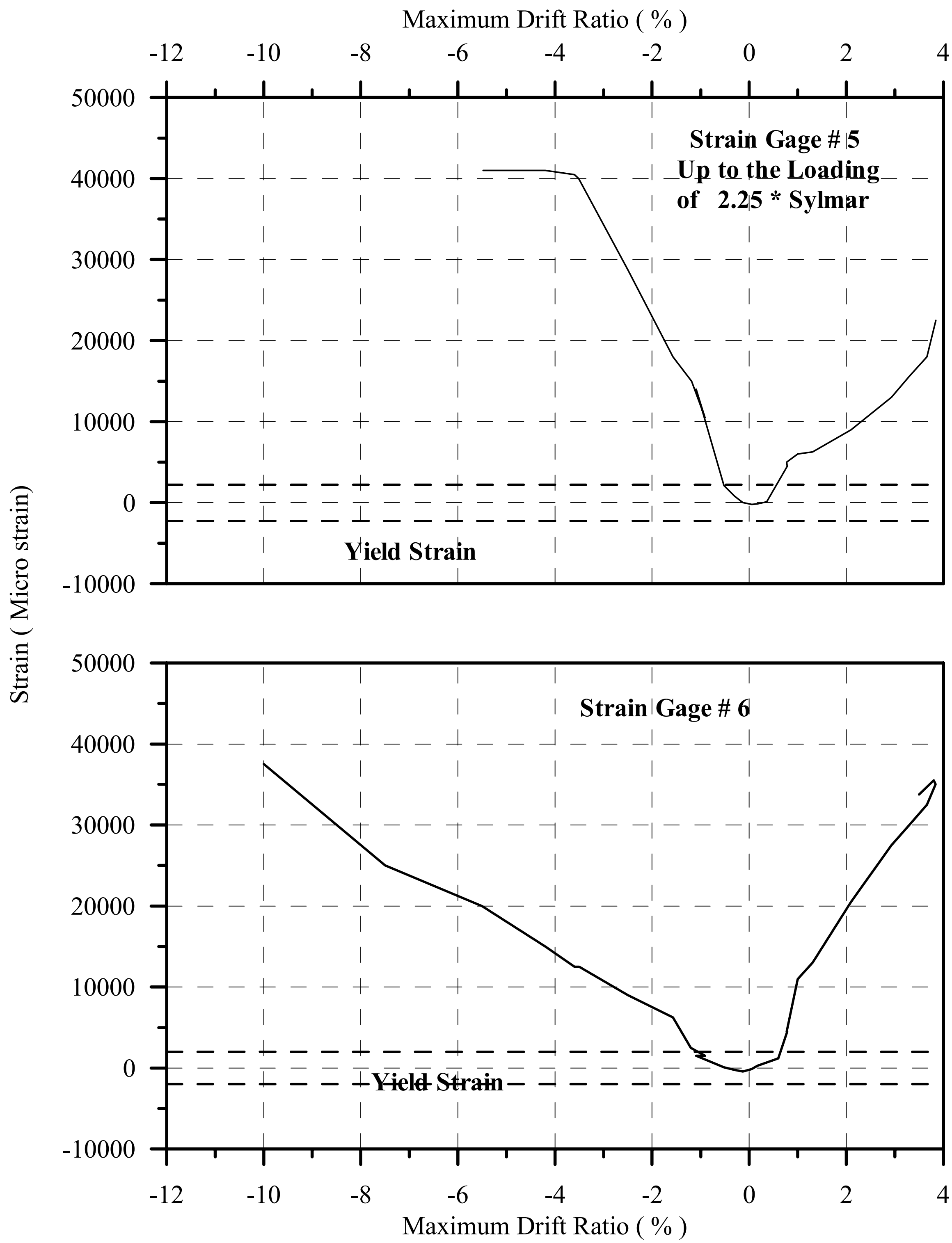

Fig. 4-91: Envelope of Strain-Displacement Hysteresis for Gages 5 and 6 in Tall Specimen B2CT

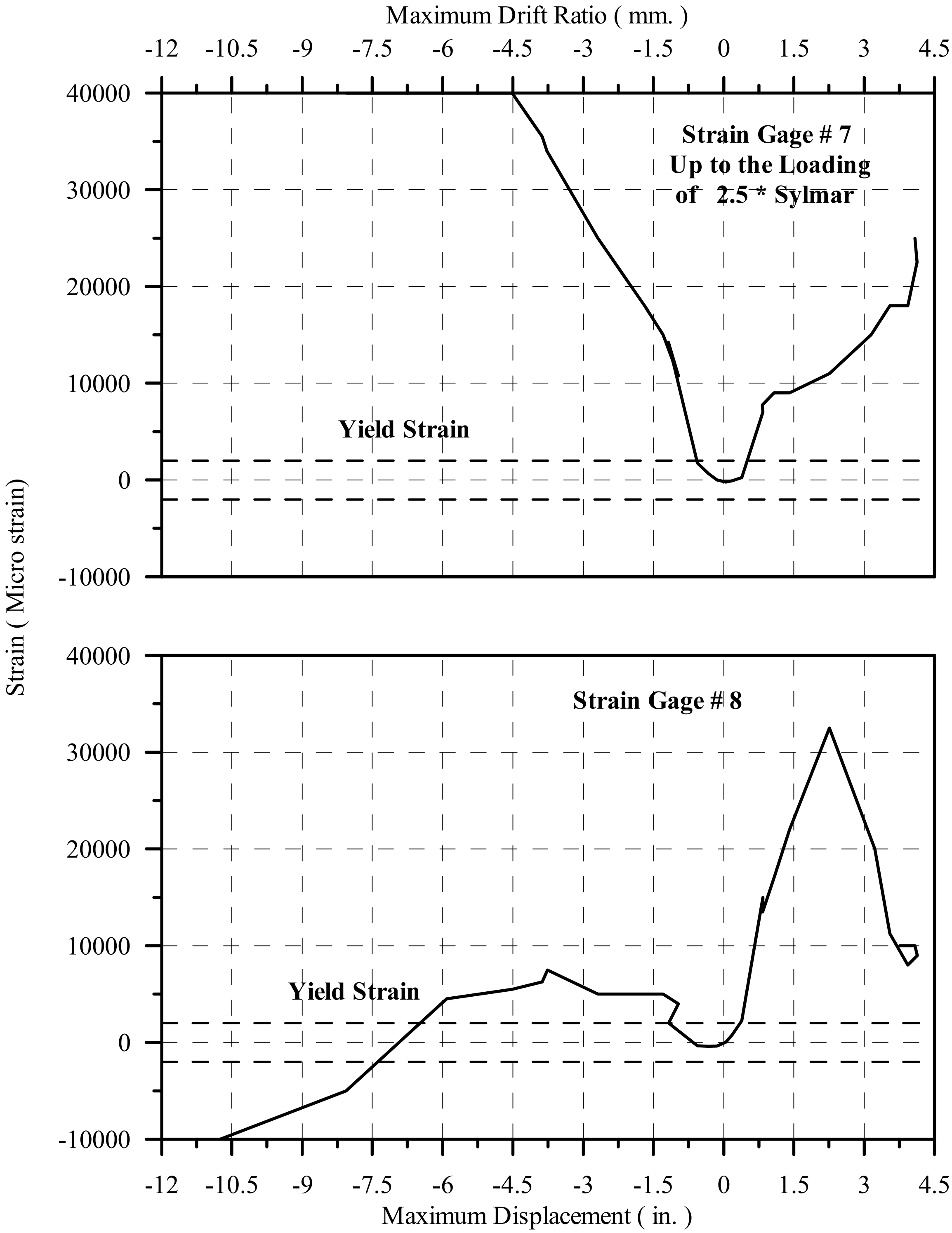

Fig. 4-92: Envelope of Strain- Displacement Hysteresis for Gages 7 and 8 in Tall Specimen B2CT

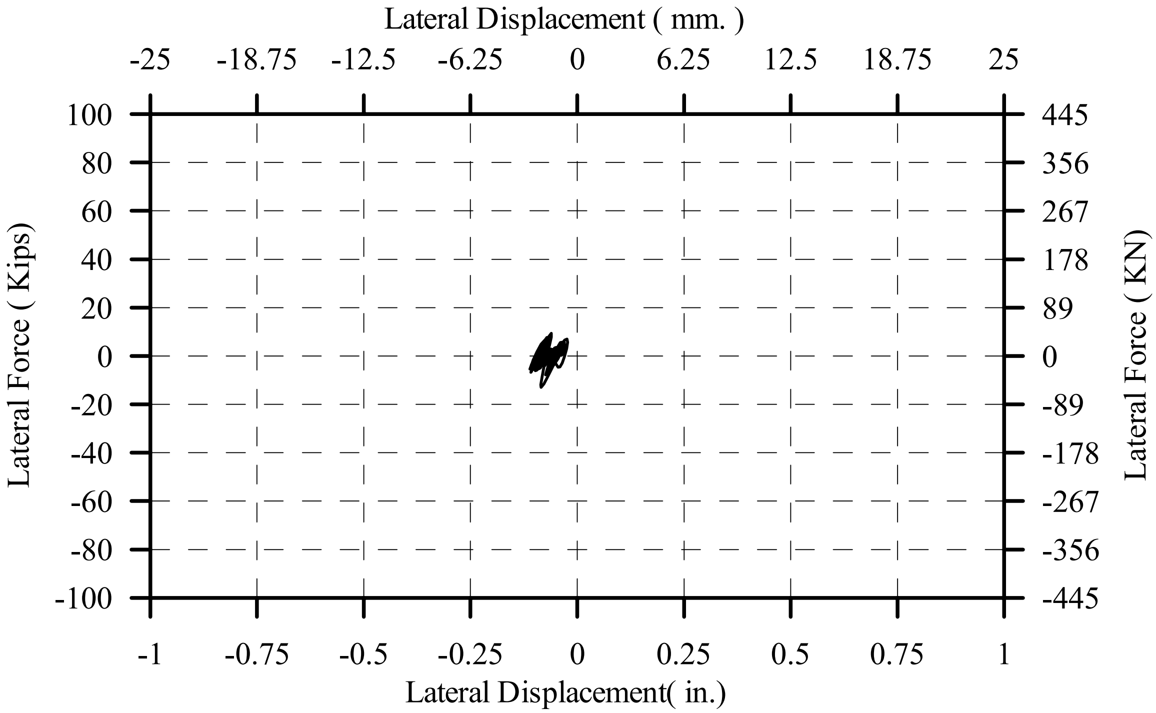

Fig. 4-93: Hysteresis Curve for B2CS at 0.2 x Sylmar

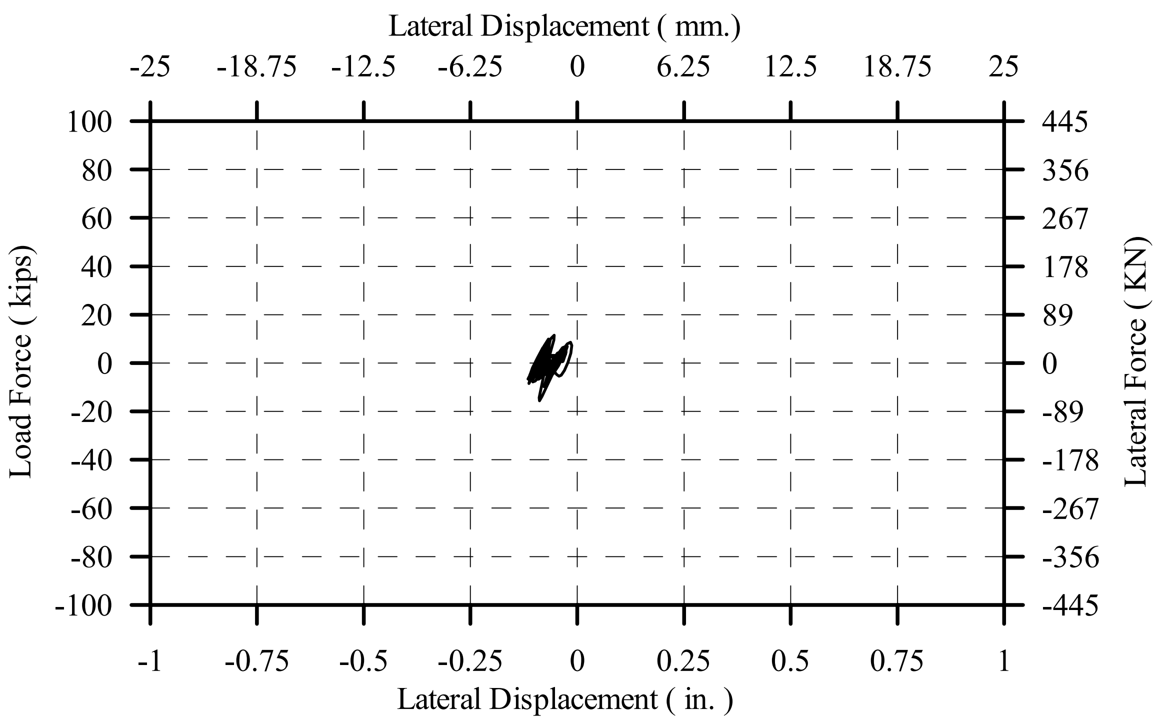

Fig. 4-94: Hysteresis Curve for B2CS at 0.25 x Sylmar

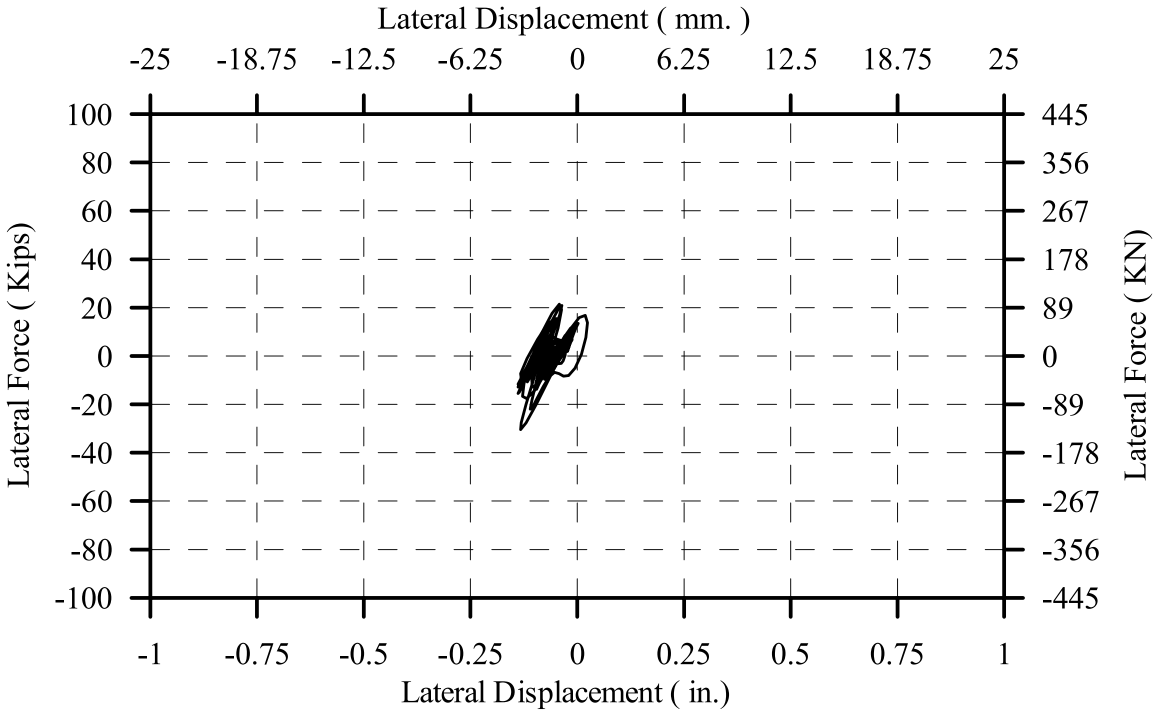

Fig. 4-95: Hysteresis Curve for B2CS at 0.5 x Sylmar

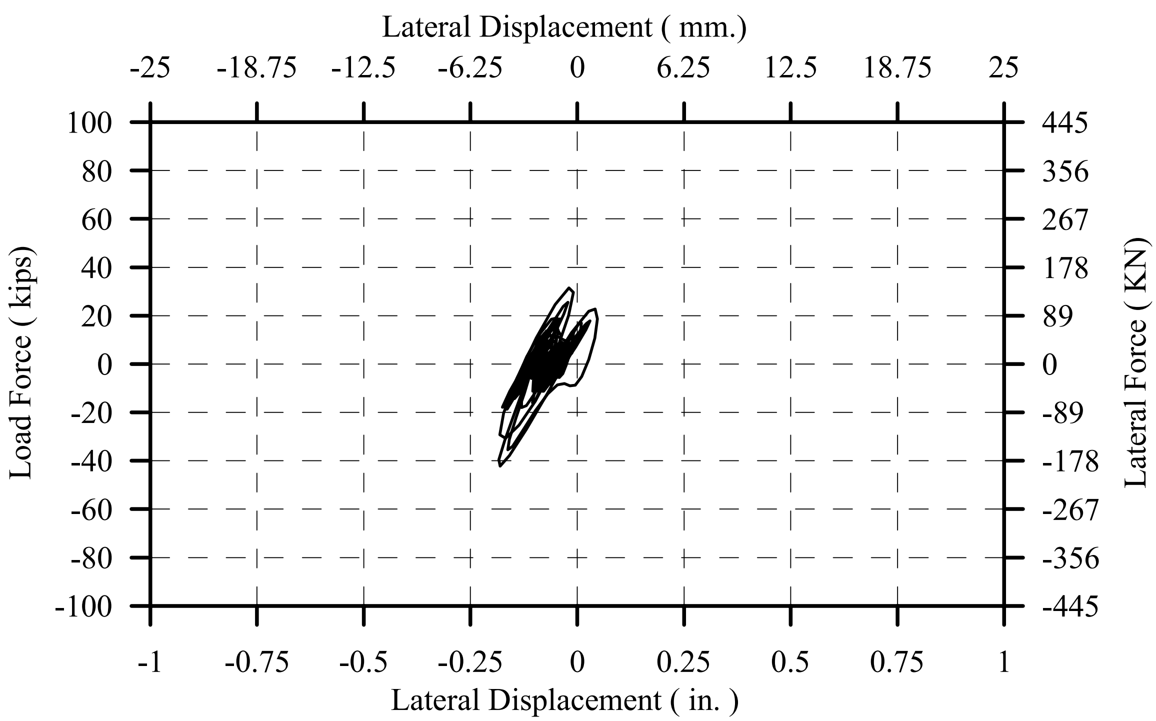

Fig. 4-96: Hysteresis Curve for B2CS at 0.75 x Sylmar

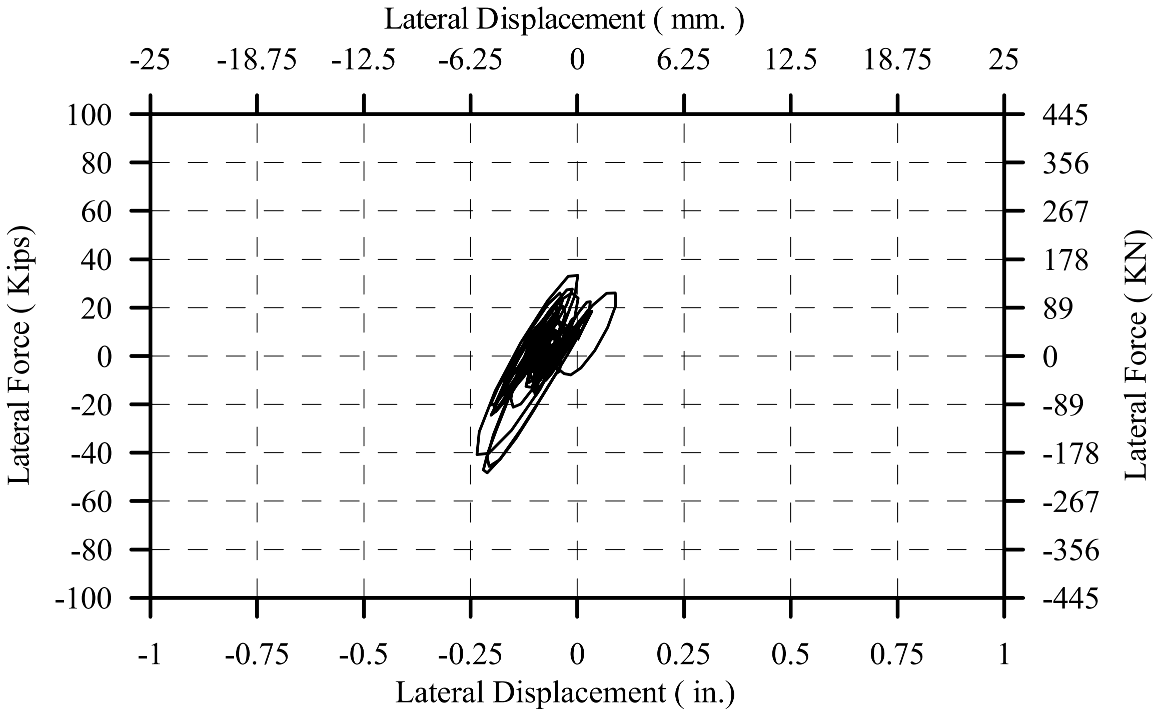

Fig. 4-97: Hysteresis Curve for B2CS at 1.00 x Sylmar

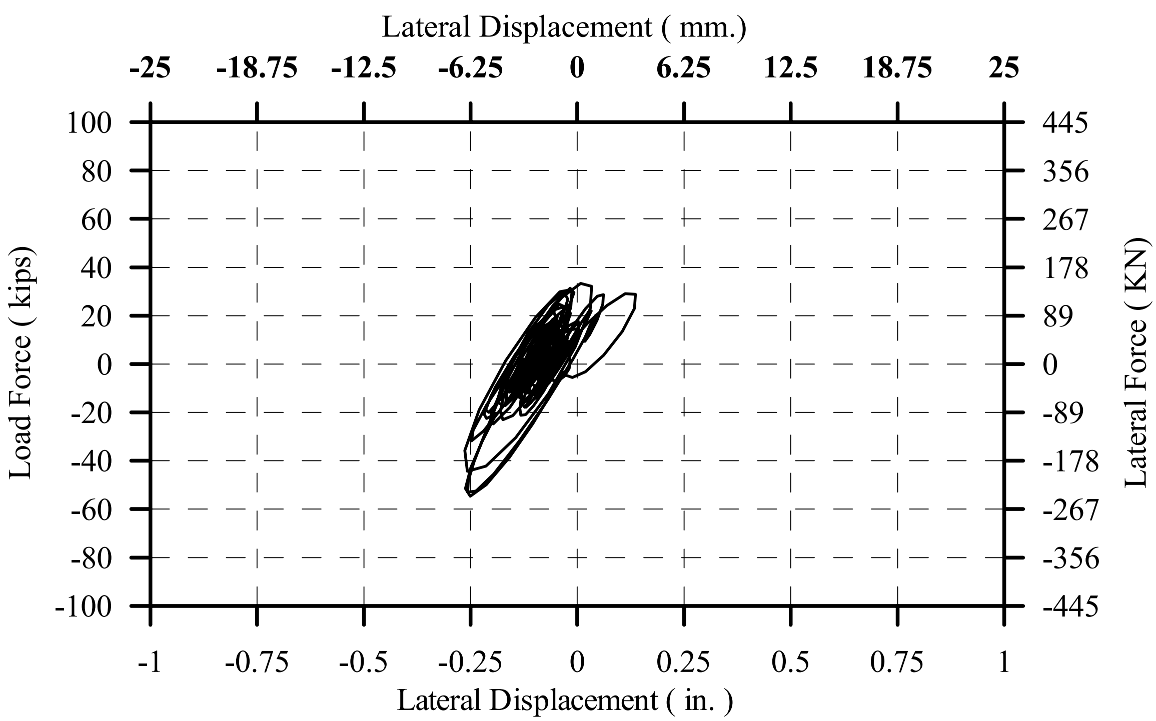

Fig. 4-98: Hysteresis Curve for B2CS at 1.25 x Sylmar

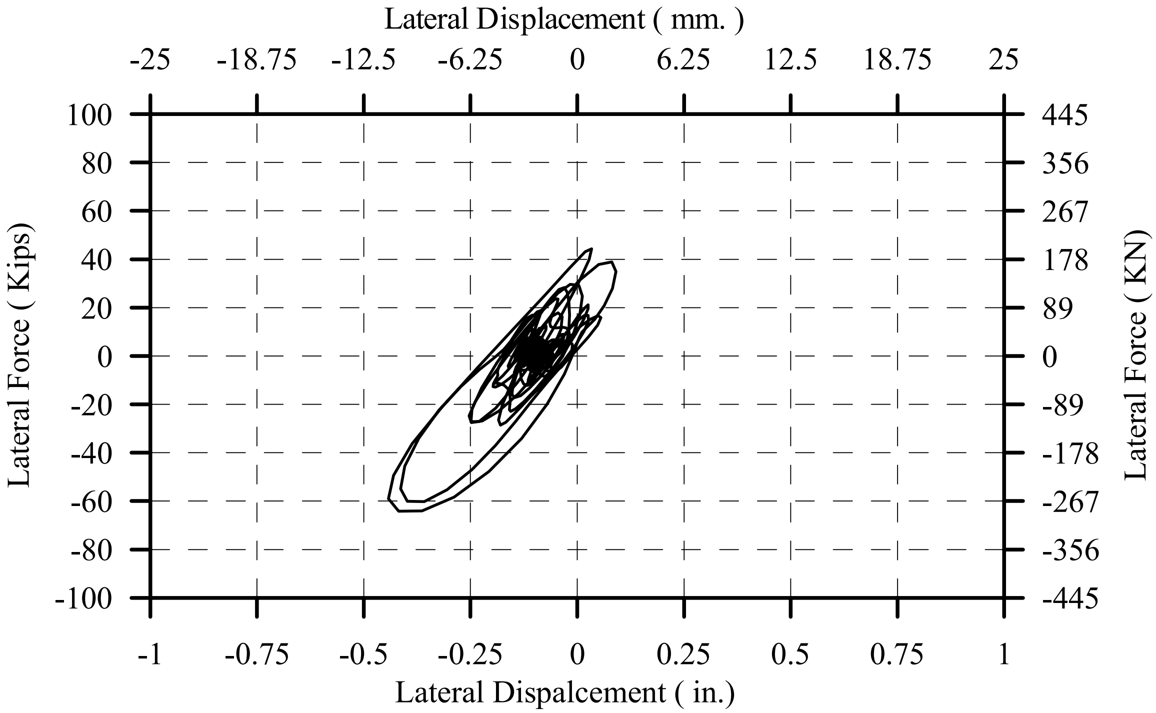

Fig. 4-99: Hysteresis Curve for B2CS at 1.40 x Sylmar

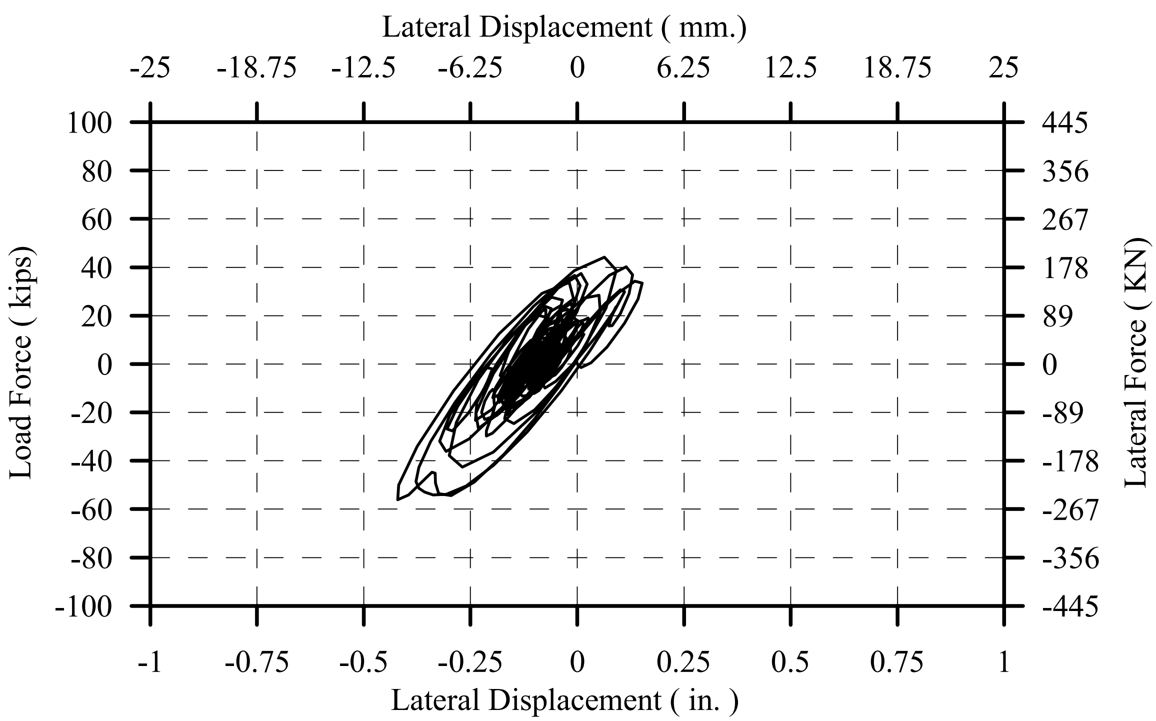

Fig. 4-100: Hysteresis Curve for B2CS at 1.75 x Sylmar

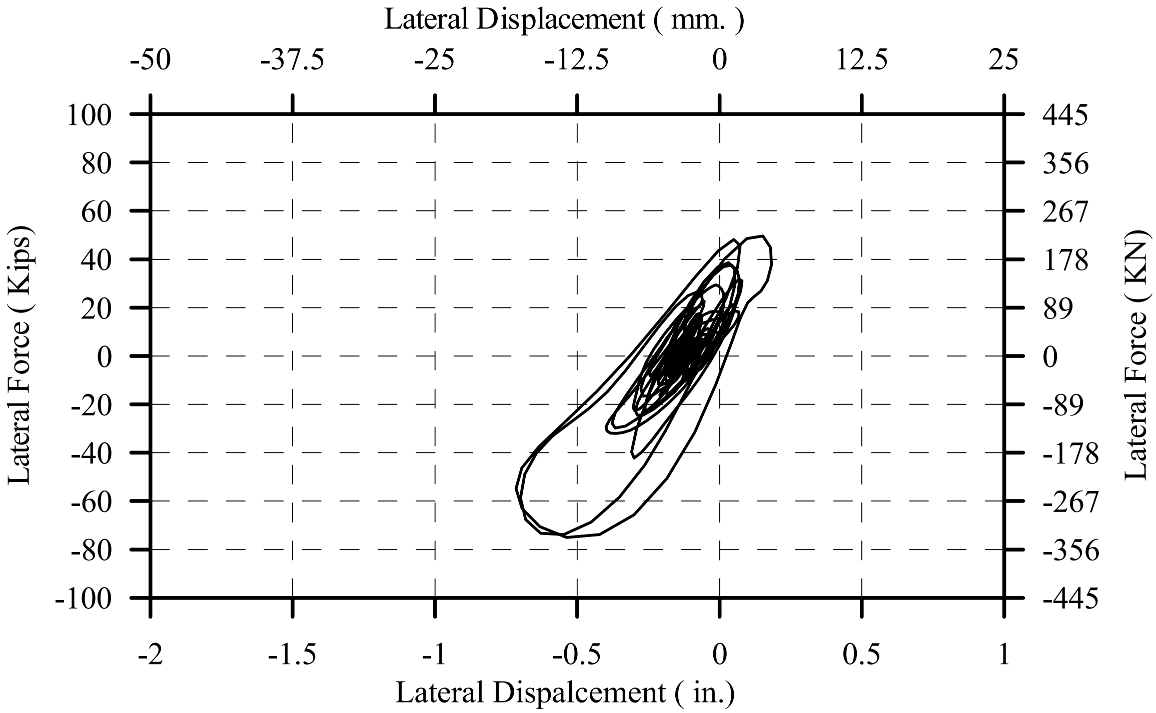

Fig. 4-101: Hysteresis Curve for B2CS at 2.0 x Sylmar

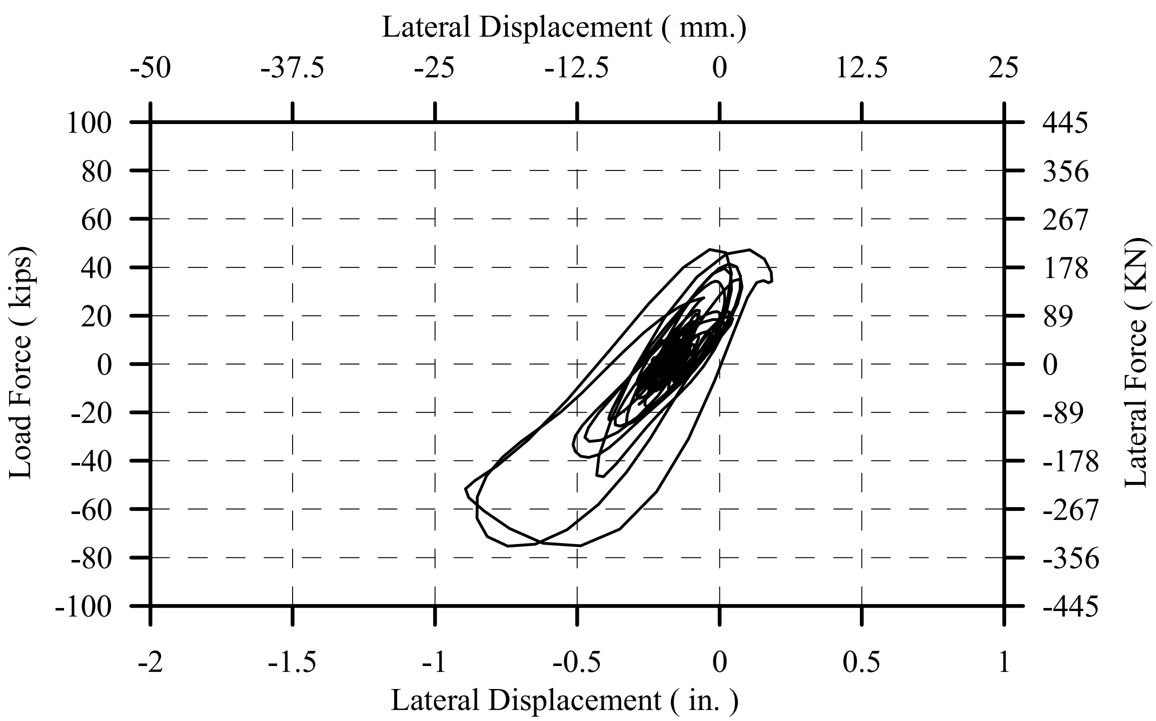

Fig. 4-102: Hysteresis Curve for B2CS at 2.125 x Sylmar

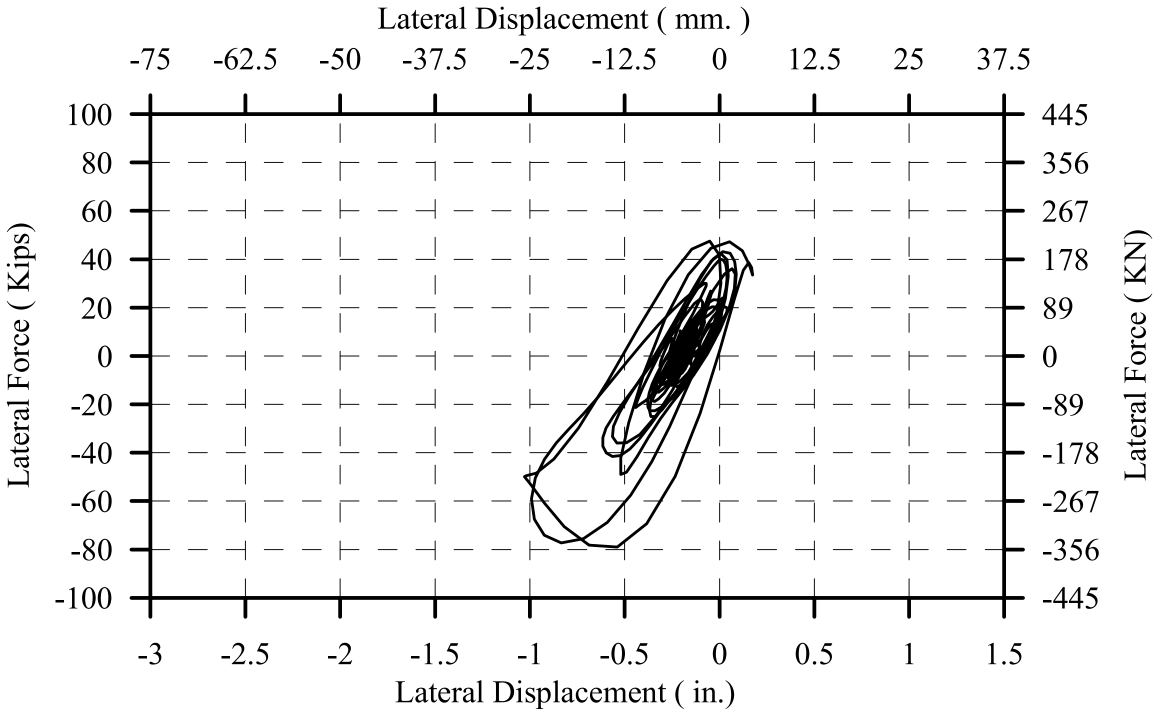

Fig. 4-103: Hysteresis Curve for B2CS at 2.25 x Sylmar

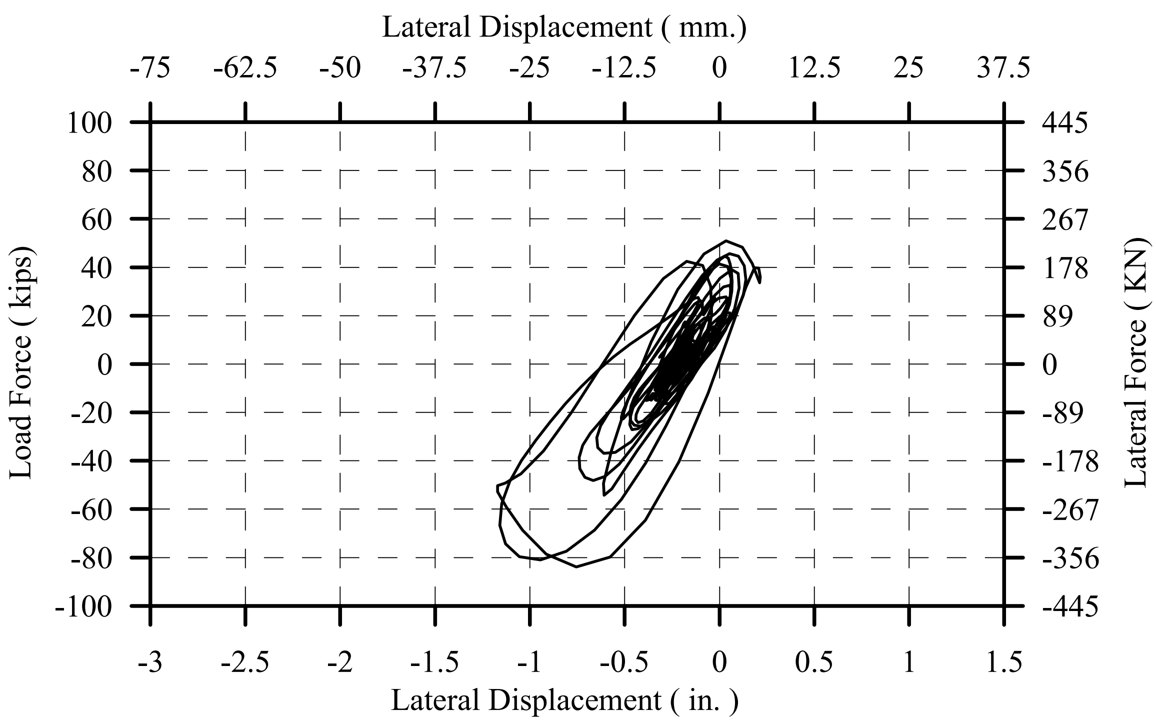

Fig. 4-104: Hysteresis Curve for B2CS at 2.375 x Sylmar

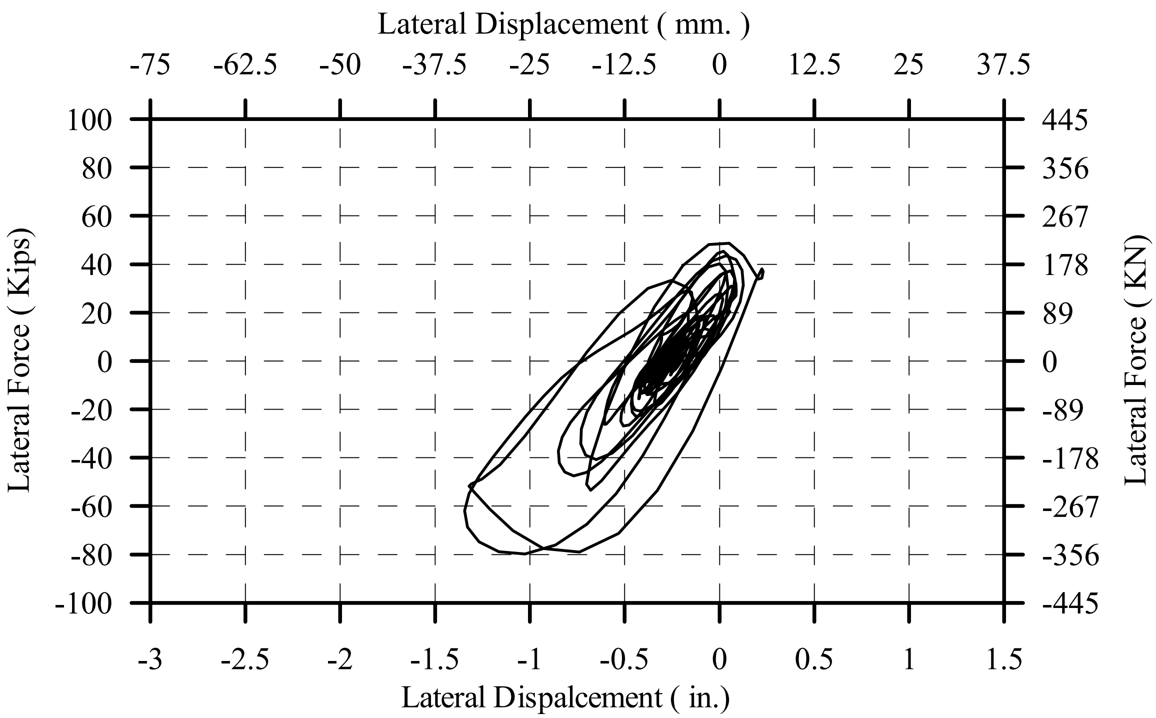

Fig. 4-105: Hysteresis Curve for B2CS at 2.5 x Sylmar

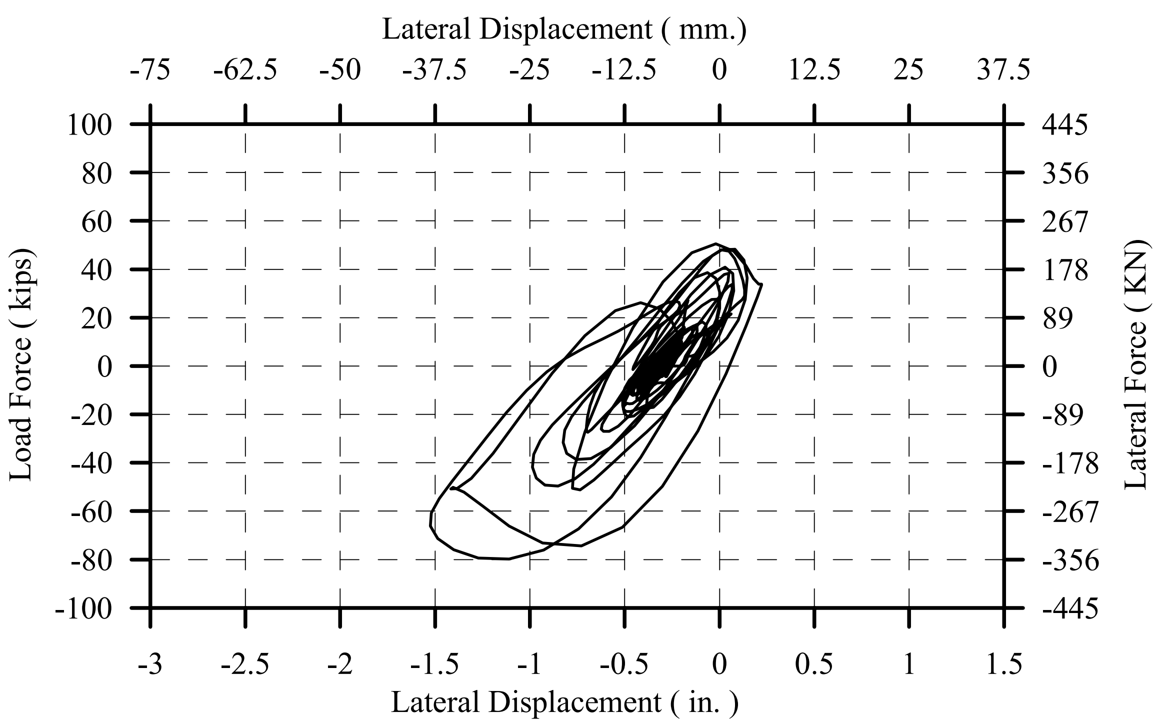

Fig. 4-106: Hysteresis Curve for B2CS at 2.625 x Sylmar

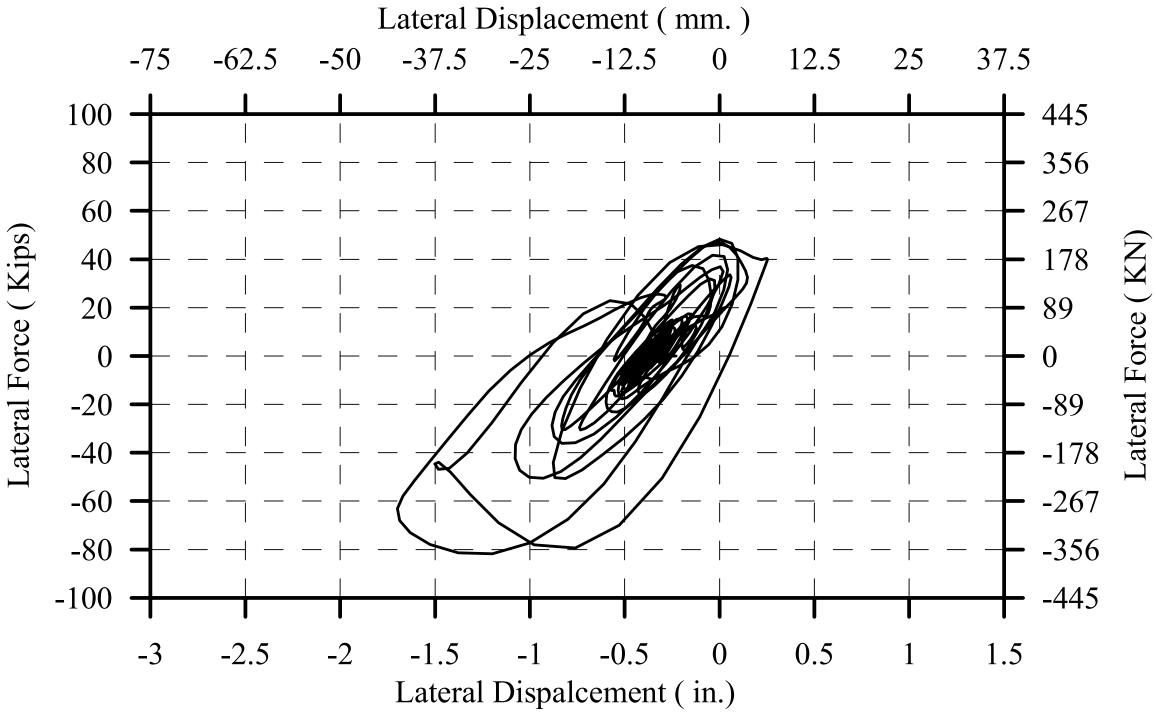

Fig. 4-107: Hysteresis Curve for B2CS at 2.75 x Sylmar

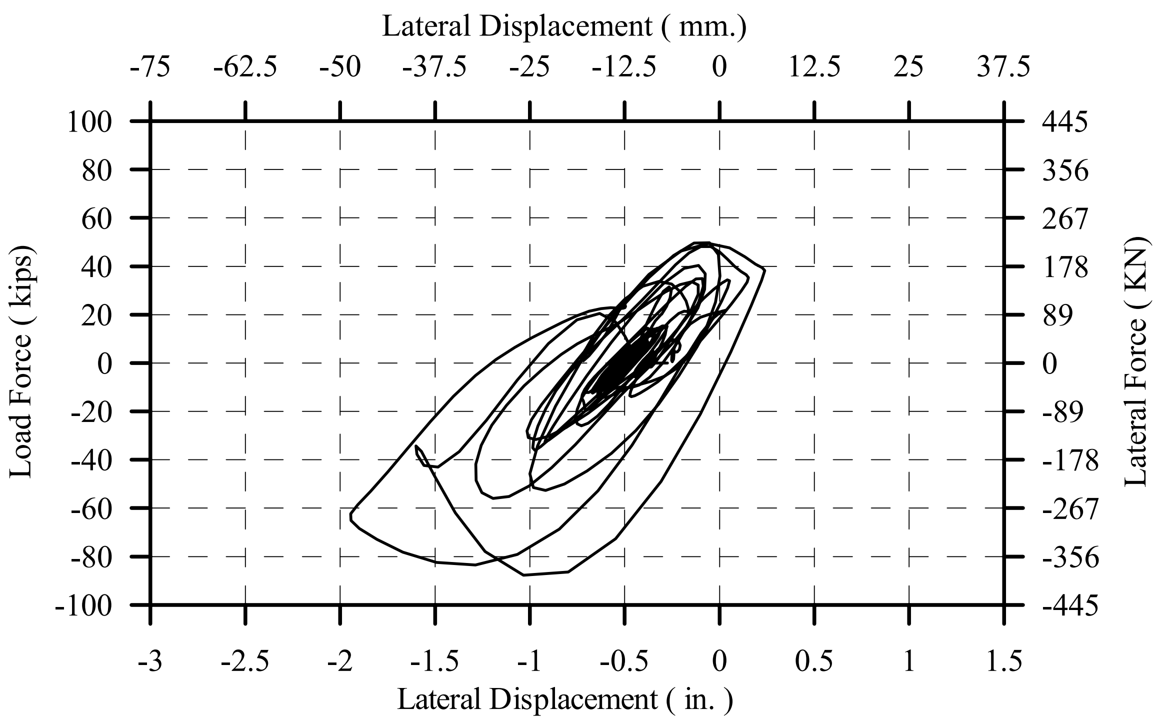

Fig. 4-108: Hysteresis Curve for B2CS at 3.0 x Sylmar

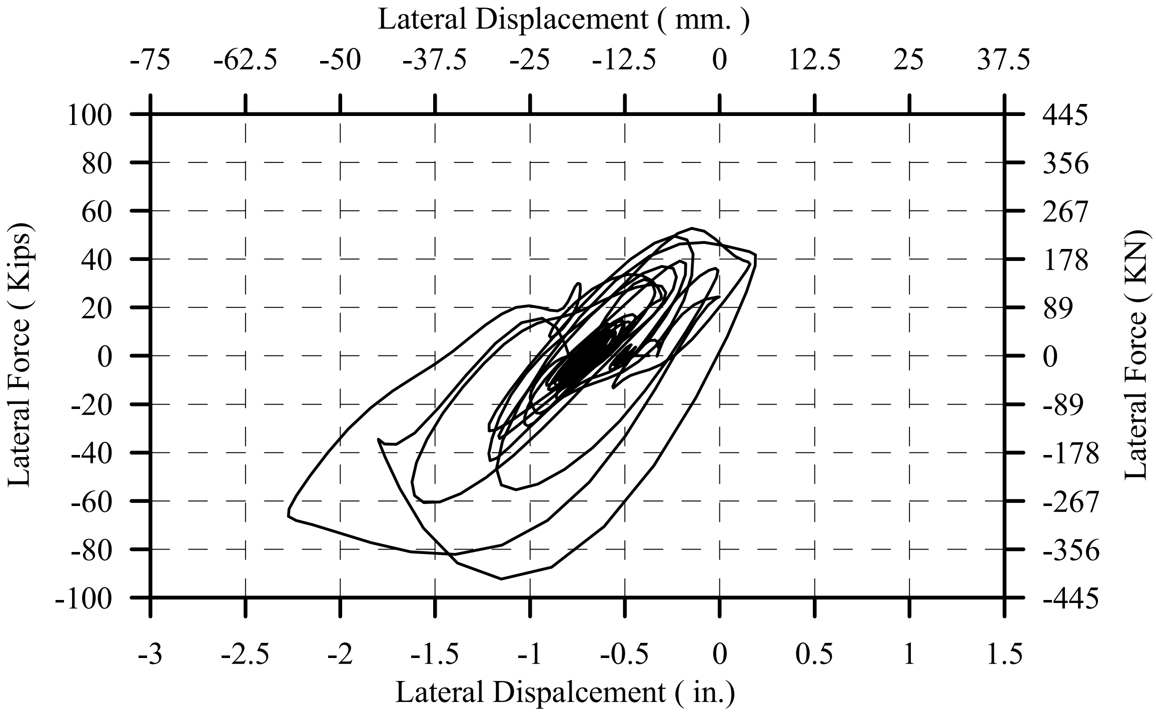

Fig. 4-109: Hysteresis Curve for B2CS at 3.25 x Sylmar

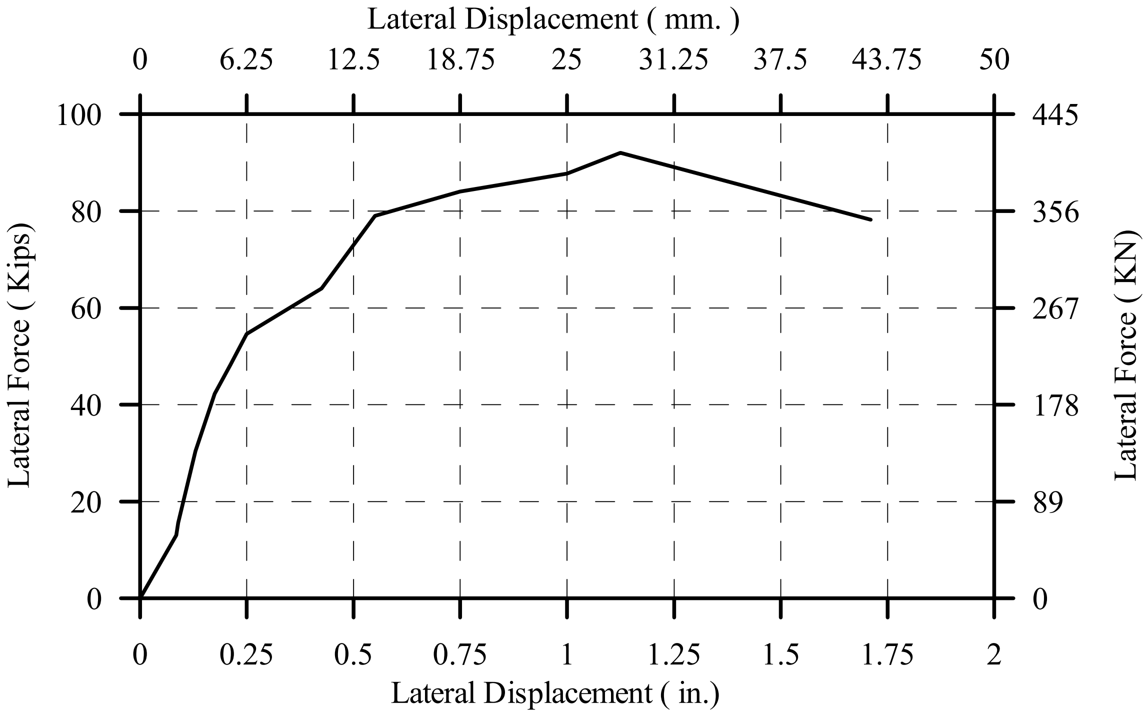

Fig. 4-110: Envelope of Load-Displacement Hystereses for B2CS

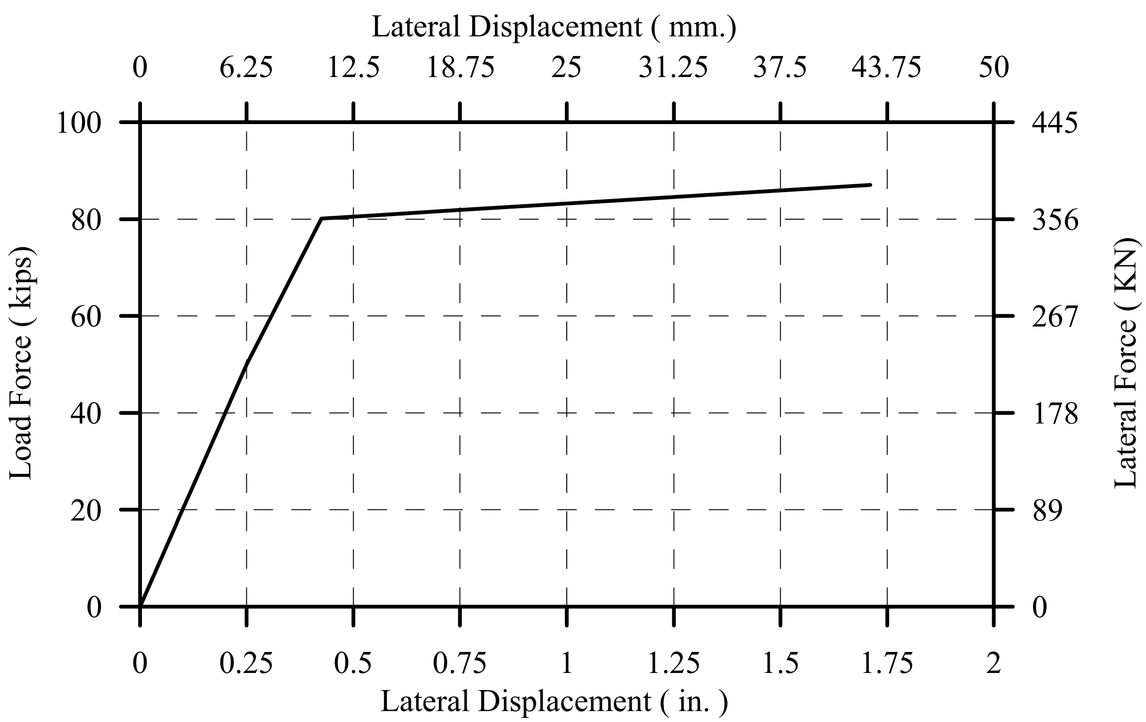

Fig. 4-111: Bilinear Representation of Previous Envelope for B2CS

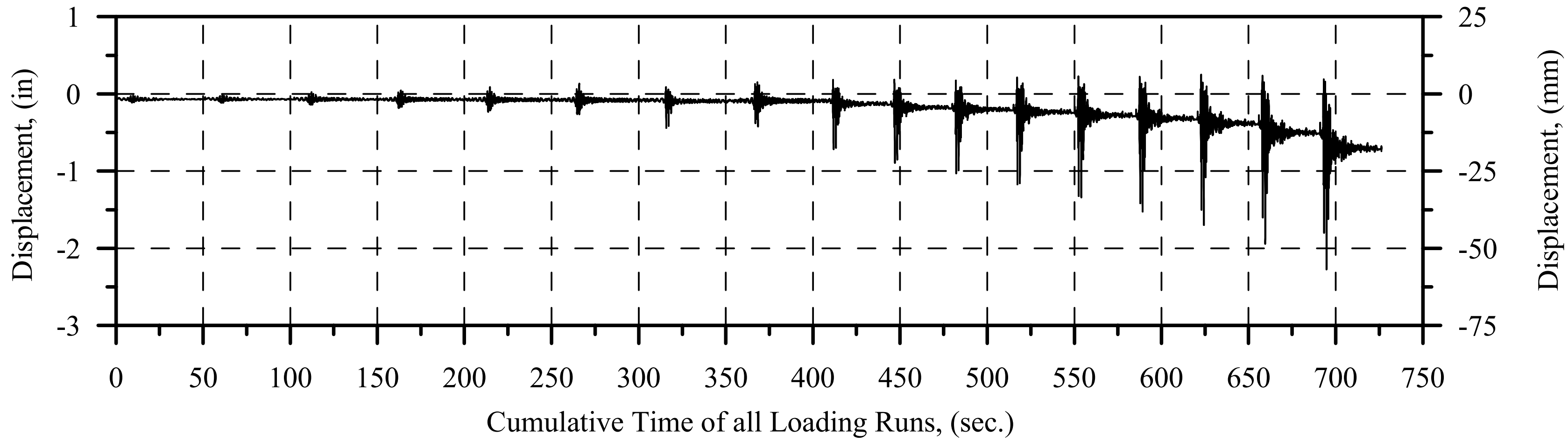

Fig. 4-112: Measured Relative Displacement History in Main Direction for Specimen B2CS

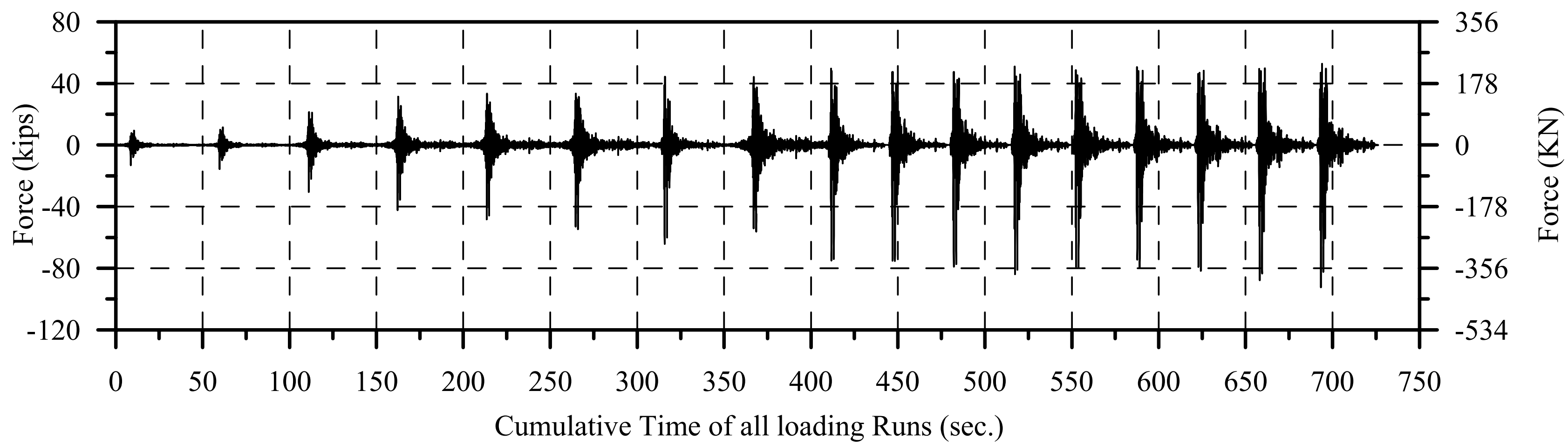

Fig. 4-113: Measured Resisting Force History in Main Direction for Specimen B2CS

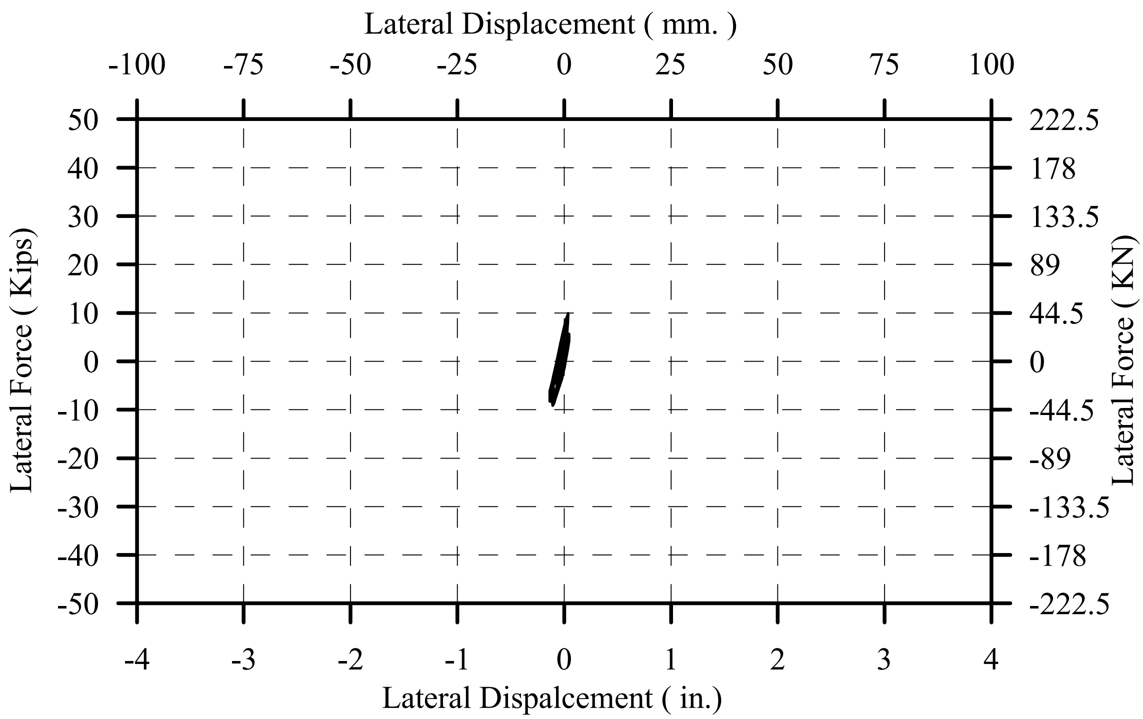

Fig. 4-114: Hysteresis Curve for B2CM at 0.1 x Sylmar

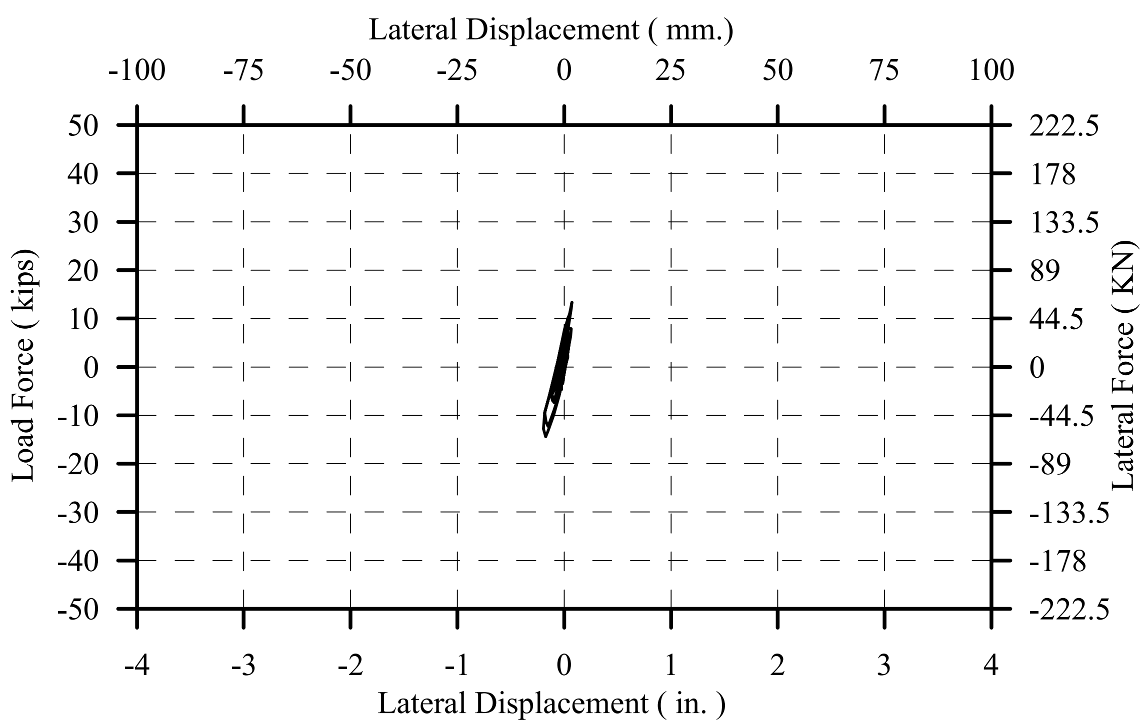

Fig. 4-115: Hysteresis Curve for B2CM at 0.20 x Sylmar

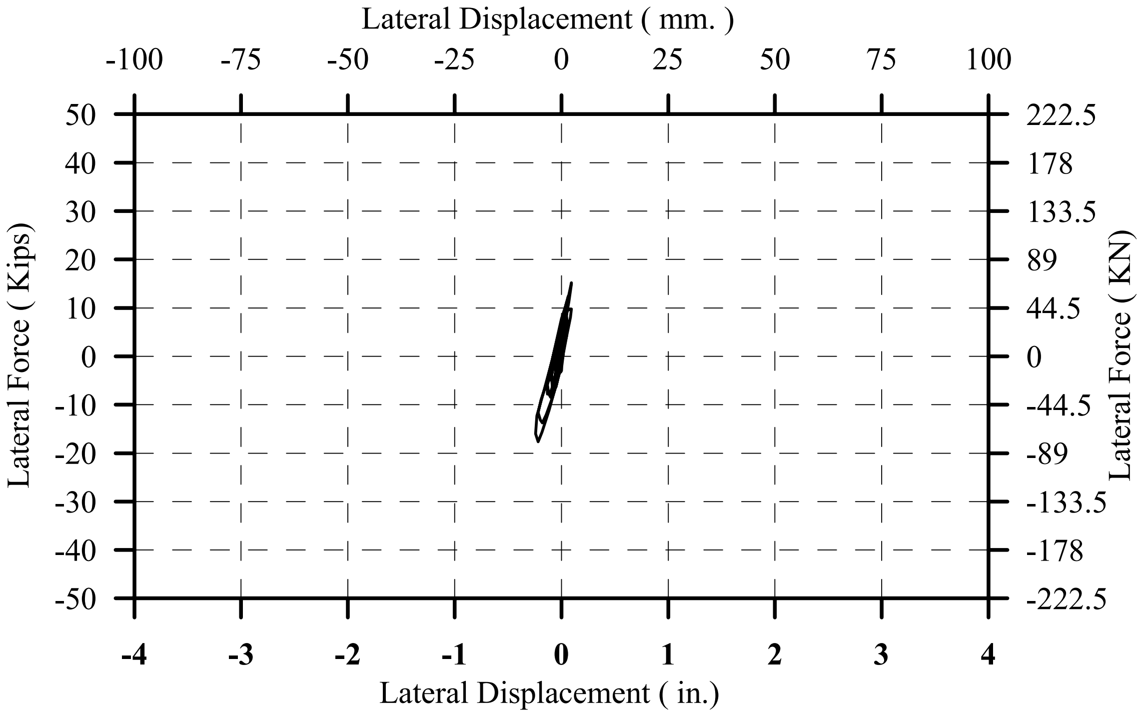

Fig. 4-116: Hysteresis Curve for B2CM at 0.25 x Sylmar

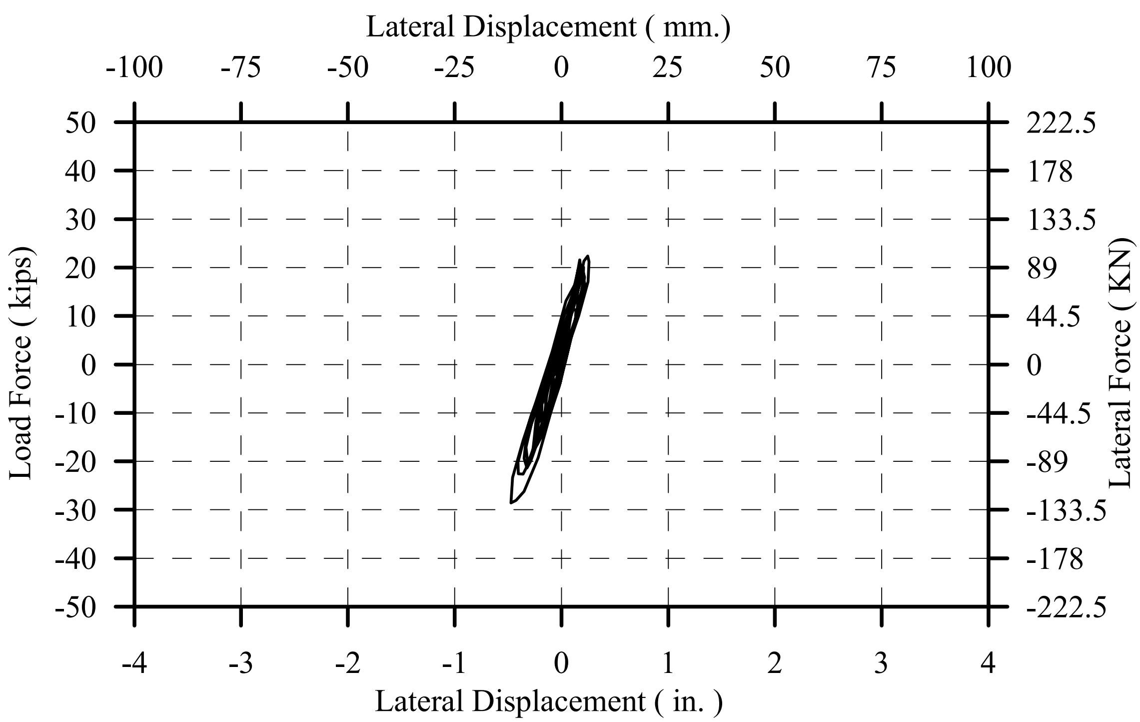

Fig. 4-117: Hysteresis Curve for B2CM at 0.50 x Sylmar

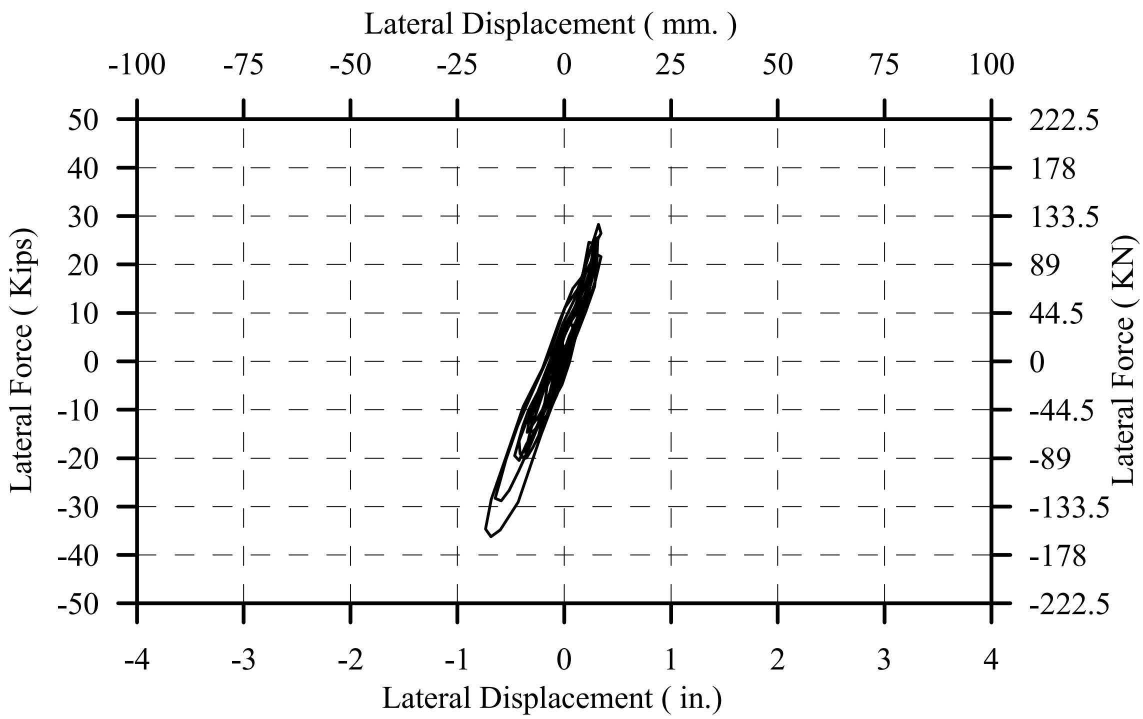

Fig. 4-118: Hysteresis Curve for B2CM at 0.75 x Sylmar

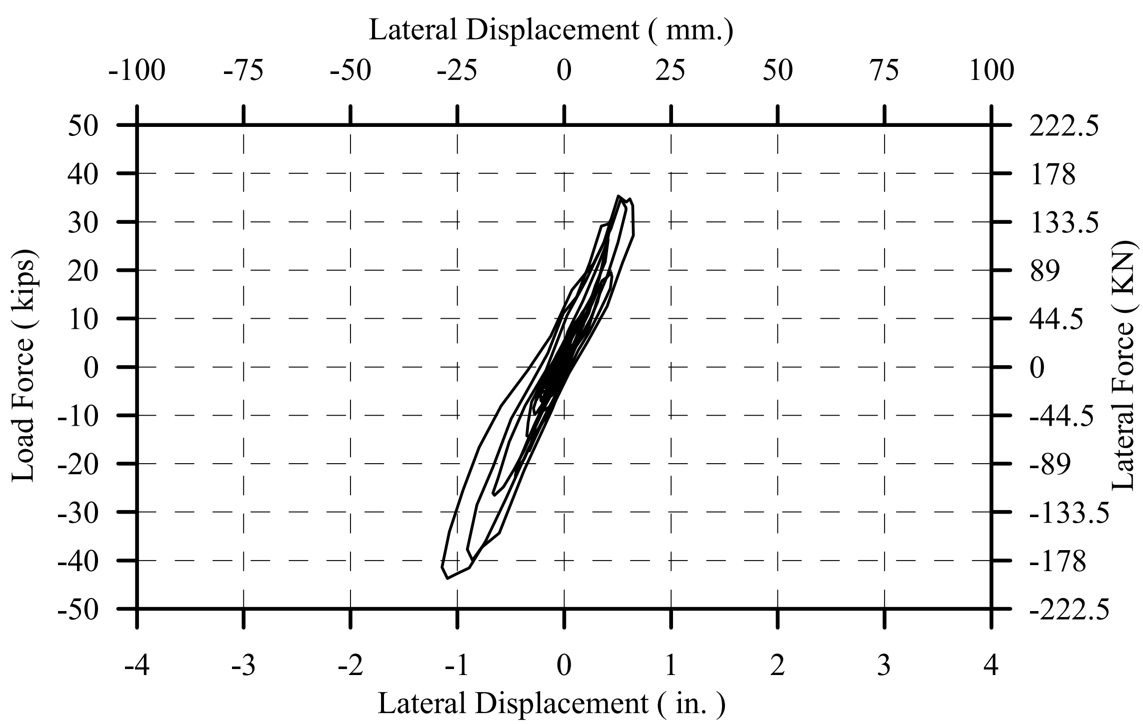

Fig. 4-119: Hysteresis Curve for B2CM at 1.00 x Sylmar

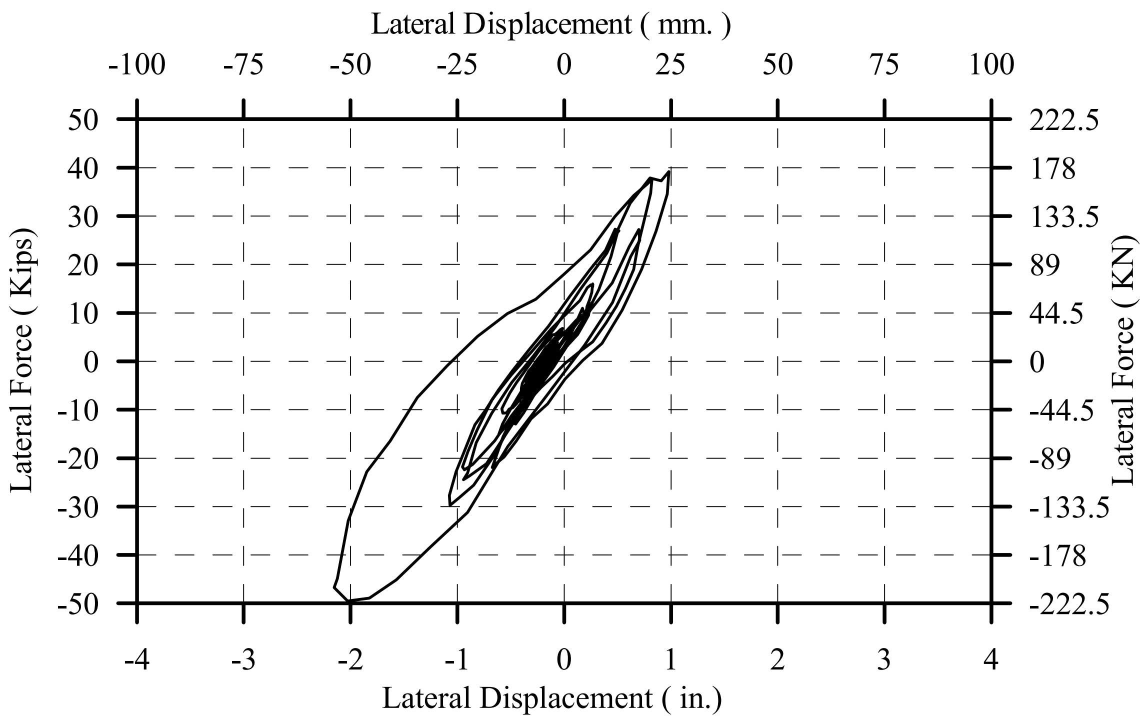

Fig. 4-120: Hysteresis Curve for B2CM at 1.25 x Sylmar

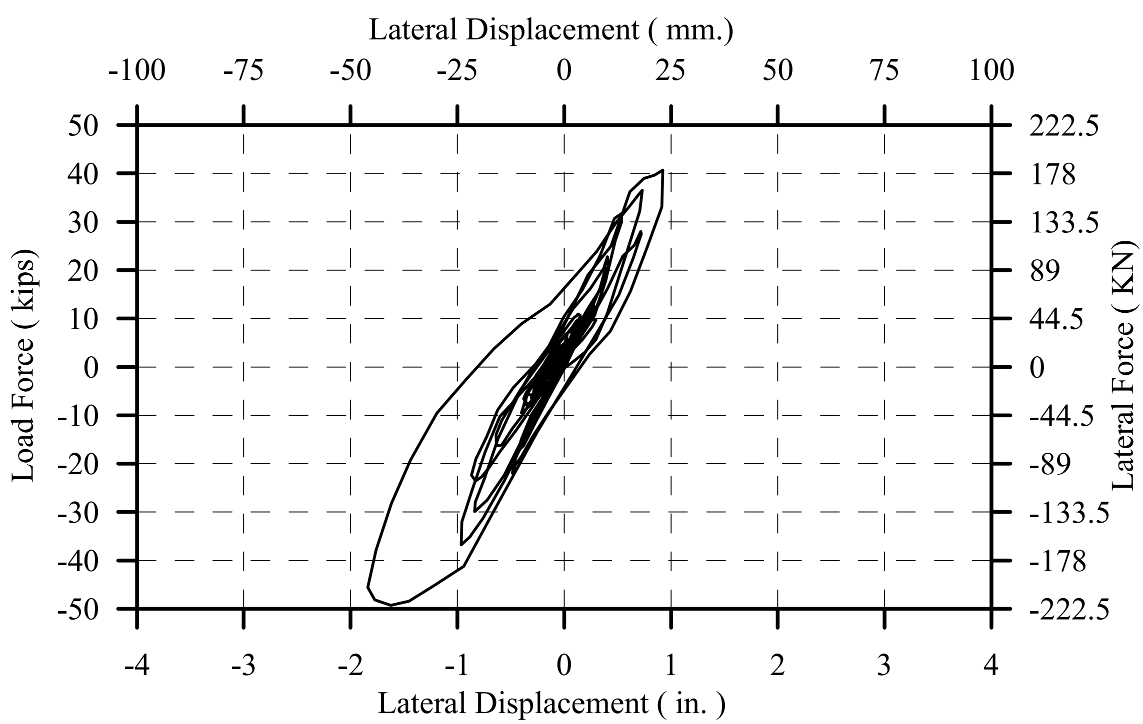

Fig. 4-121: Hysteresis Curve for B2CM at 1.40 x Sylmar

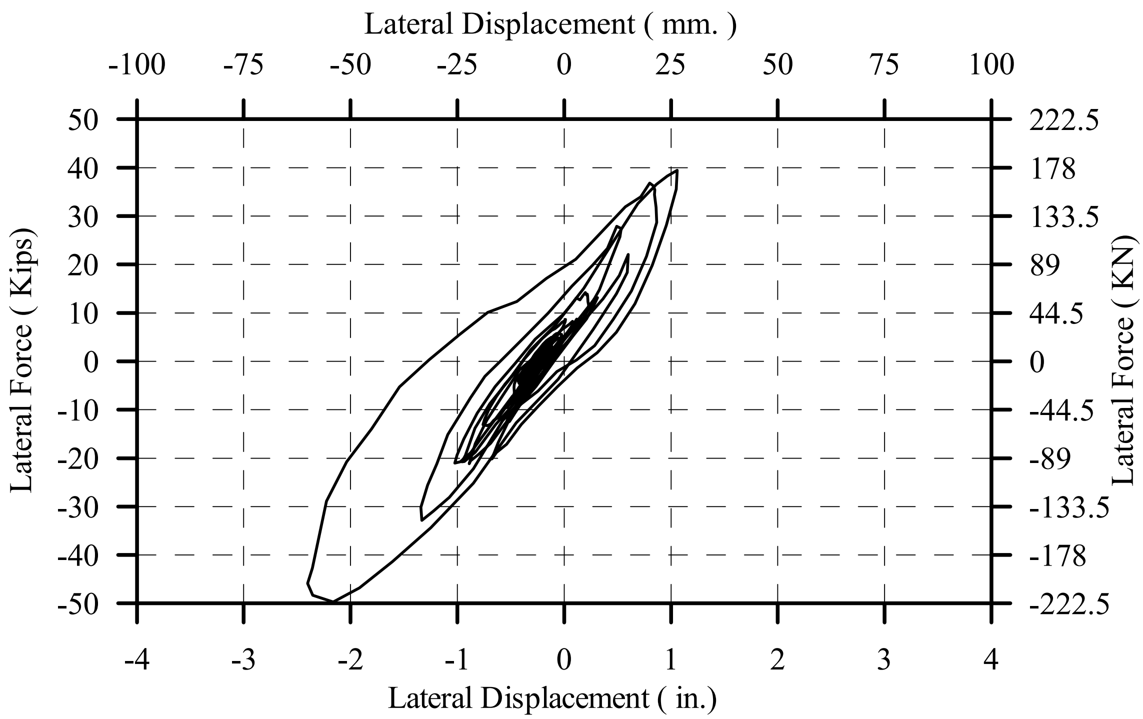

Fig. 4-122: Hysteresis Curve for B2CM at 1.50 x Sylmar

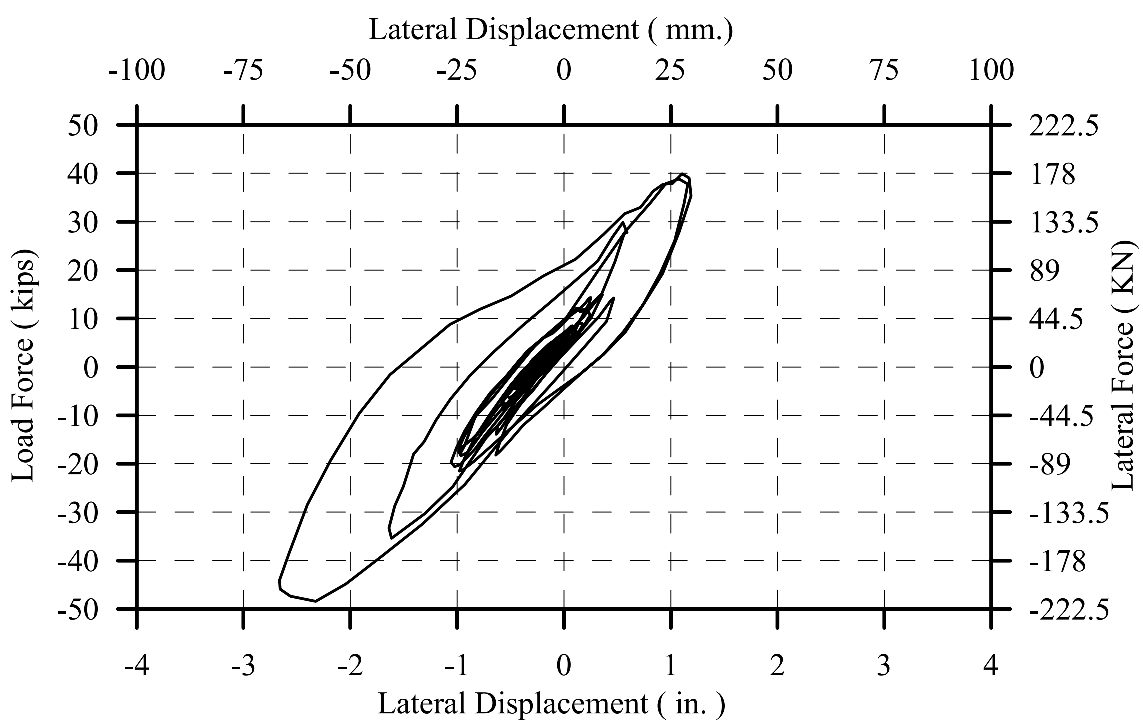

Fig. 4-123: Hysteresis Curve for B2CM at 1.75 x Sylmar

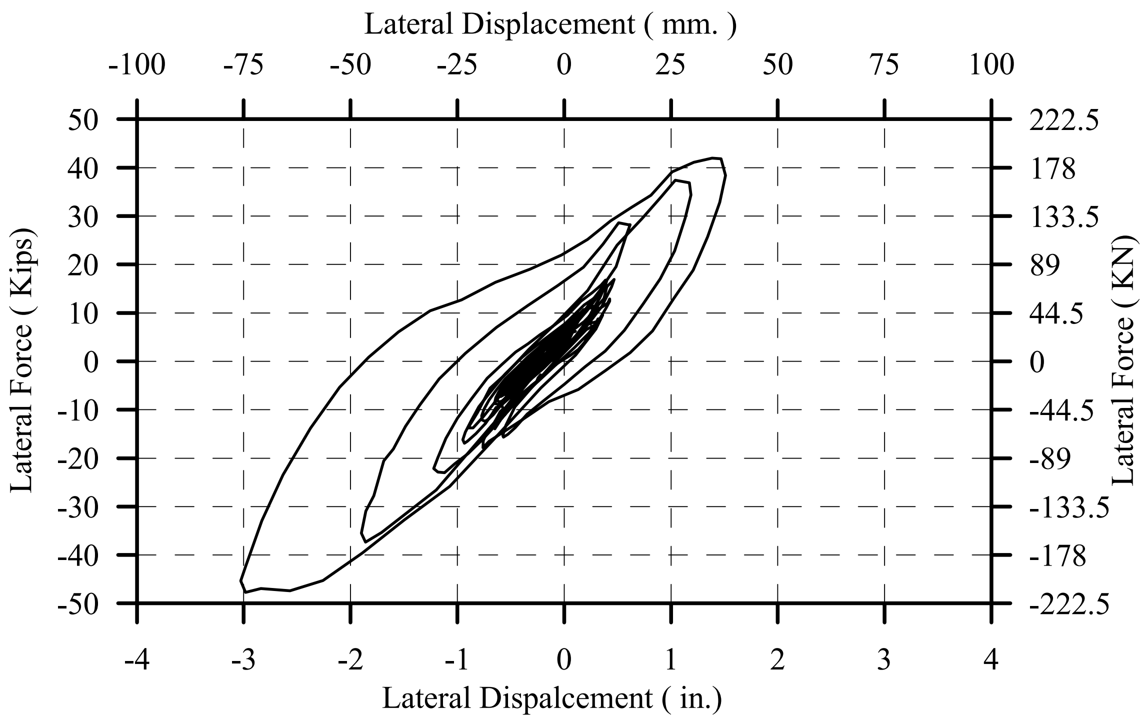

Fig. 4-124: Hysteresis Curve for B2CM at 2.00 x Sylmar

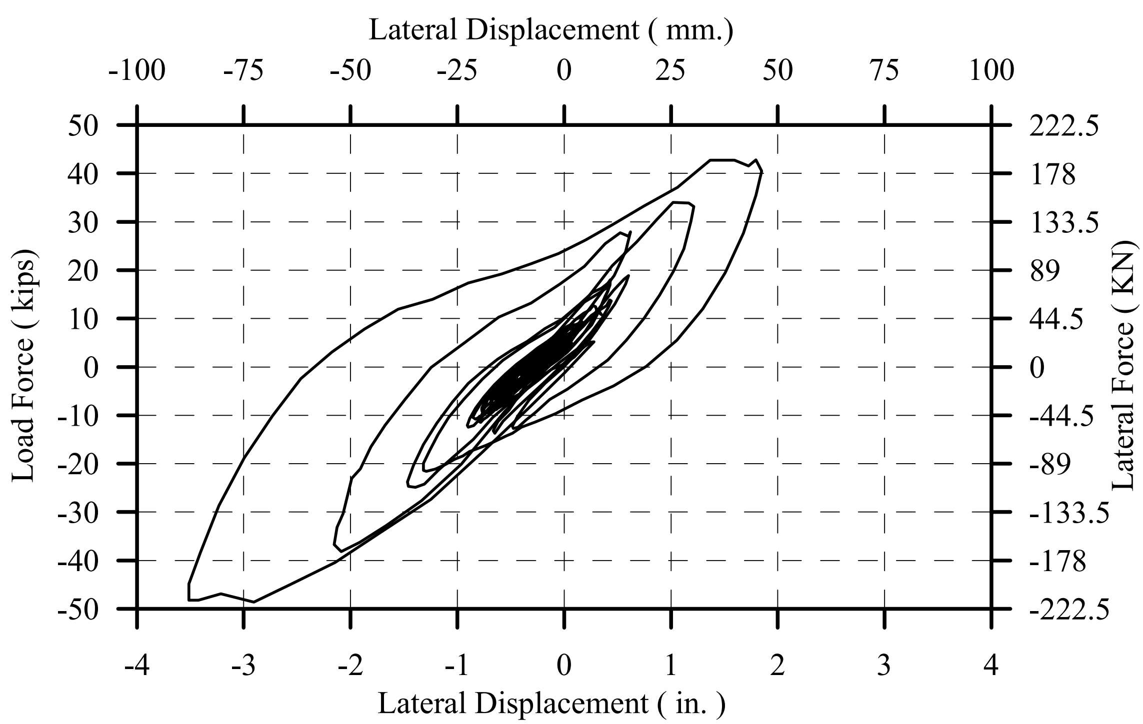

Fig. 4-125: Hysteresis Curve for B2CM at 2.25 x Sylmar

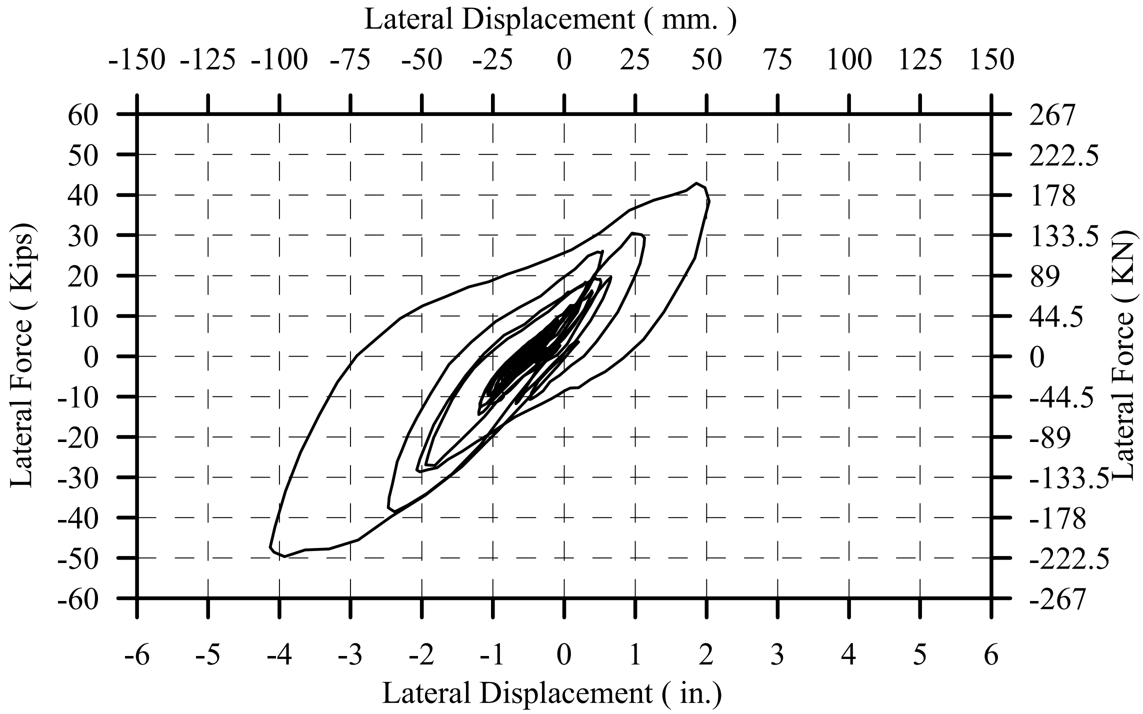

Fig. 4-126: Hysteresis Curve for B2CM at 2.50 x Sylmar

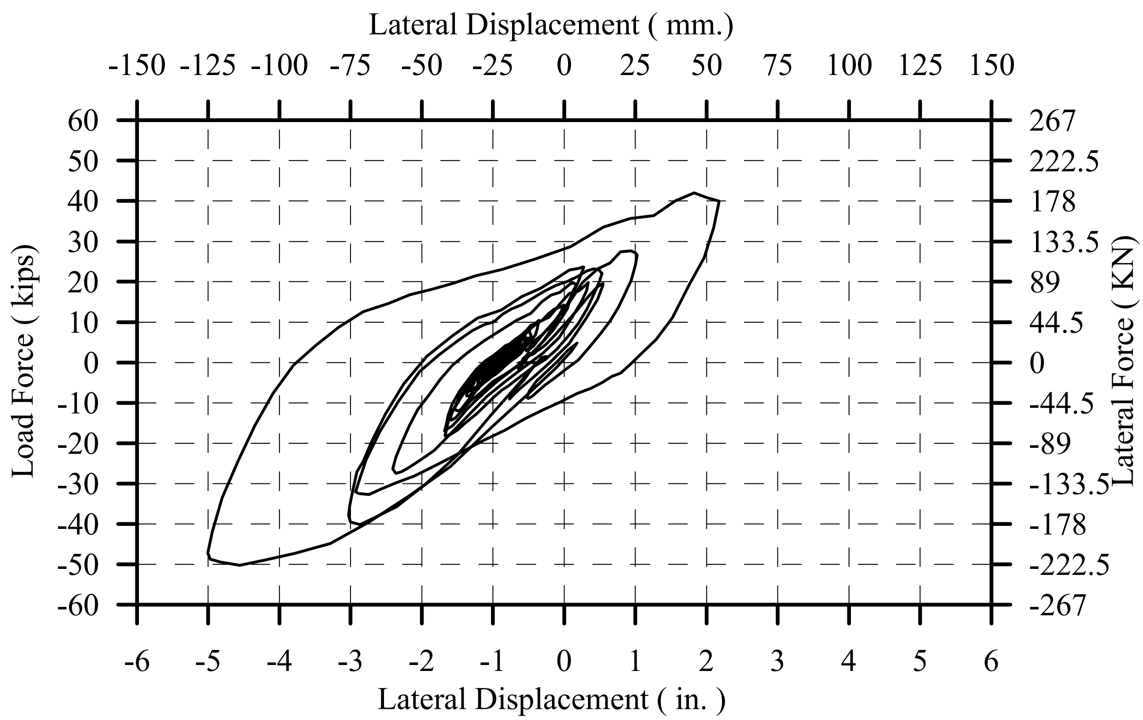

Fig. 4-127: Hysteresis Curve for B2CM at 2.75 x Sylmar

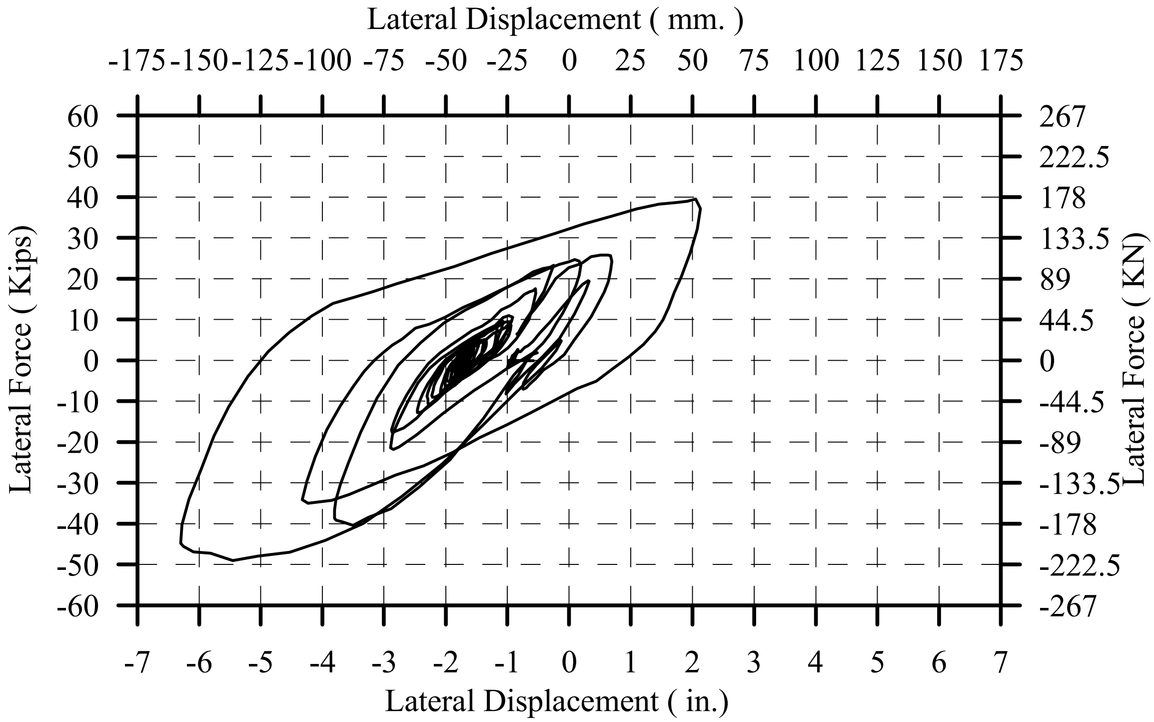

Fig. 4-128: Hysteresis Curve for B2CM at 3.00 x Sylmar

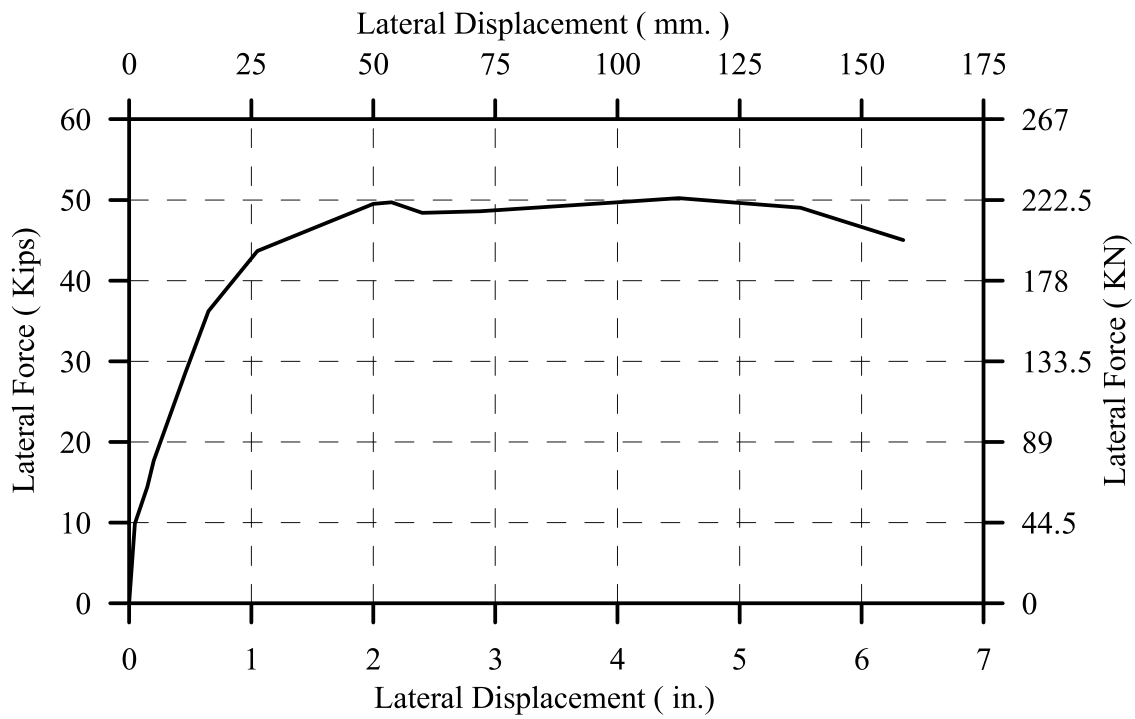

Fig. 4-129: Envelope of Load-Displacement Hystereses for B2CM

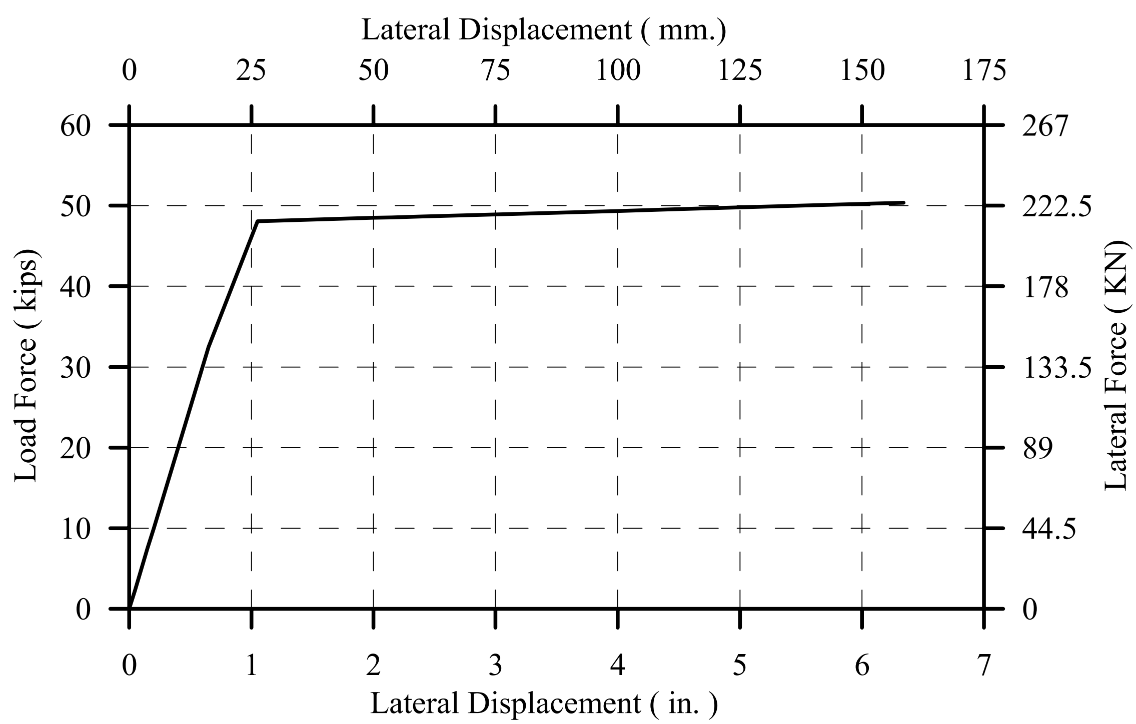

Fig. 4-130: Bilinear Representation of Previous Envelope for B2CM

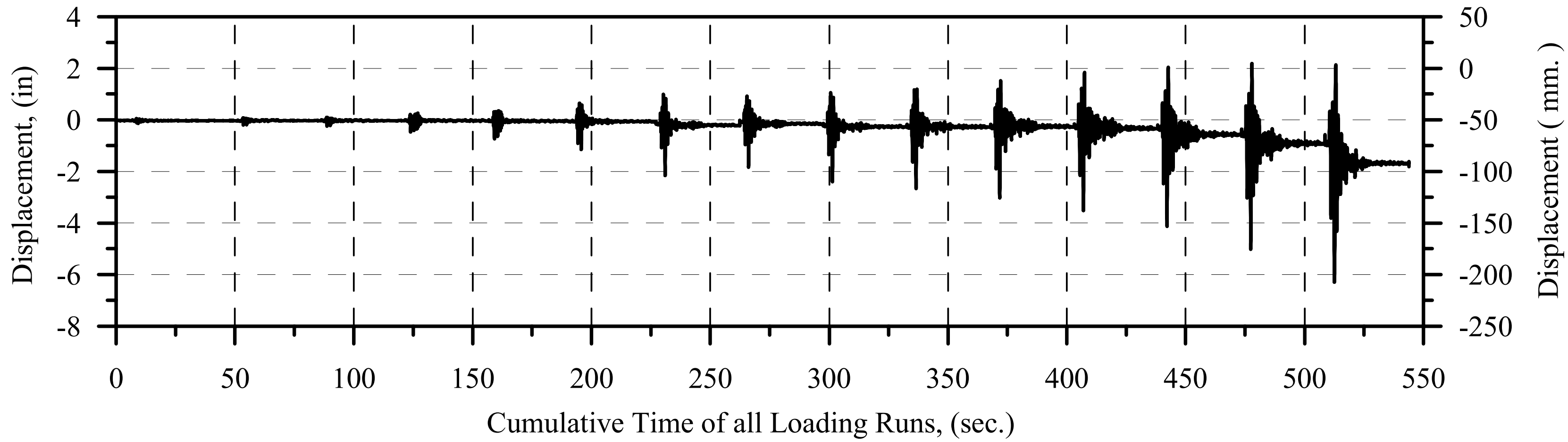

Fig. 4-131: Measured Relative Displacement History in the In-Plane Direction of Specimen B2CM

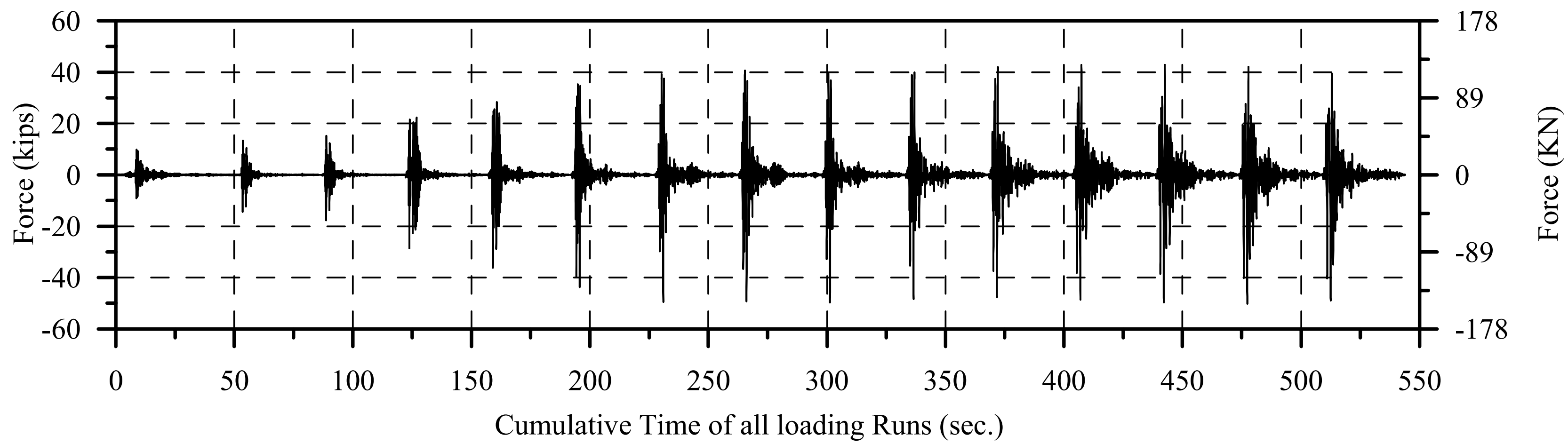

Fig. 4-132: Measured Resisting Force History in the In-Plane Direction of Specimen B2CM

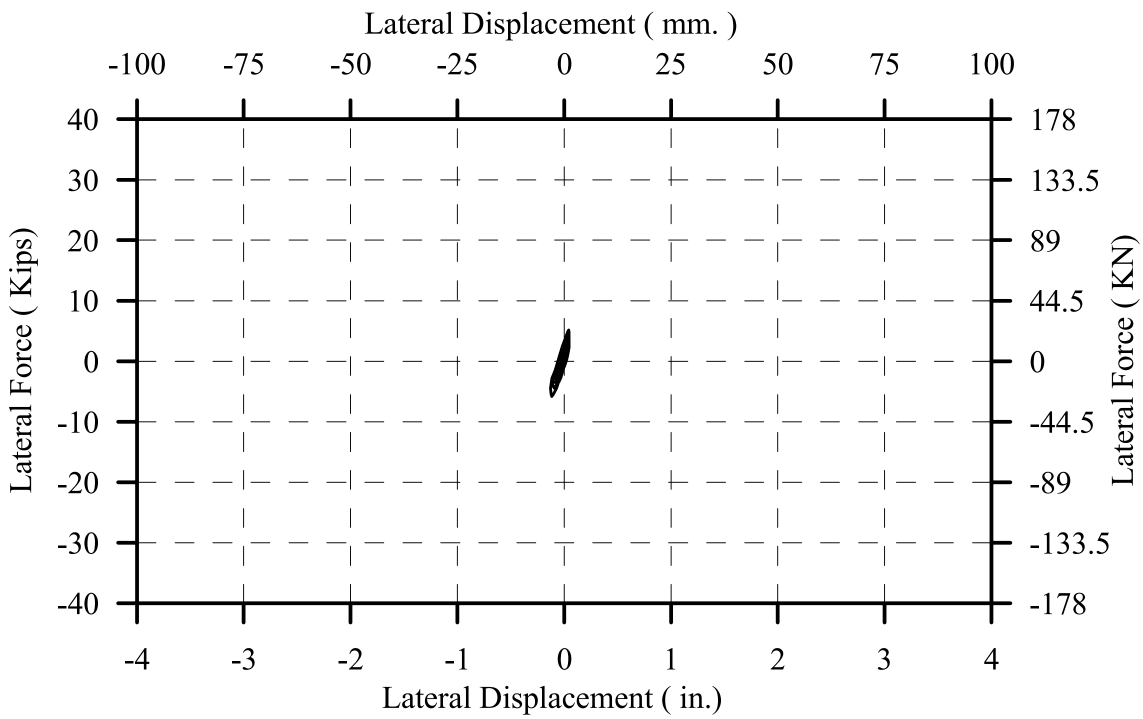

Fig. 4-133: Hysteresis Curve for B2CT at 0.1 x Sylmar

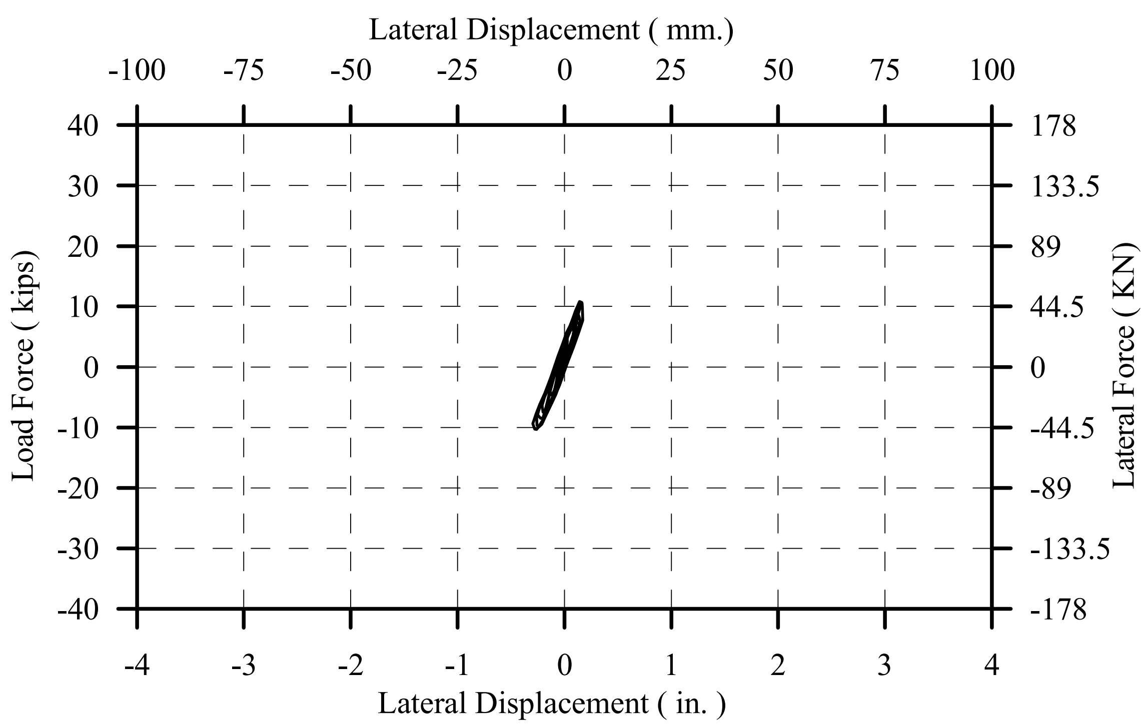

Fig. 4-134: Hysteresis Curve for B2CT at 0.20 x Sylmar

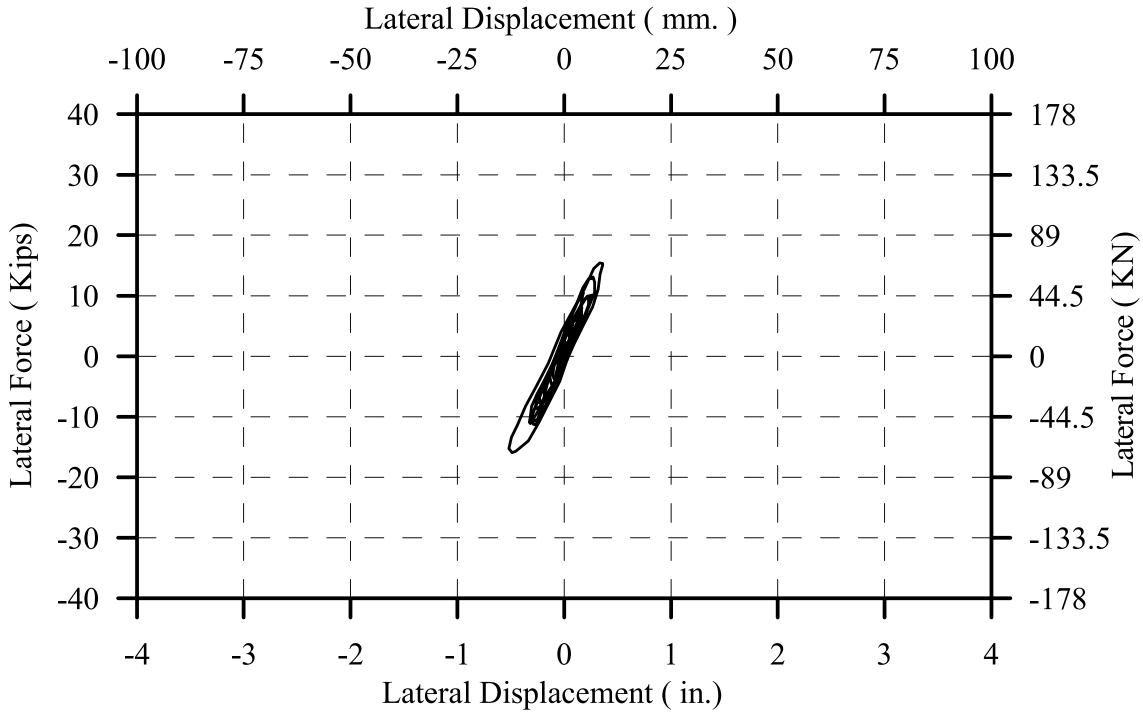

Fig. 4-135: Hysteresis Curve for B2CT at 0.25 x Sylmar

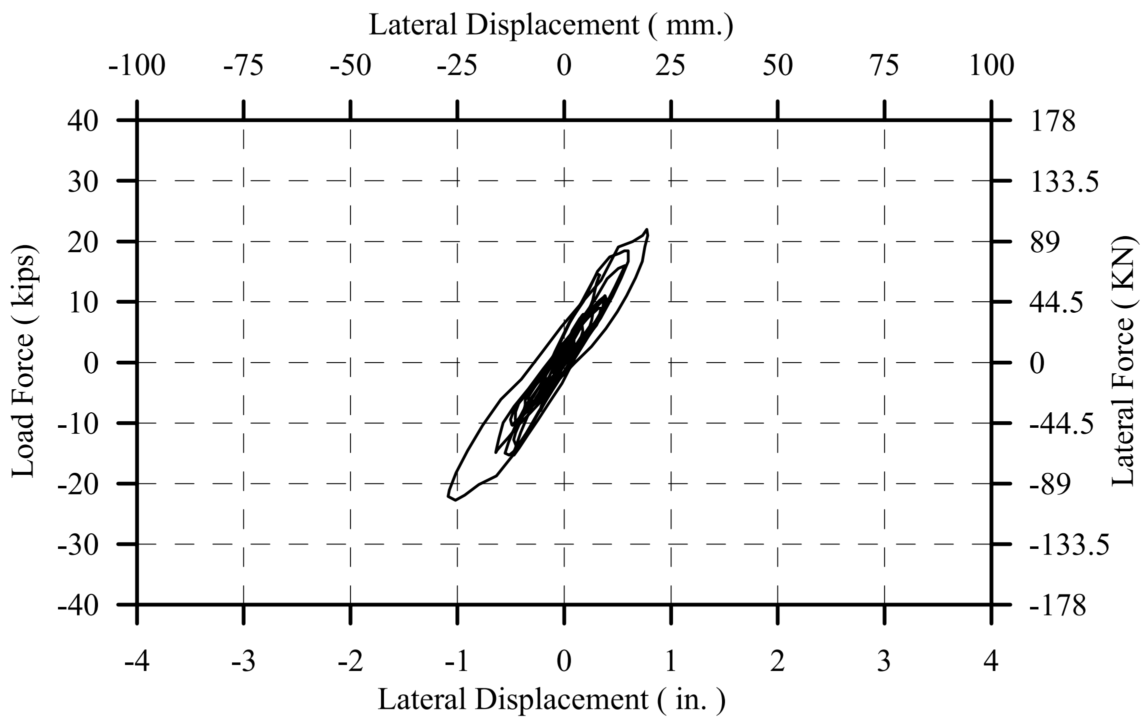

Fig. 4-136: Hysteresis Curve for B2CT at 0.50 x Sylmar

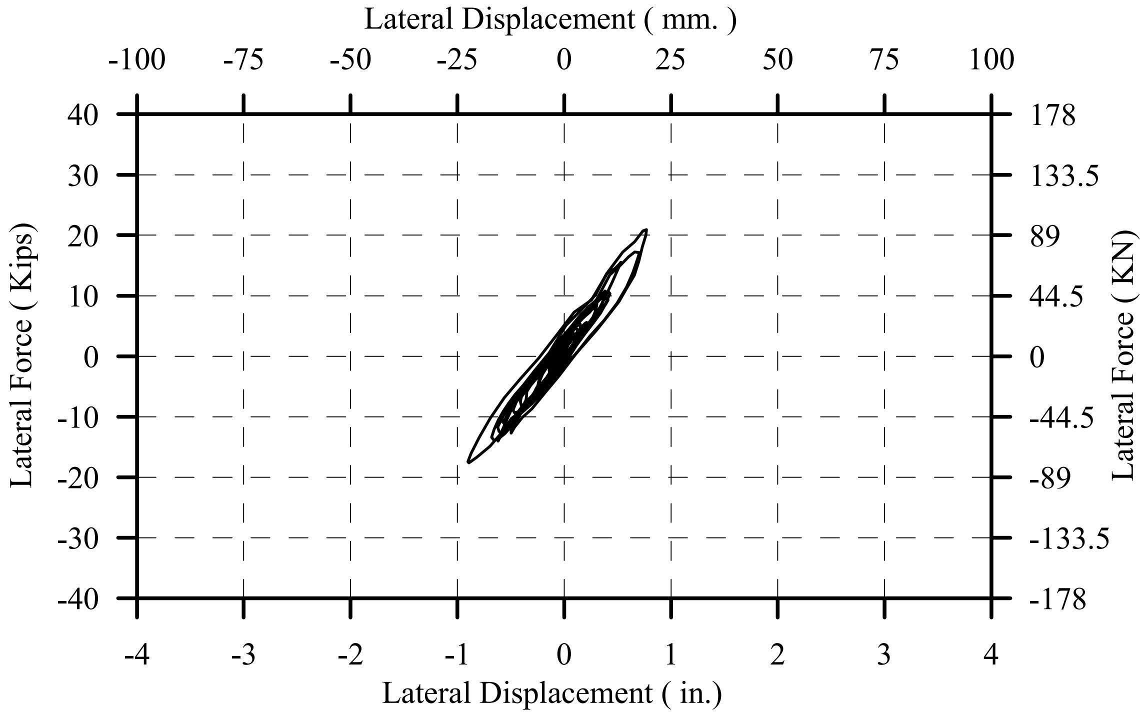

Fig. 4-137: Hysteresis Curve for B2CT at 0.75 x Sylmar

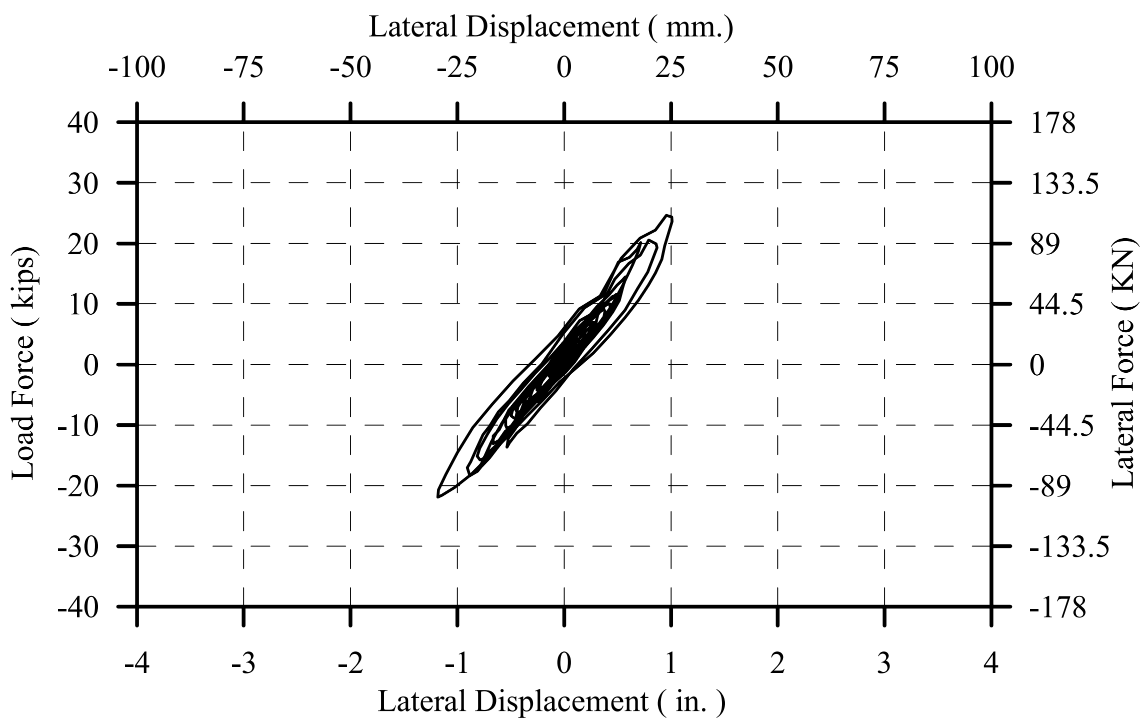

Fig. 4-138: Hysteresis Curve for B2CT at 0.85 x Sylmar

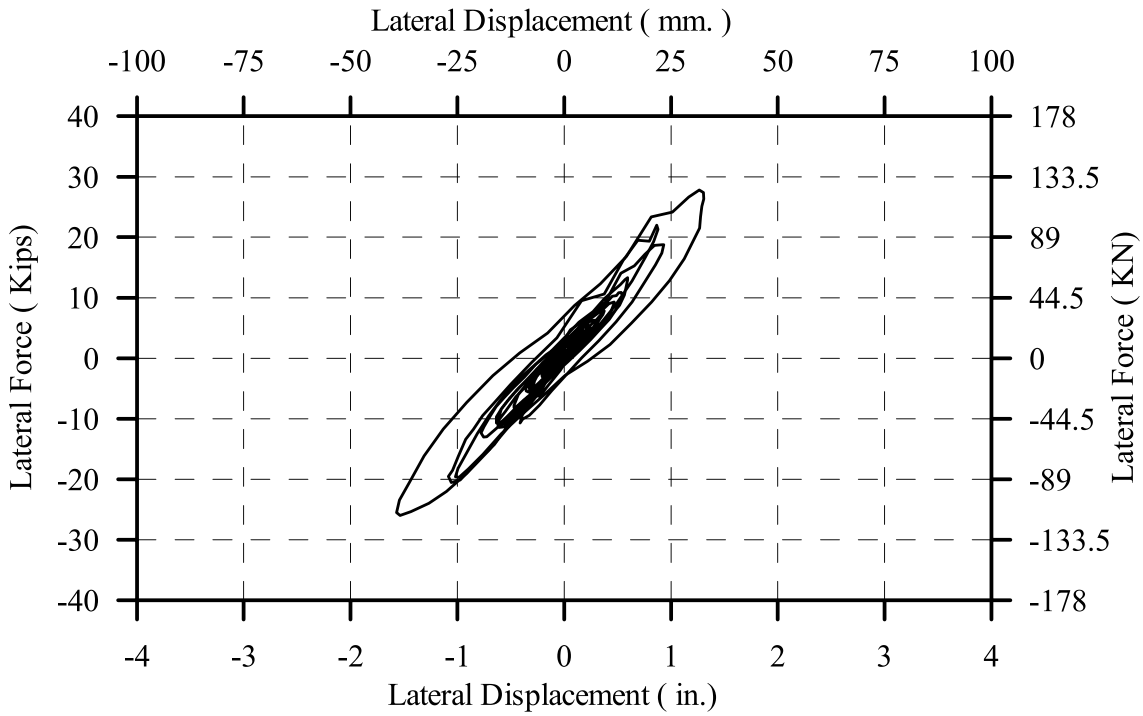

Fig. 4-139: Hysteresis Curve for B2CT at 1.00 x Sylmar

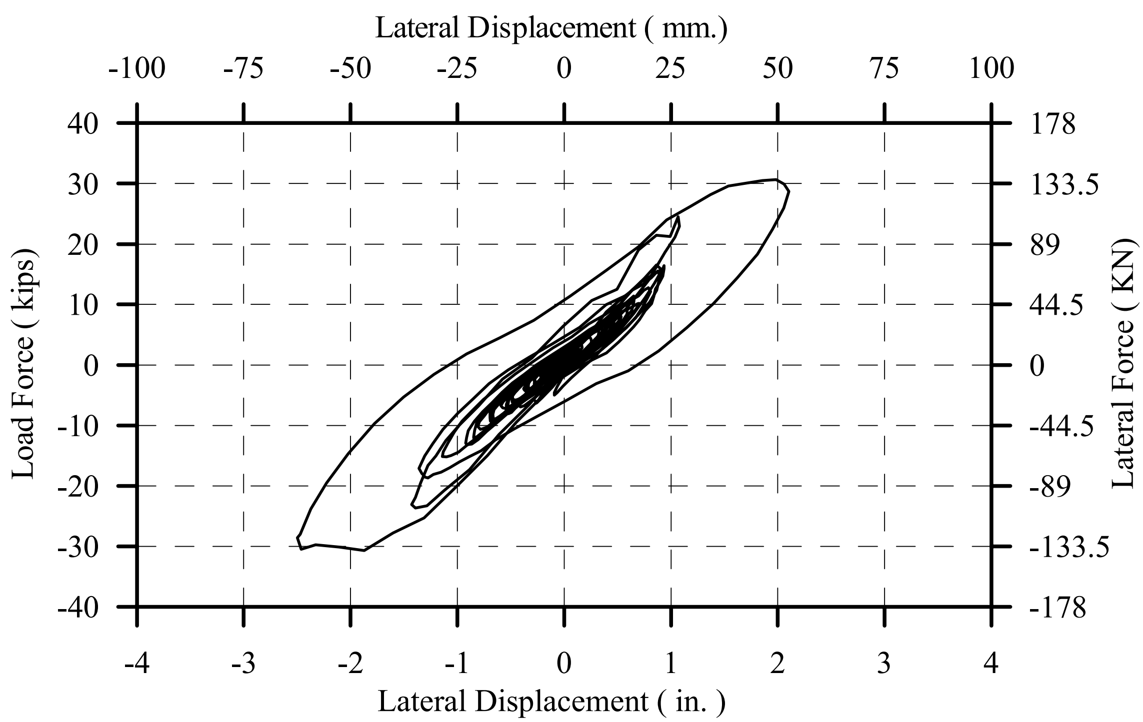

Fig. 4-140: Hysteresis Curve for B2CT at 1.25 x Sylmar

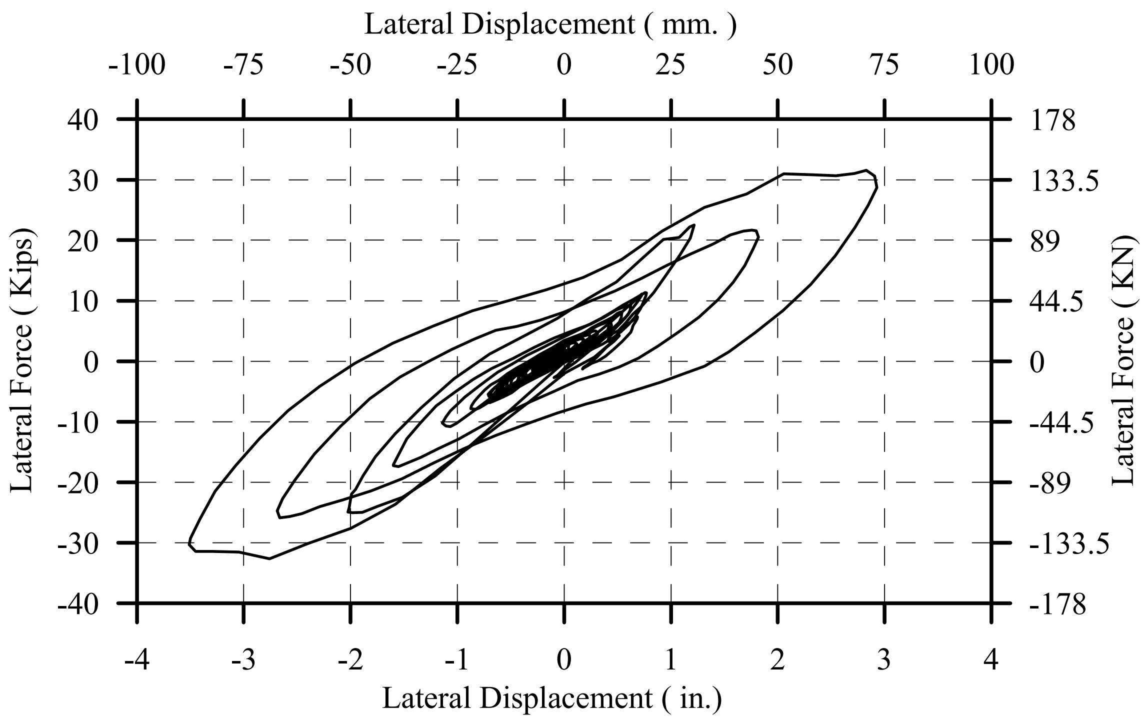

Fig. 4-141: Hysteresis Curve for B2CT at 1.50 x Sylmar

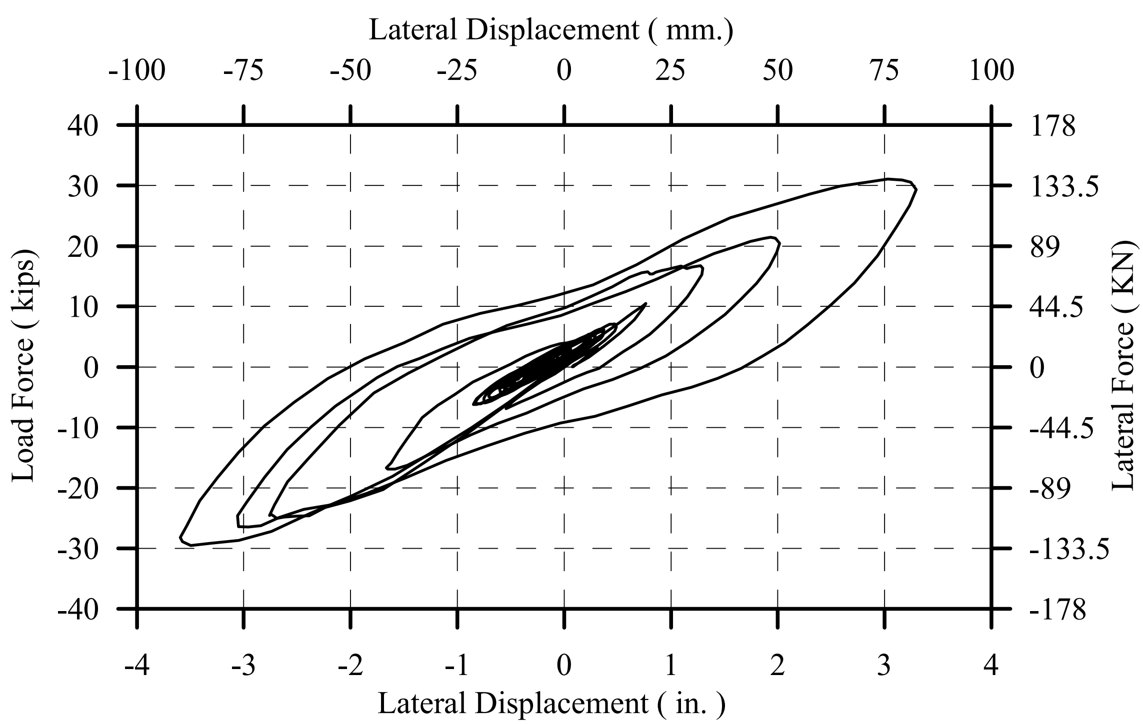

Fig. 4-142: Hysteresis Curve for B2CT at 1.75 x Sylmar

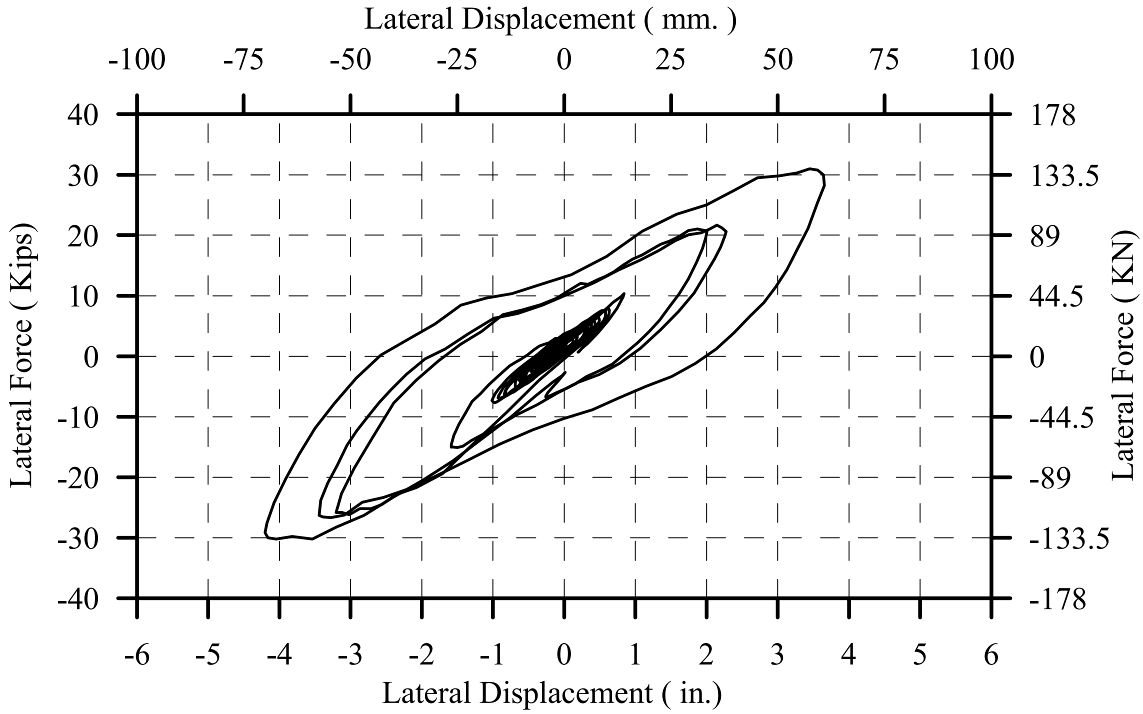

Fig. 4-143: Hysteresis Curve for B2CT at 2.00 x Sylmar

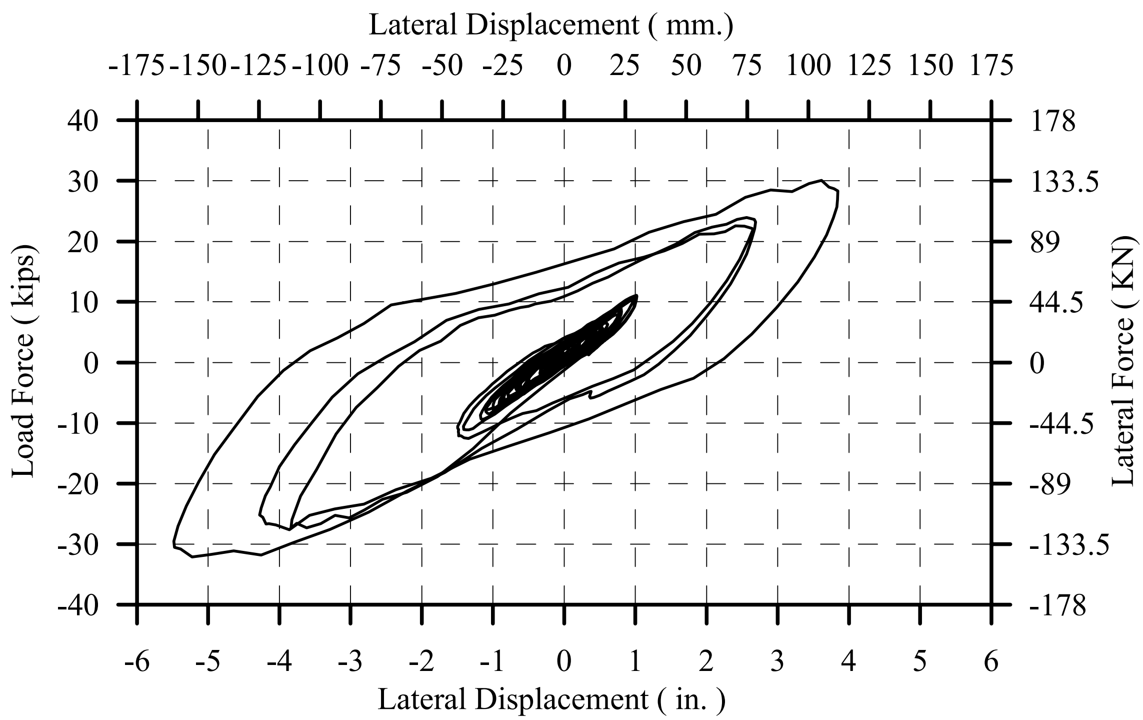

Fig. 4-144: Hysteresis Curve for B2CT at 2.25 x Sylmar

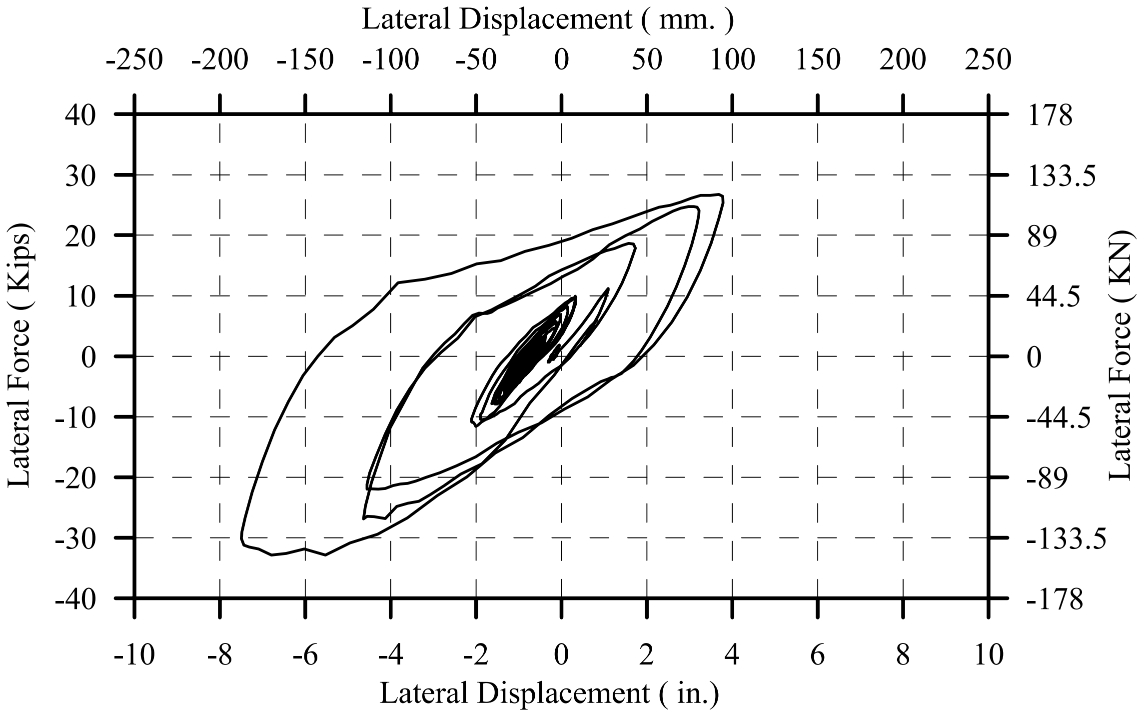

Fig. 4-145: Hysteresis Curve for B2CT at 2.50 x Sylmar

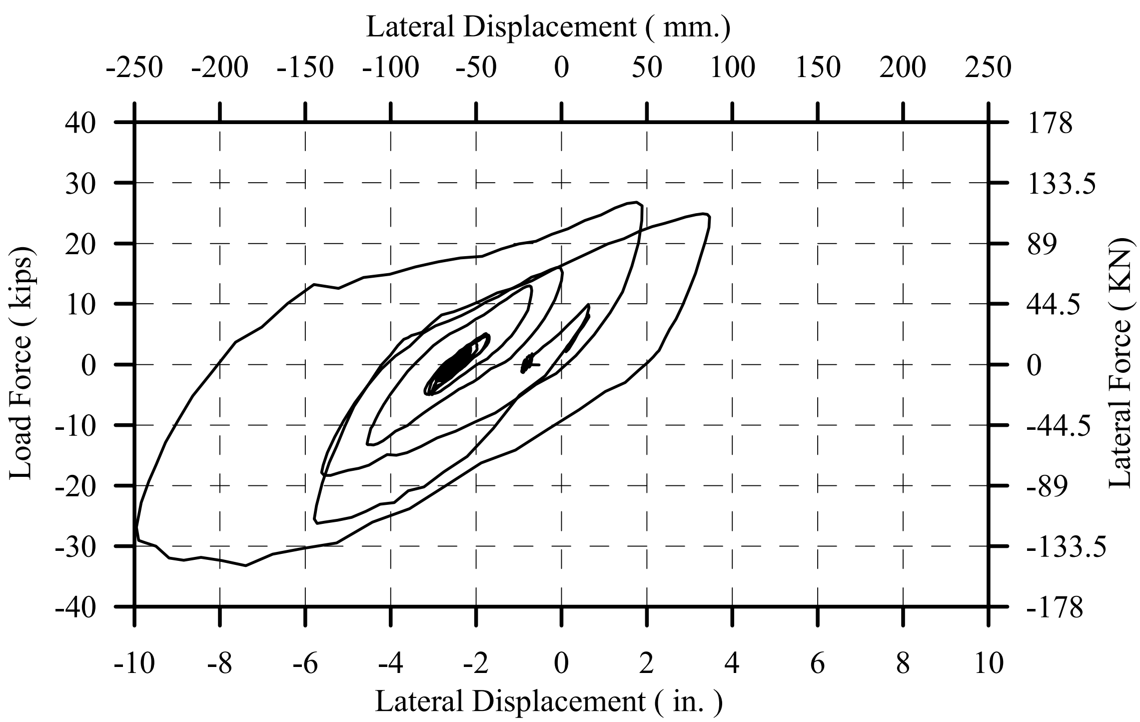

Fig. 4-146: Hysteresis Curve for B2CT at 2.75 x Sylmar

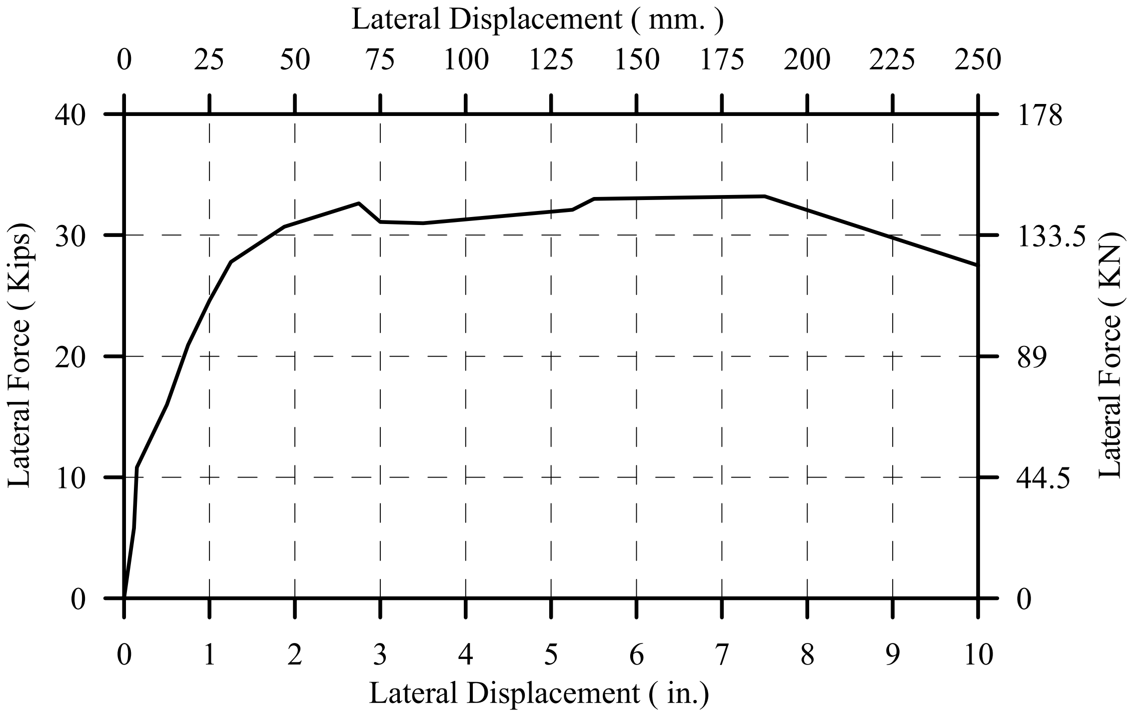

Fig. 4-147: Envelope of Load-Displacement Hystereses for B2CT

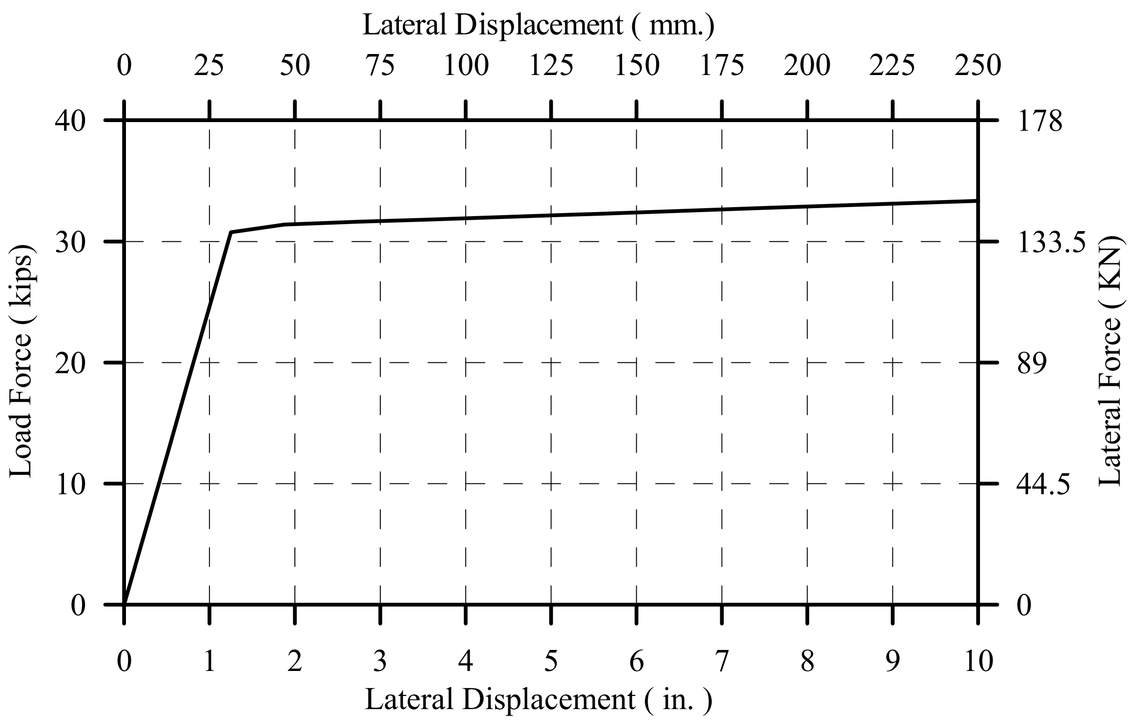

Fig. 4-148: Envelope of Load-Displacement Hystereses for B2CT

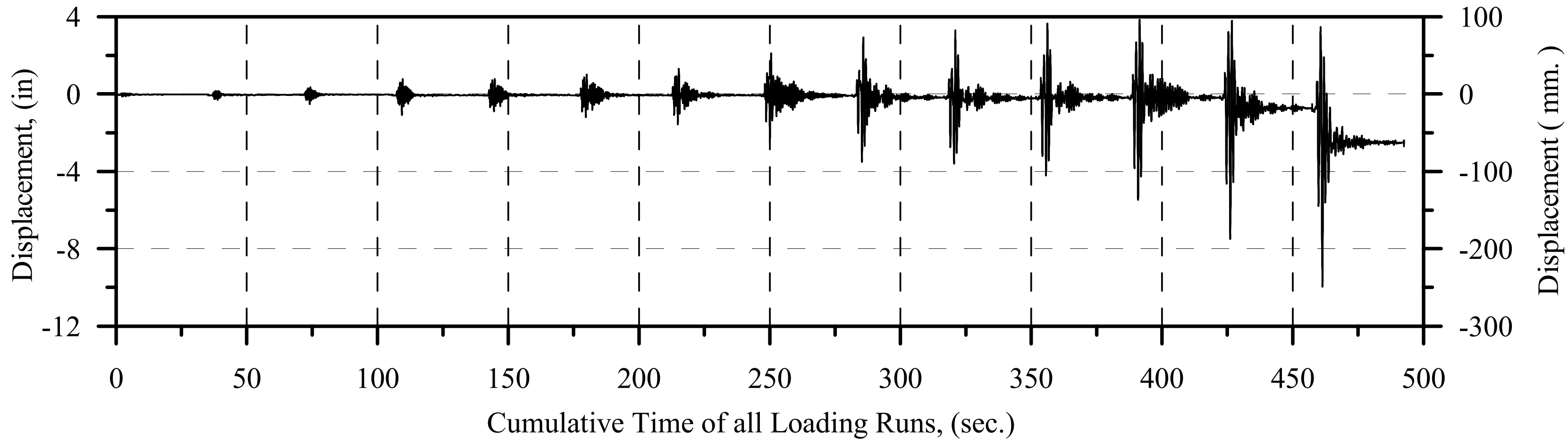

Fig. 4-149: Measured Relative Displacement History in the In-Plane Direction for Specimen B2CT

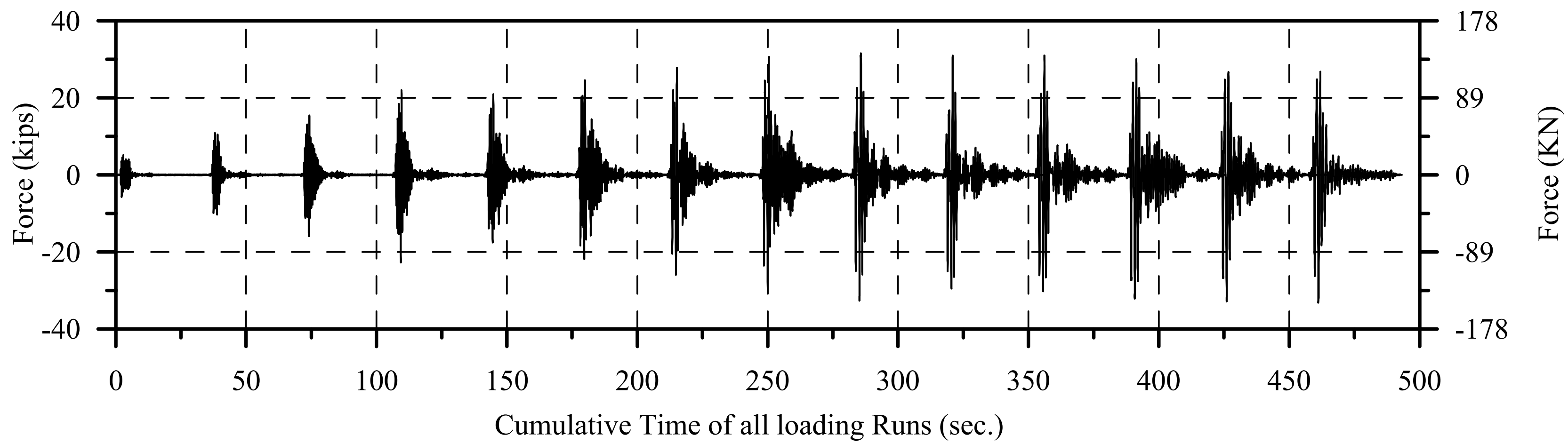

Fig. 4-150: Measured Resisting Force History in the In-Plane Direction for Specimen B2CT

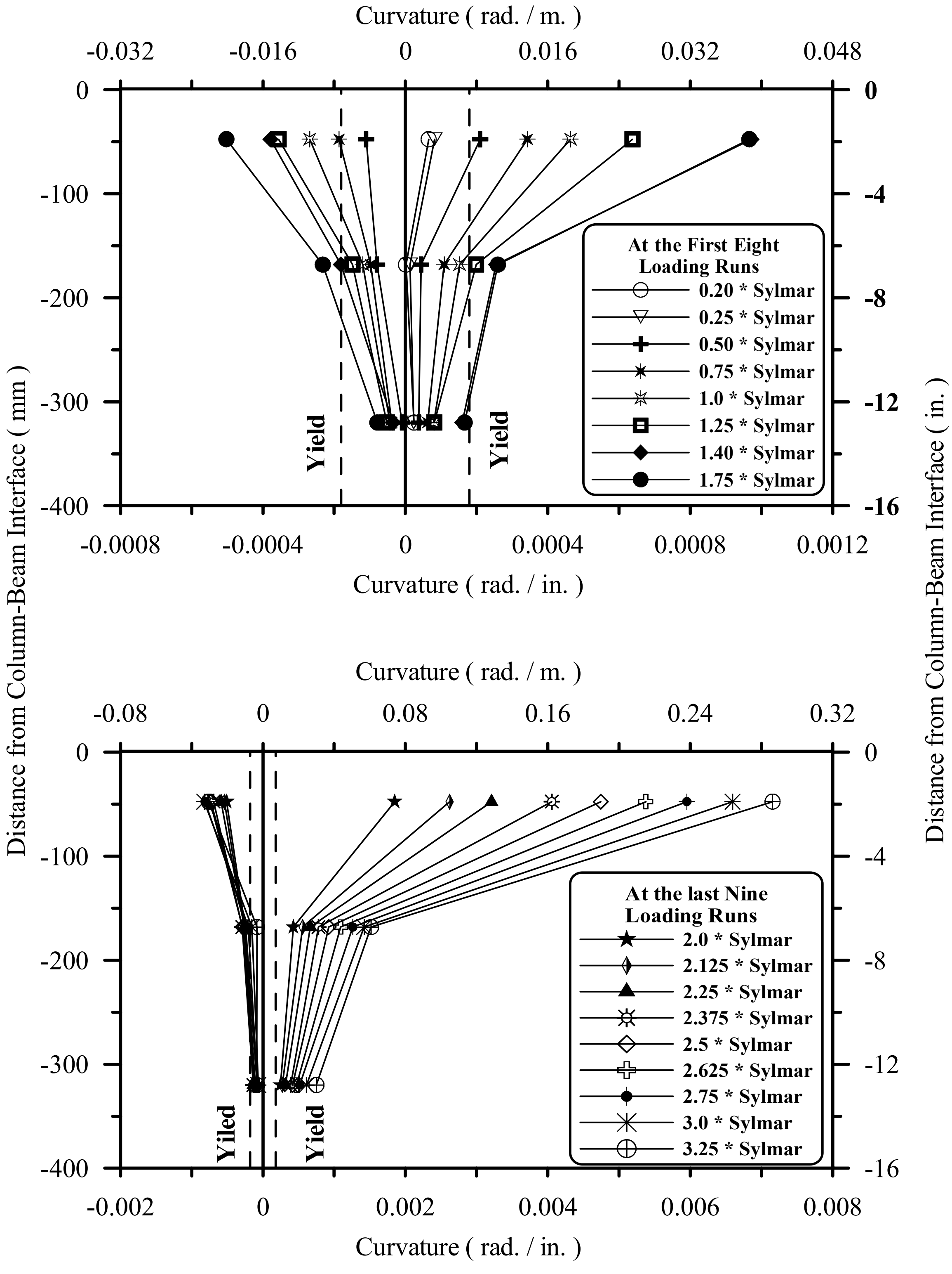

Fig. 4-151: Maximum Curvatures after each Loading at Plastic Hinge Zone of East Column in Specimen B2CS

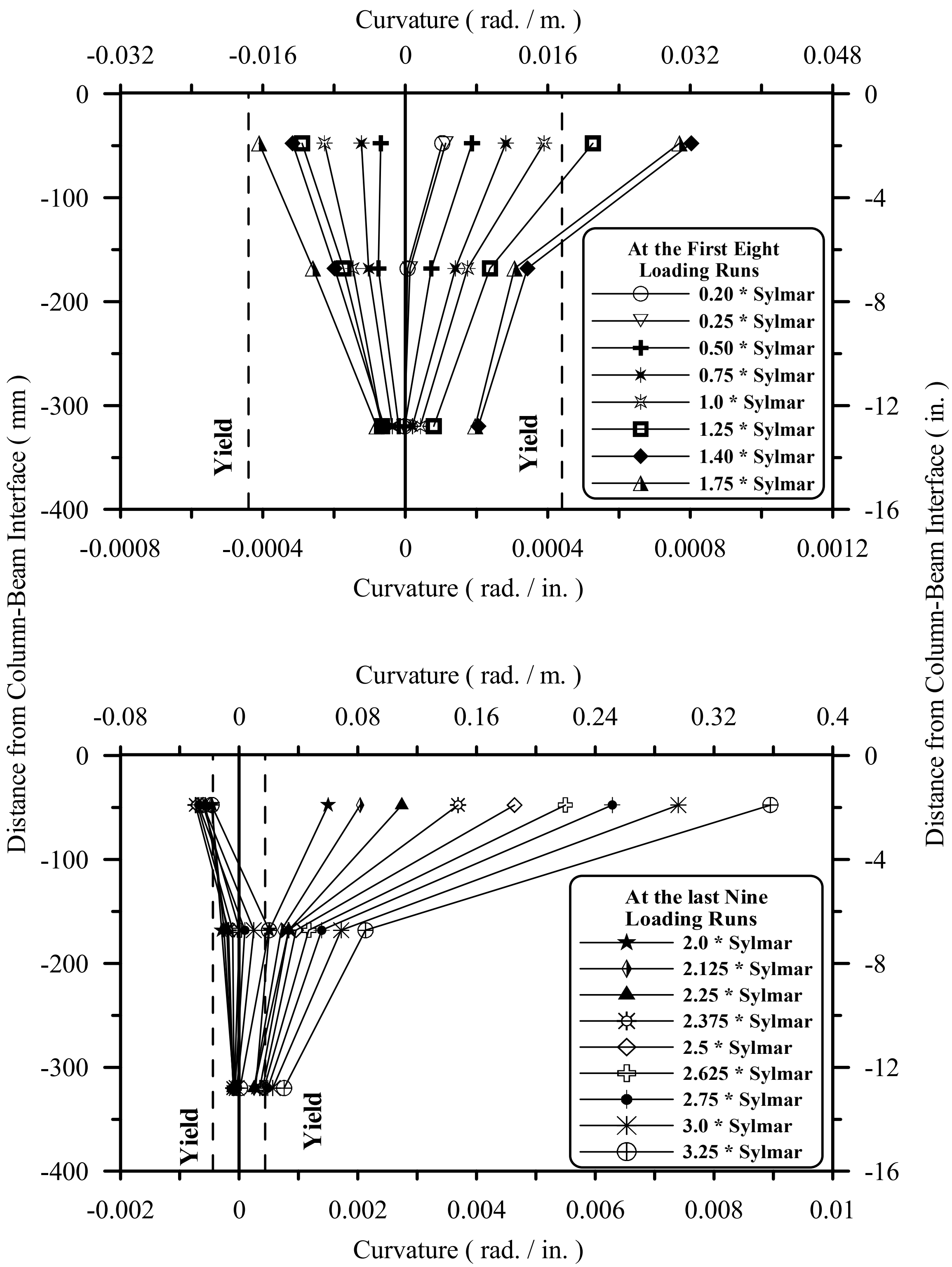

Fig. 4-152: Maximum Curvatures after each Loading at Plastic Hinge Zone of West Column in Specimen B2CS

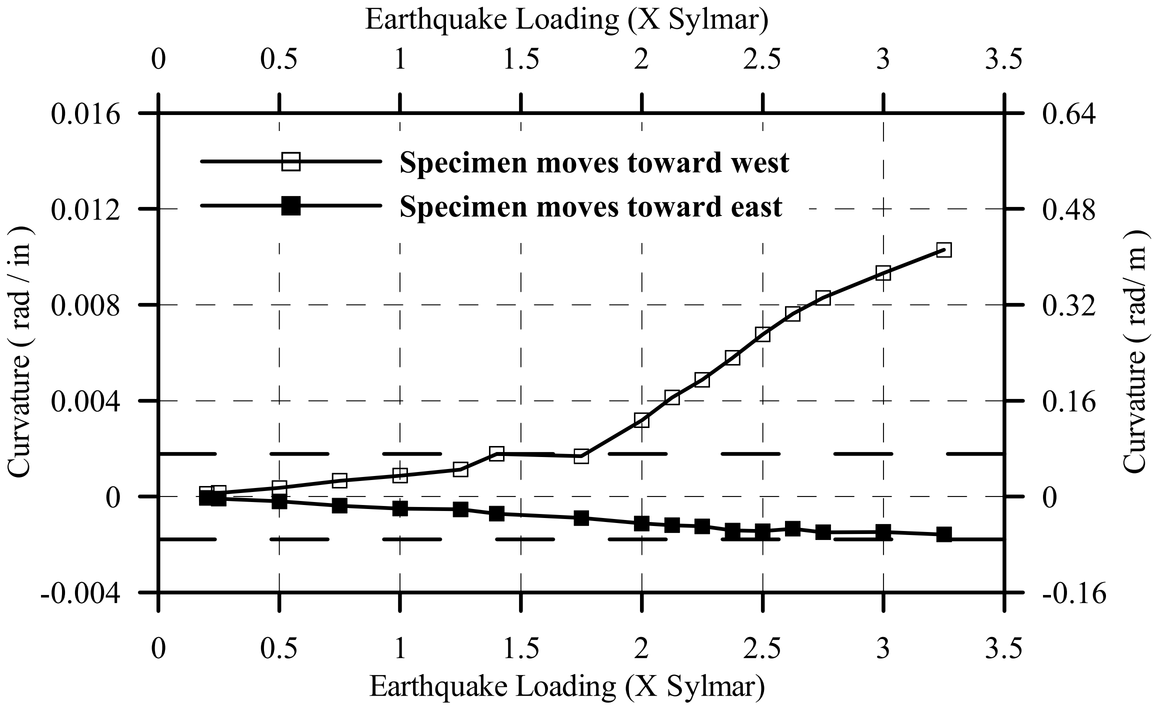

Fig. 4-153: Curvature Envelope at East Column Base in Specimen B2CS

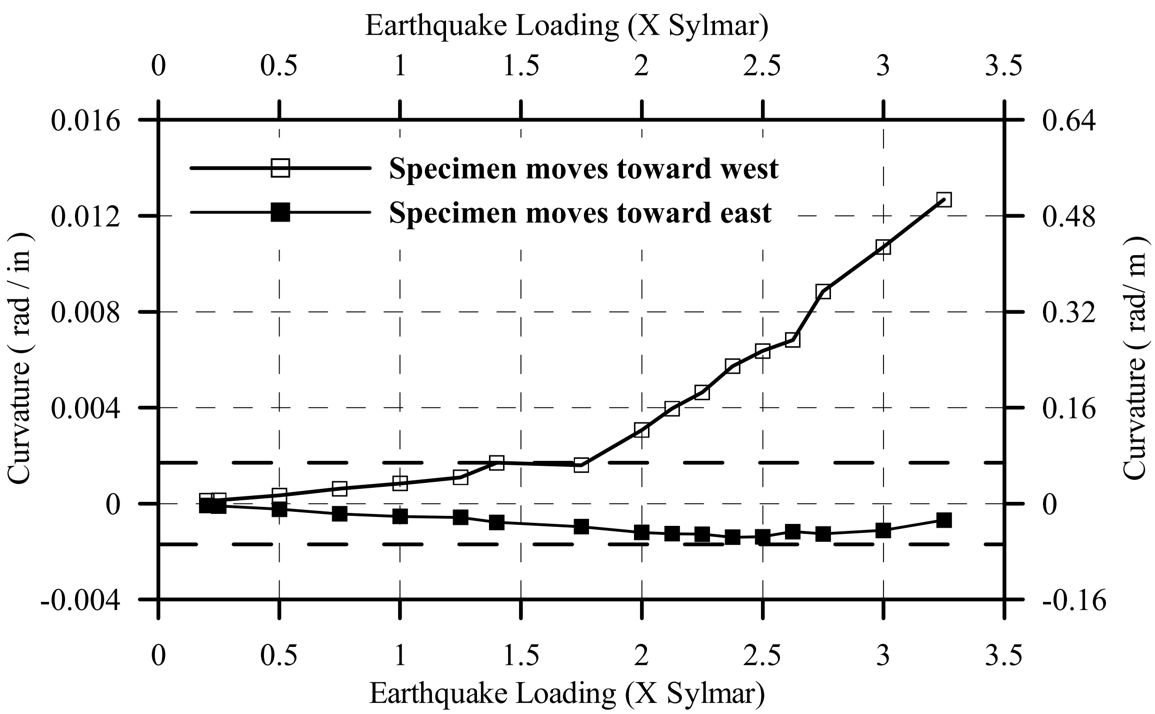

Fig. 4-154: Curvature Envelope at West Column Base in Specimen B2CS

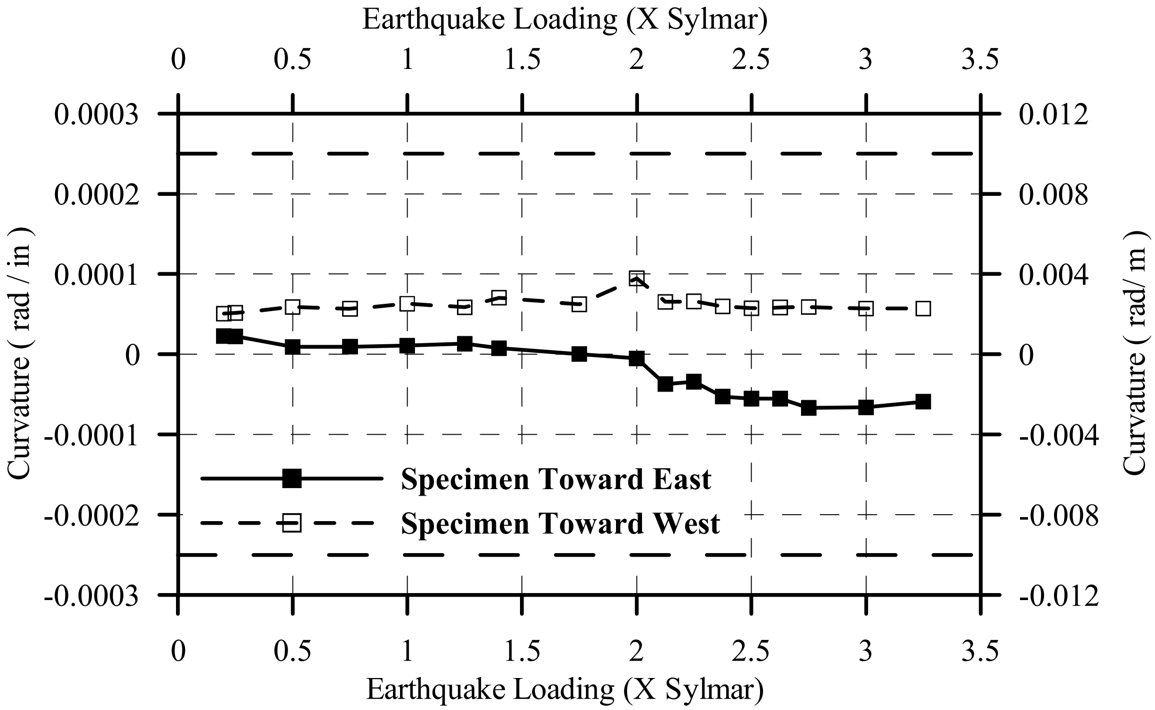

Fig. 4-155: Max. Curvature of Beam Critical Section on East Side in B2CS

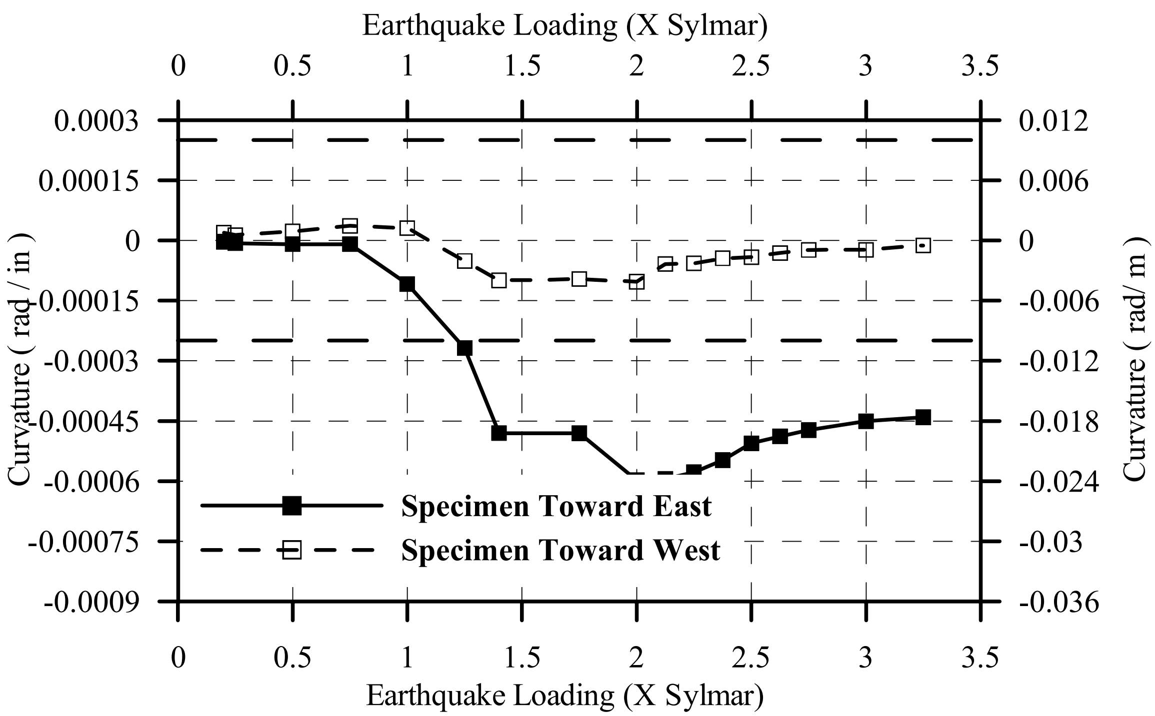

Fig. 4-156: Max. Curvature of Beam Critical Section on West Side in B2CS

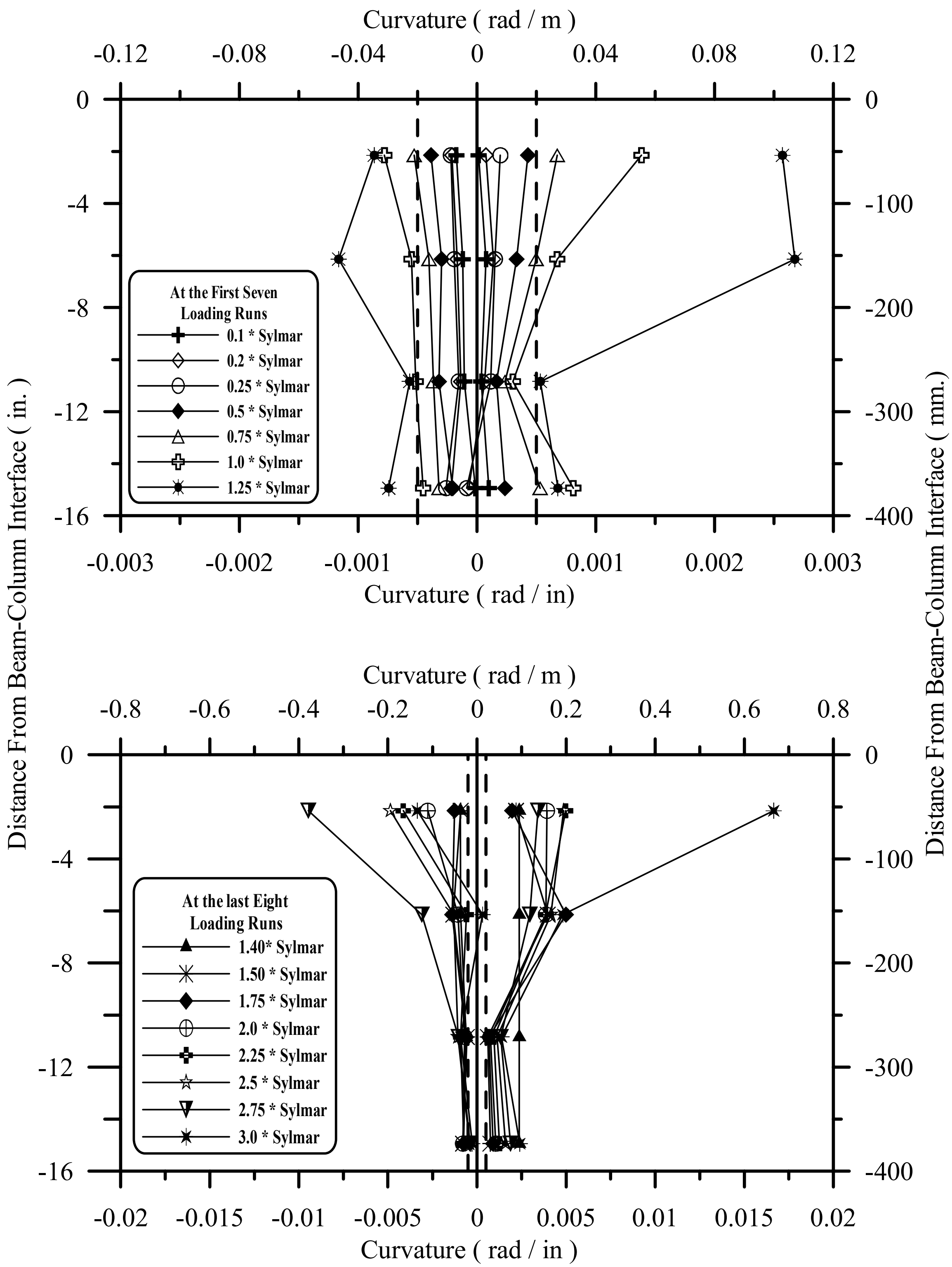

Fig. 4-157: Maximum Curvature after each Loading at Plastic Hinge Zone of East Column in Specimen B2CM

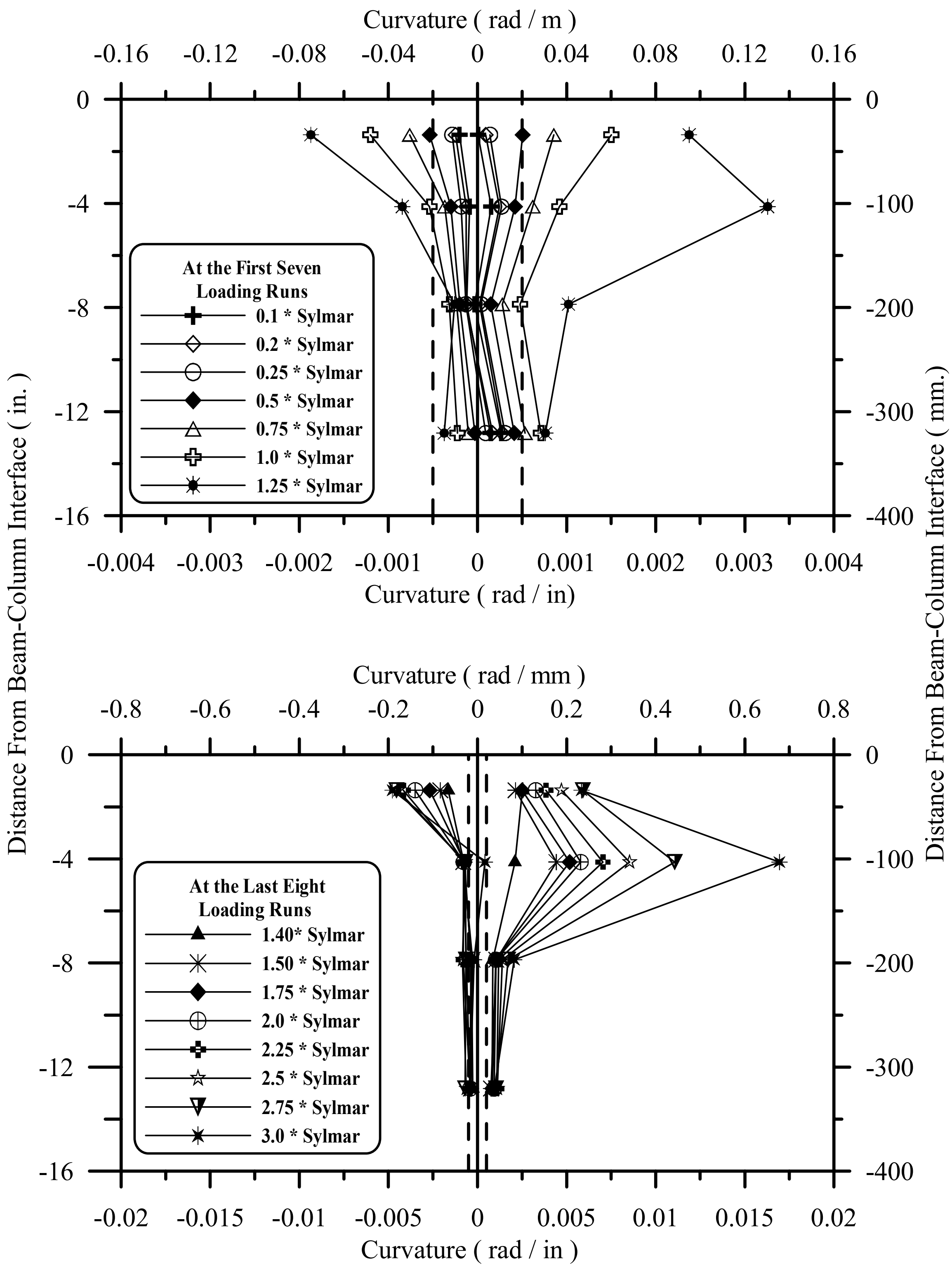

Fig. 4-158: Maximum Curvature after each Loading at Plastic Hinge Zone of West Column in Specimen B2CM

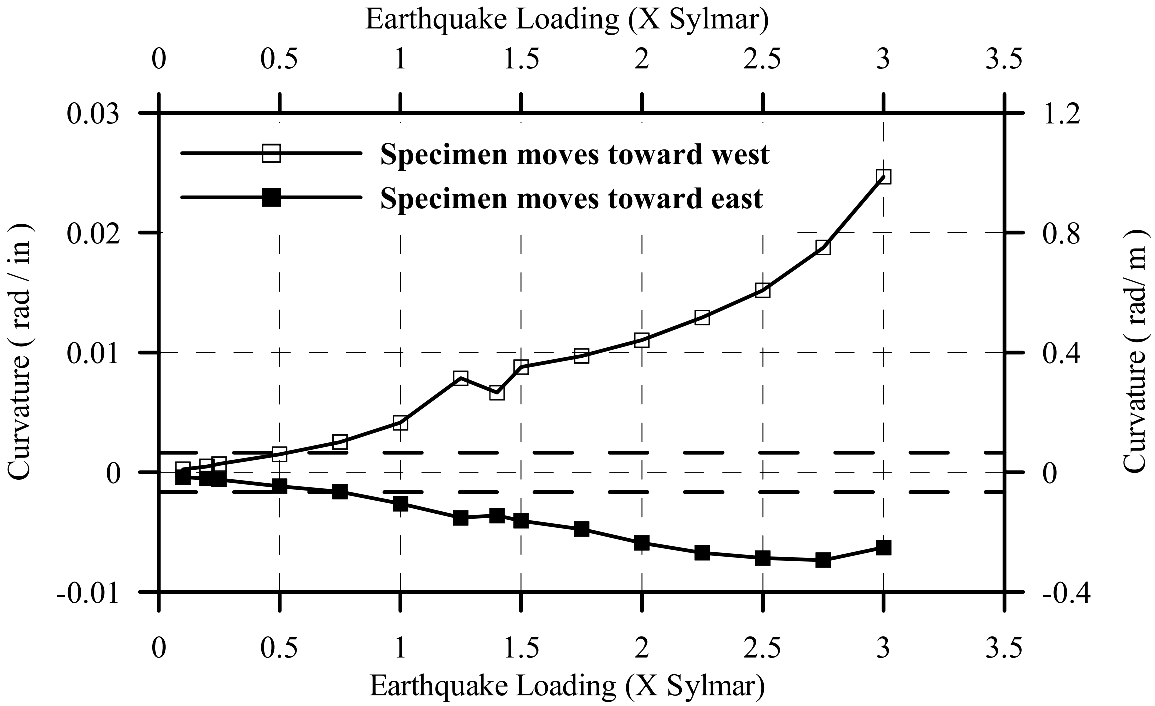

Fig. 4-159:Curvature Envelope at East Column Base in B2CM

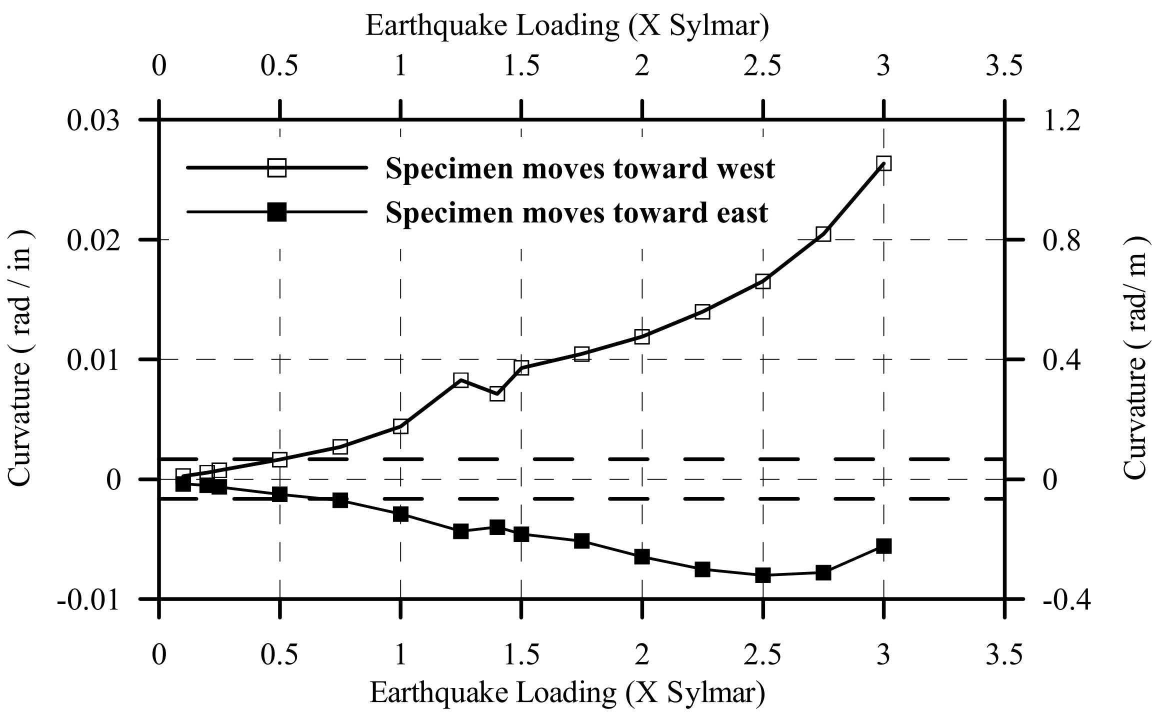

Fig. 4-160:Curvature Envelope at West Column Base in B2CM

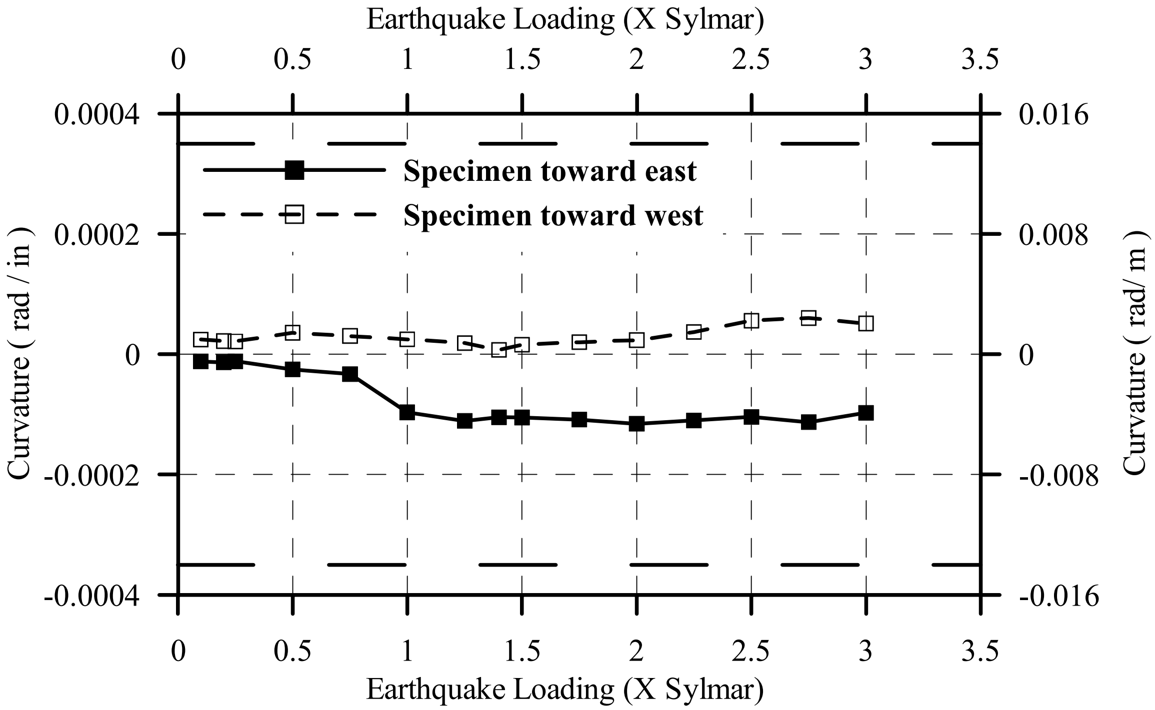

Fig. 4-161: Max. Curvature of Beam Critical Section on East Side of B2CM

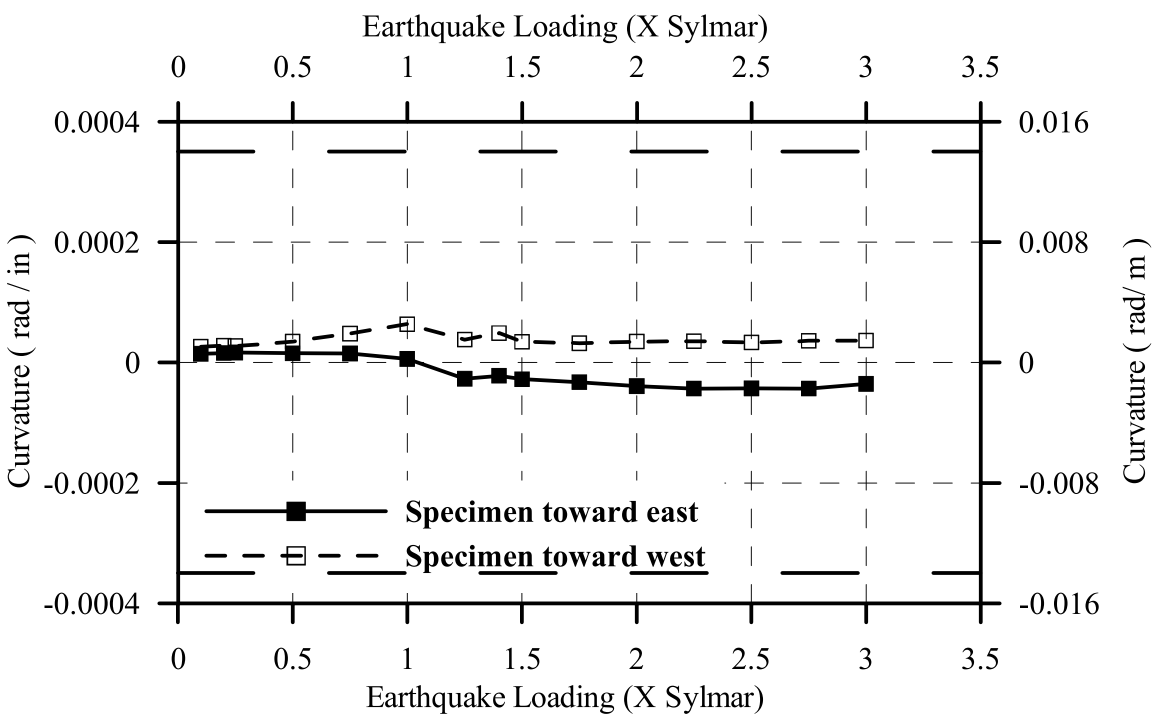

Fig. 4-162: Max. Curvature of Beam Critical Section on West Side of B2CM

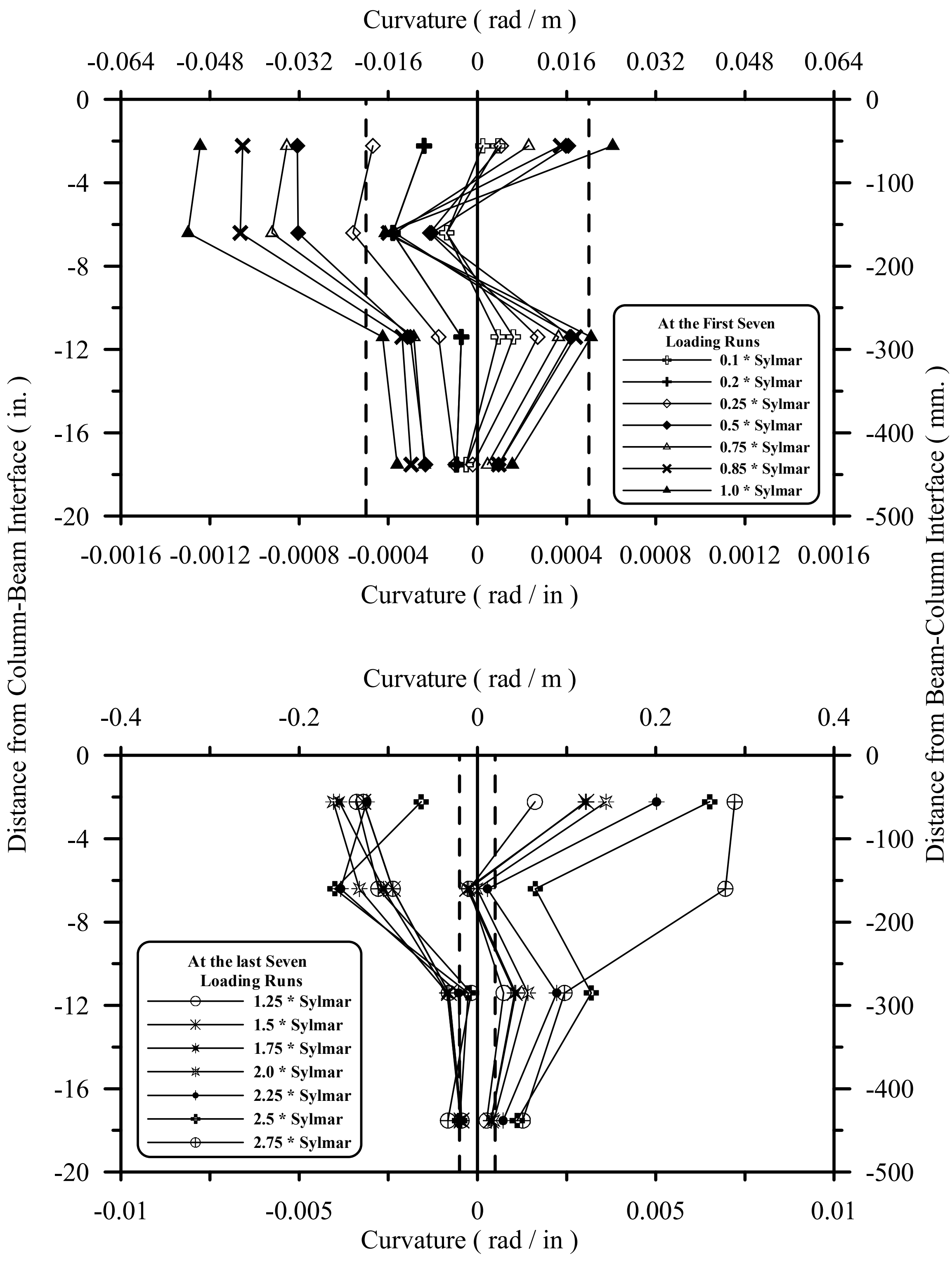

Fig. 4-163: Maximum Curvature after each Loading at Plastic Hinge Zone of East Column in Specimen B2CT

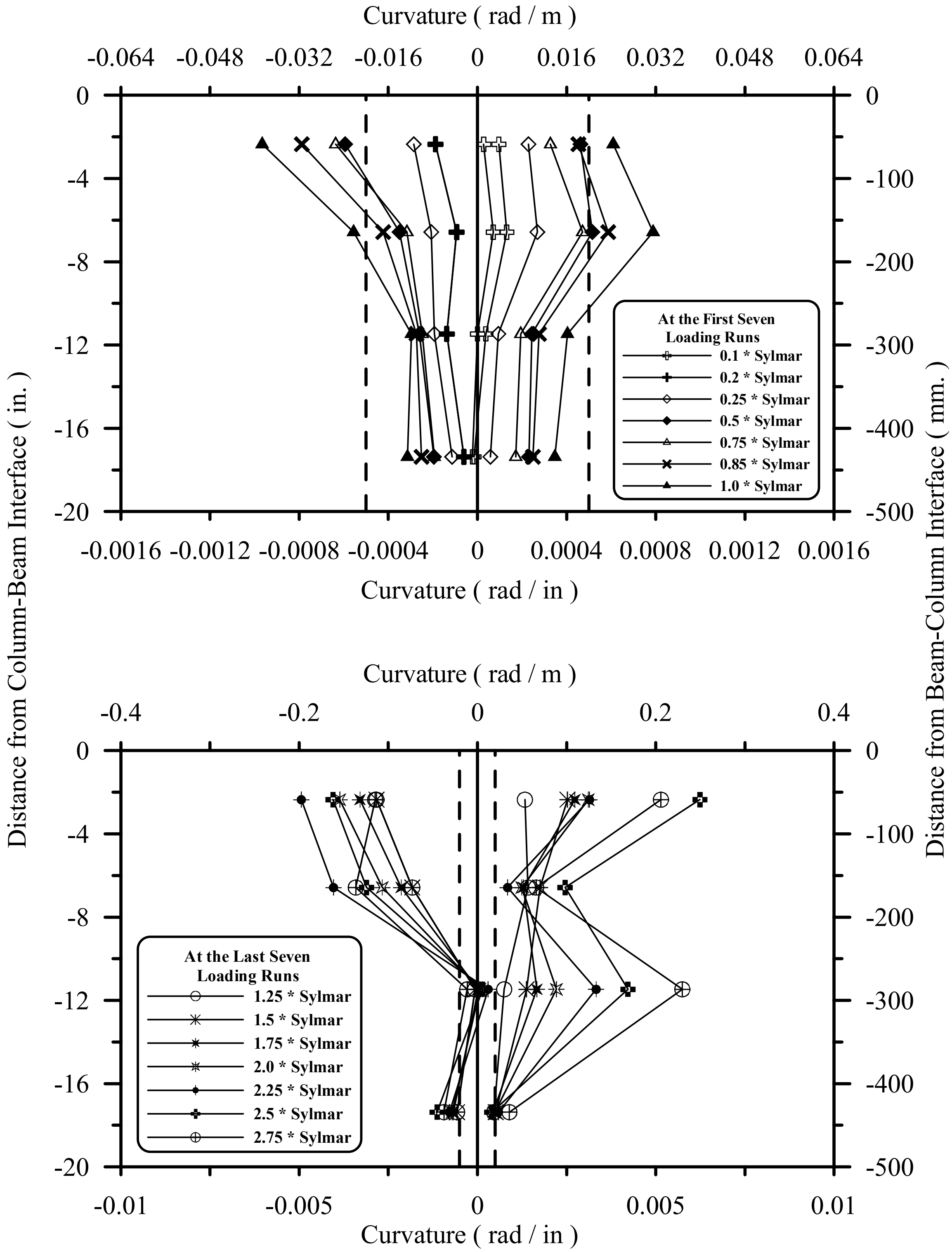

Fig. 4-164: Maximum Curvature after each Loading at Plastic Hinge Zone of West Column in Specimen B2CT

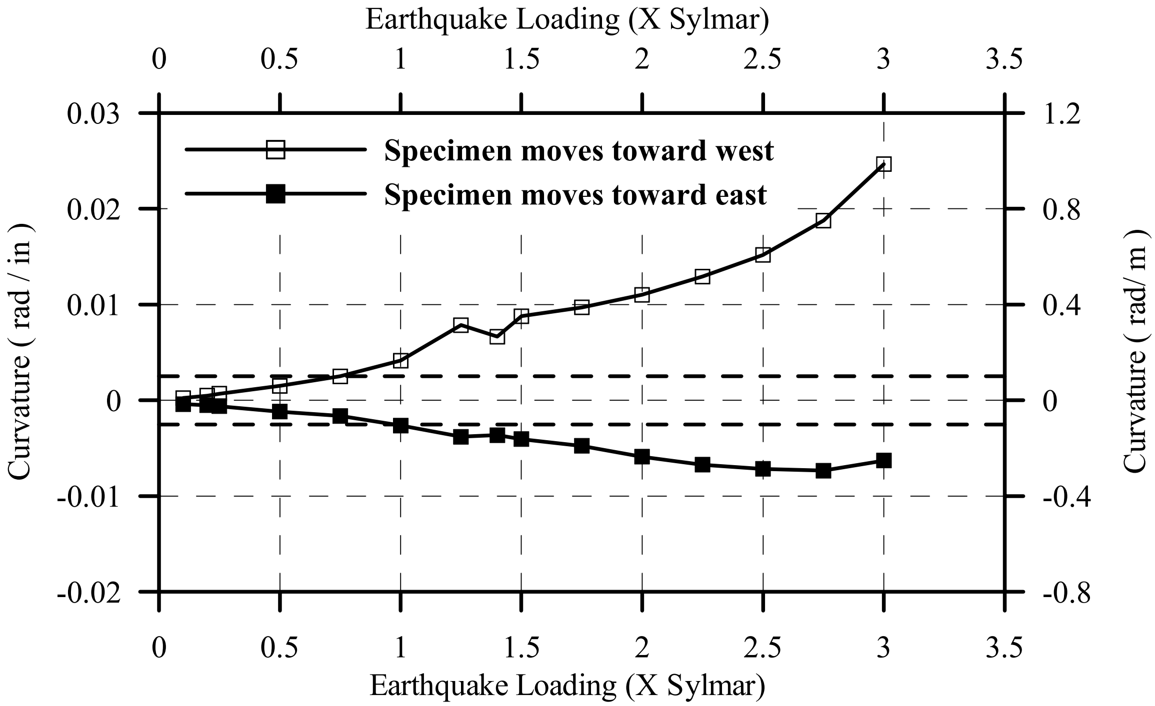

Fig. 4-165: Curvature Envelope at East Column Base in B2CT

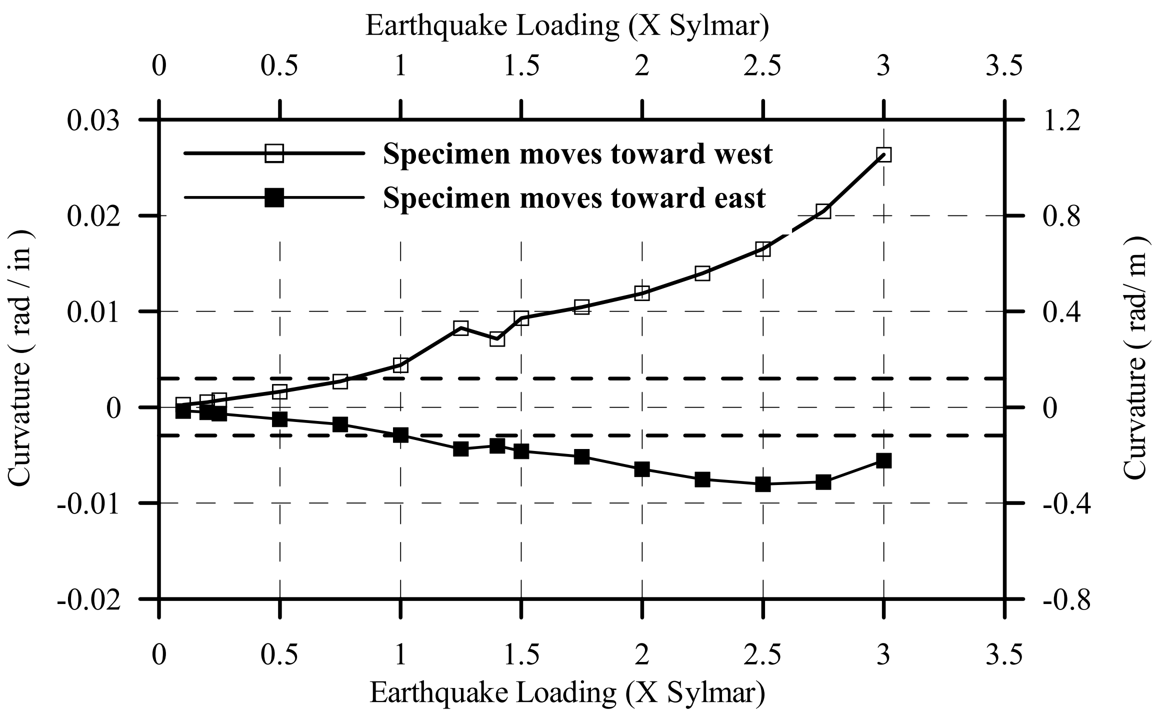

Fig. 4-166: Curvature Envelope at West Column Base in B2CT

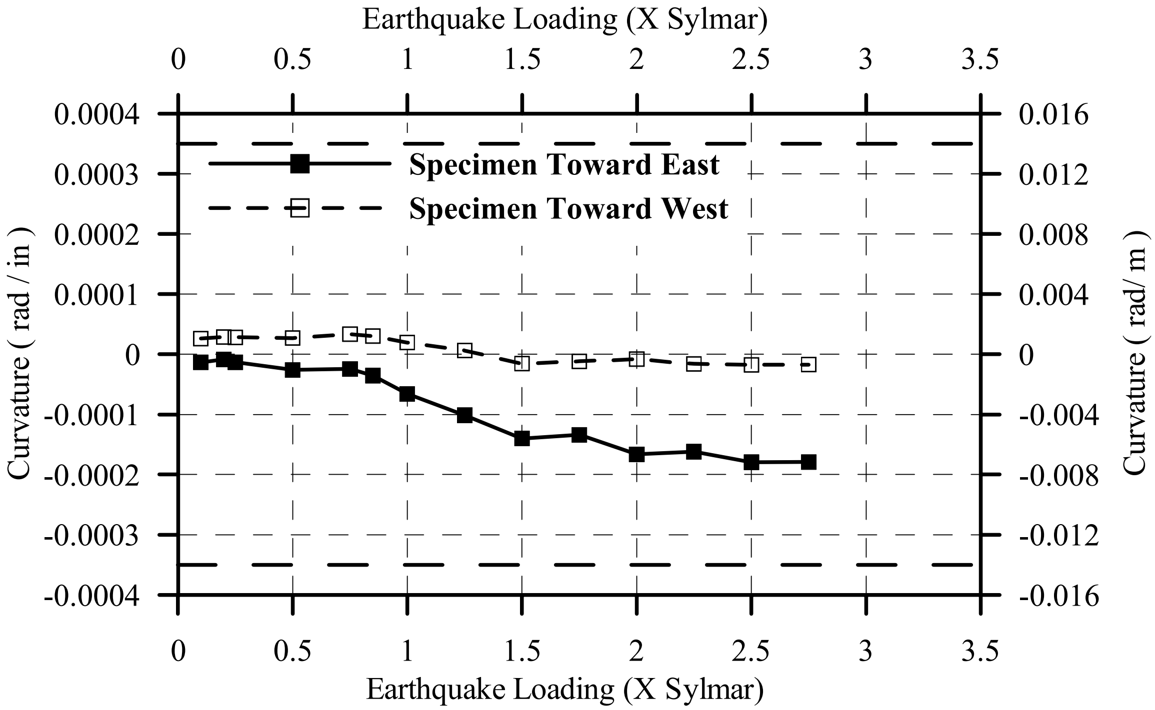

Fig. 4-167: Max. Curvature of Beam Critical Section on East side of B2CT

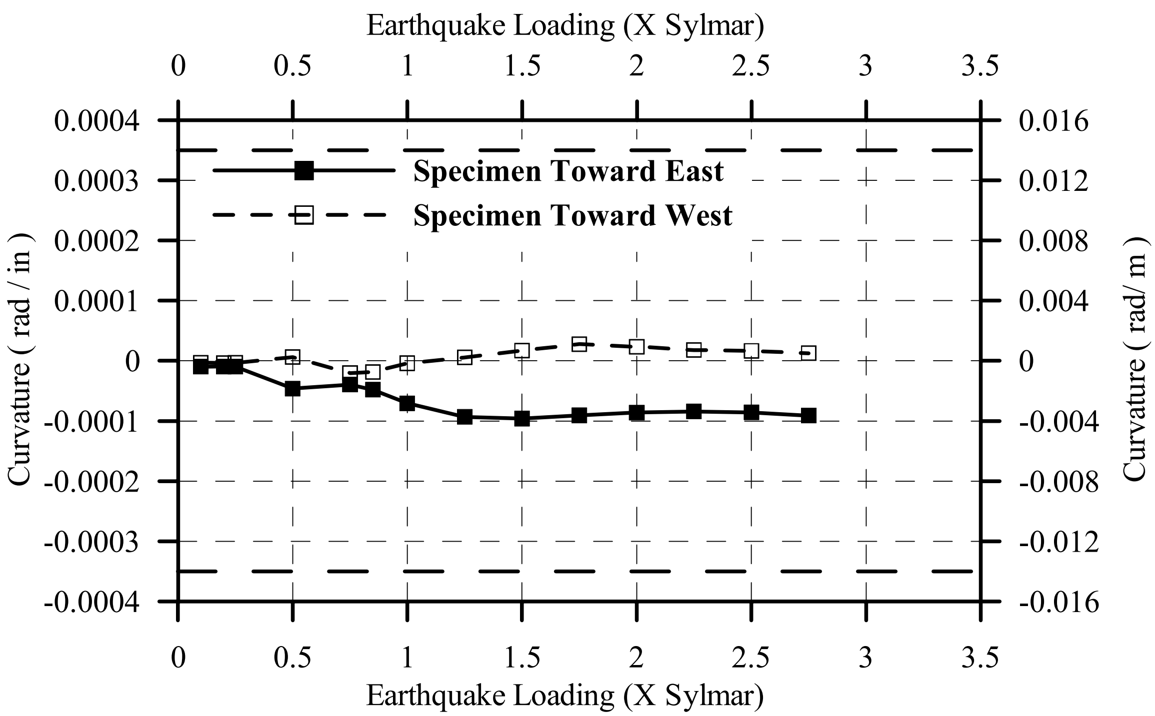

Fig. 4-168: Max. Curvature of Beam Critical Section on West Side of B2CT

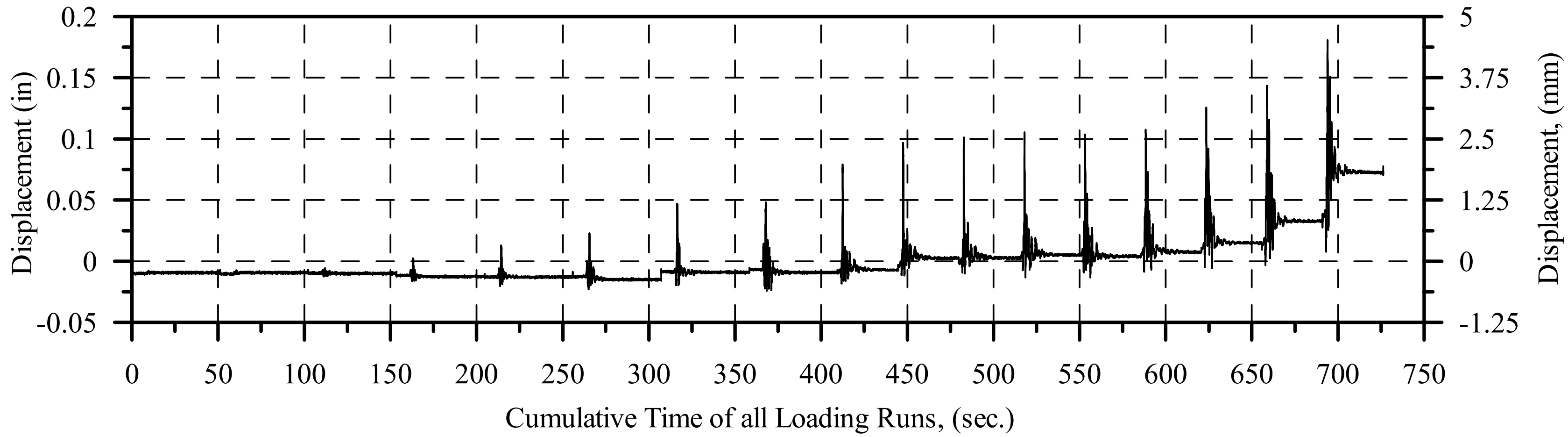

Fig. 4-169: Measured Displacement History in the Out-of-Plane Direction in Specimen B2CS

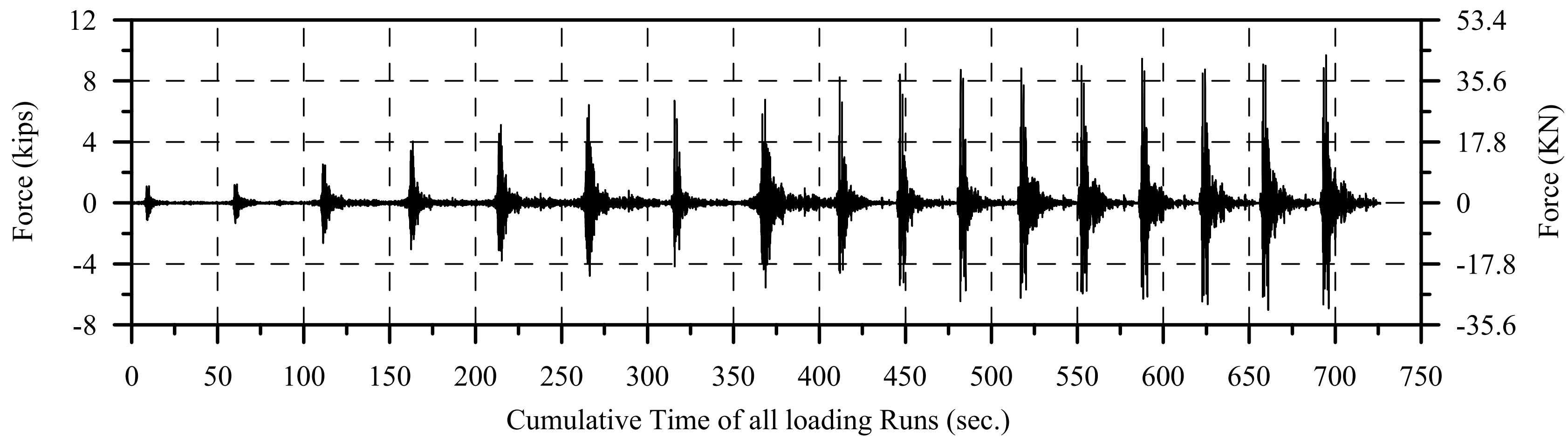

Fig. 4-170: Measured Resisting Force History in the Out-of-Plane Direction of Specimen B2CS

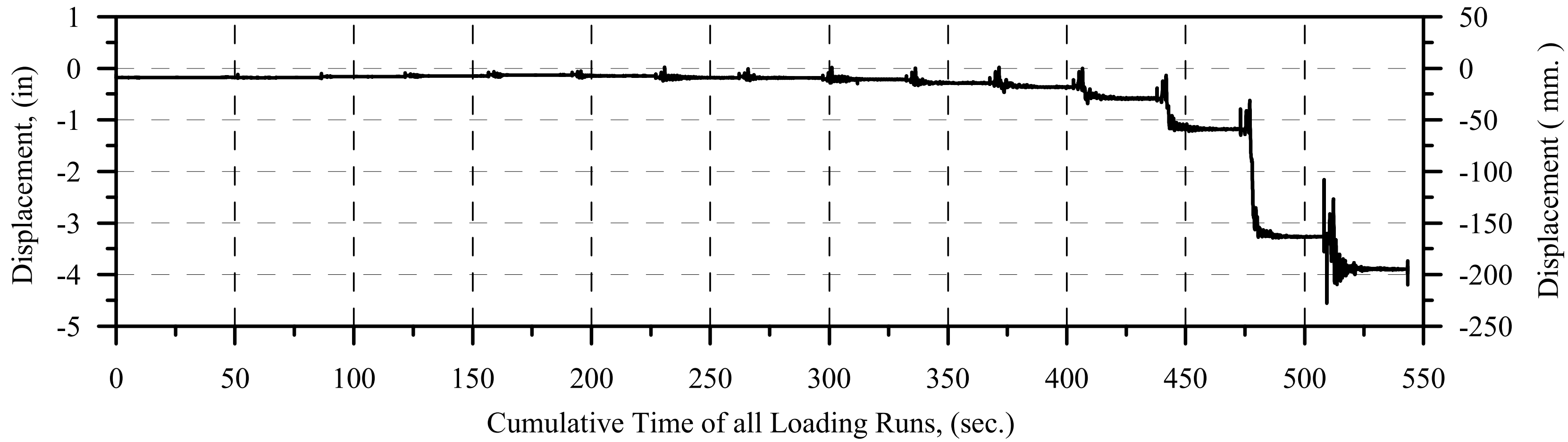

Fig. 4-171: Measured Displacement History in the Out-of_Plane Direction of Specimen B2CM

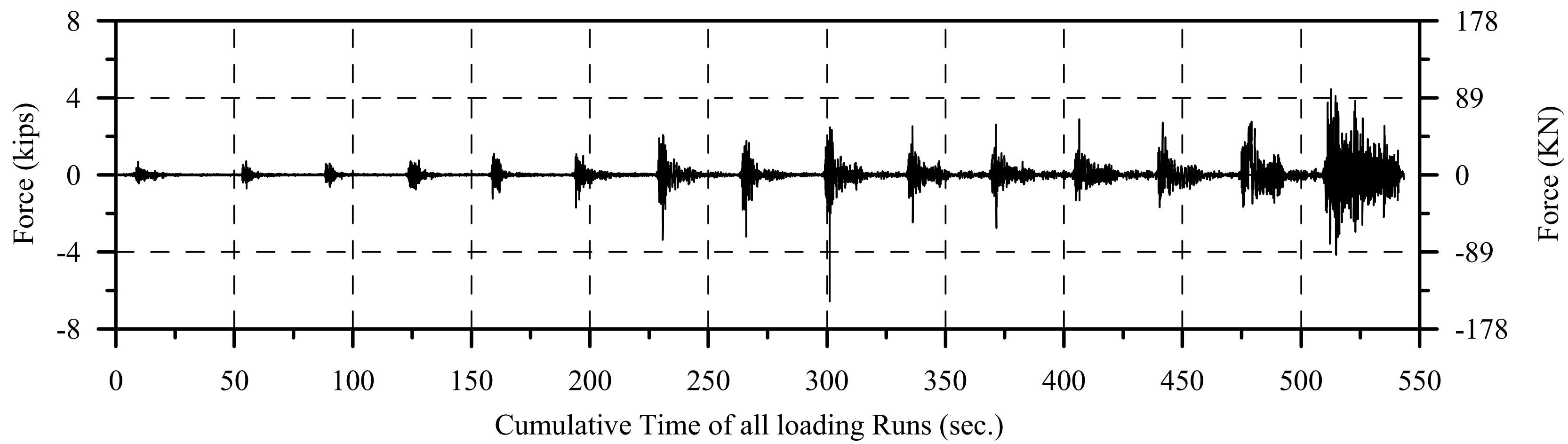

Fig. 4-172: Measured Resisting Force History in the Out-of-Plane Direction of Specimen B2CM

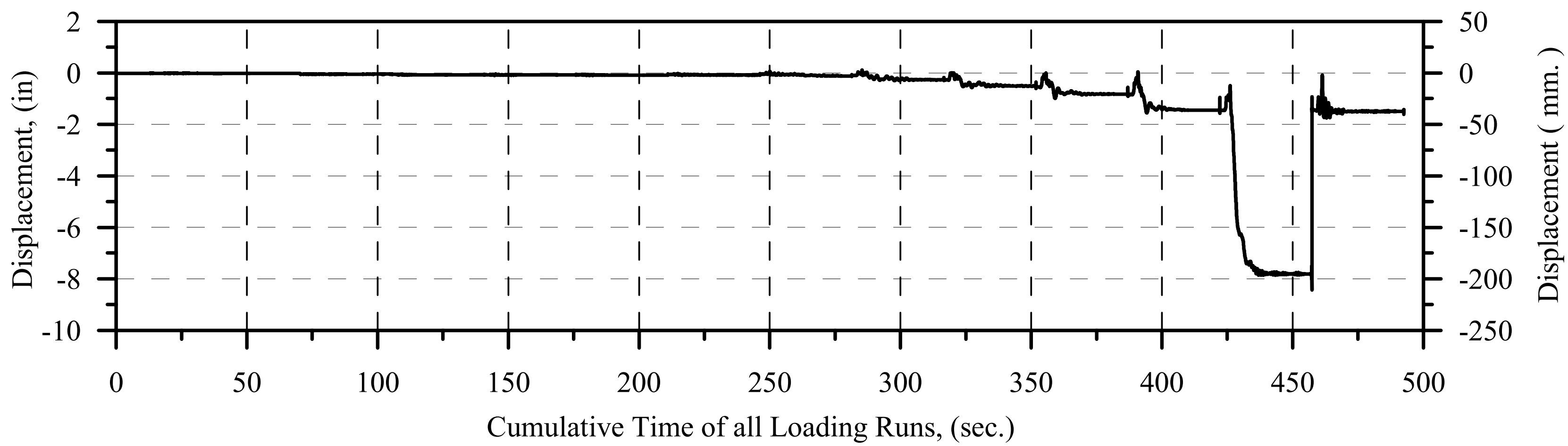

Fig. 4-173: Measured Displacement History in the Out-of-Plane Direction of Specimen B2CT

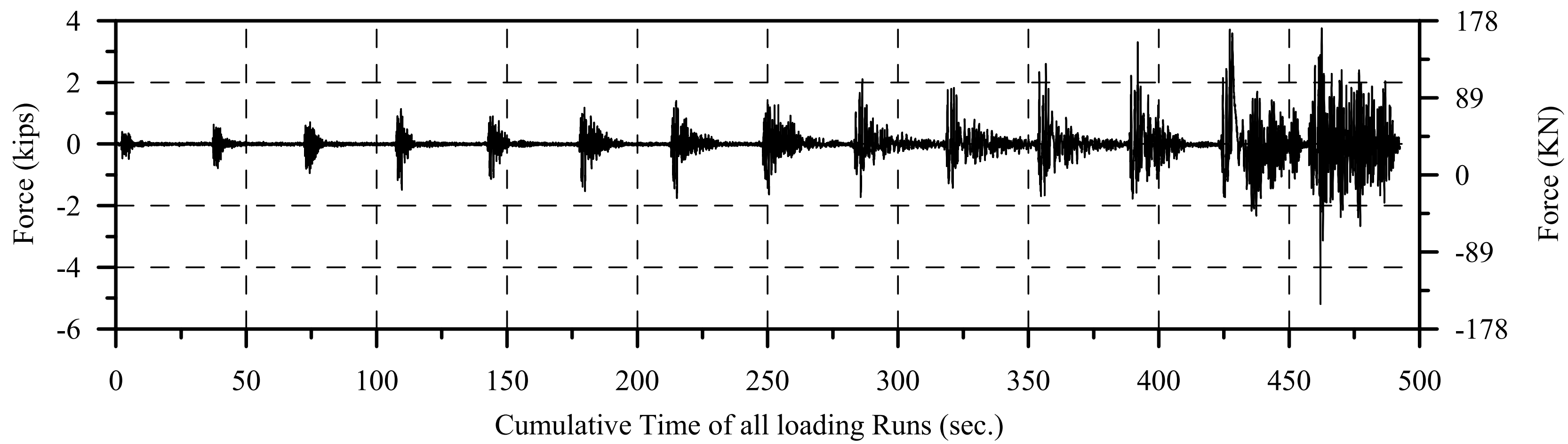

Fig. 4-174: Measured Resisting Force History in the Out-of-Plane Direction of Specimen B2CT

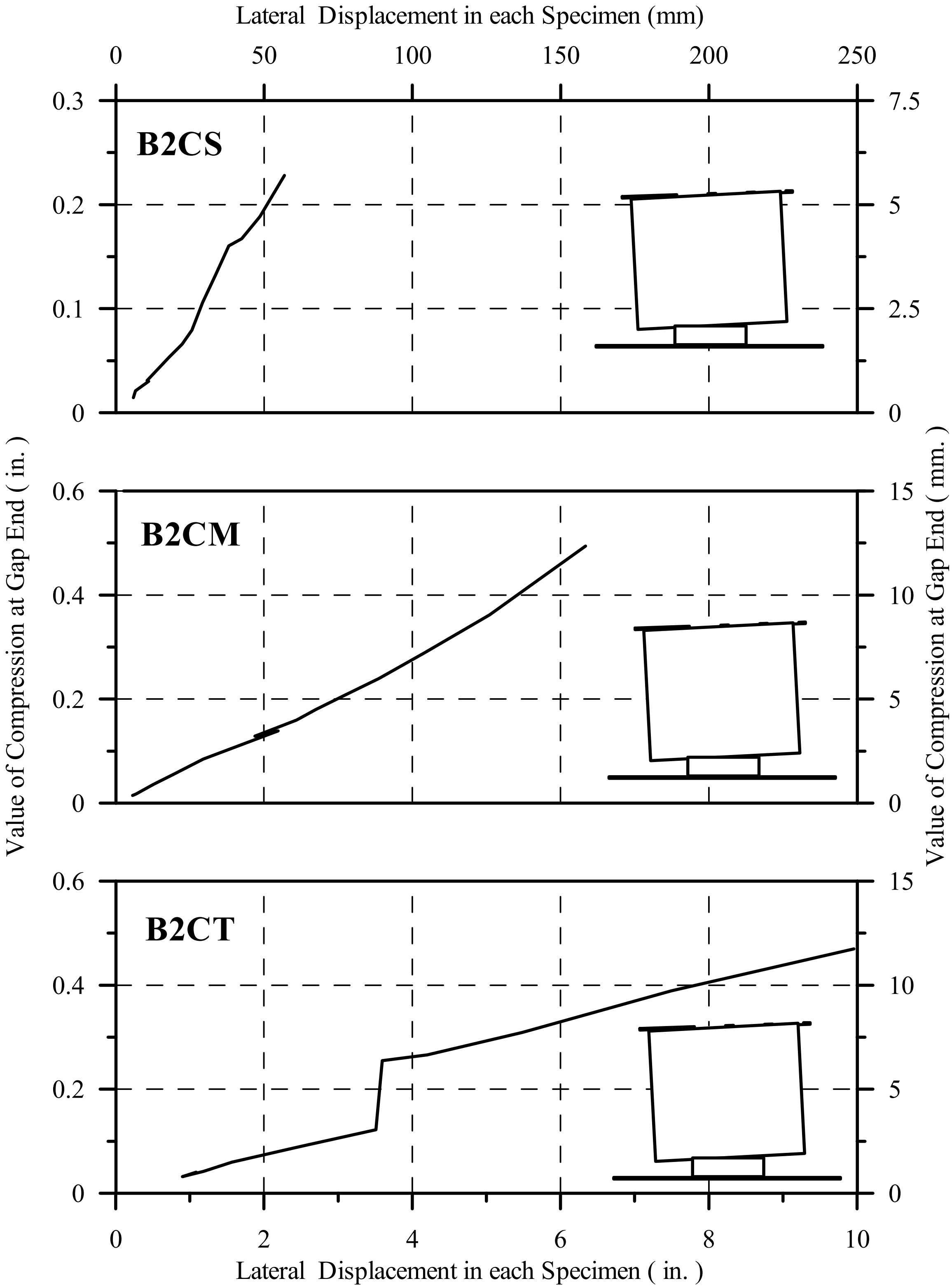

Fig. 4-175: Gap Compression on West Side of West Column Base

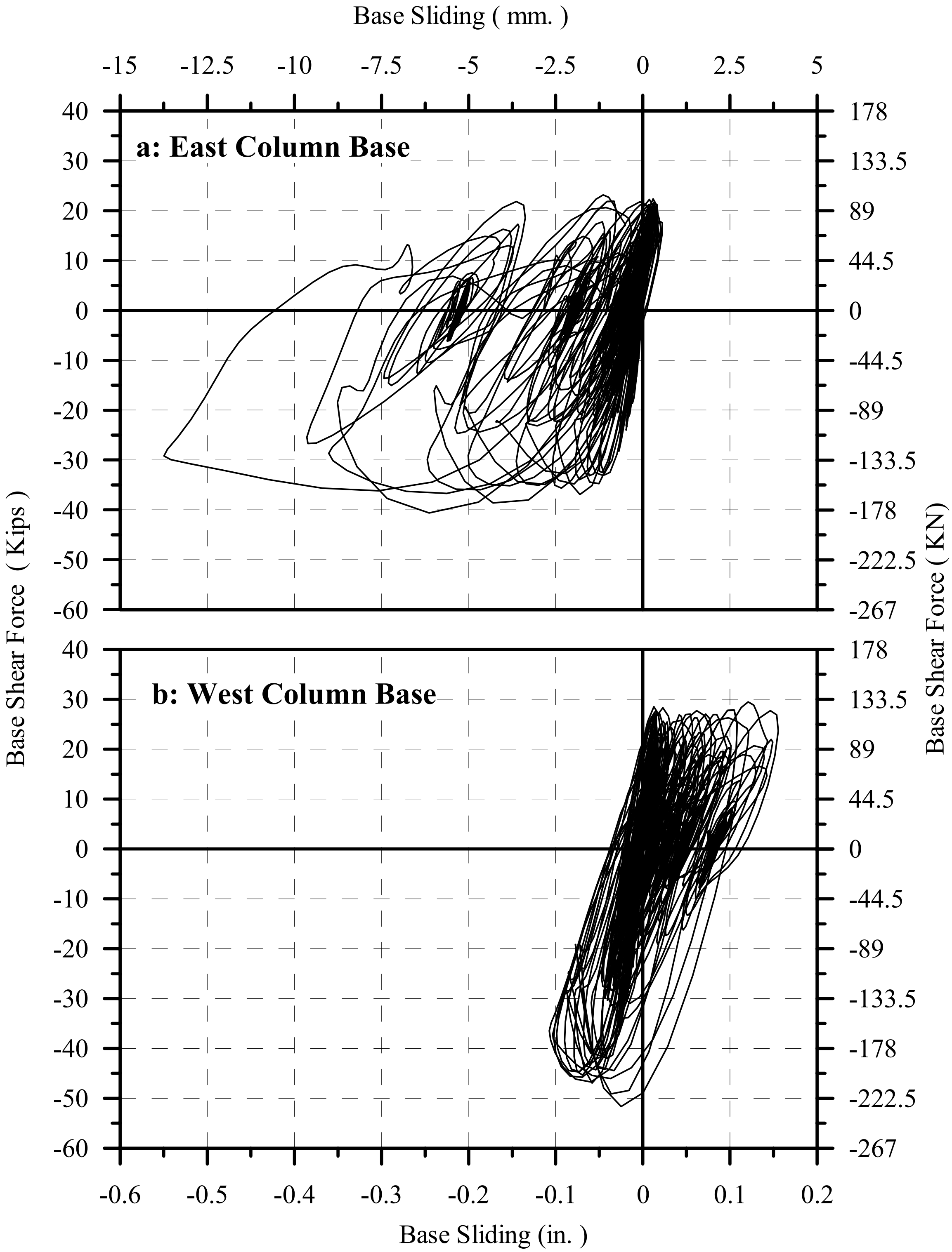

Fig. 4-176: Shear Slippage Hystereses at Column Bases of Short Specimen

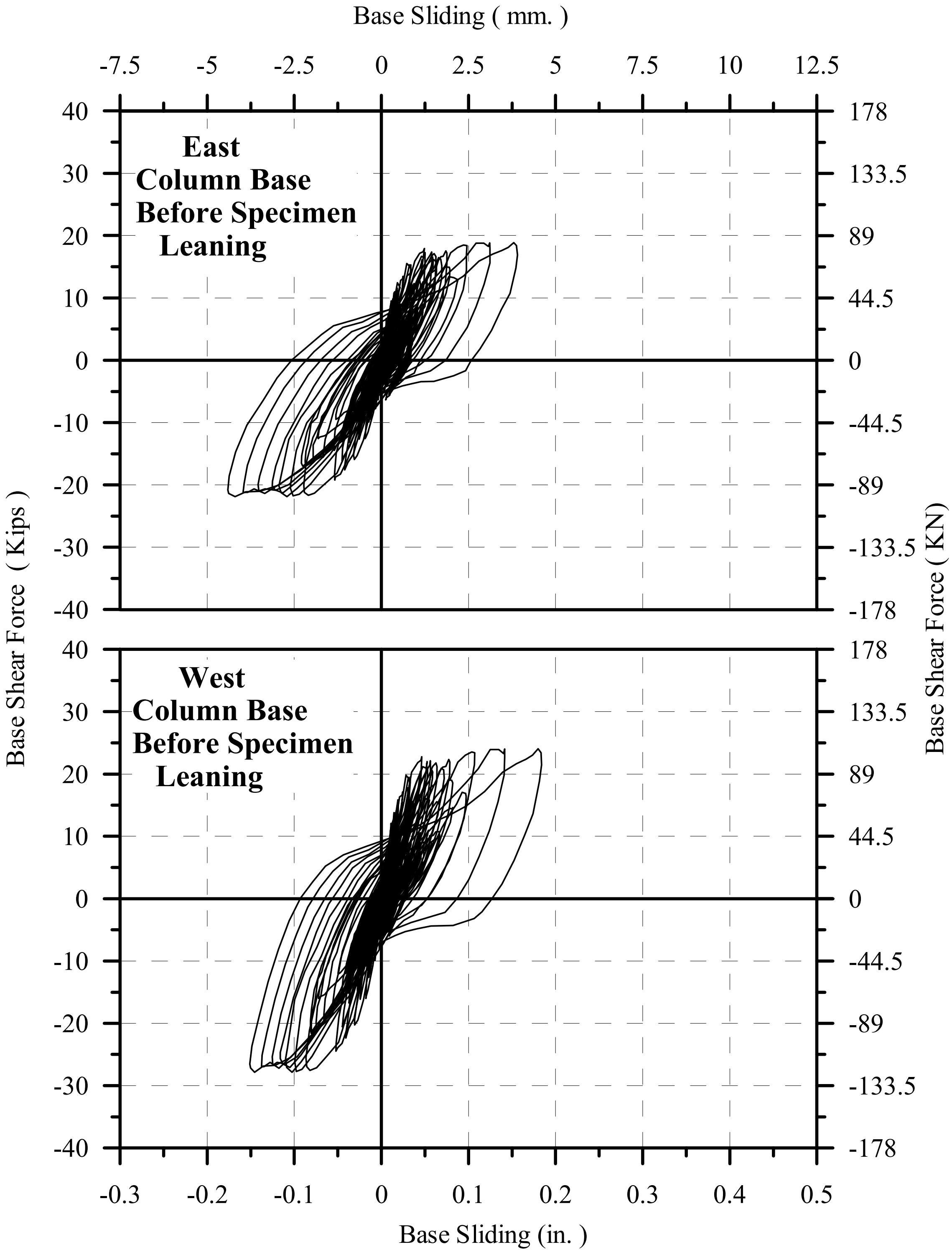

Fig. 4-177: Shear Slippage Hystereses at Column Bases of Medium Specimen

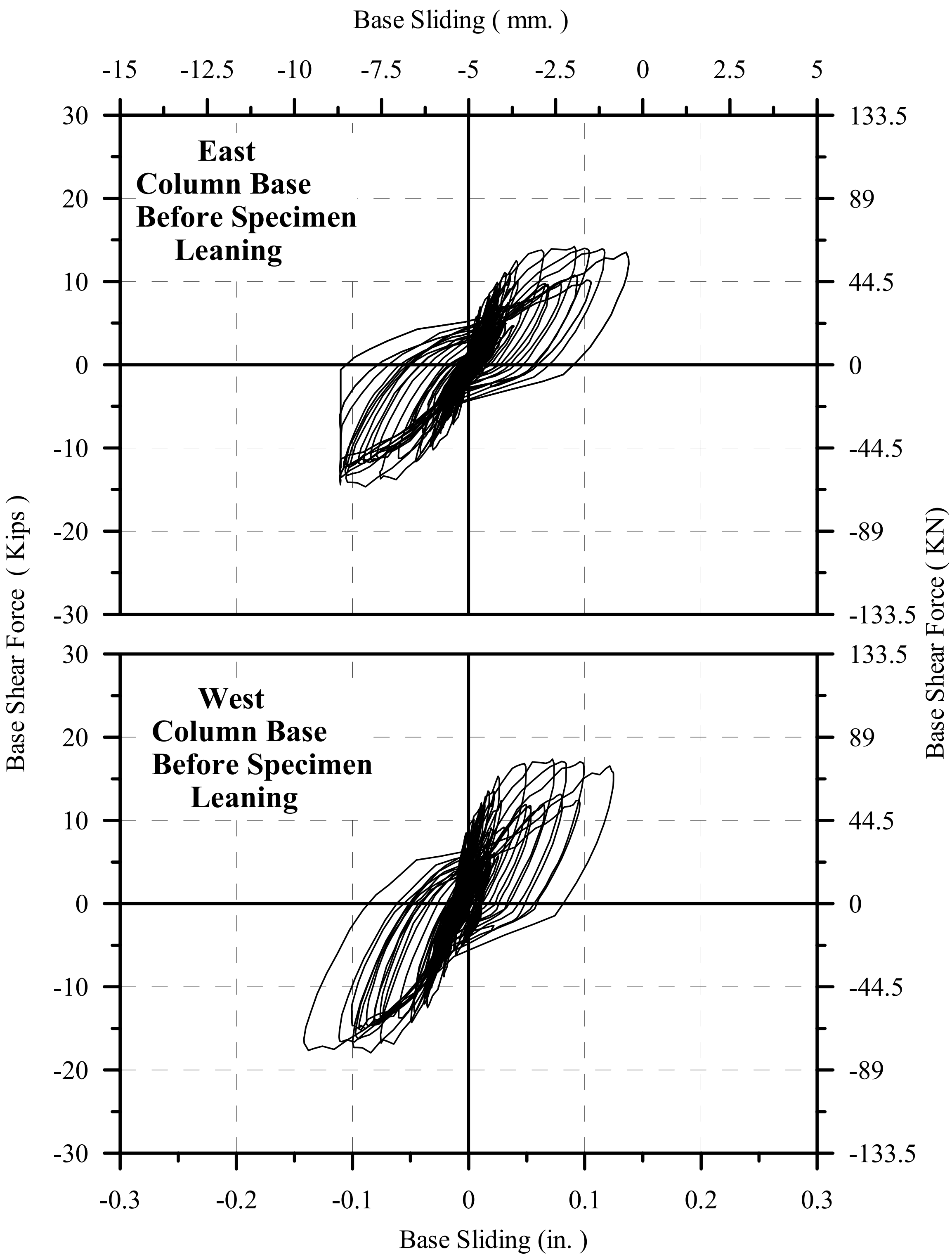

Fig. 4-178: Shear Slippage Hystereses at Column Bases of Tall Specimen

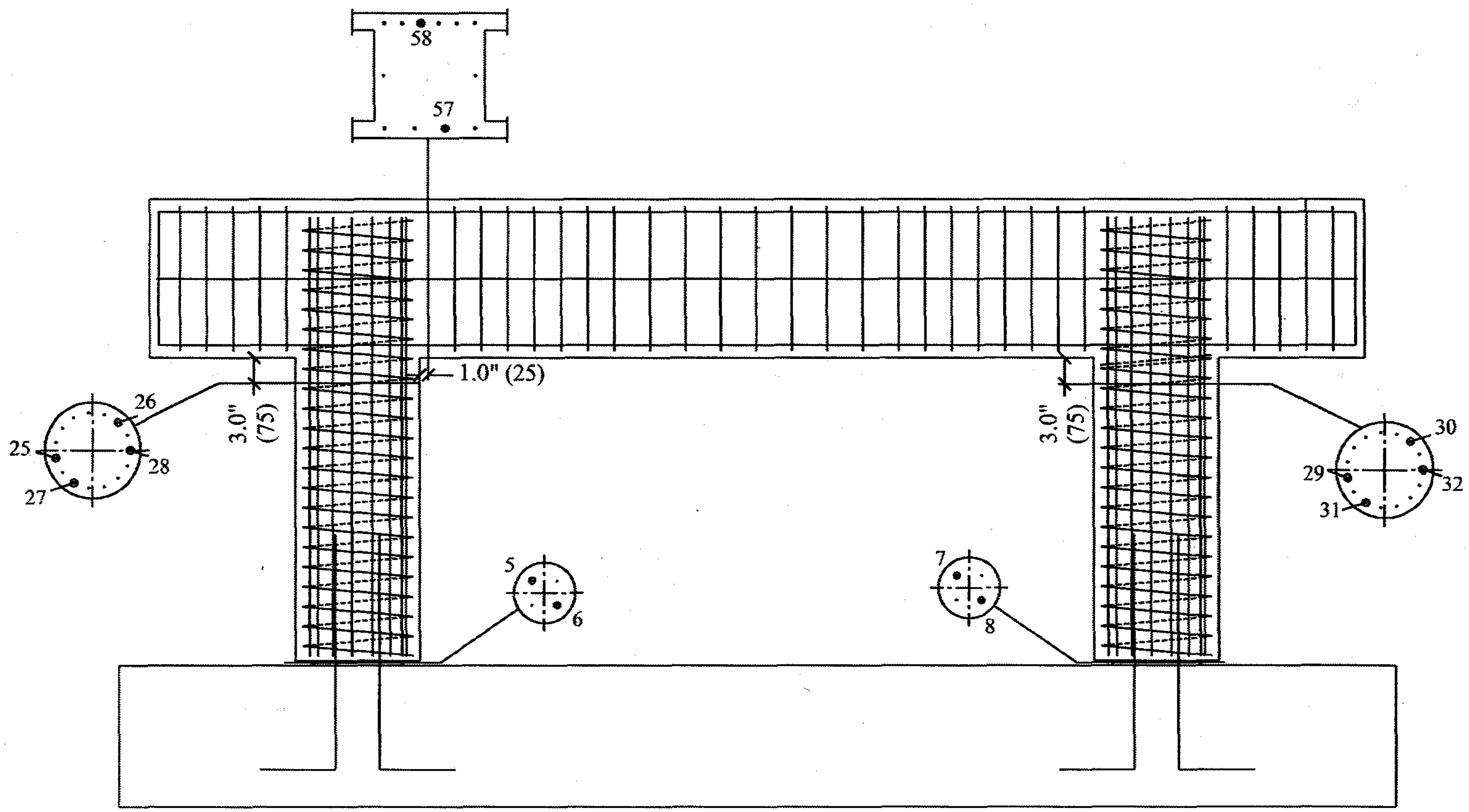

Fig. 5-1: Strain Gages used in Strain-Rate Effect Calculations in Short Specimen

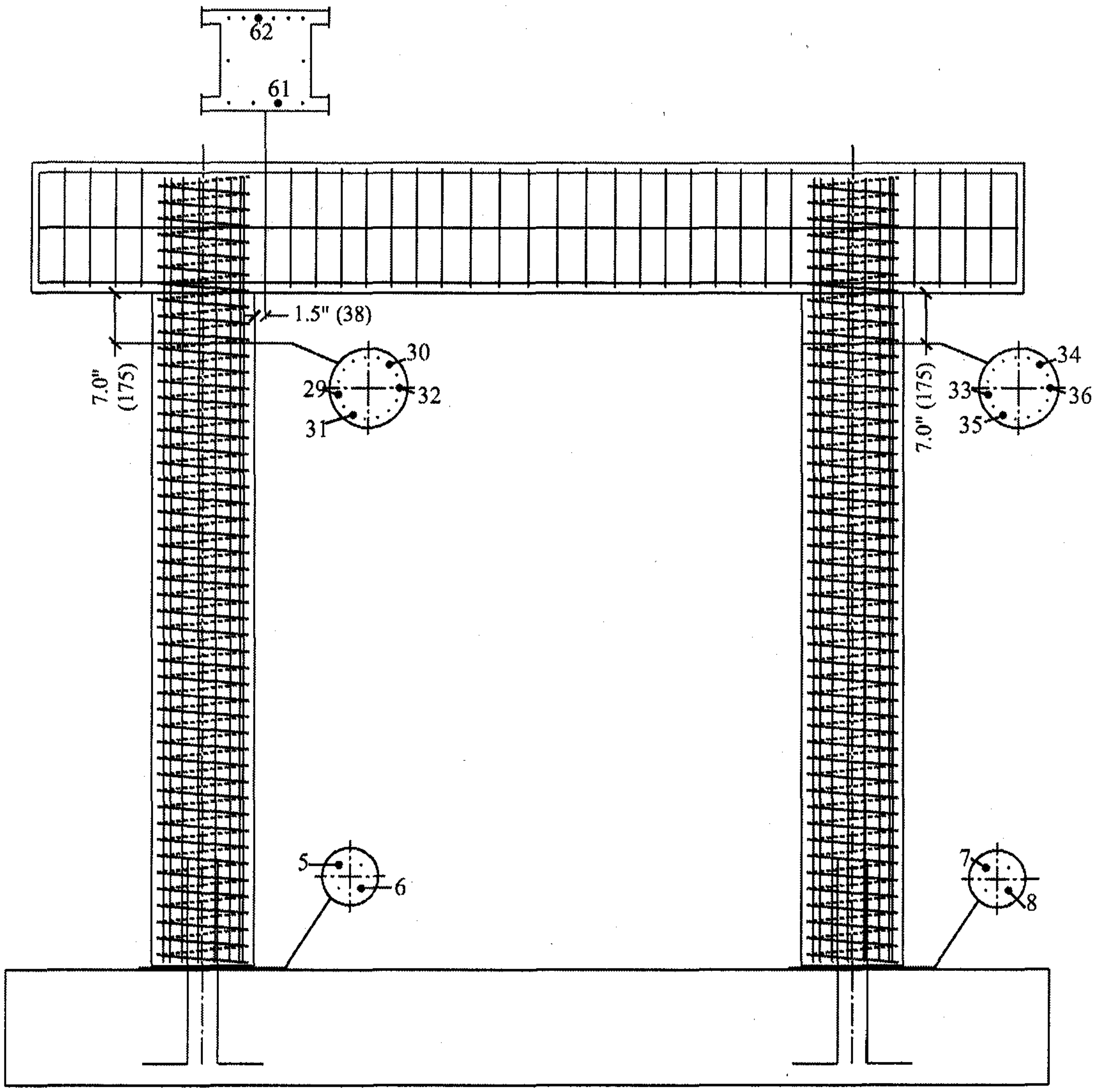

Fig. 5-2: Strain Gages used in Strain-Rate Effect Calculations
in Middle and Tall Specimens

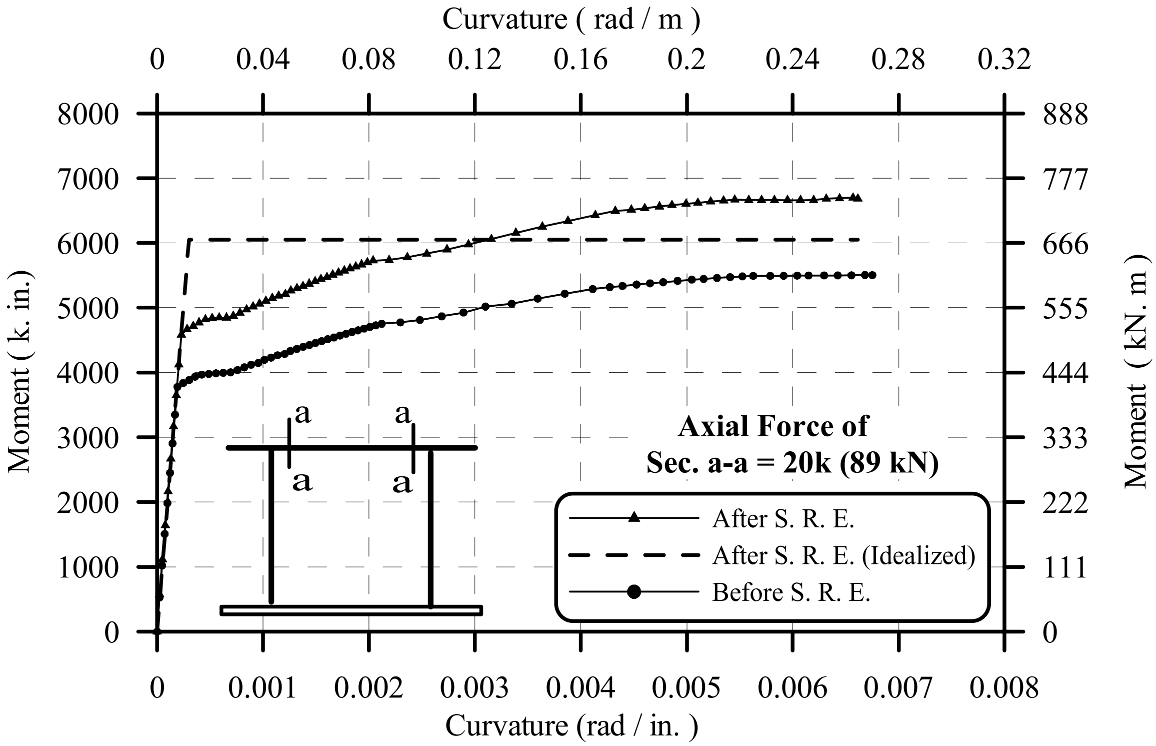

Fig. 5-3a: M-φ Diagram for Sec. a-a of Tall-Specimen Beam

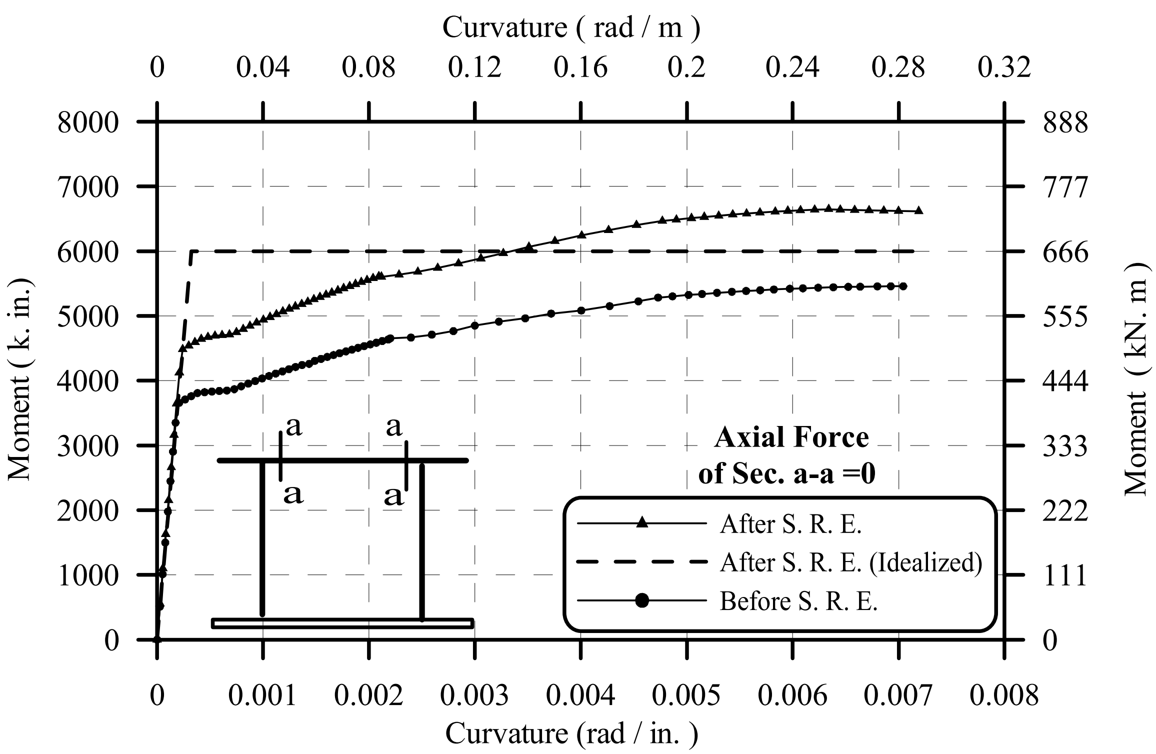

Fig. 5-3b: M-φ Diagram of Sec. a-a of Tall-Specimen Beam

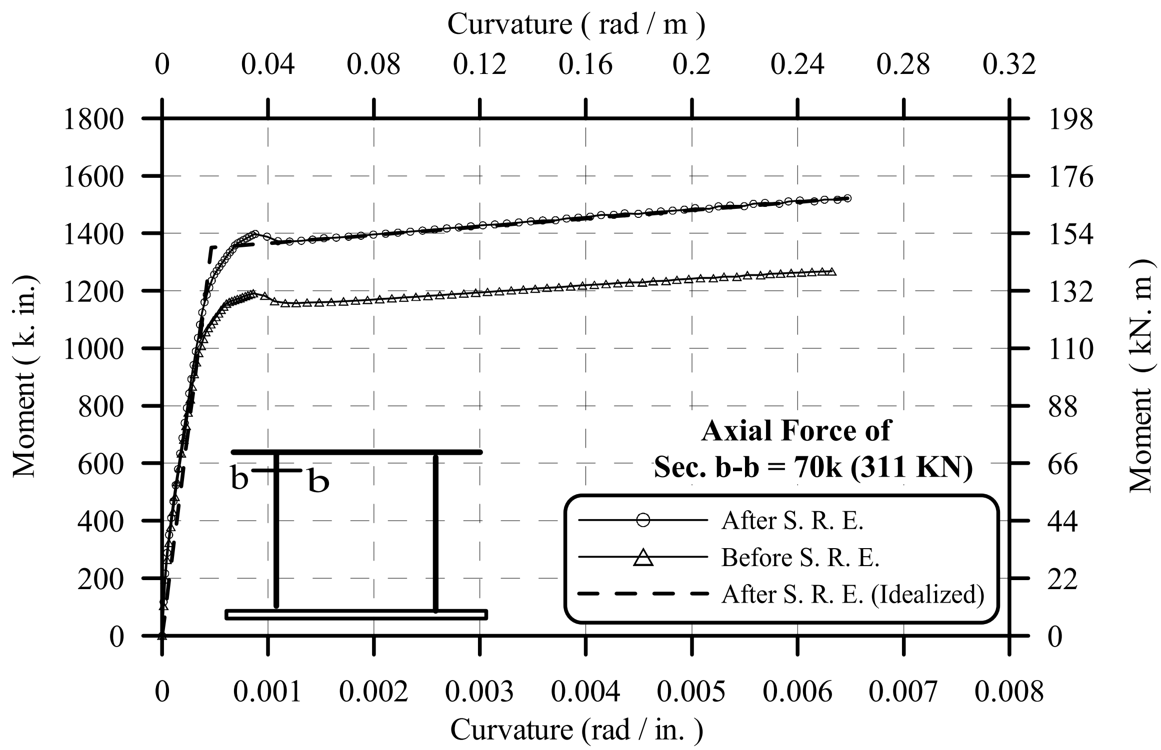

Fig. 5-4a: M-φ Diagram for Sec. b-b of Tall-Specimen Column

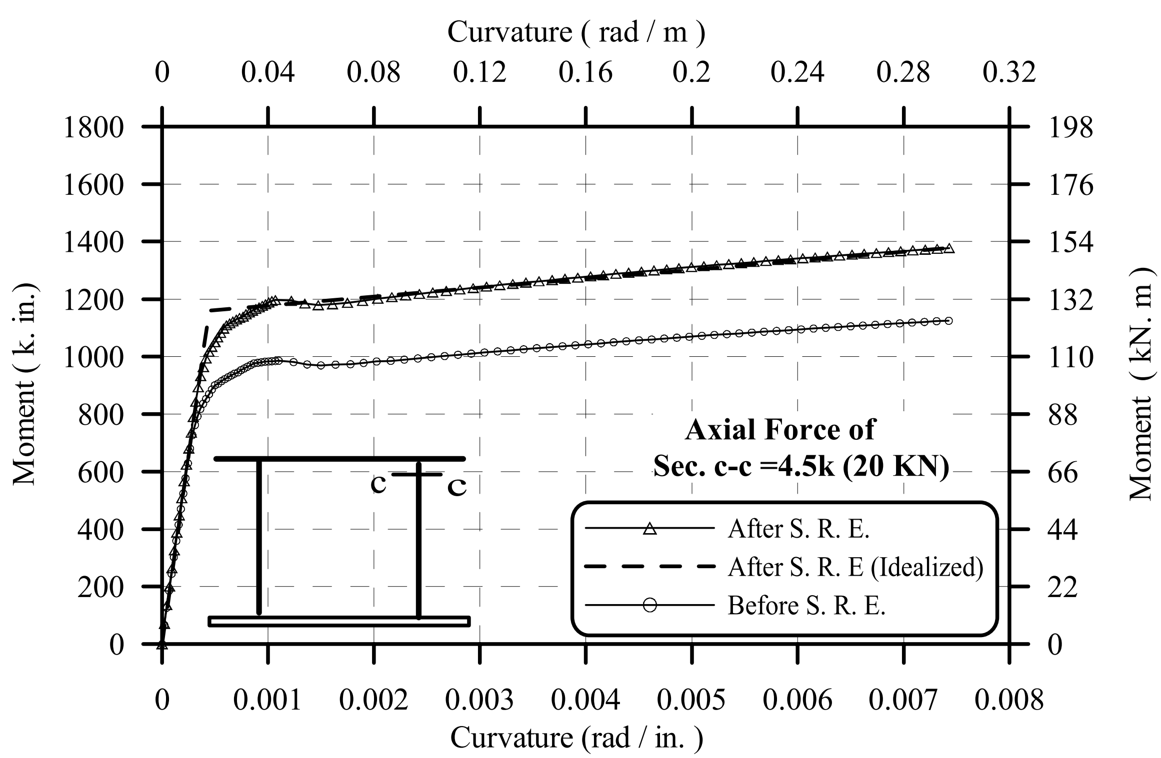

Fig. 5-4b: M-φ Diagram of Sec. c-c of Tall-Specimen Column

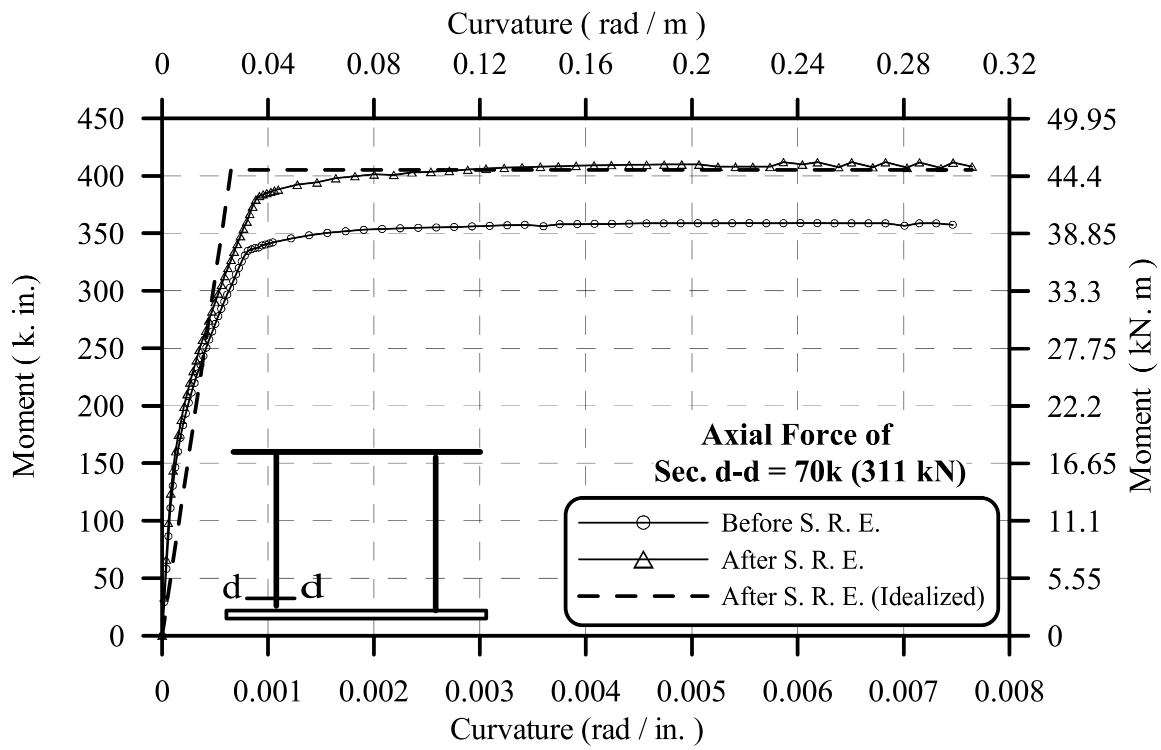

Fig. 5-5a: M-φ Diagram for Sec. d-d of Tall-column Hinge base

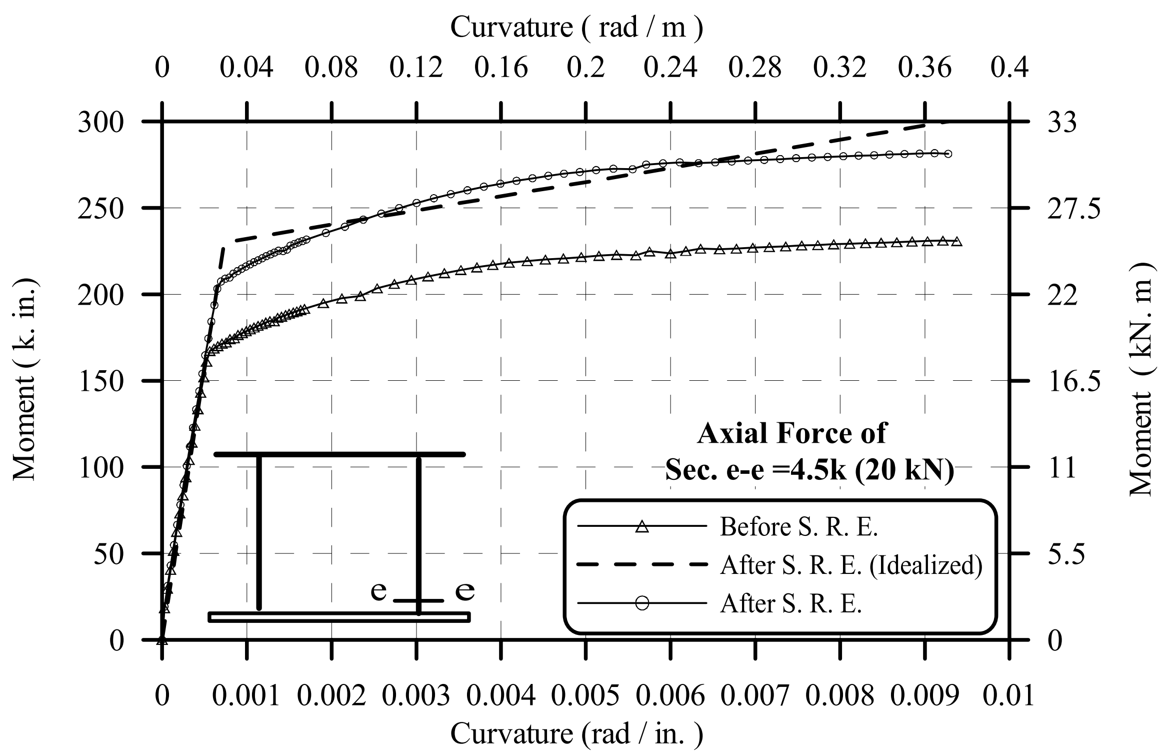

Fig. 5-5b: M-φ Diagram of Sec. e-e of Tall-Column Hinge Base

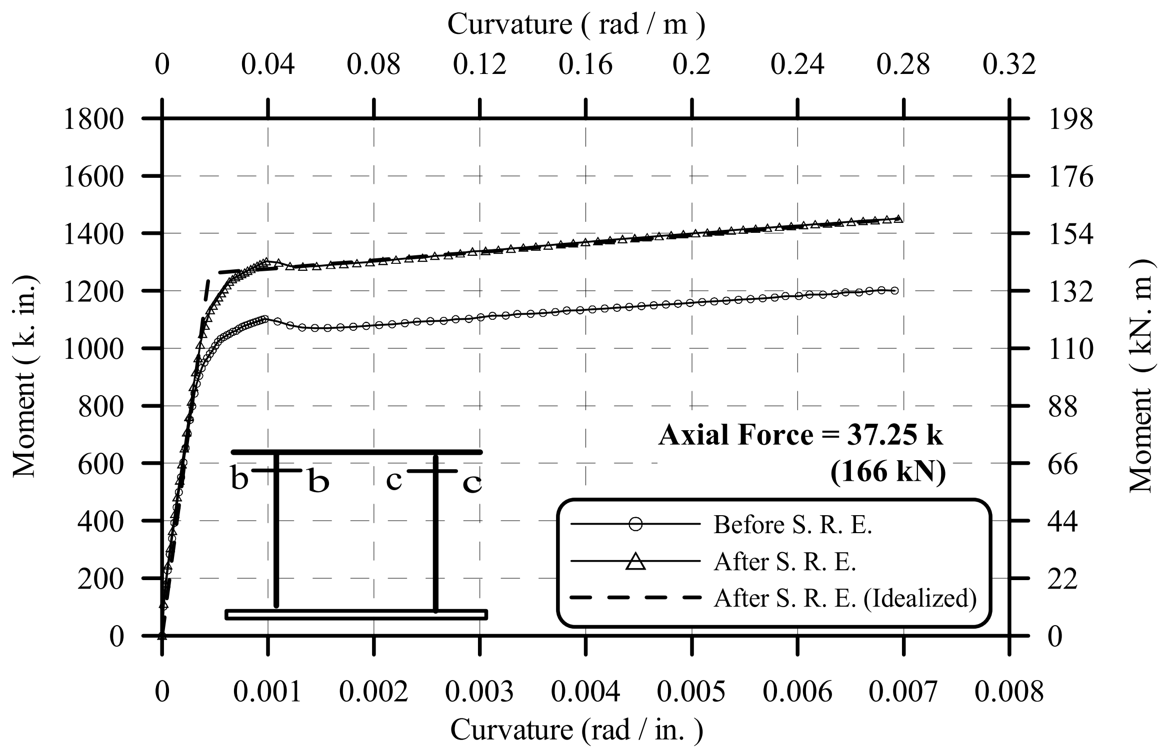

Fig. 5-6a: M-φ Diagram for Sec. b-b and c-c of Tall-Specimen Column

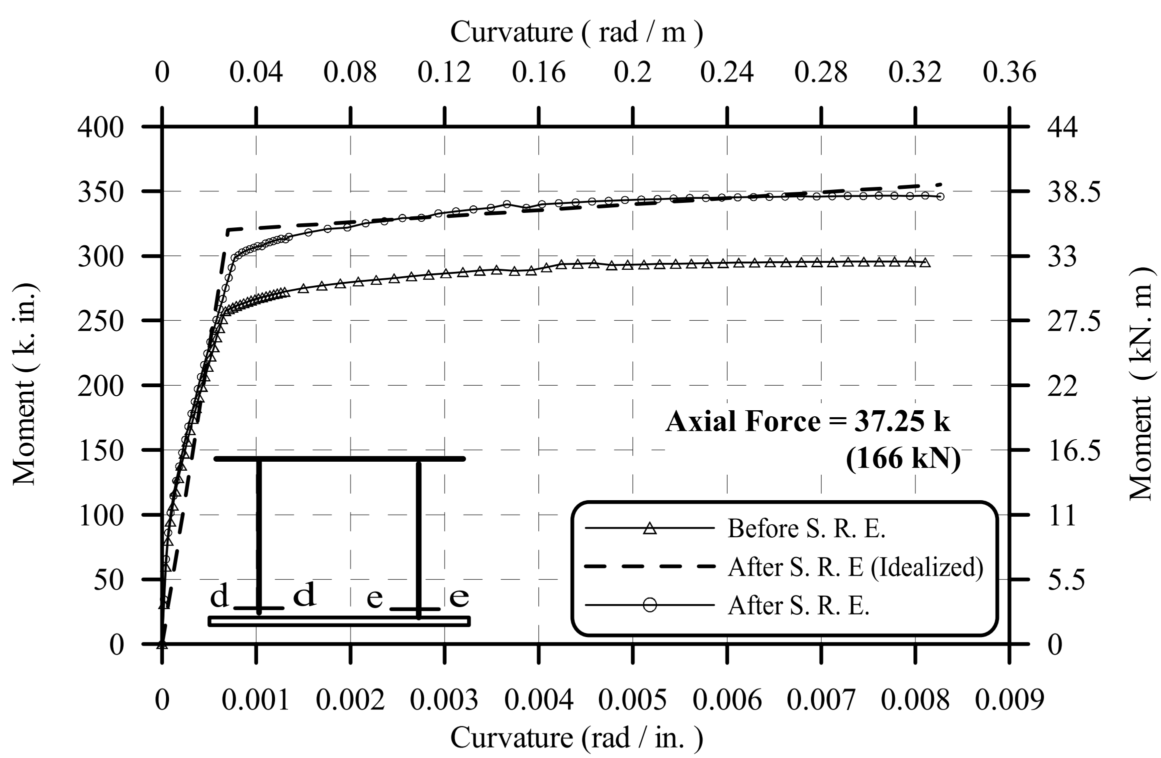

Fig. 5-6b: M-φ Diagram of Sec. d-d and e-e of Tall-Column Base Hinge

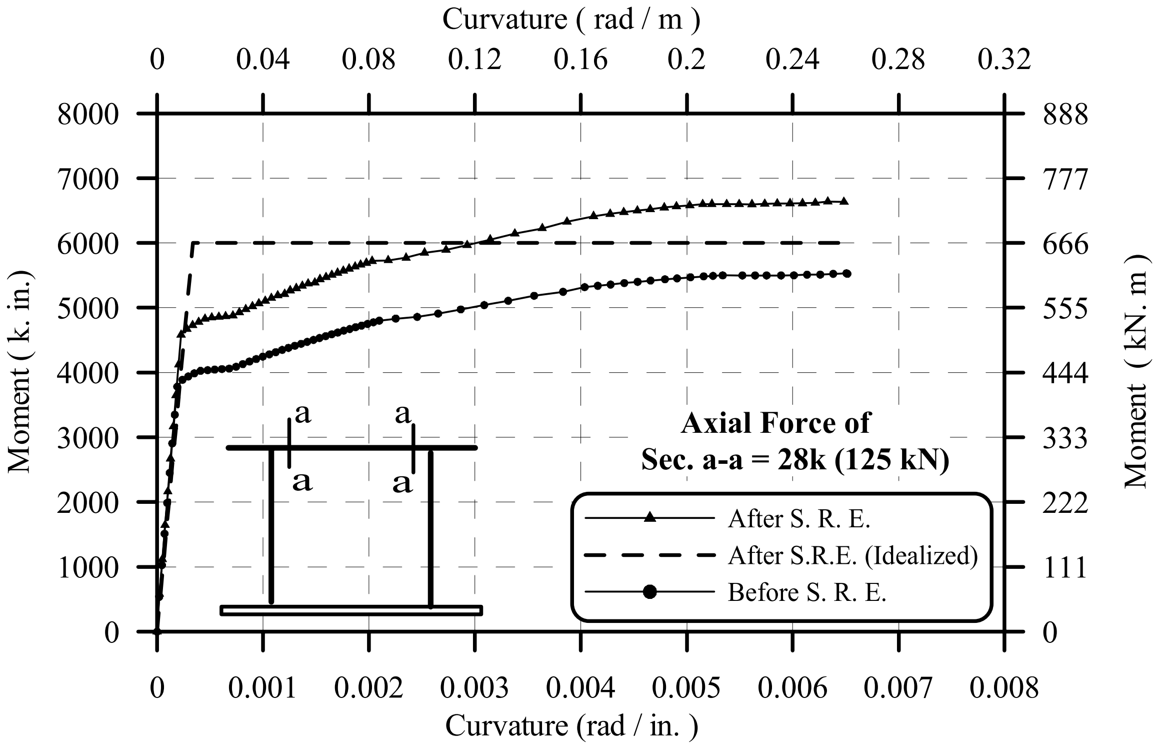

Fig. 5-7a: M-φ Diagram for Sec. a-a of Middle-Specimen Beam

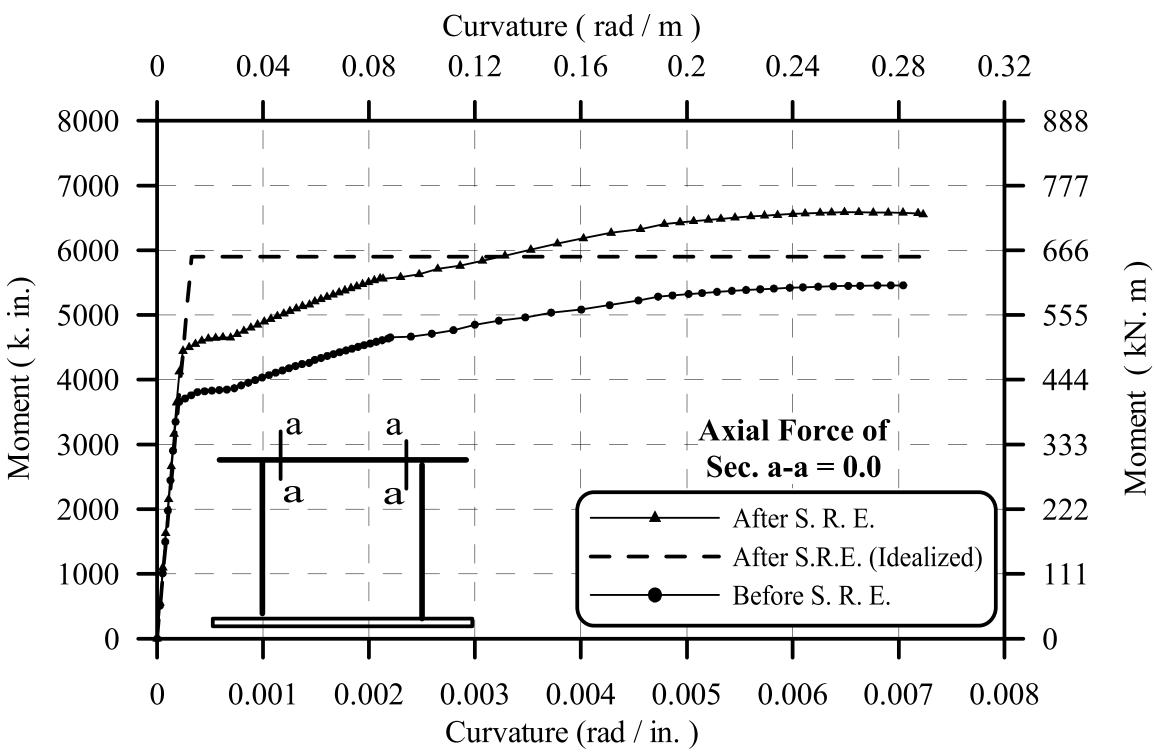

Fig. 5-7b: M-φ Diagram of Sec. a-a of Middle-Specimen Beam

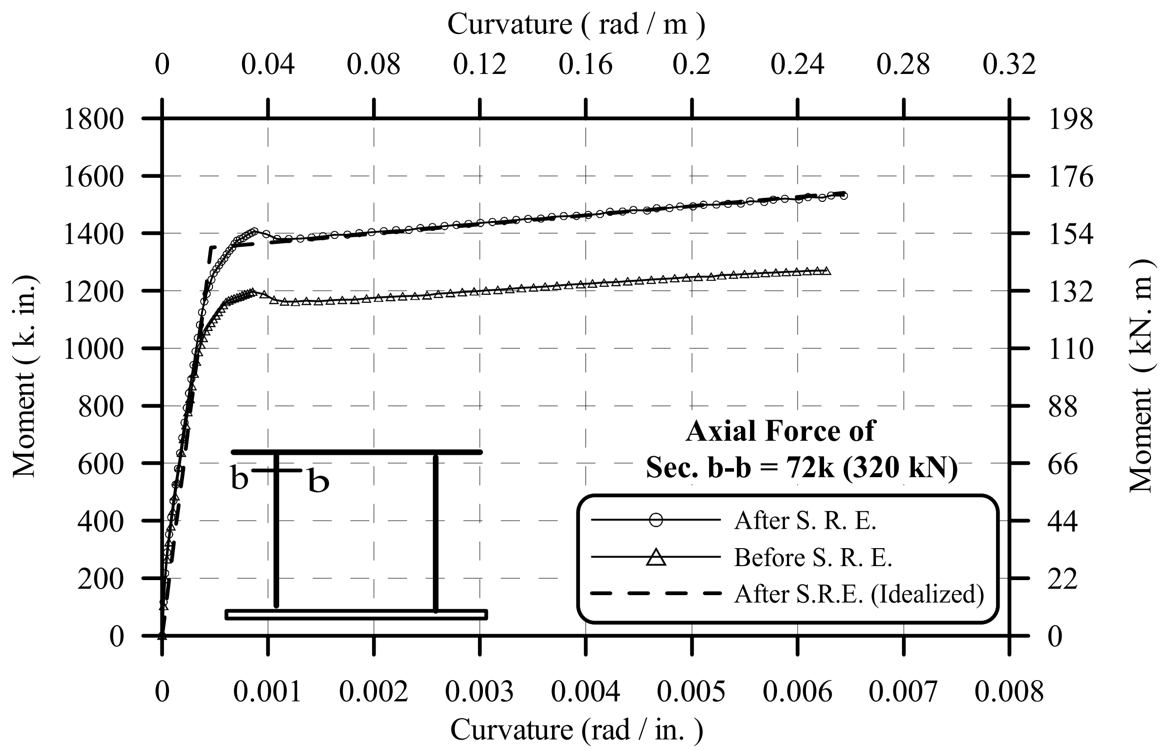

Fig. 5-8a :M-φ Diagram for Sec. b-b of Middle-Specimen Column

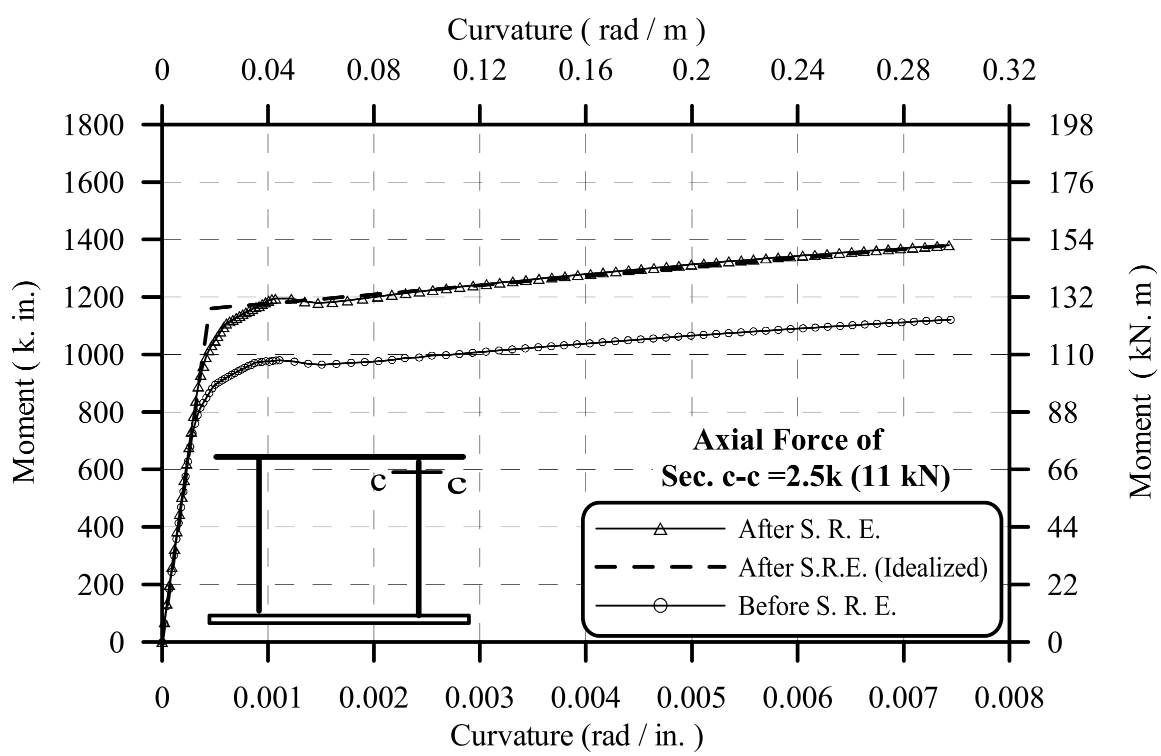

Fig. 5-8b :M-φ Diagram of Sec. c-c of Middle-Specimen Column

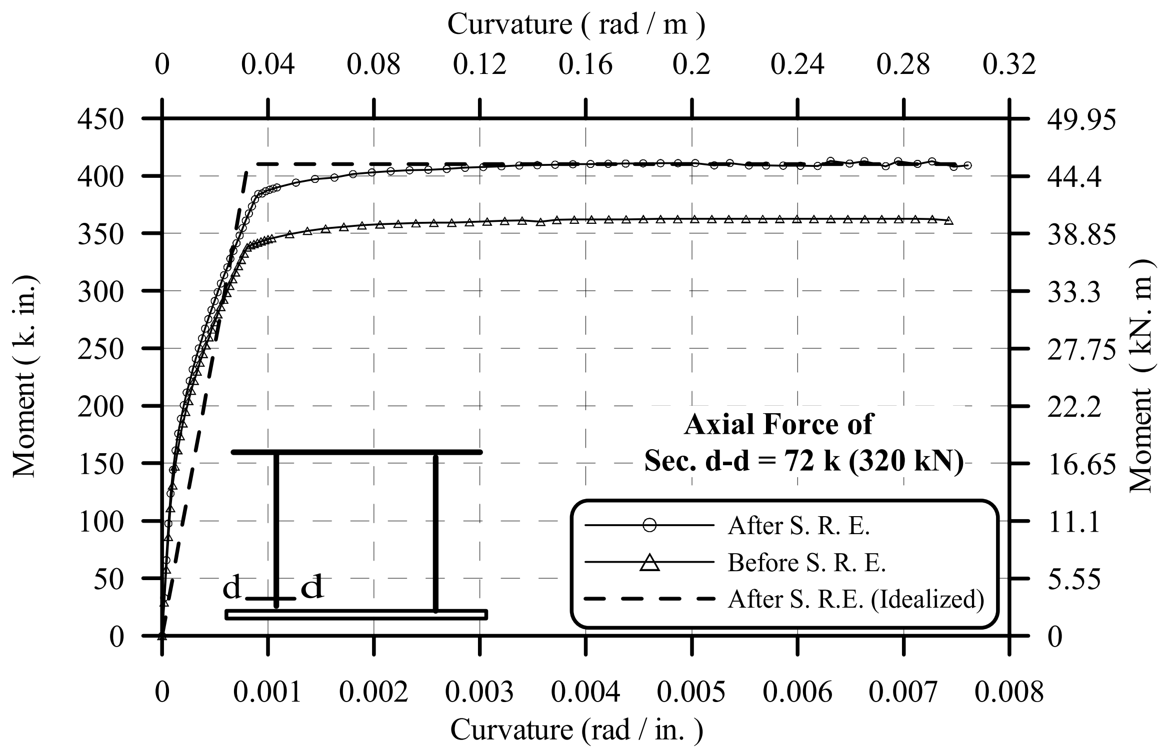

Fig. 5-9a: M-φ for Sec. d-d of Middle-Column Hinge Base

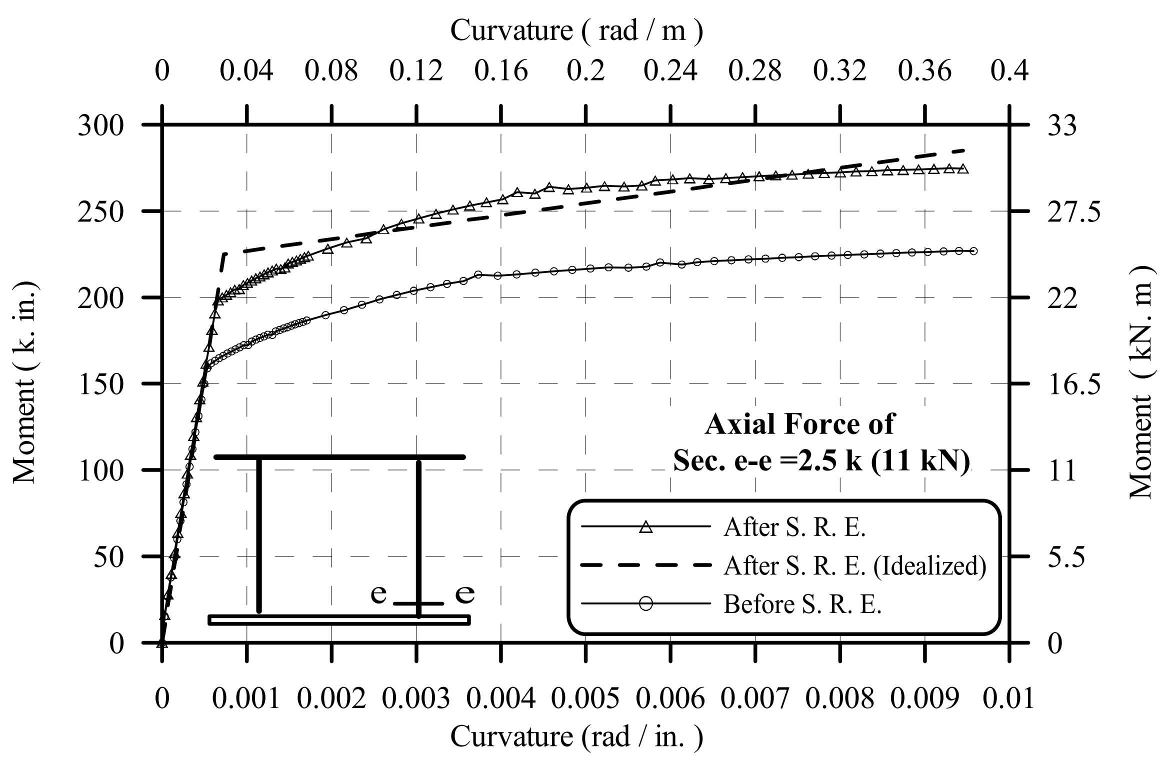

Fig. 5-9b: M-φ of Sec. e-e of Middle-Column Hinge Base

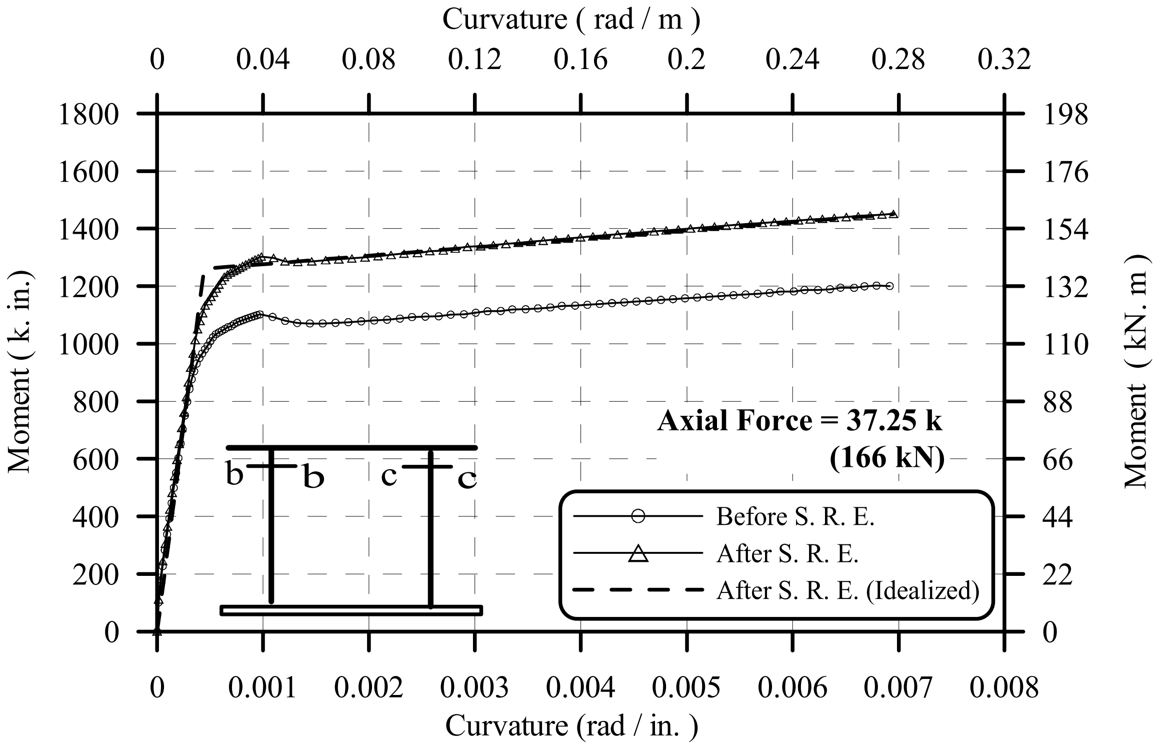

Fig. 5-10a: M-φ Diagram for Sec. b-b and c-c of Middle-Specimen Column

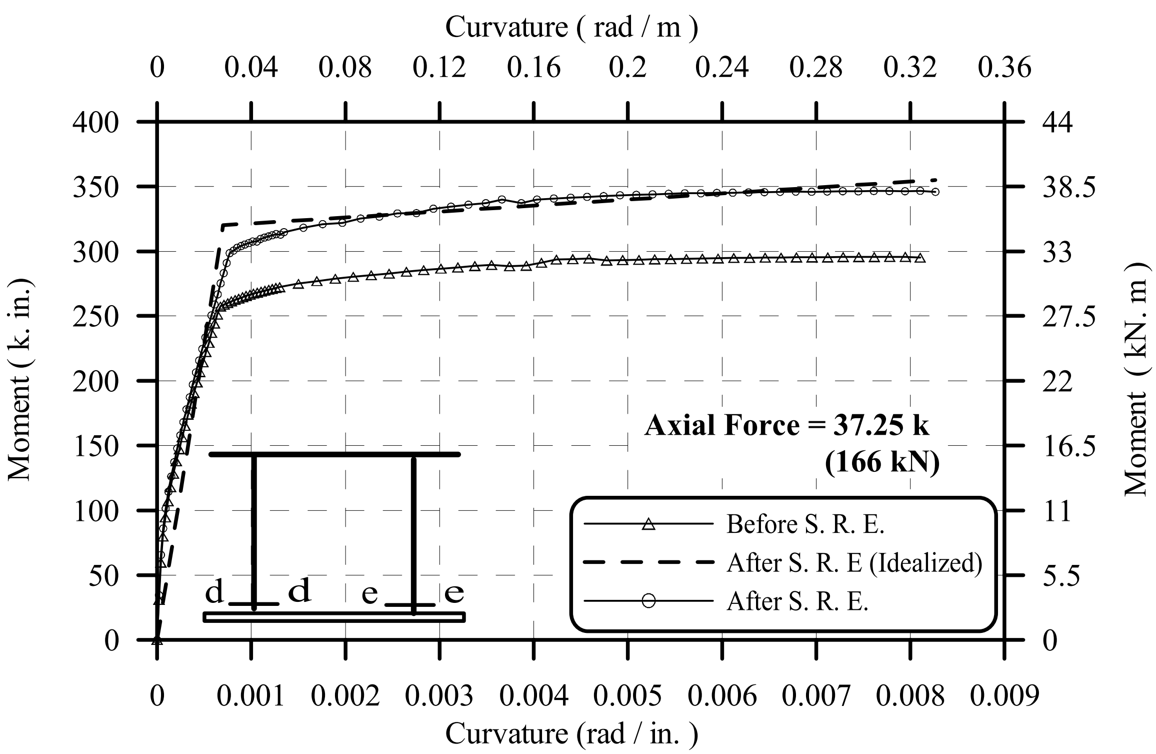

Fig. 5-10b: M-φ Diagram of Sec. d-d and e-e of Middle-Column Base Hinge

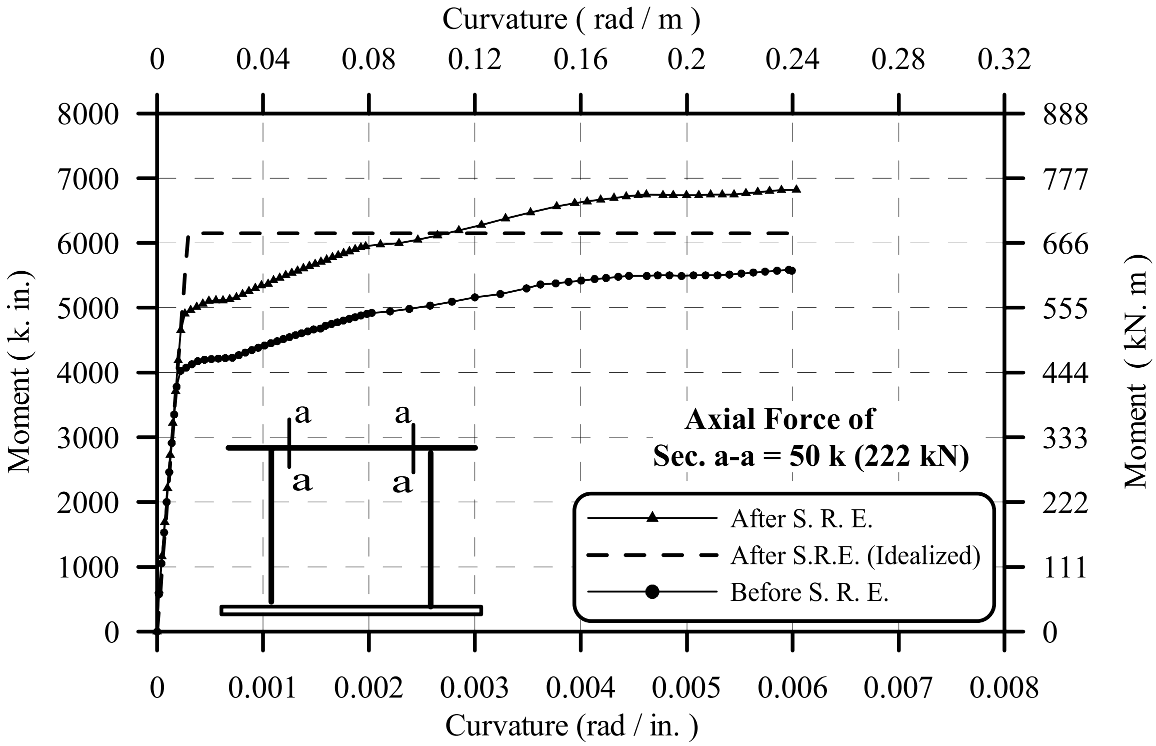

Fig. 5-11a: M-φ Diagram for Sec. a-a of Short-Specimen Beam

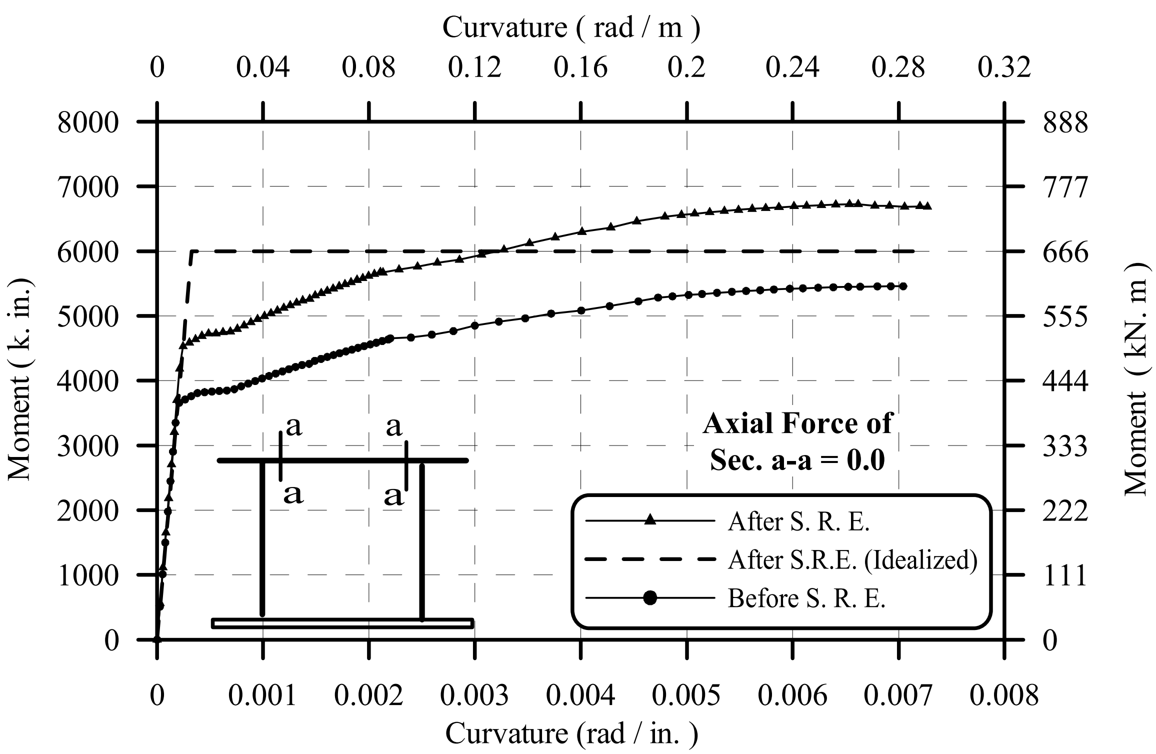

Fig. 5-11b: M-φ Diagram of Sec. a-a of Short-Specimen Beam

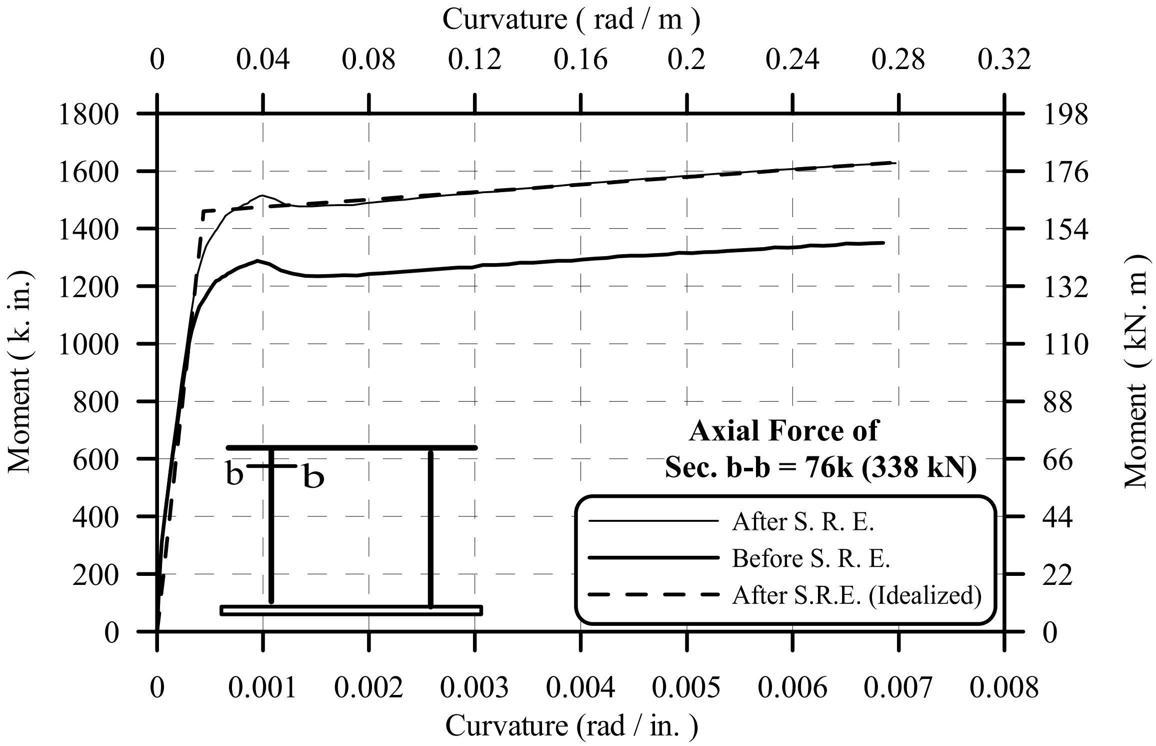

Fig. 5-12a: M-φ Diagram for Sec. b-b of Short-Specimen Column

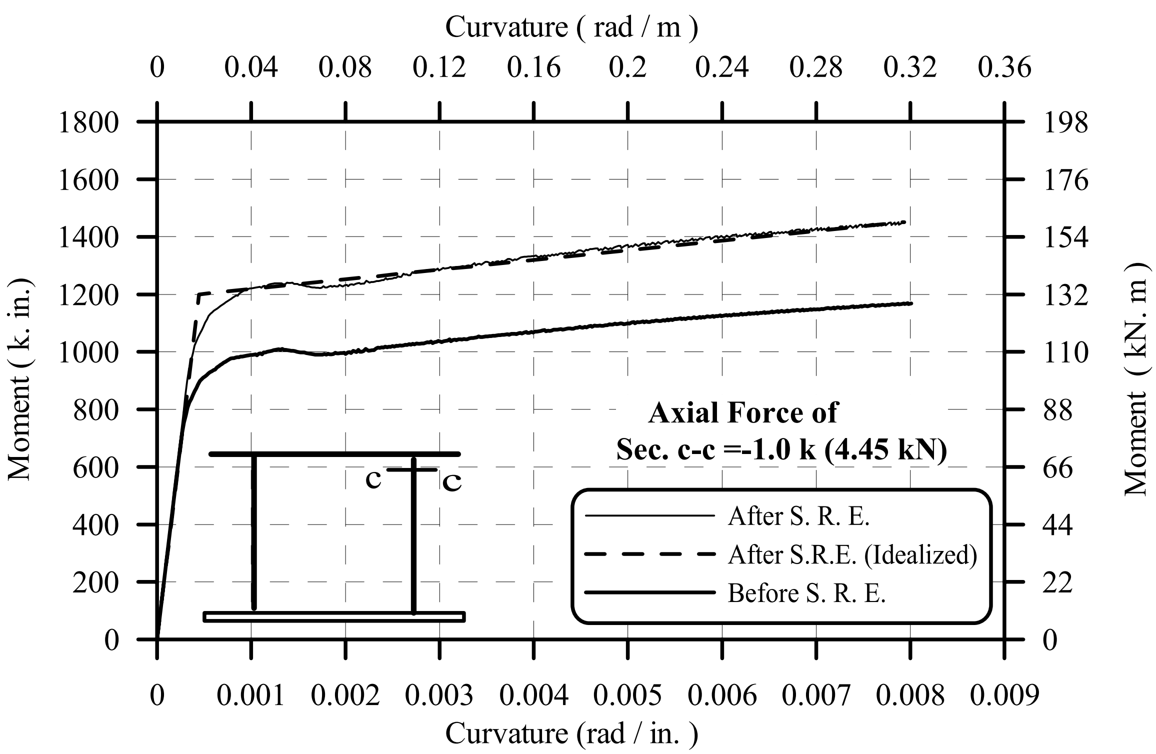

Fig. 5-12b: M-φ Diagram of Sec. c-c of Short-Specimen Column

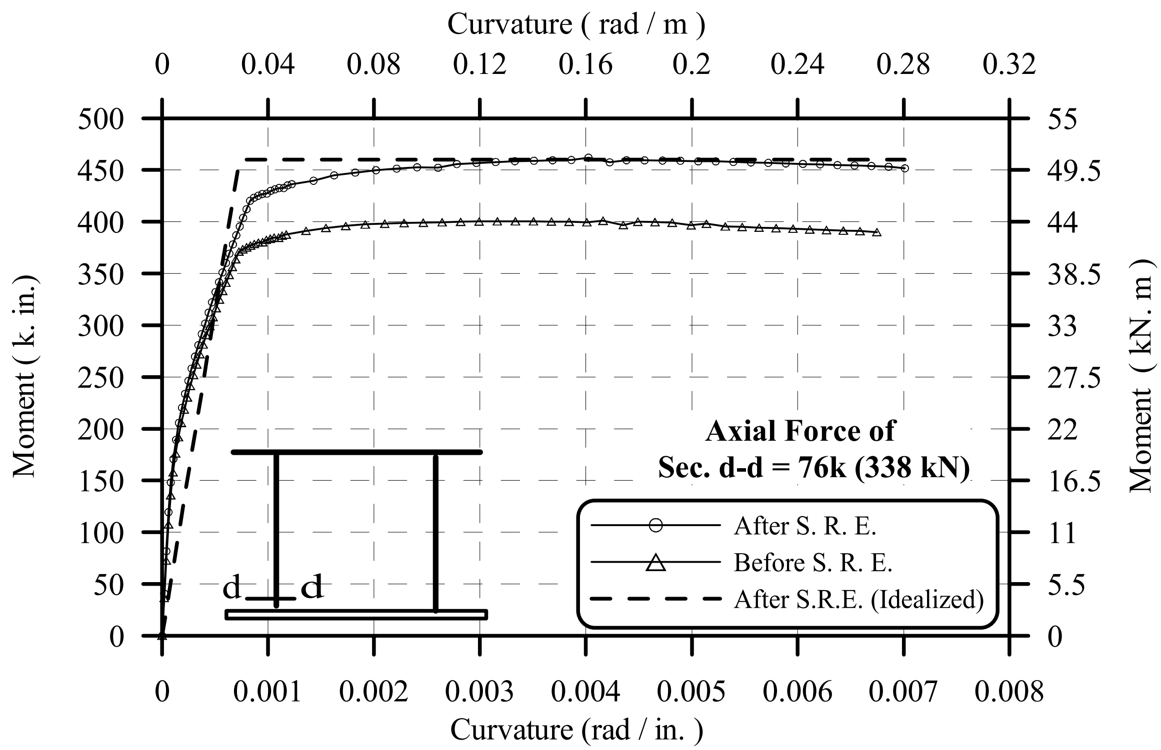

Fig. 5-13a: M-φ Diagram for Sec. d-d of Short-Column Base

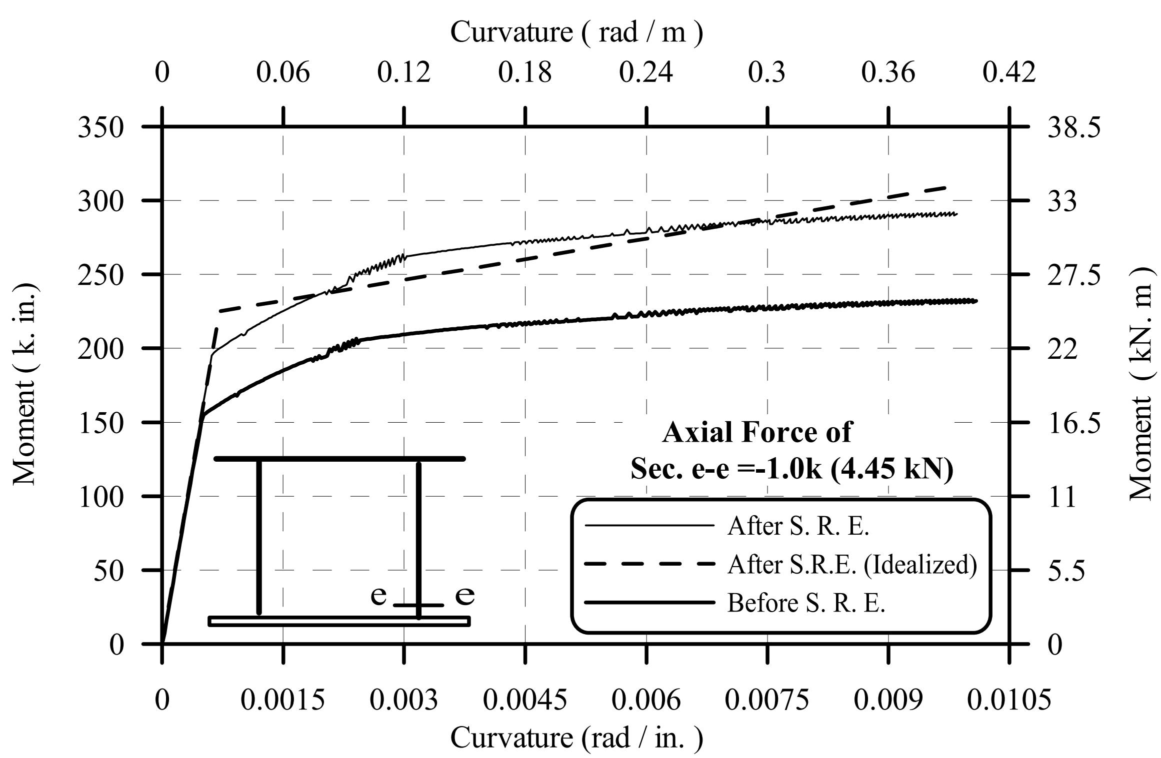

Fig. 5-13b: M-φ Diagram of Sec. e-e of Short-Column Base

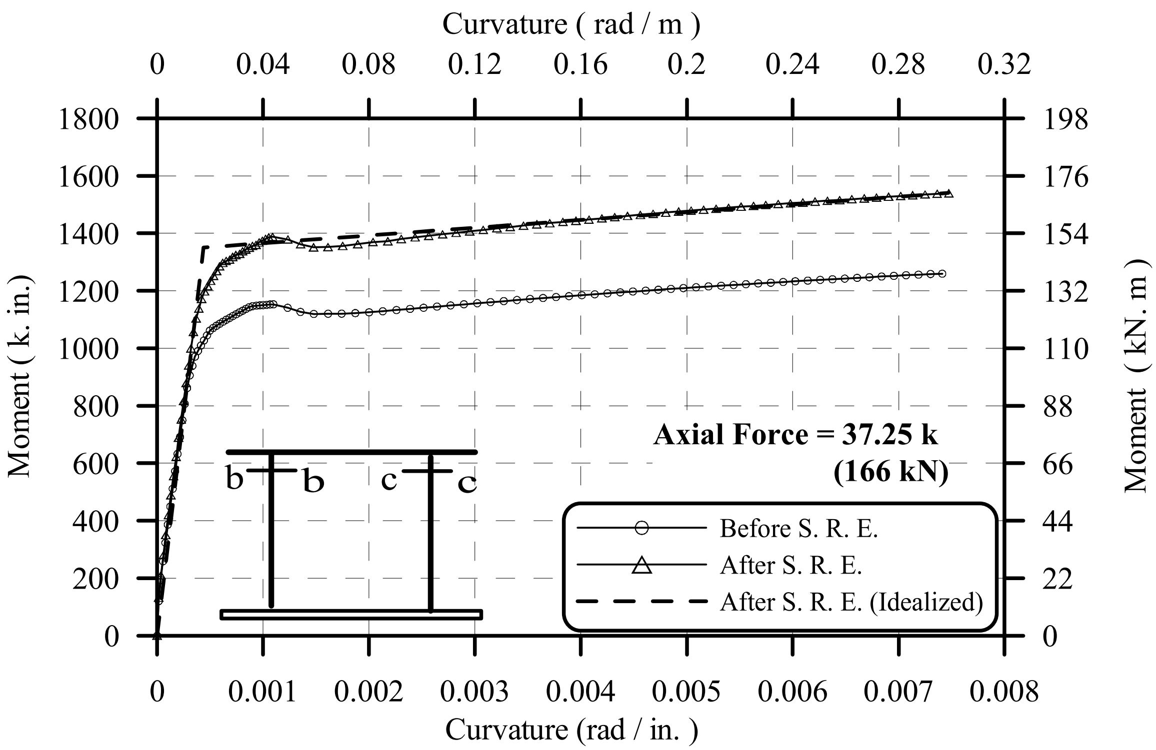

Fig. 5-14a: M-φ Diagram for Sec. b-b and c-c of Short-Specimen Column

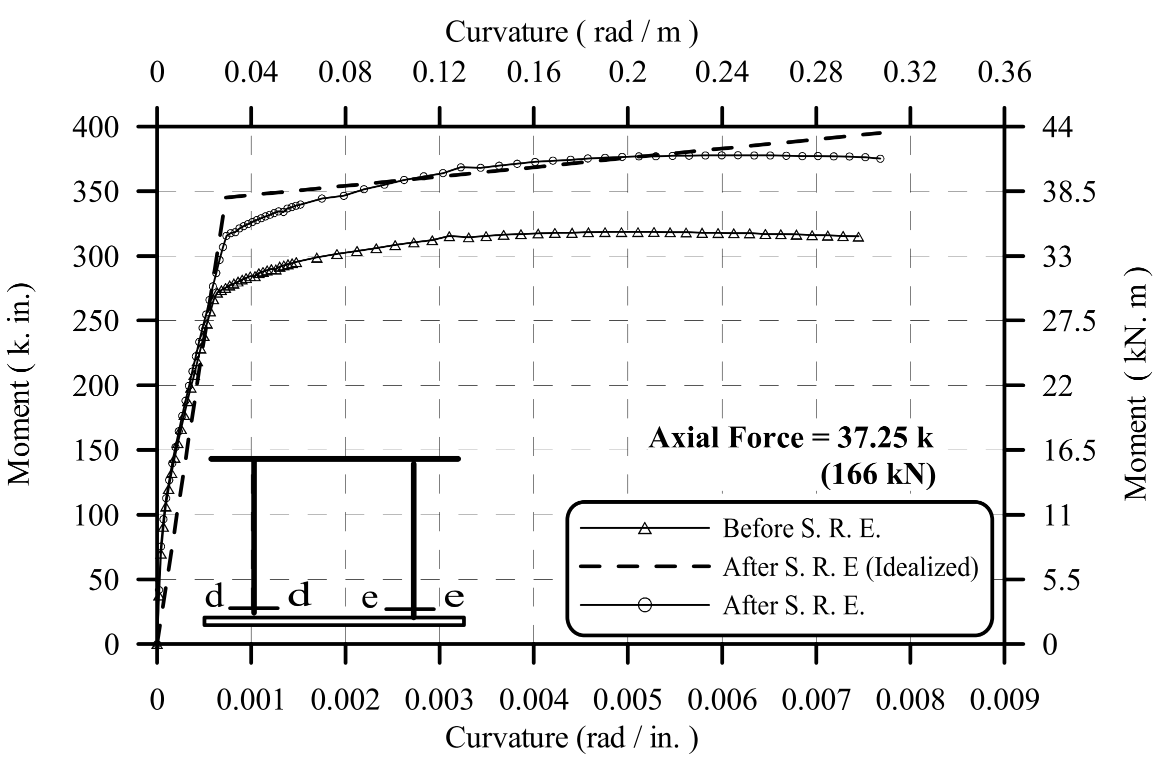

Fig. 5-14b: M-φ Diagram of Sec. d-d and e-e of Short-Column Base Hinge

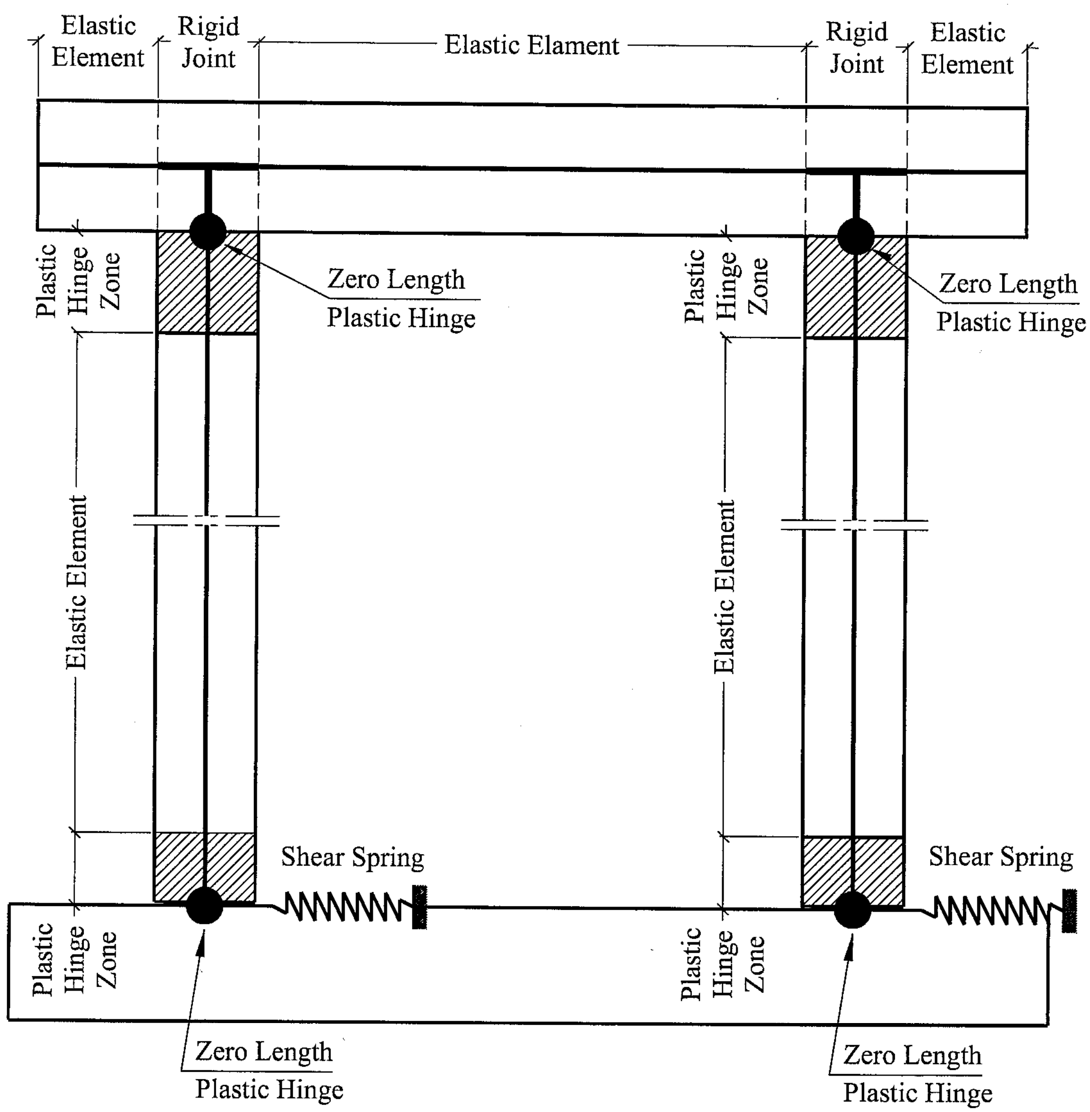

Fig. 5-15: Lumped Plasticity Model

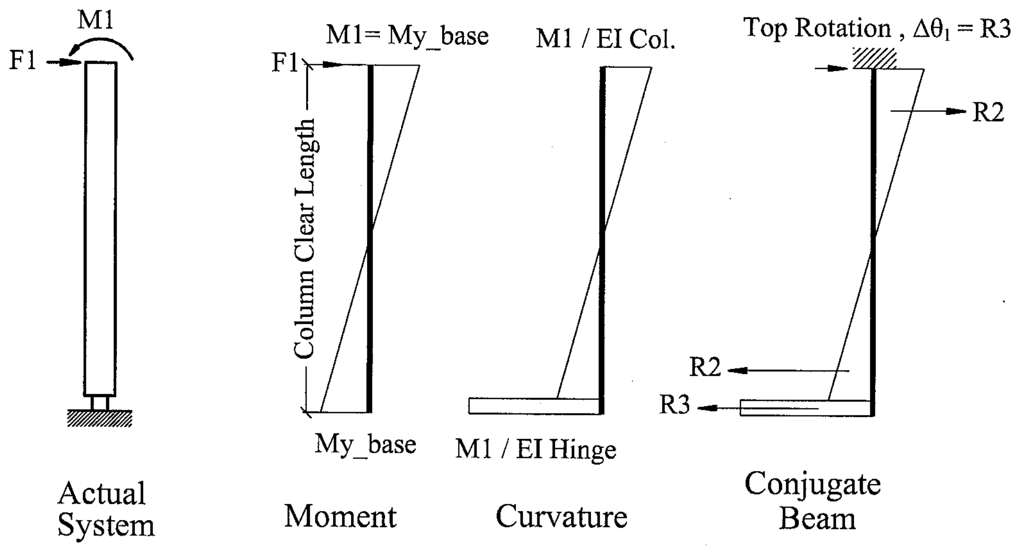

a: Forming the First Hinge at Column Base

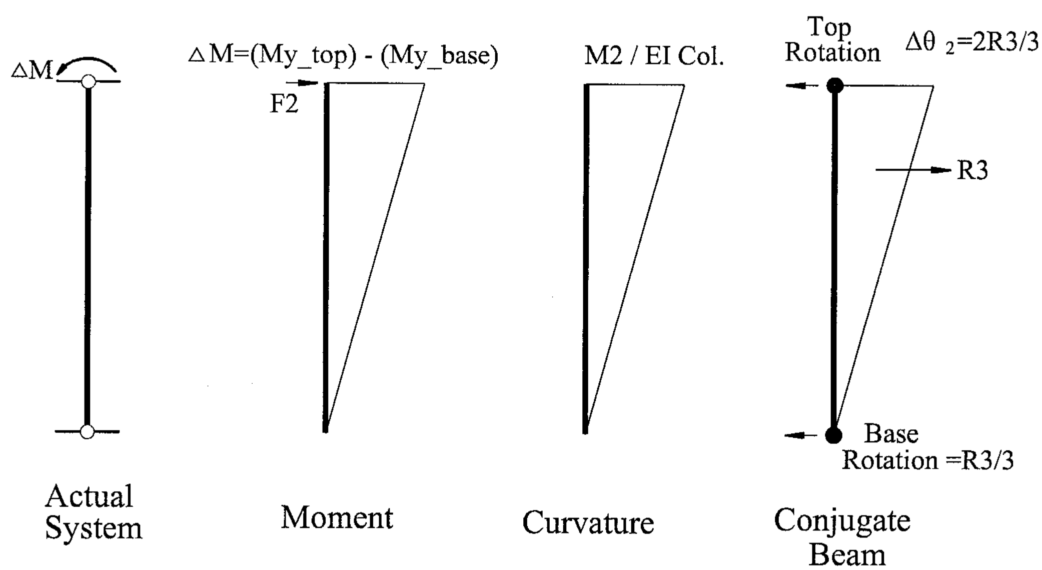

b: Forming the Second Hinge at Column Top

Fig. 5-16: Calculation of Moment-Rotation at Critical Sections

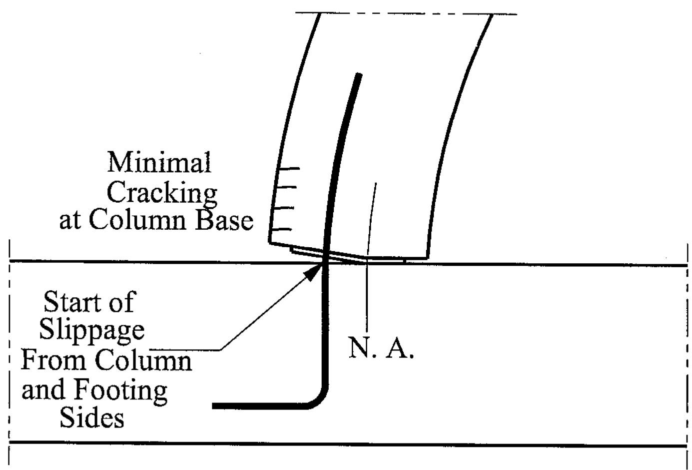

a: Slippage at Column-Footing interface

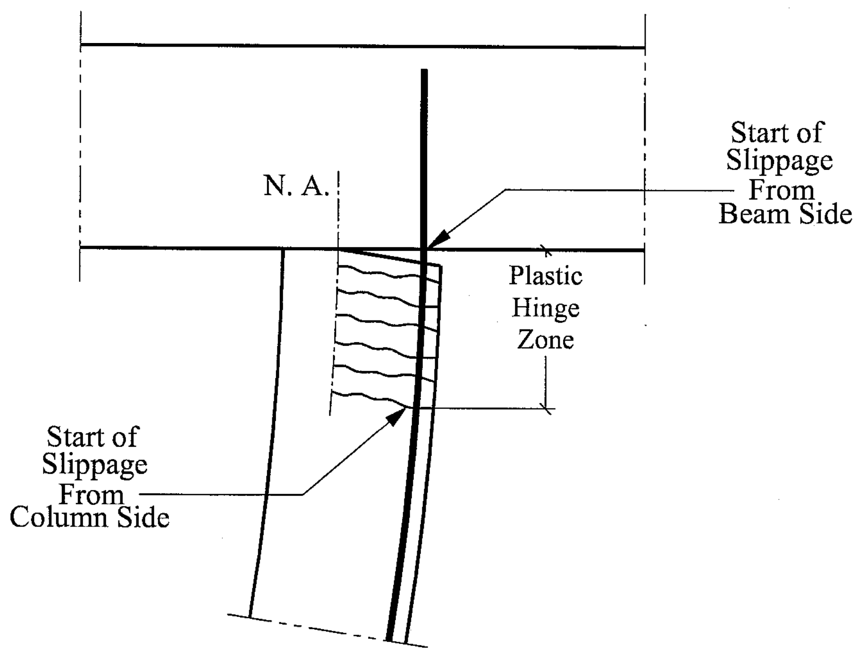

b: Slippage at Beam-Column Interface

Fig. 5-17: Slippage Mechanism at Critical Sections

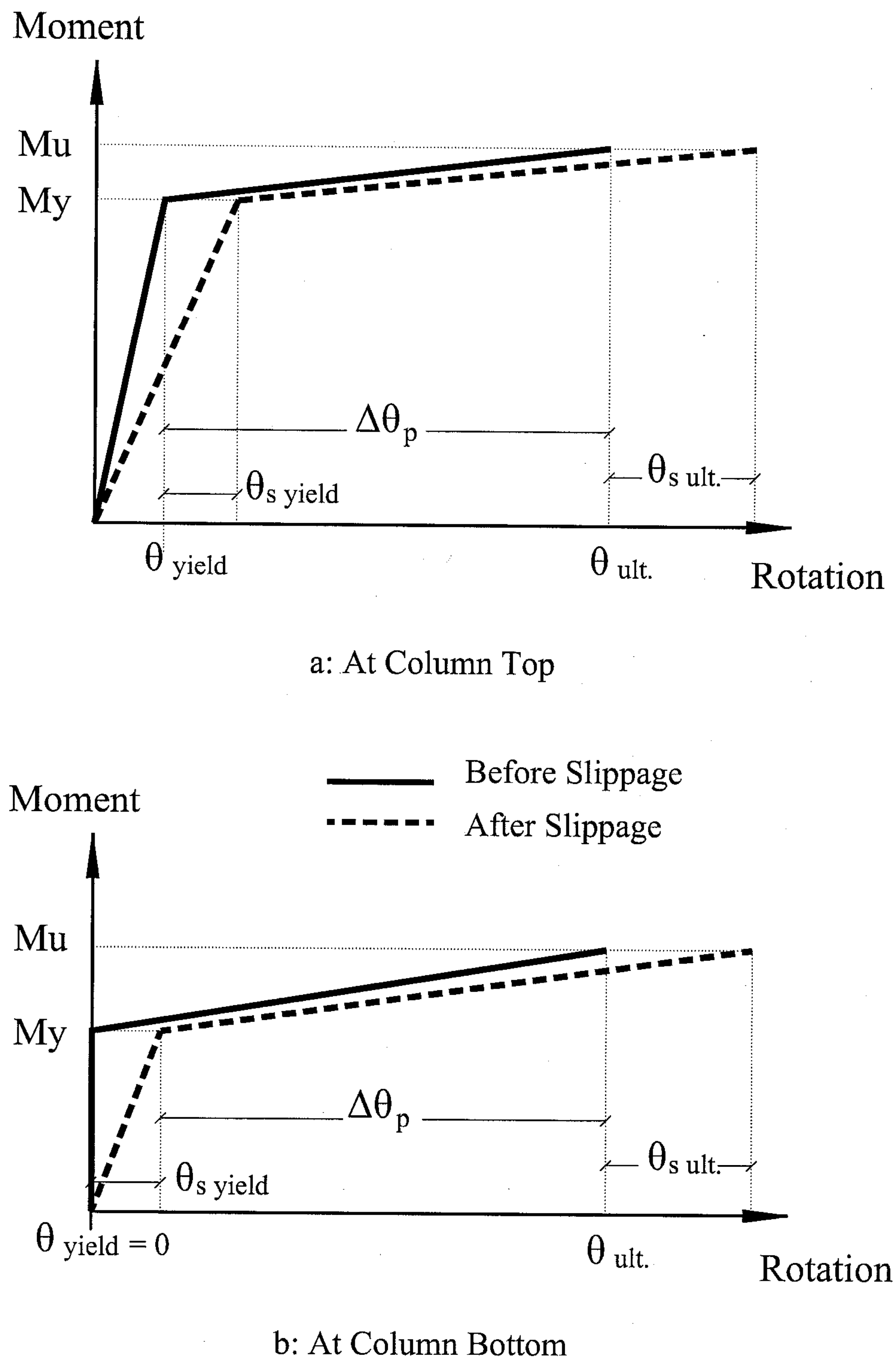

Fig. 5-18: Moment-Rotation Relationships for Column Plastic Hinges

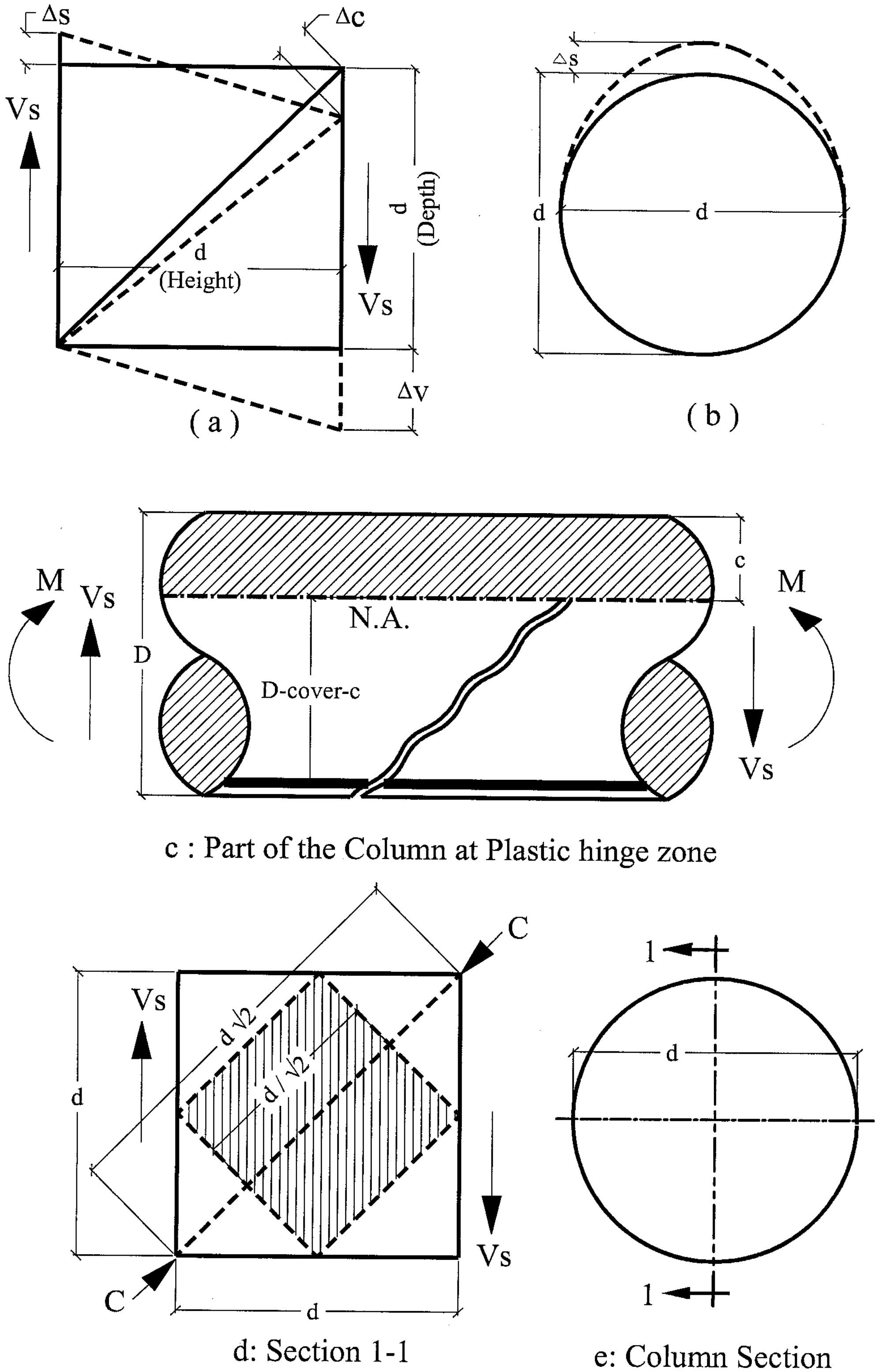

Fig. 5-19: Cracked Shear Area in Circular Cross-Sections

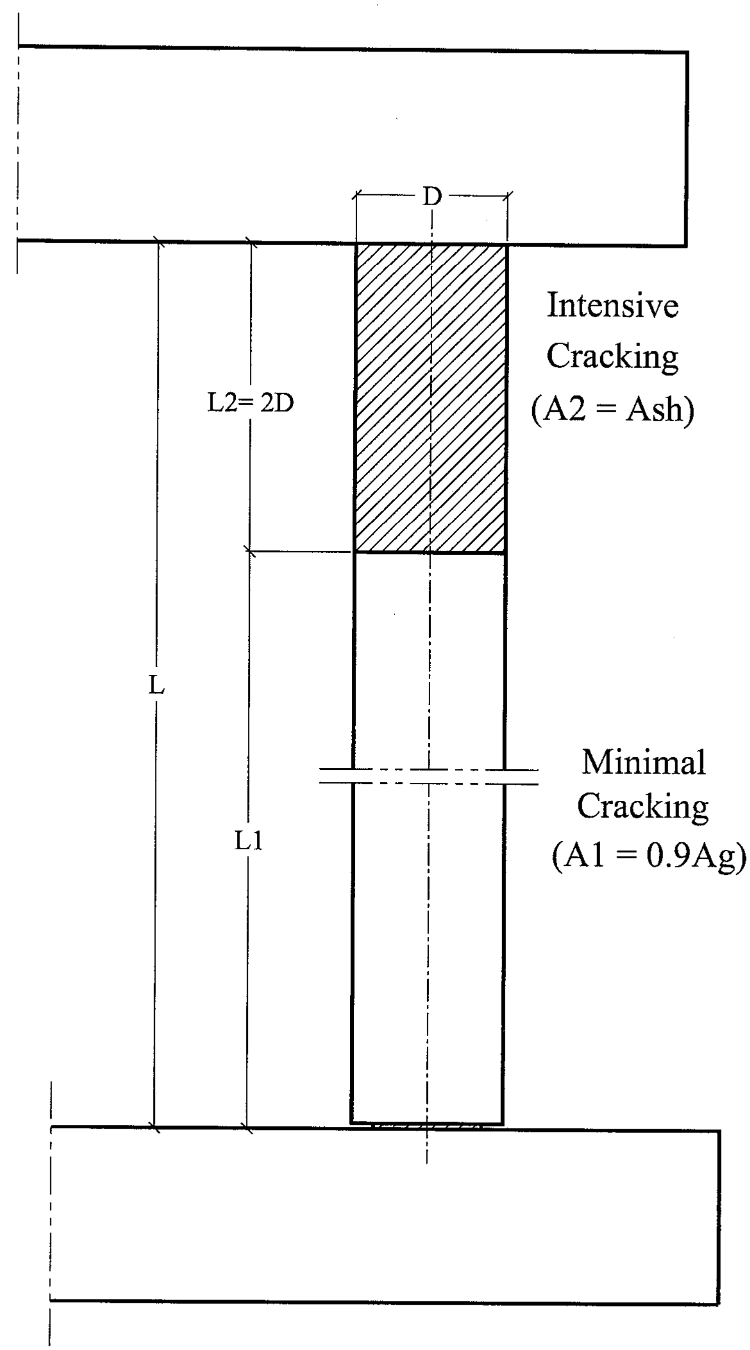

$$\text{Equivalent Column Shear Area} = \frac{L\,(A1\;A2)}{(L1\;A2 + L2\;A1)}$$

Fig. 5-20 a: Calculation of Column Shear Area (for Tall and middle Columns)

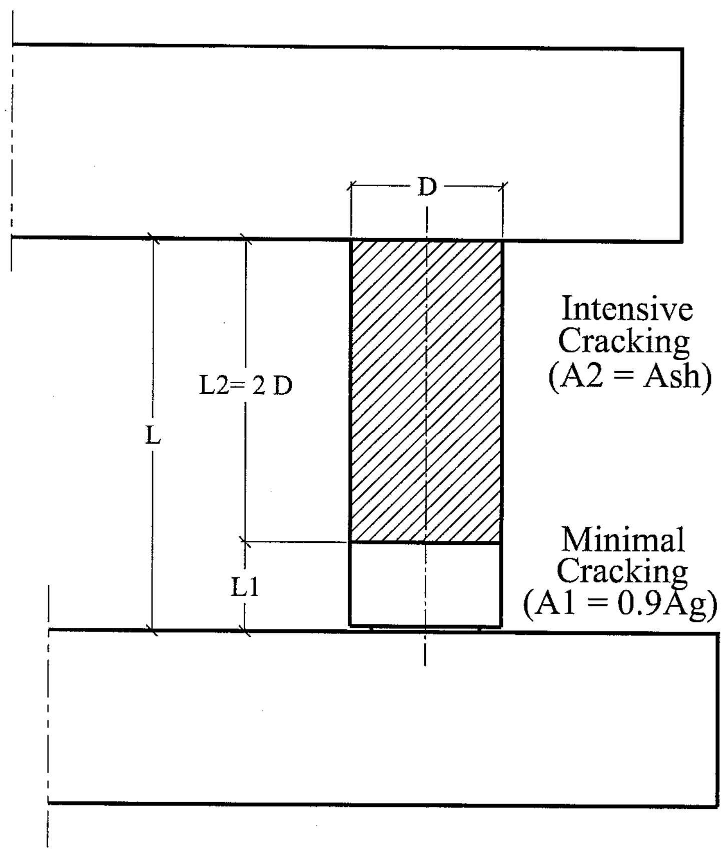

$$\text{Equivalent Column Shear Area} = \frac{L\,(A1\ A2)}{(L1\ A2 + L2\ A1)}$$

Fig. 5-20 b: Calculation of Column Shear Area (For Short Columns)

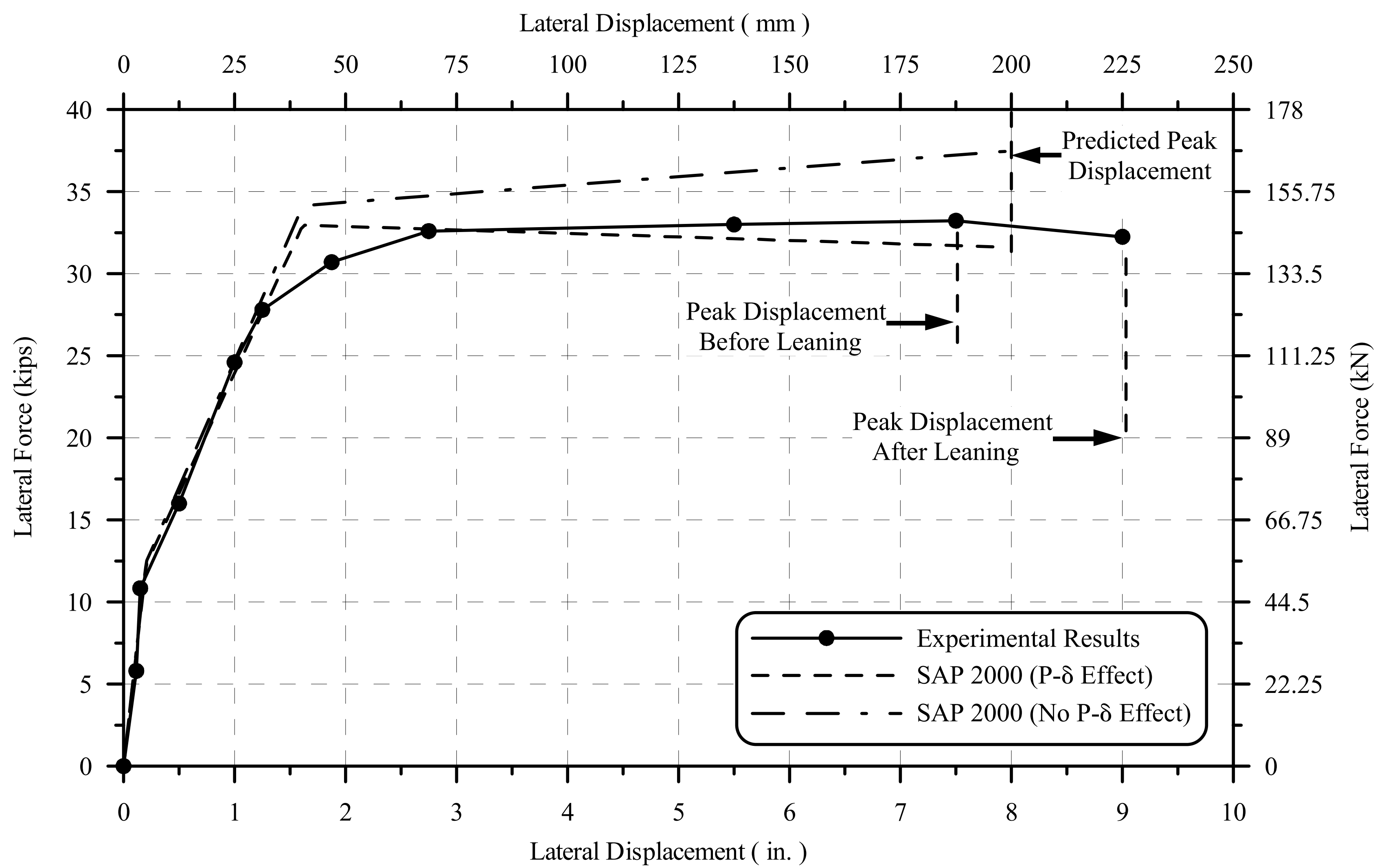

Fig. 5-21: Push-Over Diagram for Tall Specimen B2CT (SAP 2000 Program)

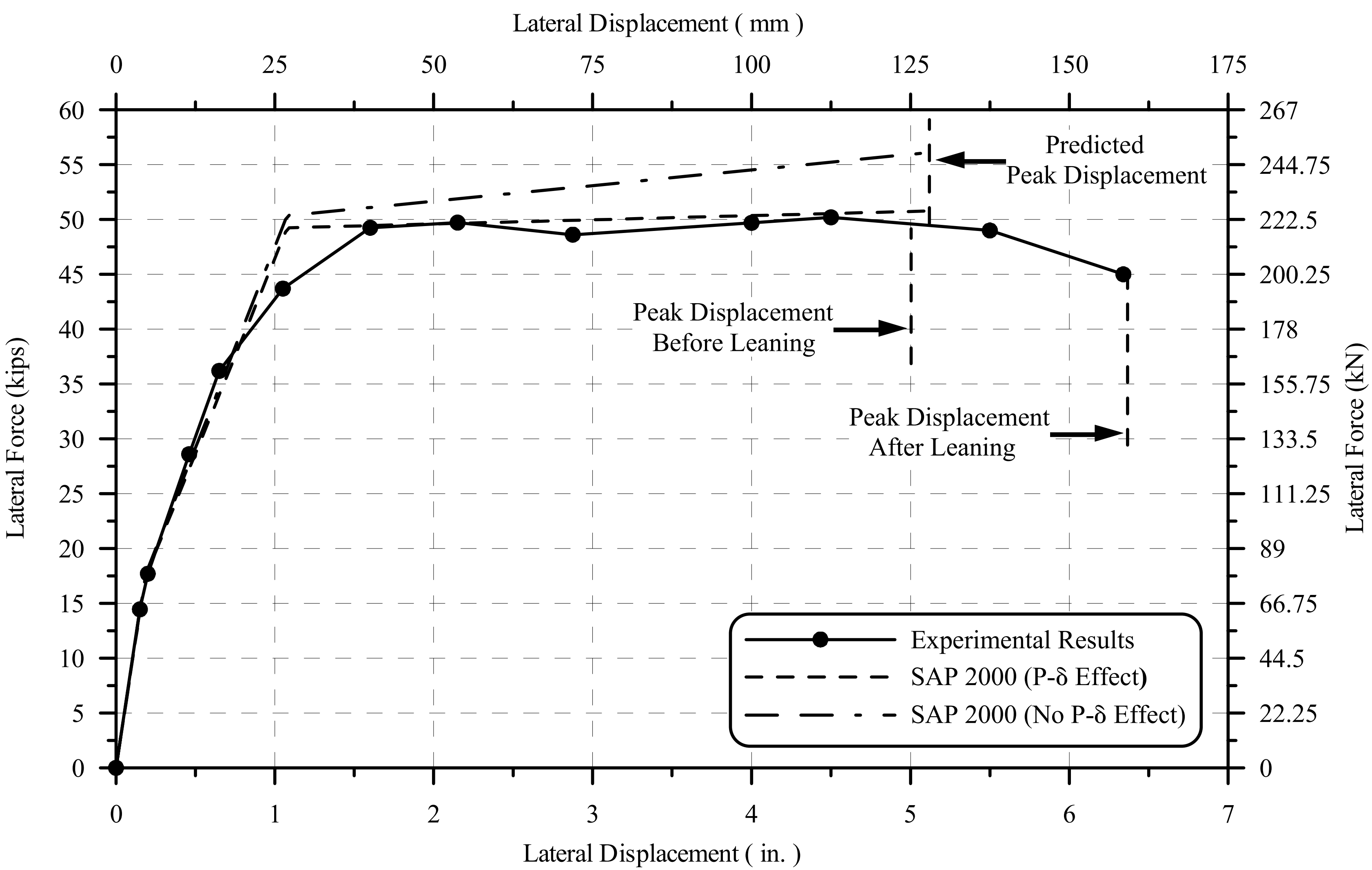

Fig. 5-22: Push-Over Diagram for Middle Specimen B2CM (SAP 2000 Program)

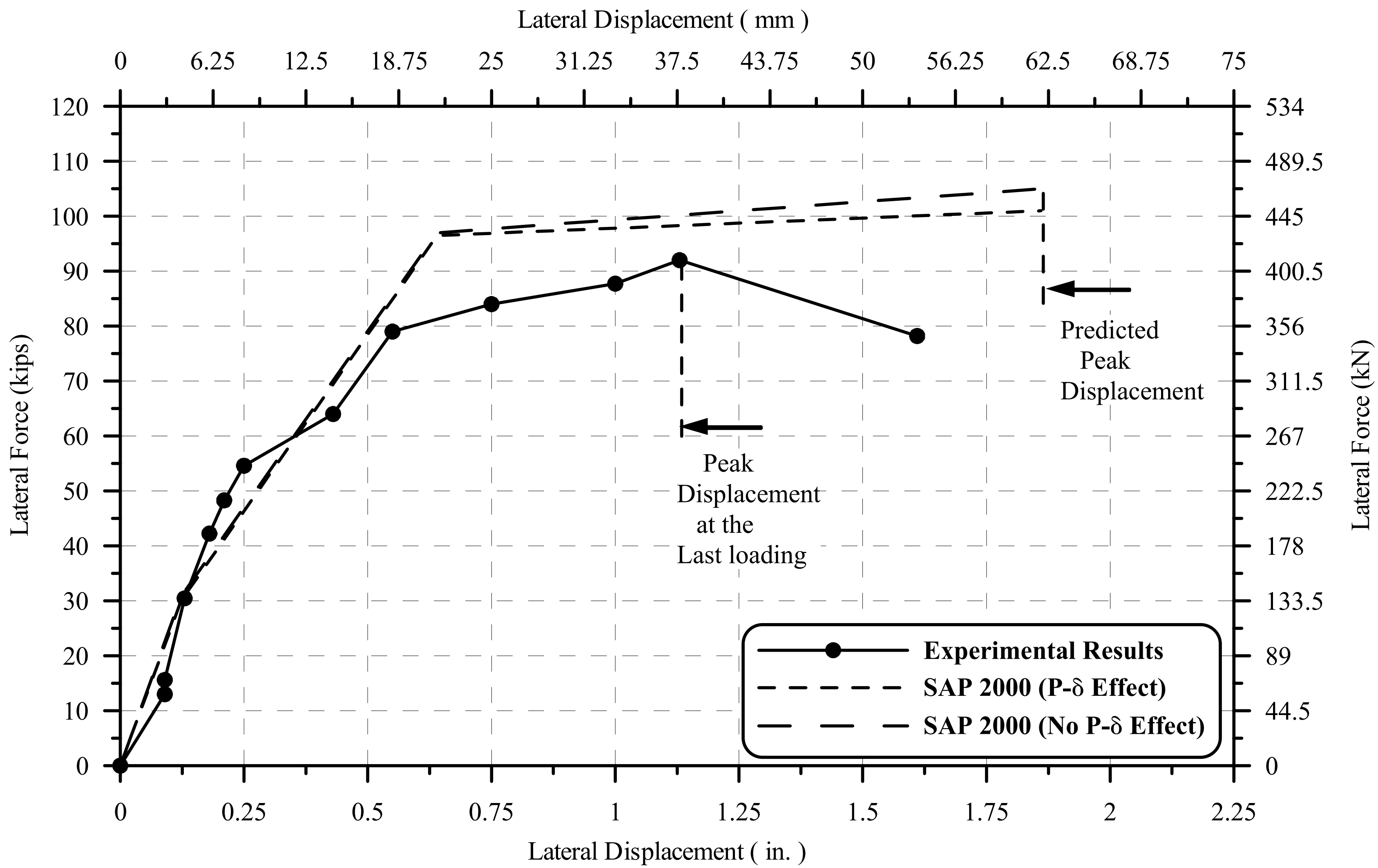

Fig. 5-23: Push-Over Diagram for Short Specimen B2CS (SAP 2000 Program)

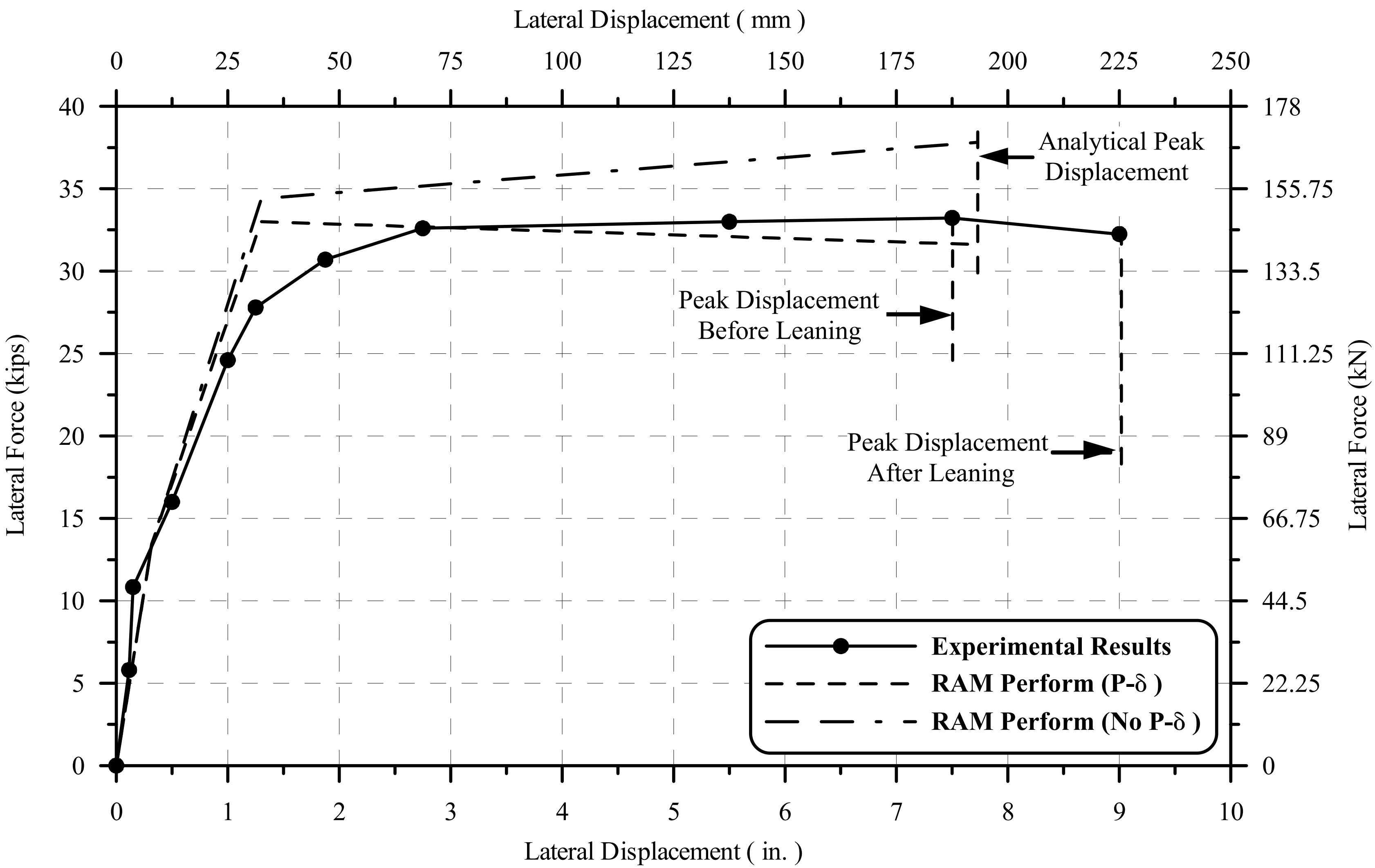

Fig. 5-24: Push-Over Diagram for Tall Specimen B2CT (RAM Perform Program)

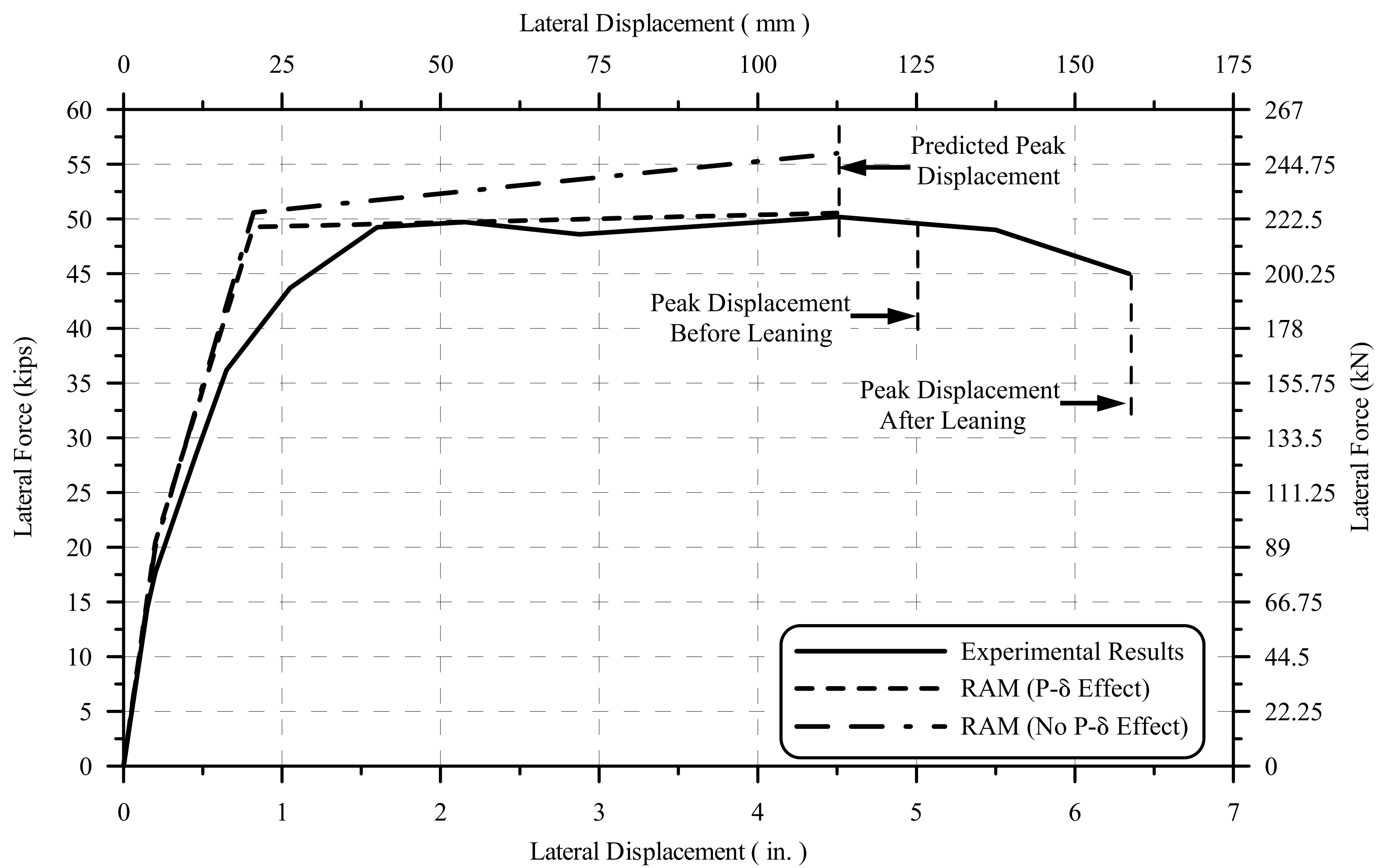

Fig. 5-25: Push-Over Diagram for Middle Specimen B2CM (RAM Perform Program)

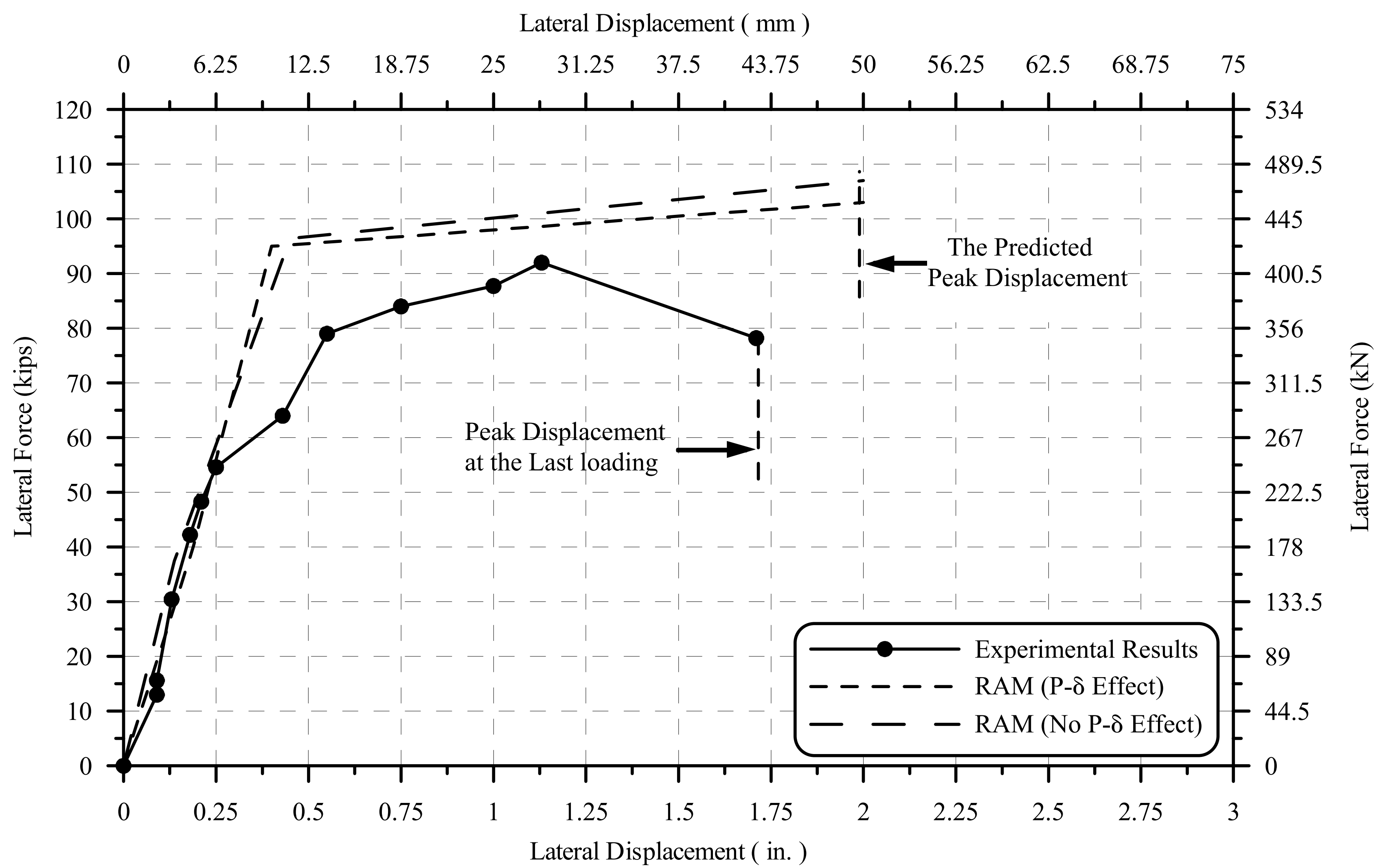

Fig. 5-26: Push-Over Diagram for Short Specimen B2CS (RAM Perform Program)

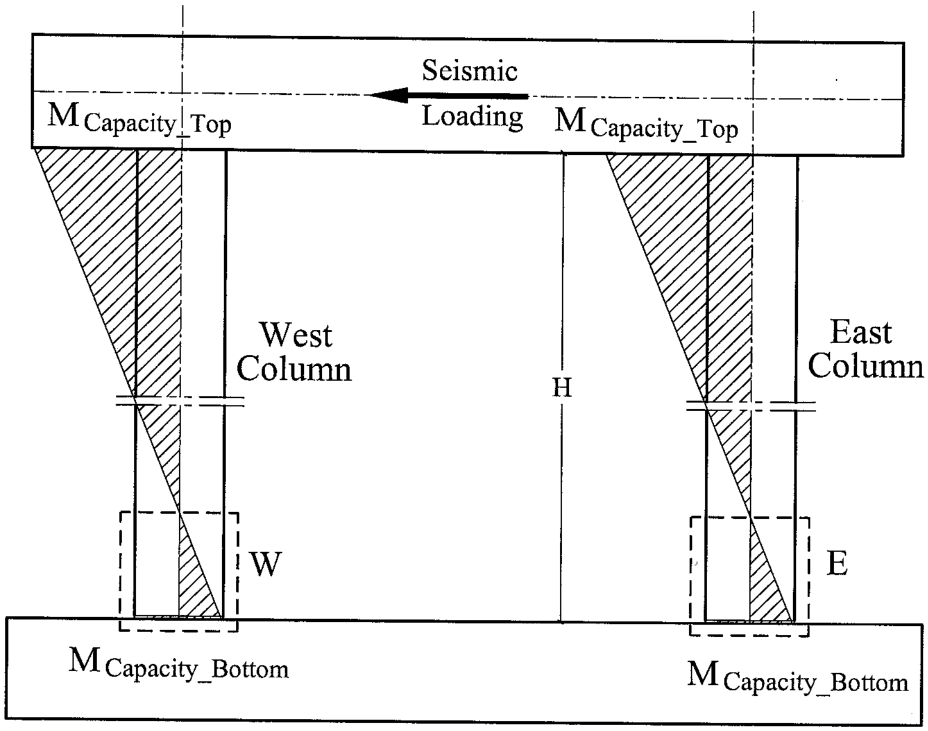

a: Seismic Demands

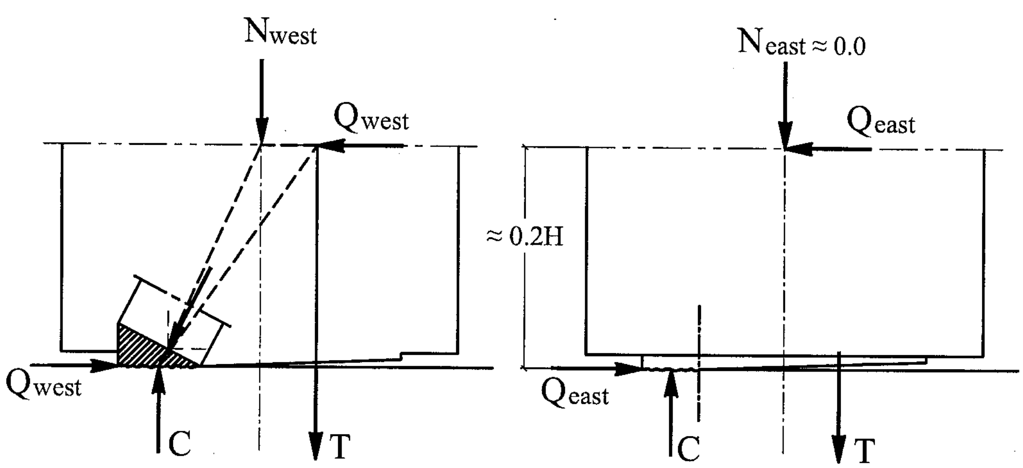

b: Part W

c: Part E

Fig. 5-27: Shear-Friction Mechanism at Column Bases

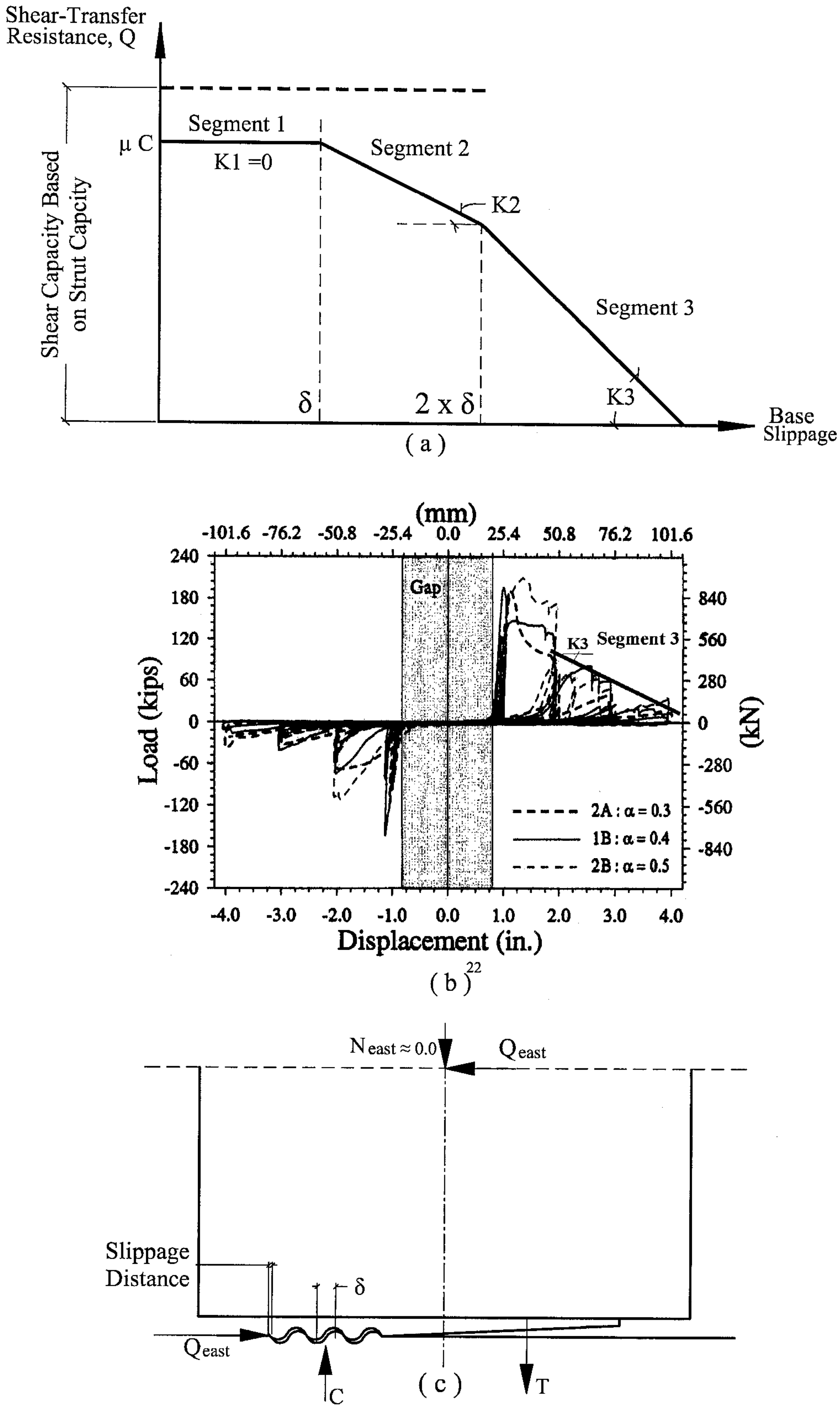

Fig. 5-28: Shear-Sliding Model For East Column Base

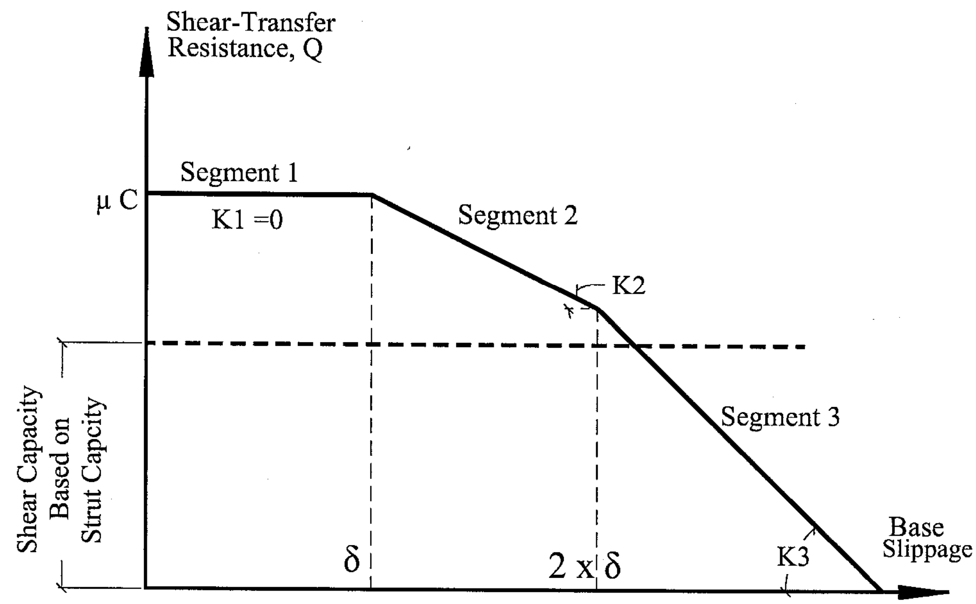

(a)

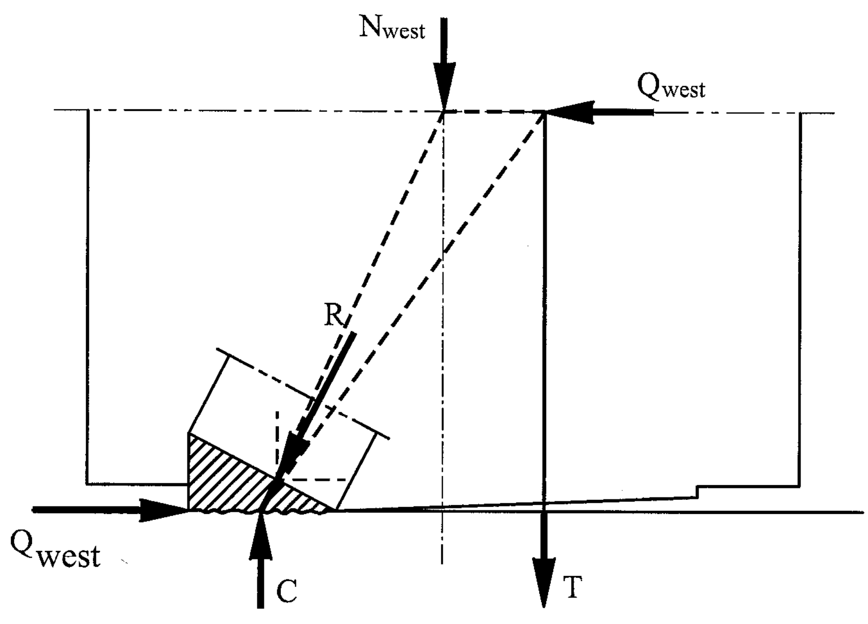

(b)

Fig. 5-29: Shear-Sliding Model For West Column Base

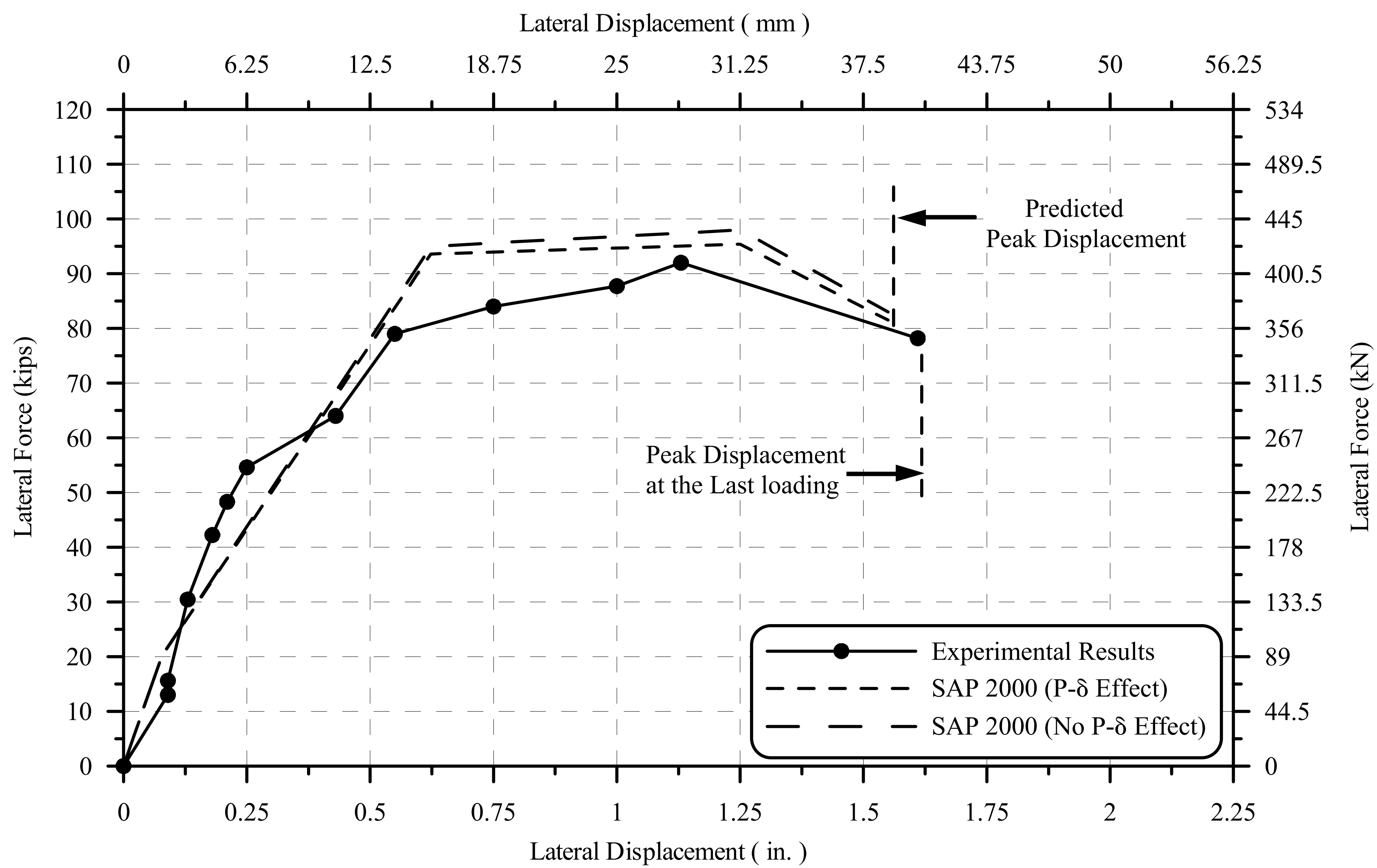

Fig. 5-30: Push-Over Diagram for Short Specimen B2CS after Including Base Slippage(SAP 2000 Program)

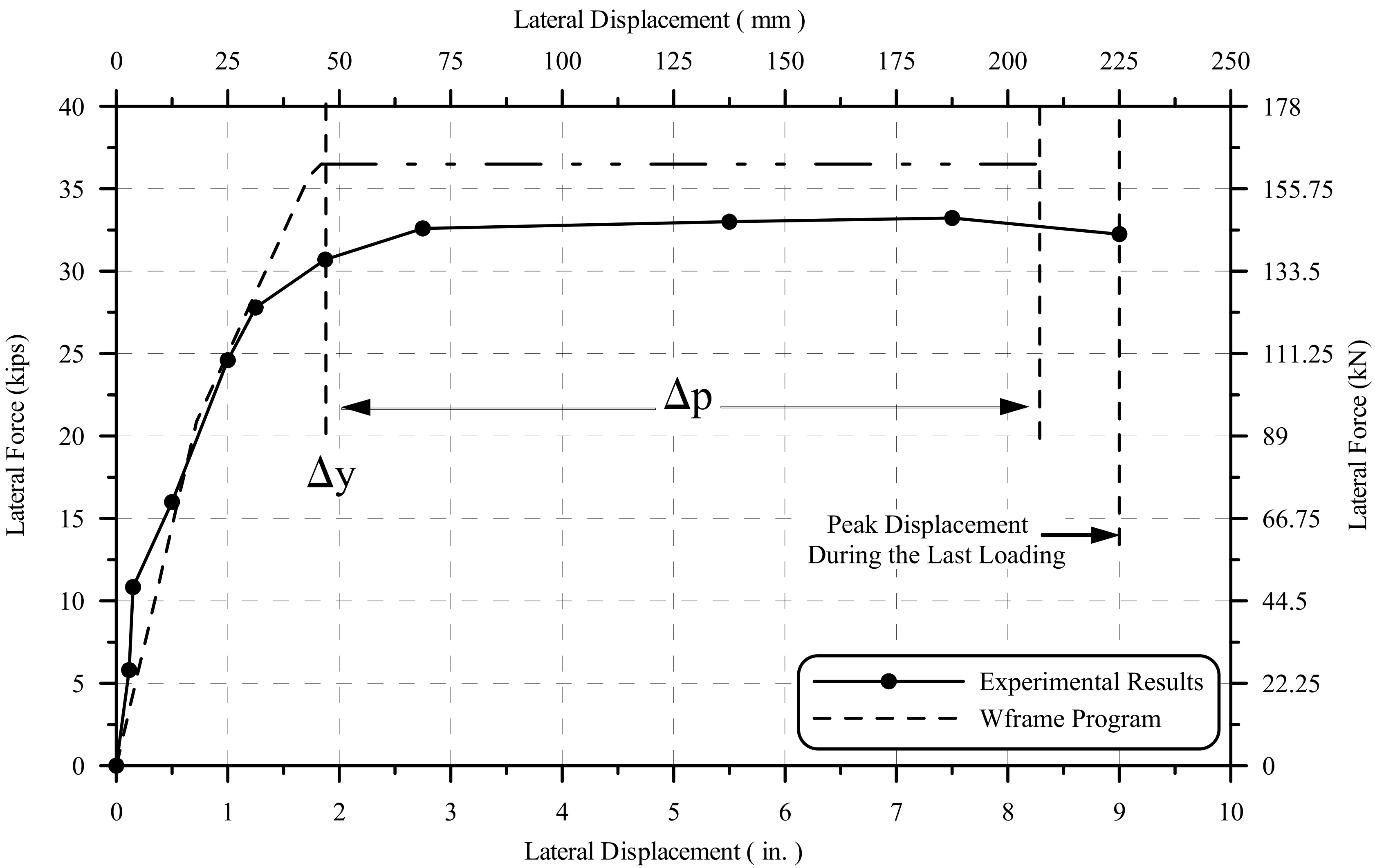

Fig. 5-31: Push-Over Diagram for Tall Specimen B2CT (wFRAME Program)

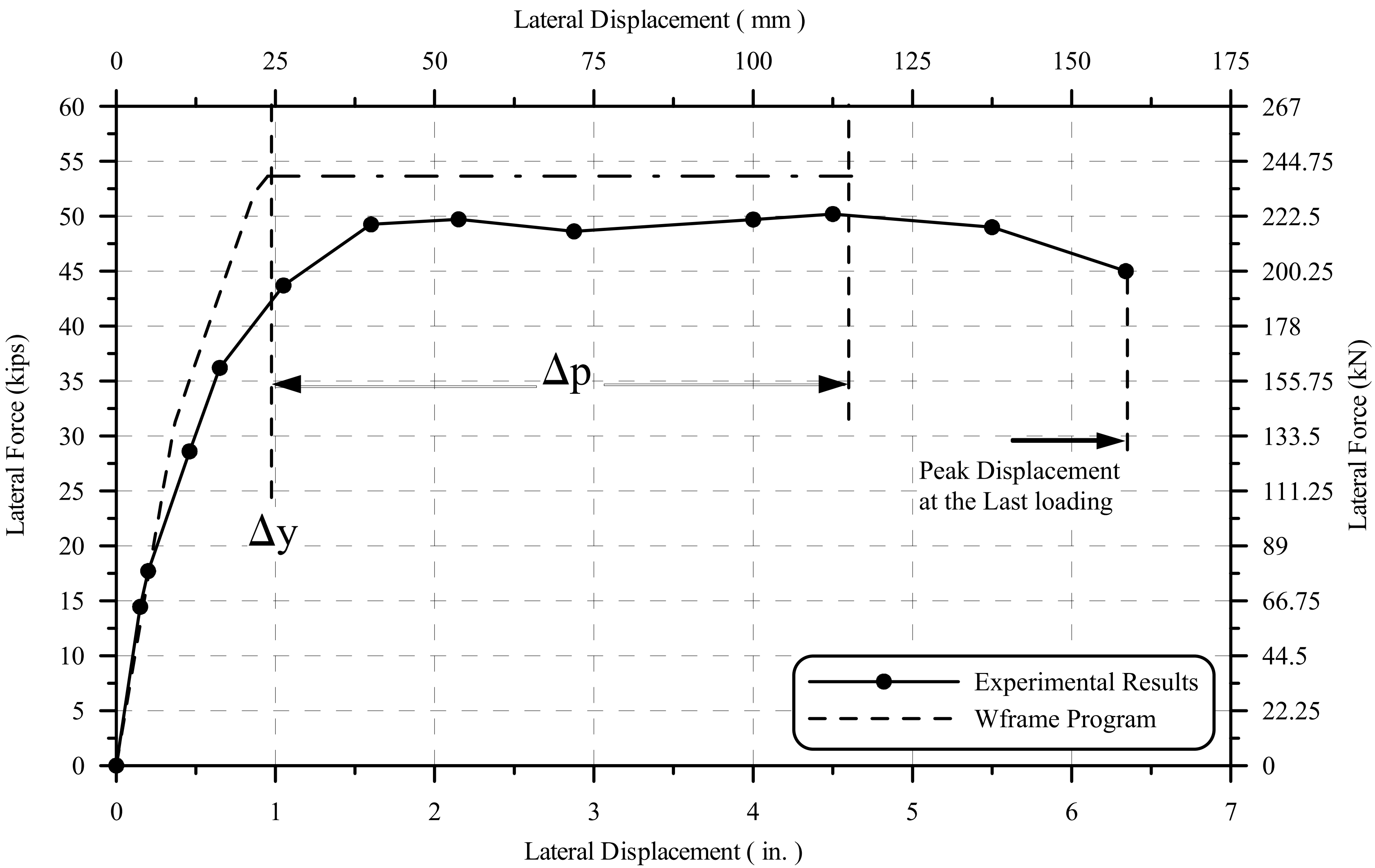

Fig. 5-32: Push-Over Diagram for Middle Specimen B2CM (wFRAME Program)

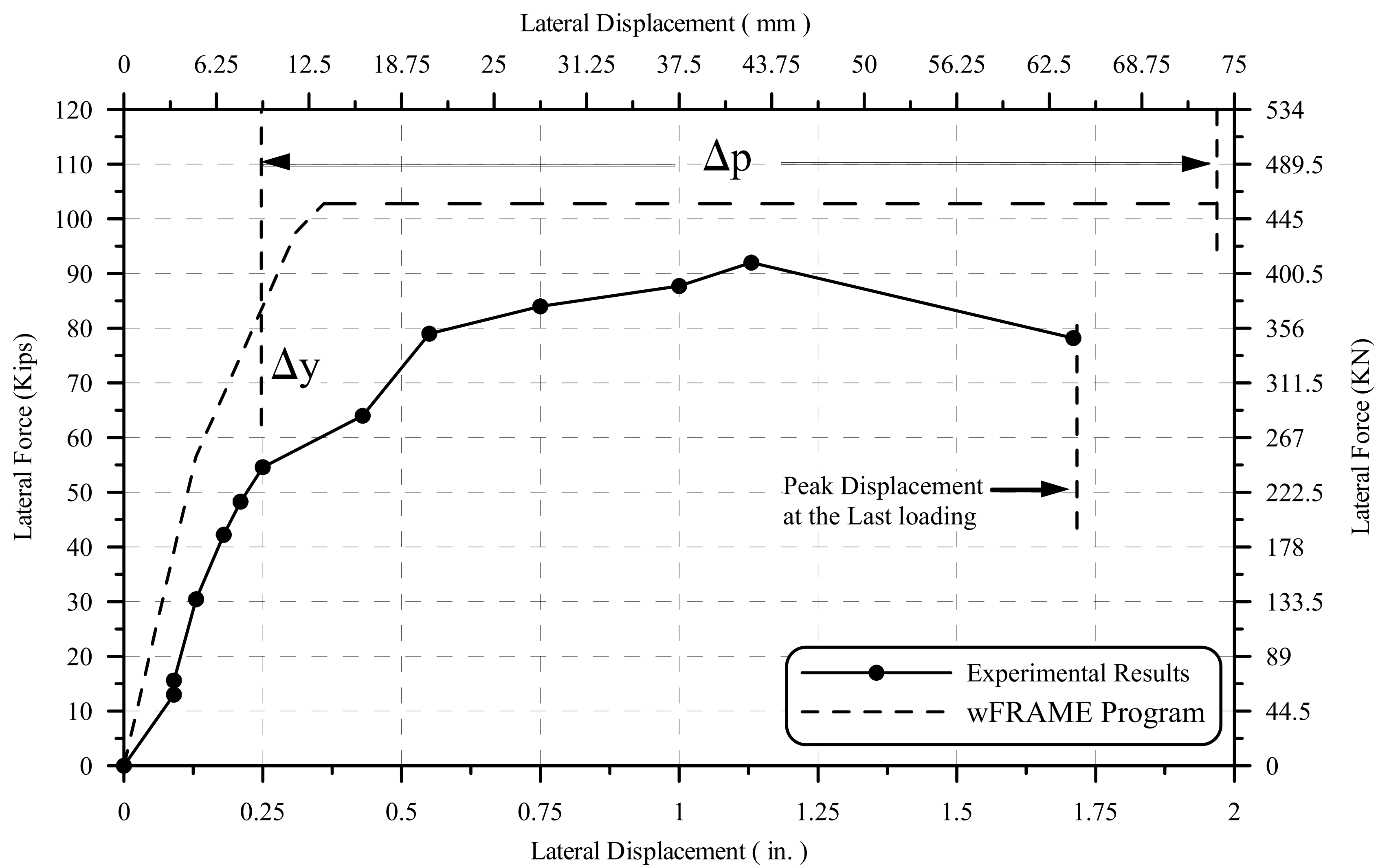

Fig. 5-33: Push-Over Diagram for Short Specimen B2CS (wFRAME Program)

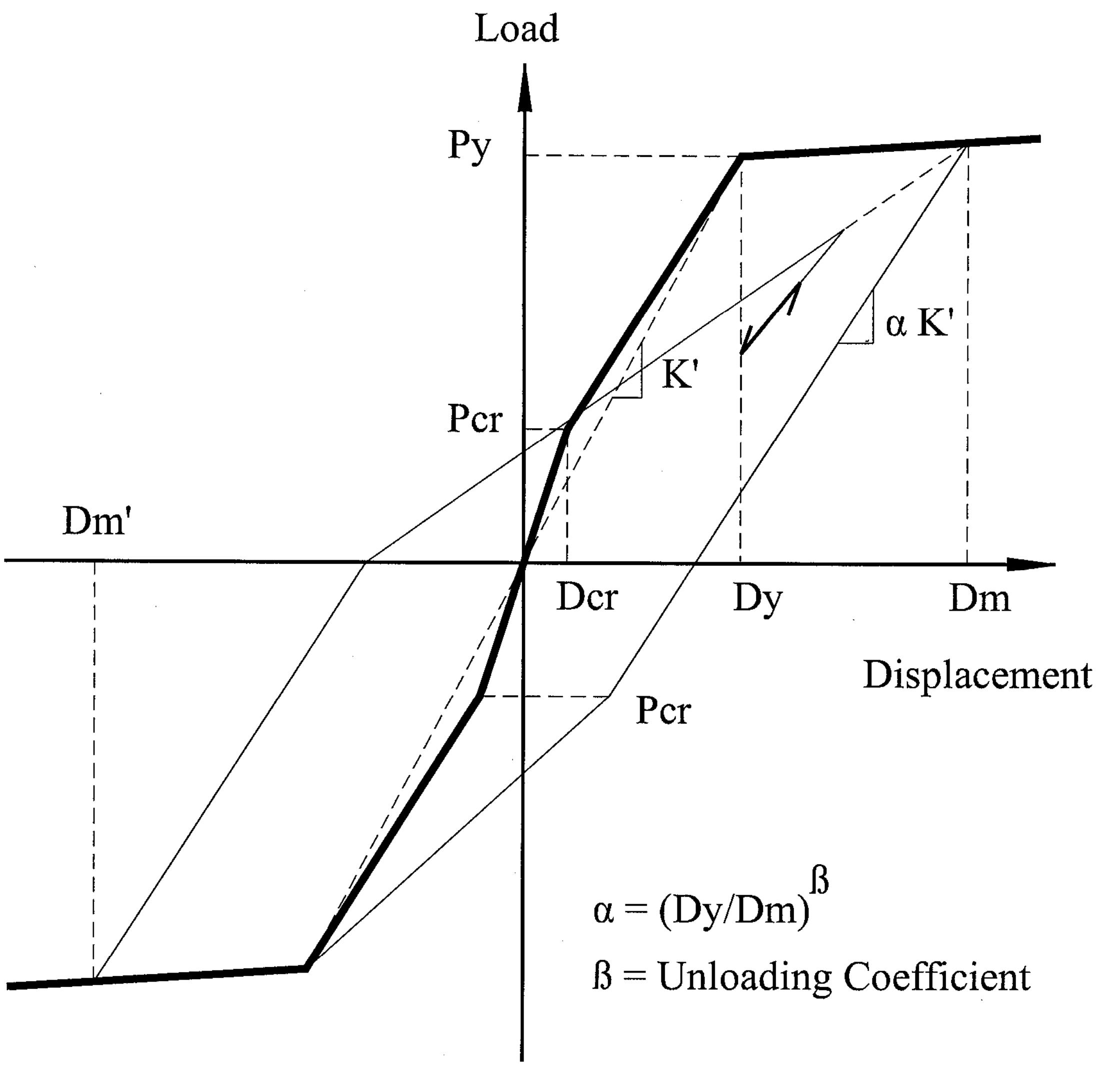

Fig. 5-34: The Takeda Model

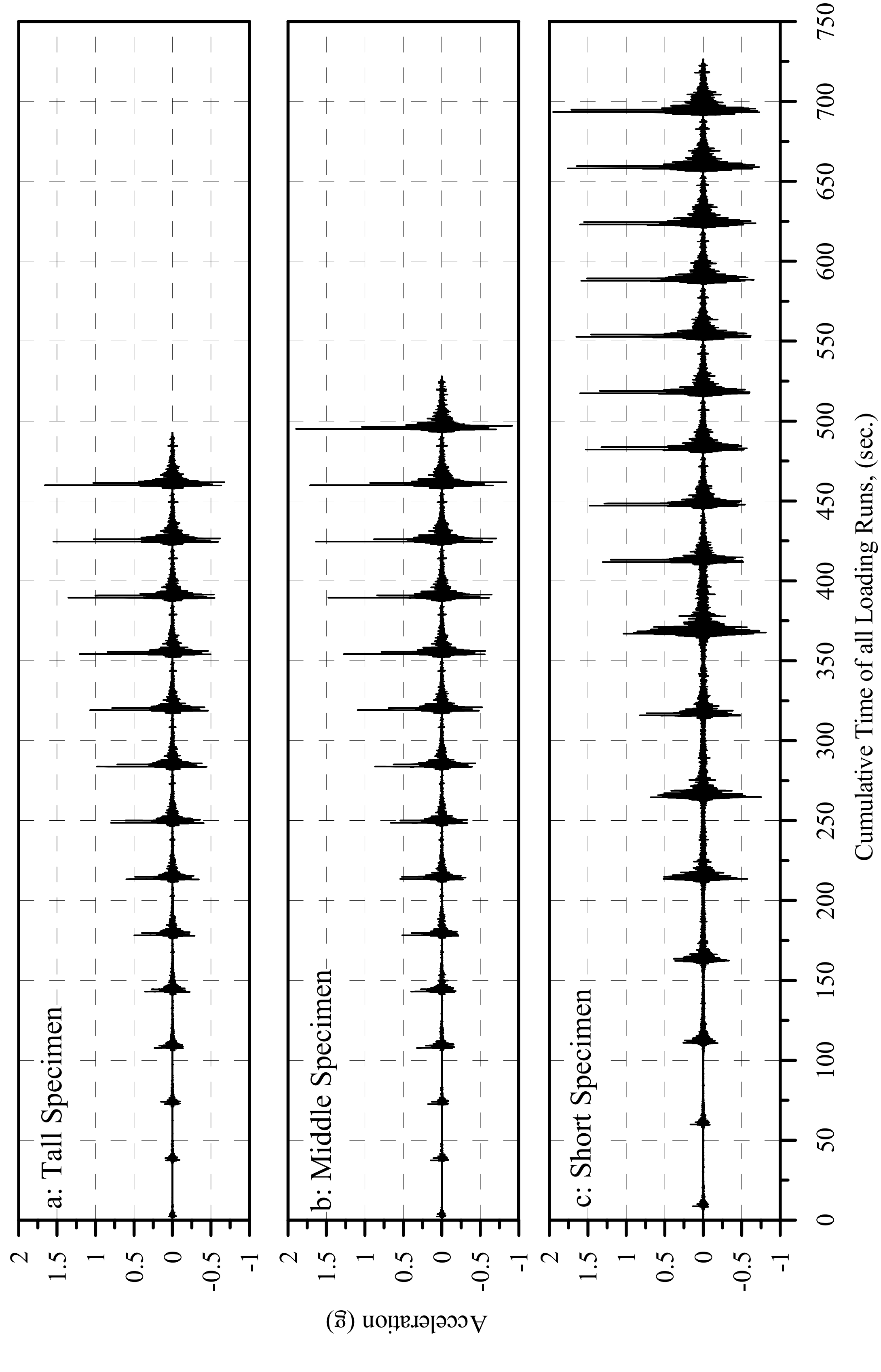

Fig. 5-35a: Actual Dynamic Loading for the Three Specimens Before Resampling

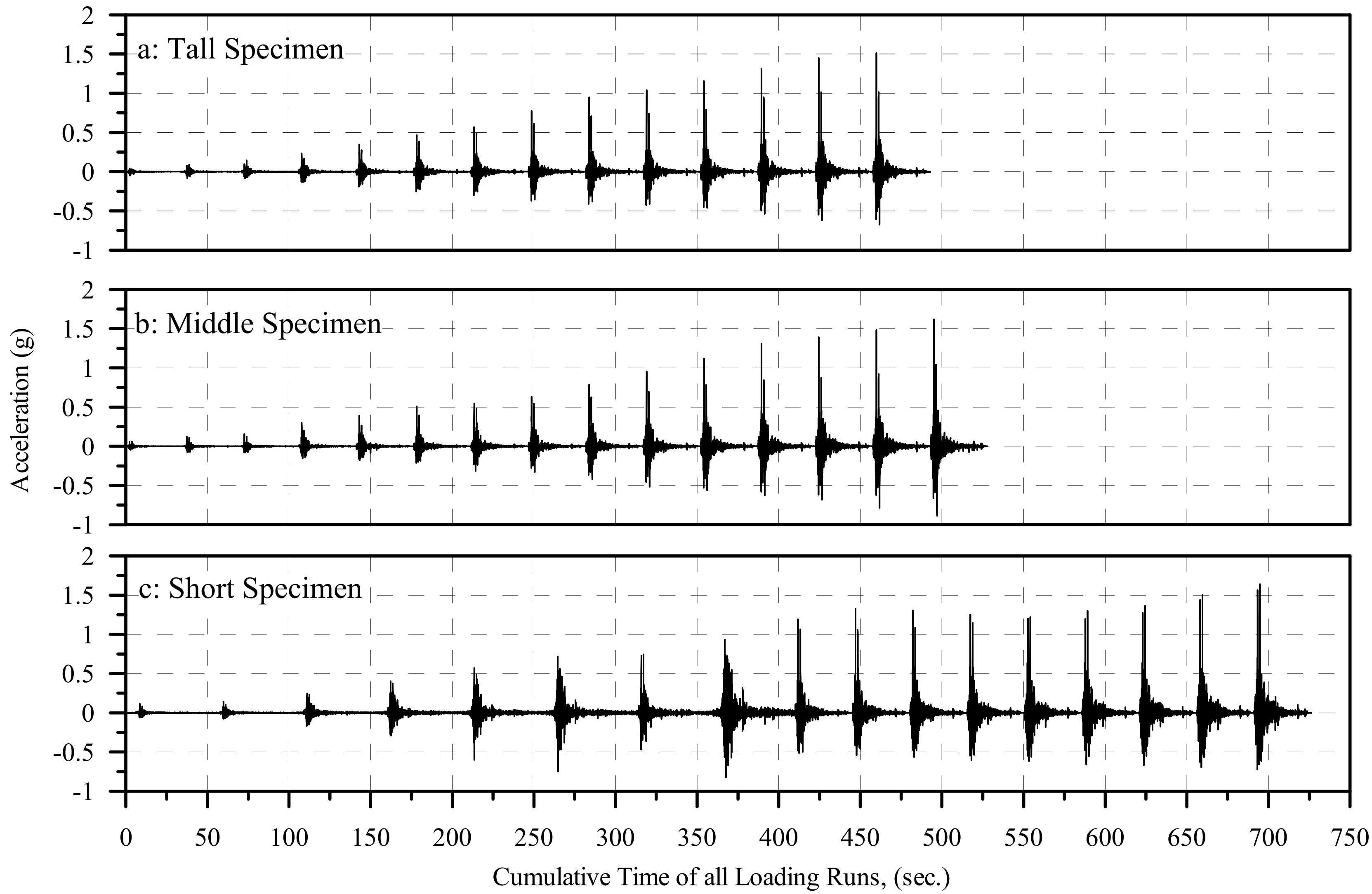

Fig. 5-35b: Dynamic Loading Input for the Three Specimens After Resampling

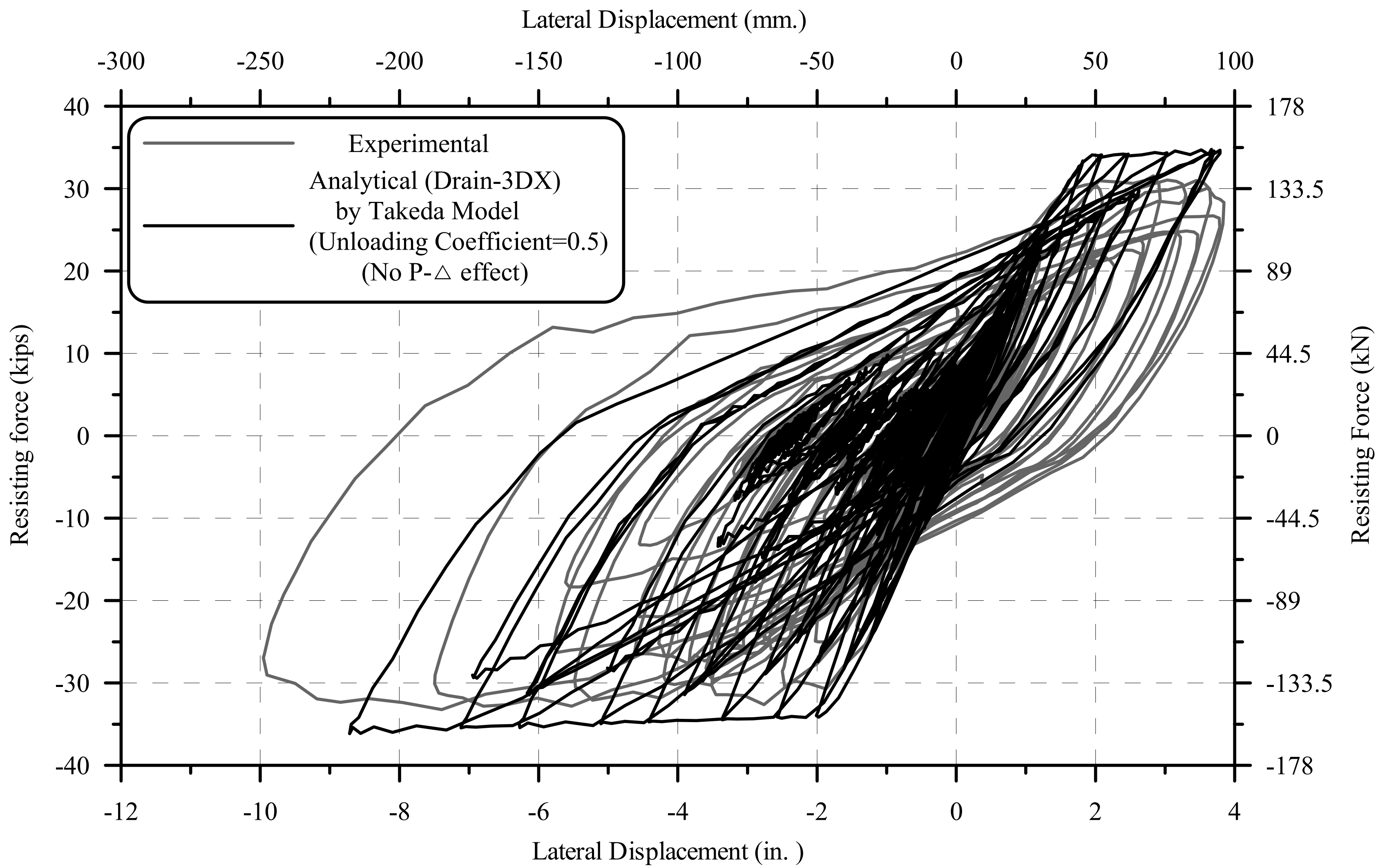

Fig. 5-36a: Load-Displacement Hystereses for Specimen B2CT under the Fourteen Loading Runs

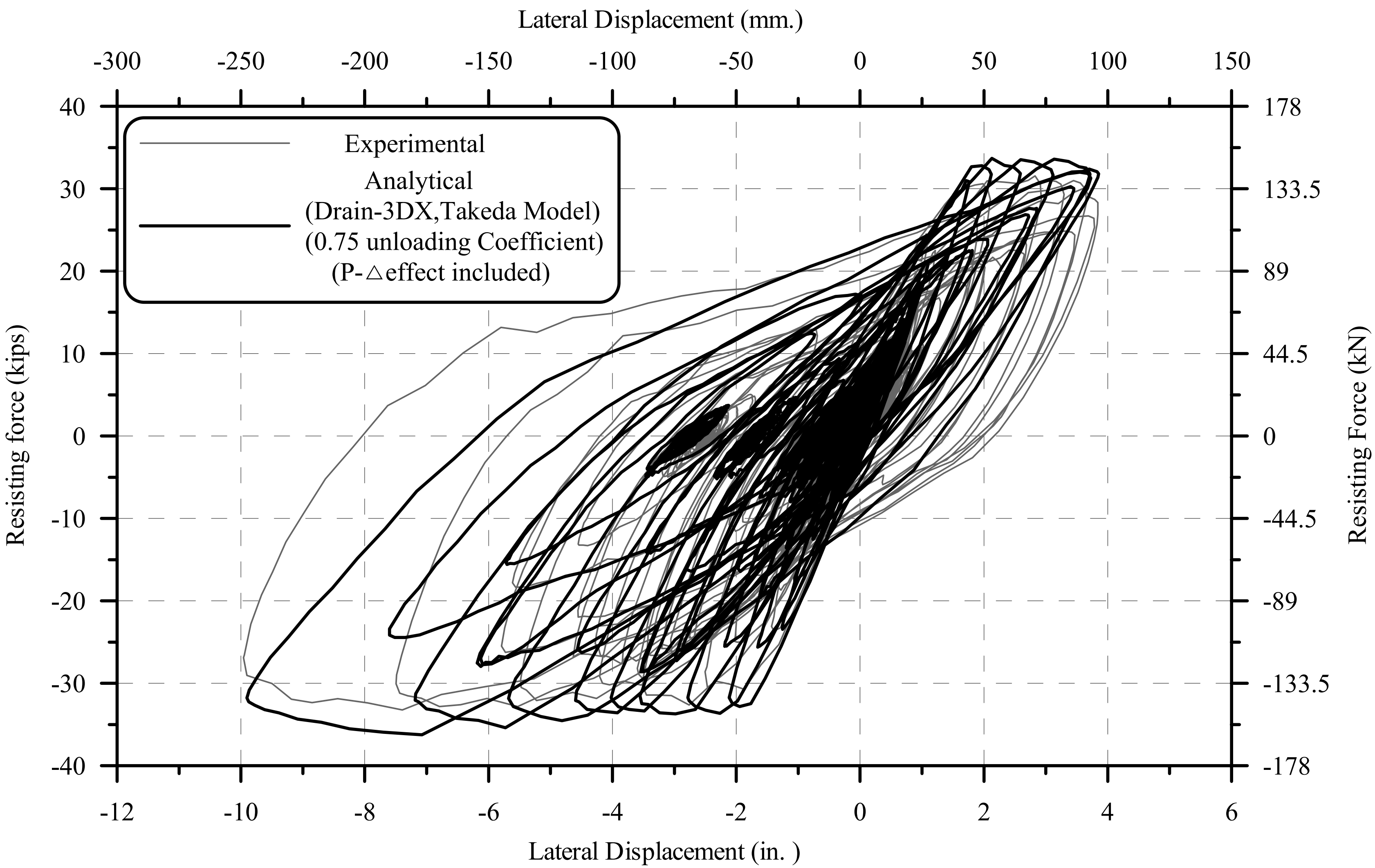

Fig. 5-36b: Load-Displacement Hystereses for Specimen B2CT under the Fourteen Loading Runs

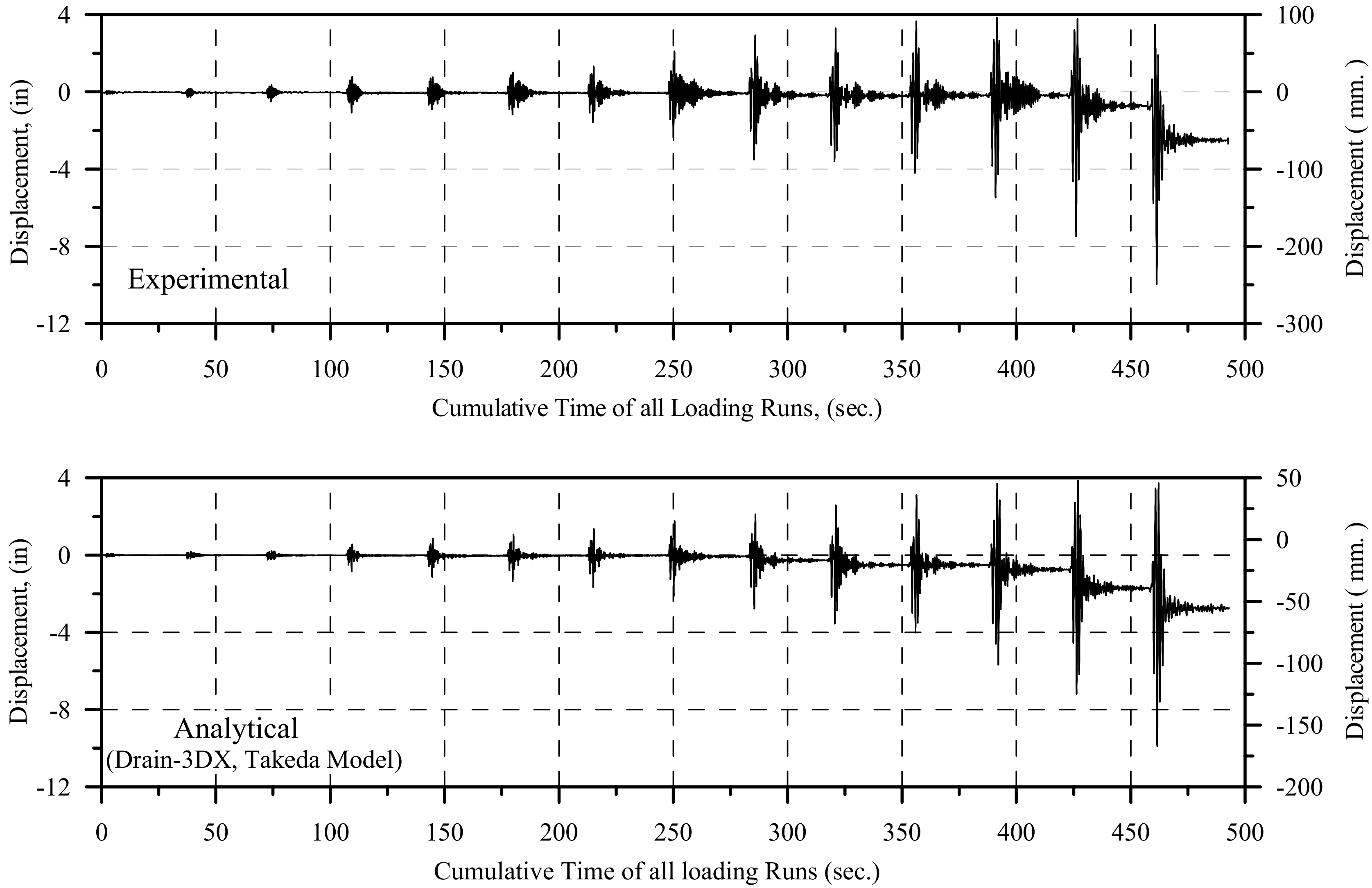

Fig. 5-37: Relative Displacement History for Specimen B2CT unfer the Fourteen Loading Runs

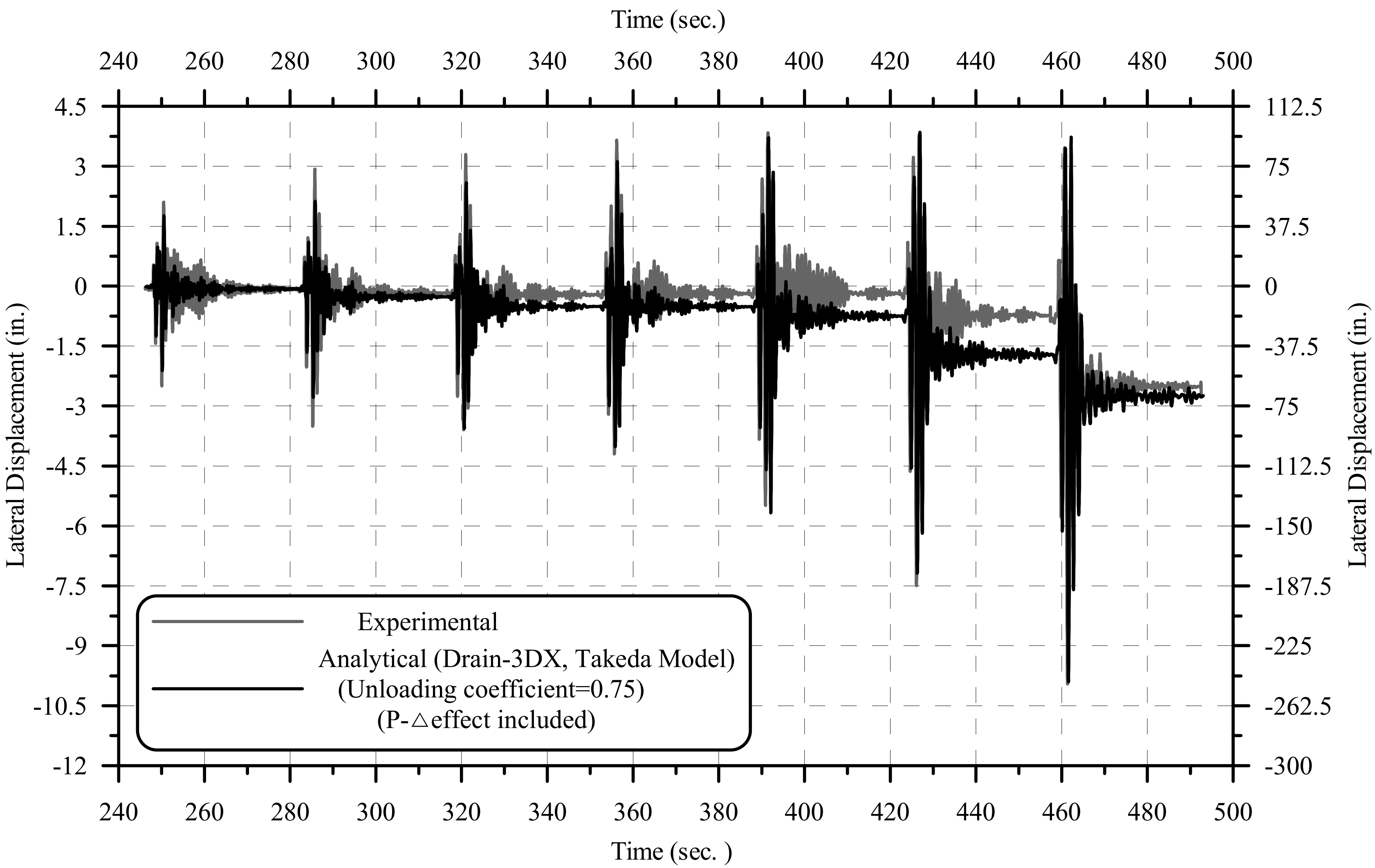

Fig. 5-38: Displacement Time-History for Specimen B2CT under the Last Seven Loadings

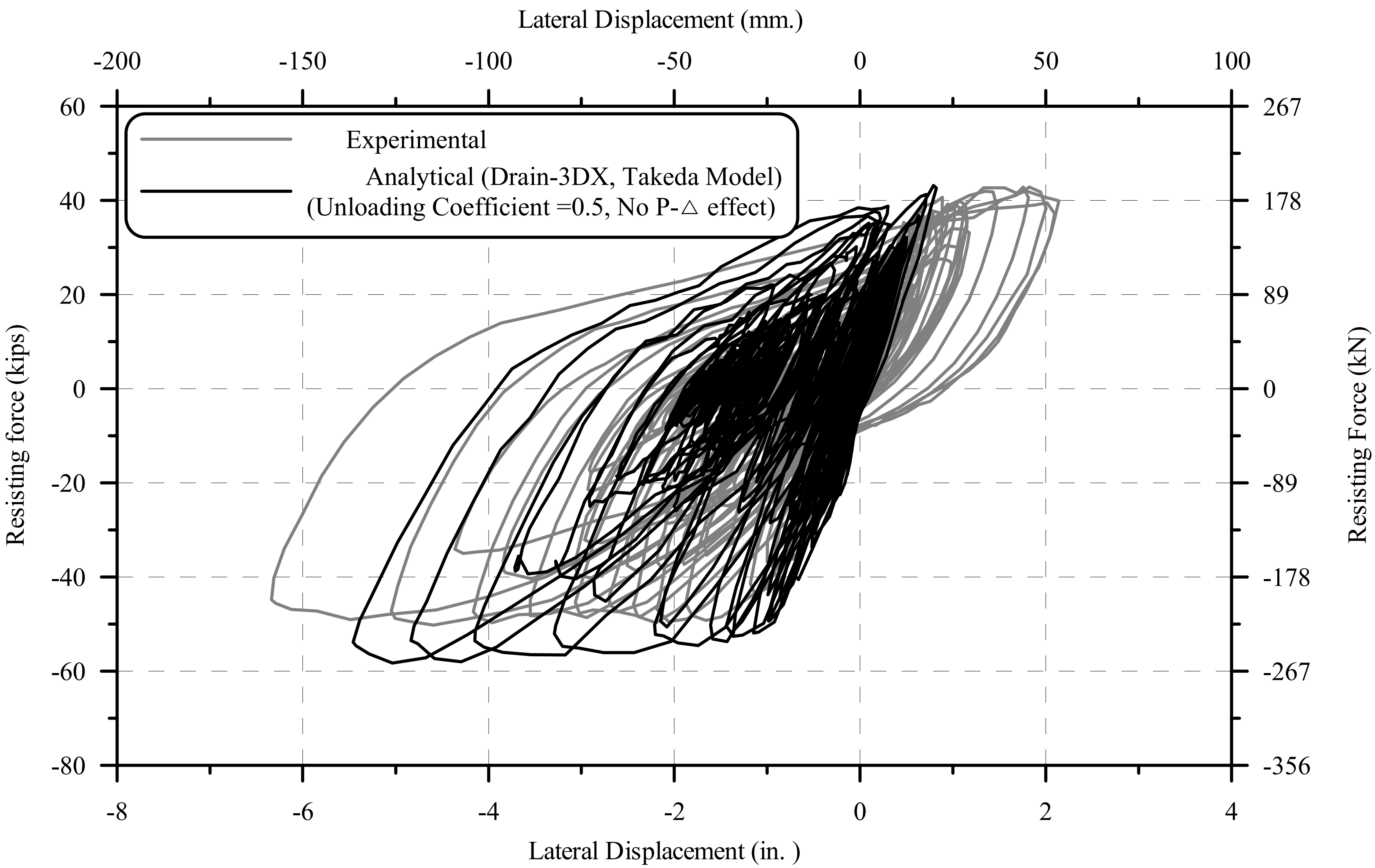

Fig. 5-39a: Load-Displacement Hystereses for Specimen B2CM under the Fifteen Loading Runs

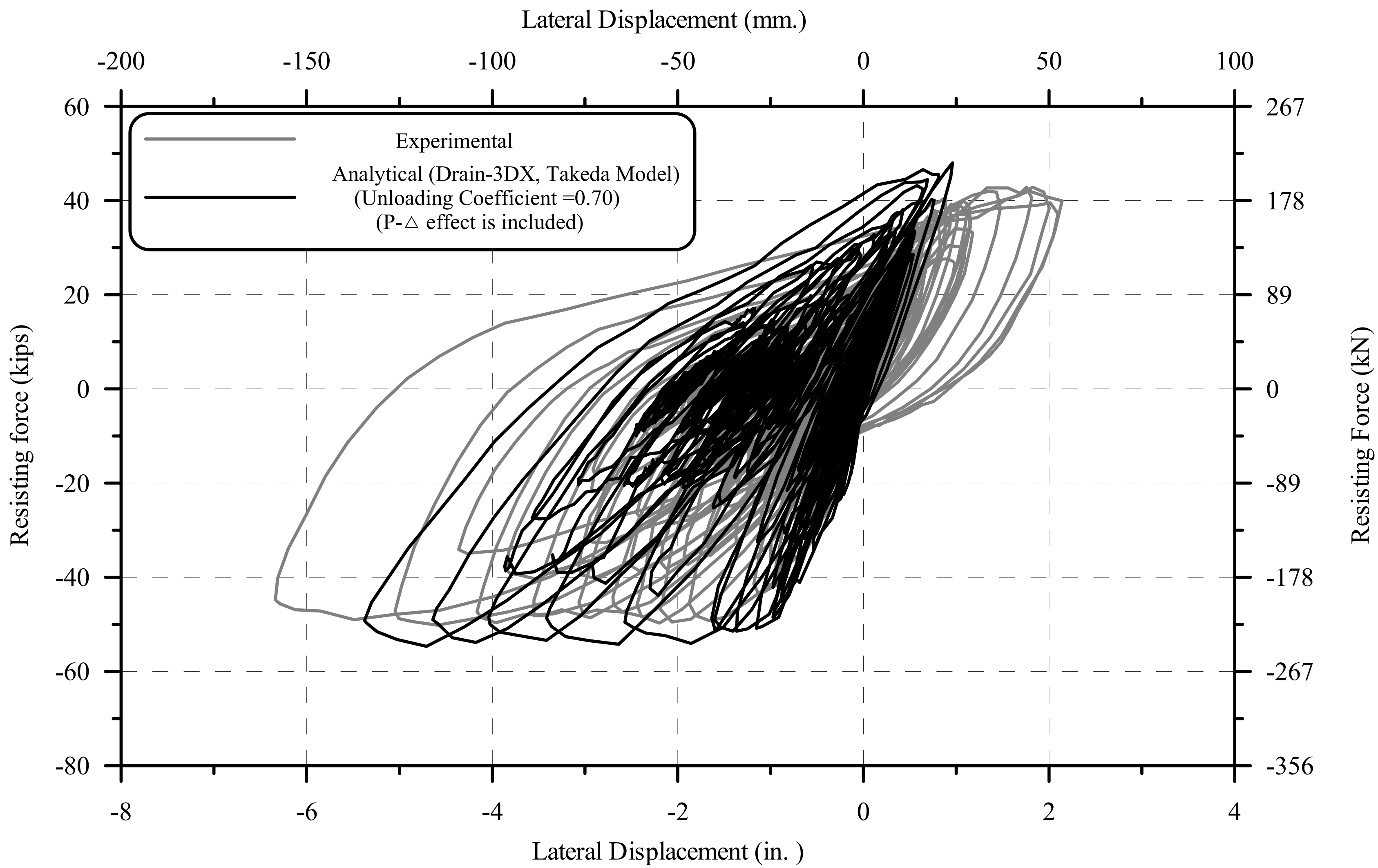

Fig. 5-39b: Load-Displacement Hystereses for Specimen B2CM under the Fifteen Loading Runs

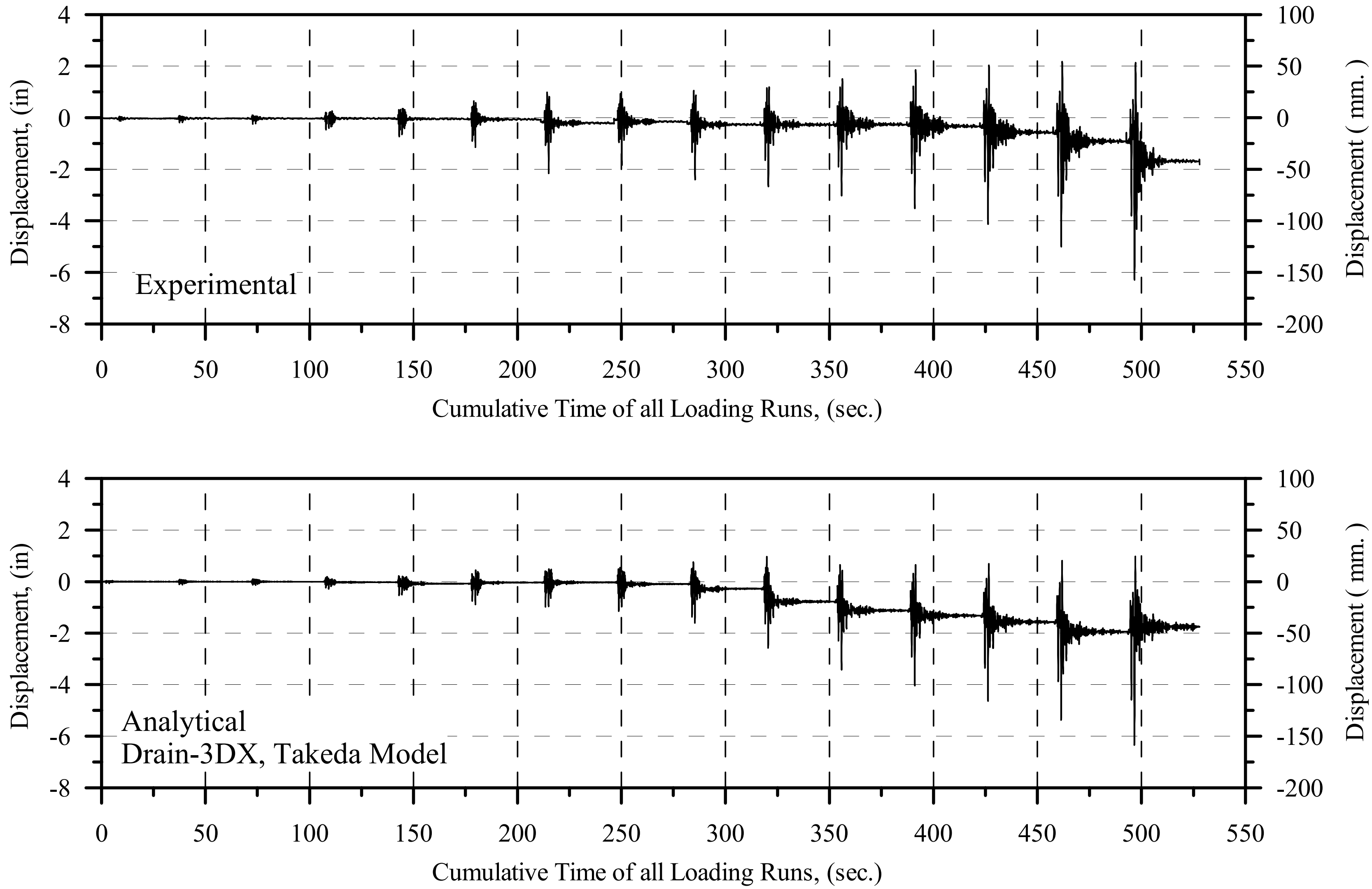

Fig. 5-40: Relative Displacement History for Specimen B2CM under the Fifteen Loading Runs

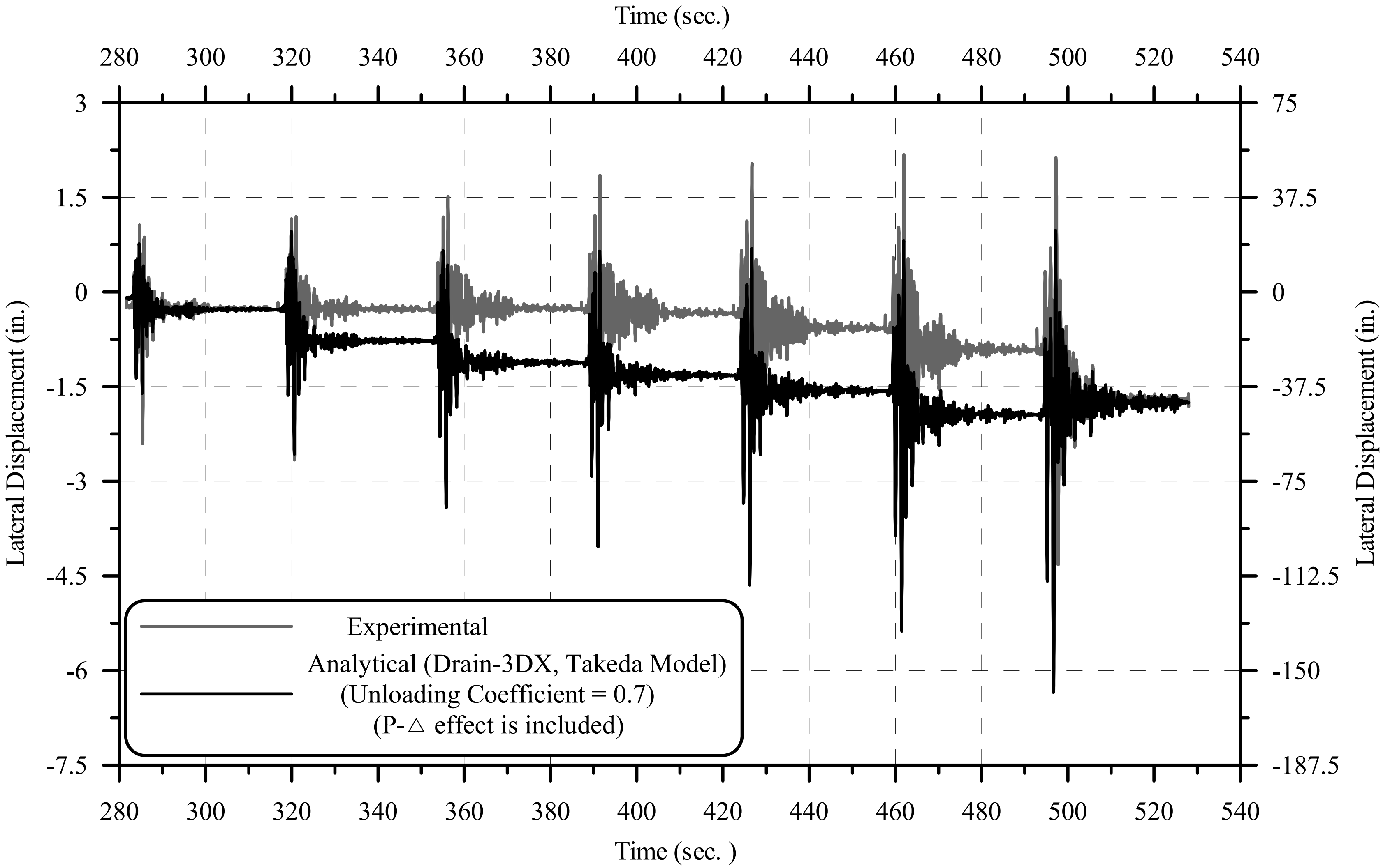

Fig. 5-41: Displacement Time-History for Specimen B2CM under the Last Seven Loadings

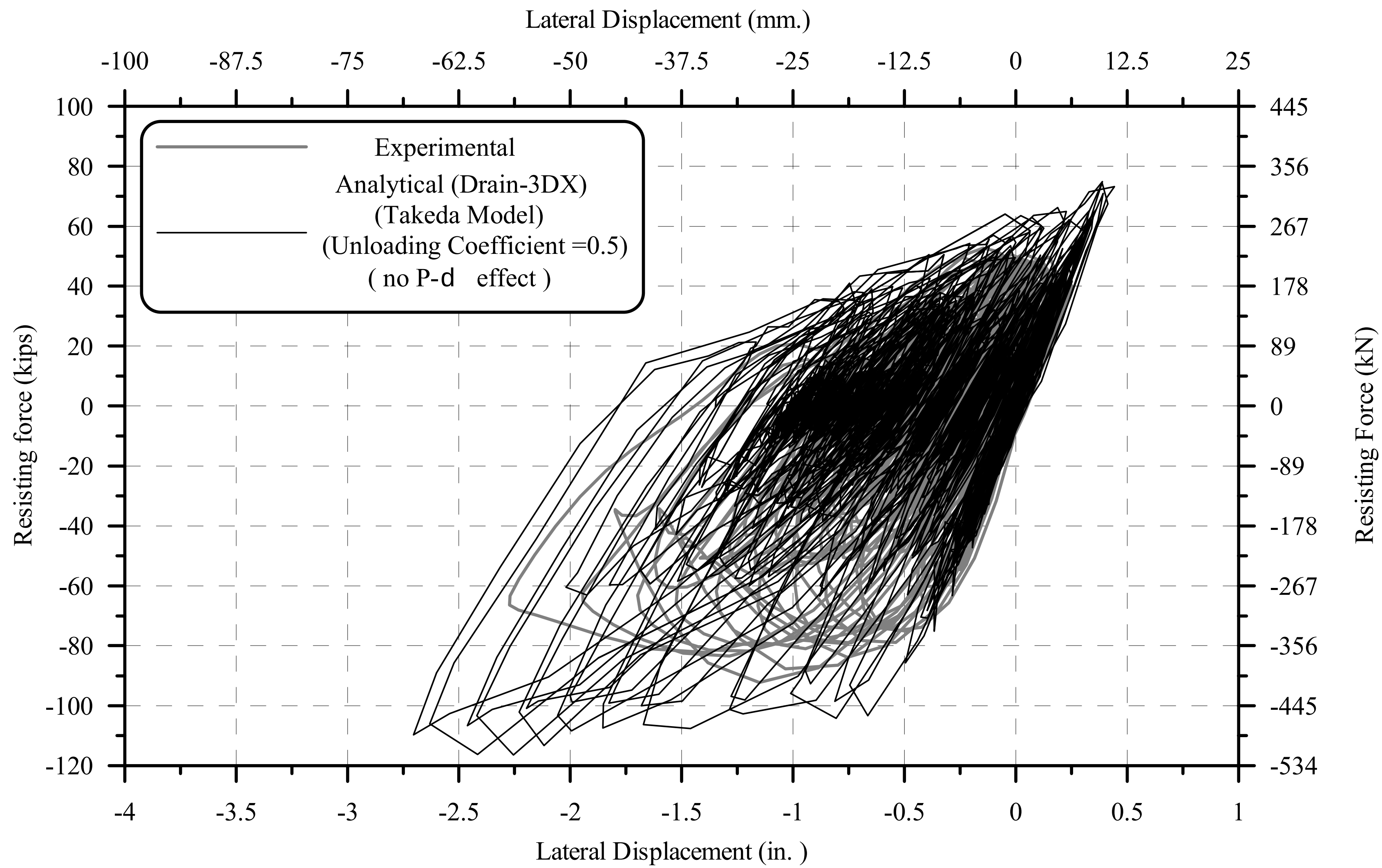

Fig. 5-42a: Load-Displacement Hystereses for Specimen B2CS under the Seventeen Loading Runs

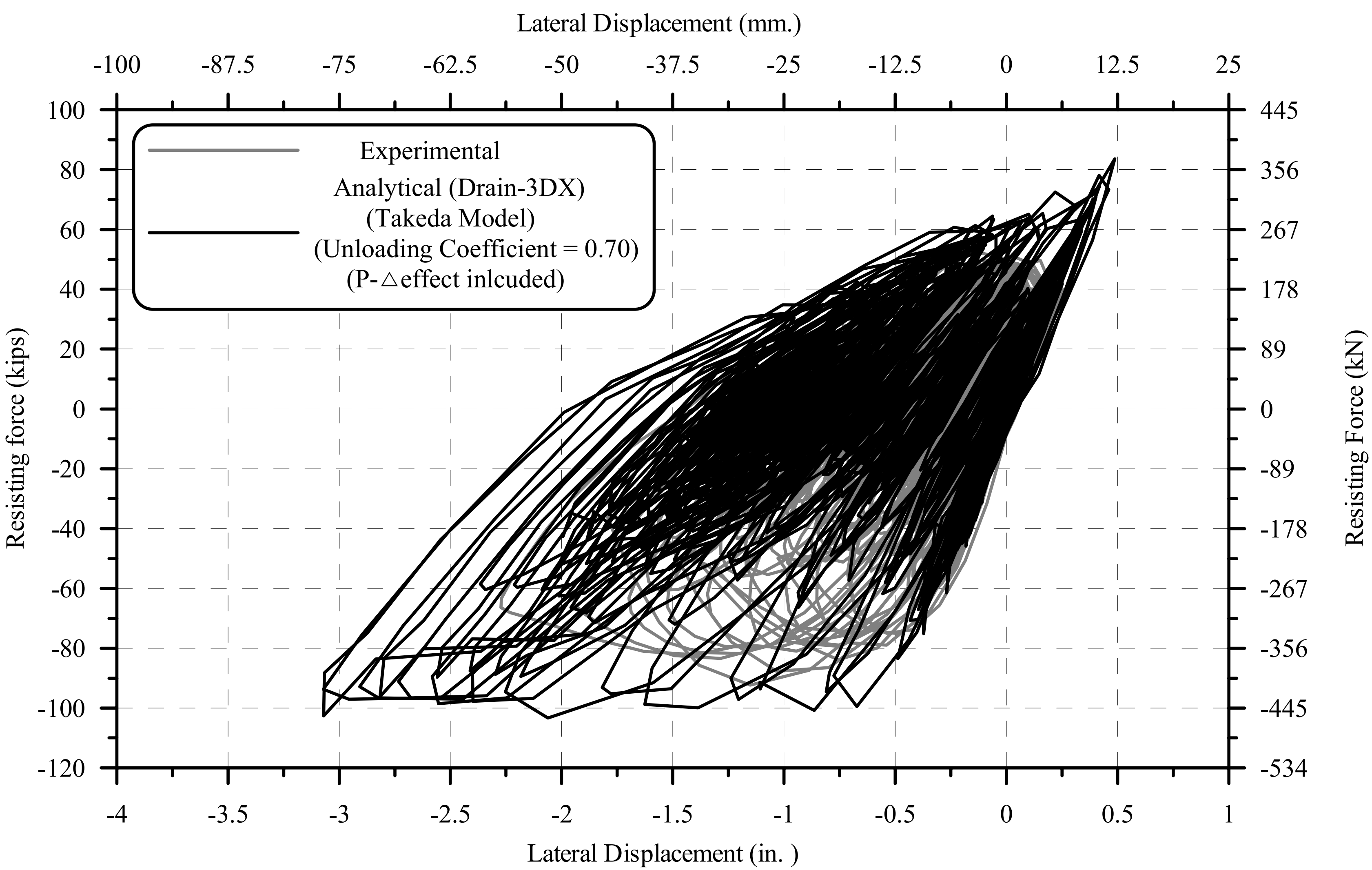

Fig. 5-42b: Load-Displacement Hystereses for Specimen B2CS under the Seventeen Loading Runs

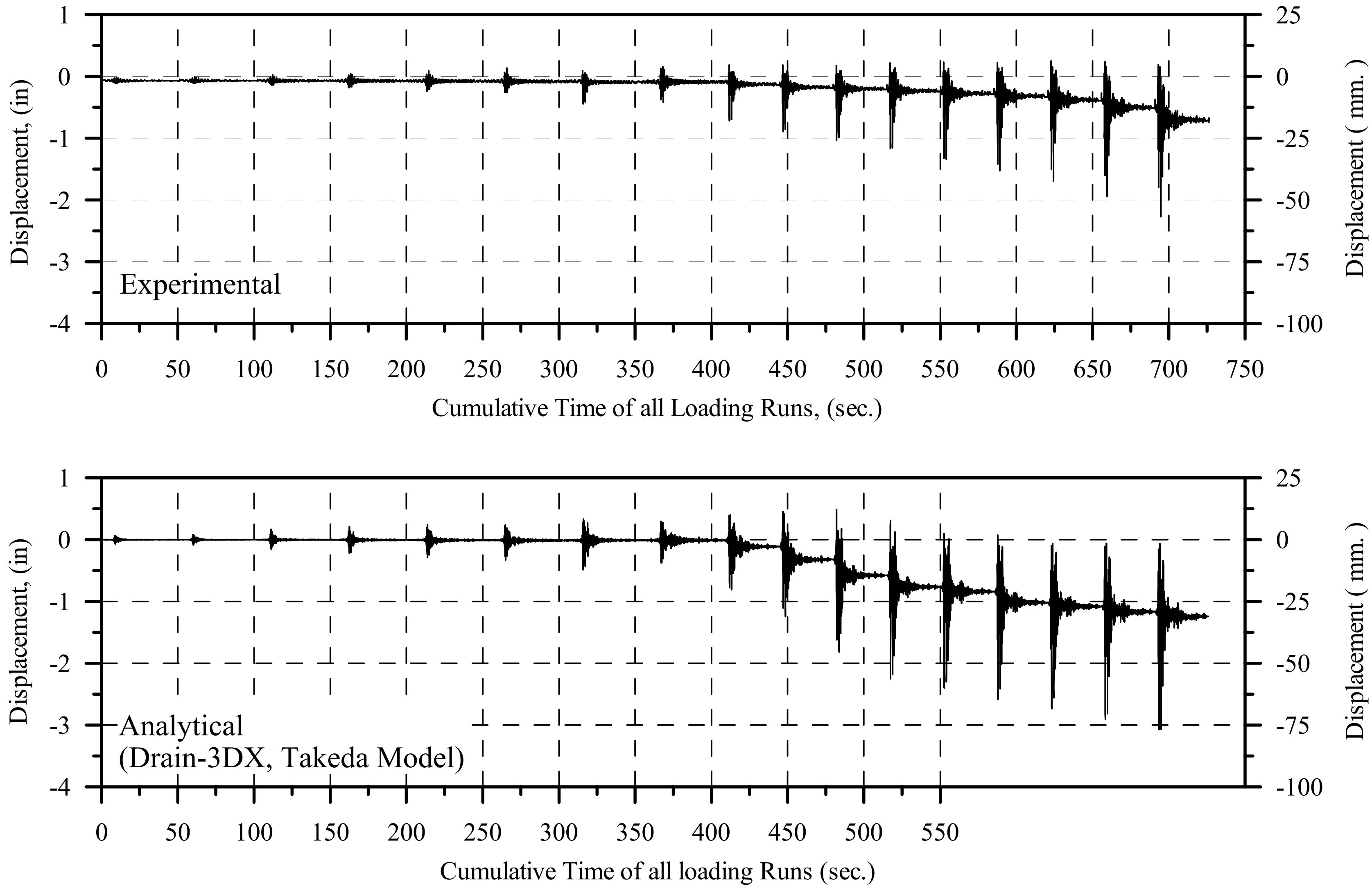

Fig. 5-43: Relative Displacement History for Specimen B2CS under the Seventeen Loading Runs

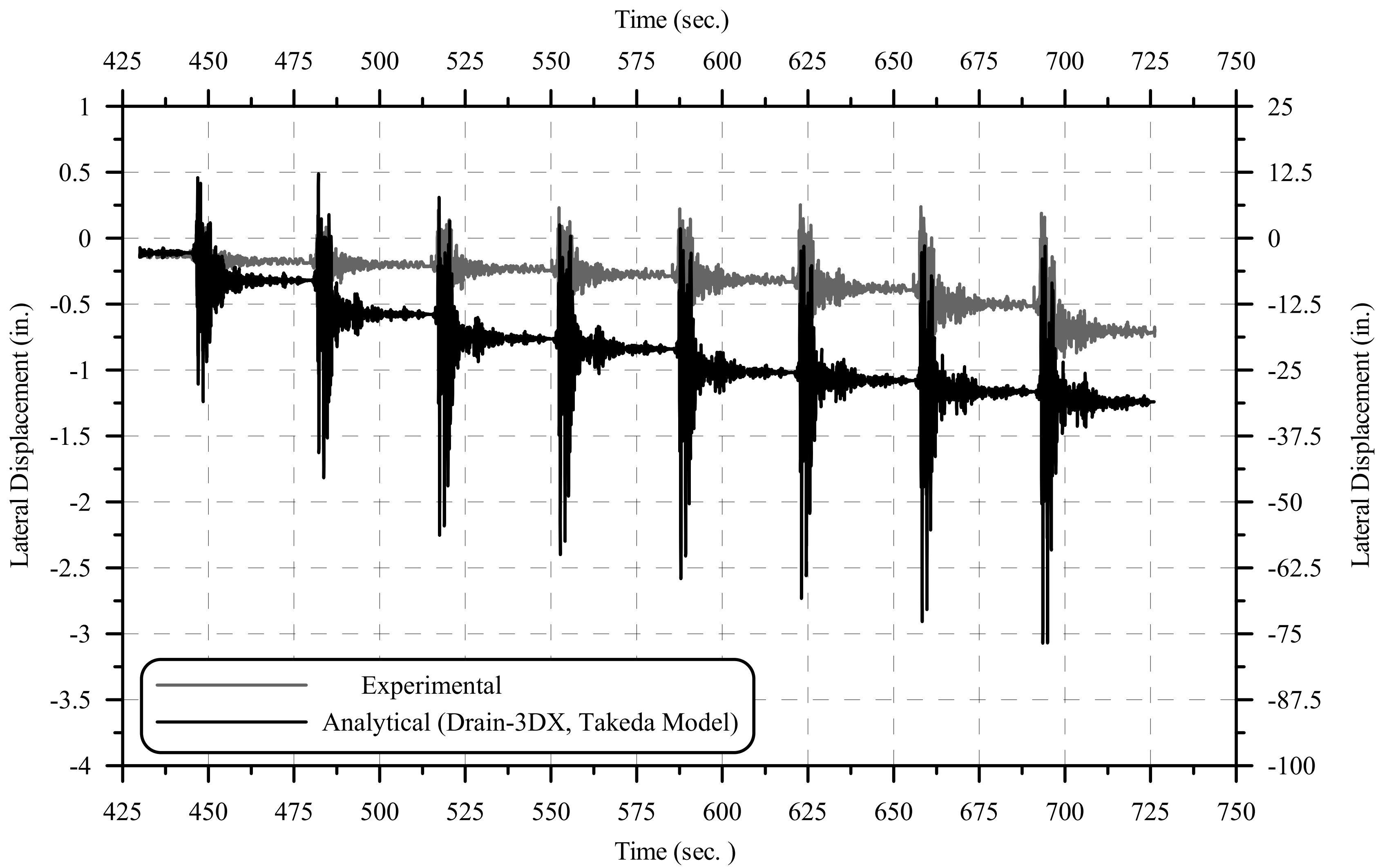

Fig. 5-44:Displacement Time-History for Specimen B2CS under the Last Eight Loadings

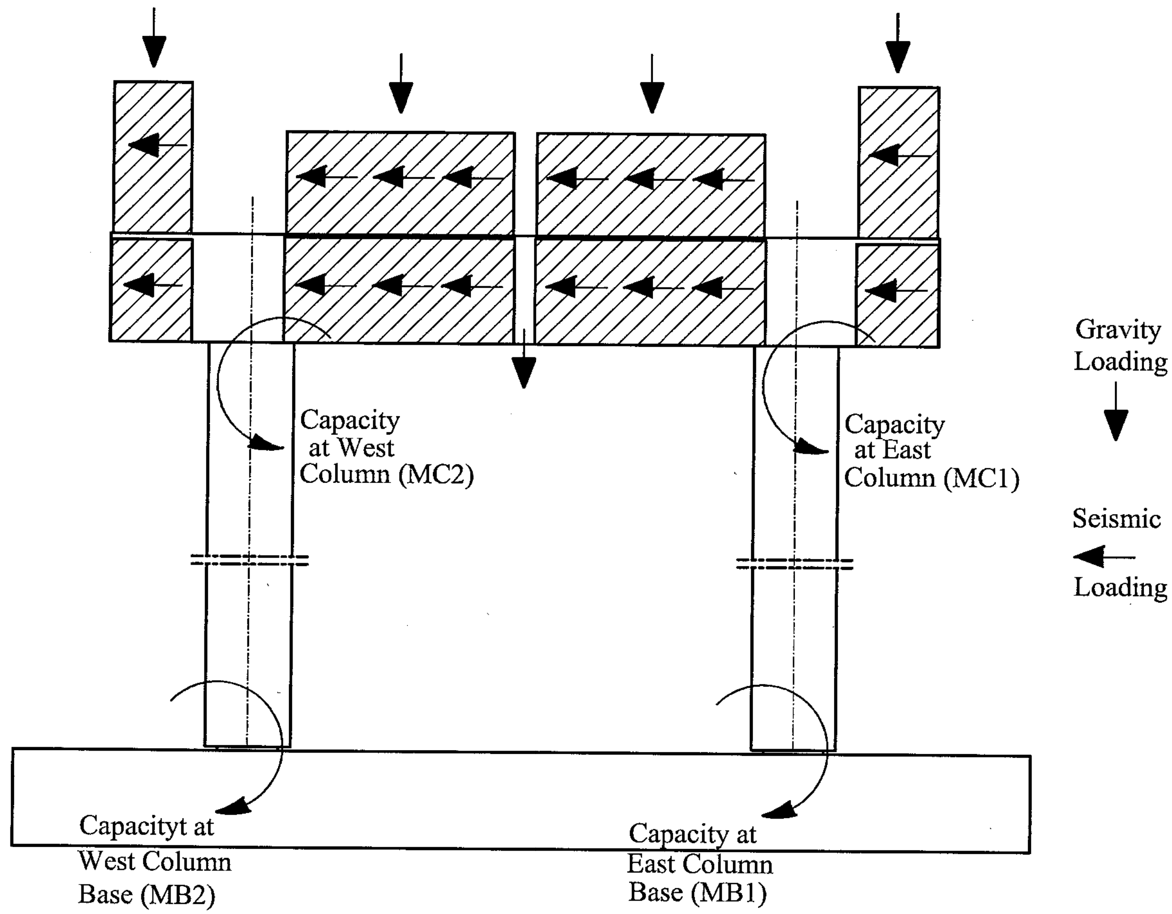

Fig. 5-45: Modeling of Gravity and Seismic Loadings

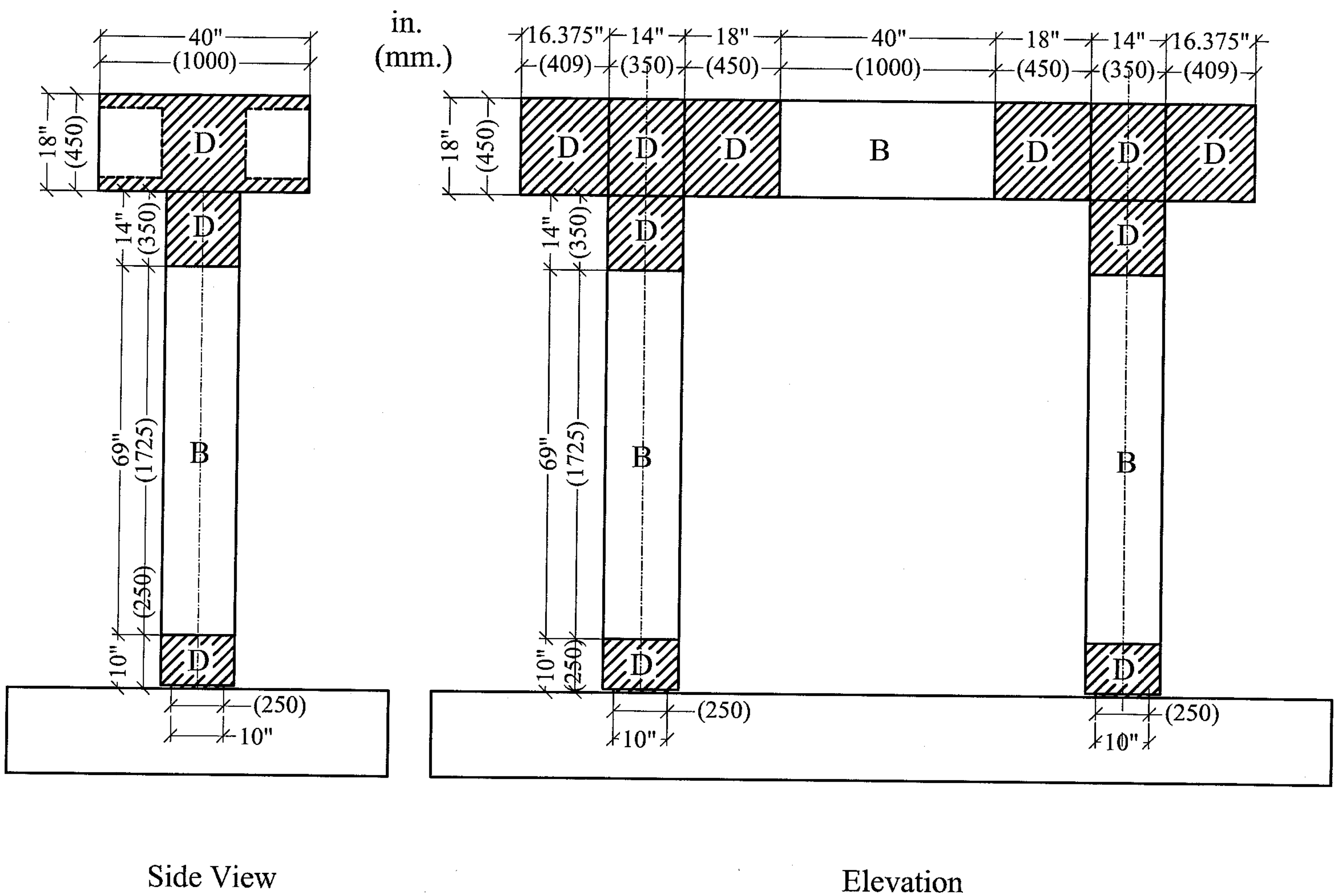

Fig. 5-46a :D and B regions in Tall Specimen B2CT

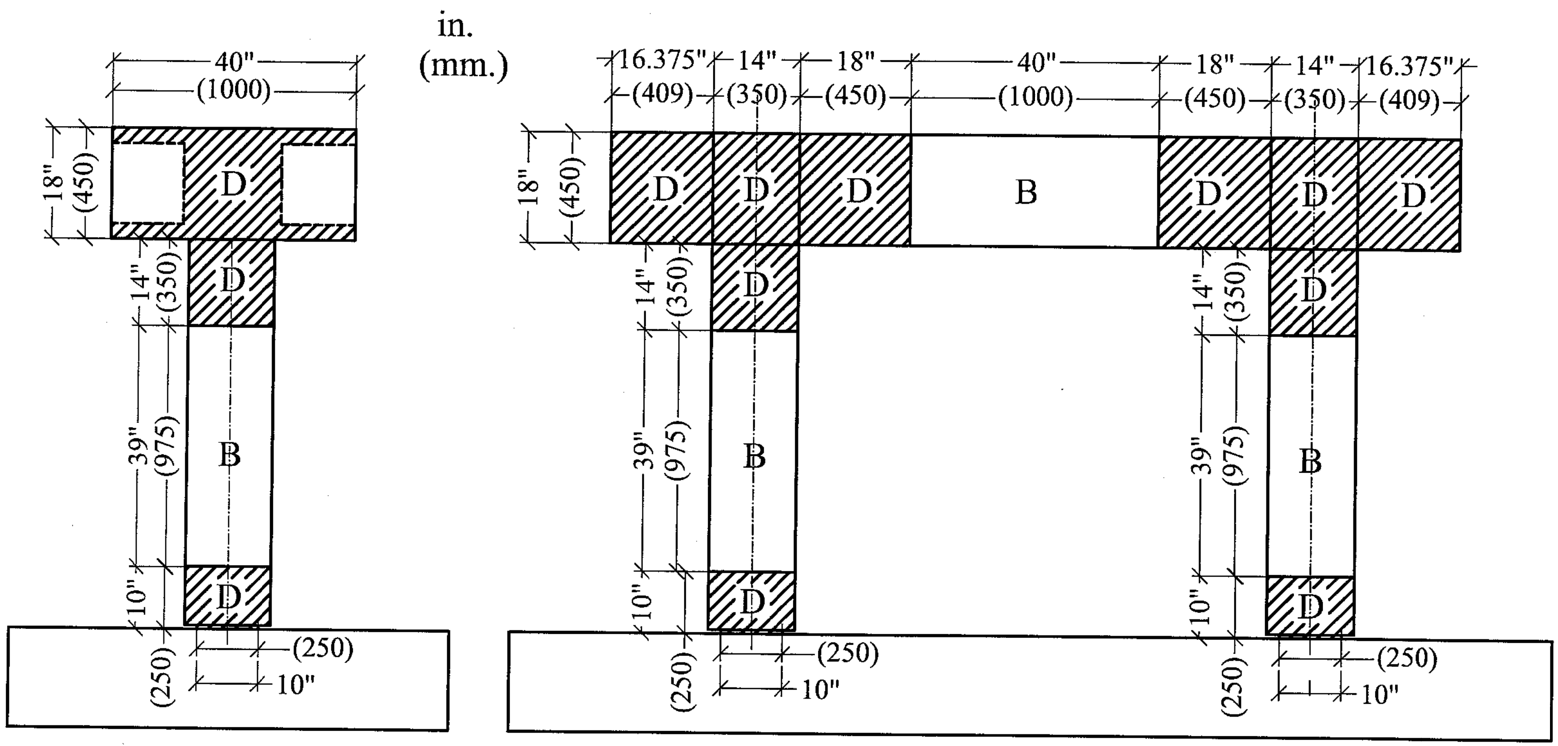

Fig. 5-46b: D and B regions in Middle Specimen B2CM

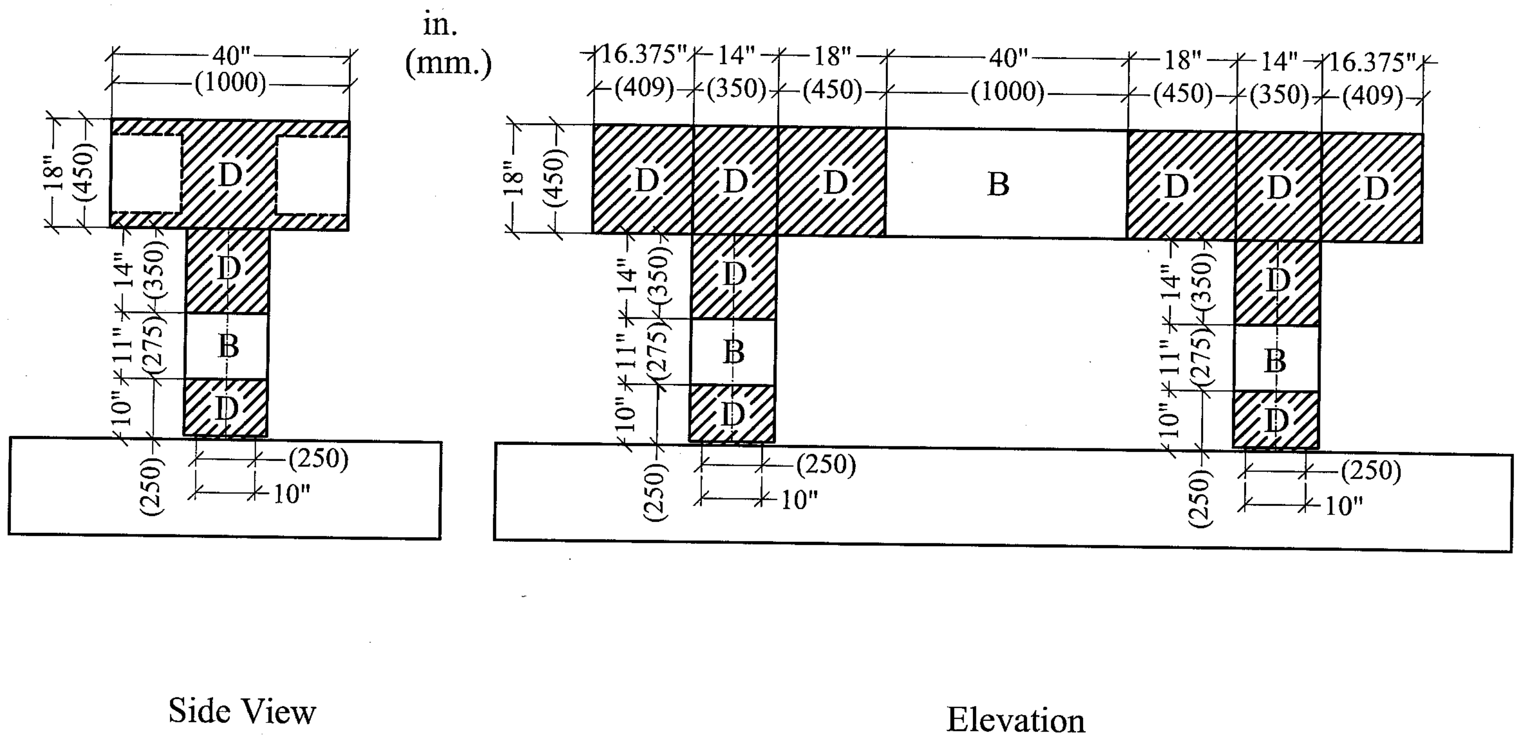

Fig. 5-46c: D and B Regions in Short Specimen B2CS

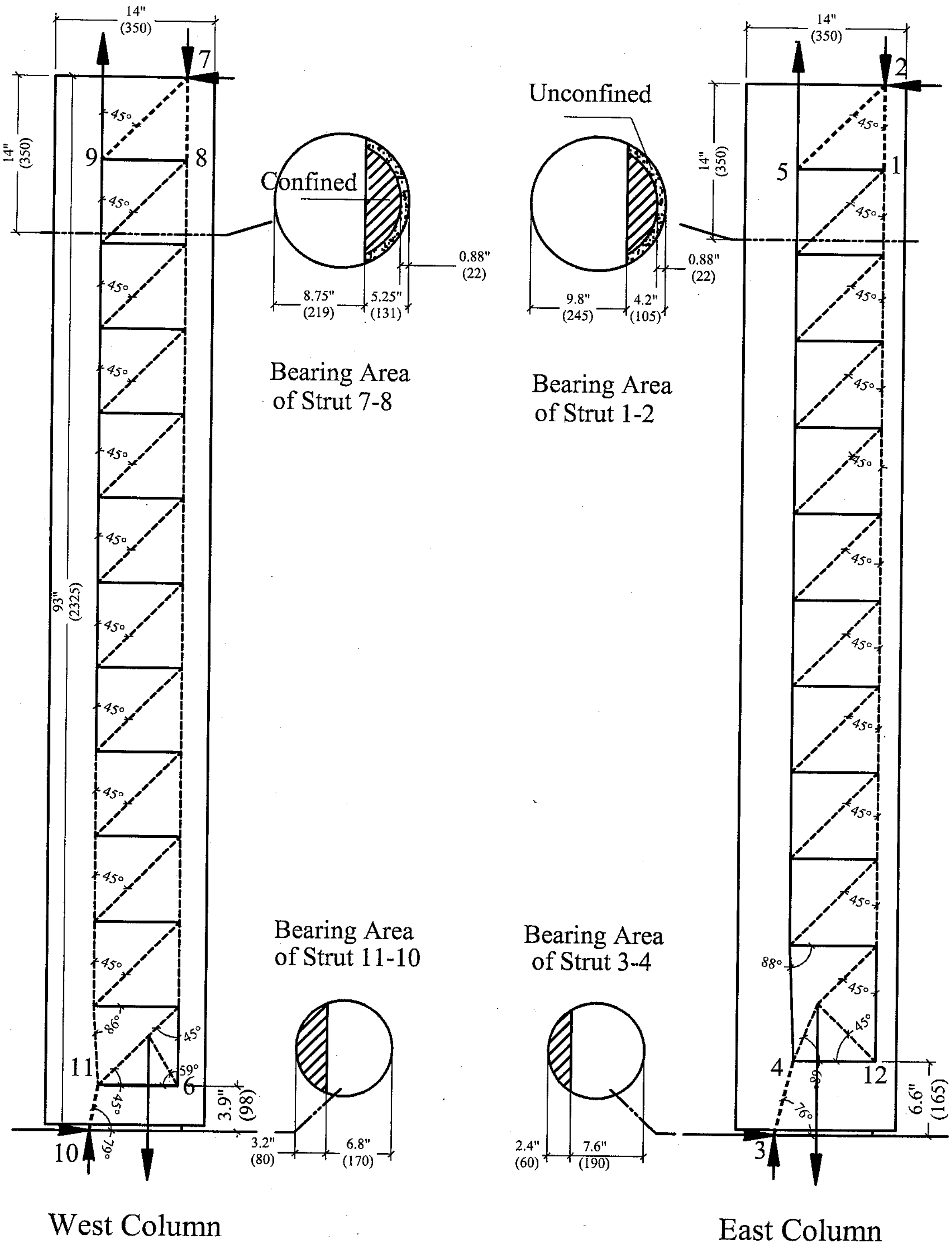

Fig. 5-47: Strut-and-Tie Model in Tall Specimen Columns

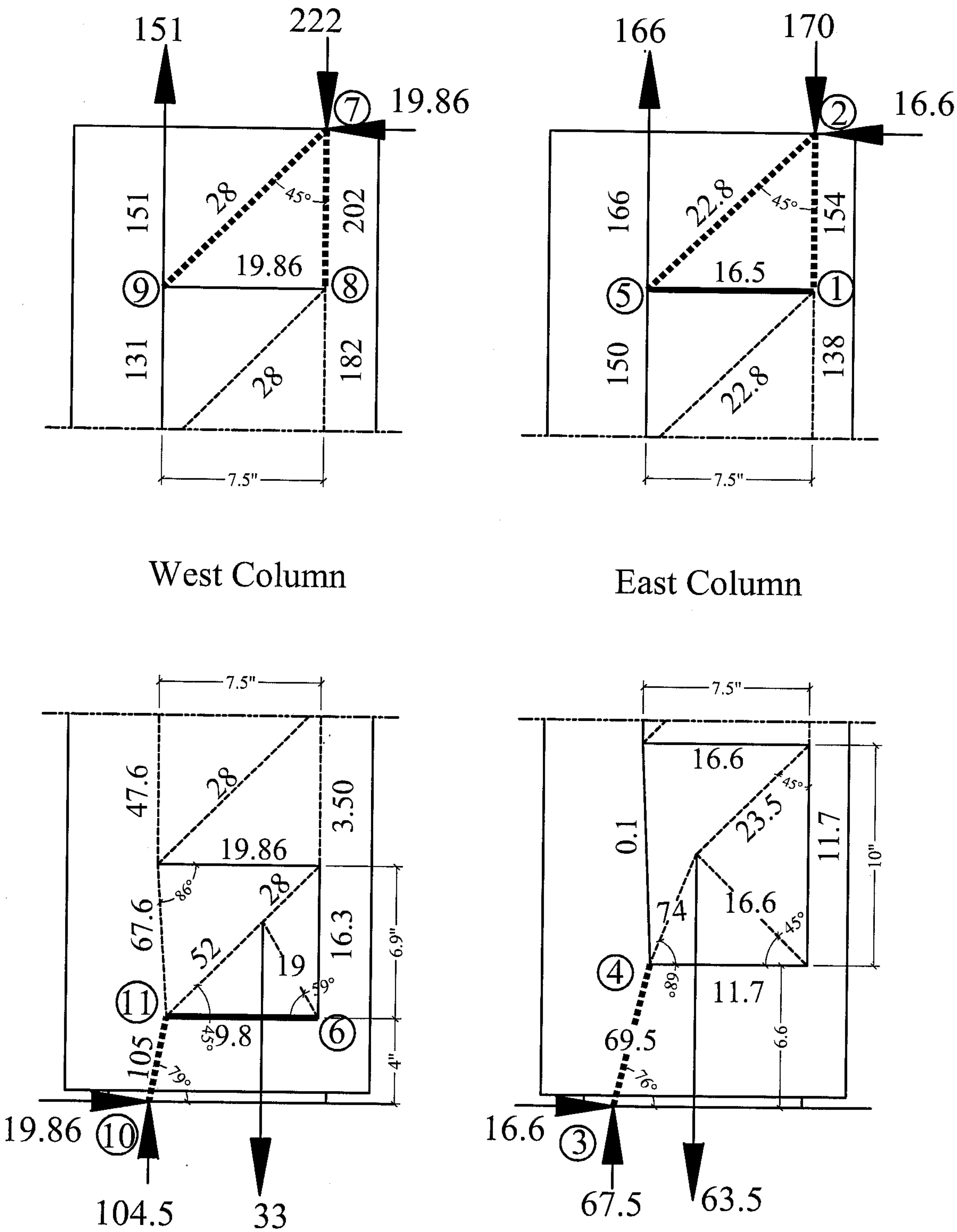

Fig. 5-48a: Model Forces in D-Regions of Tall Columns (kips, in.)

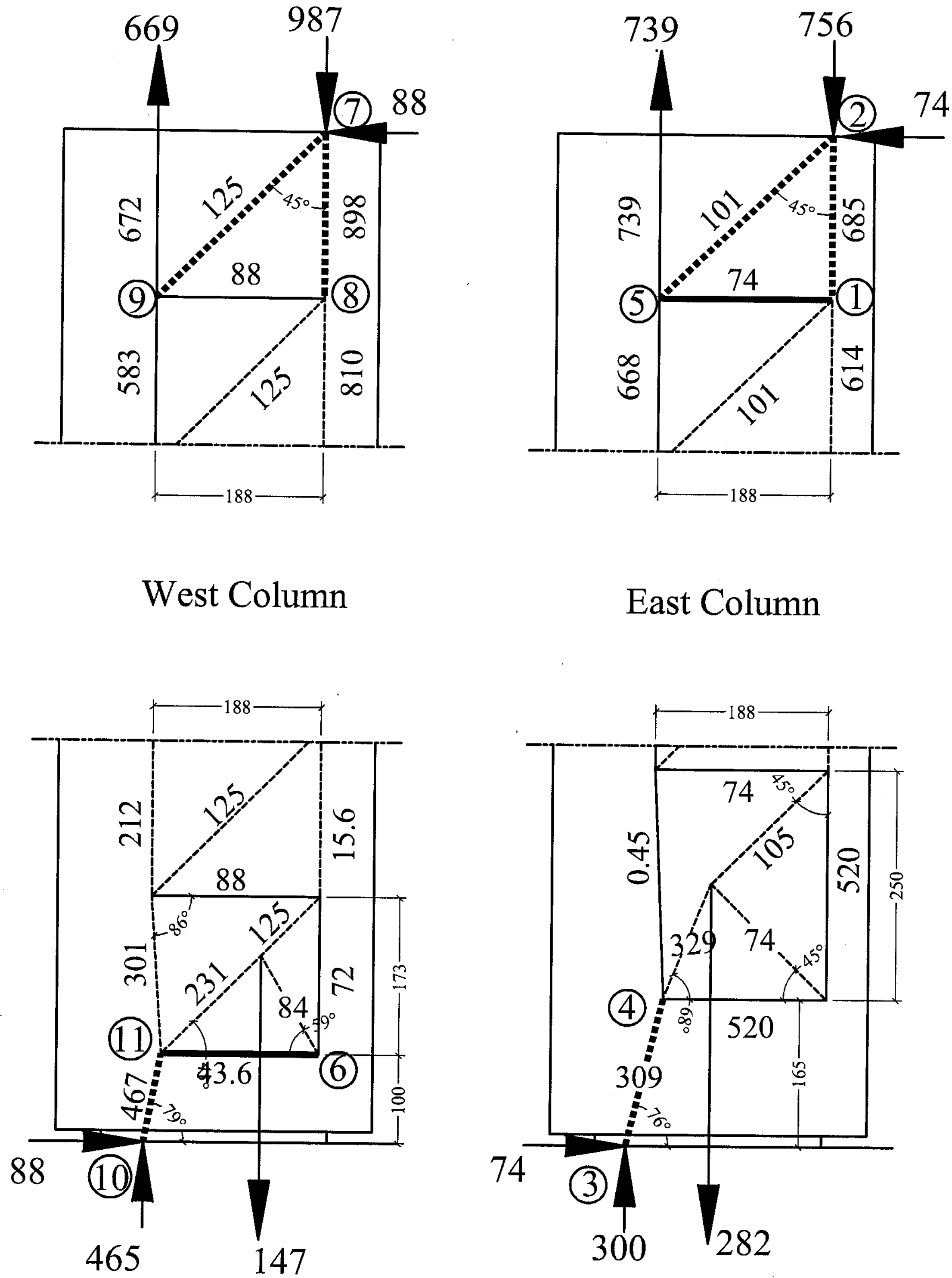

Fig. 5-48b: Model Forces in D-Regions of Tall Columns (kN, mm.)

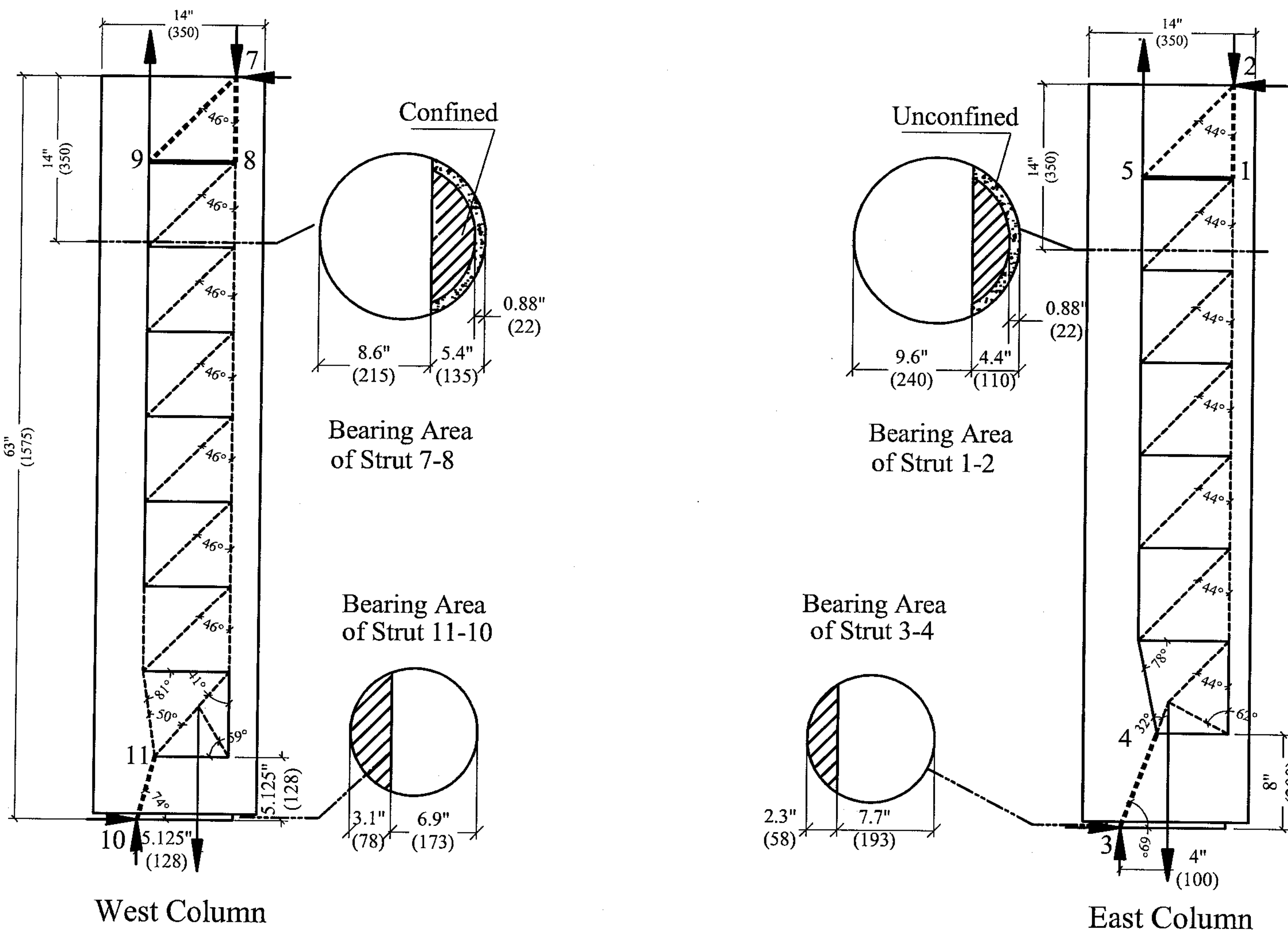

Fig. 5-49: Strut-and-Tie Model in Middle Specimen Columns

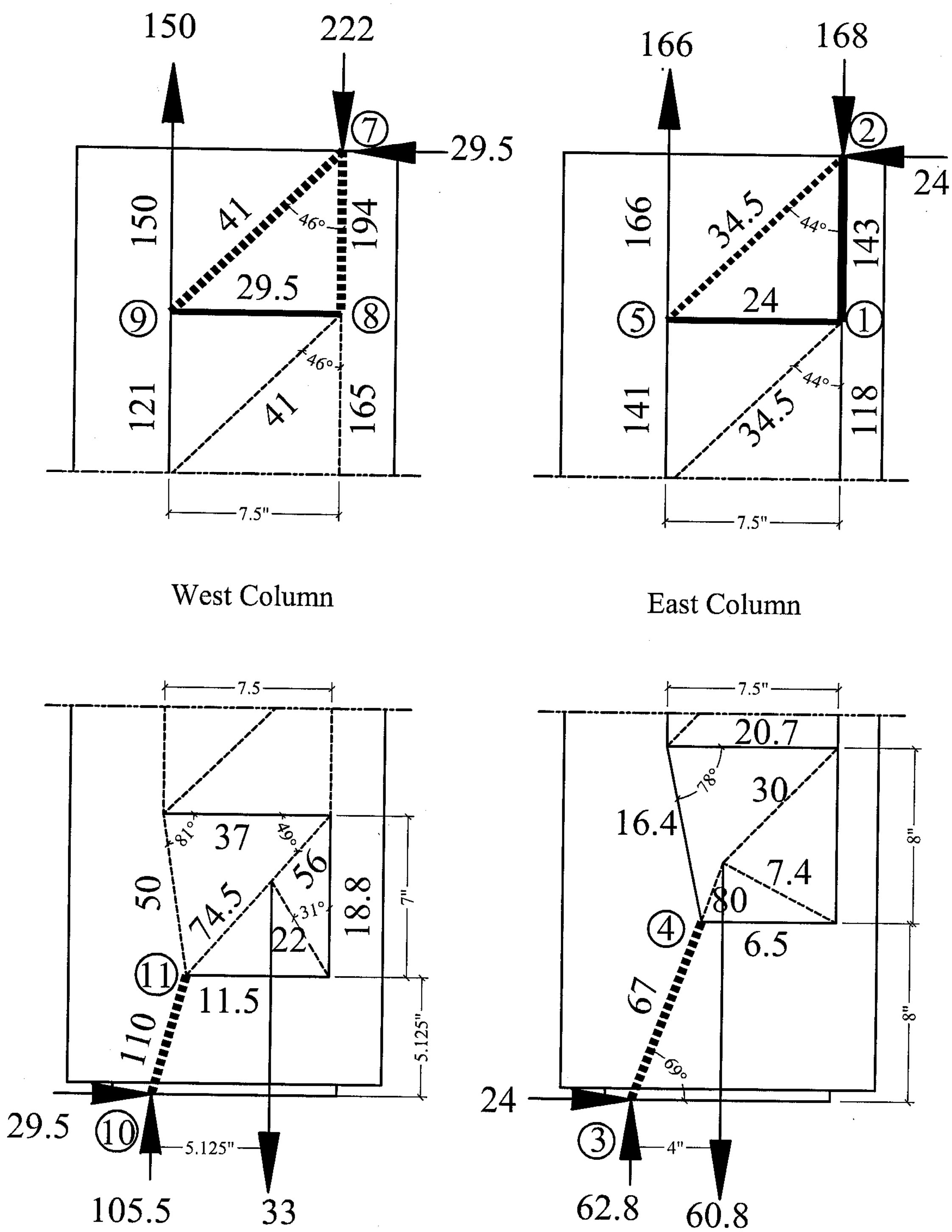

Fig. 5-50a: Model Forces in D-Regions of Middle Columns (kips, in.)

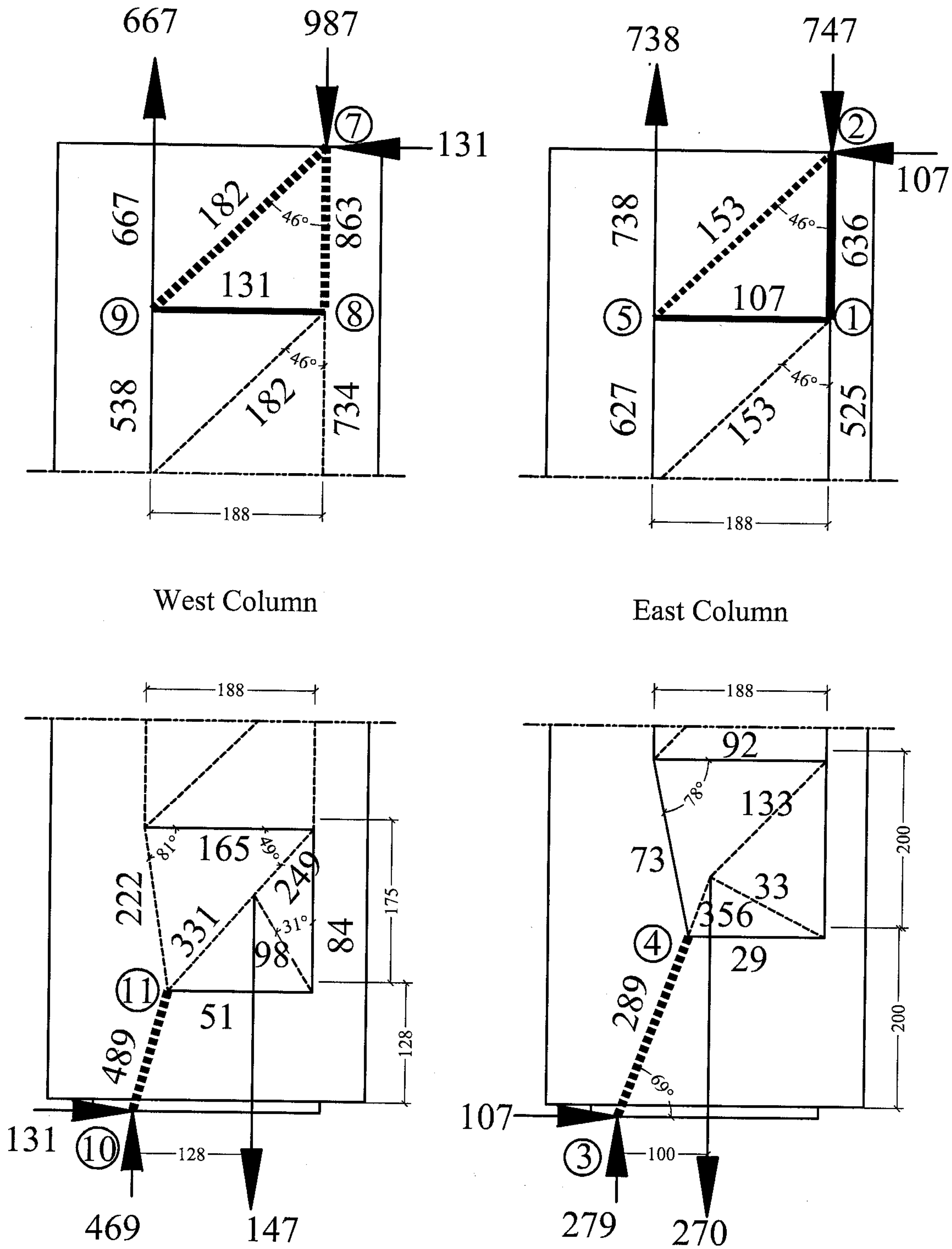

Fig. 5-50b: Model Forces in D-Regions of Middle Columns (kN, mm.)

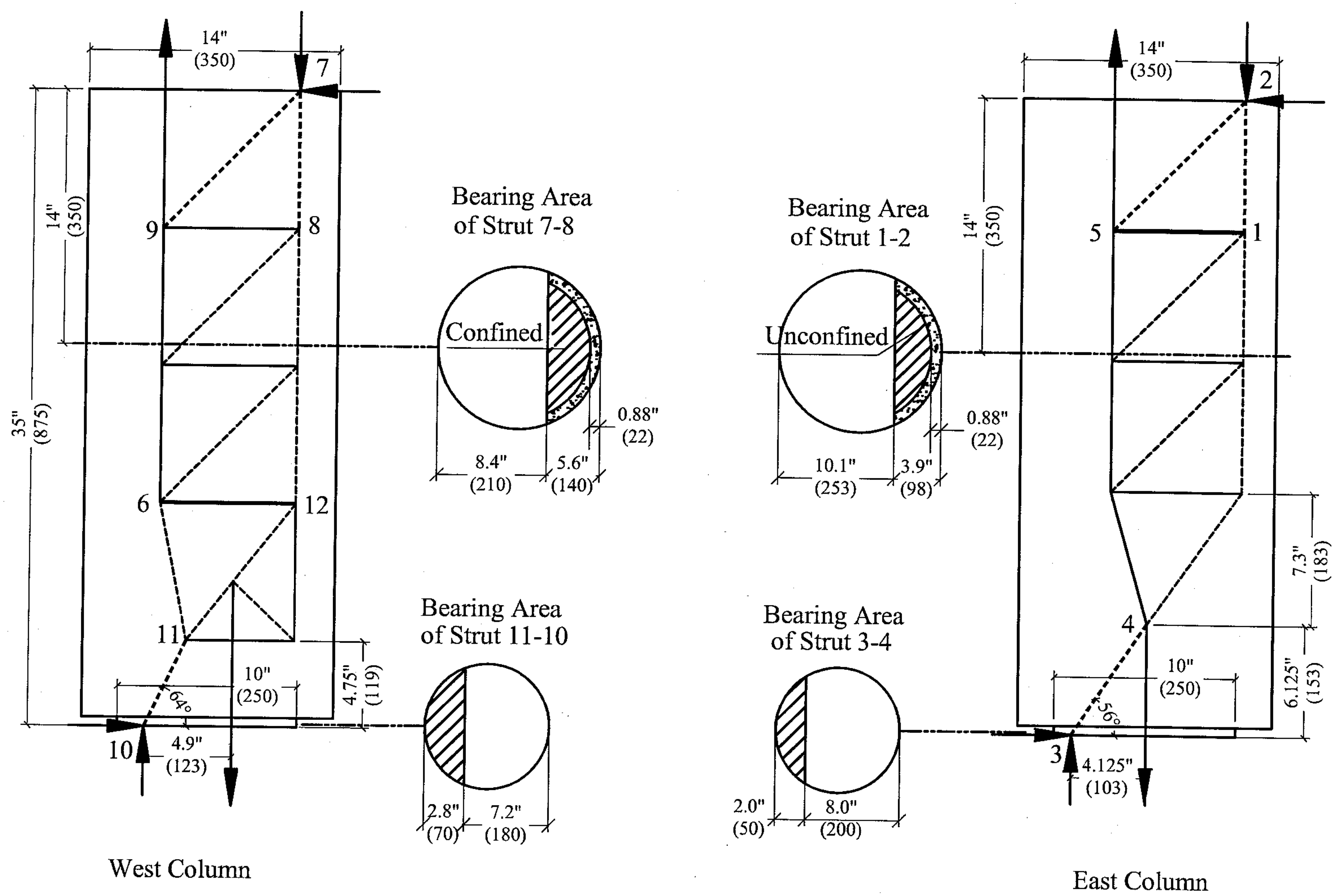

Fig. 5-51: Strut-and Tie-Model in Short Specimen Columns

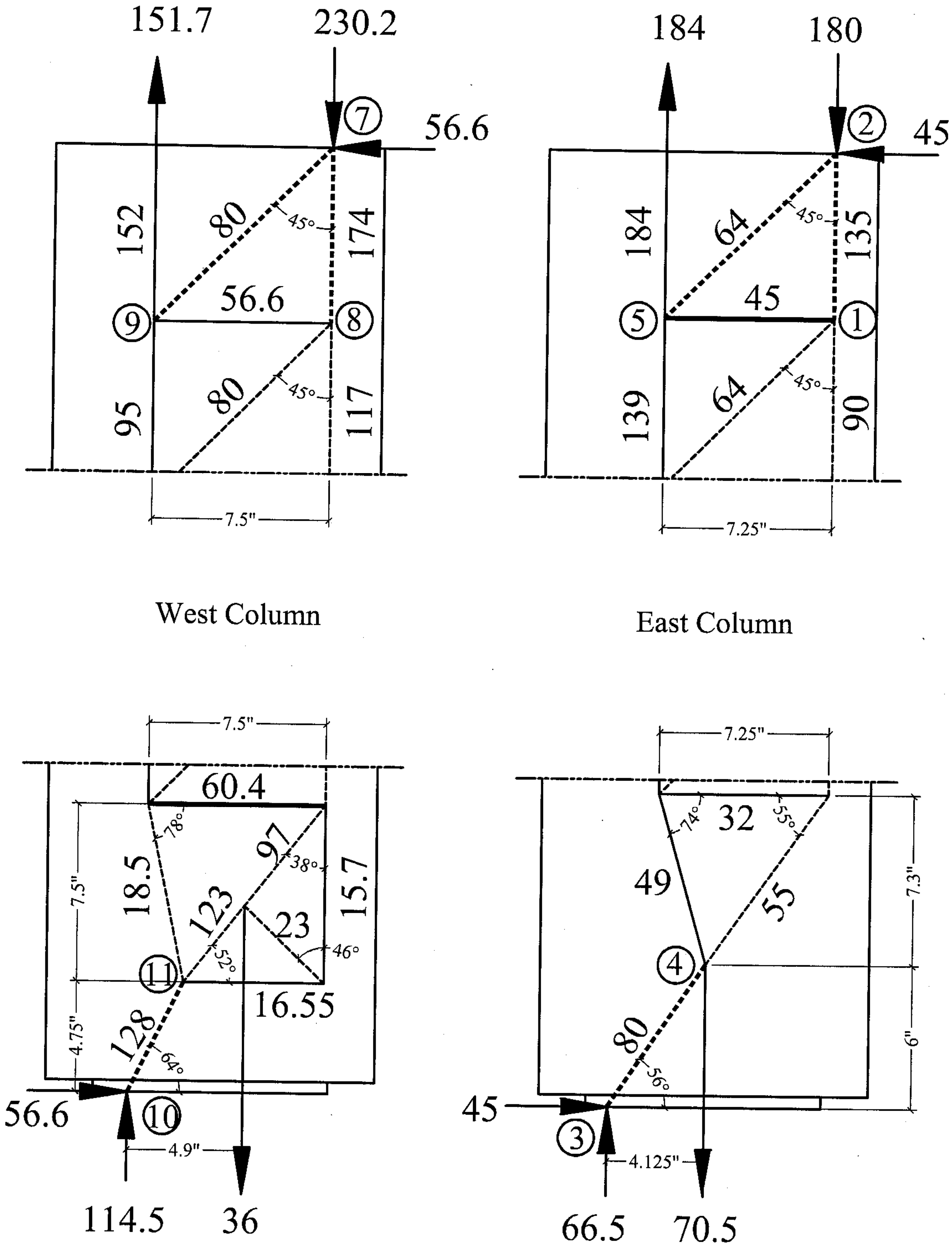

Fig. 5-52a: Model Forces in D-Regions of Short Columns (kips, in.)

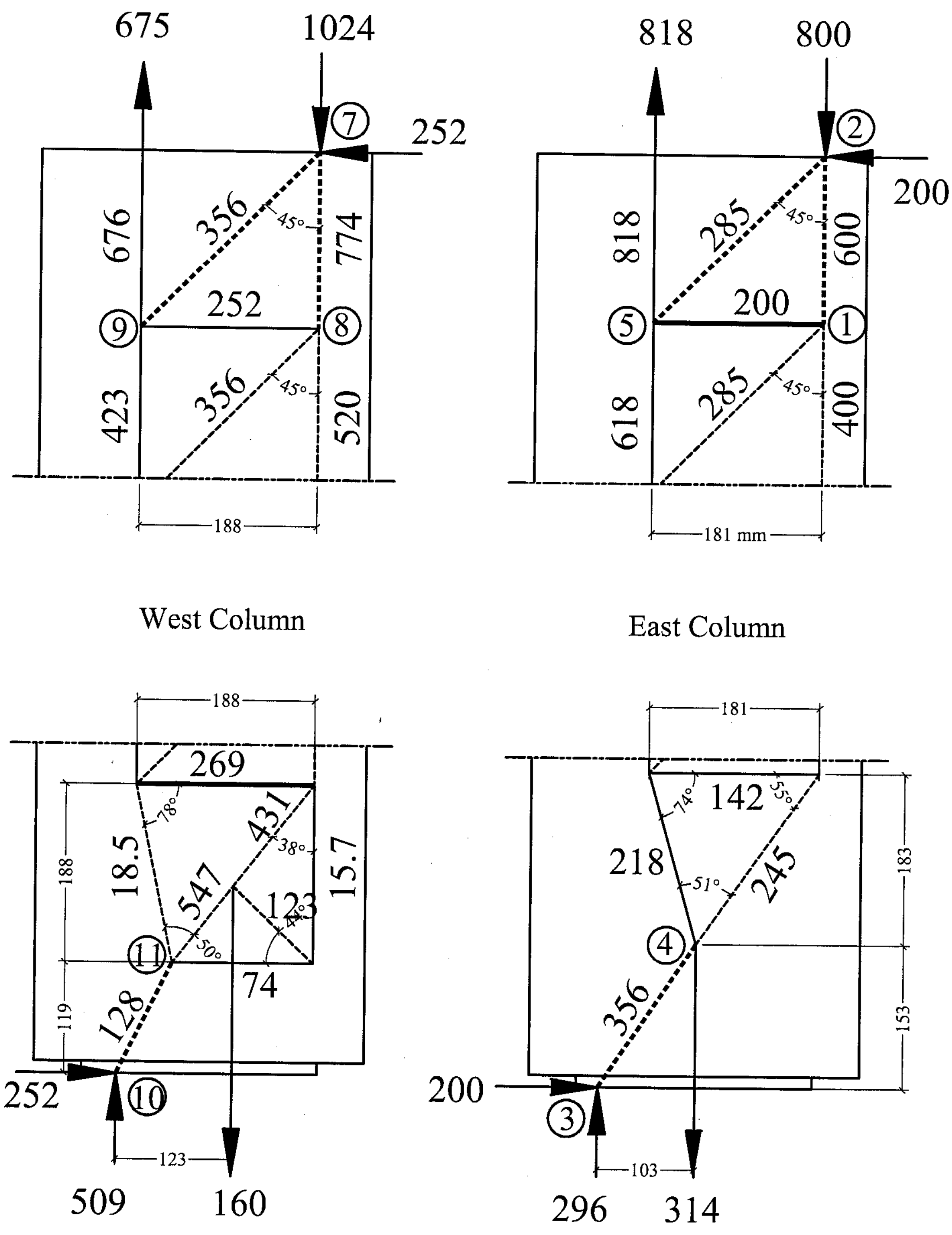

Fig. 5-52b: Model Forces in D-Regions of Short Columns (kN, mm.)

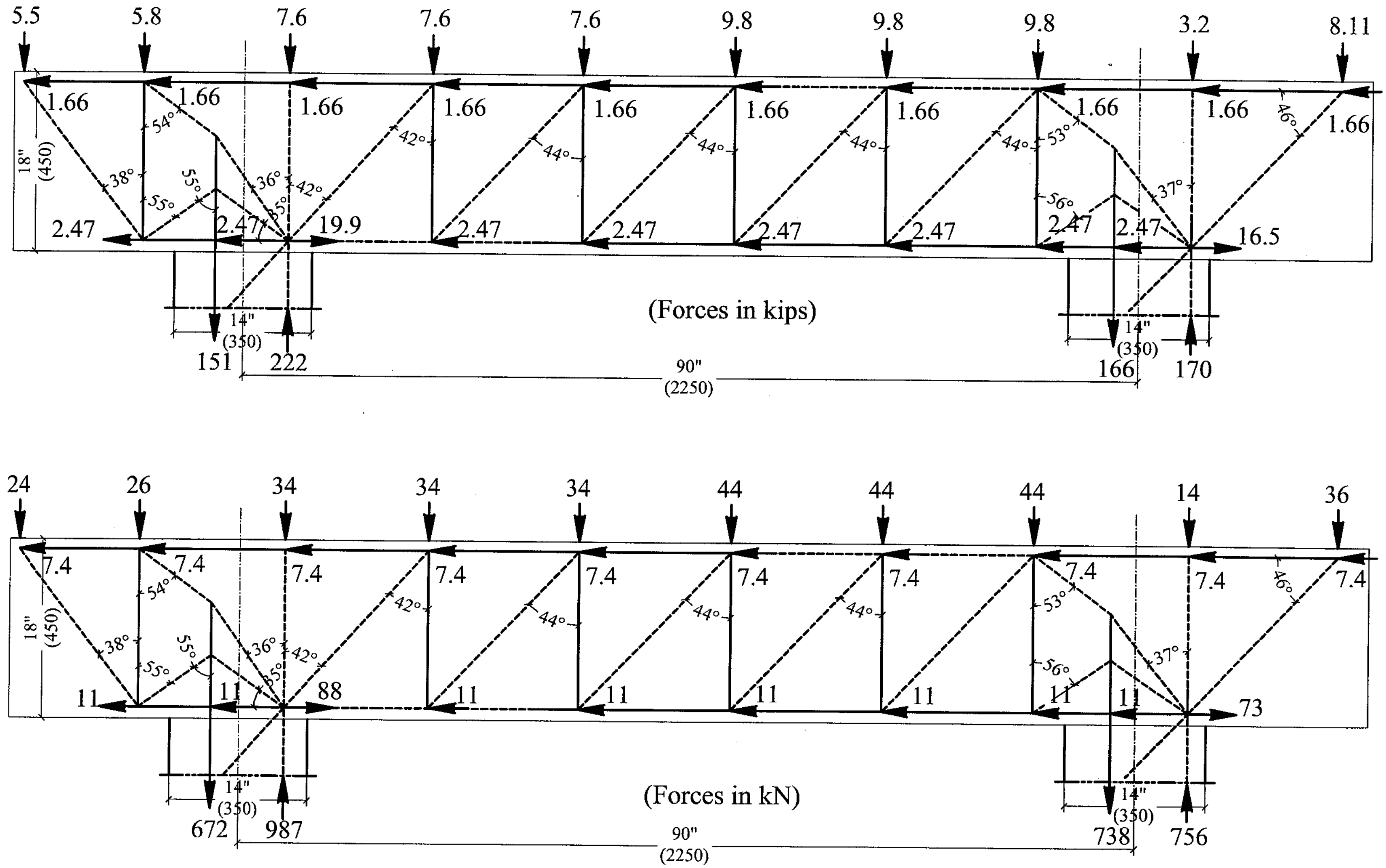

Fig. 5-53a: Strut-and-Tie Model in Tall Specimen Beam

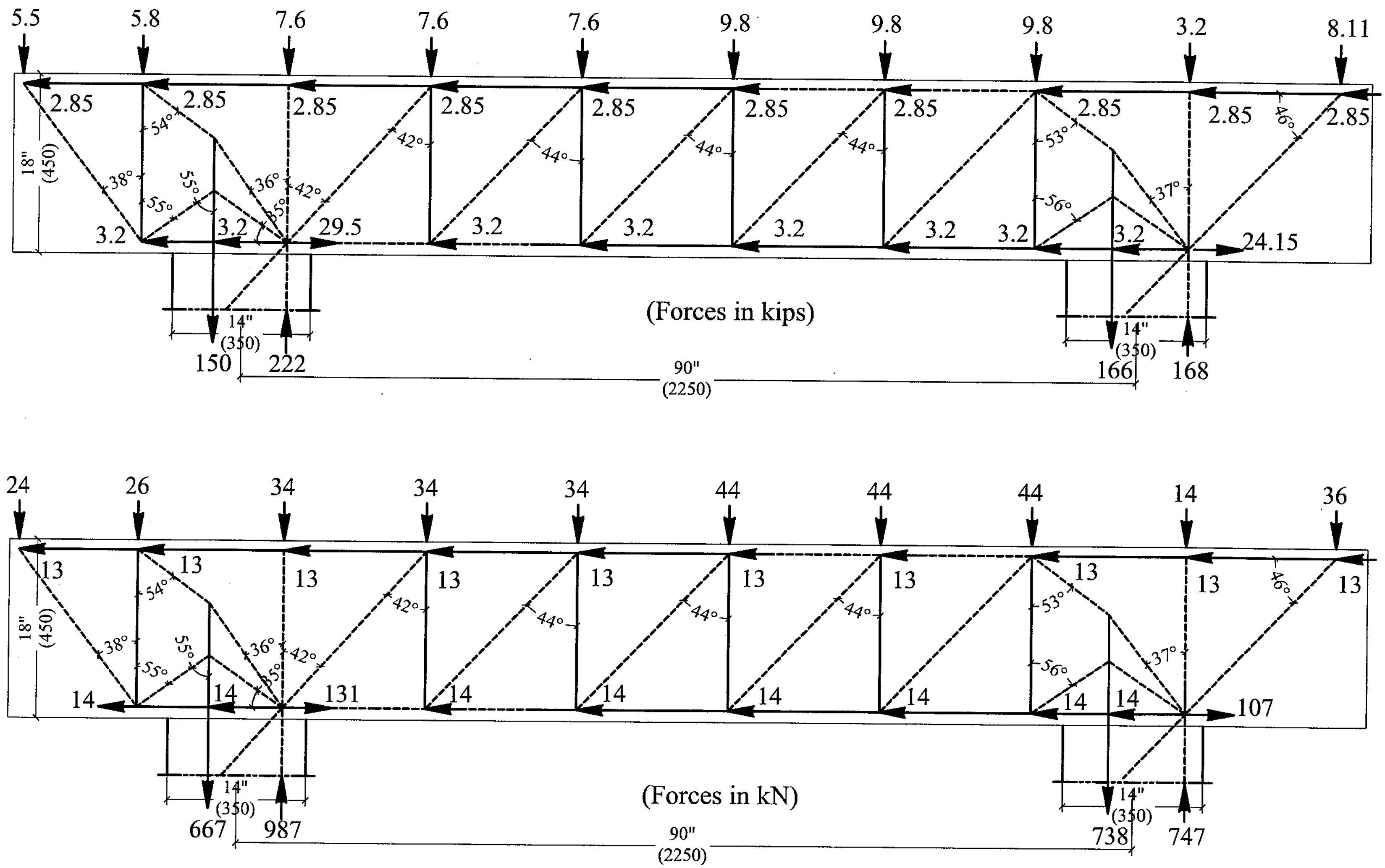

Fig. 5-53b: Strut-and-Tie Model in Middle Specimen Beam

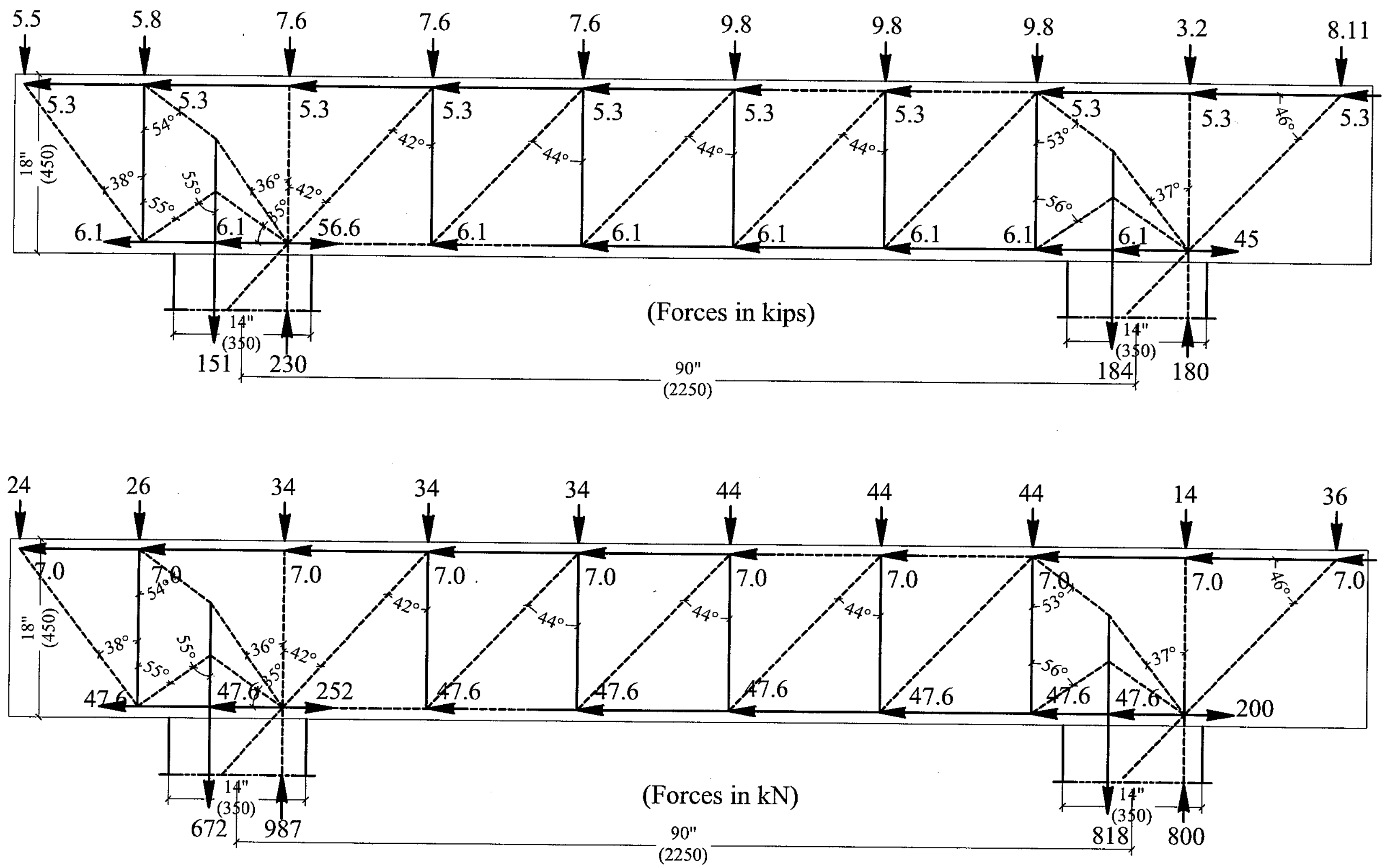

Fig. 5-53c: Strut-and-Tie Model in Short Specimen Beam

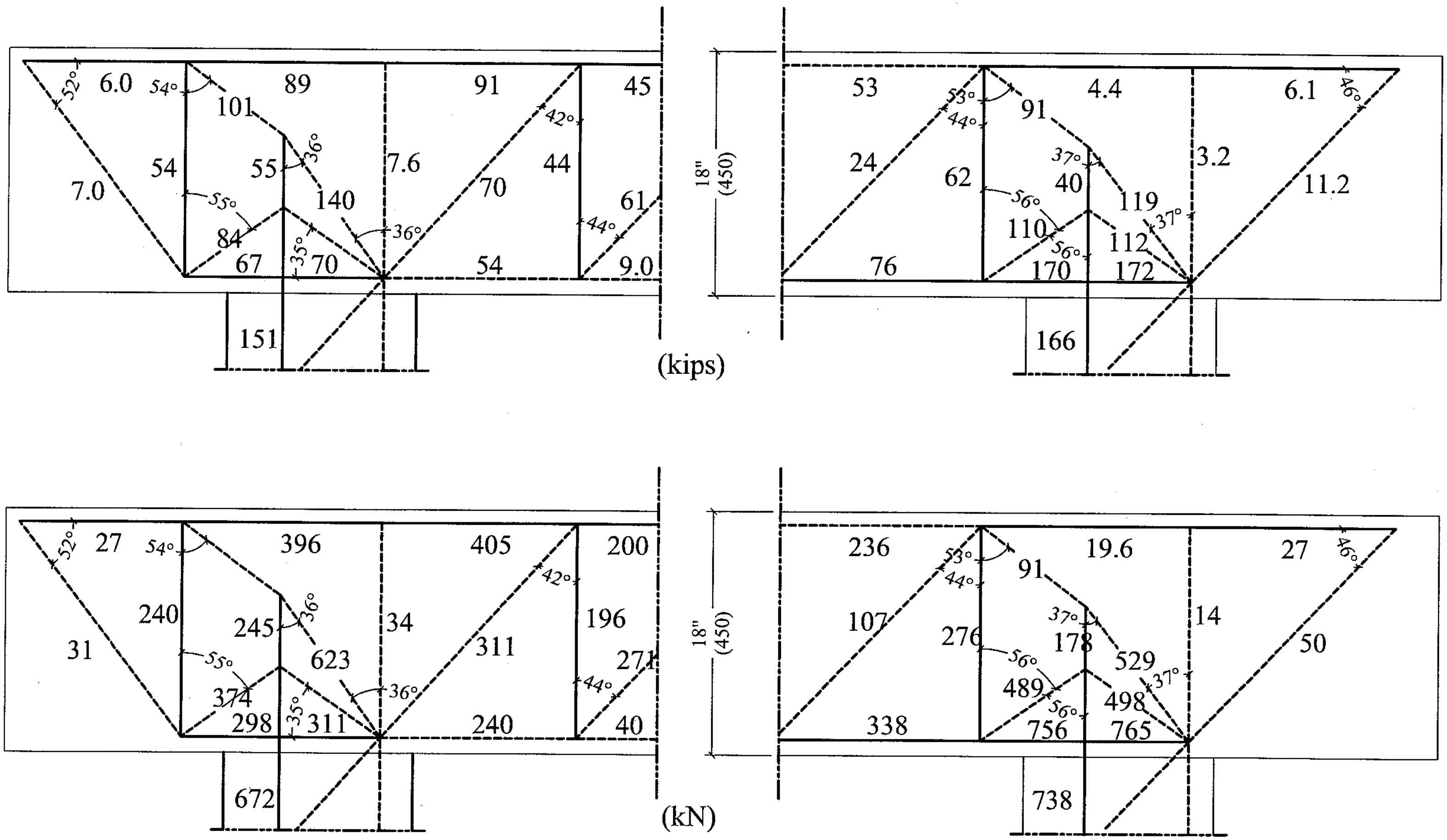

Fig. 5-54a: Model Forces in D-Regions of Tall Specimen Beam

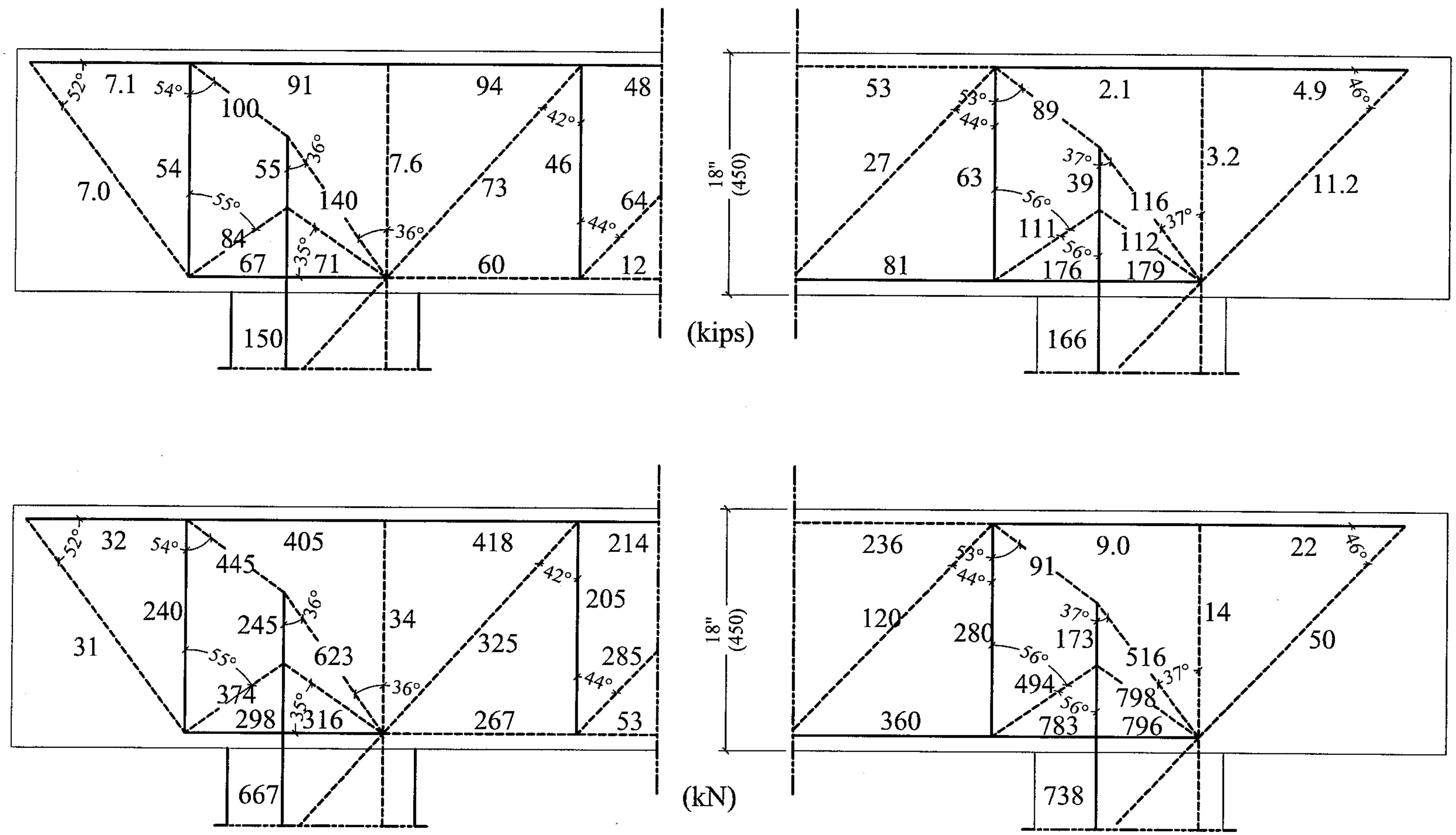

Fig. 5-54b: Model Forces in D-Regions of Middle Specimen Beam

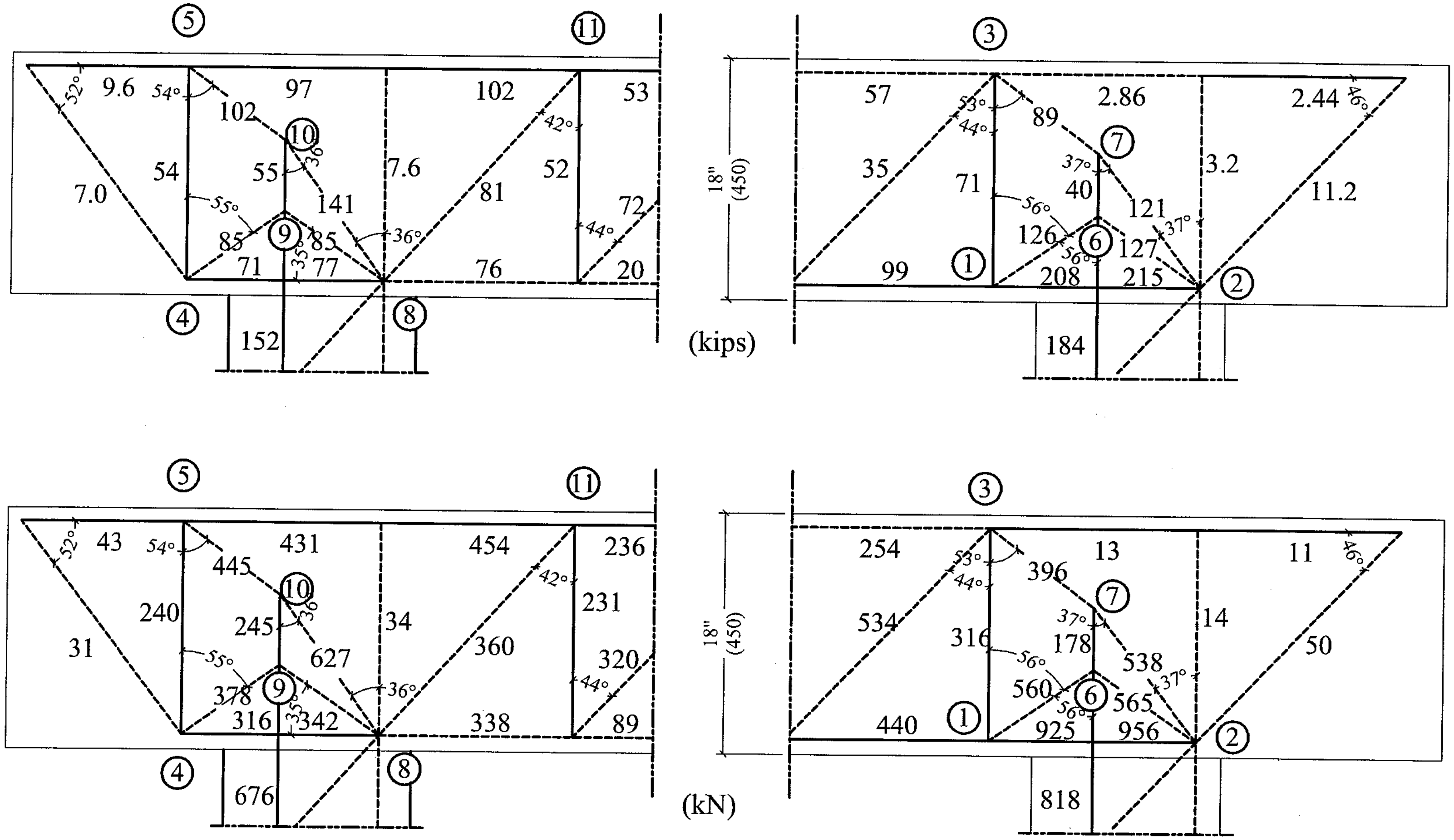

Fig. 5-54c: Model Forces in D-Regions of Short Specimen Beam

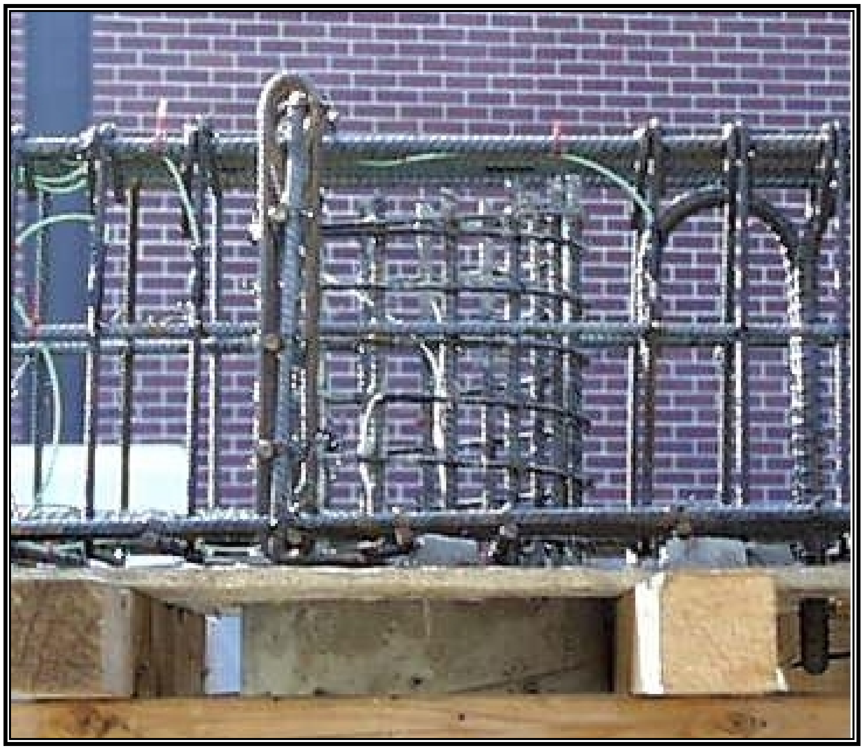

Fig. 6-1: Reinforcement Details of the Beam-Column Joint

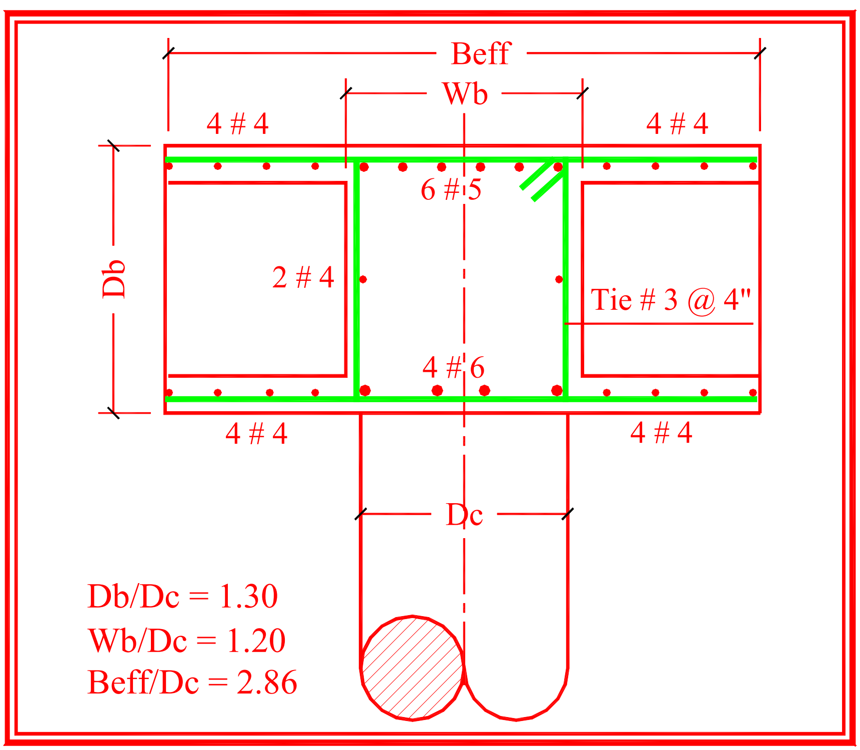

Fig. 6-2: Beam-Column Joint Proportions in Two-Column Bent

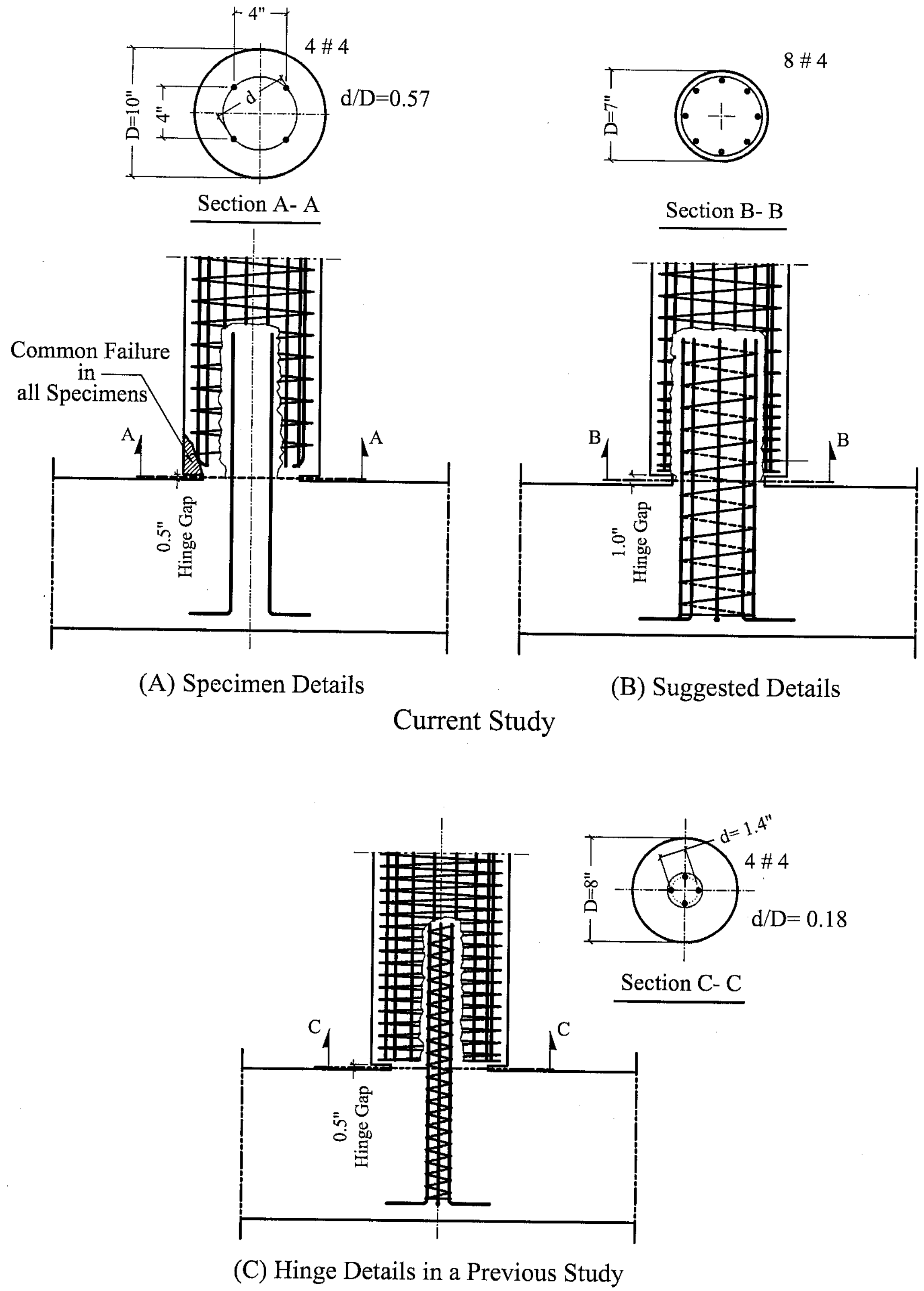

Fig. 6-3: Hinge Details in the Current and Previous Studies

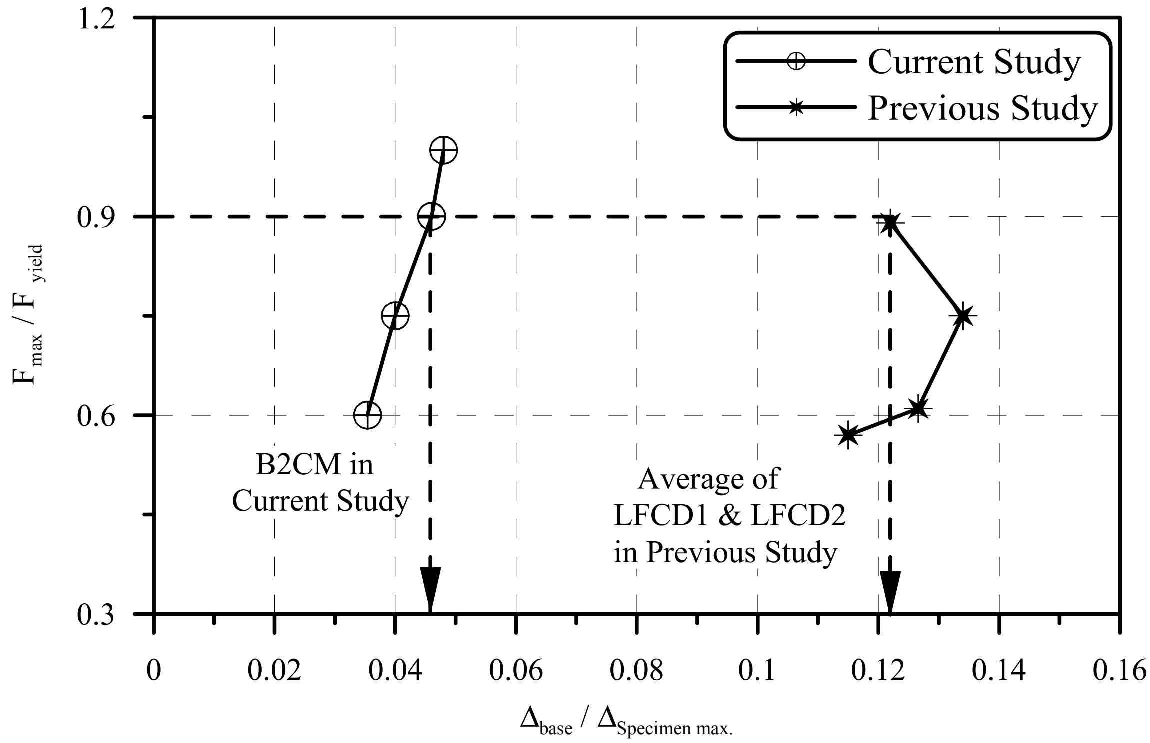

Fig. 6-4a: Base Slippage in Current and Previous Study

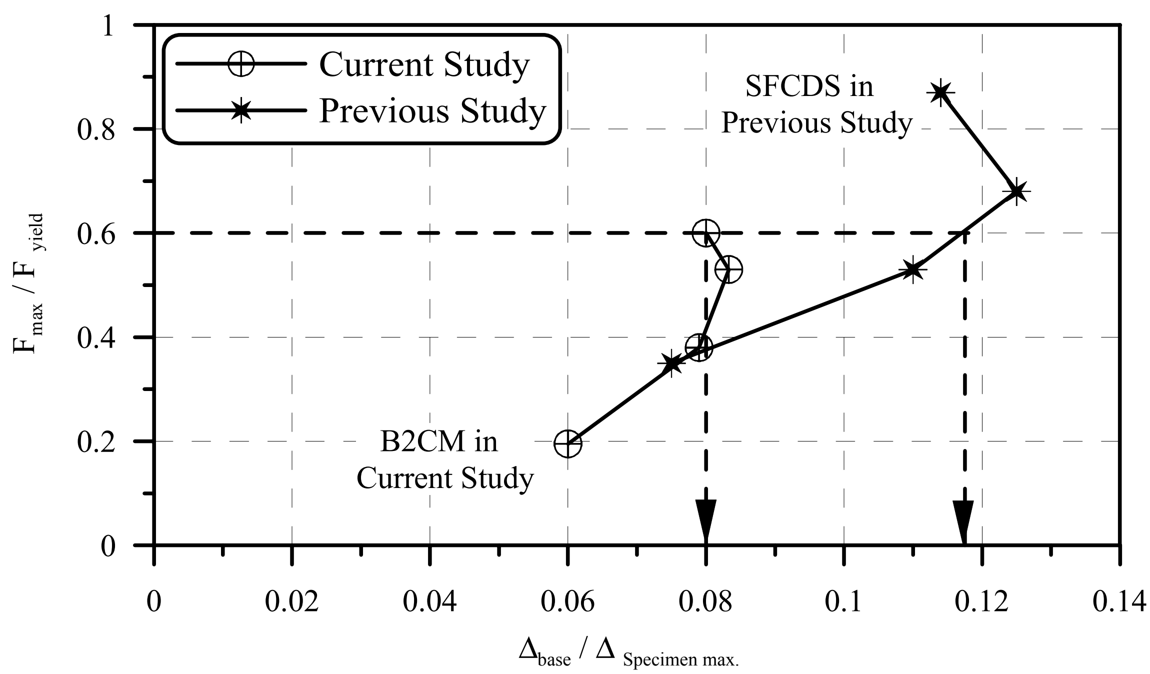

Fig. 6-4b: Base Slippage in Current and Previous Study (Short Specimens)

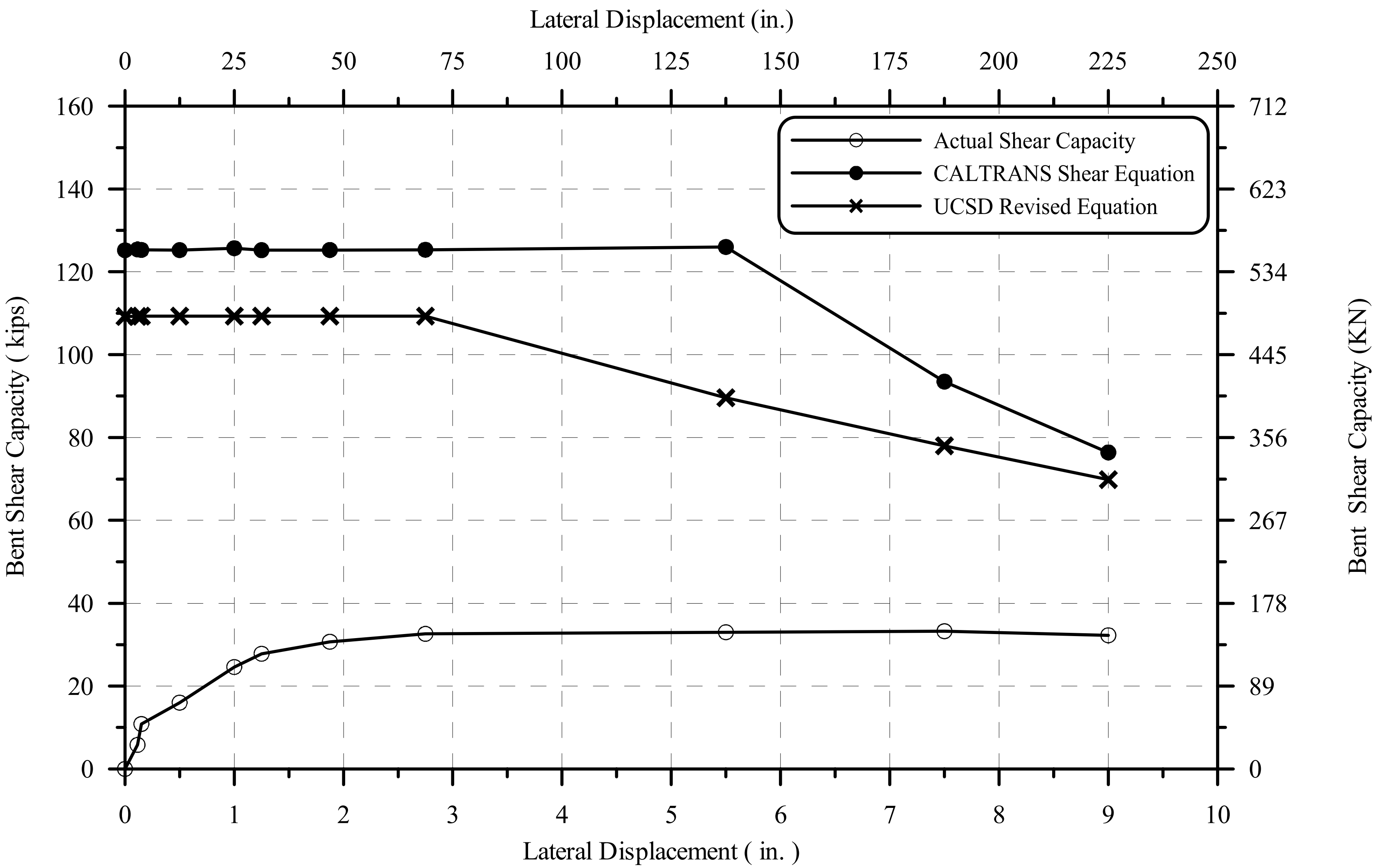

Fig. 6-5: Shear Capacity for Tall Specimen B2CT

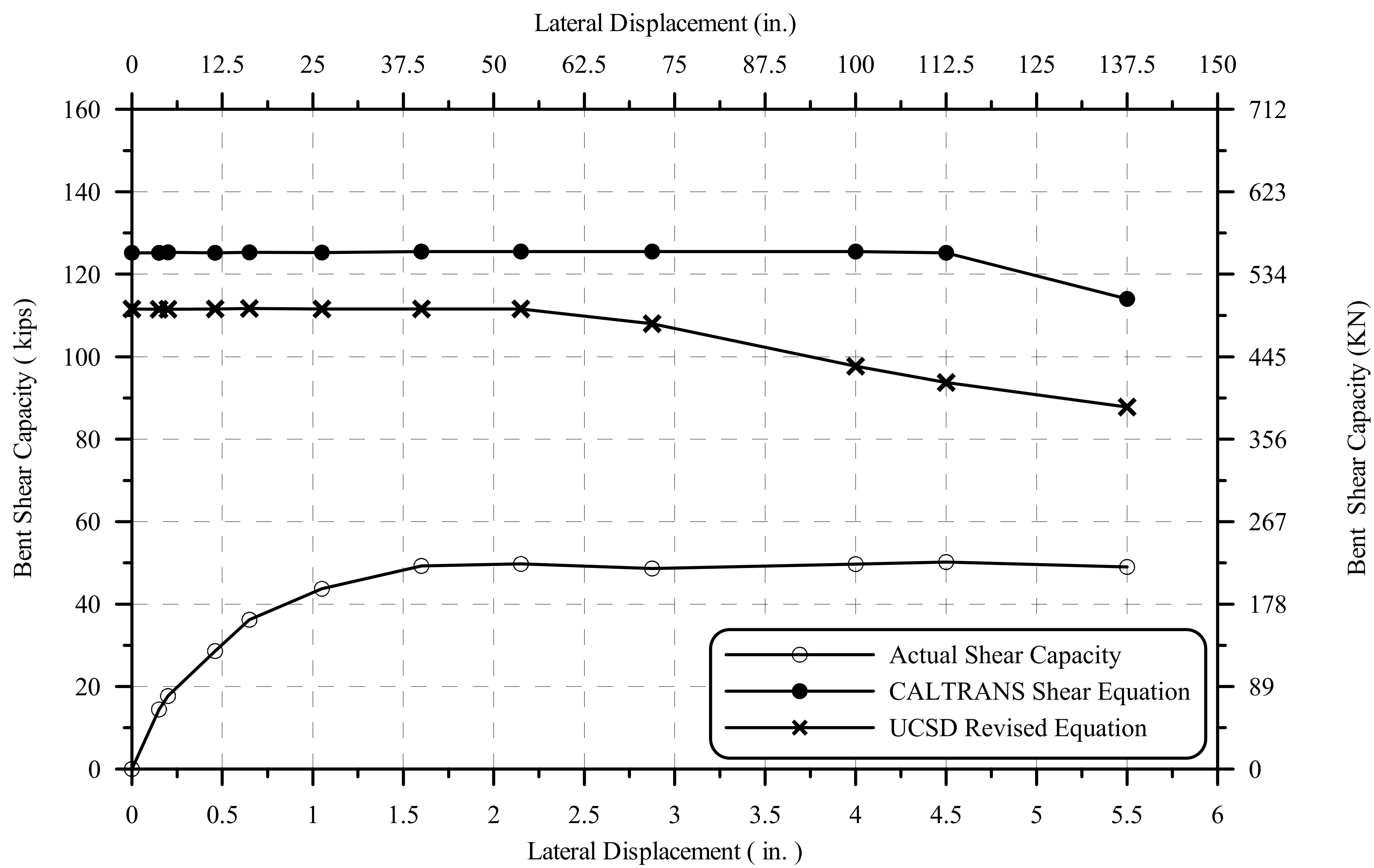

Fig. 6-6: Shear Capacity for Middle Specimen B2CM

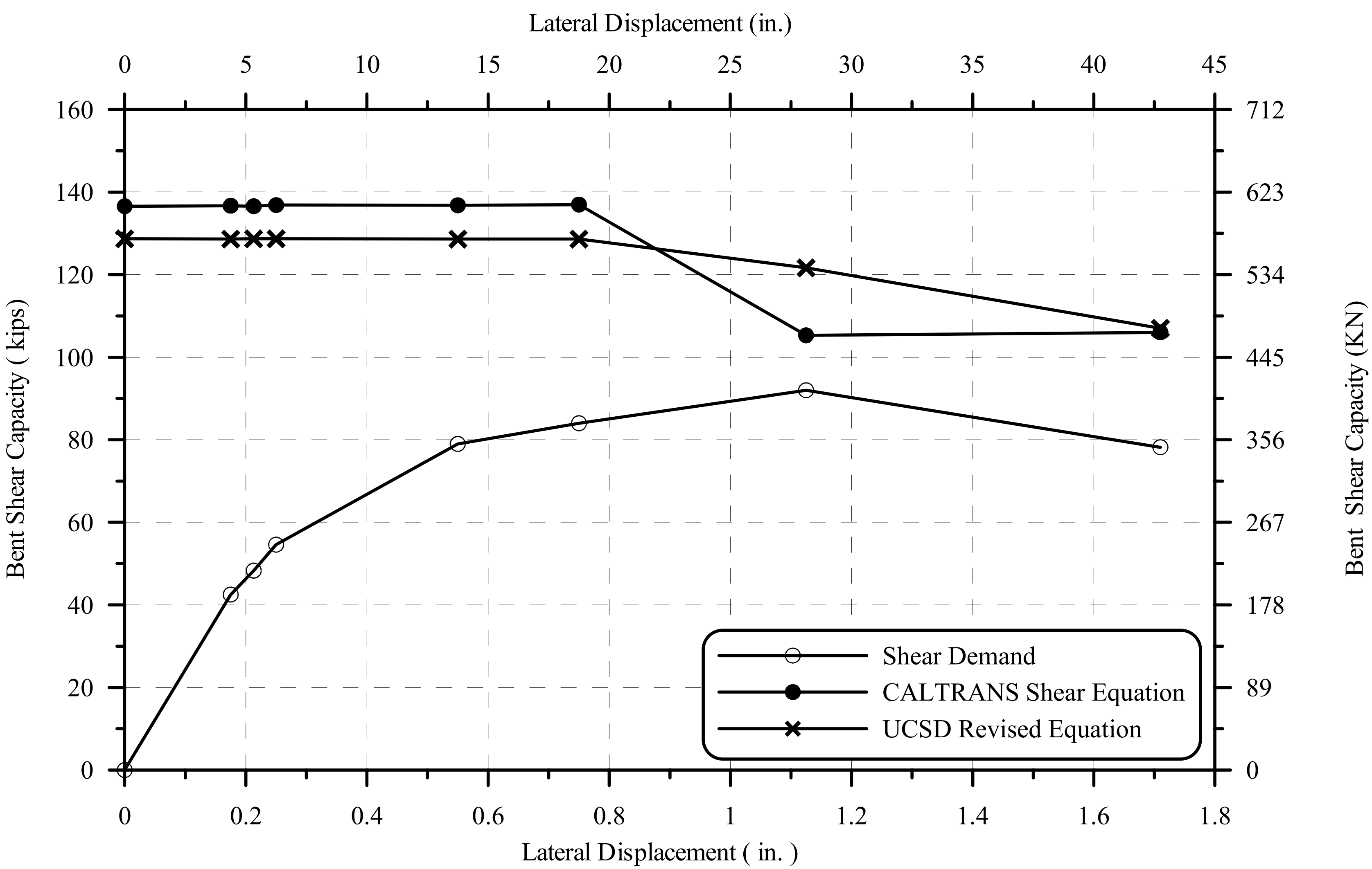

Fig. 6-7: Shear Capacity for Short Specimen B2CS

APPENDIX A

STRAIN-TIME HISTORY FOR GAGES IN SHORT SPECIMEN B2CS

(See Figs. 2-38 and 2-39 for the locations of each gage)

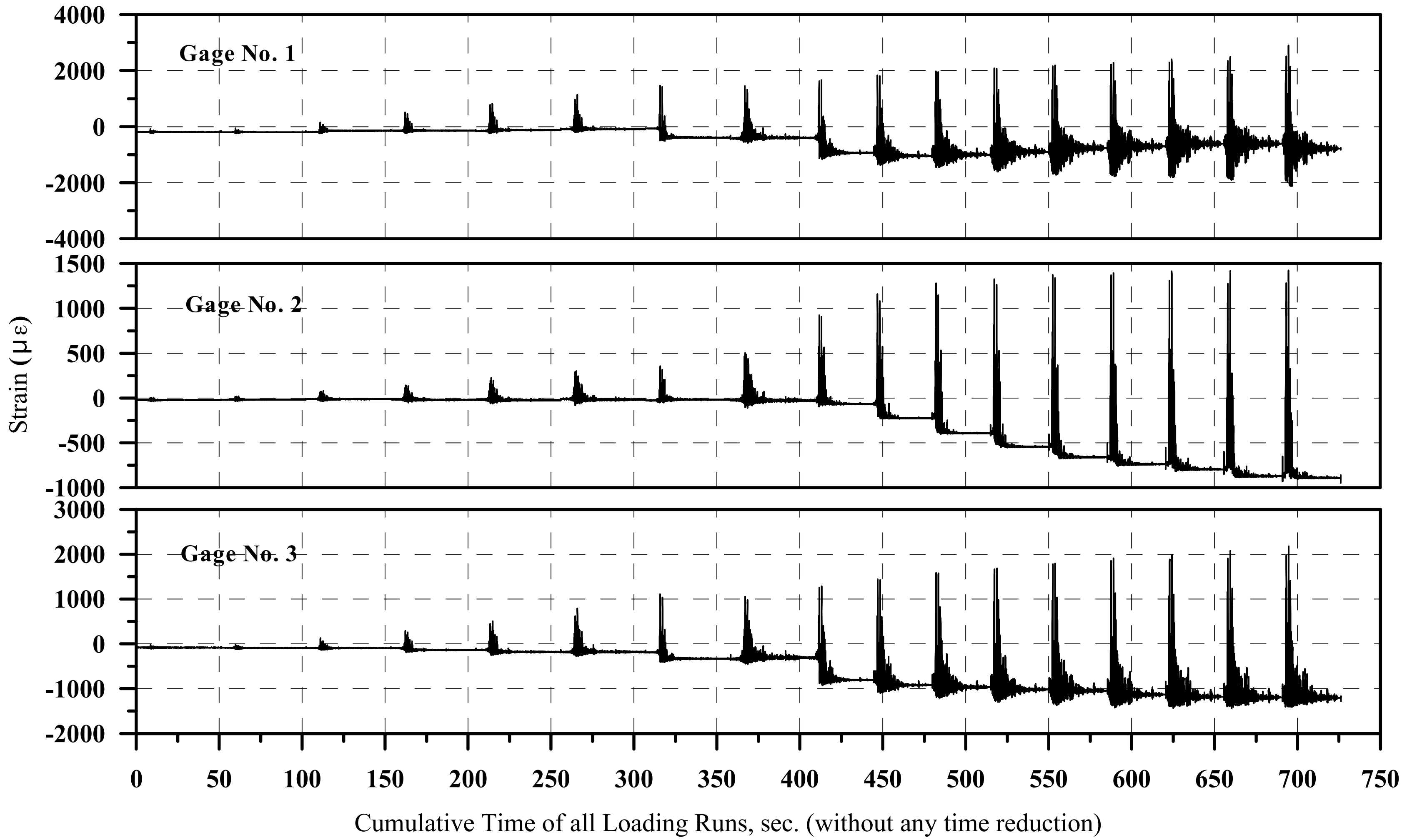

Fig. A-1: Strain History for Gages 1, 2 and 3 in Specimen B2CS

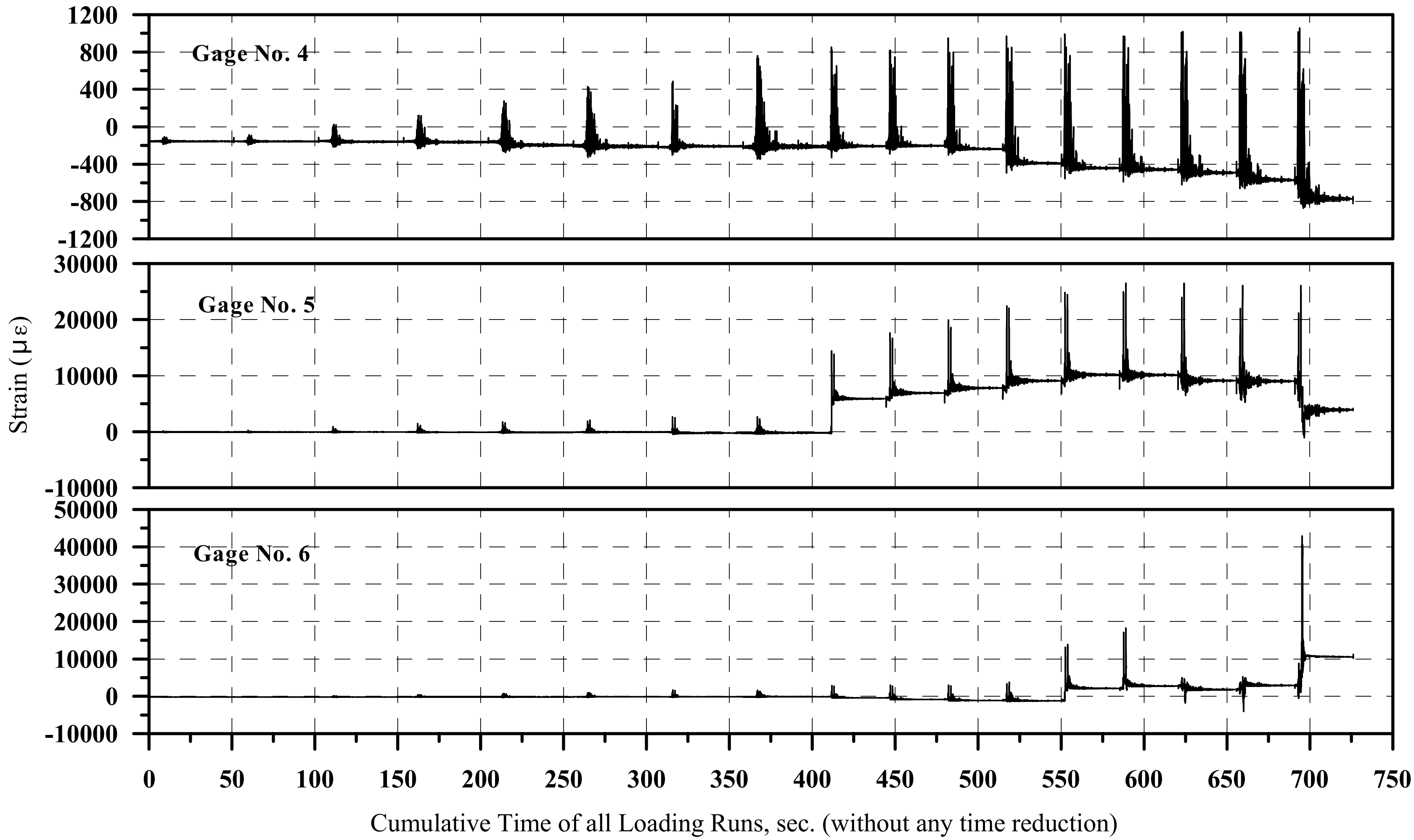

Fig. A-2: Strain History for Gages 4, 5 and 6 in Specimen B2CS

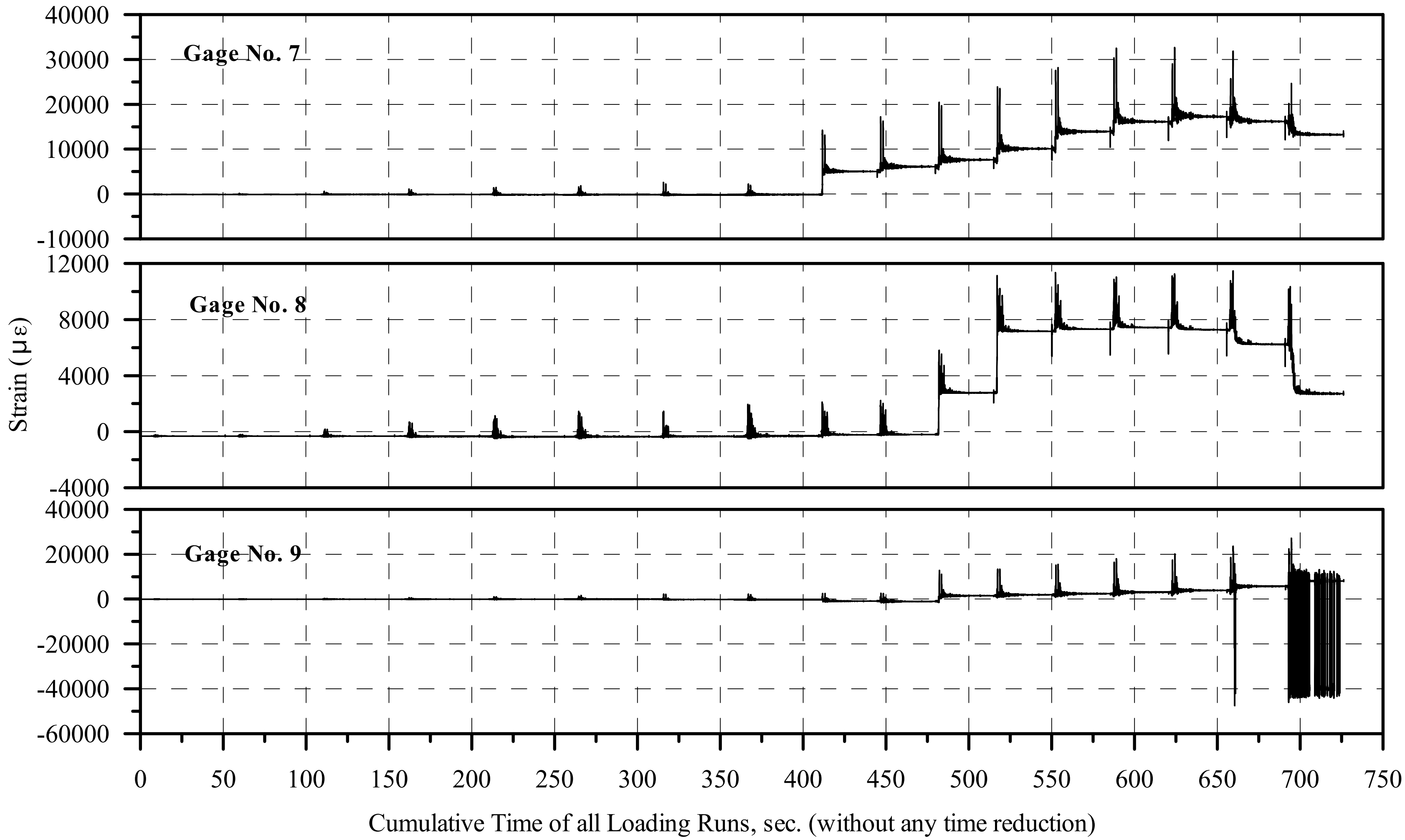

Fig. A-3: Strain History for Gages 7, 8 and 9 in Specimen B2CS

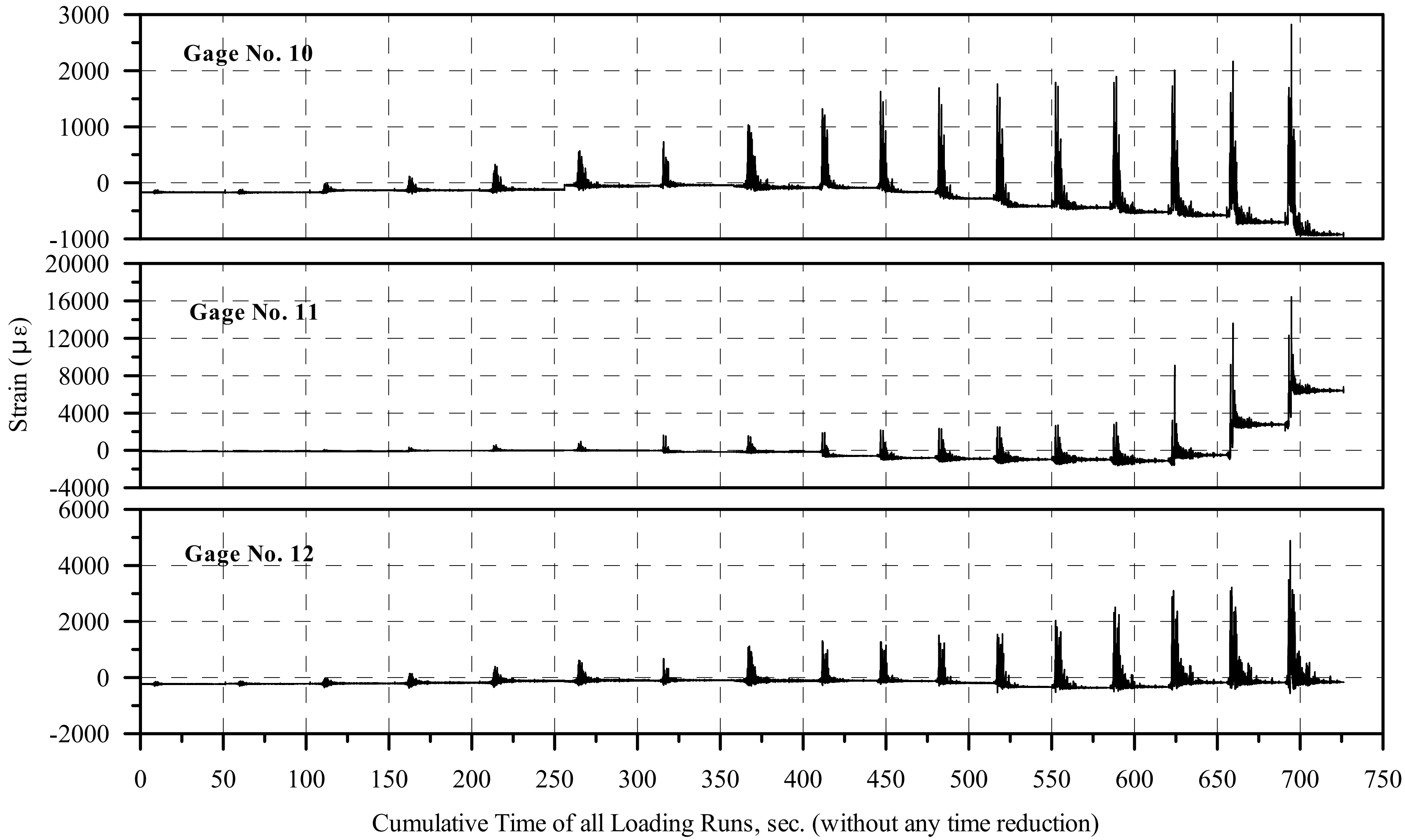

Fig. A-4: Strain History for Gages 10, 11 and 12 of Specimen B2CS

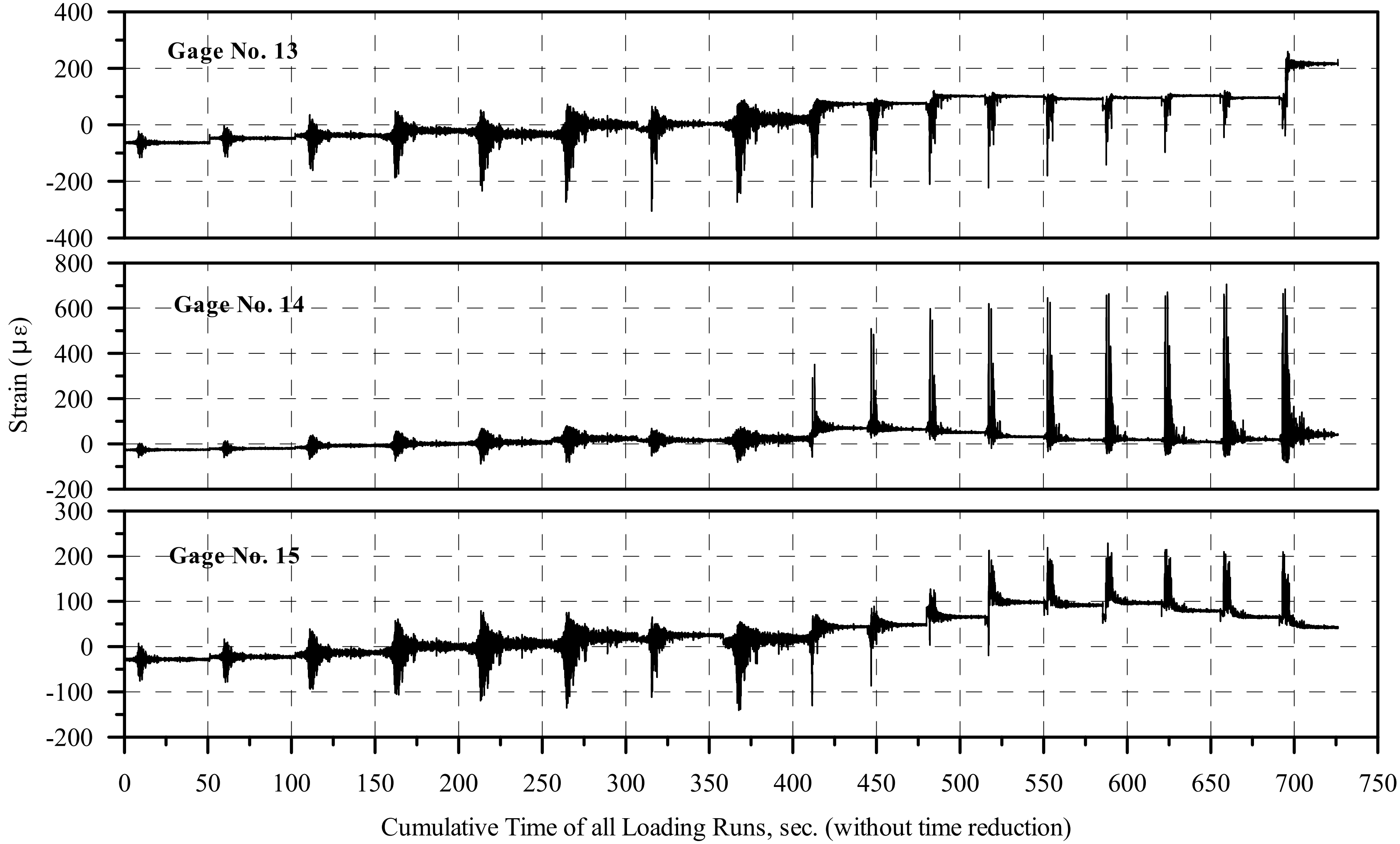

Fig. A-5: Strain History of Gages 13, 14 and 15 in Specimen B2CS

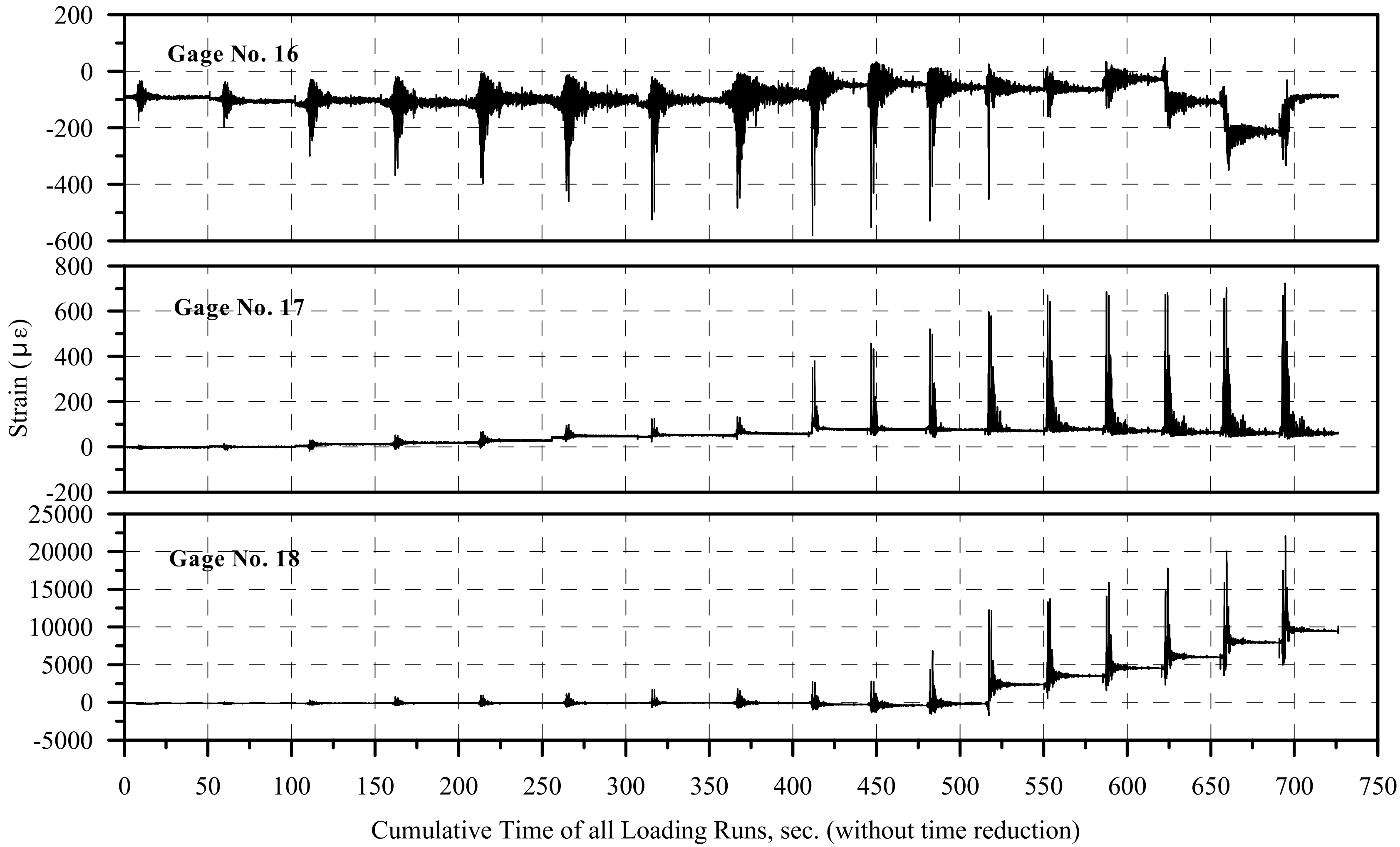

Fig. A-6: Strain History of Gages 16, 17 and 18 in Specimen B2CS

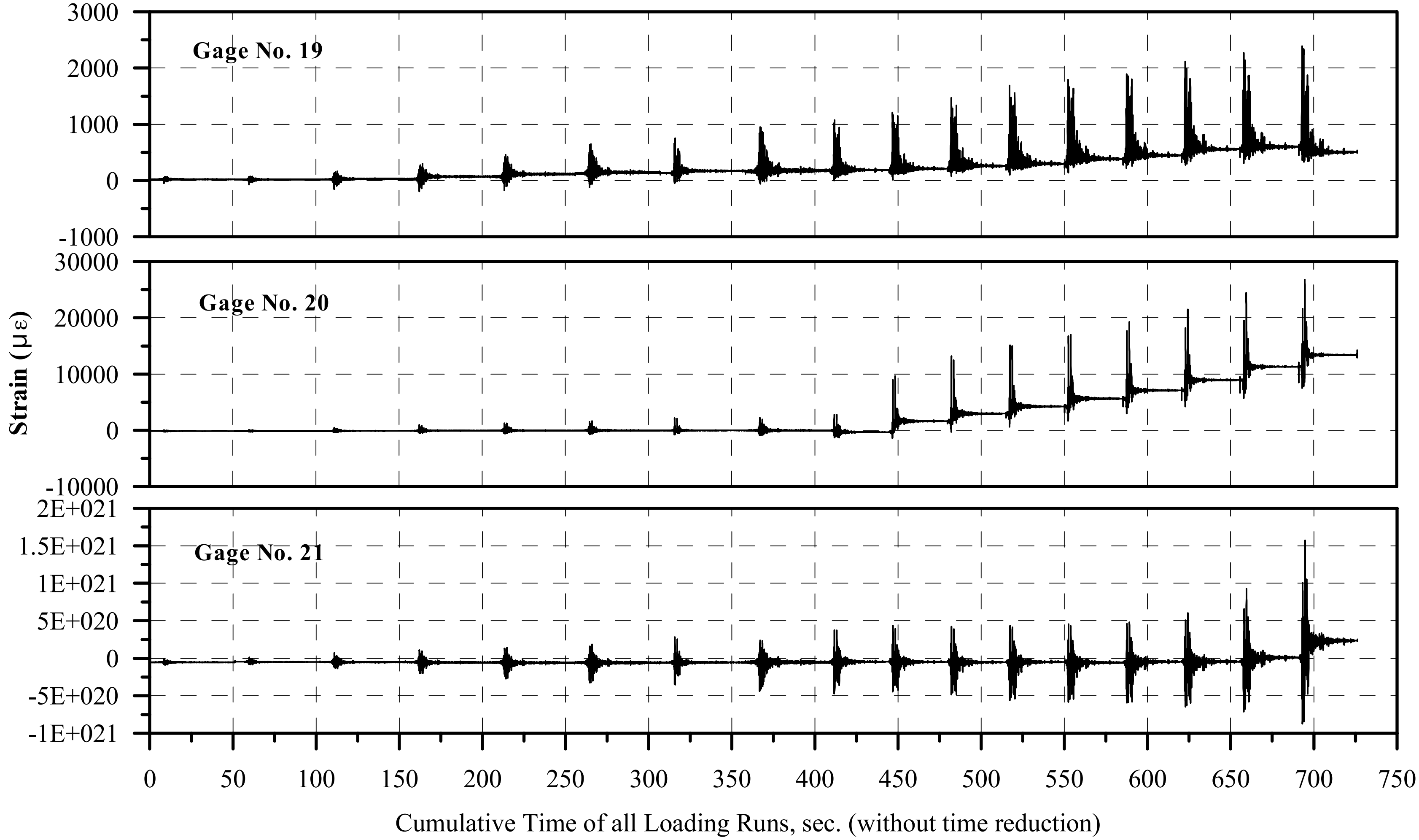

Fig. A-7: Strain History of Gages 19, 20 and 21 in Specimen B2CS

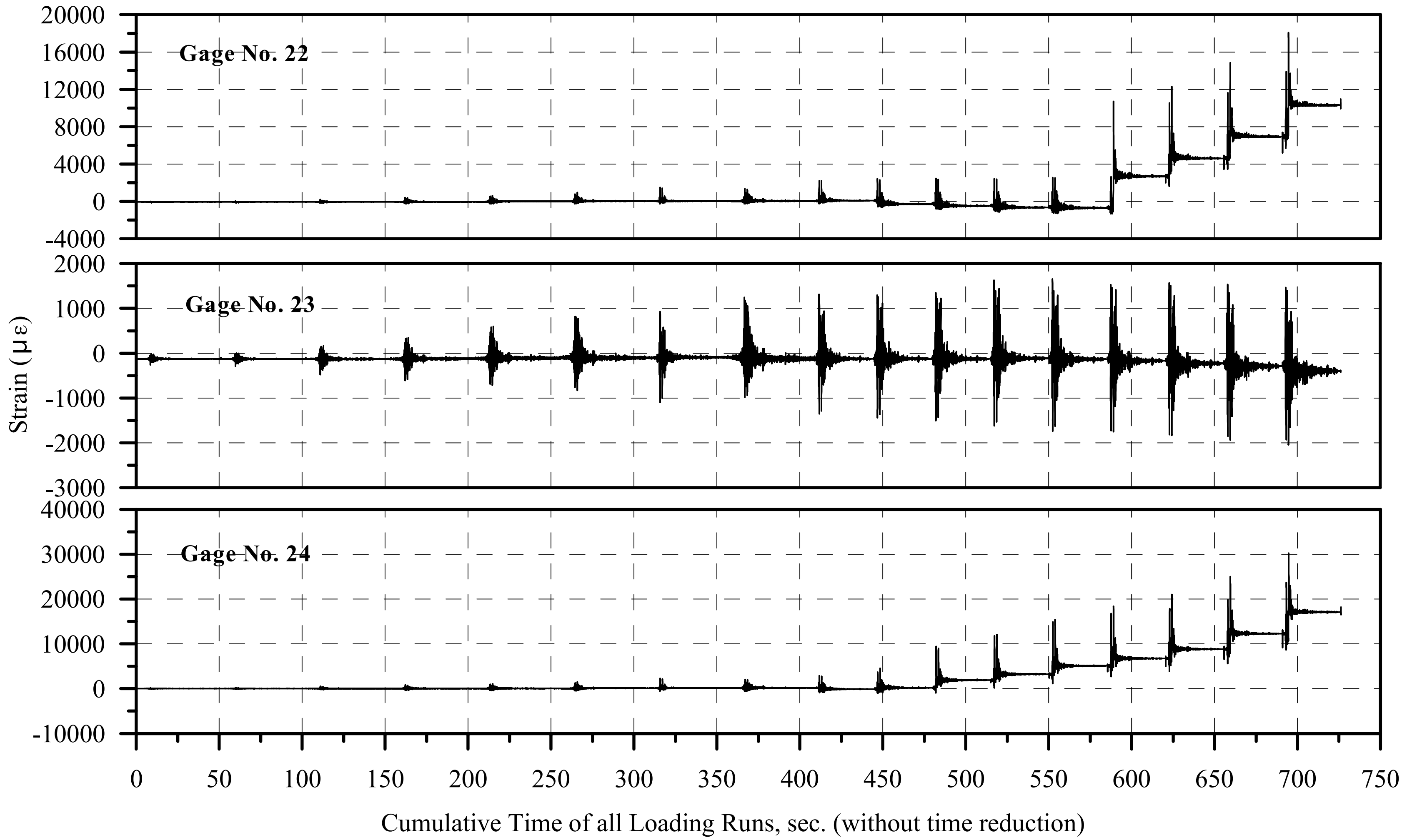

Fig. A-8: Strain History of Gages 22, 23 and 24 in Specimen B2CS

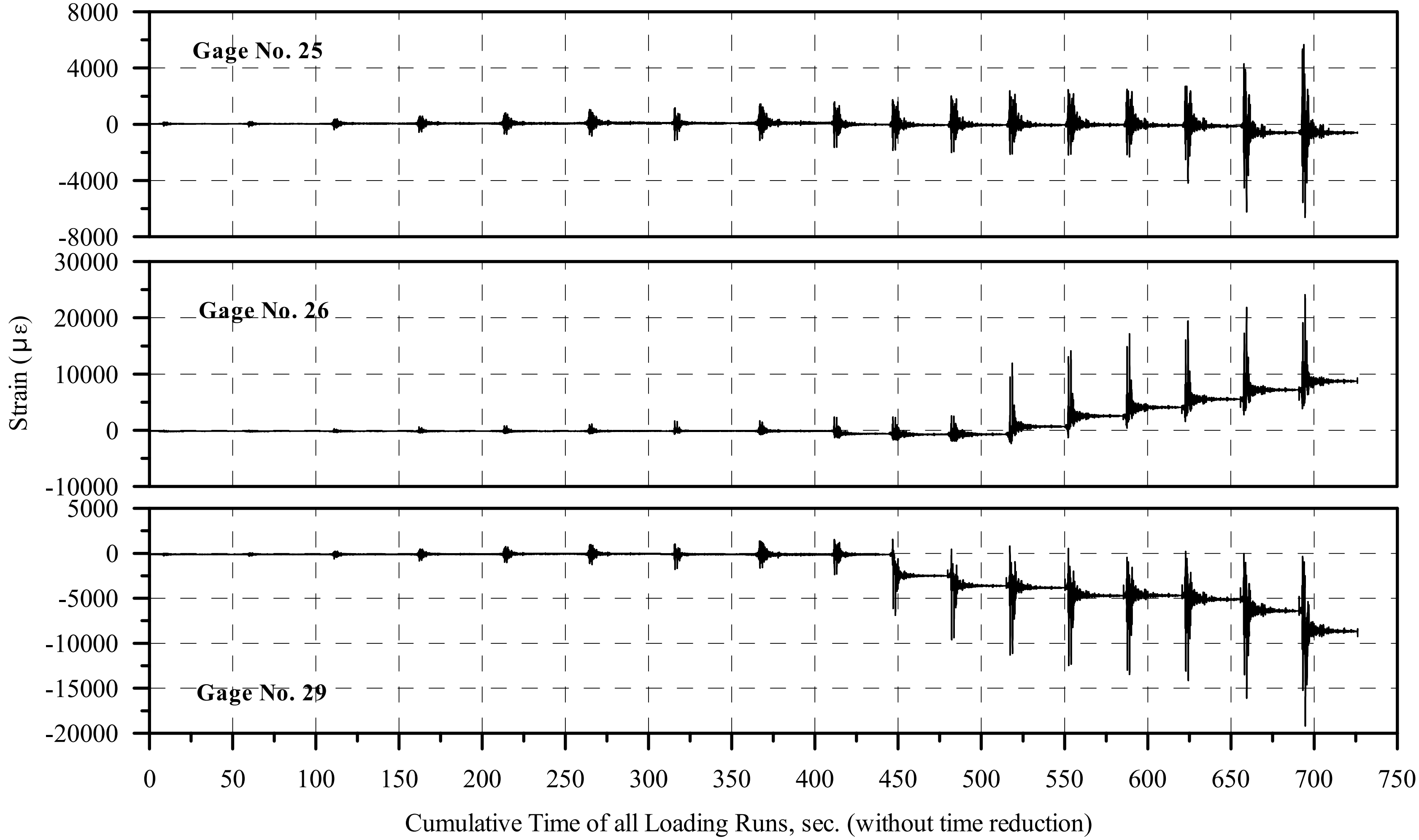

Fig. A-9: Strain History of Gages 25, 26 and 29 in Specimen B2CS

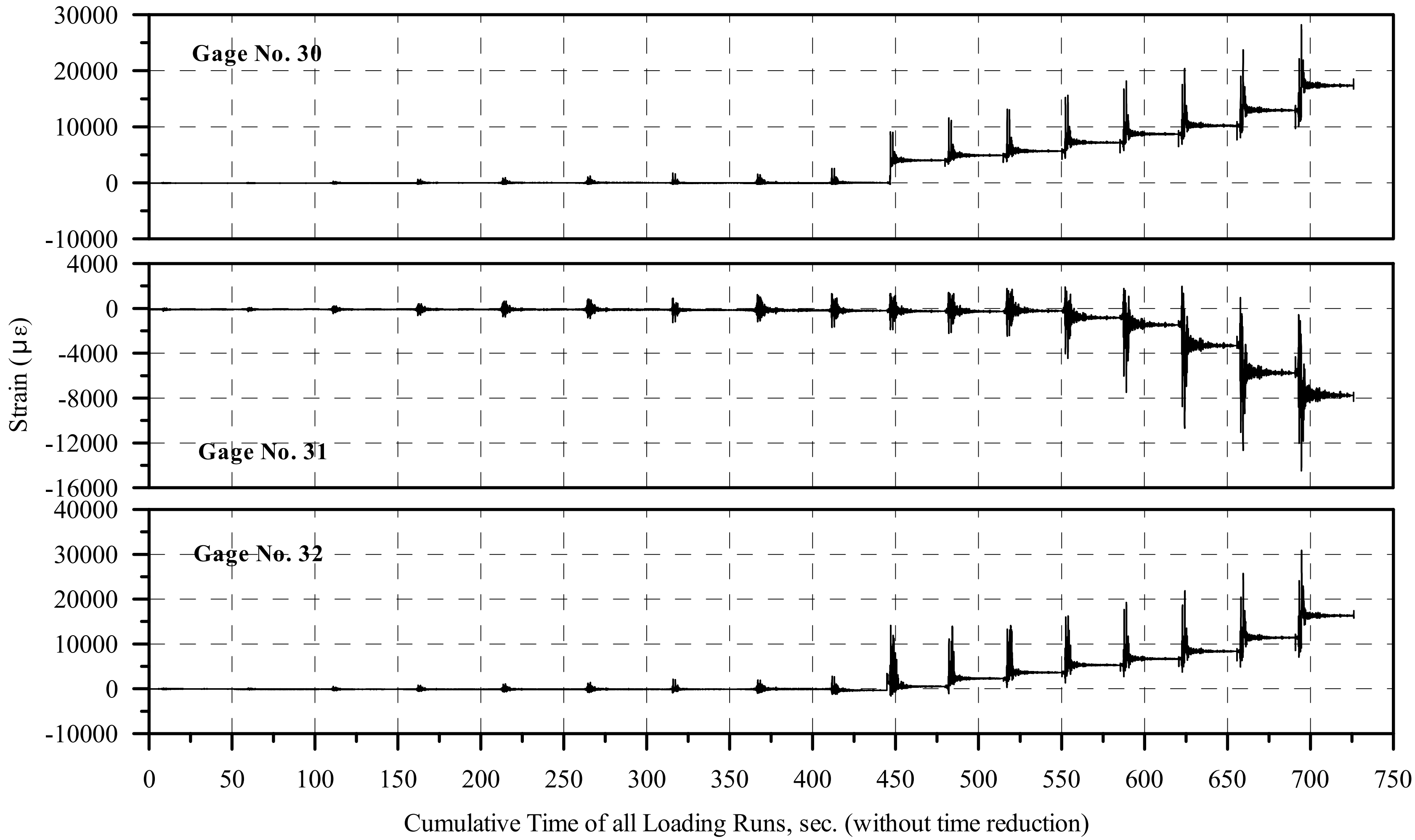

Fig. A-10: Strain History of Gages 30, 31 and 32 in Specimen B2CS

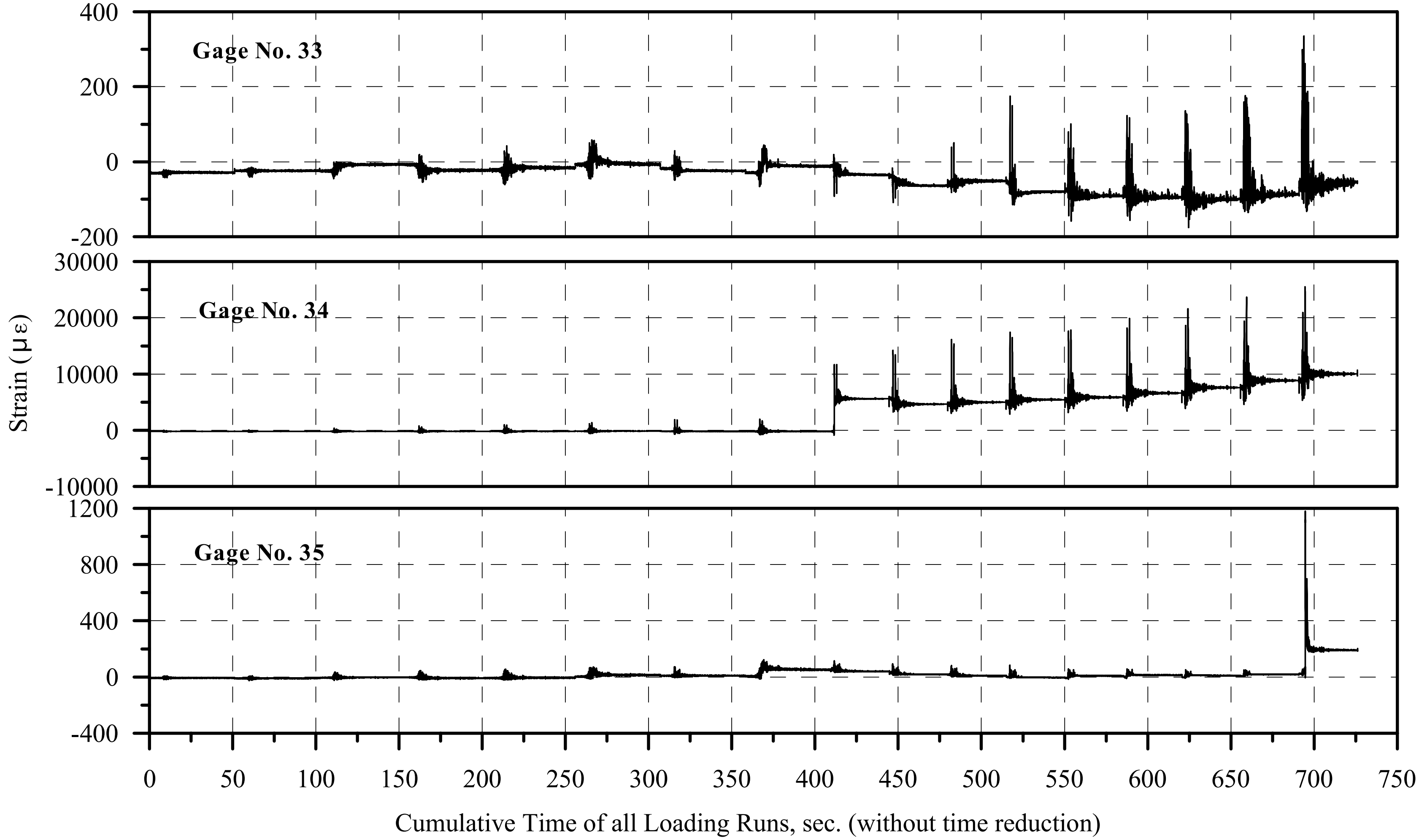

Fig. A-11: Strain History of Gages 33, 34 and 35 in Specimen B2CS

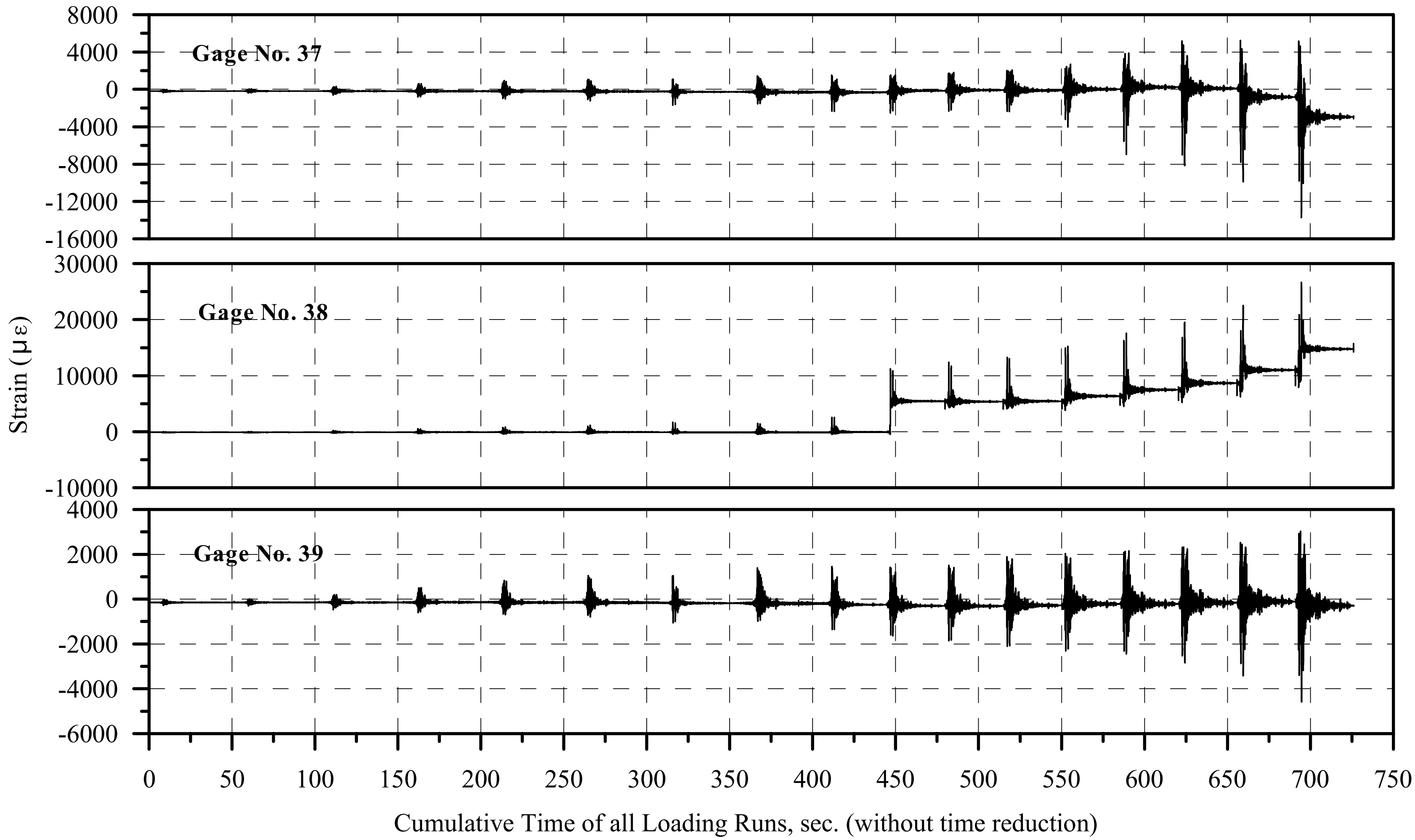

Fig. A-12: Strain History of Gages 37, 38 and 39 in Specimen B2CS

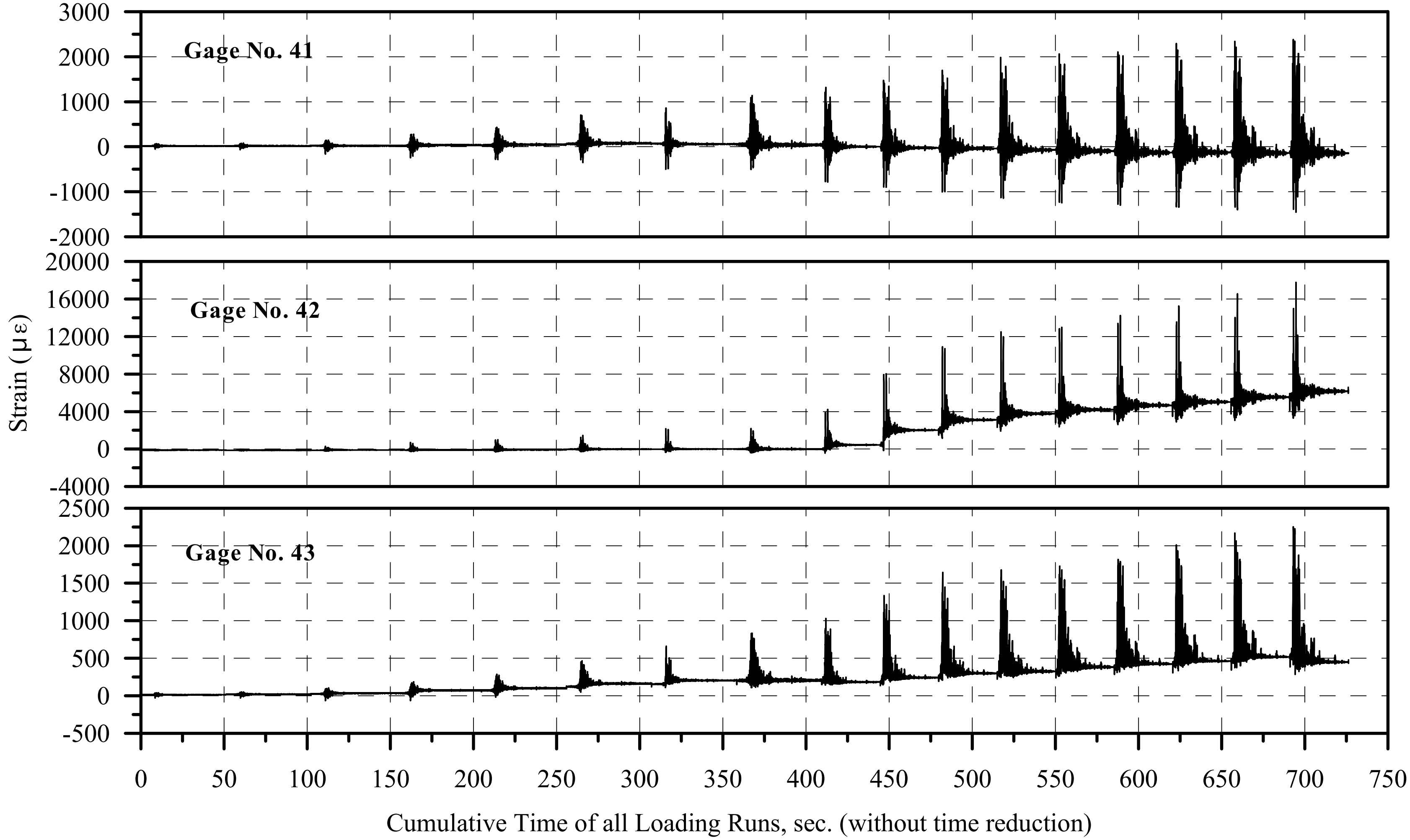

Fig. A-13: Strain History of Gages 41, 42 and 43 in Specimen B2CS

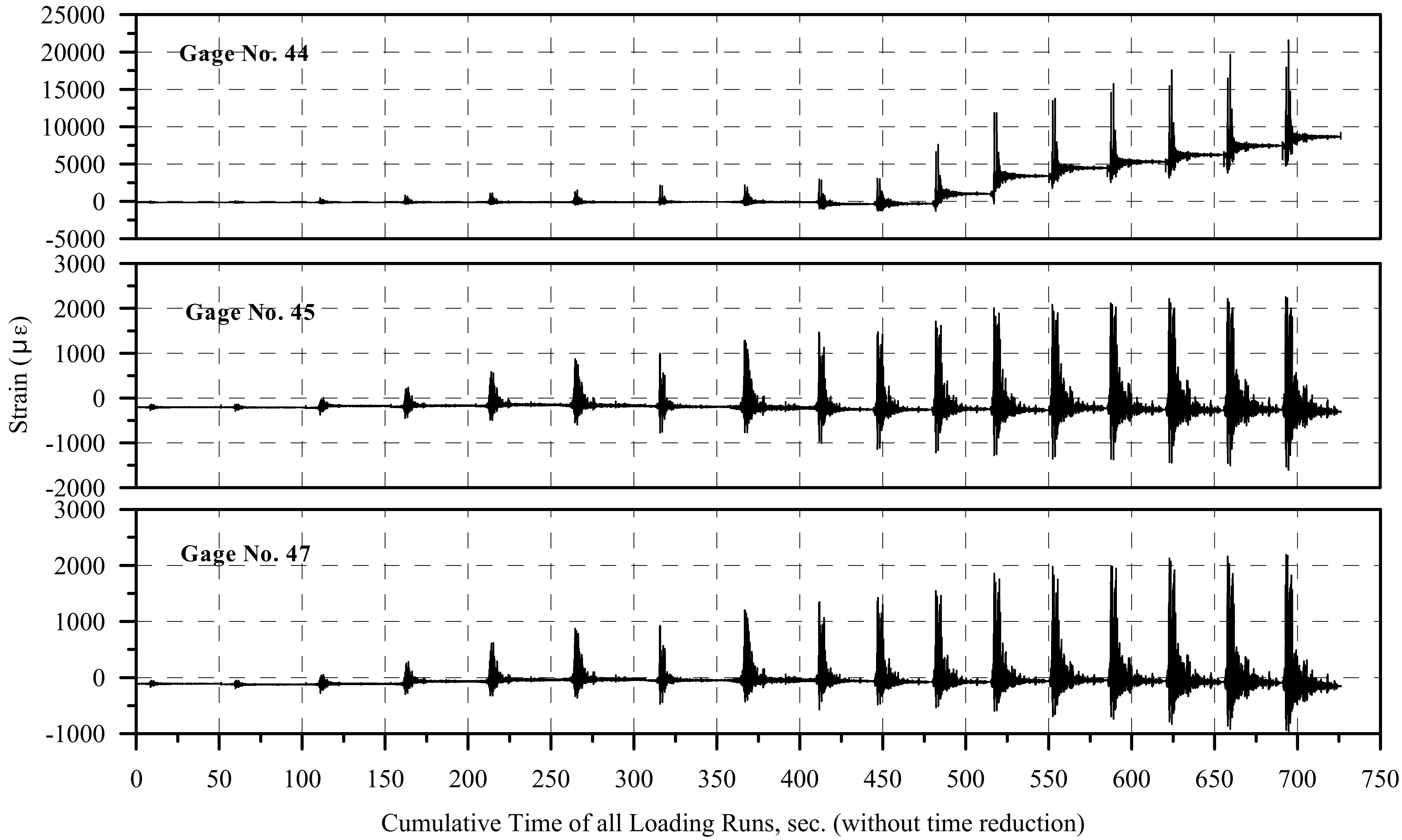

Fig. A-14: Strain History of Gages 44, 45 and 47 in Specimen B2CS

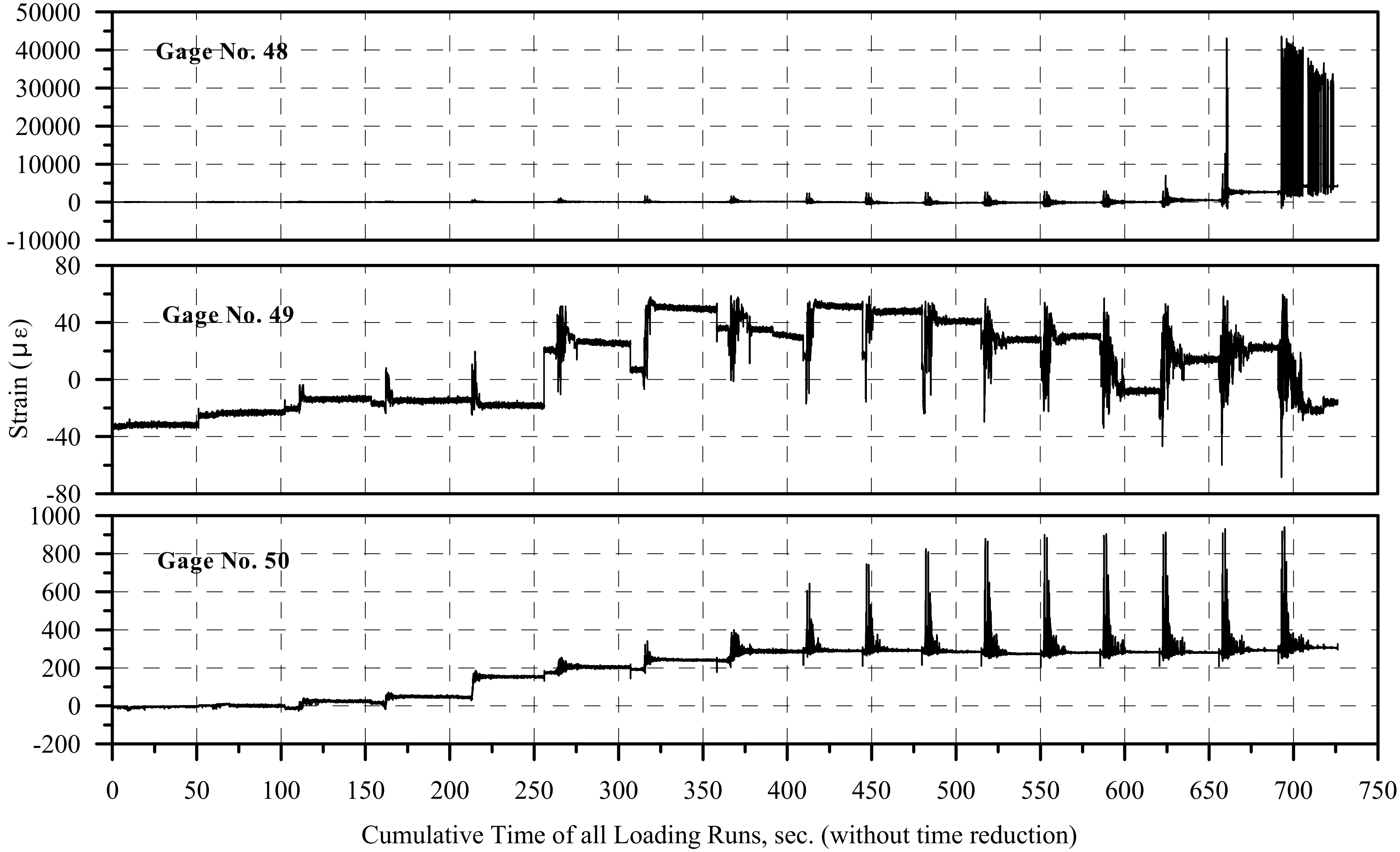

Fig A-15: Strain History for Gages 48, 49 and 50 of Specimen B2CS

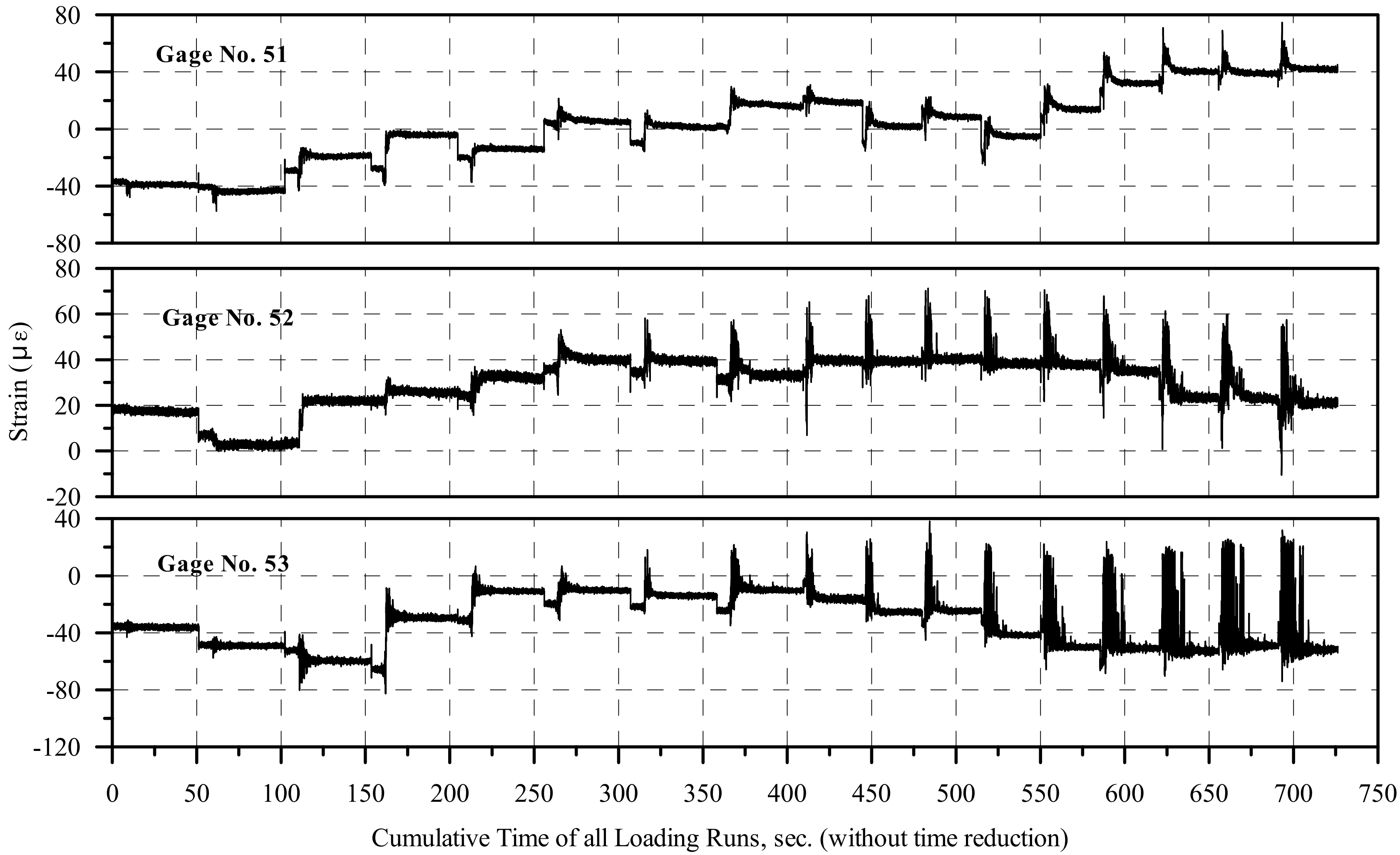

Fig. A-16: Strain History of Gages 51, 52 and 53 in Specimen B2CS

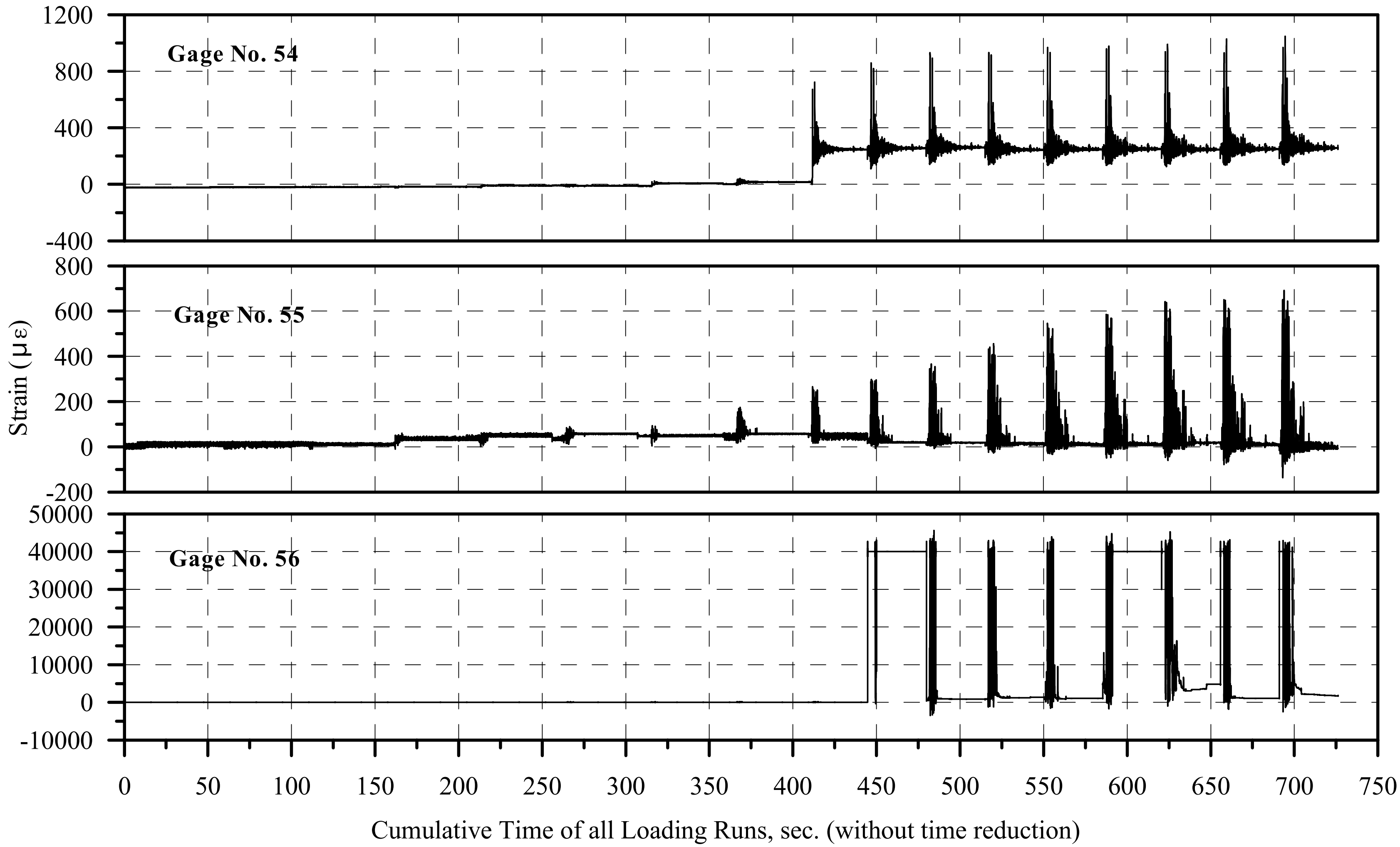

Fig. A-17: Strain History of Gages 54, 55 and 56 in Specimen B2CS

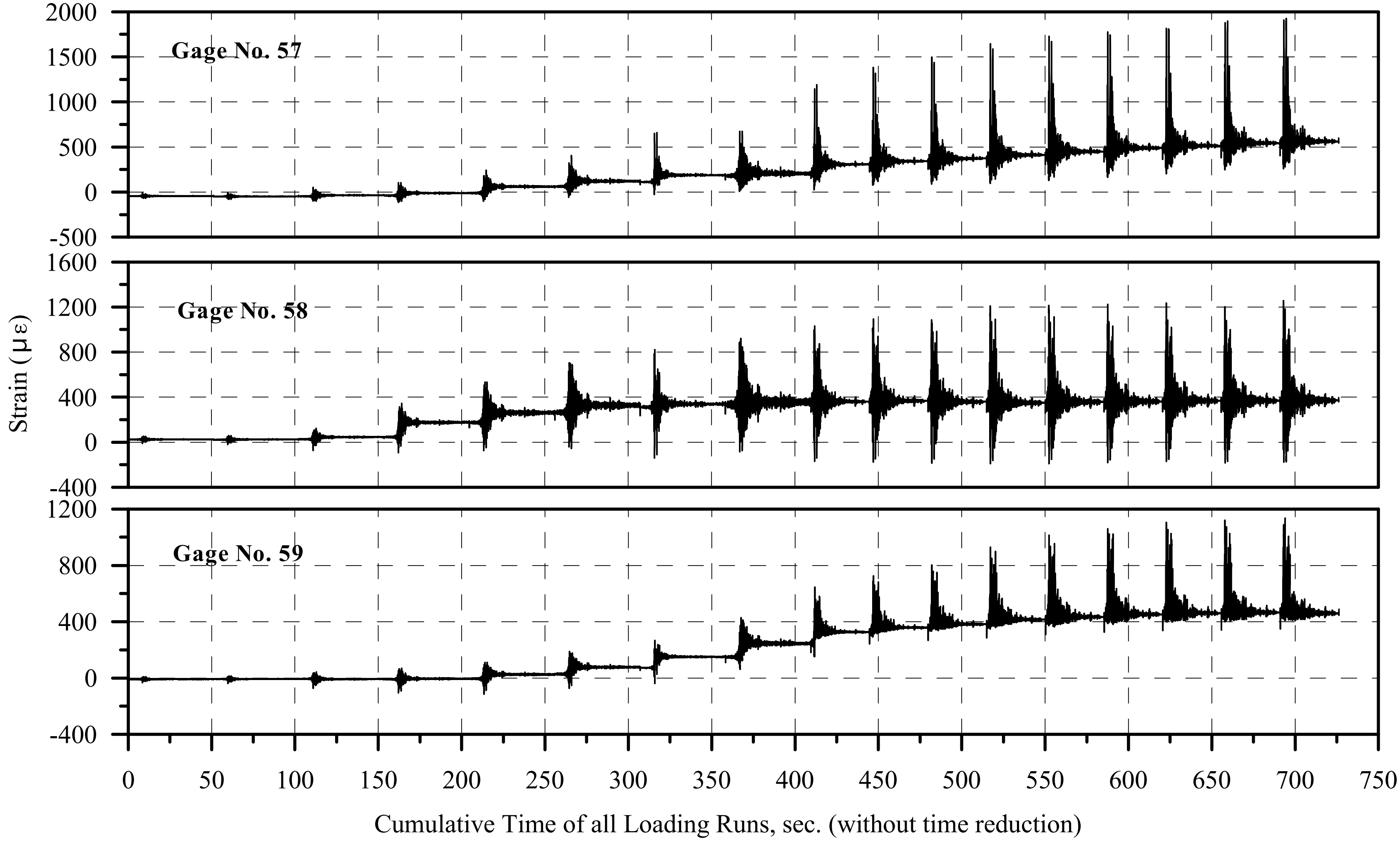

Fig. A-18: Strain History of Gages 57, 58 and 59 in Specimen B2CS

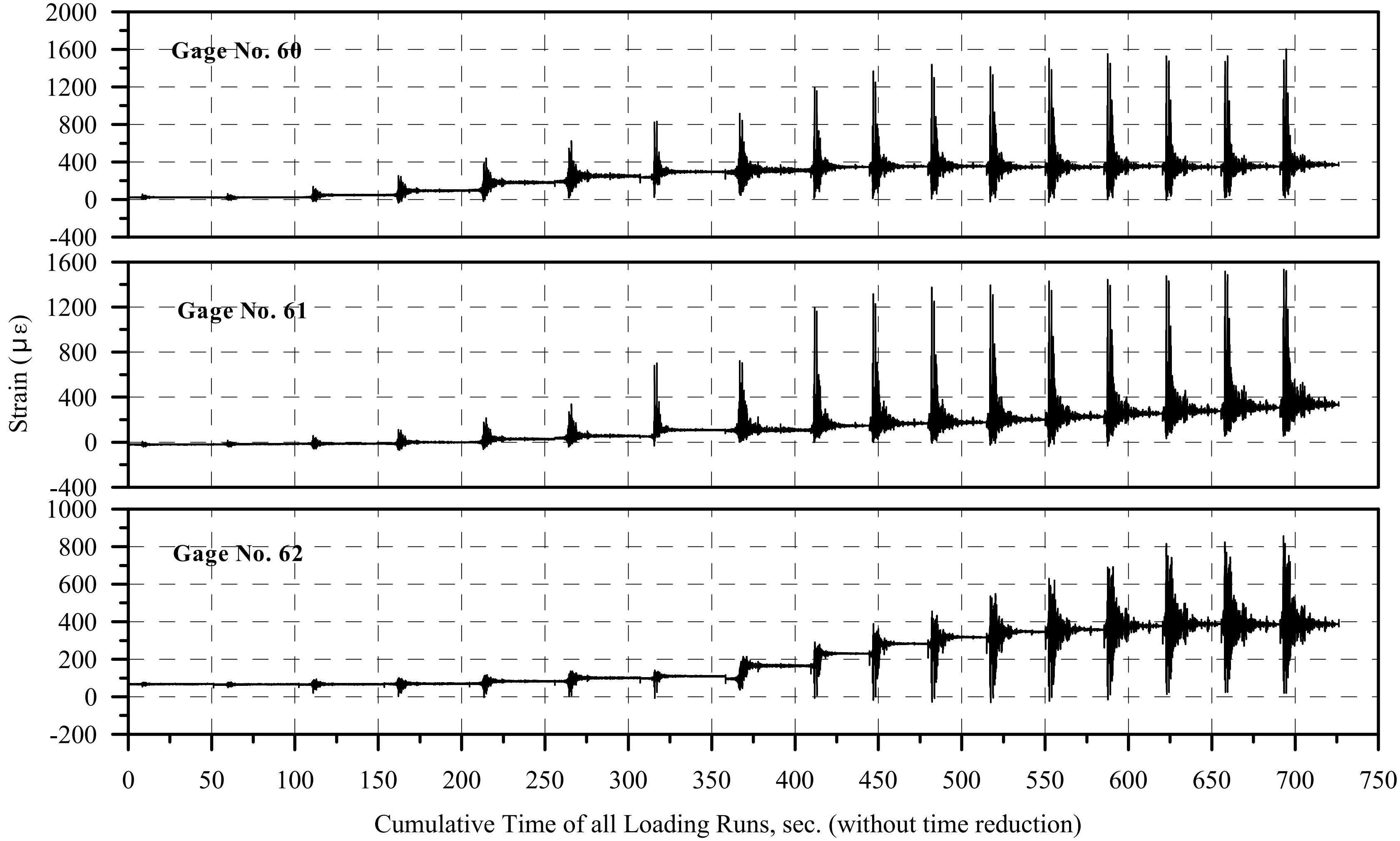

Fig. A-19: Strain History of Gages 60, 61 and 62 in Specimen B2CS

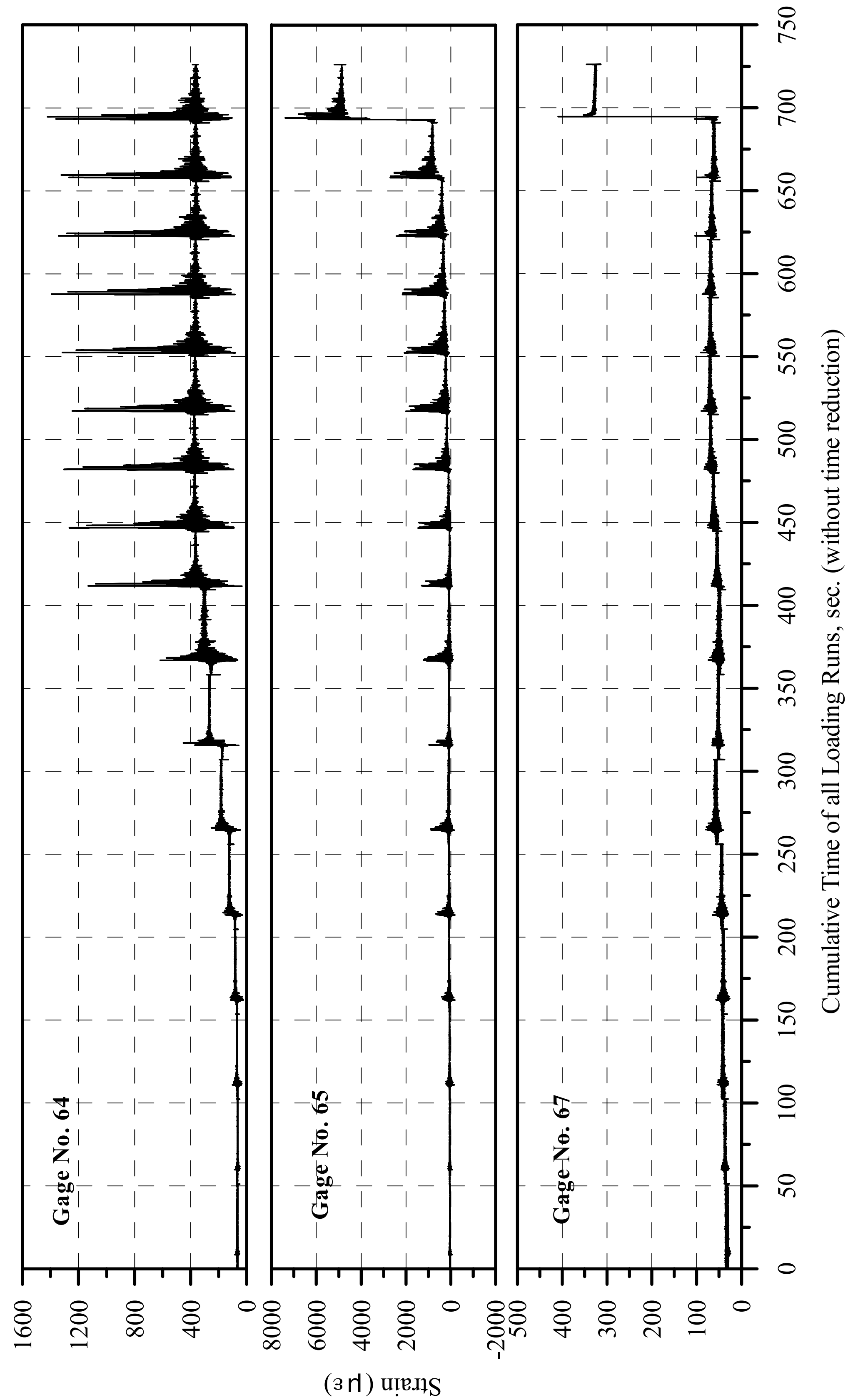

Fig. A-20: Strain History of Gages 64, 65 and 67 in Specimen B2CS

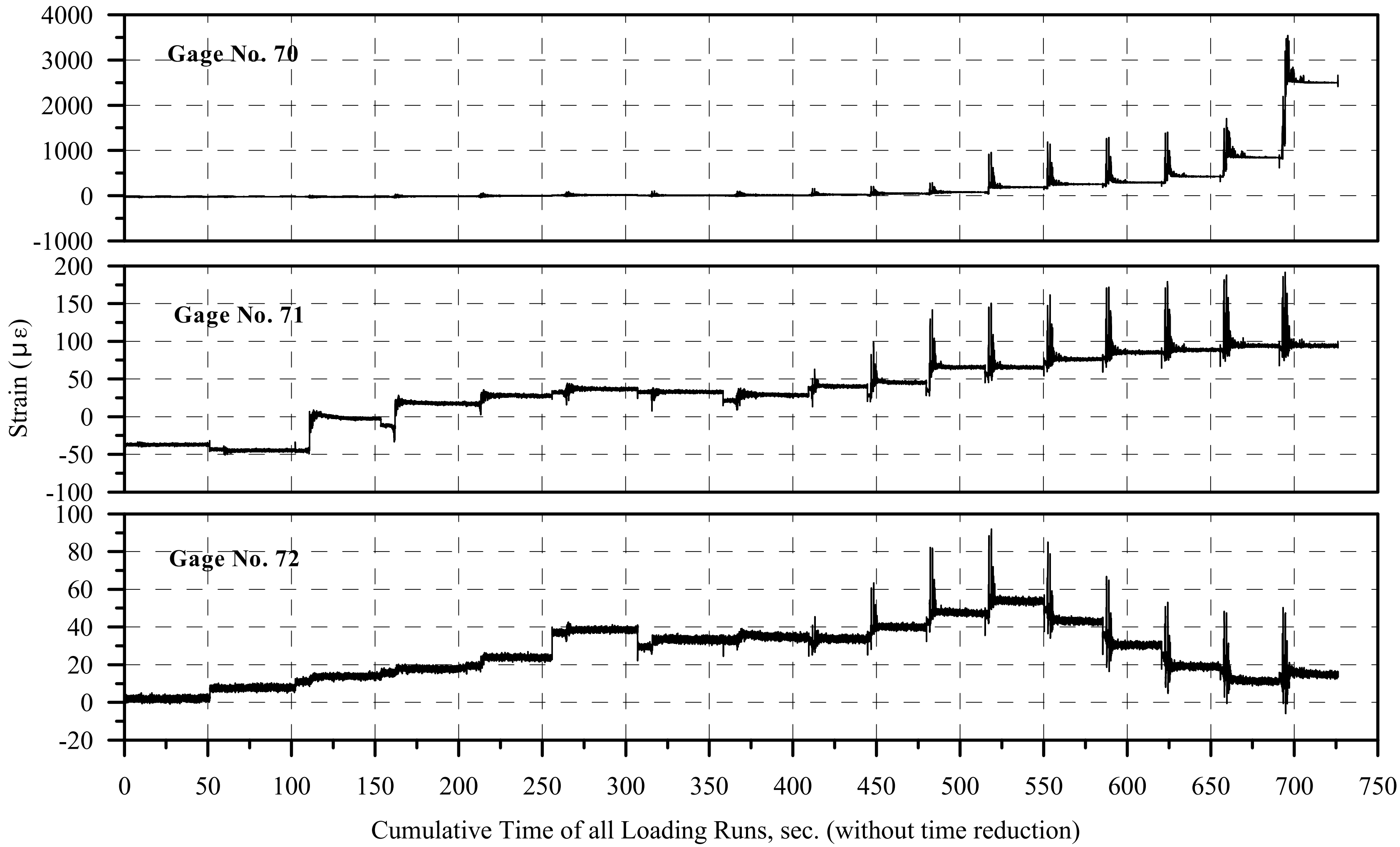

Fig. A-21: Strain History of Gages 70, 71 and 72 in Specimen B2CS

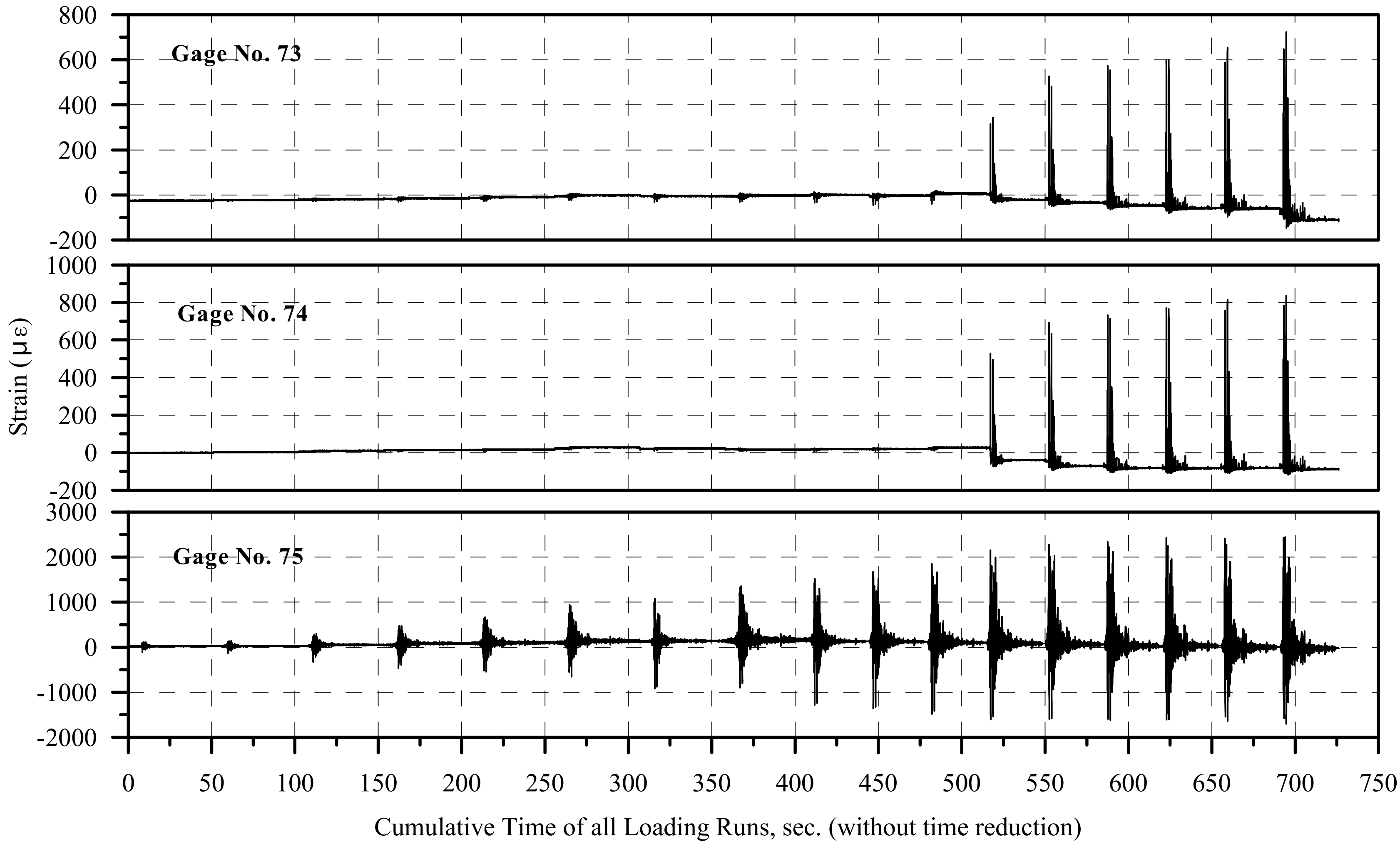

Fig. A-22: Strain History of Gages 73, 74 and 75 in Specimen B2CS

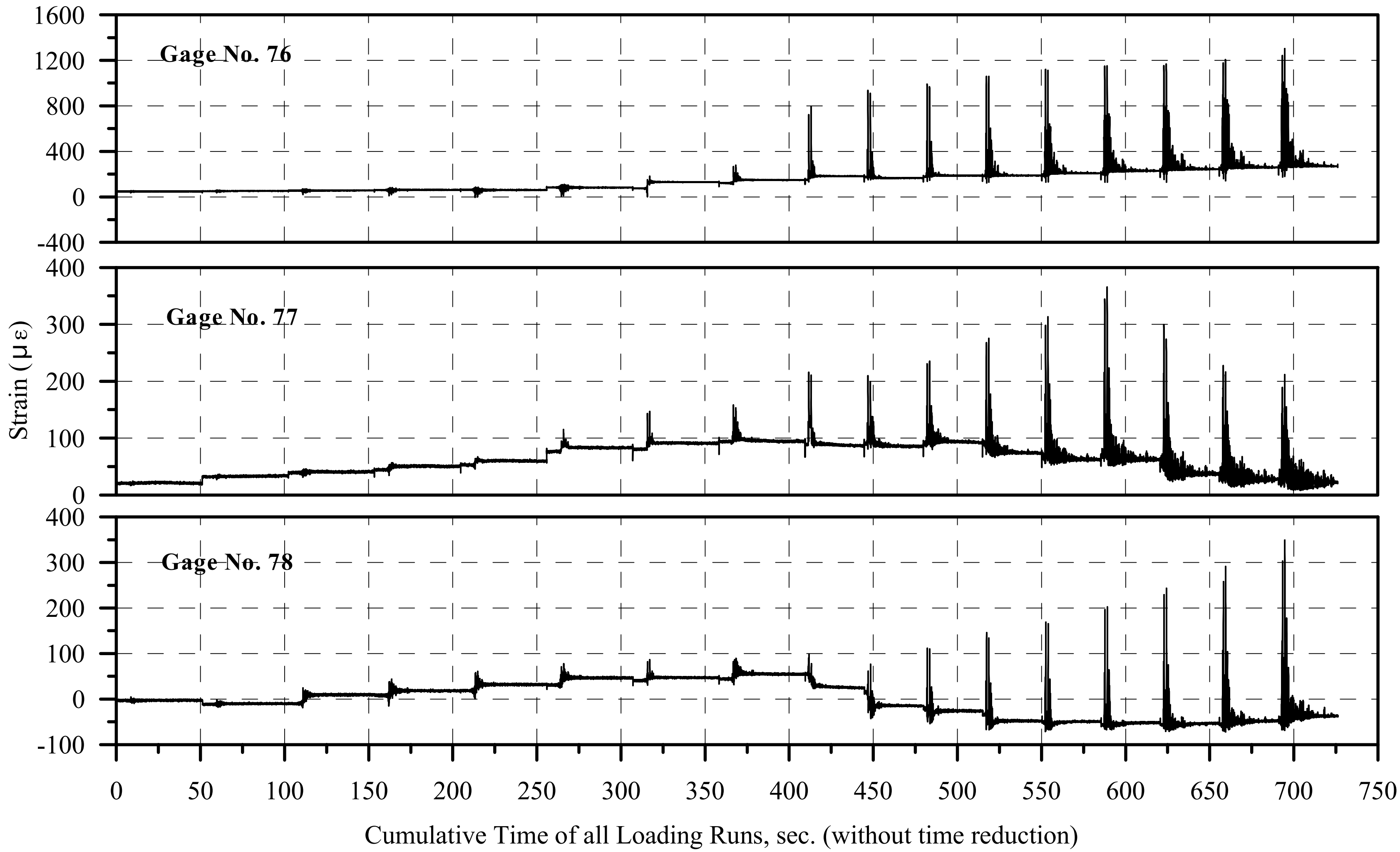

Fig. A-23: Strain History of Gages 76, 77 and 78 in Specimen B2CS

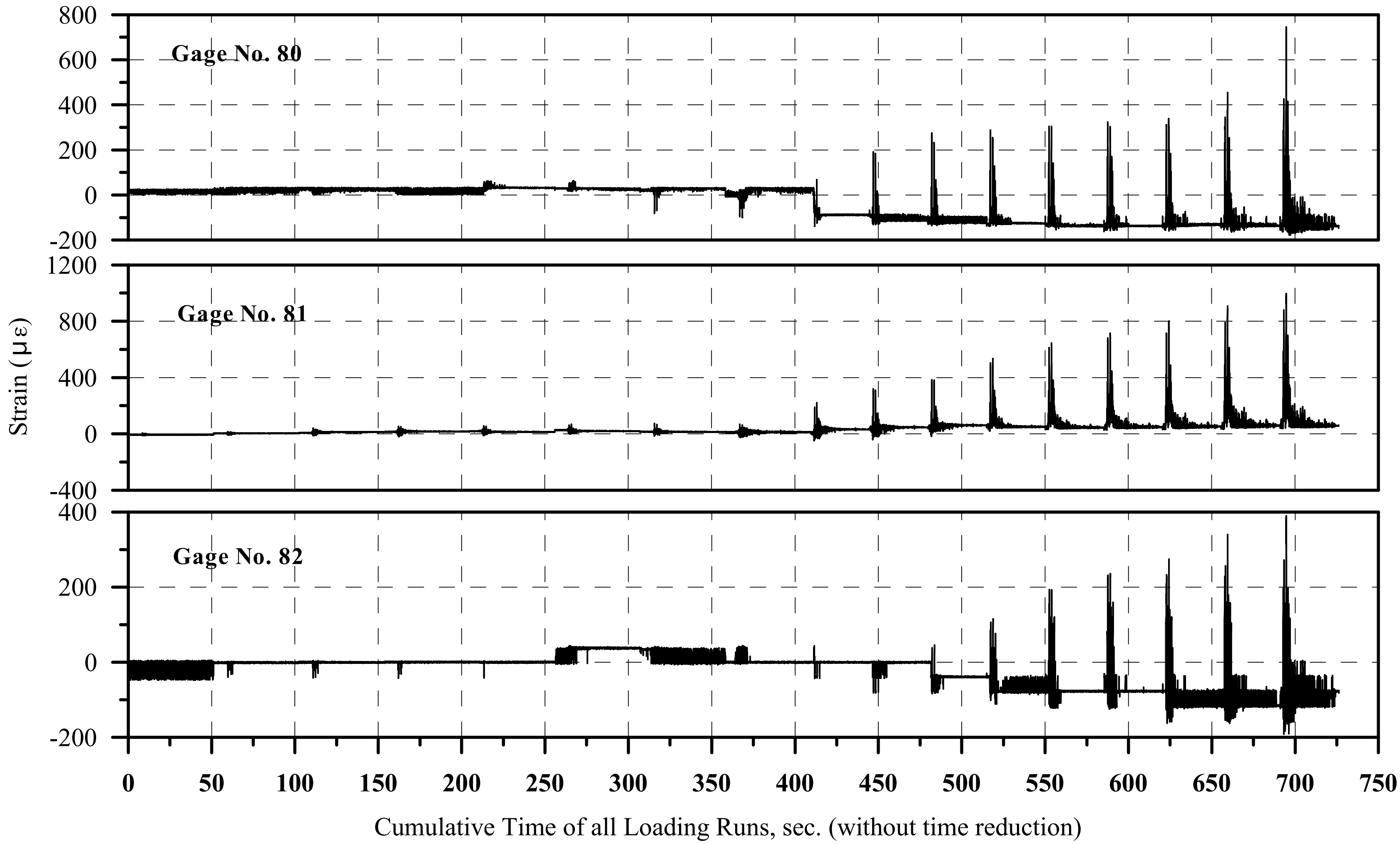

Fig. A-24: Strain History of Gages 80, 81 and 82 in Specimen B2CS

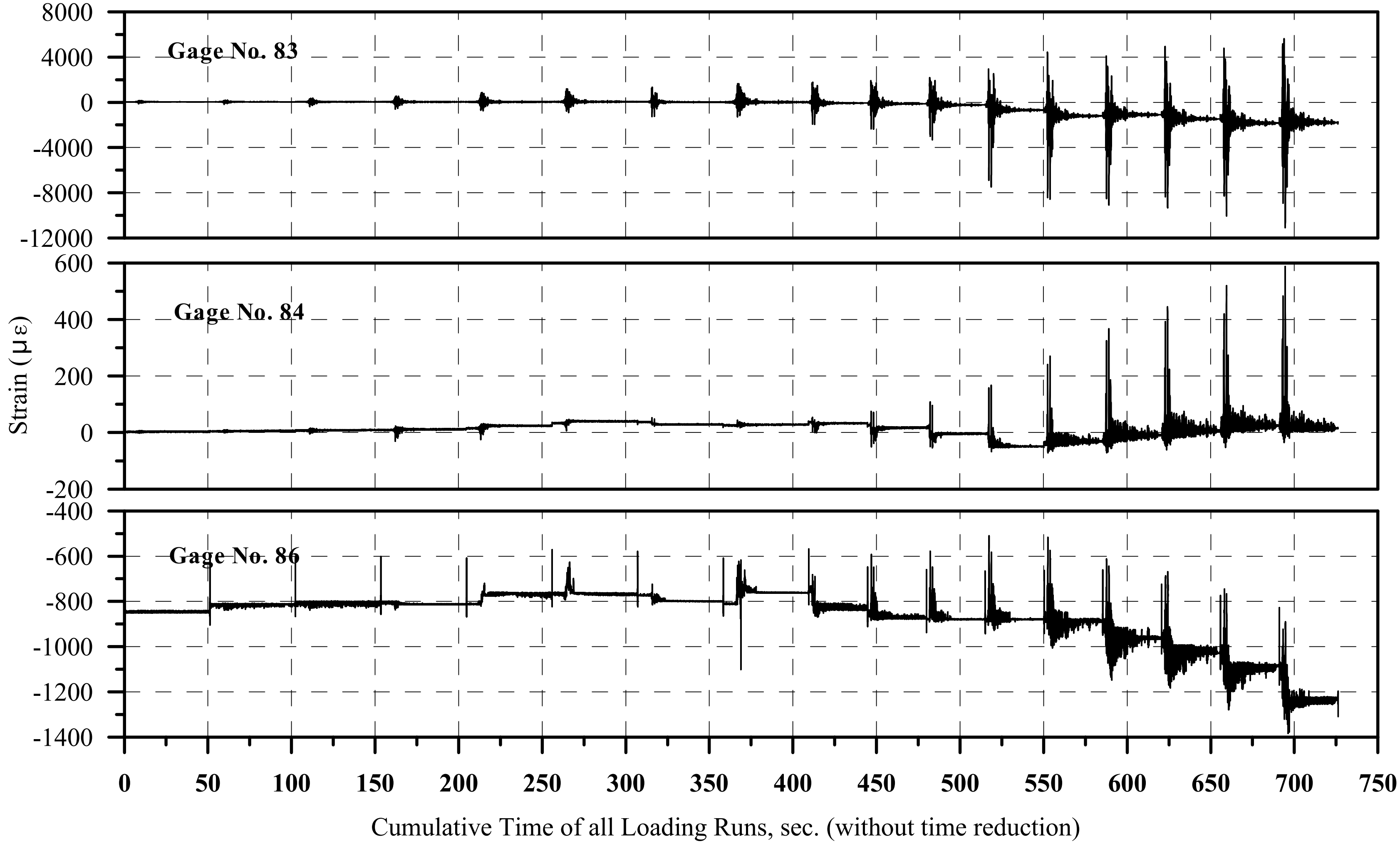

Fig. A-25: Strain History of Gages 83, 84 and 86 in Specimen B2CS

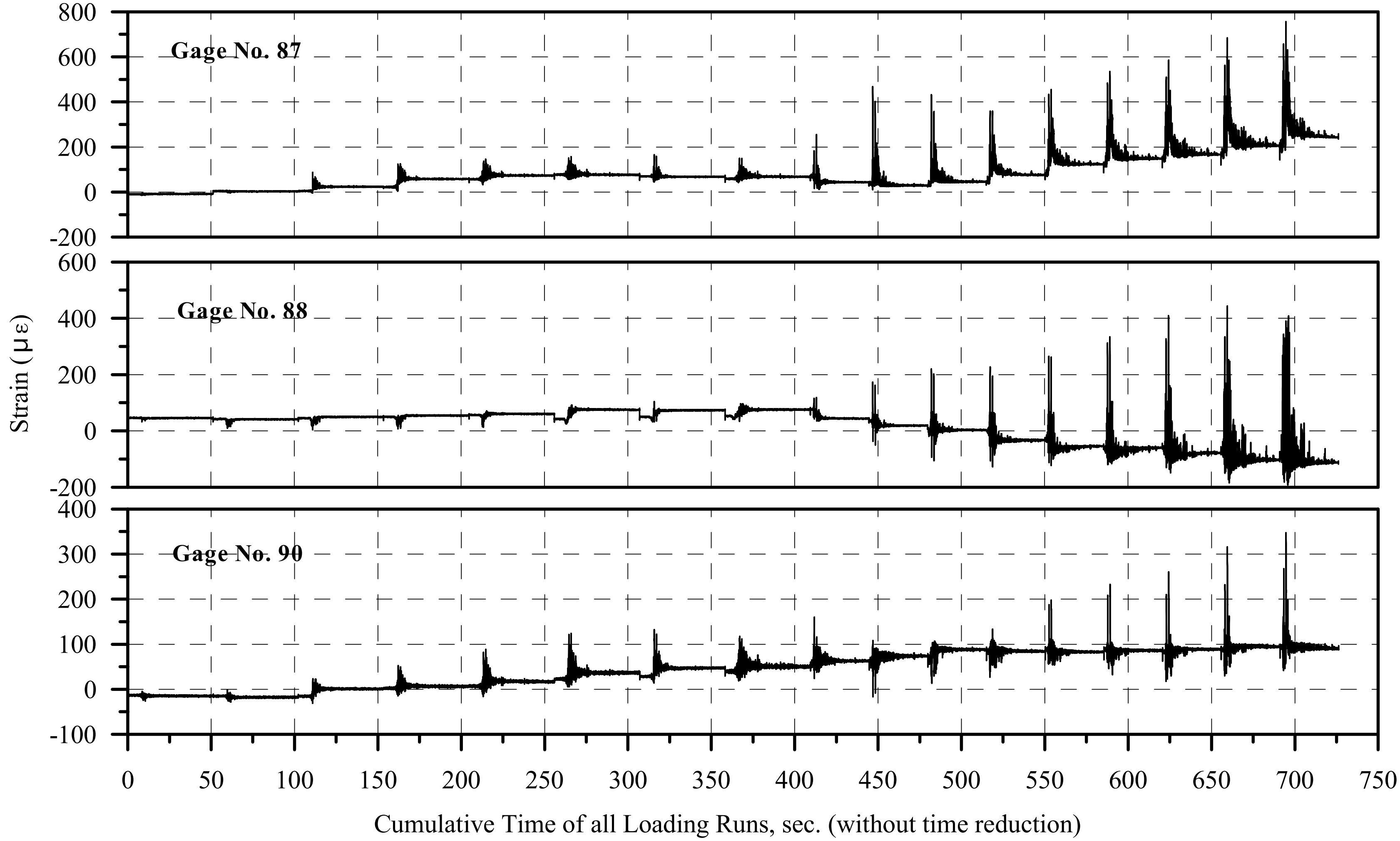

Fig. A-26: Strain History of Gages 87, 88 and 90 in Specimen B2CS

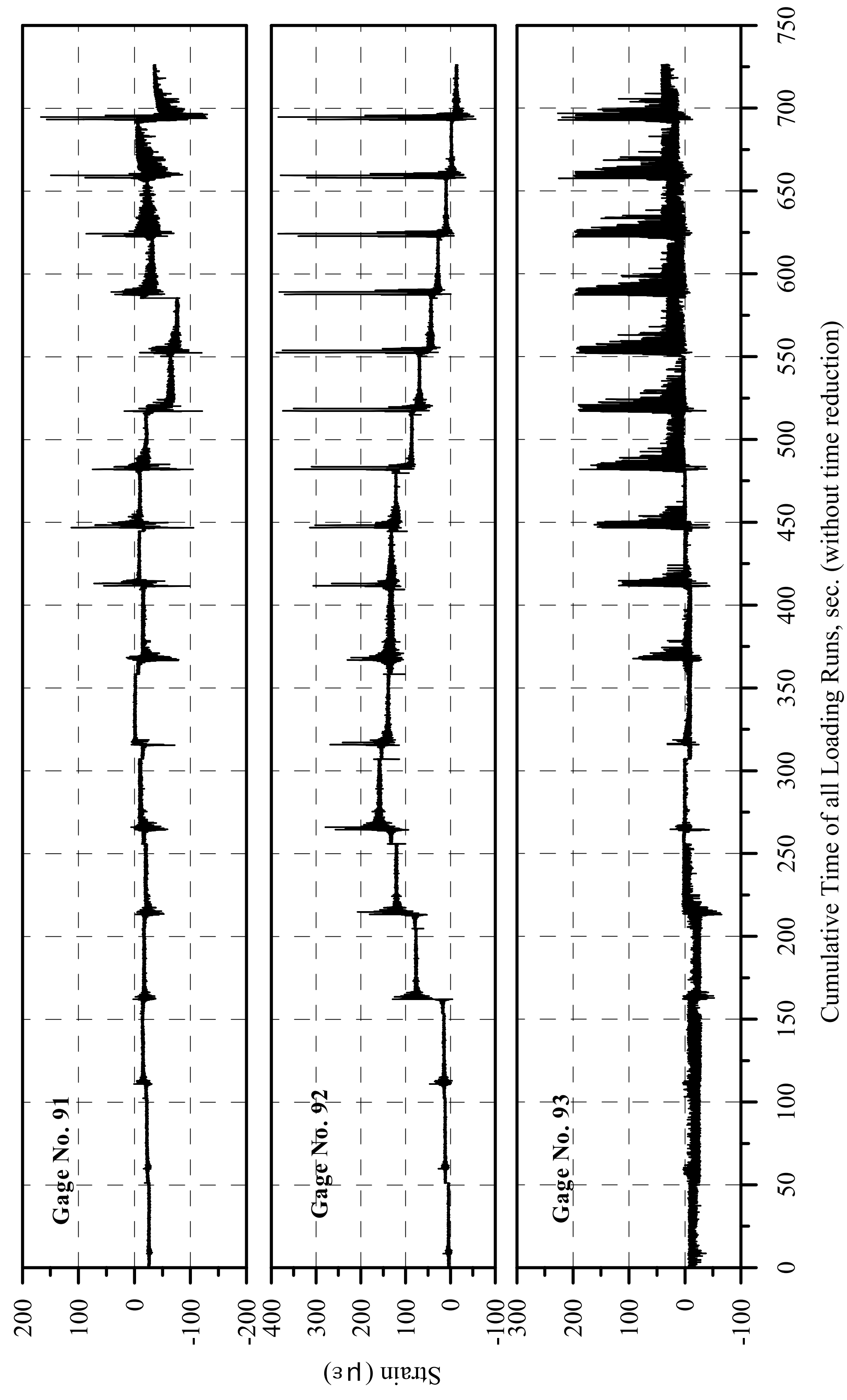

Fig. A-27: Strain History of Gages 91, 92 and 93 in Specimen B2CS

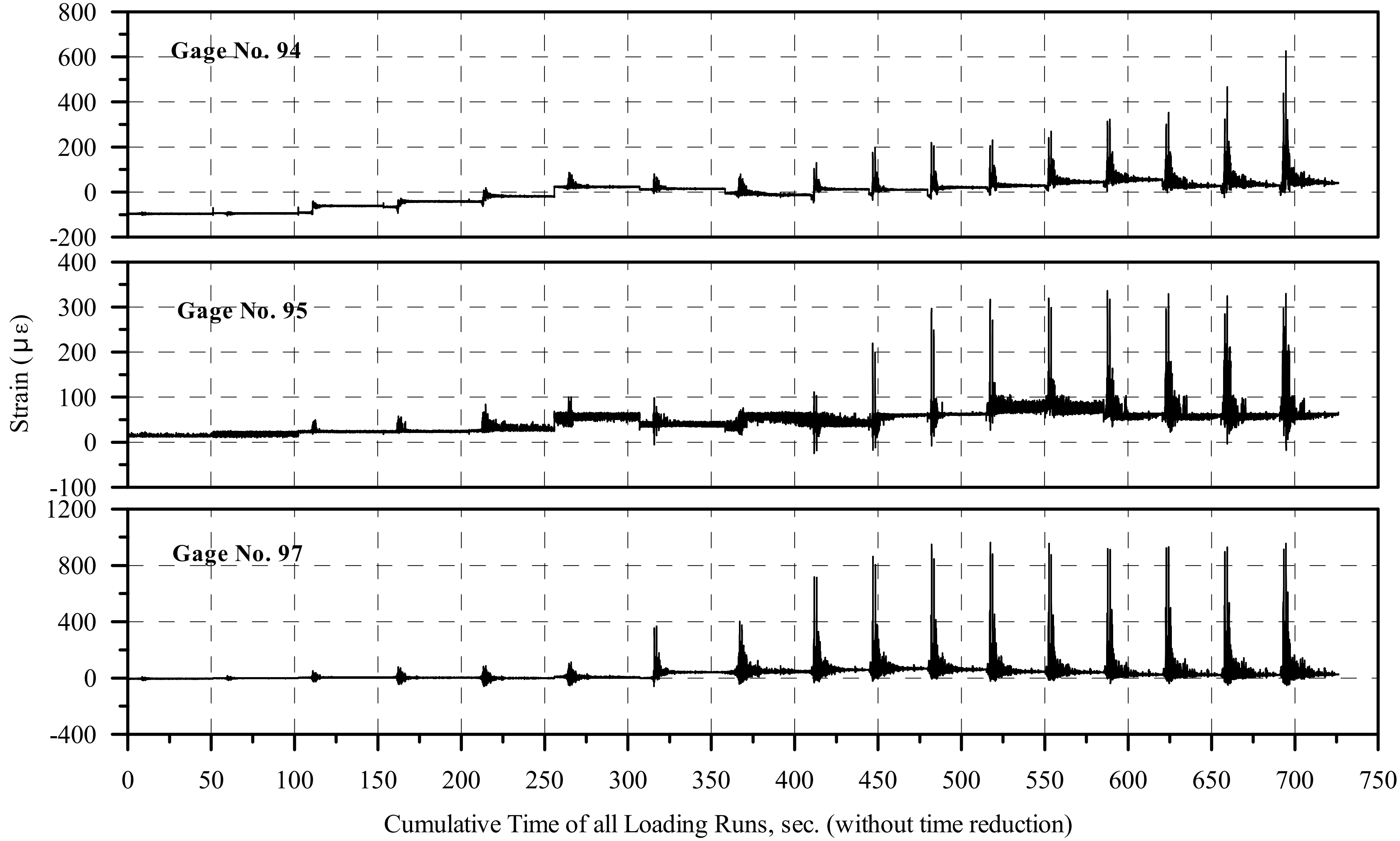

Fig. A-28: Strain History of Gages 94, 95 and 97 in Specimen B2CS

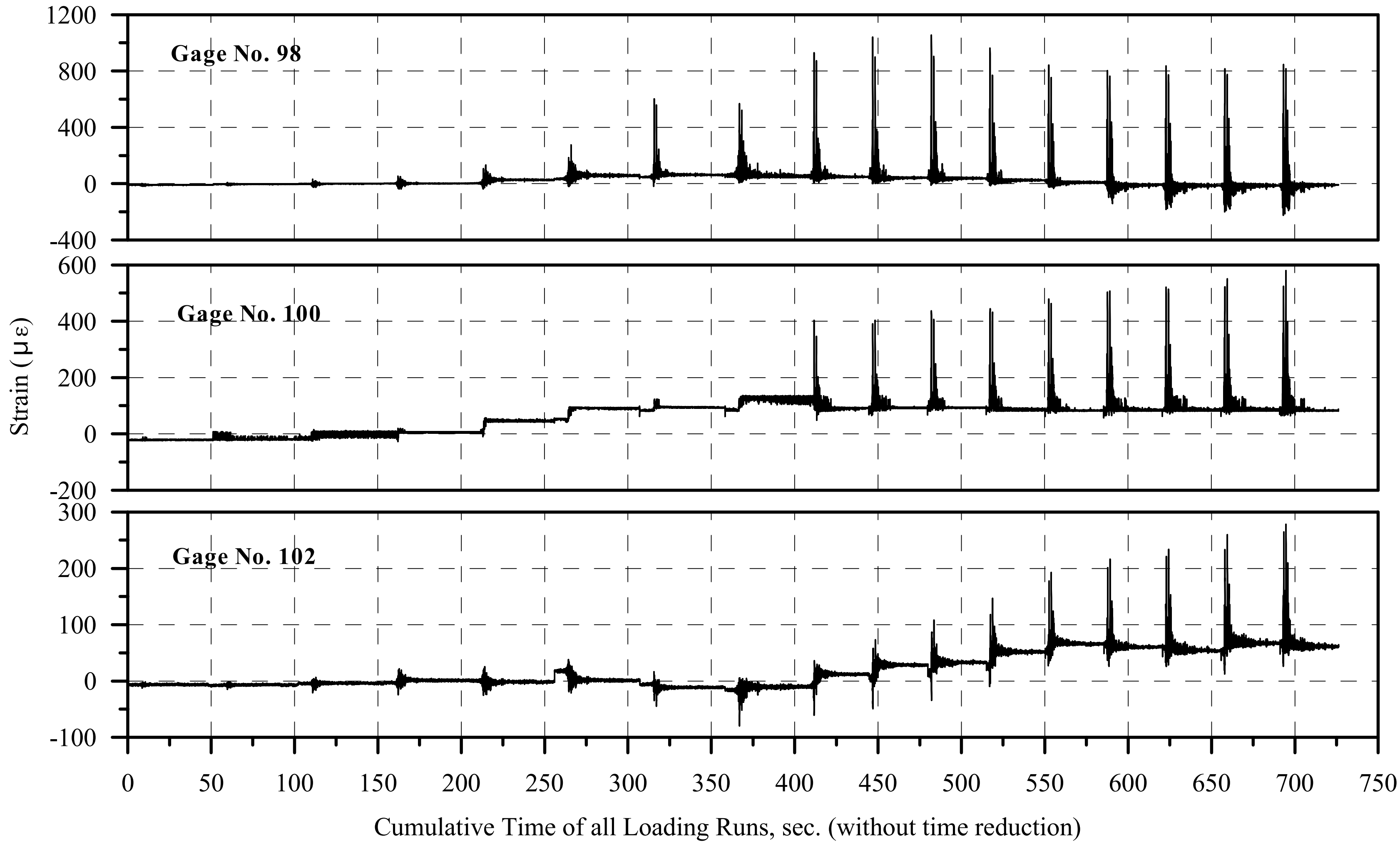

Fig. A-29: Strain History of Gages 98, 100 and 102 in Specimen B2CS

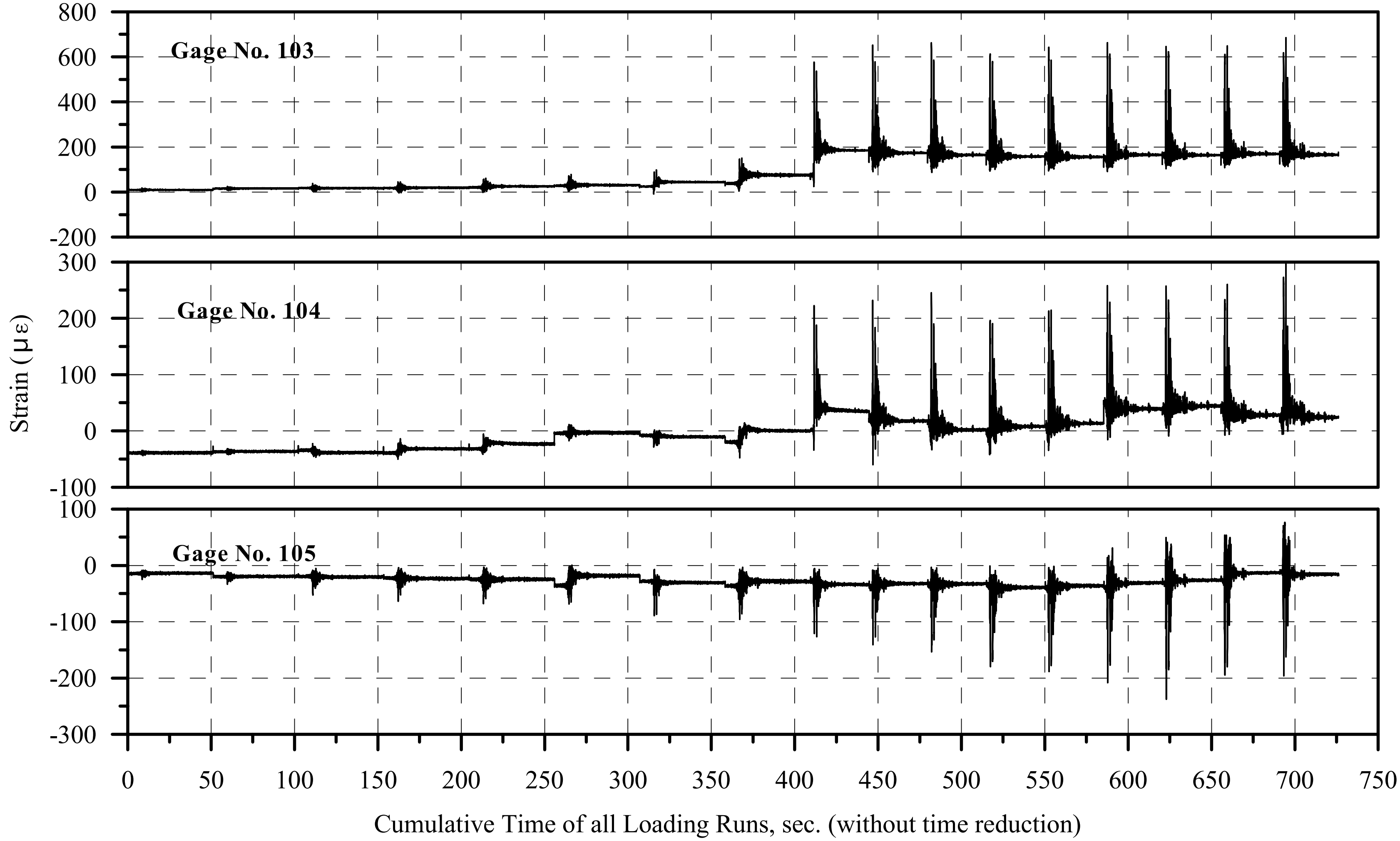

Fig. A-30: Strain History of Gages 103, 104 and 105 in Specimen B2CS

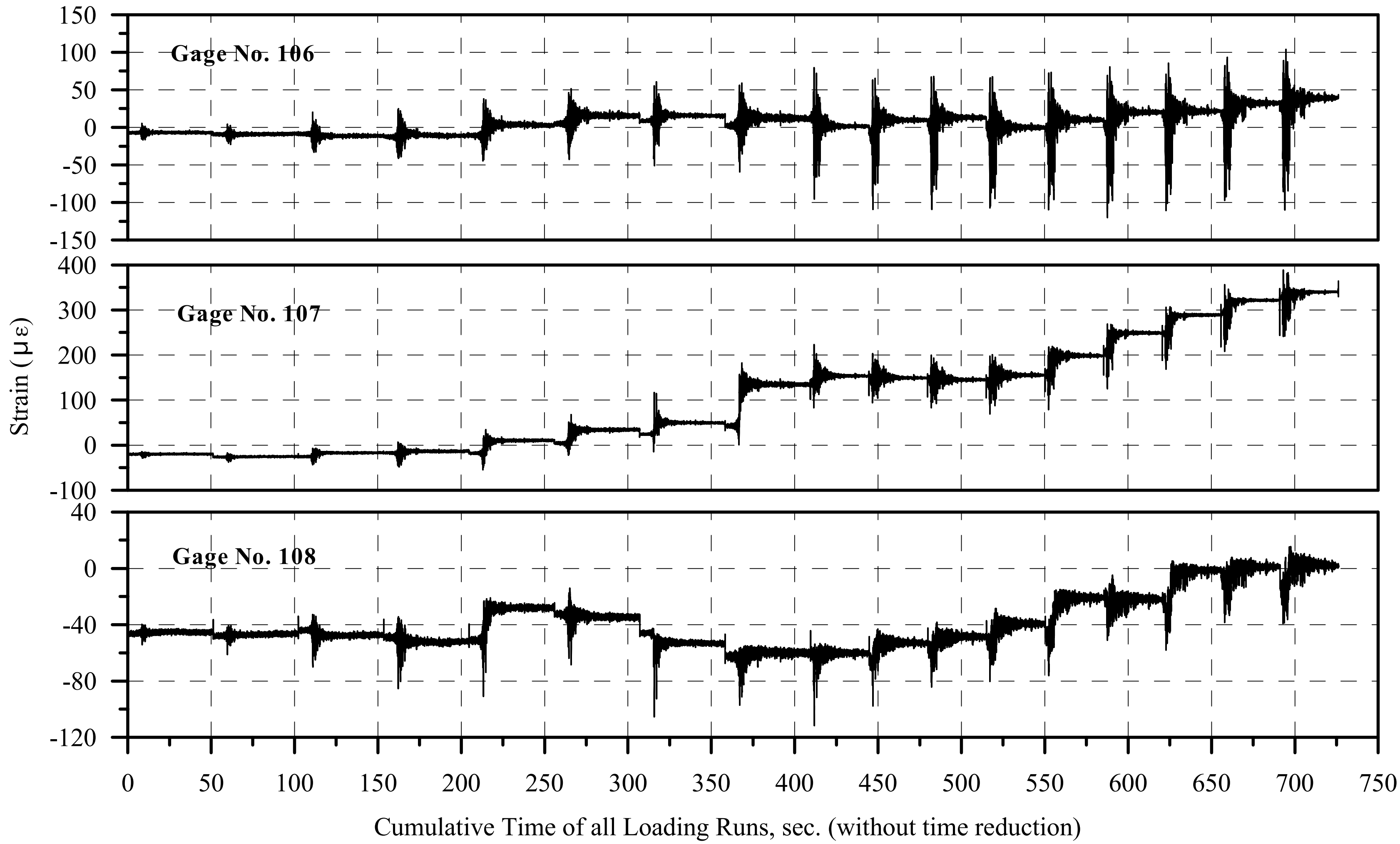

Fig. A-31: Strain History of Gages 106, 107 and 108 in Specimen B2CS

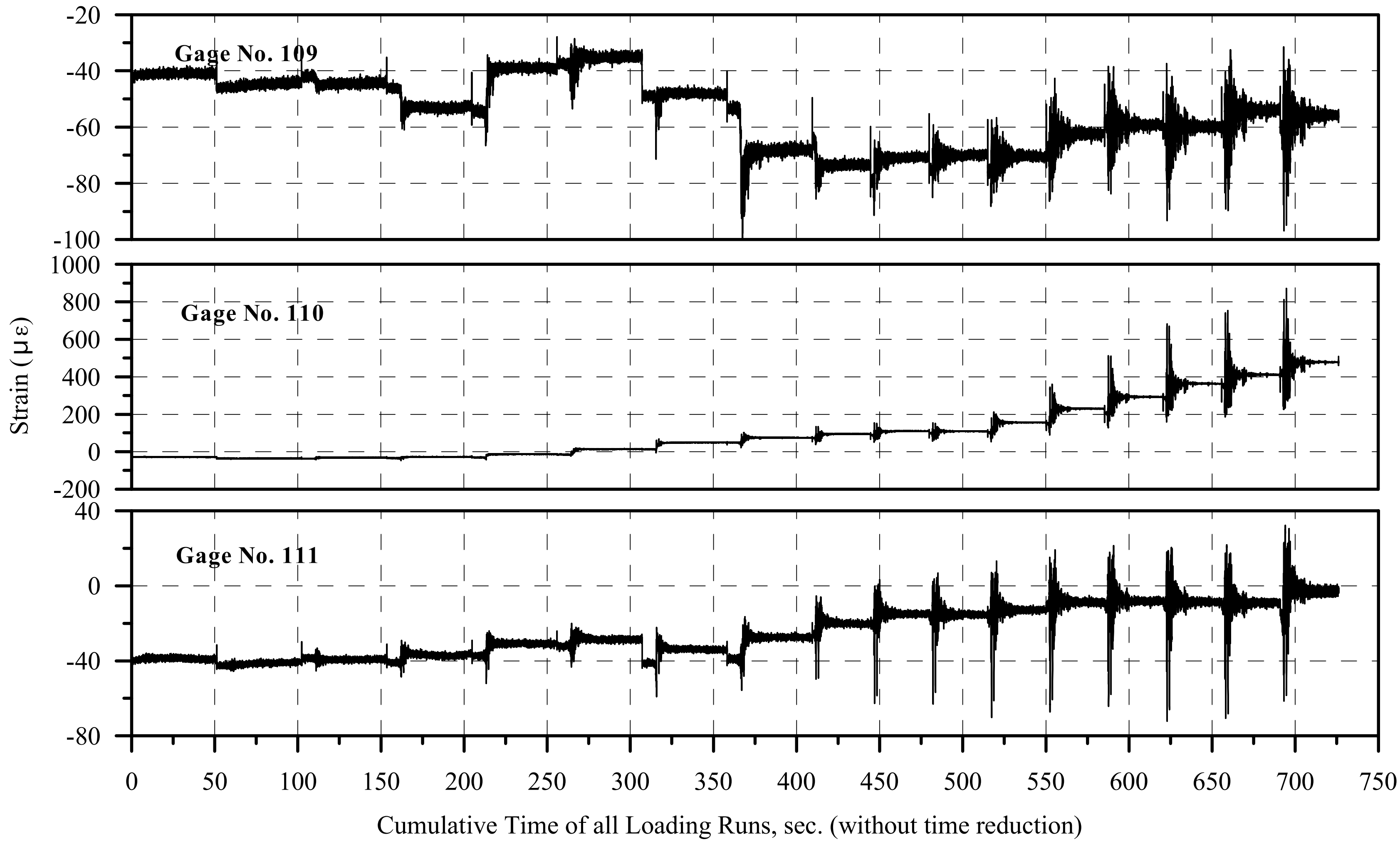

Fig. A-32: Strain History for Gages 109, 110 and 111 of Specimen B2CS

APPENDIX B

STRAIN-TIME HISTORY FOR GAGES IN MIDDLE SPECIMEN B2CM

(See Figs. 2-34 and 2-35 for the locations of each gage)

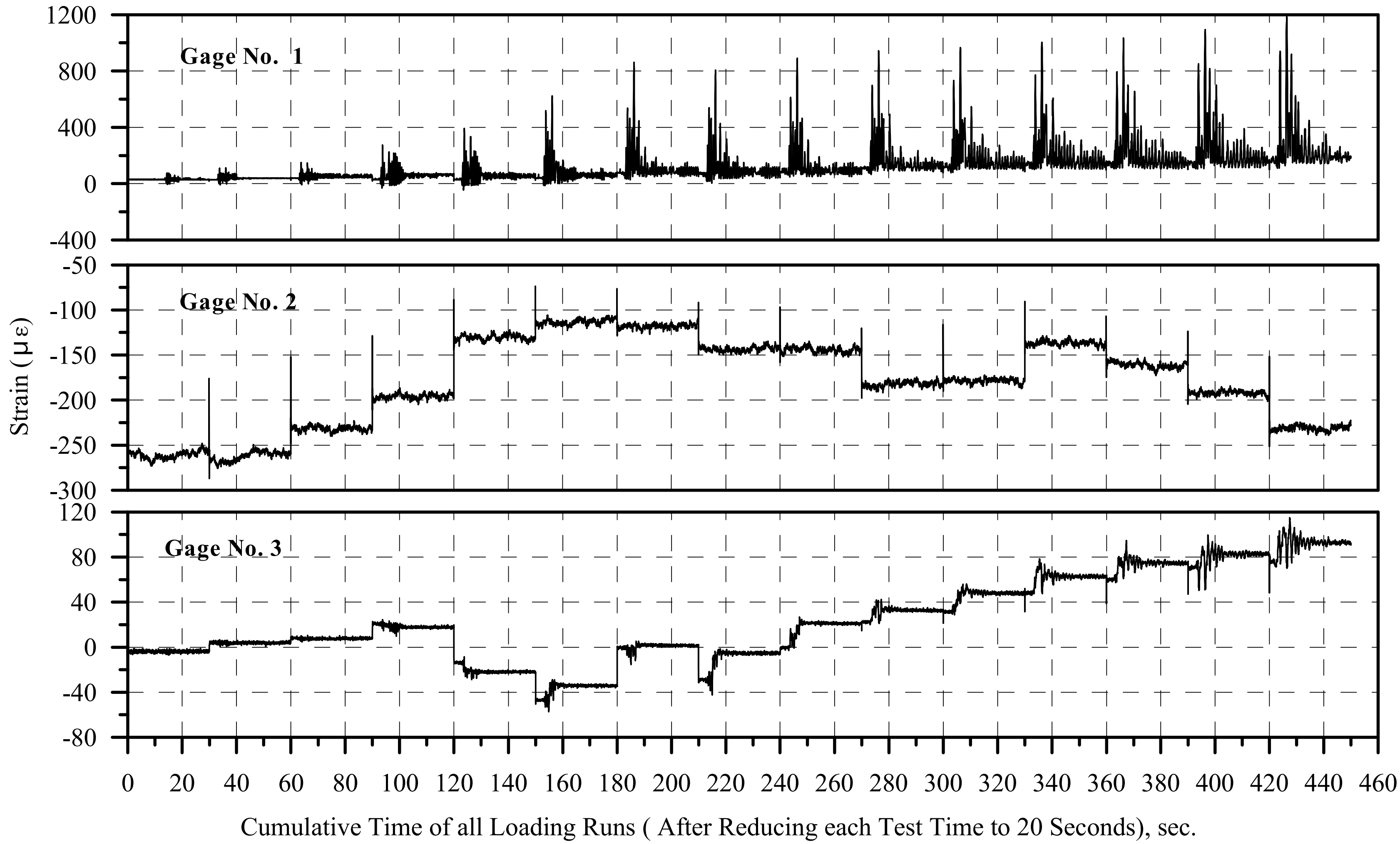

Fig. B-1: Strain History of Gages 1, 2 and 3 in Specimen B2CM

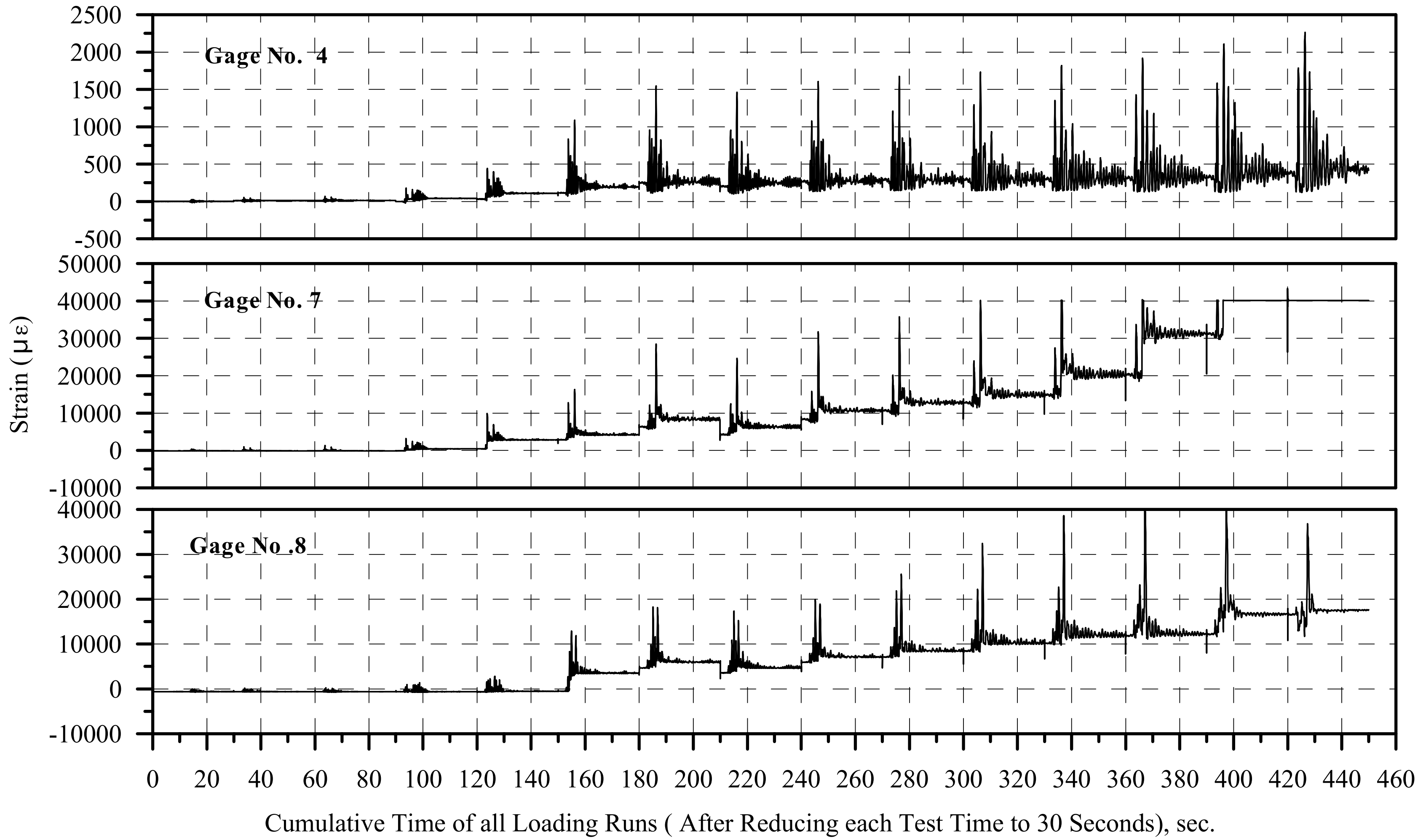

Fig. B-2: Strain History of Gages 4, 7 and 8 in Specimen B2CM

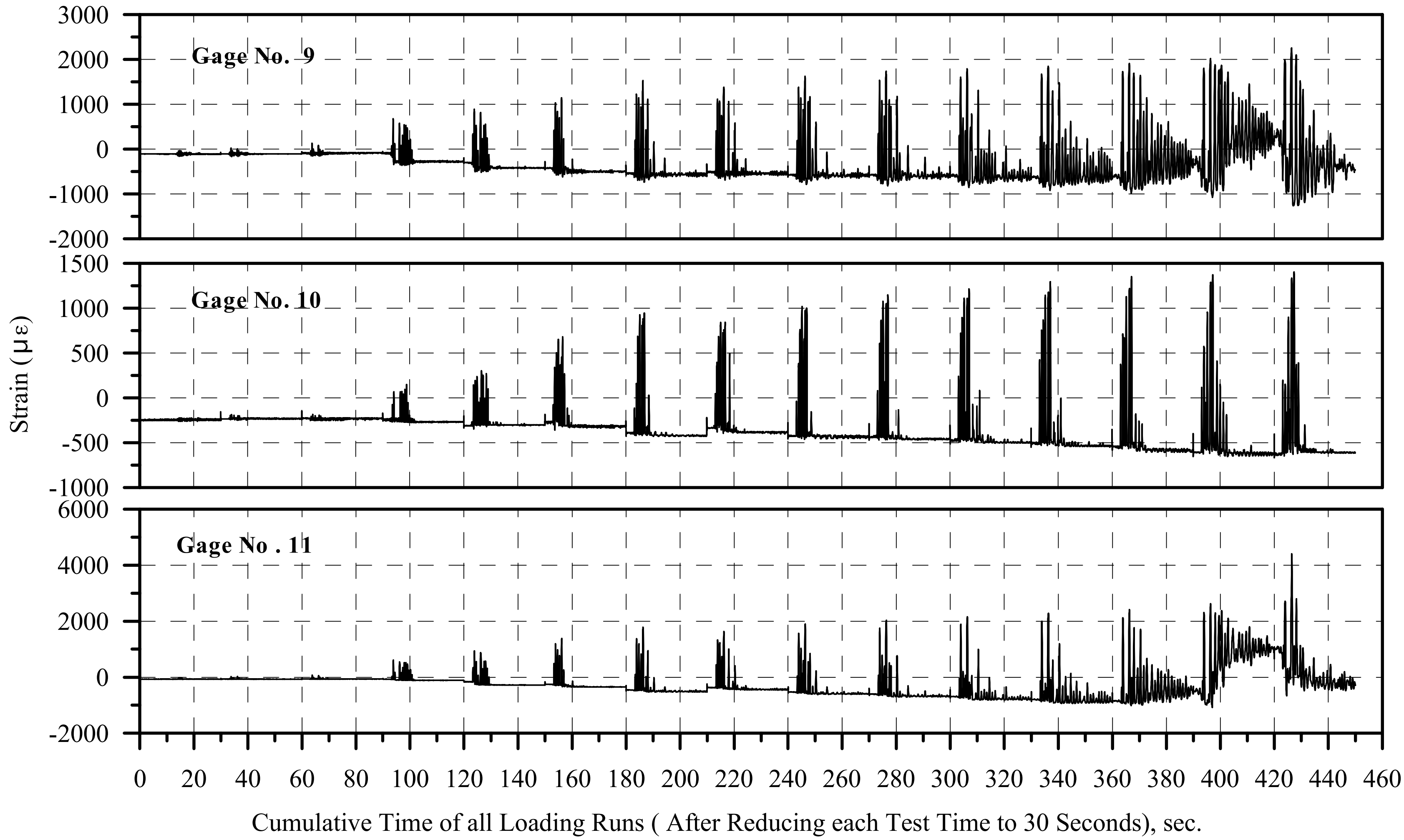

Fig. B-3: Strain History of Gages 9, 10 and 11 in Specimen B2CM

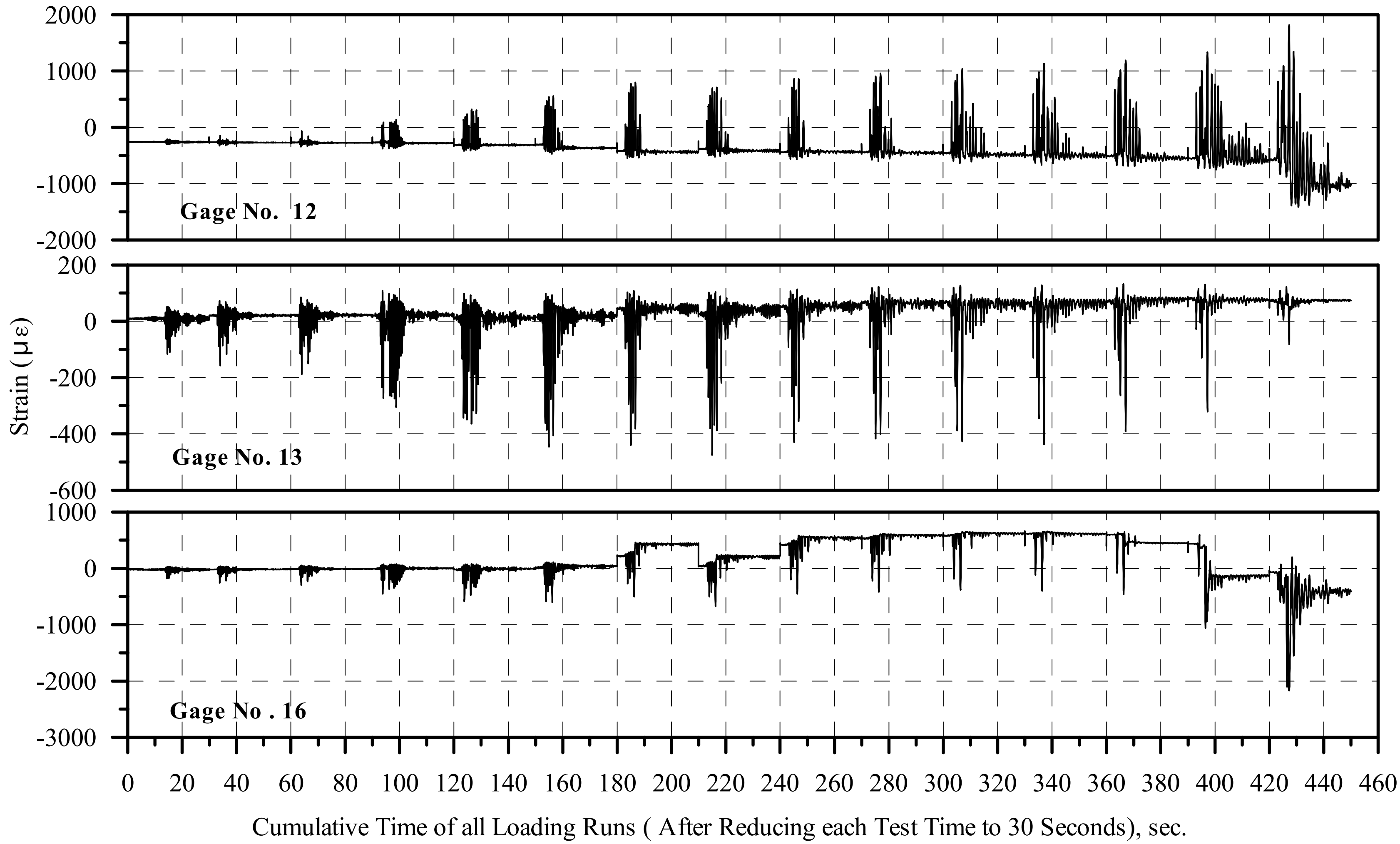

Fig. B-4: Strain History of Gages 12, 13 and 16 in Specimen B2CM

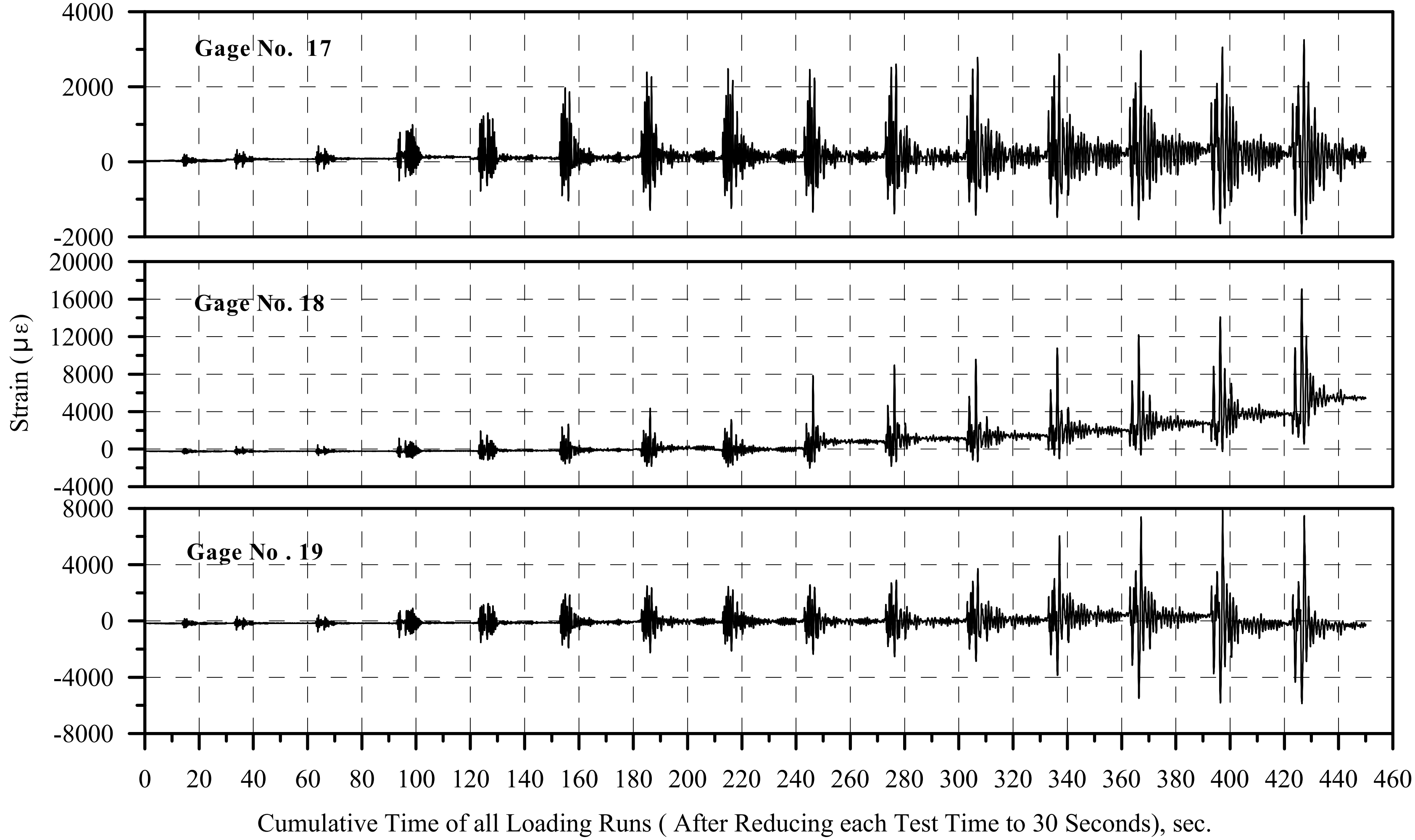

Fig. B-5: Strain History of Gages 17, 18 and 19 in Specimen B2CM

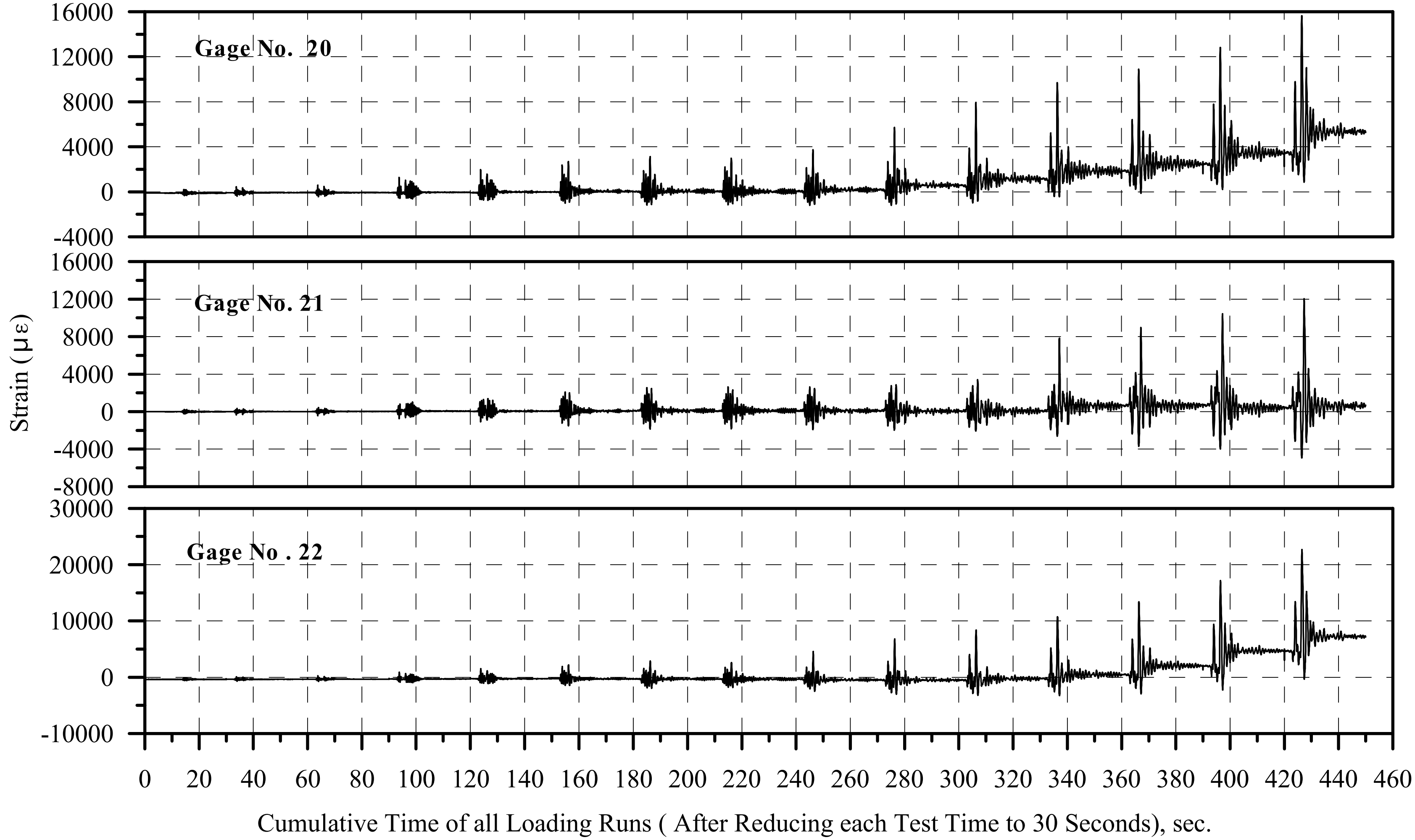

Fig. B-6: Strain History of Gages 20, 21 and 22 in Specimen B2CM

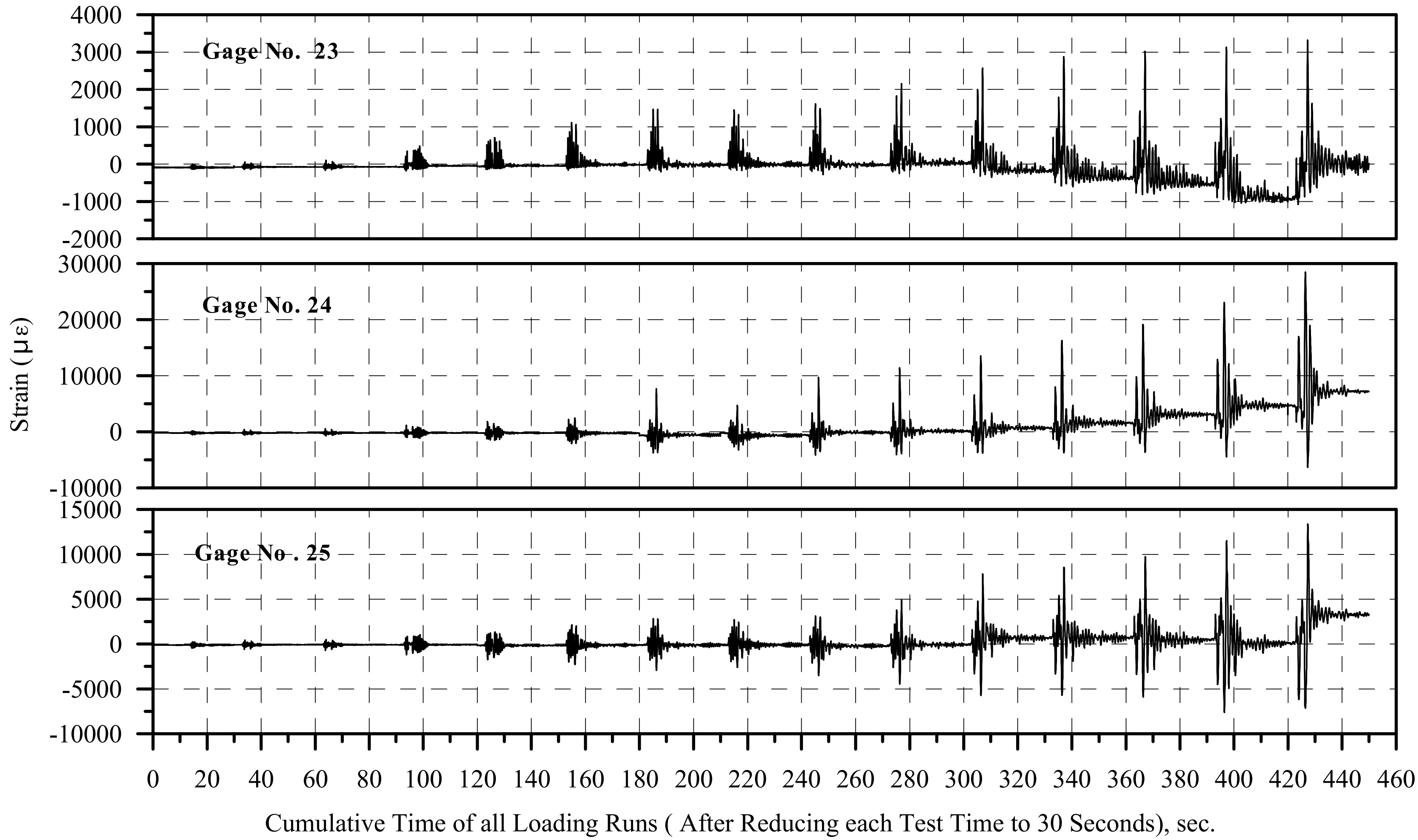

Fig. B-7 Strain History of Gages 23, 24 and 25 in Specimen B2CM

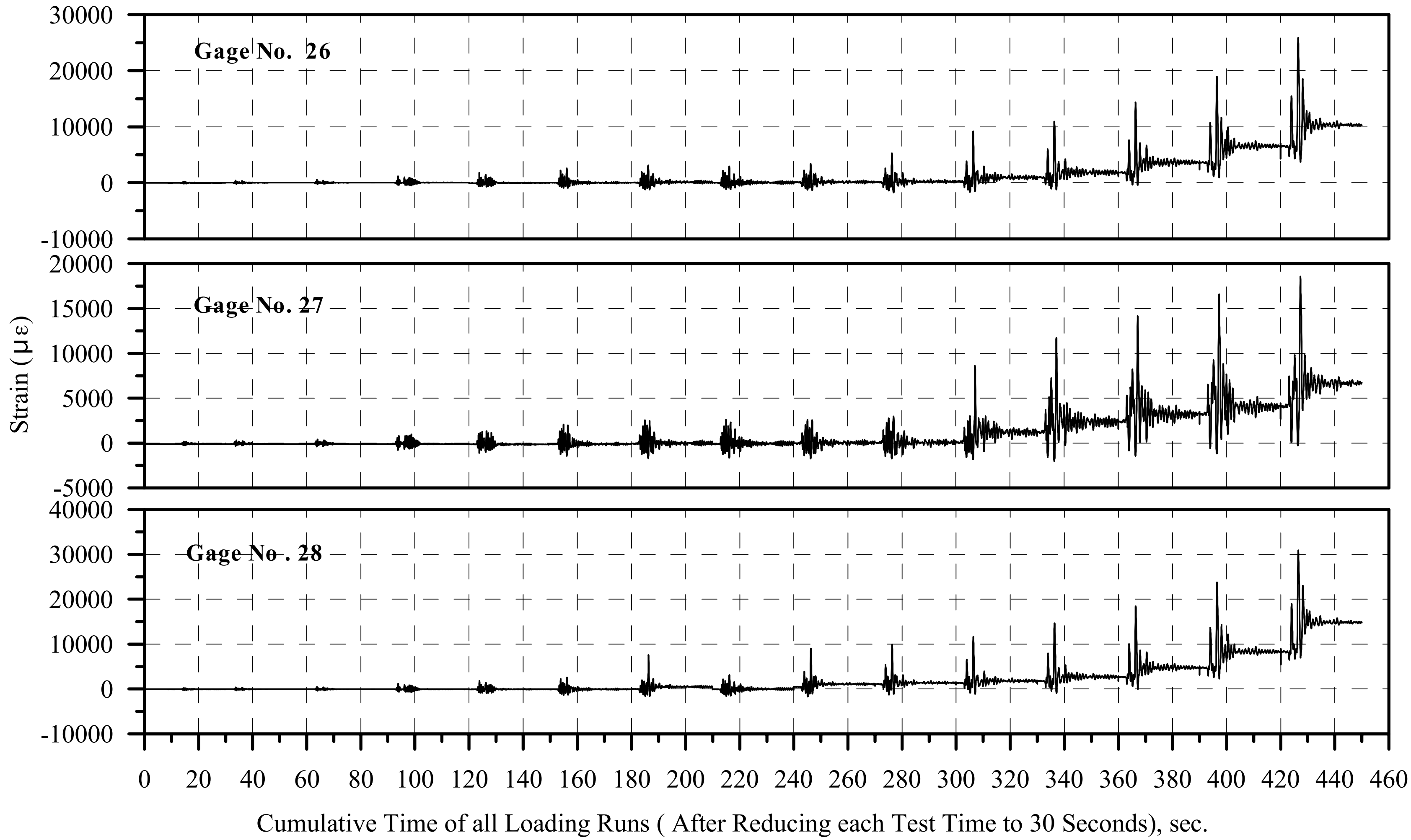

Fig. B-8: Strain History of Gages 26, 27 and 28 in Specimen B2CM

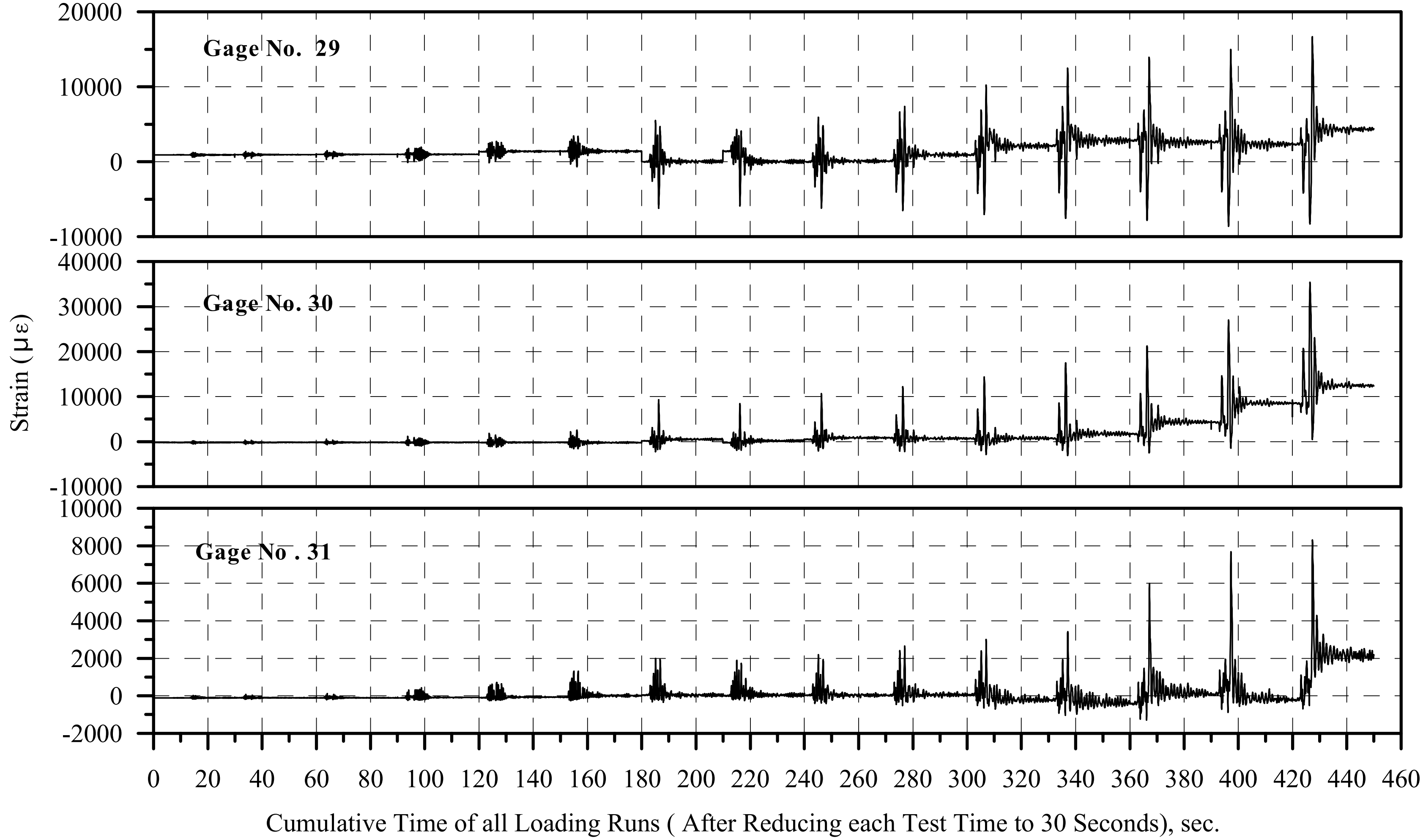

Fig. B-9: Strain History of Gages 29, 30 and 31 in Specimen B2CM

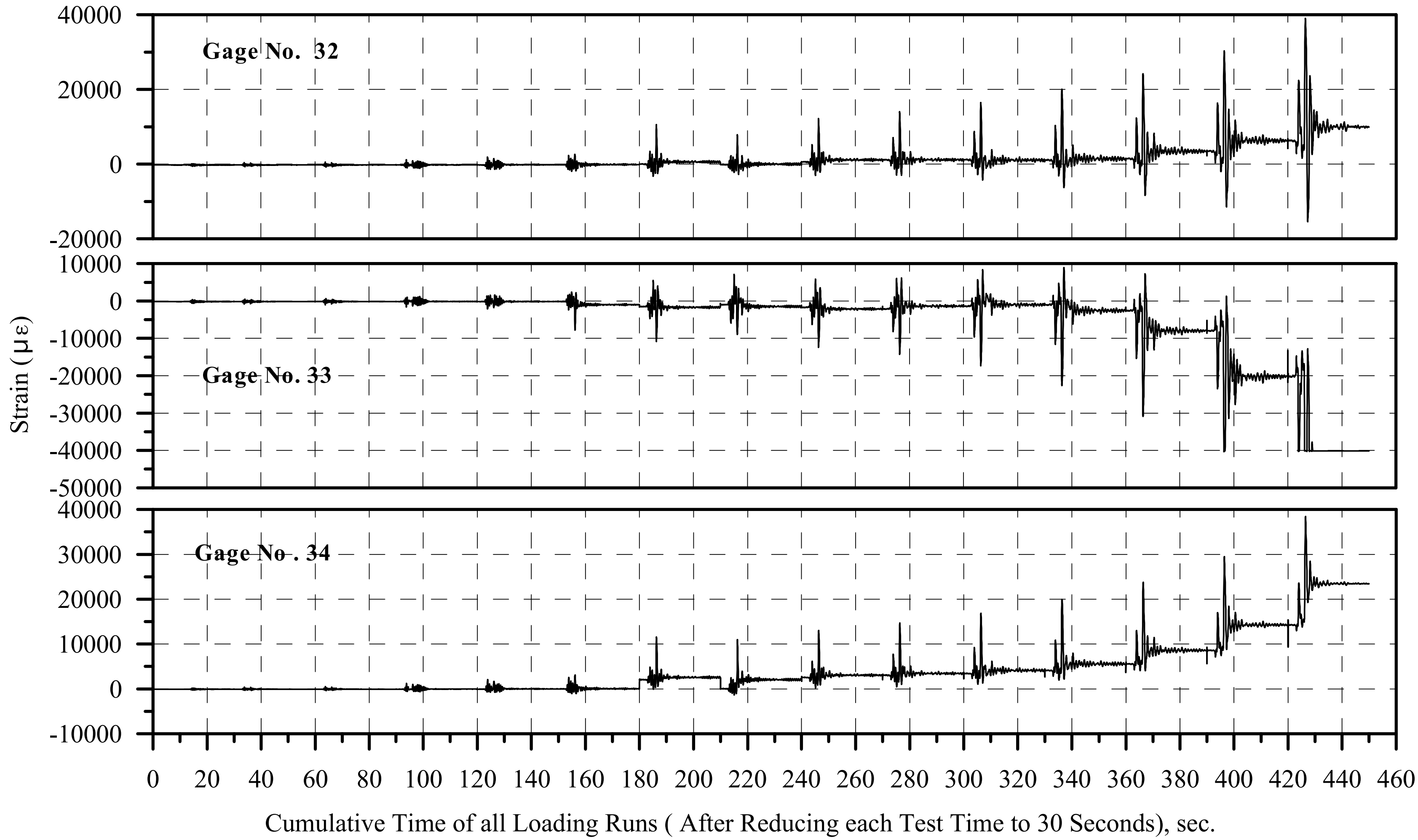

Fig. B-10: Strain History of Gages 32, 33 and 34 in Specimen B2CM

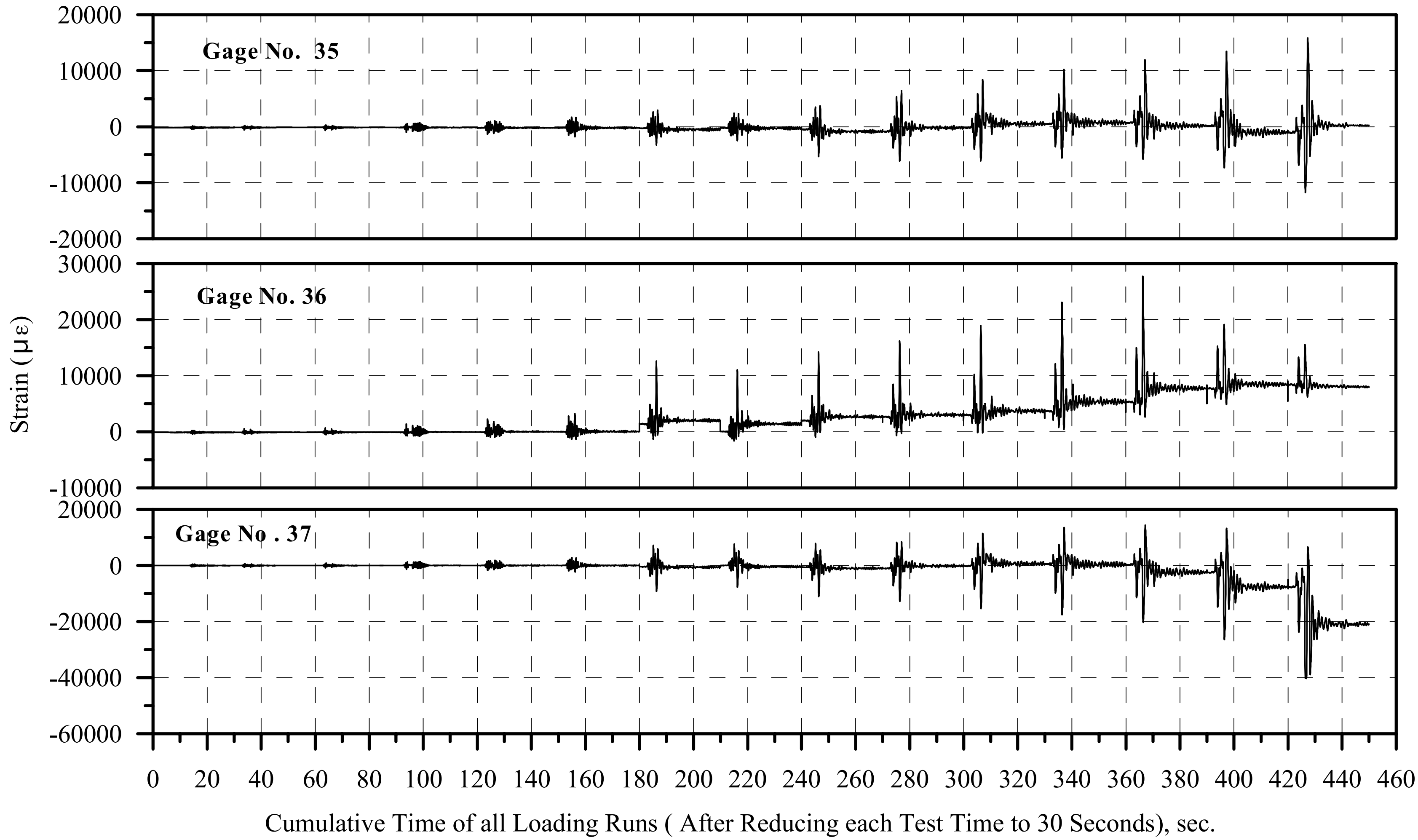

Fig. B-11: Strain History of Gages 35, 36 and 37 in Specimen B2CM

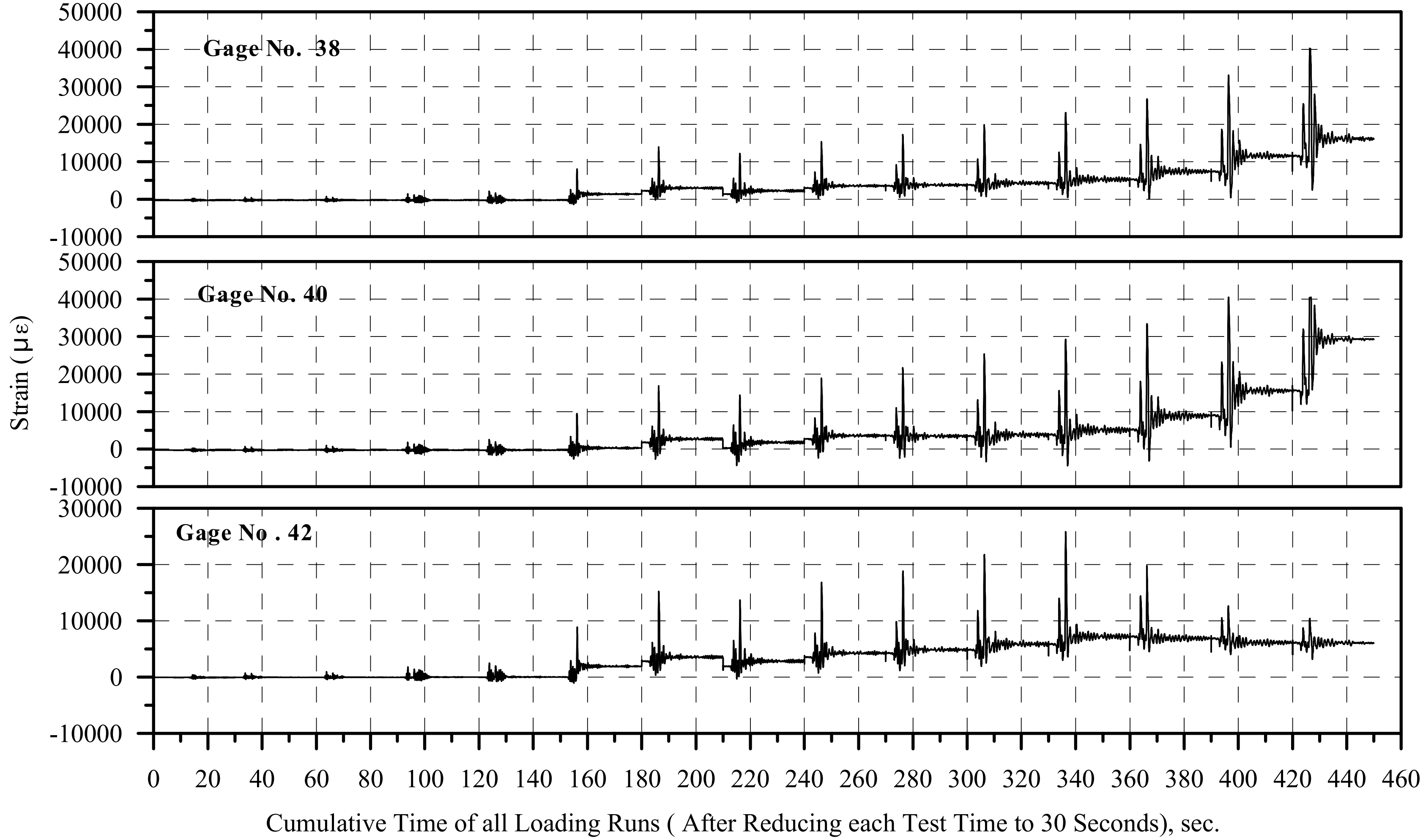

Fig. B-12: Strain History of Gages 38, 40 and 42 in Specimen B2CM

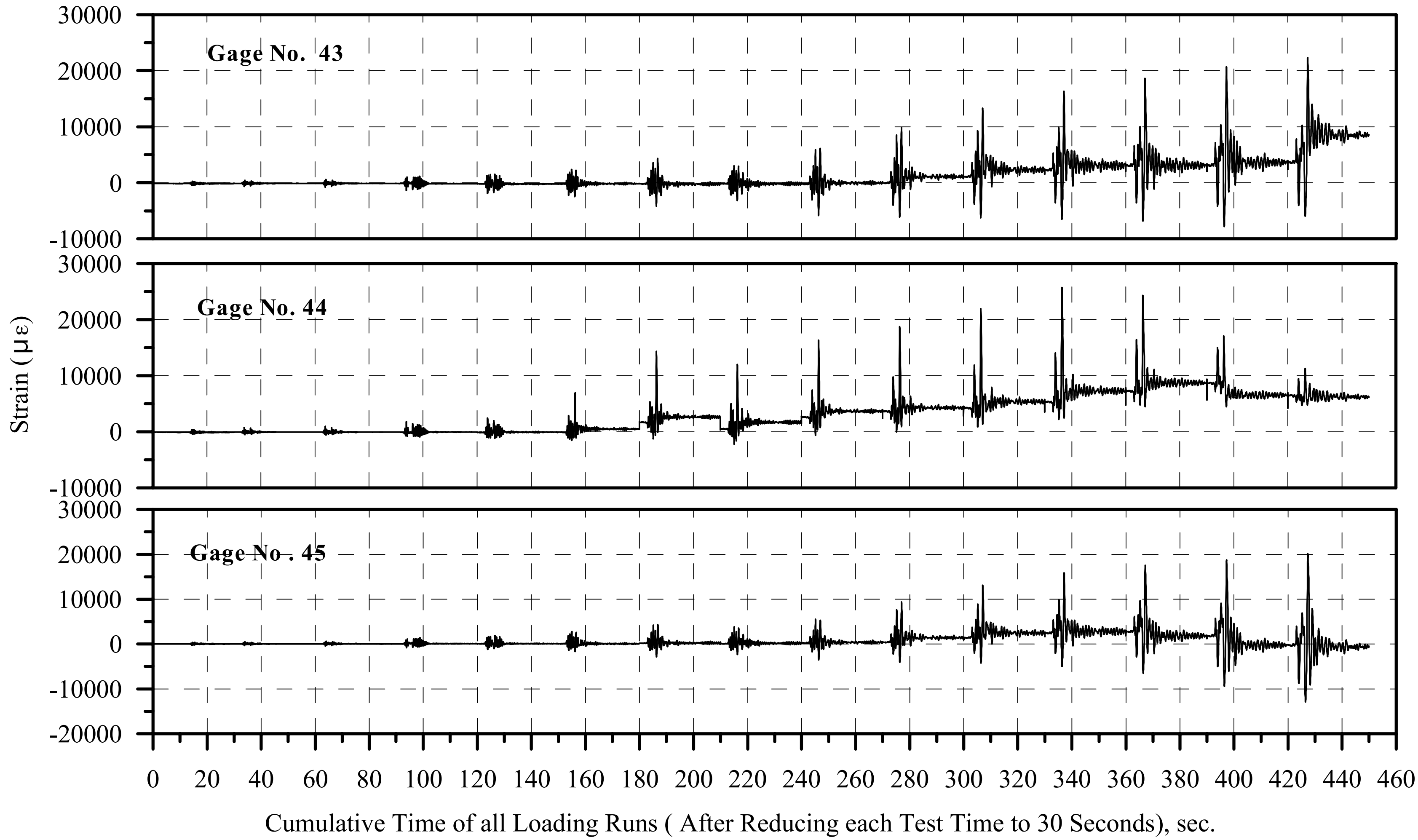

Fig. B-13: Strain History of Gages 43, 44 and 45 in Specimen B2CM

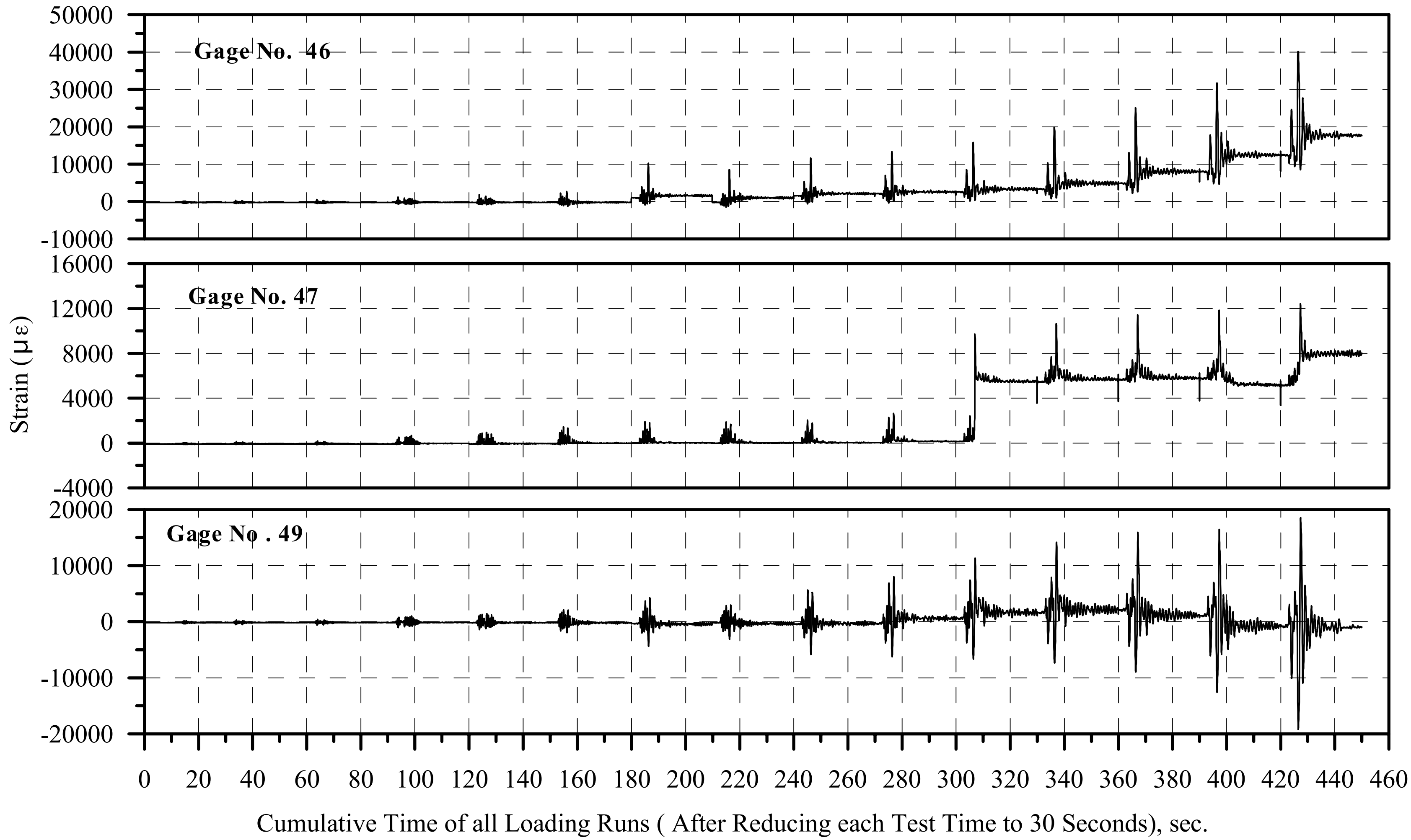

Fig. B-14: Strain History of Gages 46, 47 and 49 in Specimen B2CM

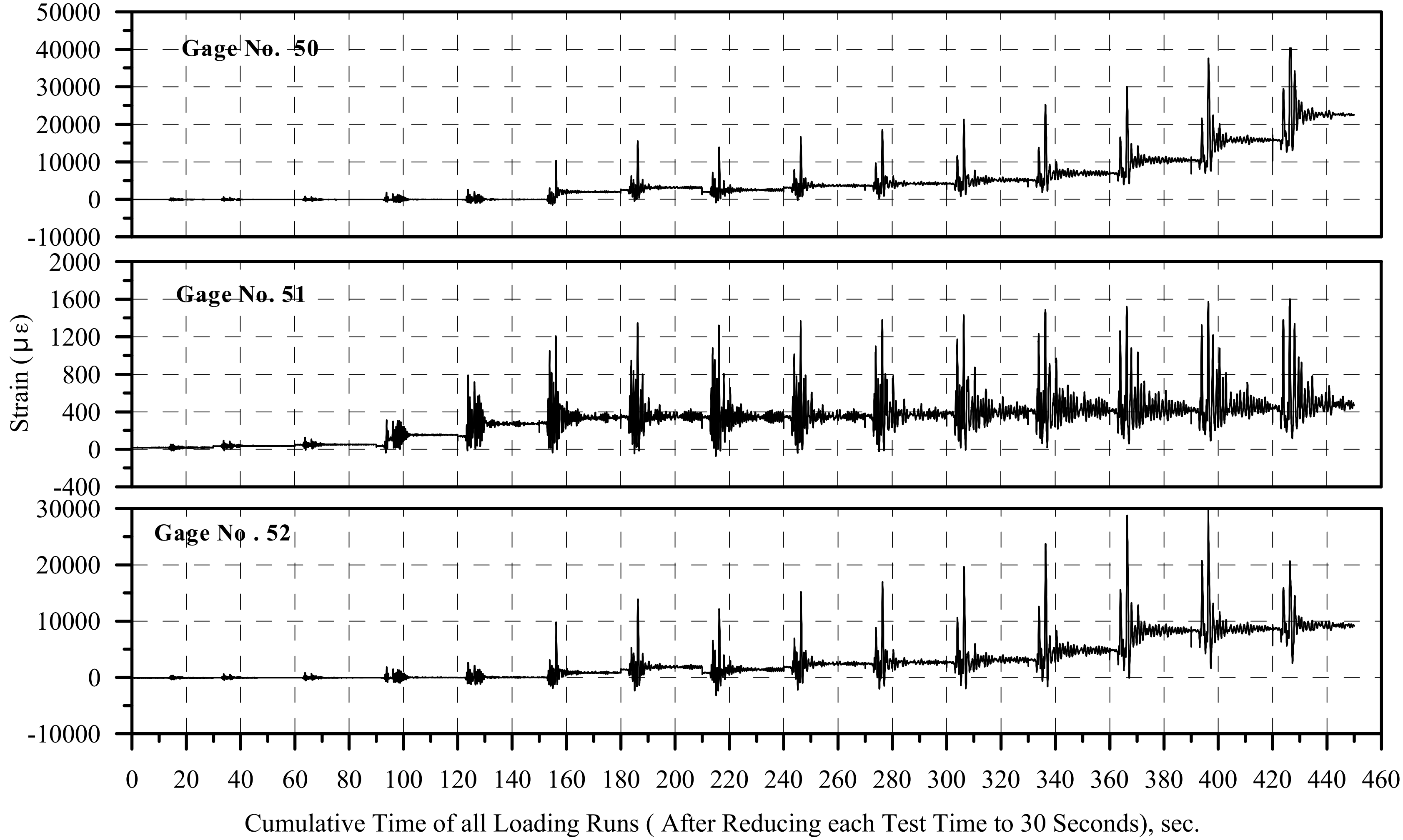

Fig. B-15: Strain History of Gages 50, 51 and 52 in Specimen B2CM

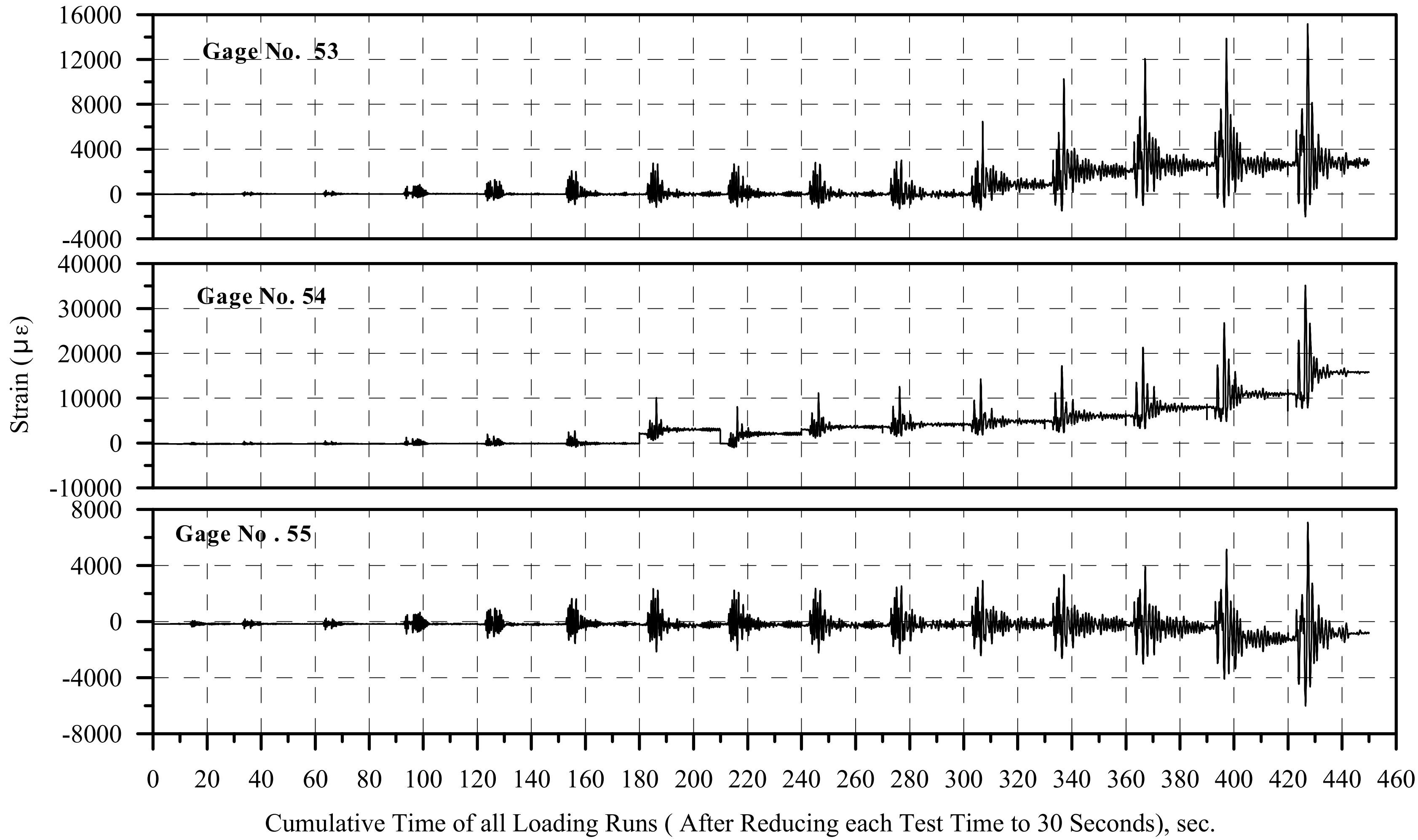

Fig. B-16: Strain History of Gages 53, 54 and 55 in Specimen B2CM

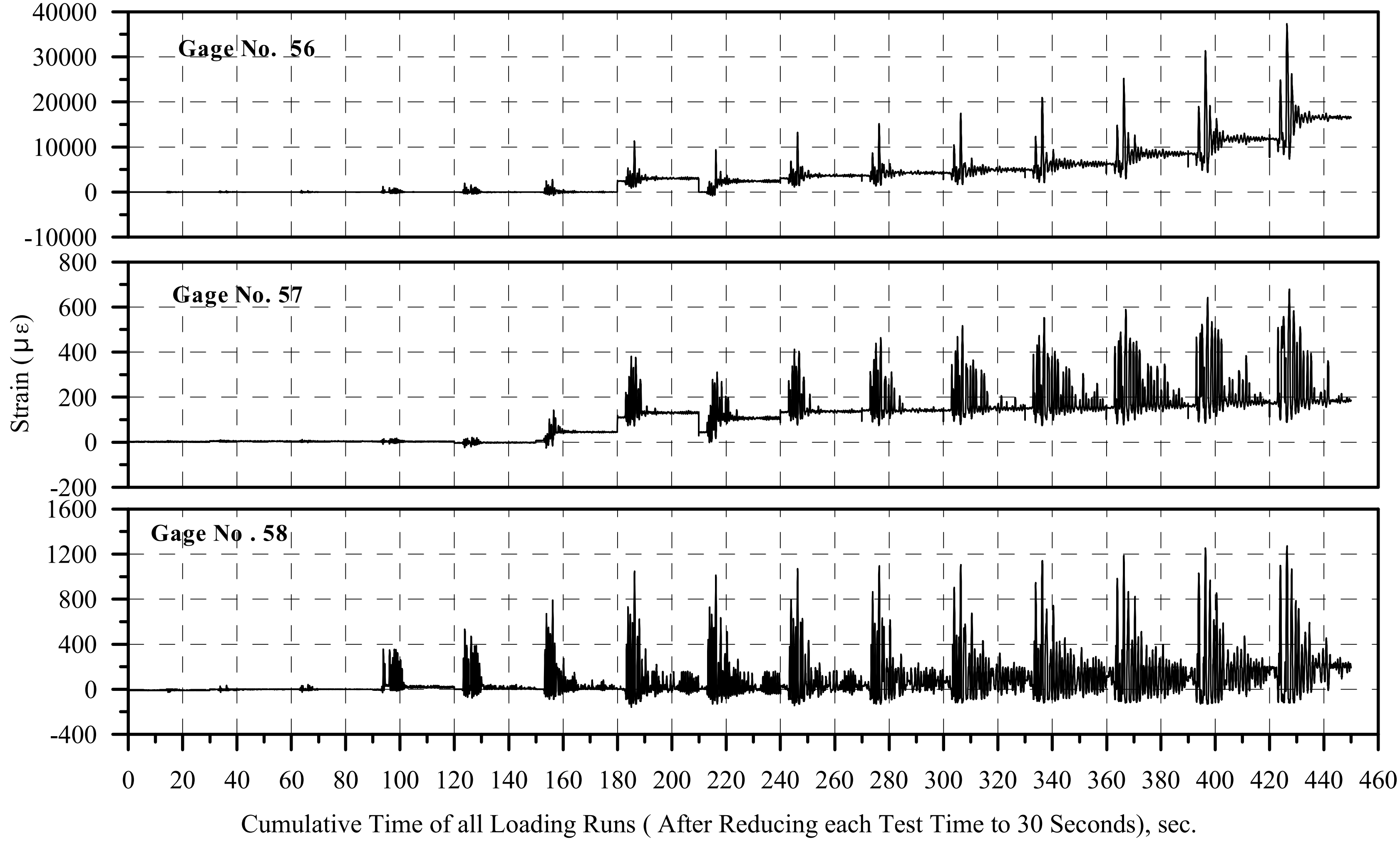

Fig. B-17: Strain History of Gages 56, 57 and 58 in Specimen B2CM

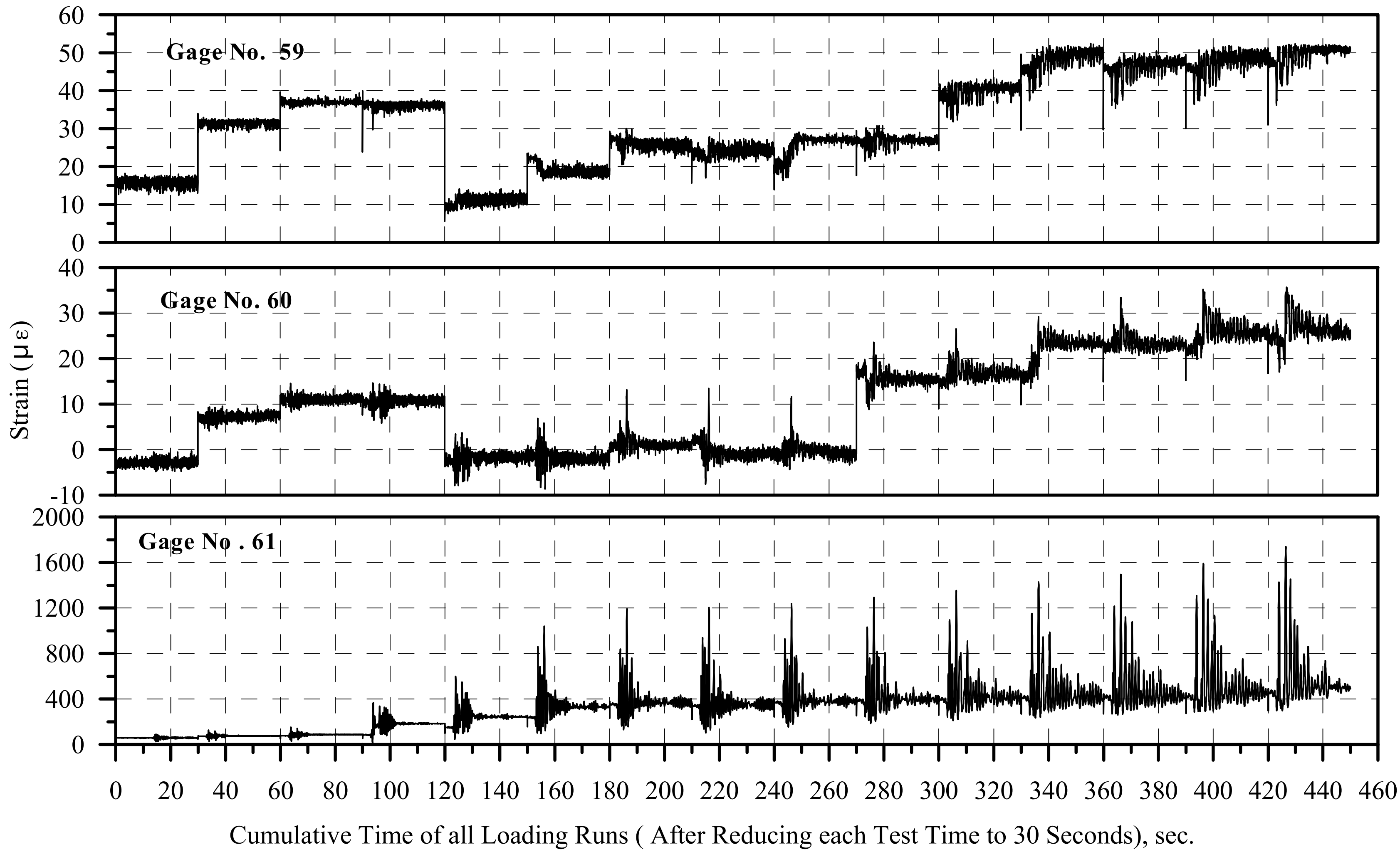

Fig. B-18: Strain History of Gages 59, 60 and 61 in Specimen B2CM

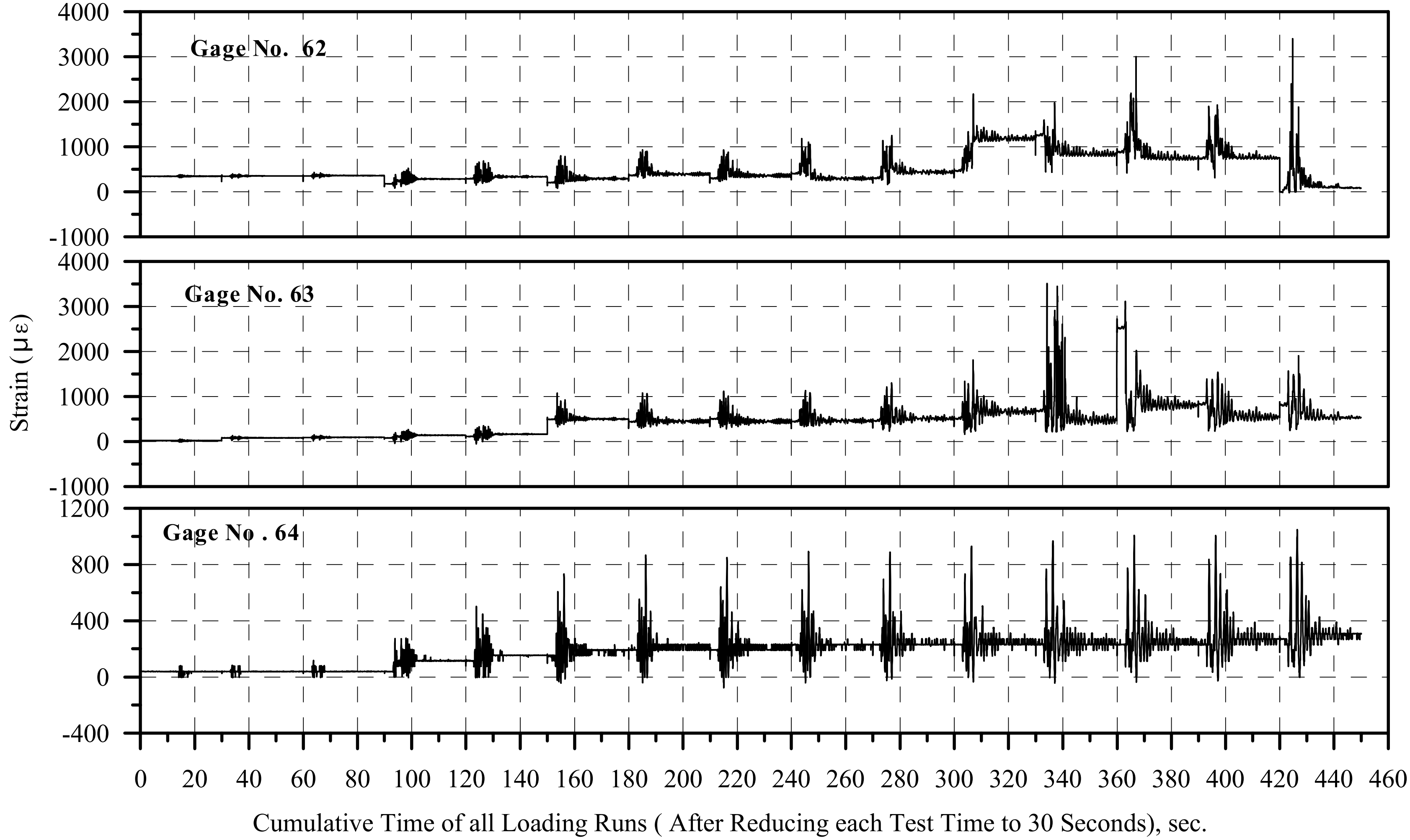

Fig. B-19: Strain History of Gages 62, 63 and 64 in Specimen B2CM

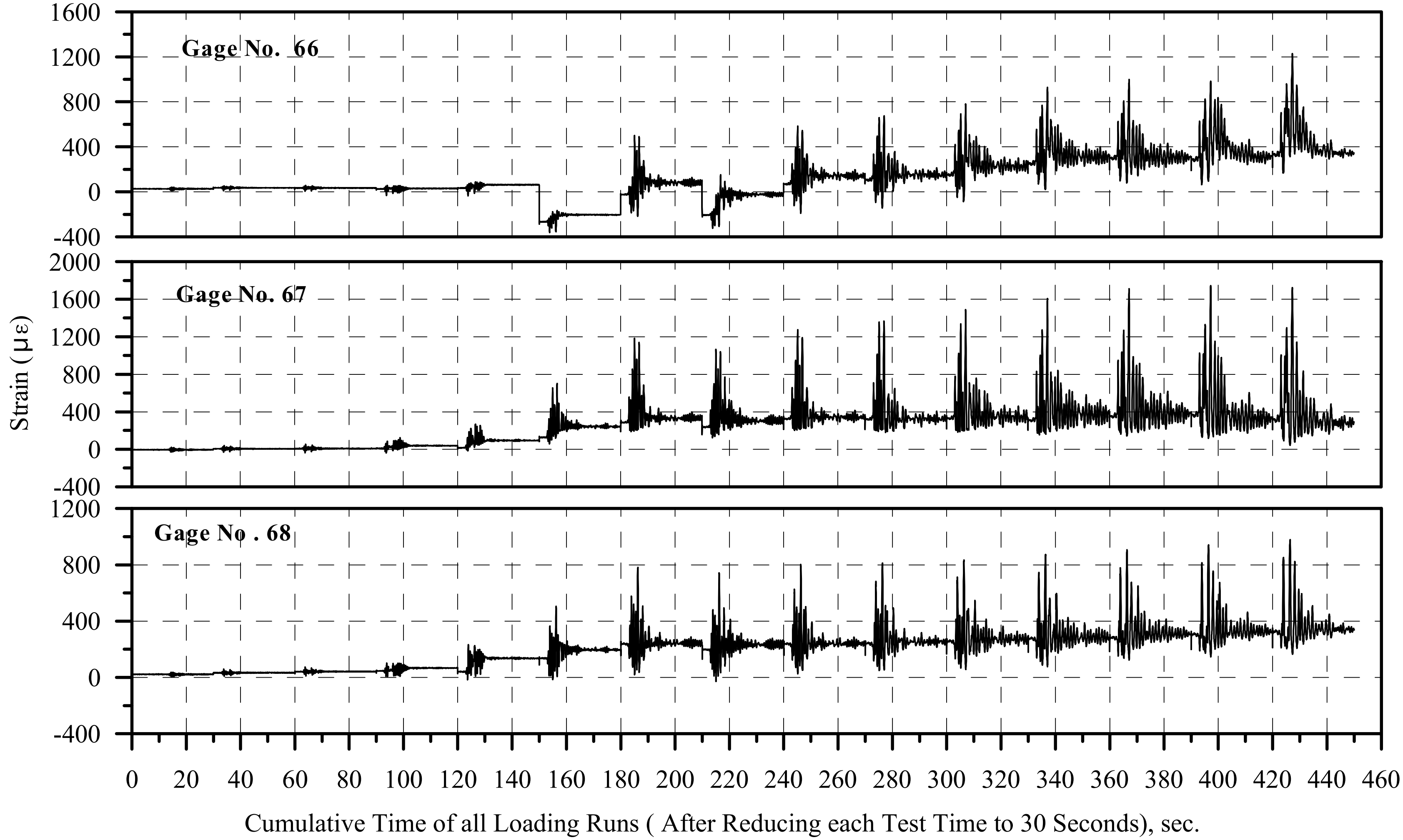

Fig. B-20: Strain History of Gages 66, 67 and 68 in Specimen B2CM

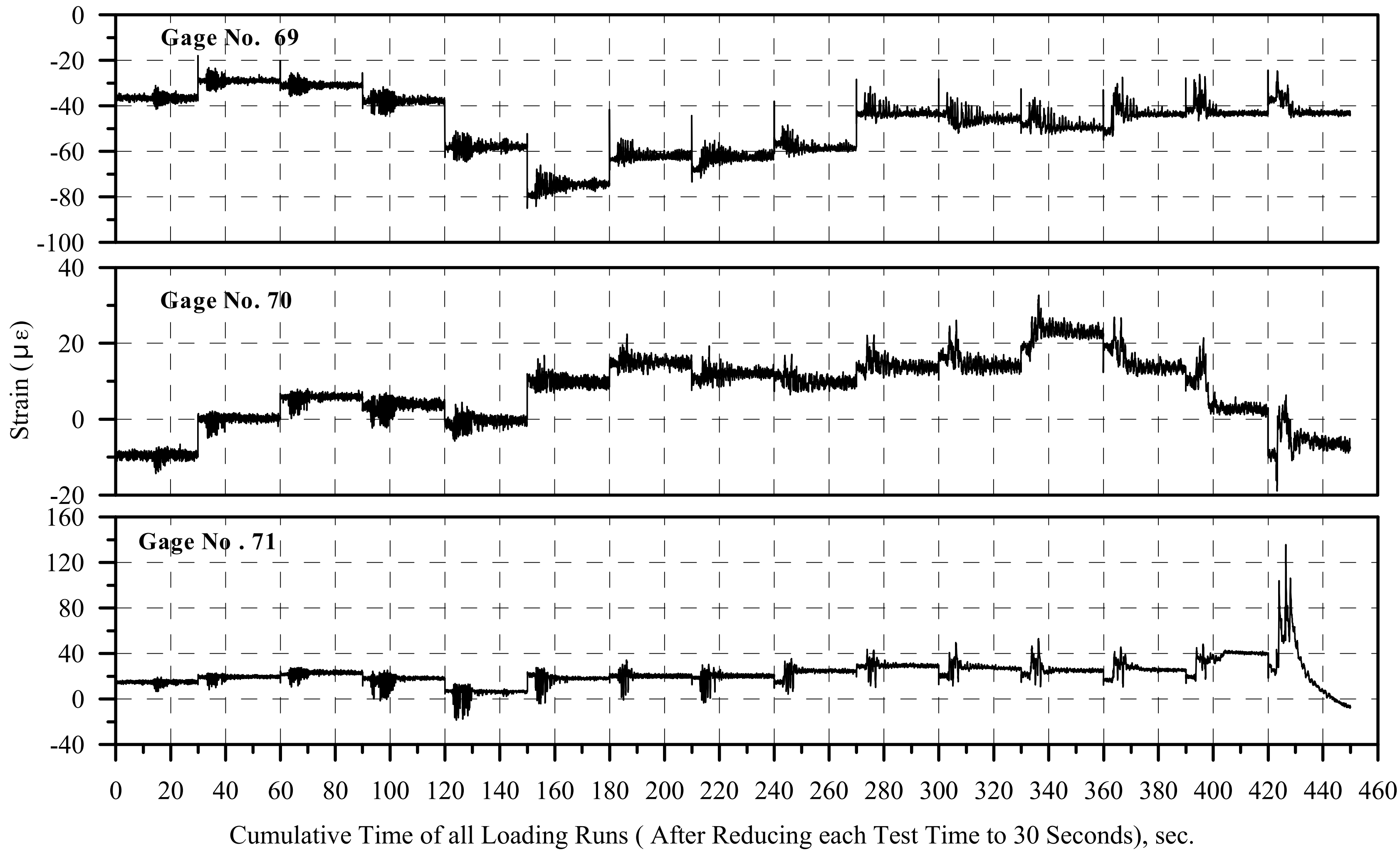

Fig. B-21: Strain History of Gages 69, 70 and 71 in Specimen B2CM

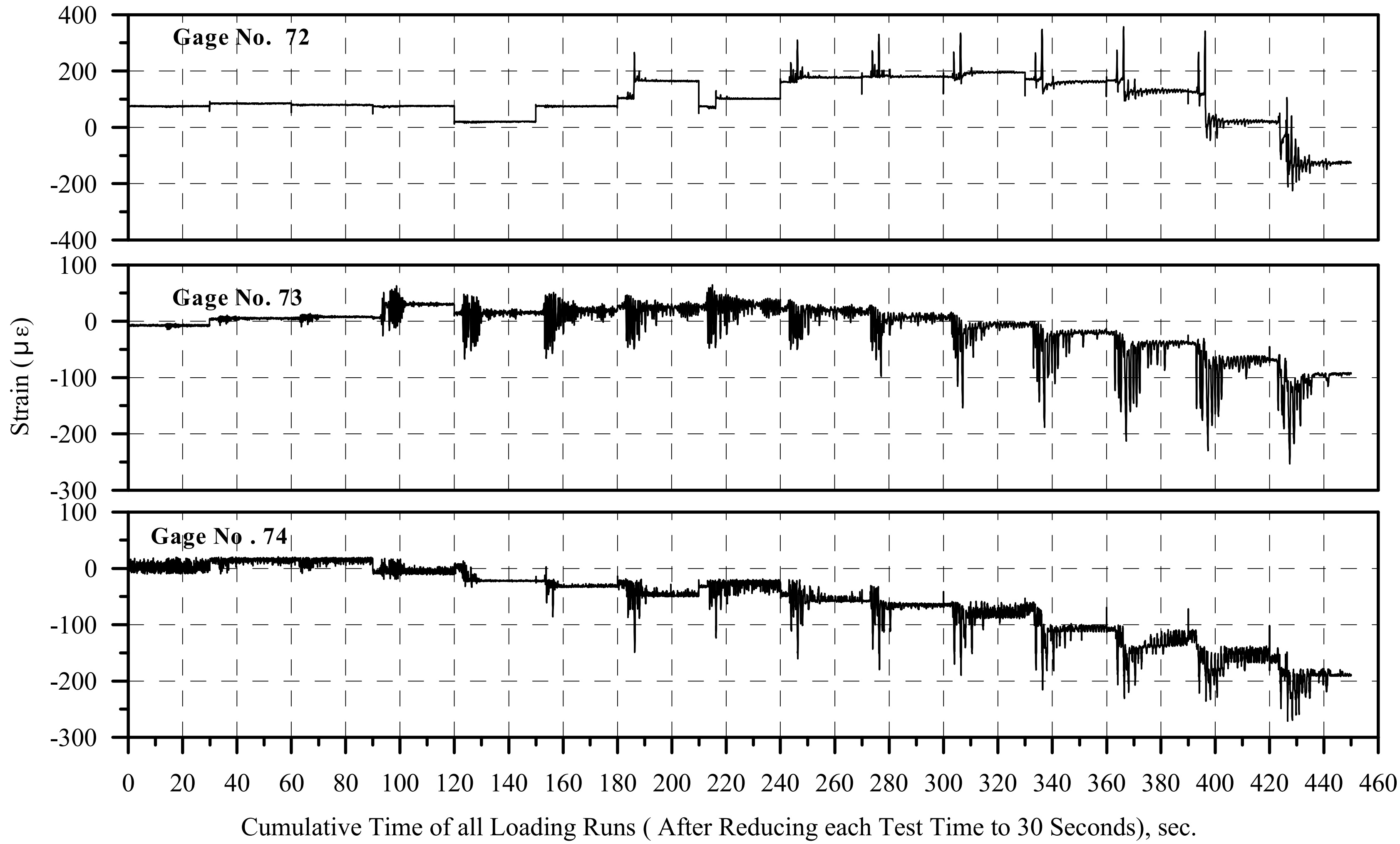

Fig. B-22: Strain History of Gages 72, 73 and 74 in Specimen B2CM

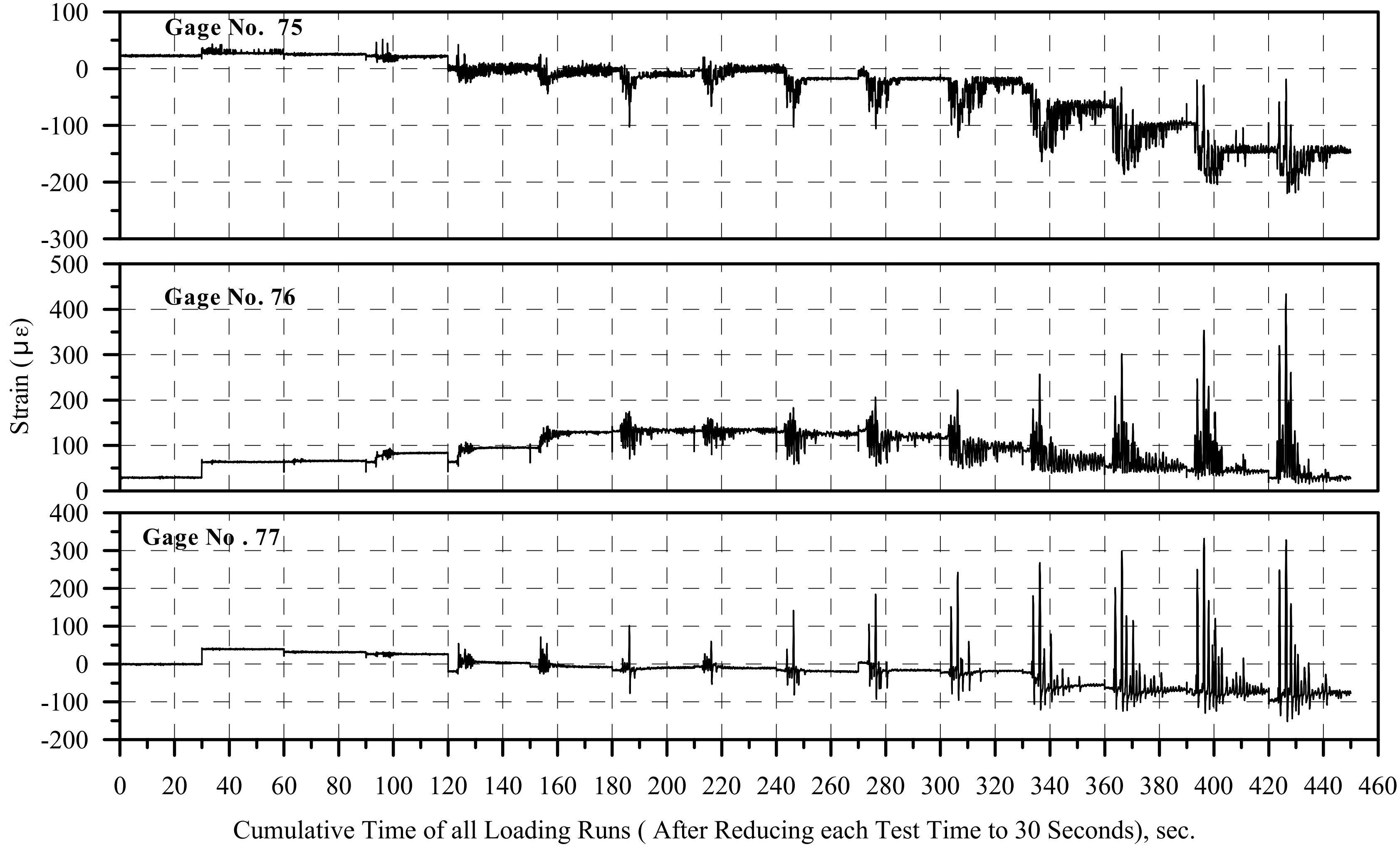

Fig. B-23: Strain History of Gages 75, 76 and 77 in Specimen B2CM

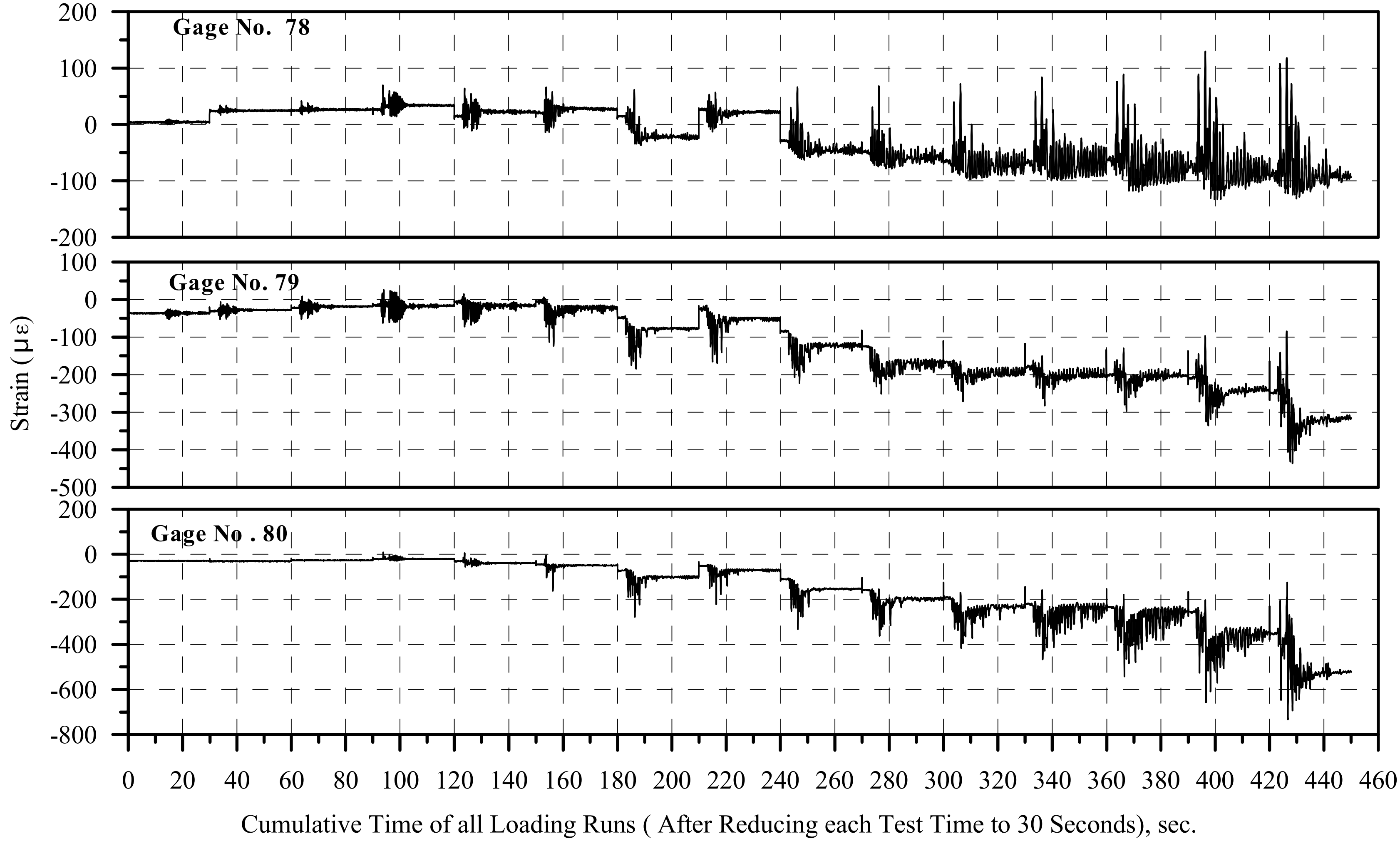

Fig. B-24: Strain History of Gages 78, 79 and 80 in Specimen B2CM

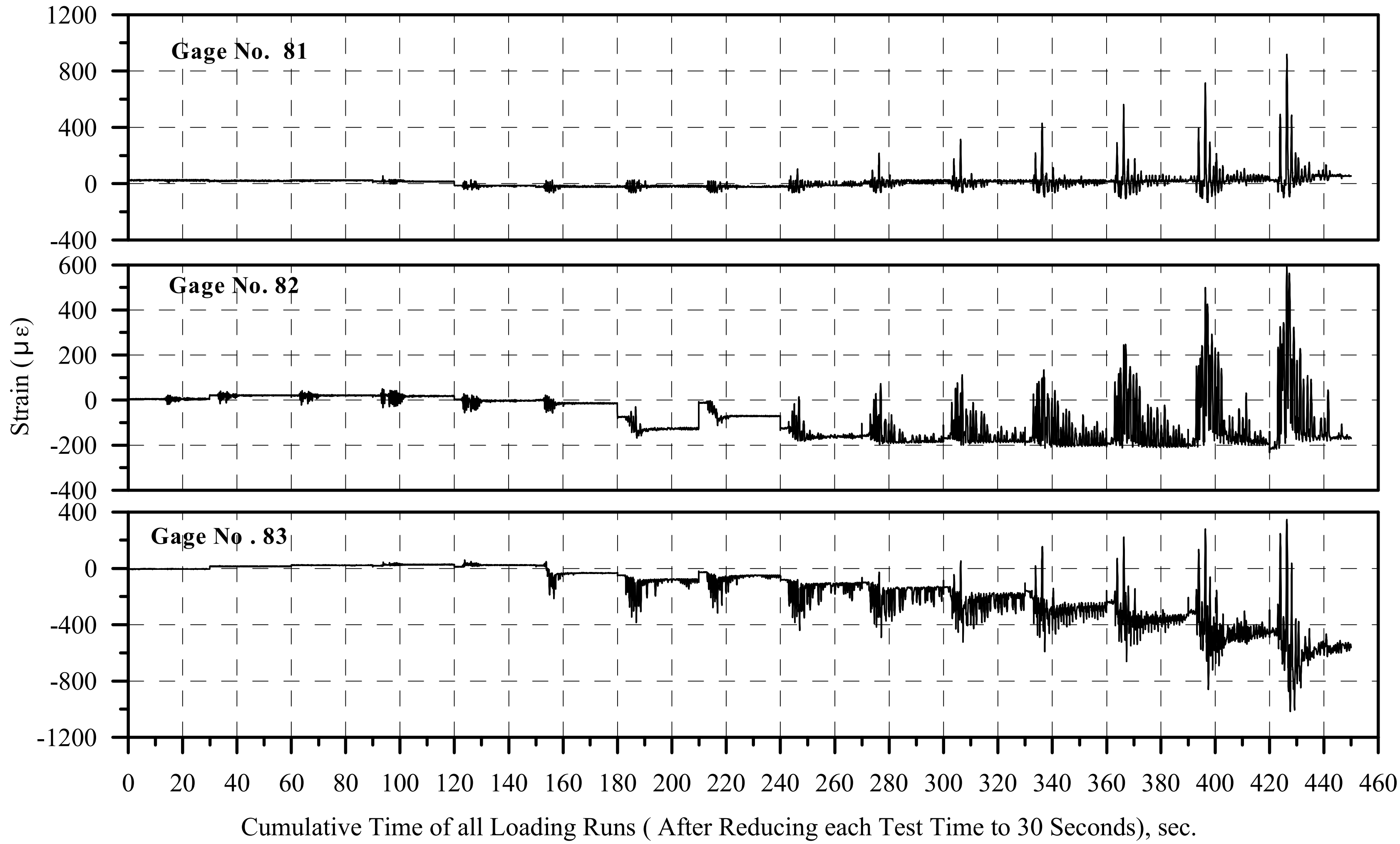

Fig. B-25: Strain History of Gages 81, 82 and 83 in Specimen B2CM

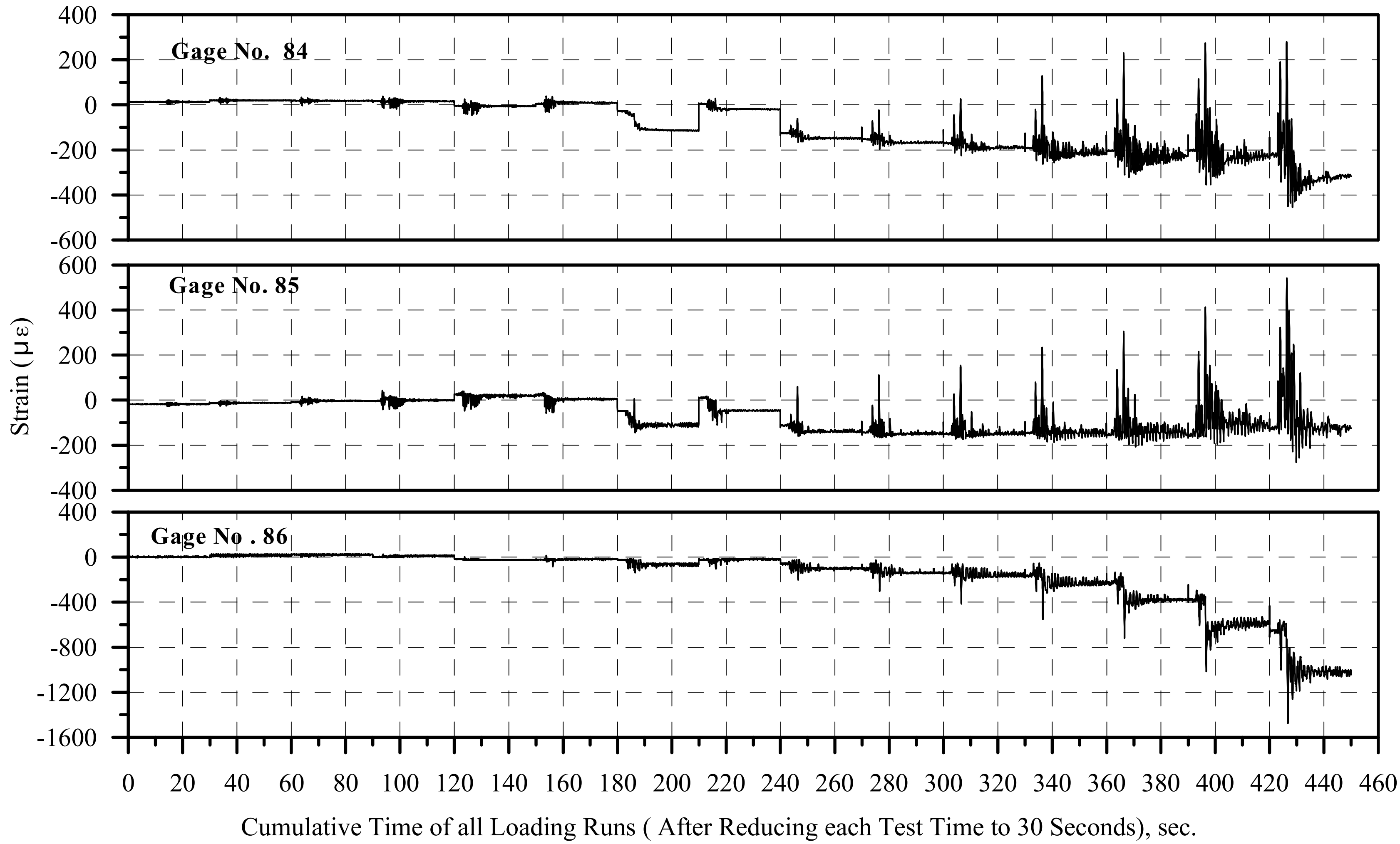

Fig. B-26: Strain History of Gages 84, 85 and 86 in Specimen B2CM

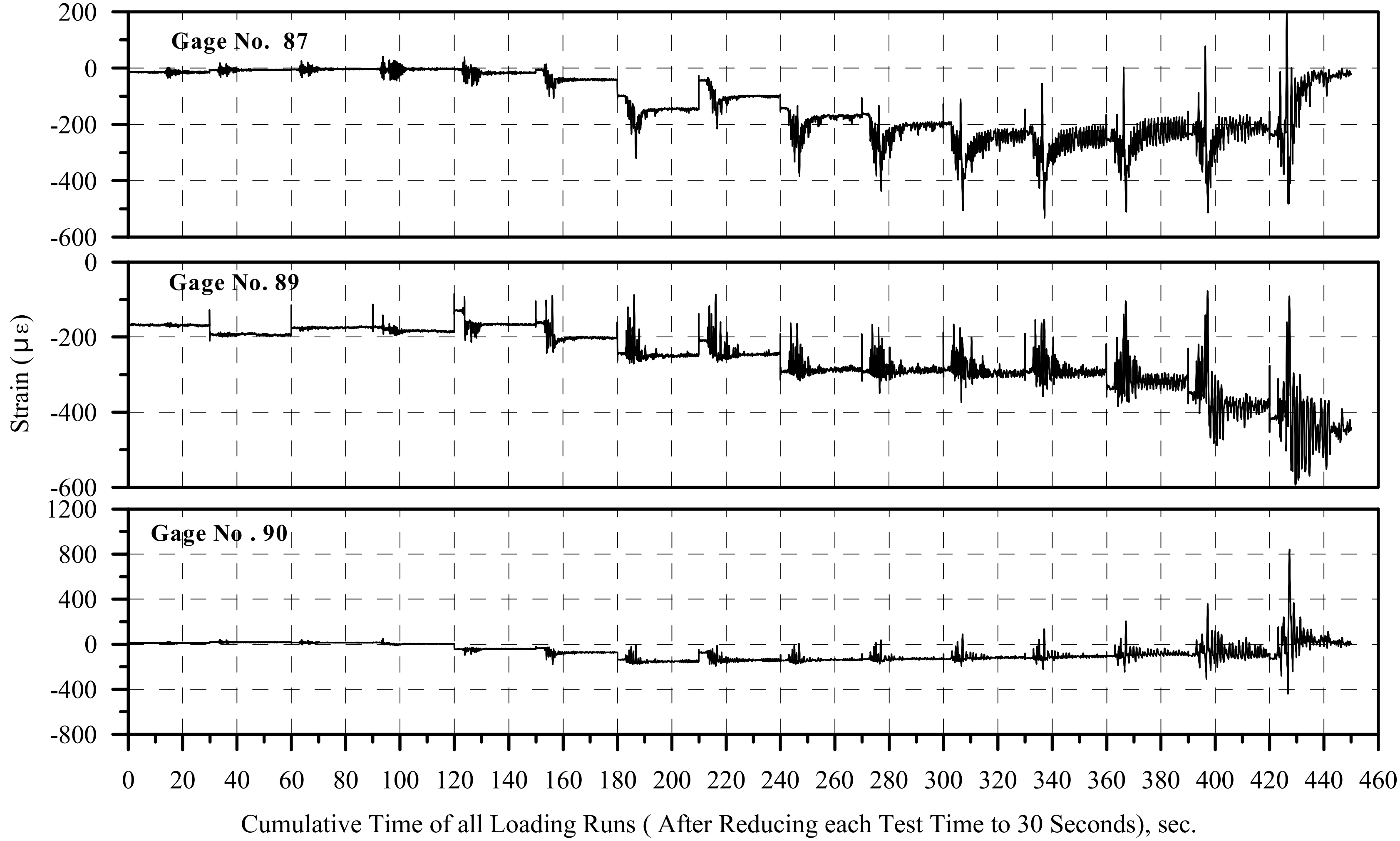

Fig. B-27: Strain History of Gages 87, 89 and 90 in Specimen B2CM

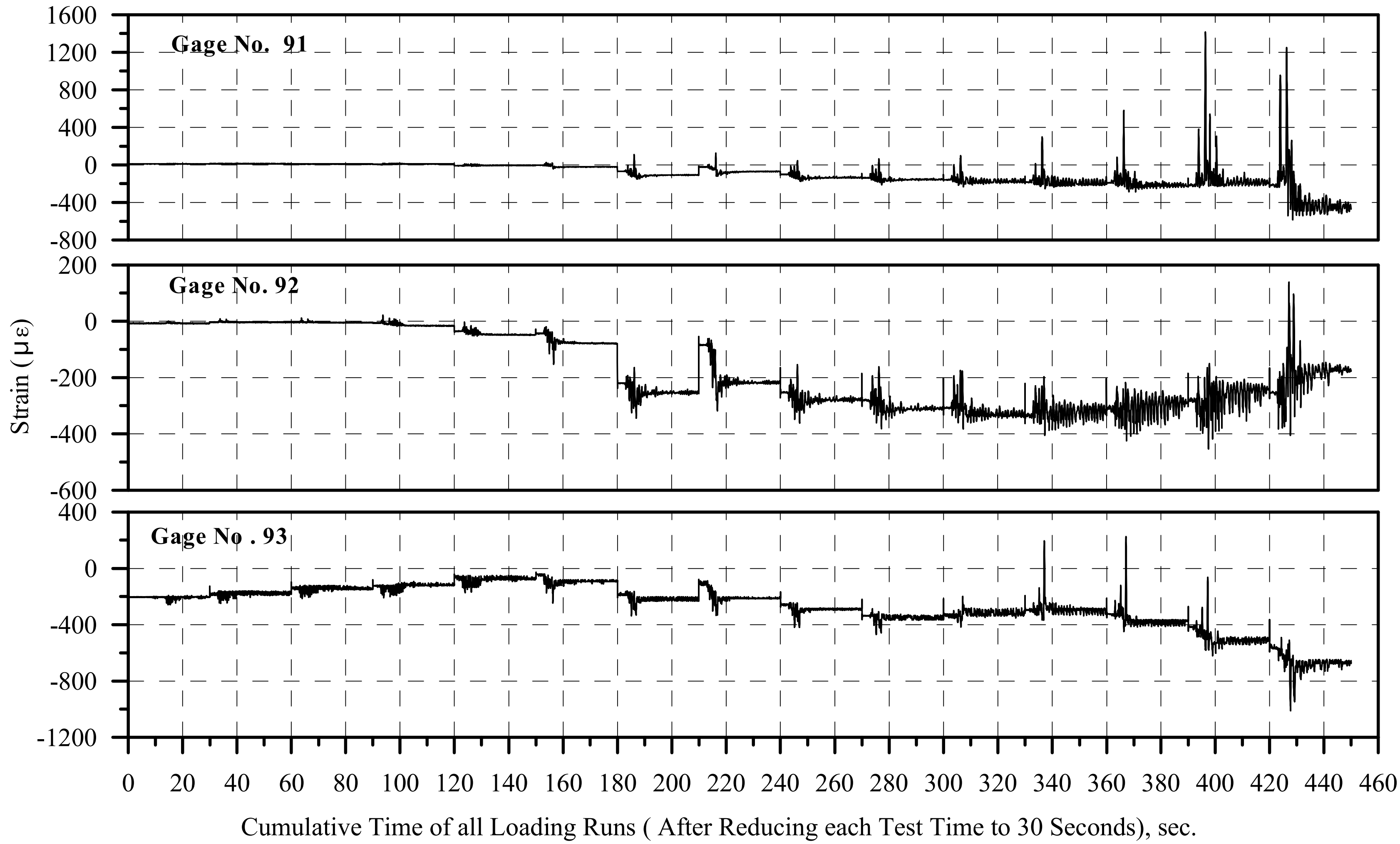

Fig. B-28: Strain History of Gages 91, 92 and 93 in Specimen B2CM

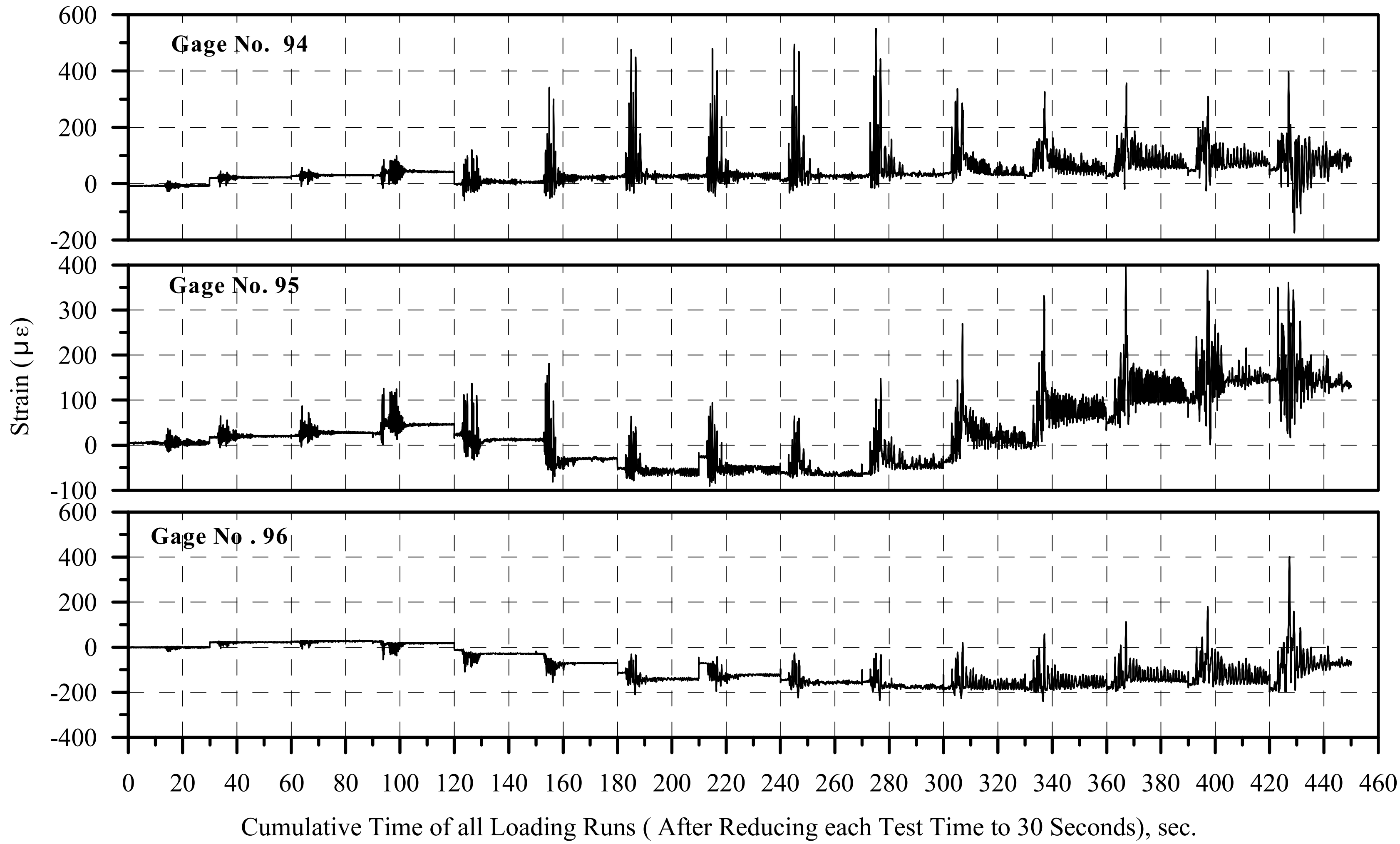

Fig. B-29: Strain History of Gages 94, 95 and 96 in Specimen B2CM

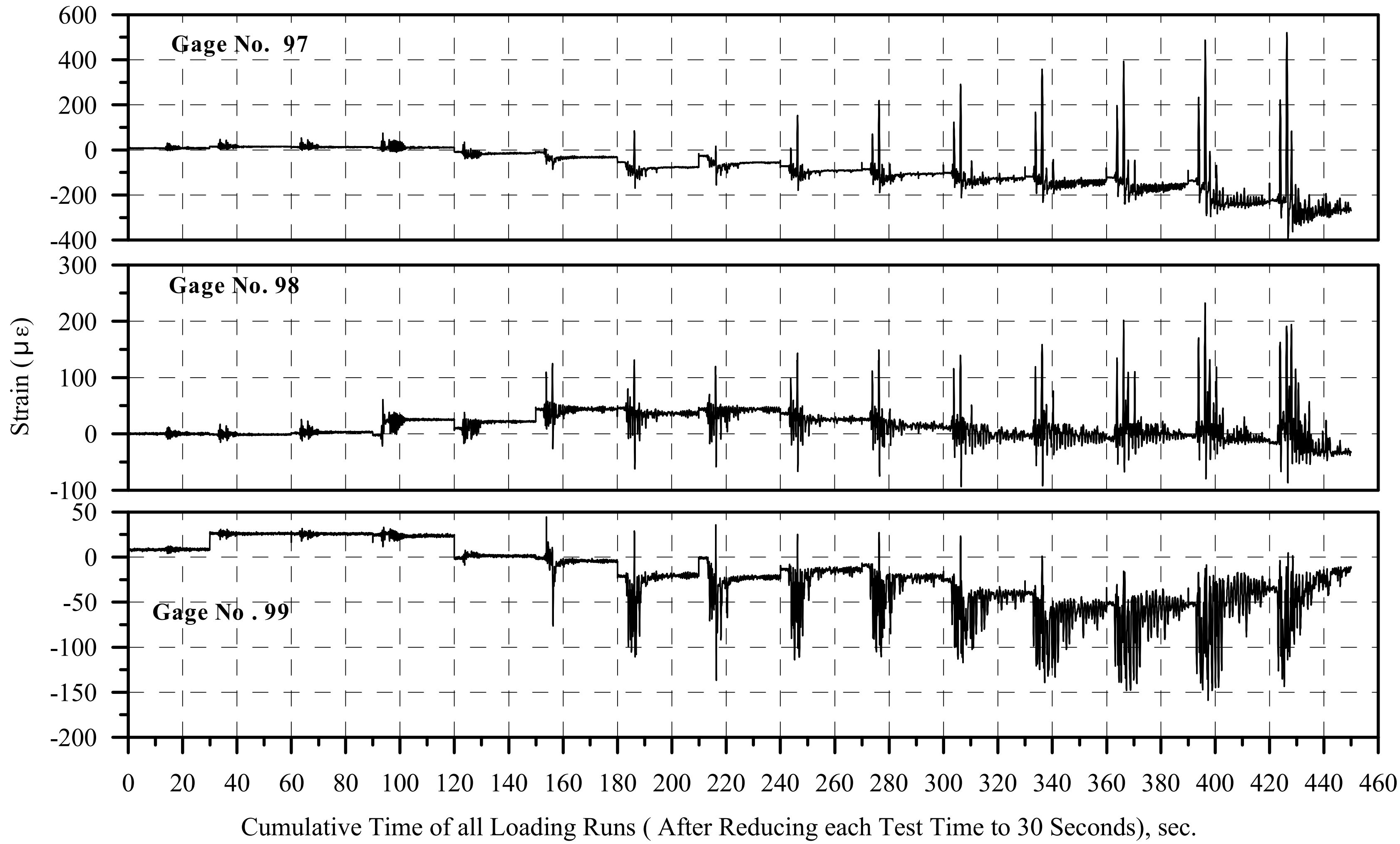

Fig. B-30: Strain History of Gages 97, 98 and 99 in Specimen B2CM

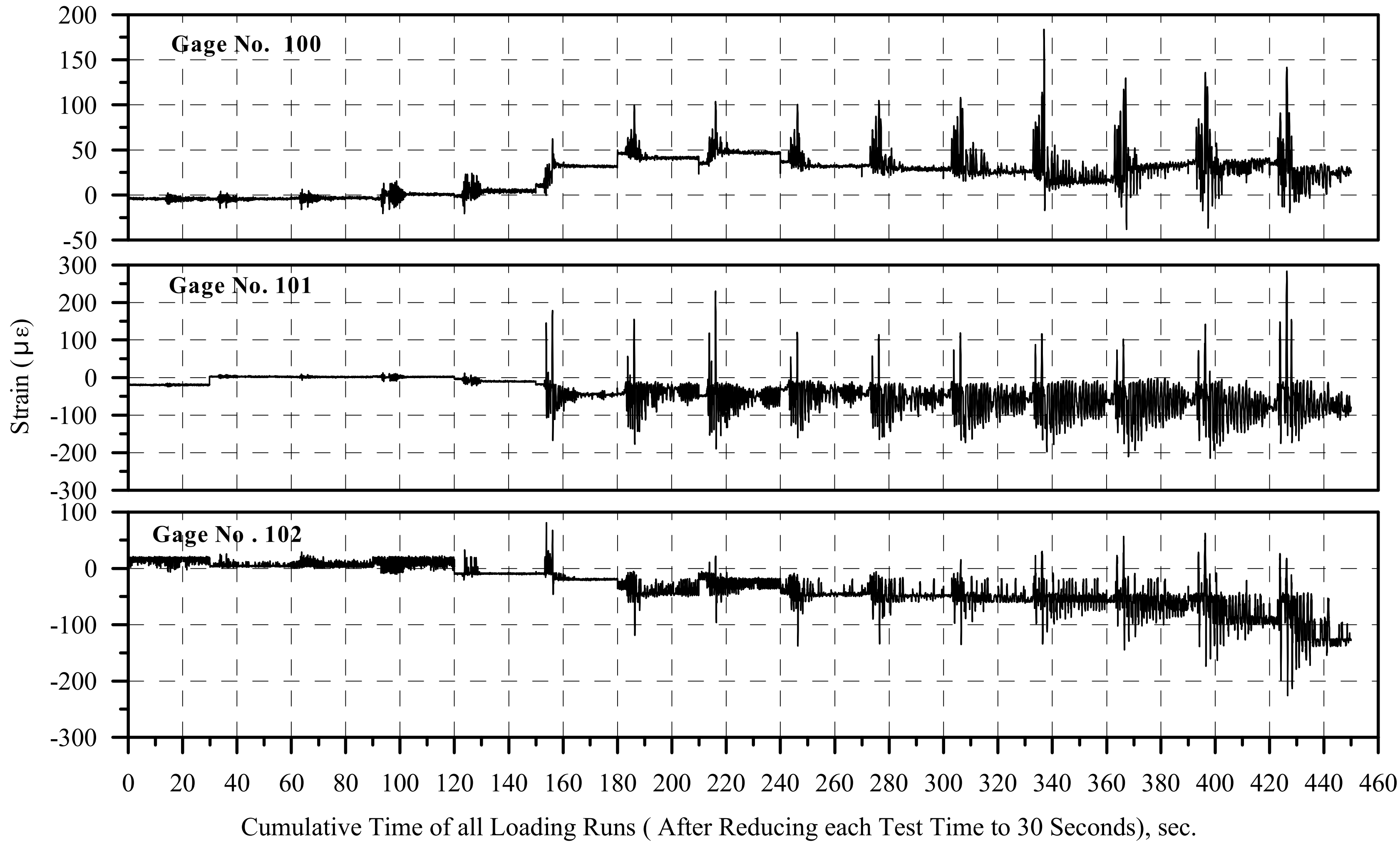

Fig. B-31: Strain History of Gages 100, 101 and 102 in Specimen B2CM

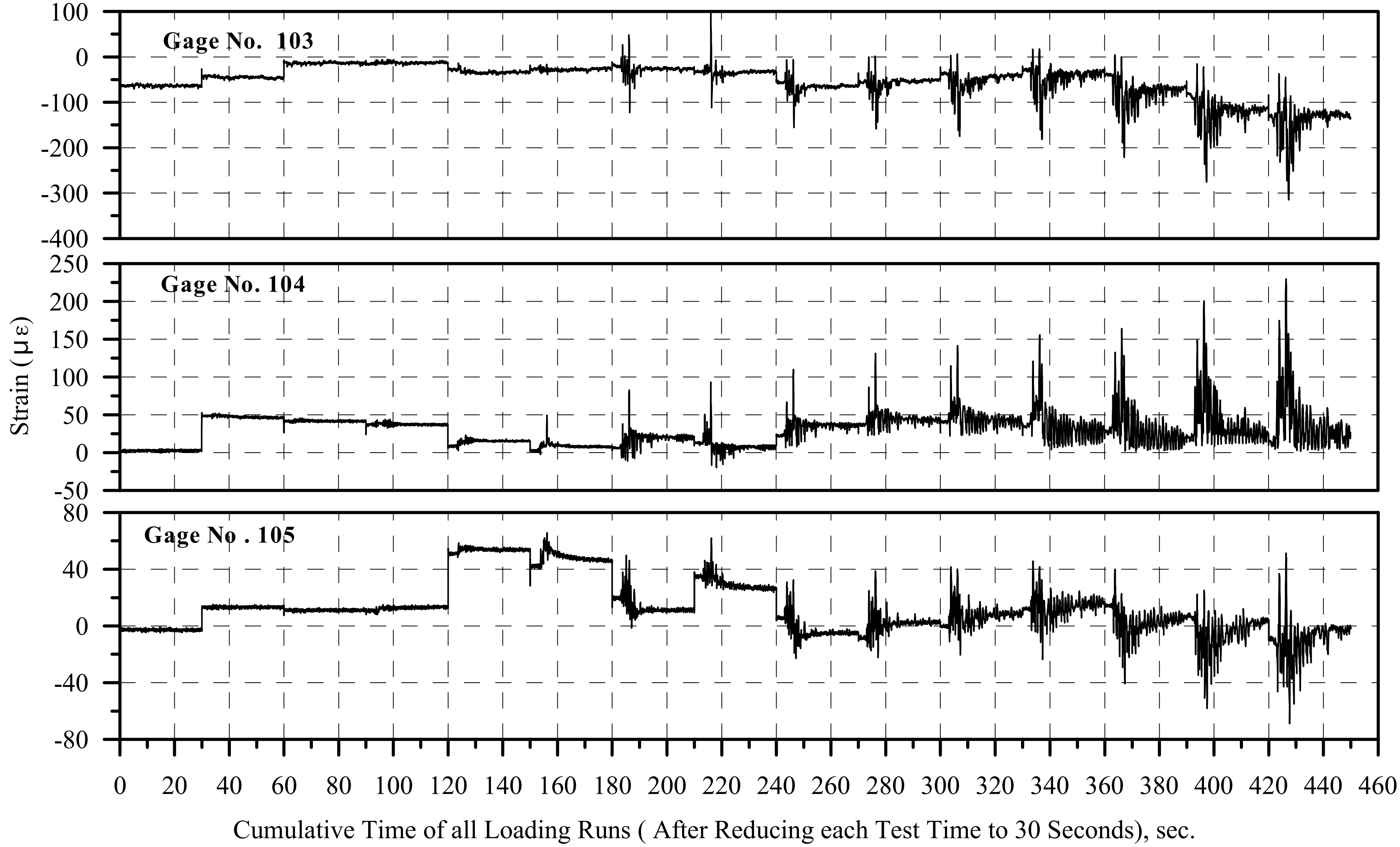

Fig. B-32: Strain History of Gages 103, 104 and 105 in Specimen B2CM

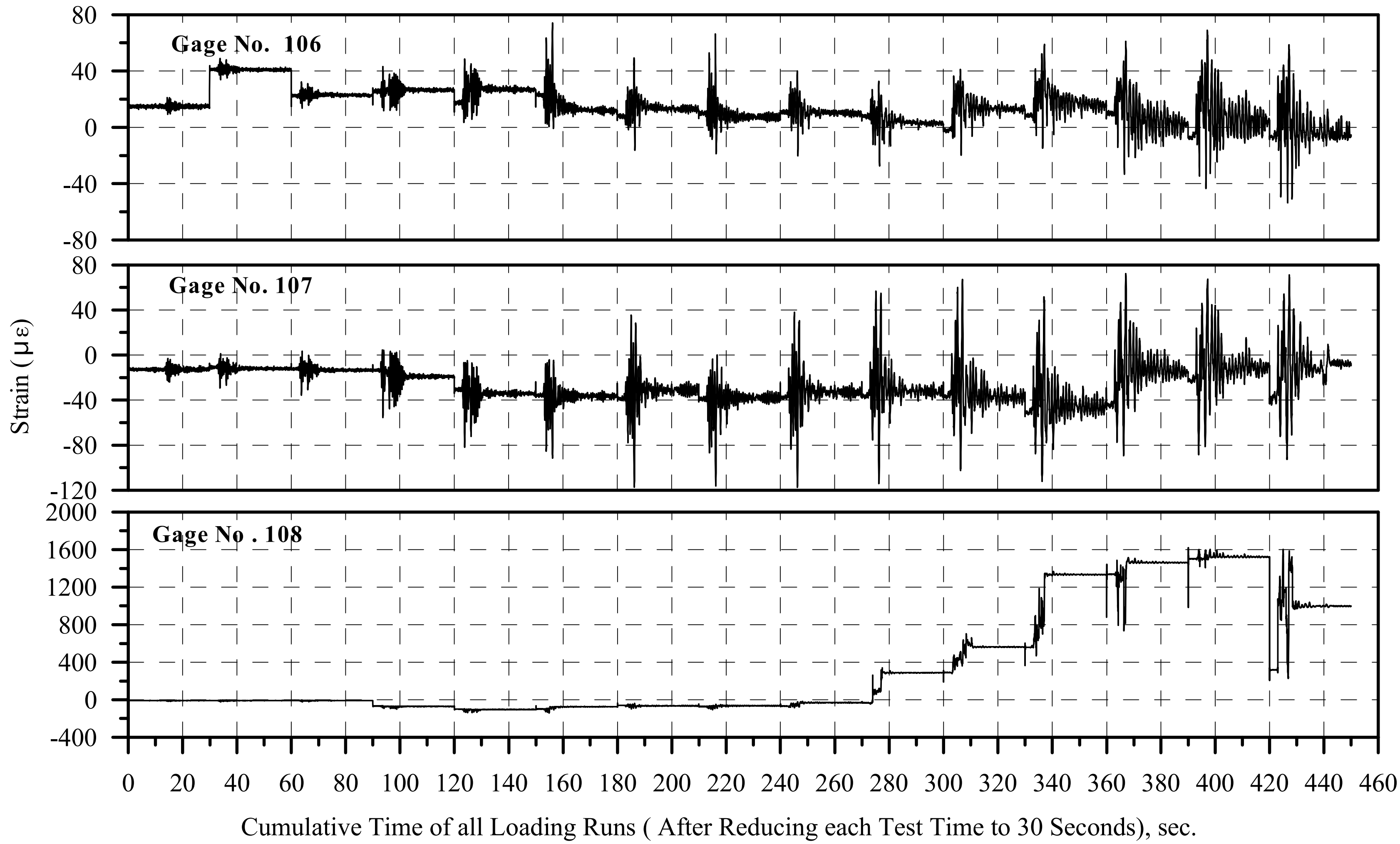

Fig. B-33: Strain History of Gages 106, 107 and 108 in Specimen B2CM

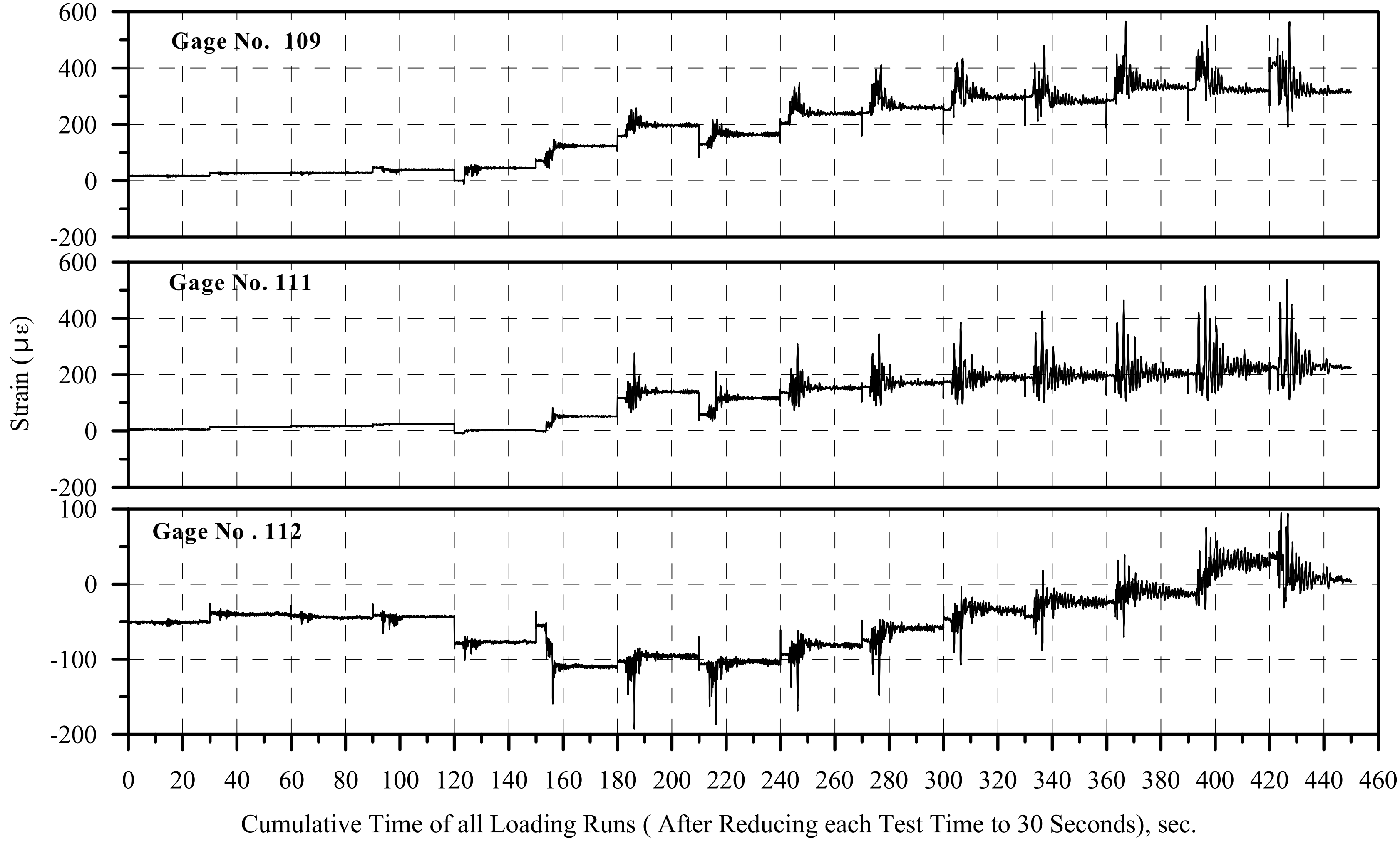

Fig. B-34: Strain History of Gages 109, 111 and 112 in Specimen B2CM

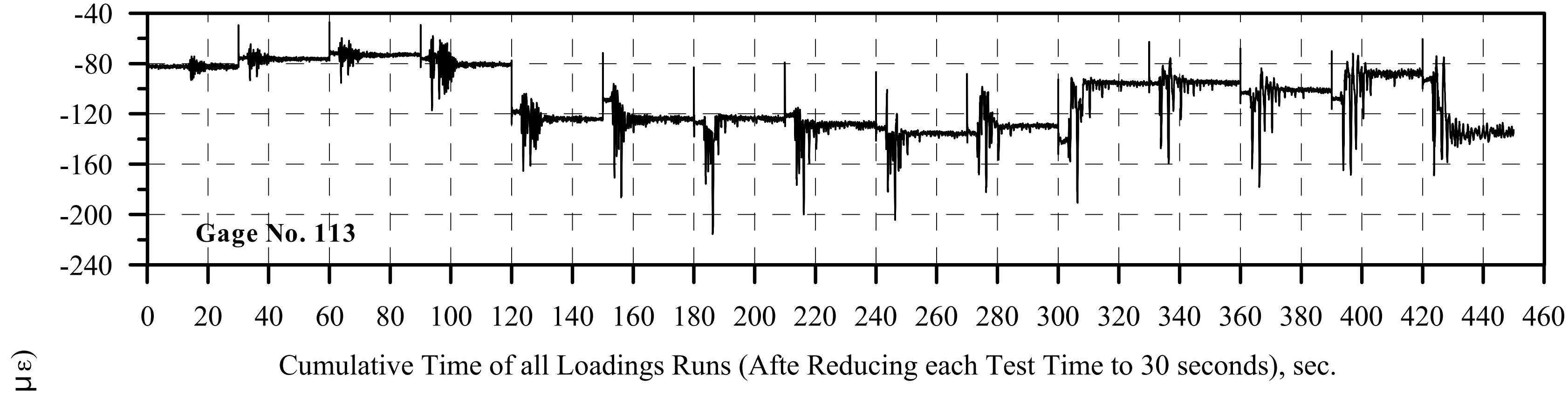

Fig. B-35: Strain History for Gages 113 of Specimen B2CM

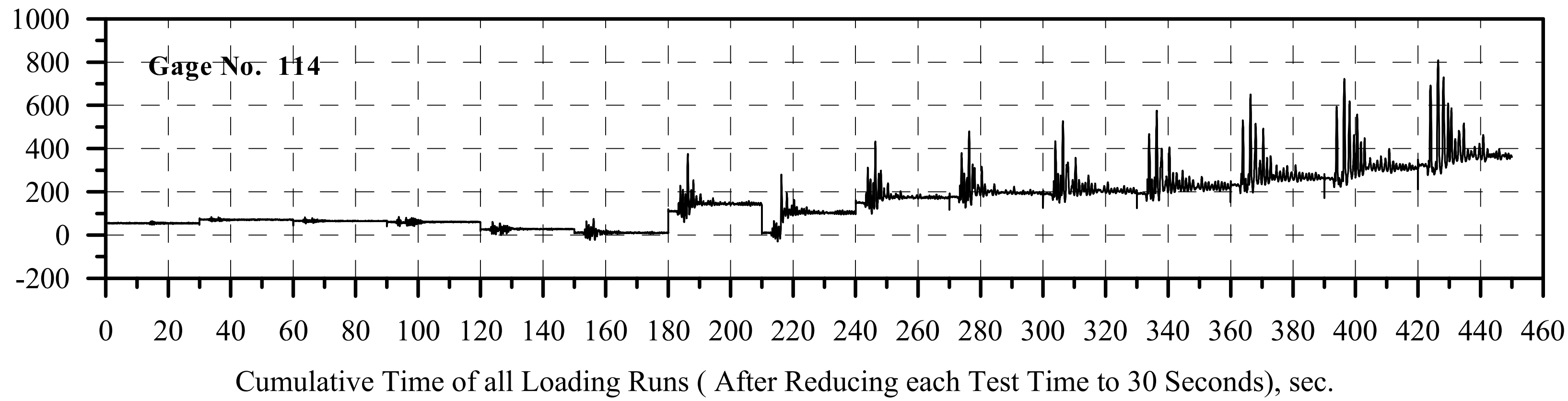

Fig. B-36: Strain History for Gages 114 of Specimen B2CM

APPENDIX C

STRAIN-TIME HISTORY FOR STRAIN GAGES IN TALL SPECIMEN B2CT

(See Figs. 2-34 and 2-35 for the locations of each gage)

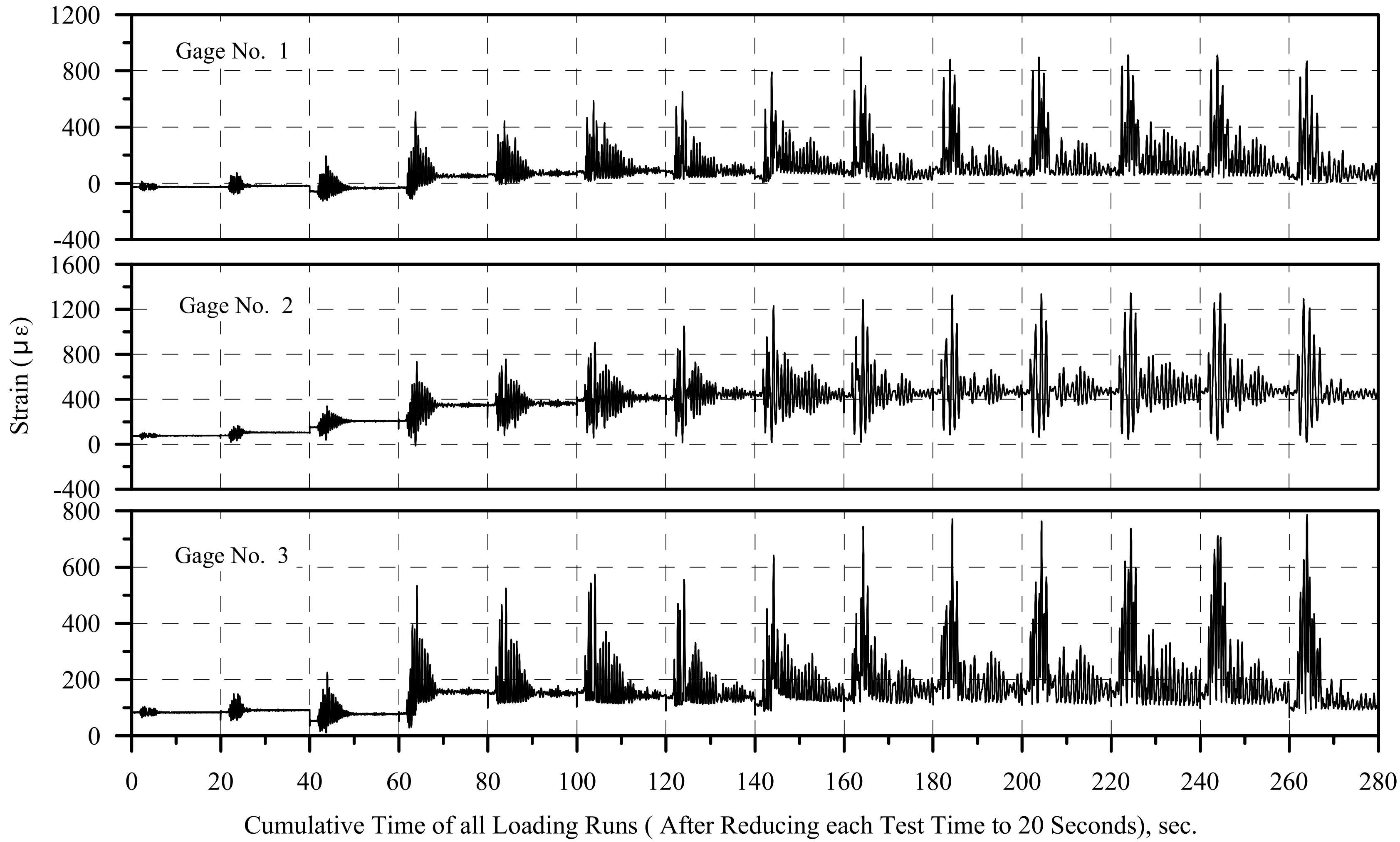

Fig. C-1: Strain History for Gages 1, 2 and 3 of Specimen B2CT

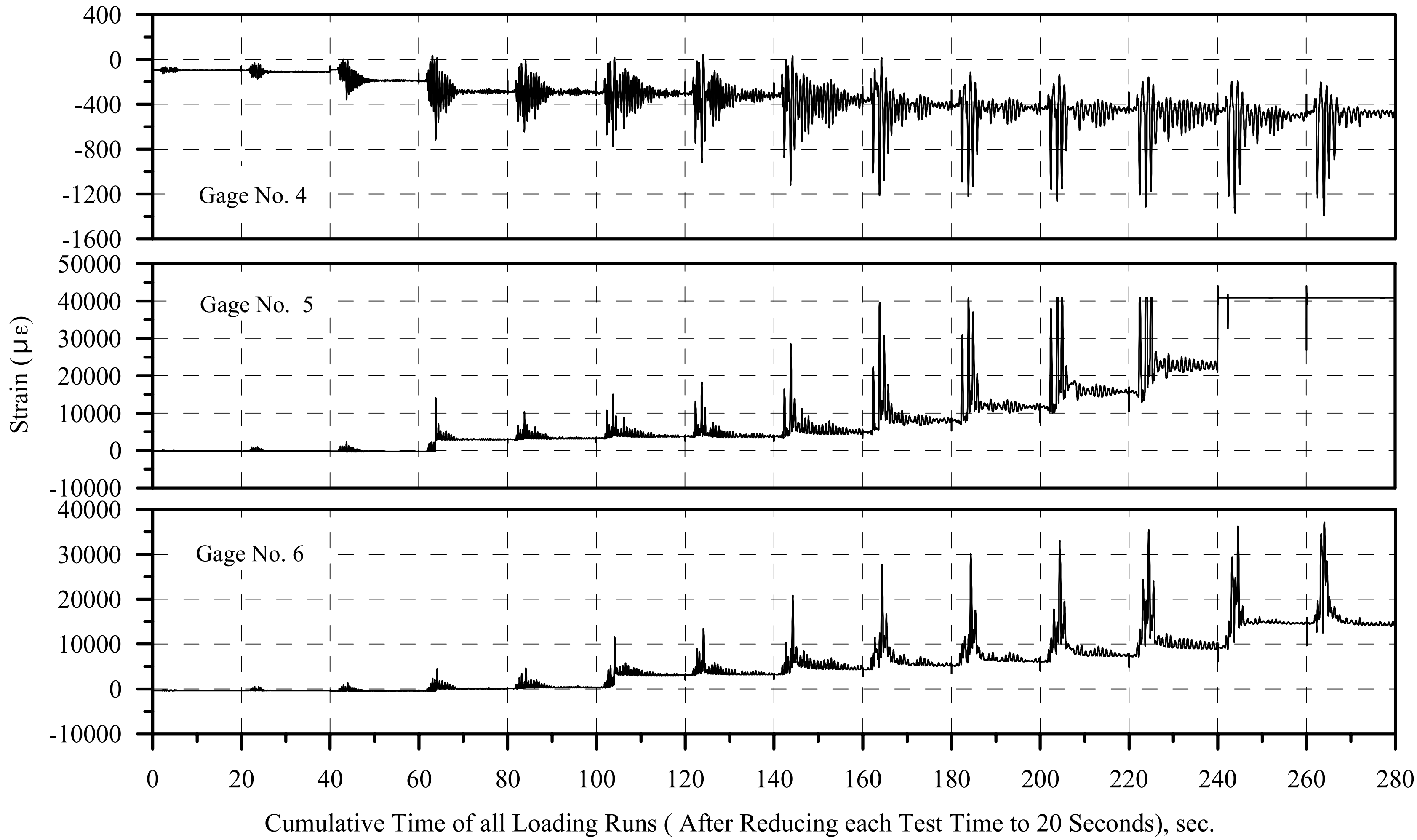

Fig. C-2: Strain History for Gages 4, 5 and 6 of Specimen B2CT

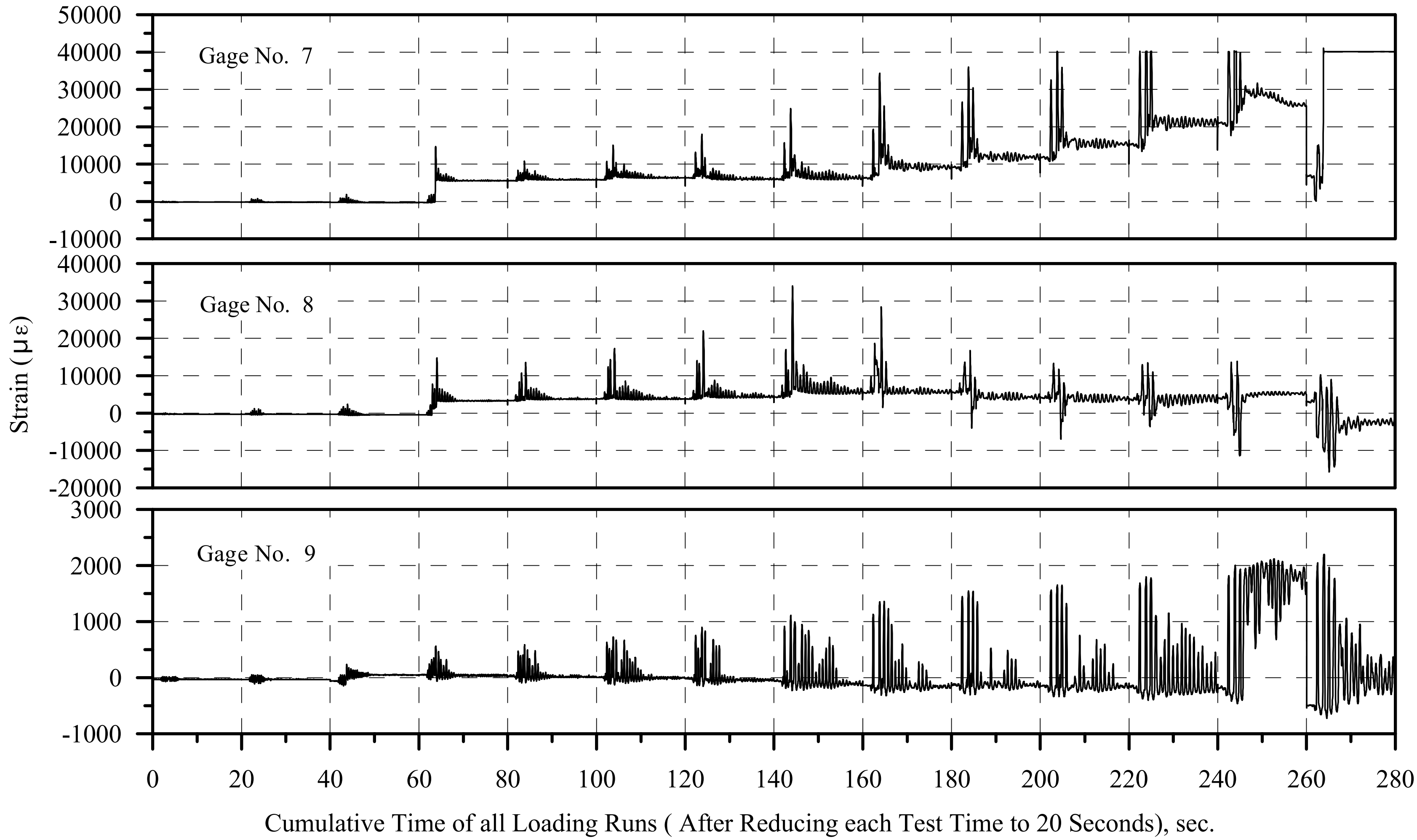

Fig. C-3: Strain History for Gages 7, 8 and 9 of Specimen B2CT

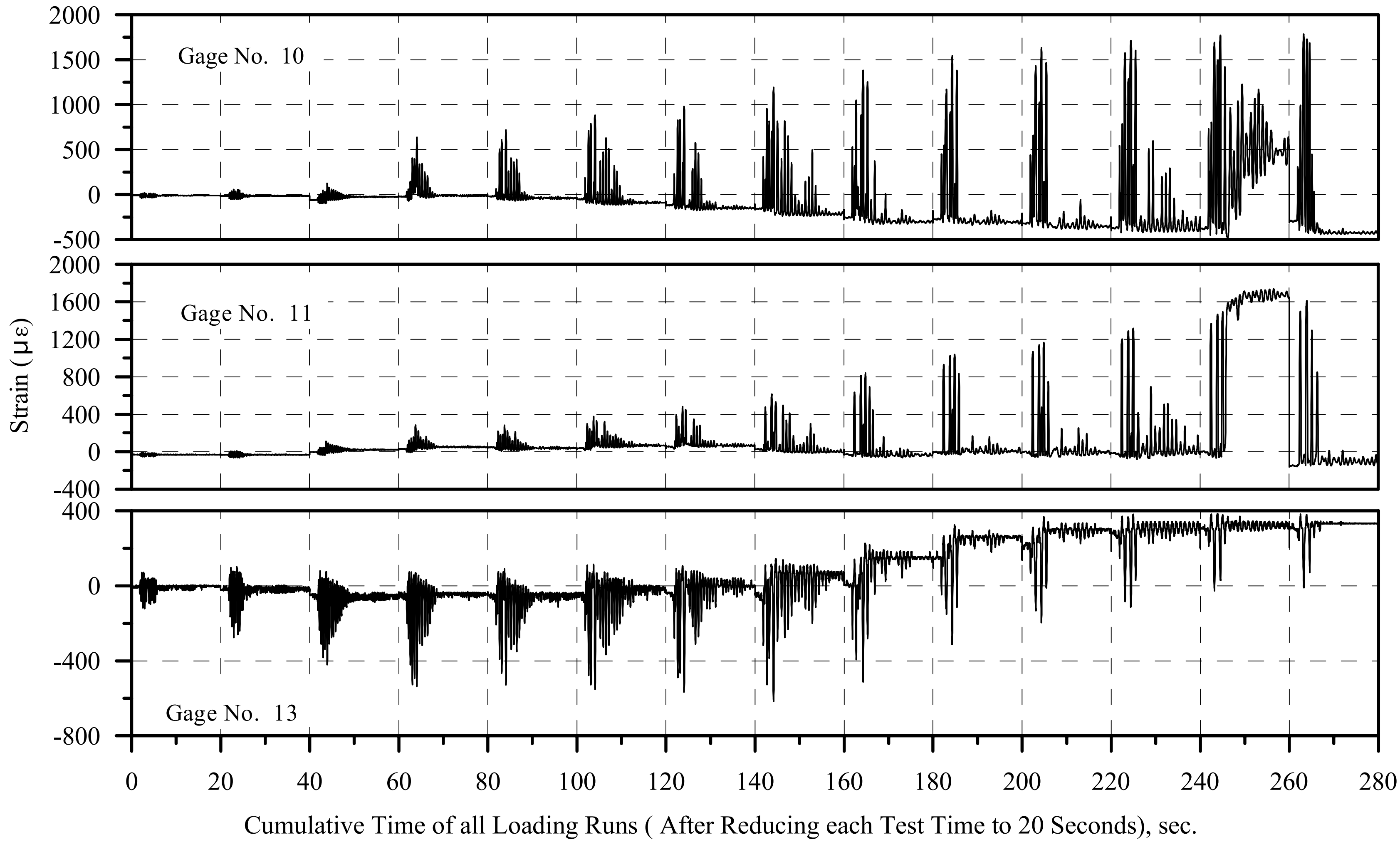

Fig. C-4: Strain History for Gages 10, 11 and 13 of Specimen B2CT

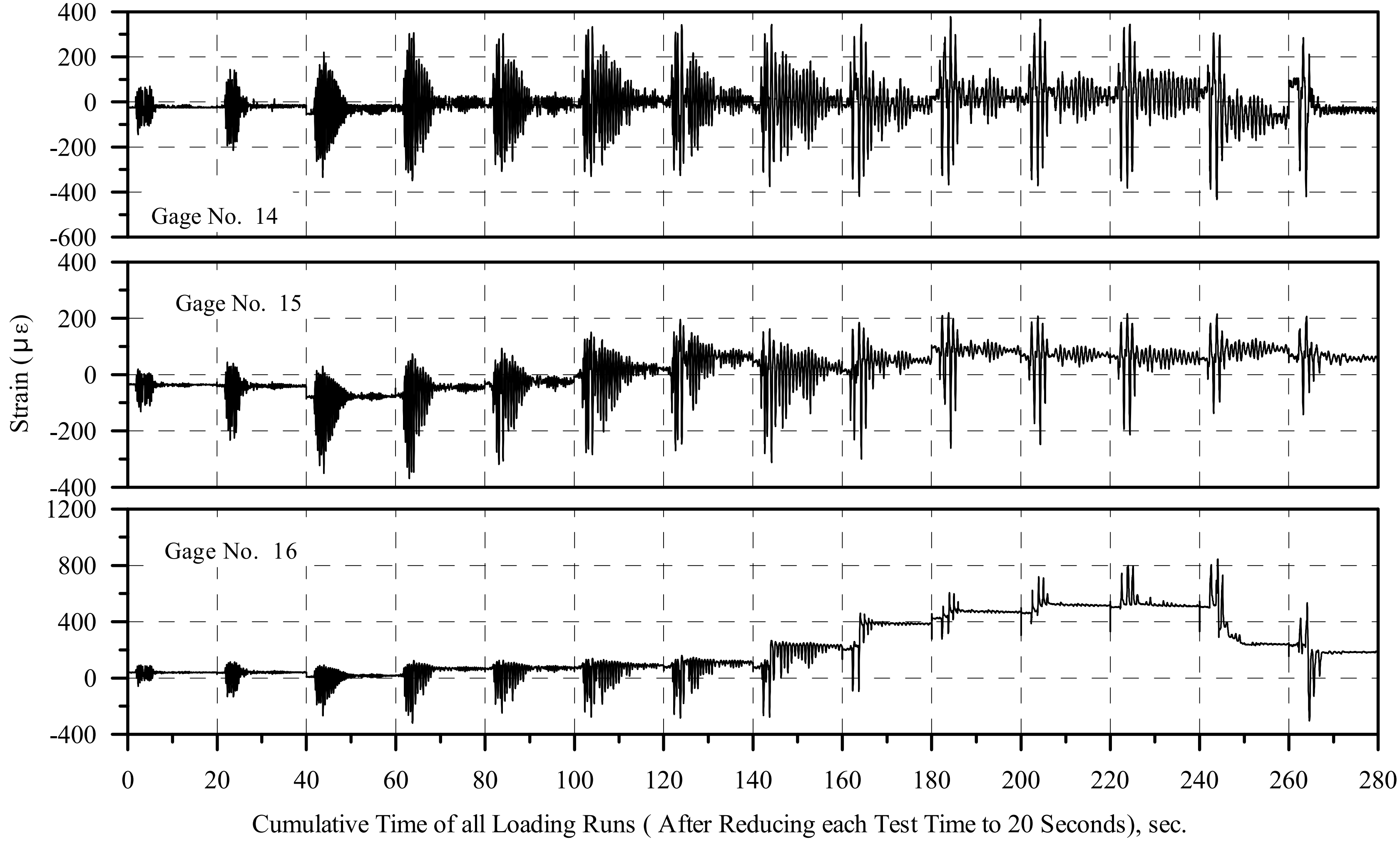

Fig. C-5: Strain History of Gages 14, 15 and 16 in Specimen B2CT

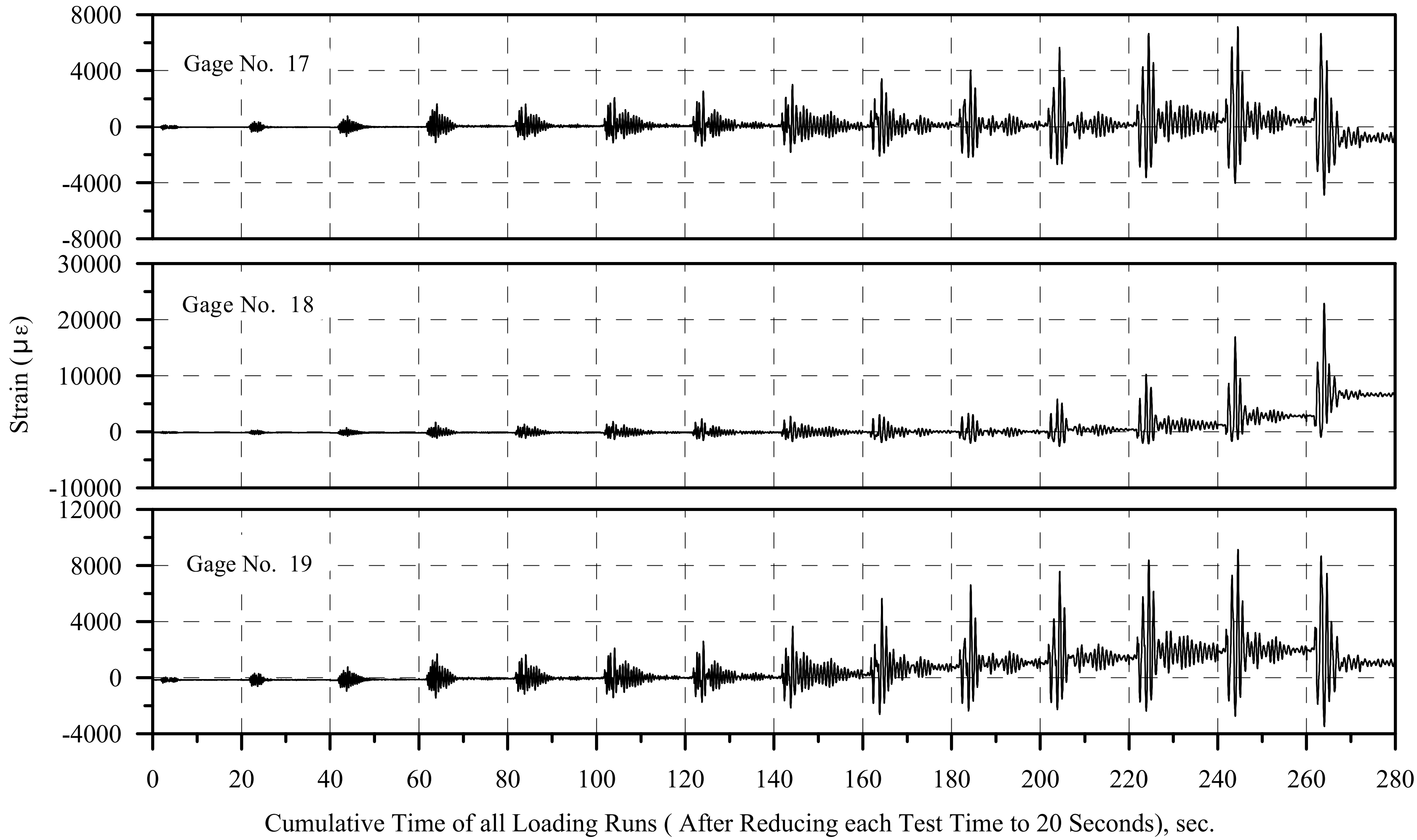

Fig. C-6: Strain History of Gages 17, 18 and 19 in Specimen B2CT

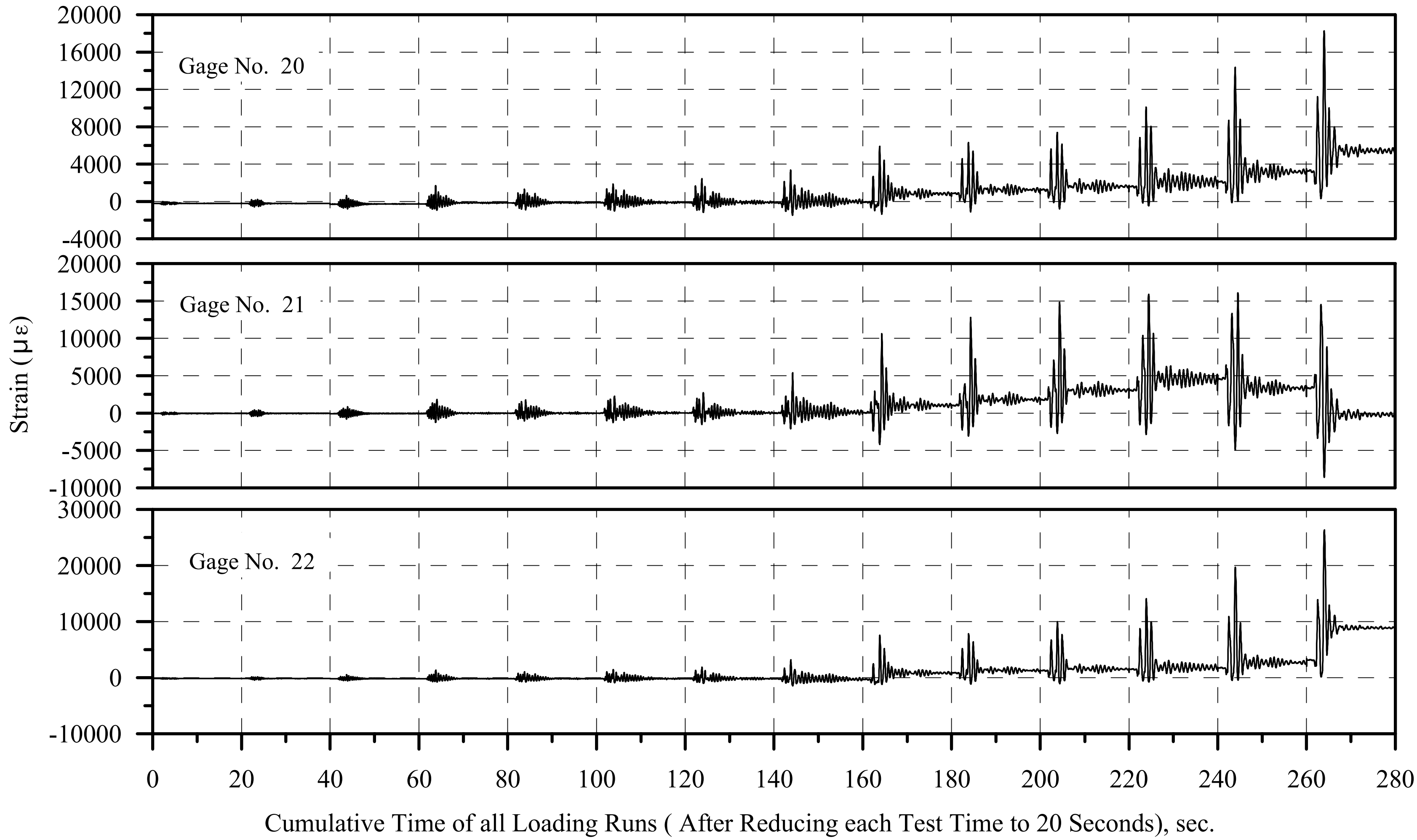

Fig. C-7: Strain History of Gages 20, 21 and 22 in Specimen B2CT

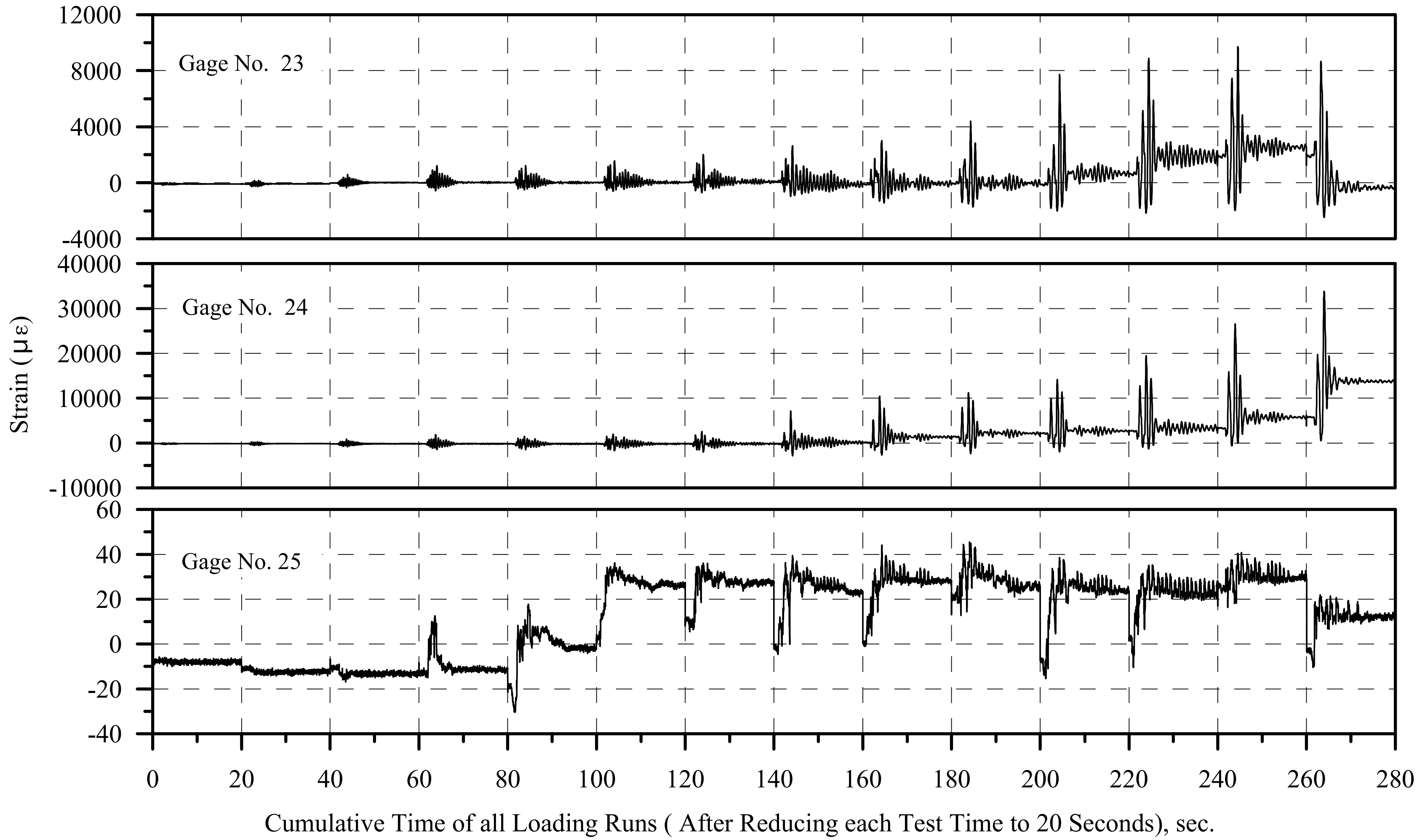

Fig. C-8: Strain History for Gages 23, 24 and 25 of Specimen B2CT

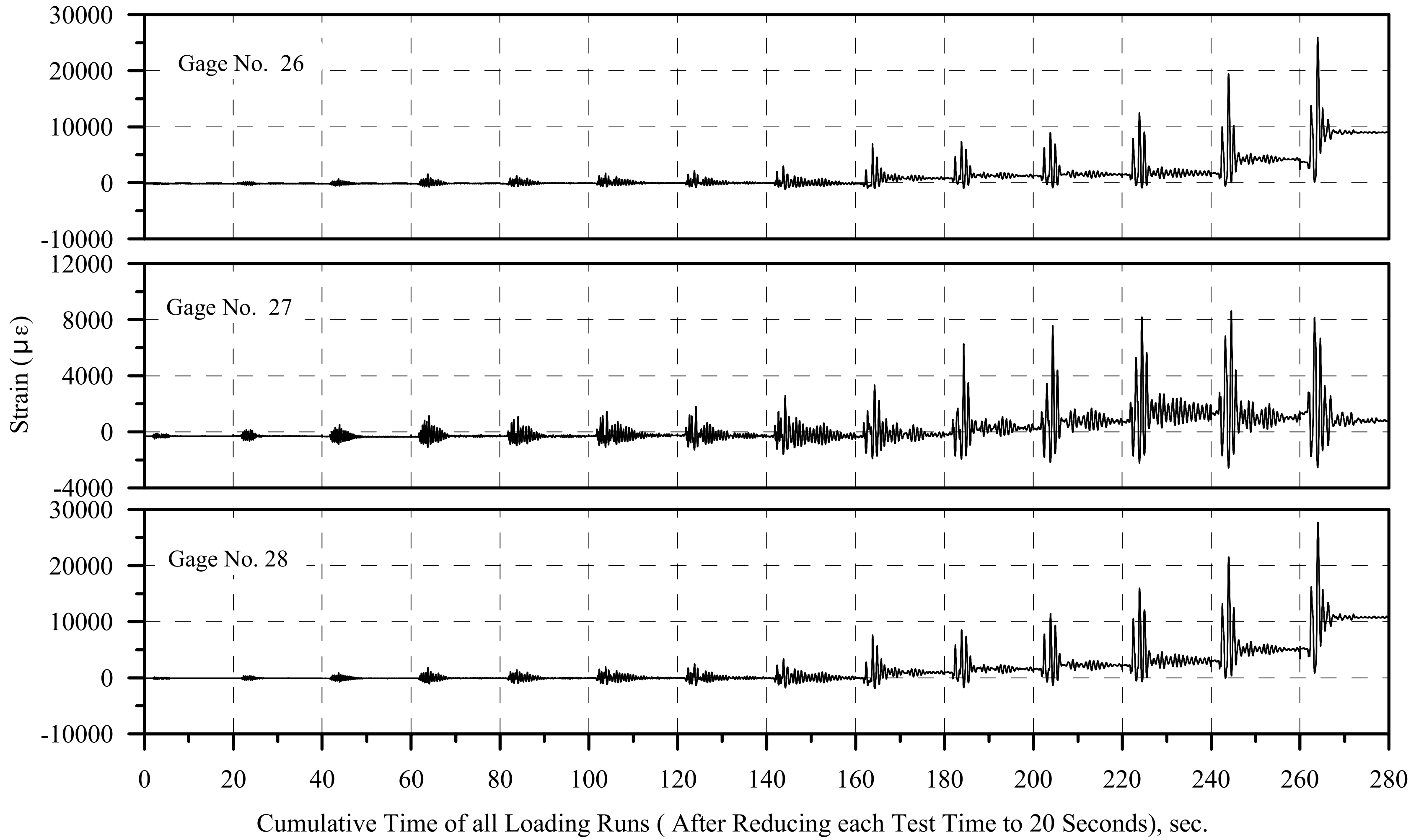

Fig. C-9: Strain History for Gages 26, 27 and 28 of Specimen B2CT

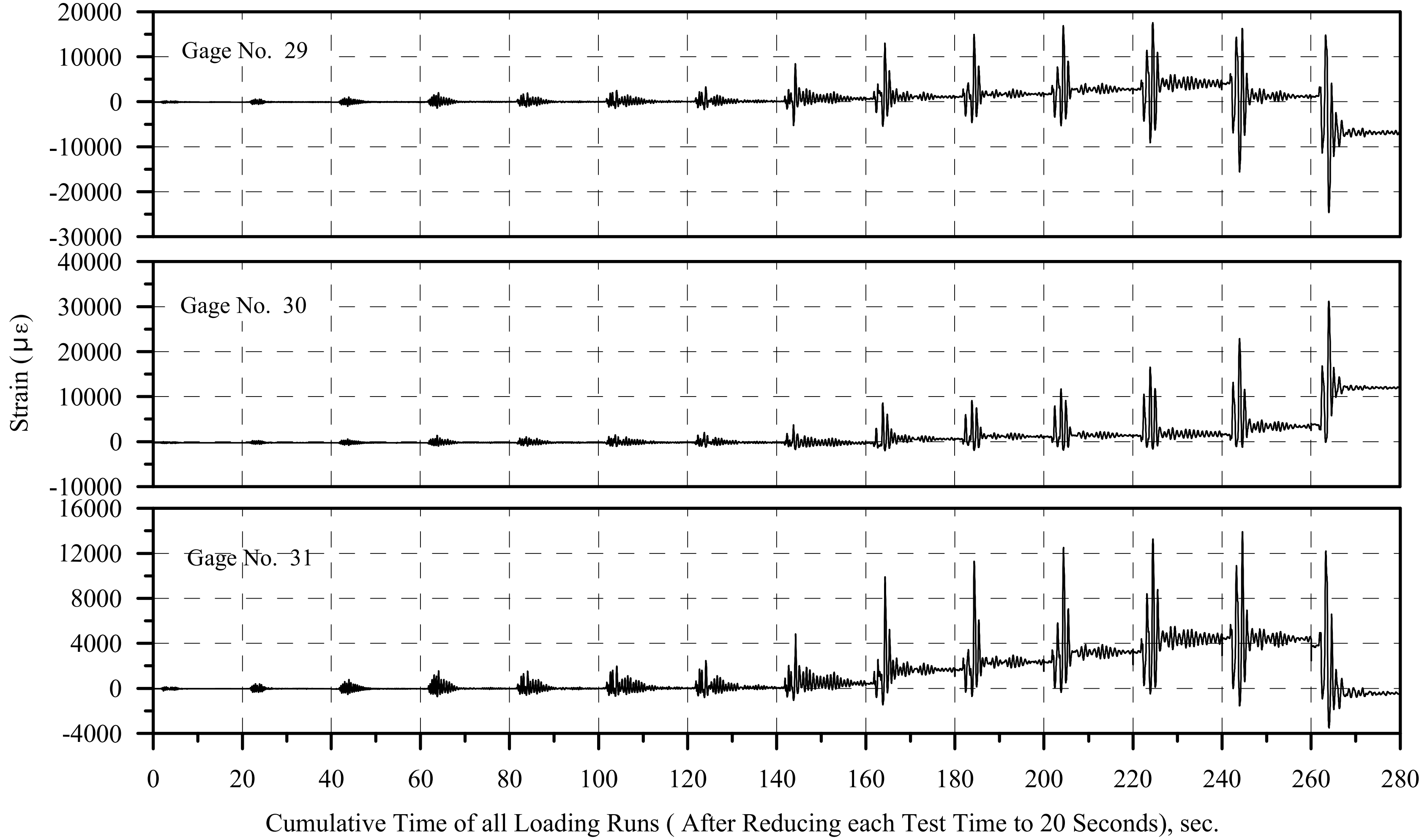

Fig C-10: Strain History for Gages 29, 30 and 31 of Specimen B2CT

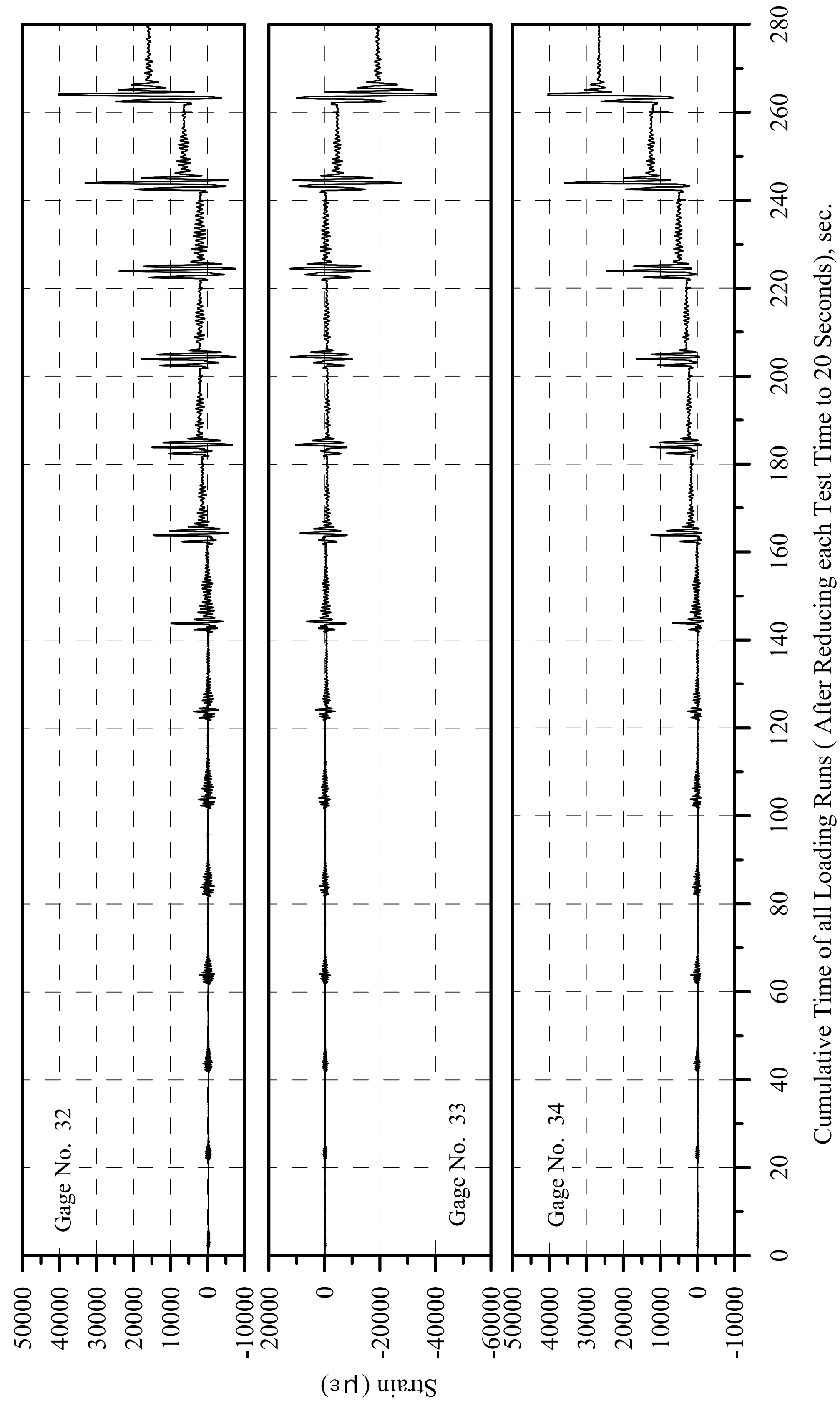

Fig. C-11: Strain History for Gages 32, 33 and 34 of Specimen B2CT

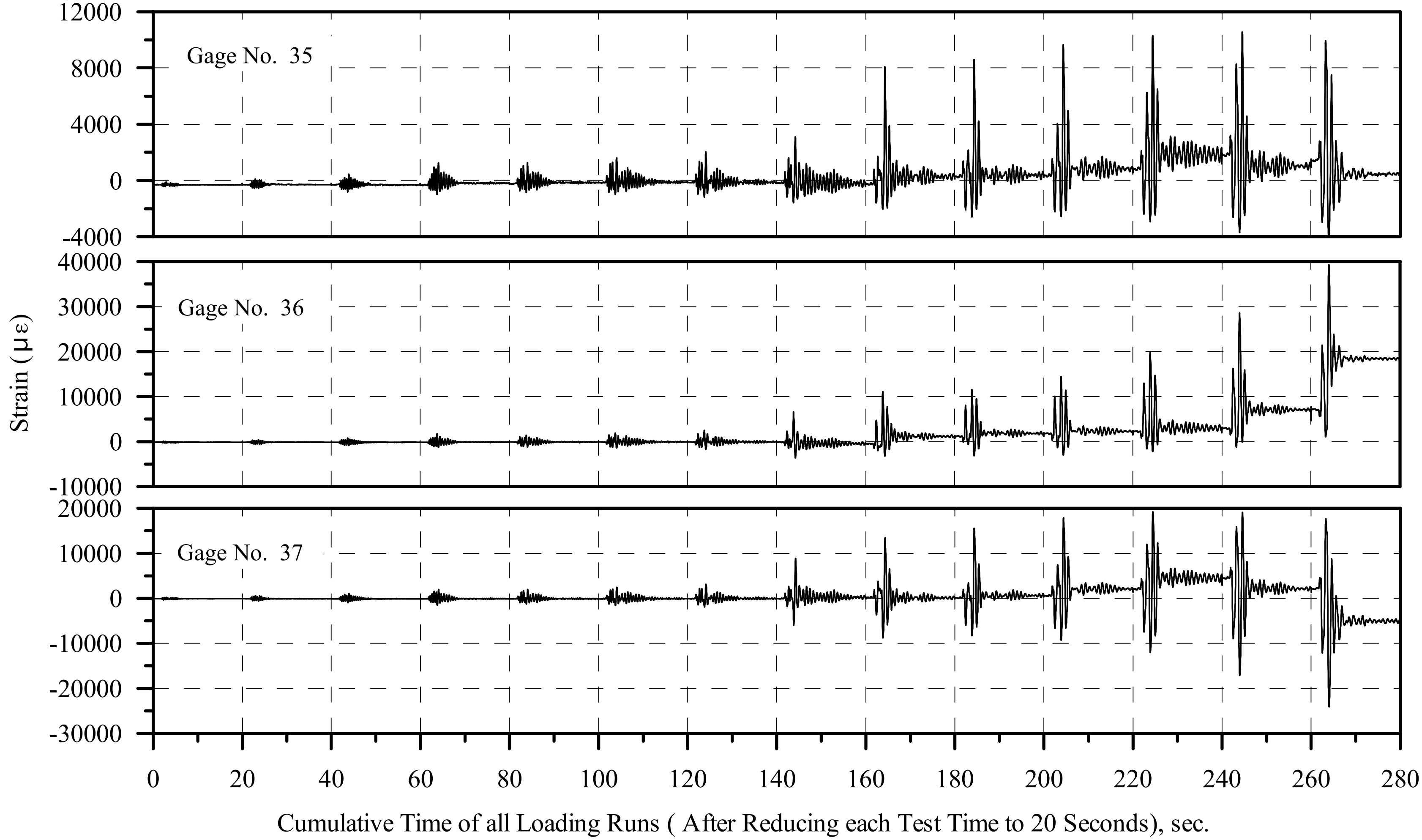

Fig. C-12: Strain History for Gages 35, 36 and 37 of Specimen B2CT

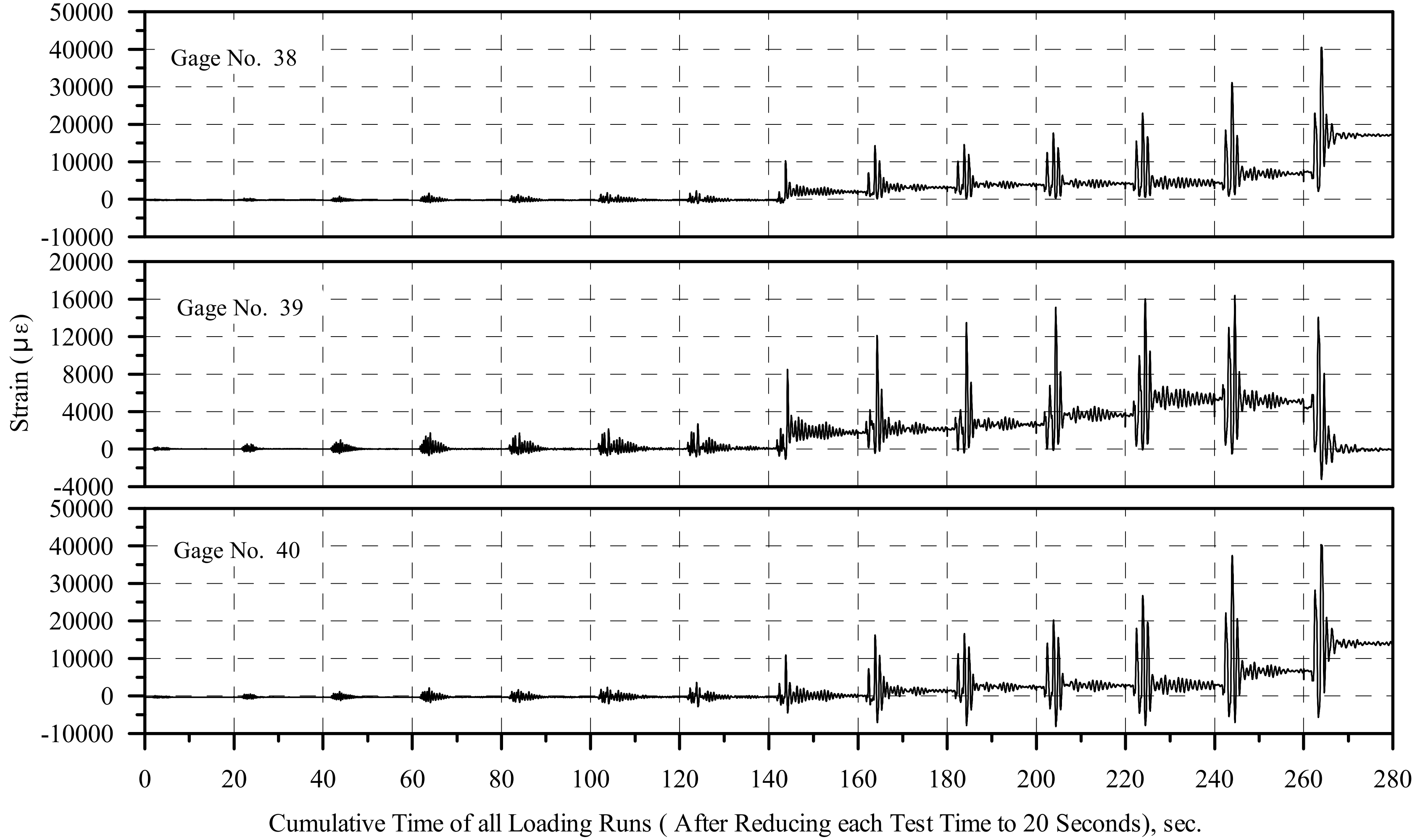

Fig. C-13: Strain History for Gages 38, 39 and 40 of Specimen B2CT

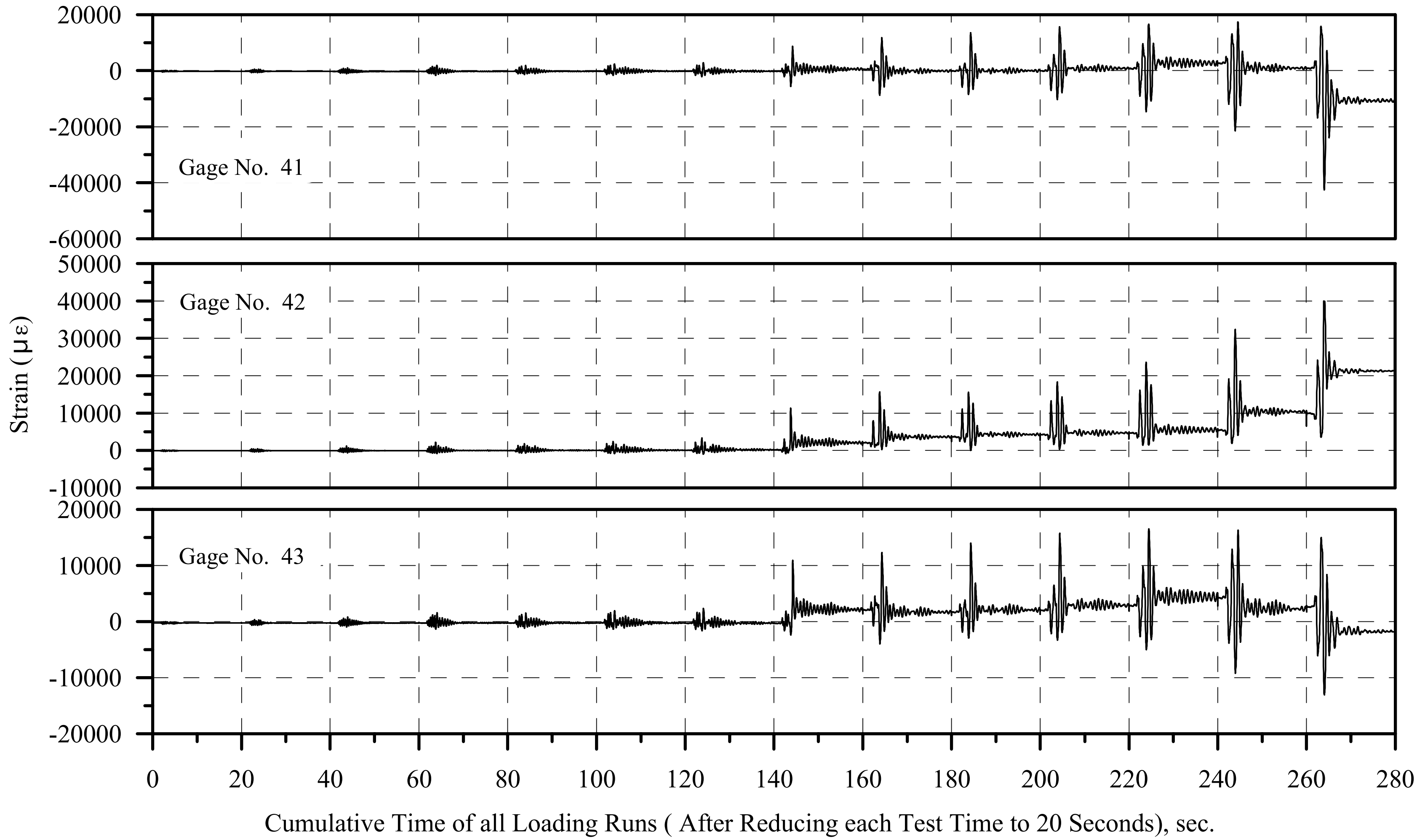

Fig. C-14: Strain History for Gages 41, 42 and 43 of Specimen B2CT

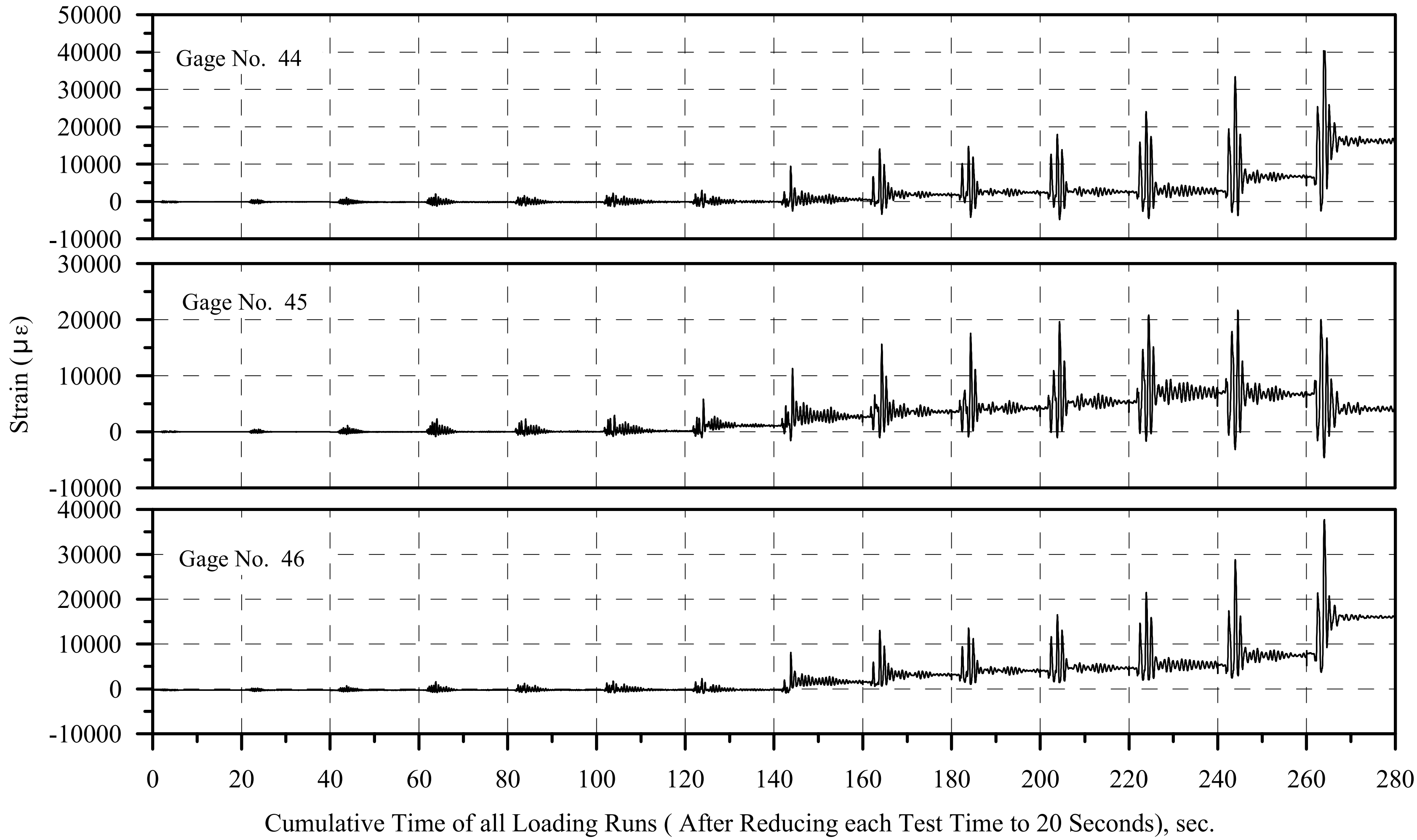

Fig. C-15: Strain History for Gages 44, 45 and 46 of Specimen B2CT

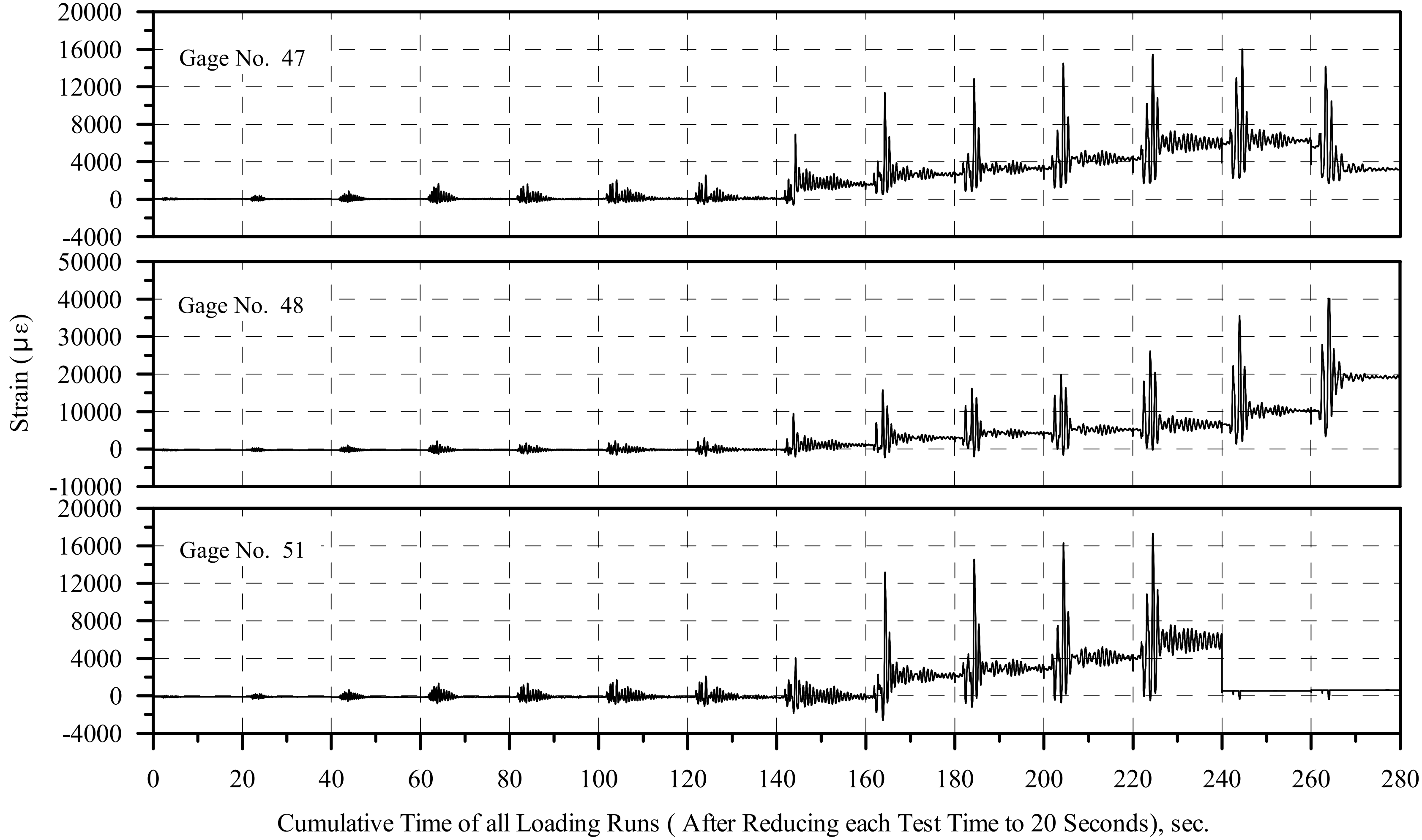

Fig. C-16: Strain History for Gages 47, 48 and 51 of Specimen B2CT

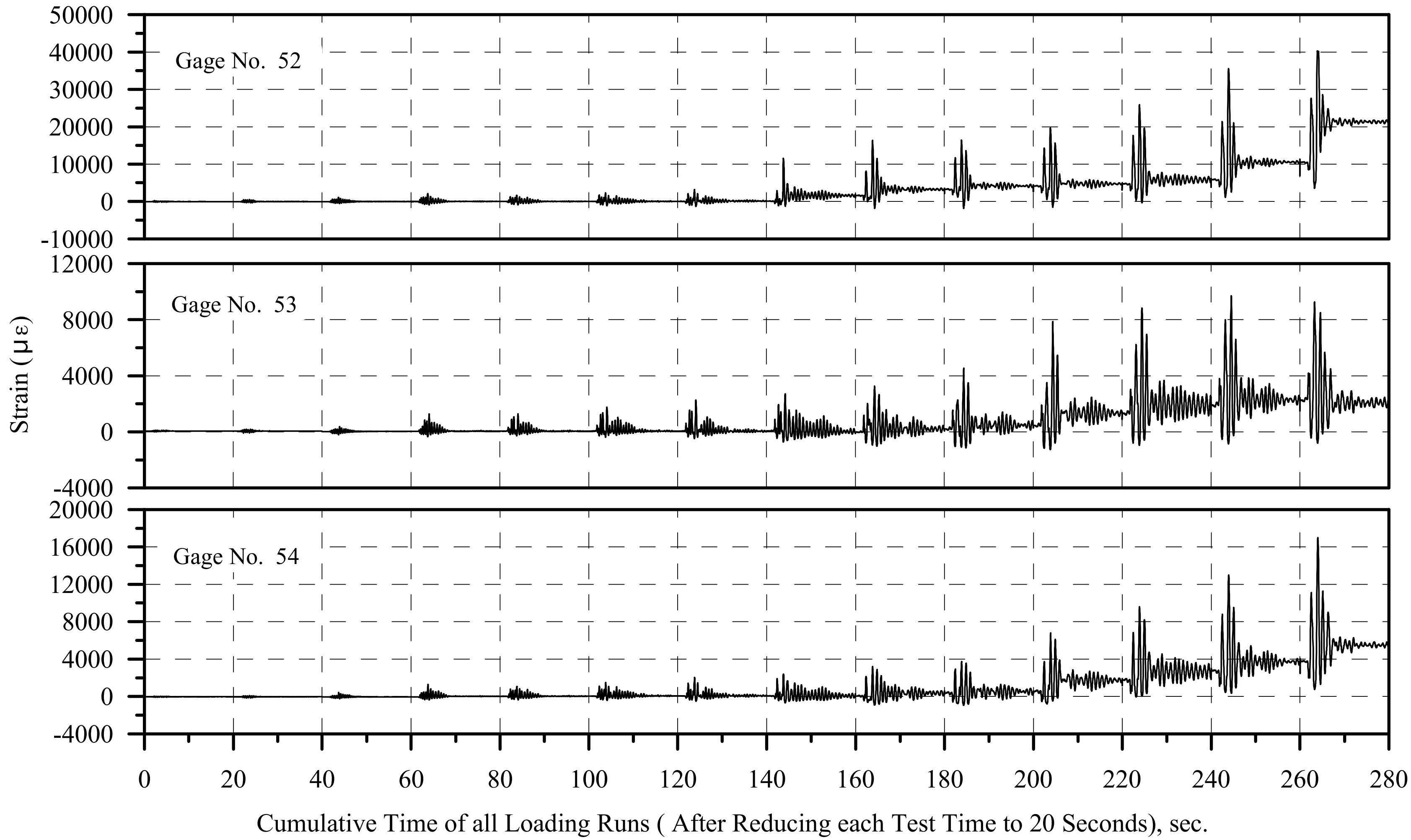

Fig. C-17: Strain History for Gages 52, 53 and 54 of Specimen B2CT

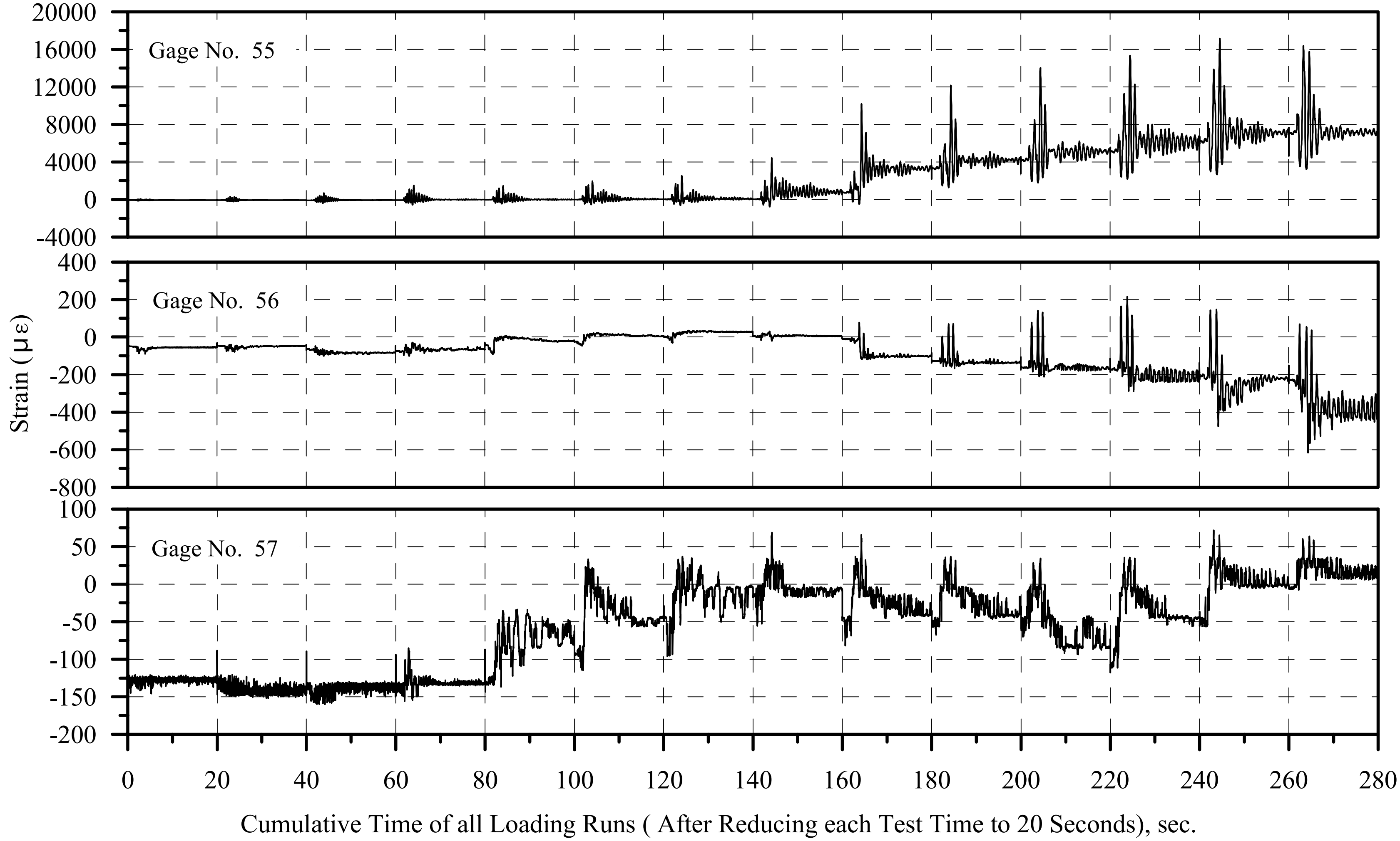

Fig. C-18: Strain History for Gages 55, 56 and 57 of Specimen B2CT

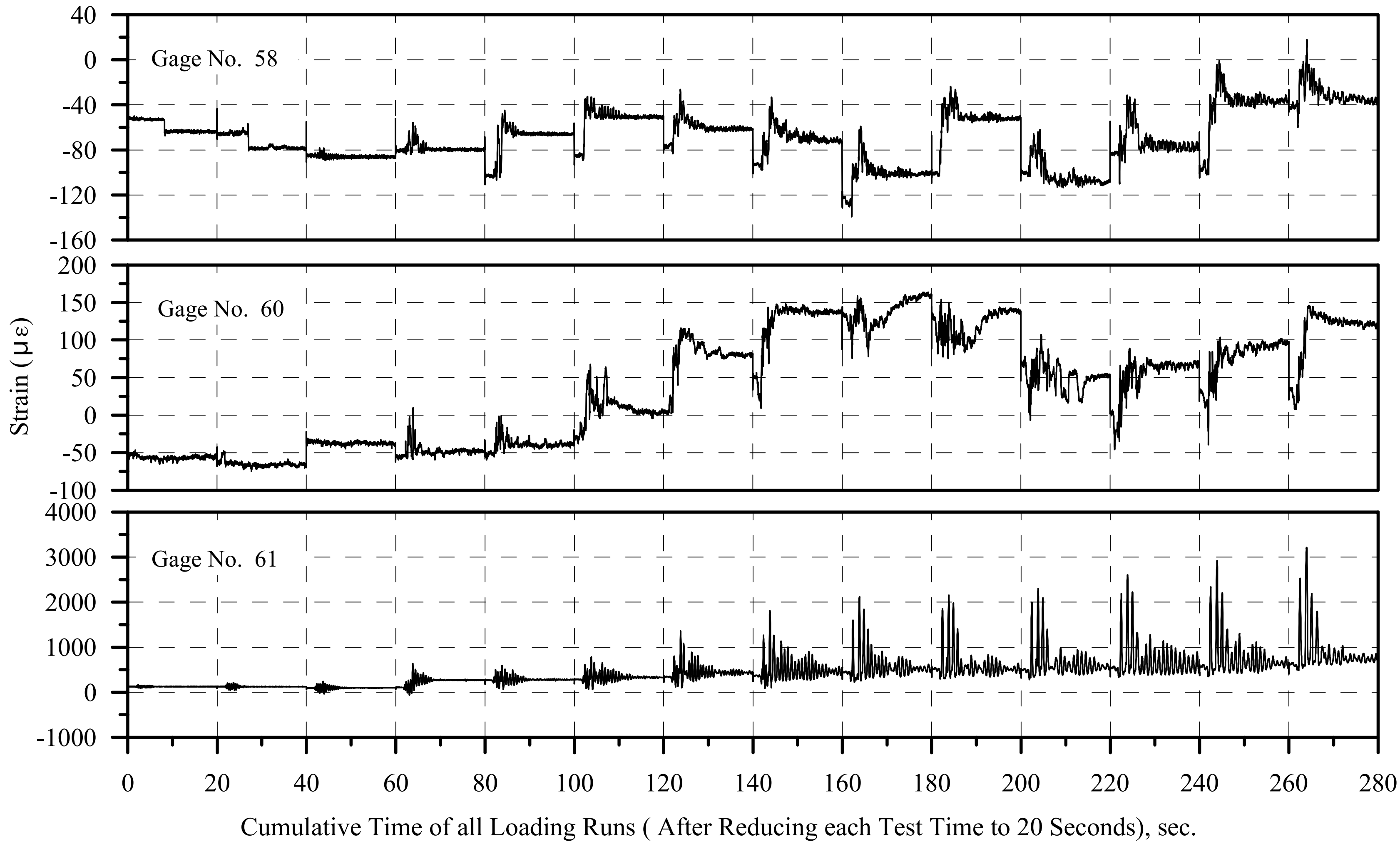

Fig. C-19: Strain History for Gages 58, 60 and 61 of Specimen B2CT

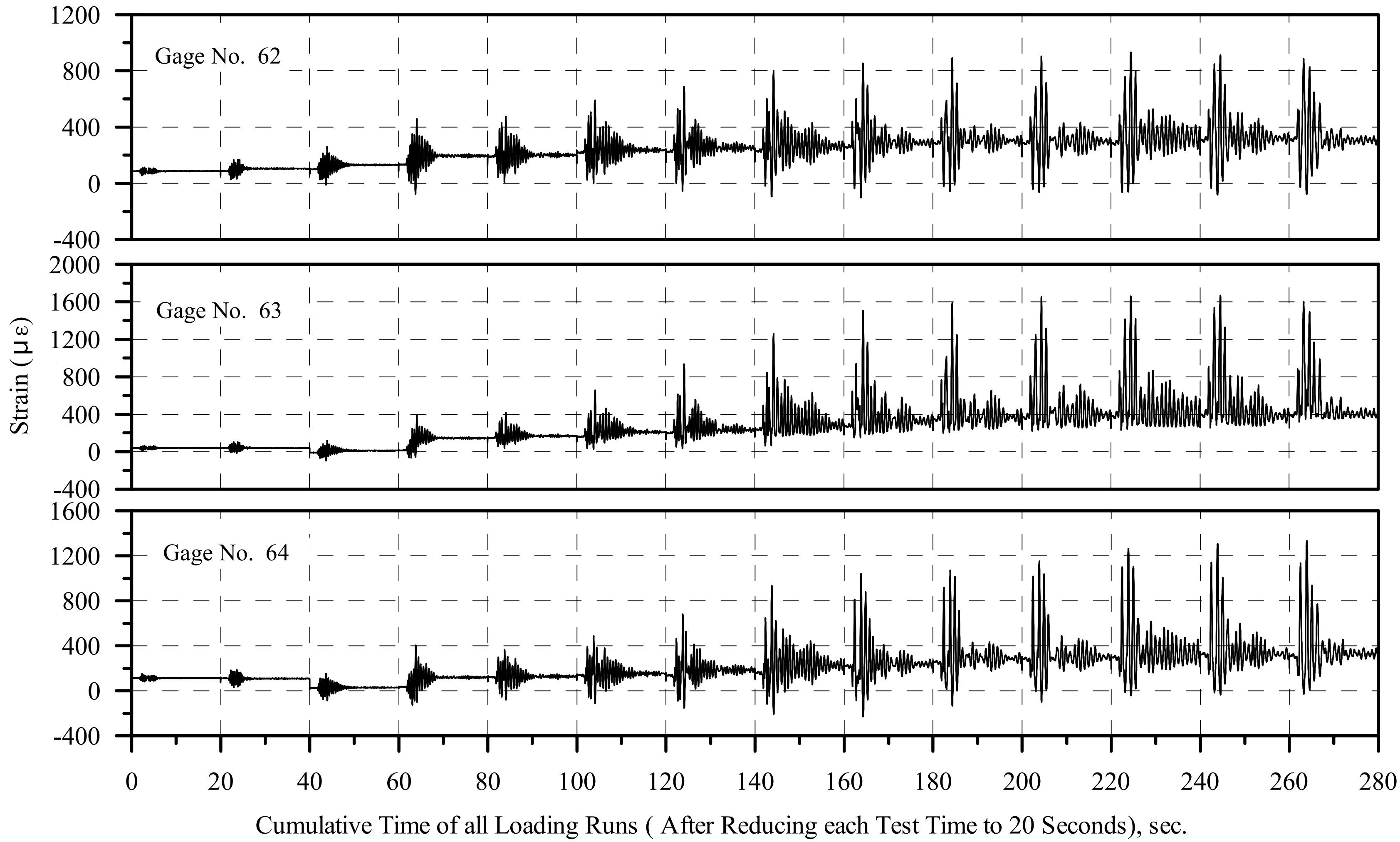

Fig. C-20: Strain History for Gages 62, 63 and 64 of Specimen B2CT

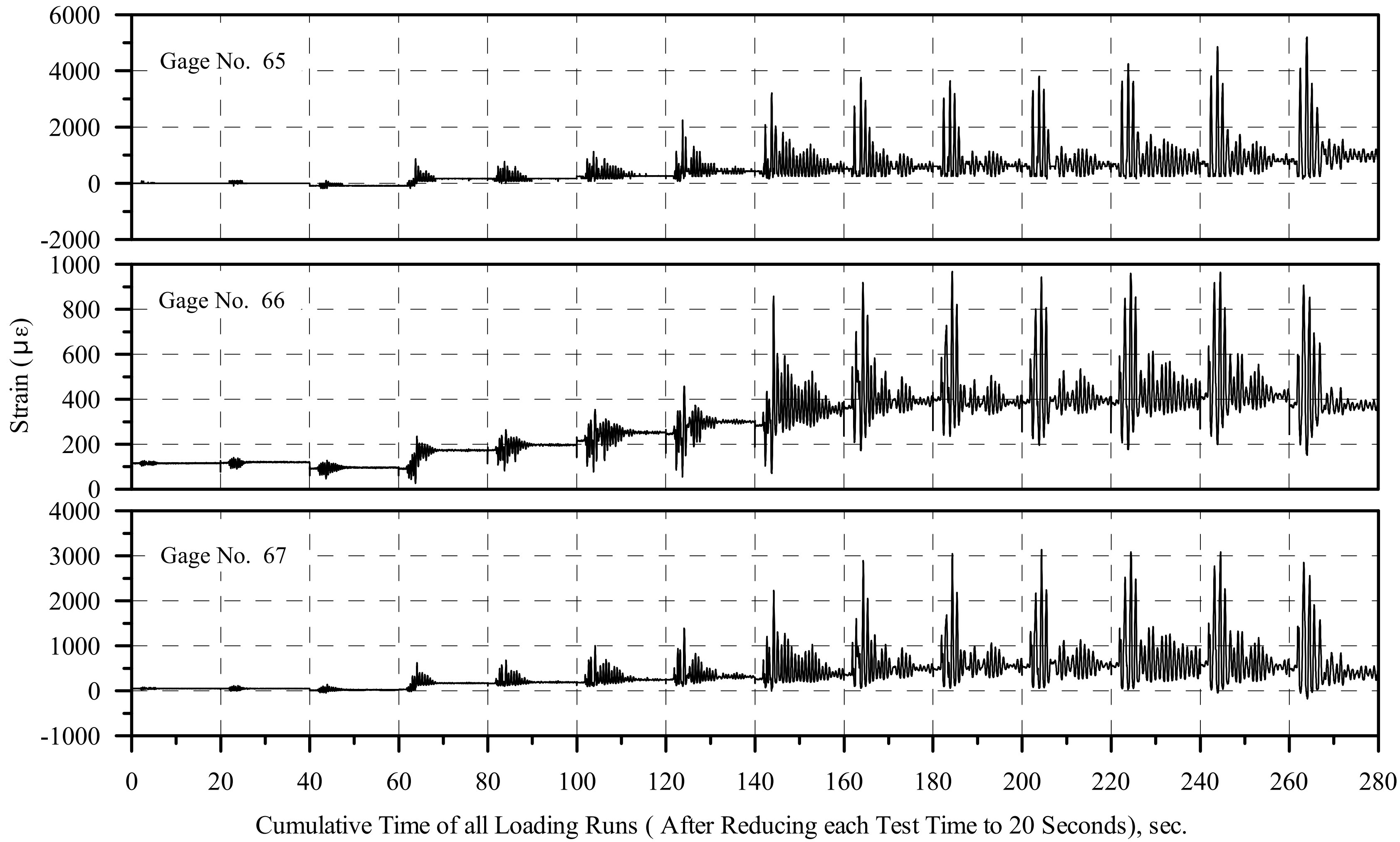

Fig. C-21: Strain History for Gages 65, 66 and 67 of Specimen B2CT

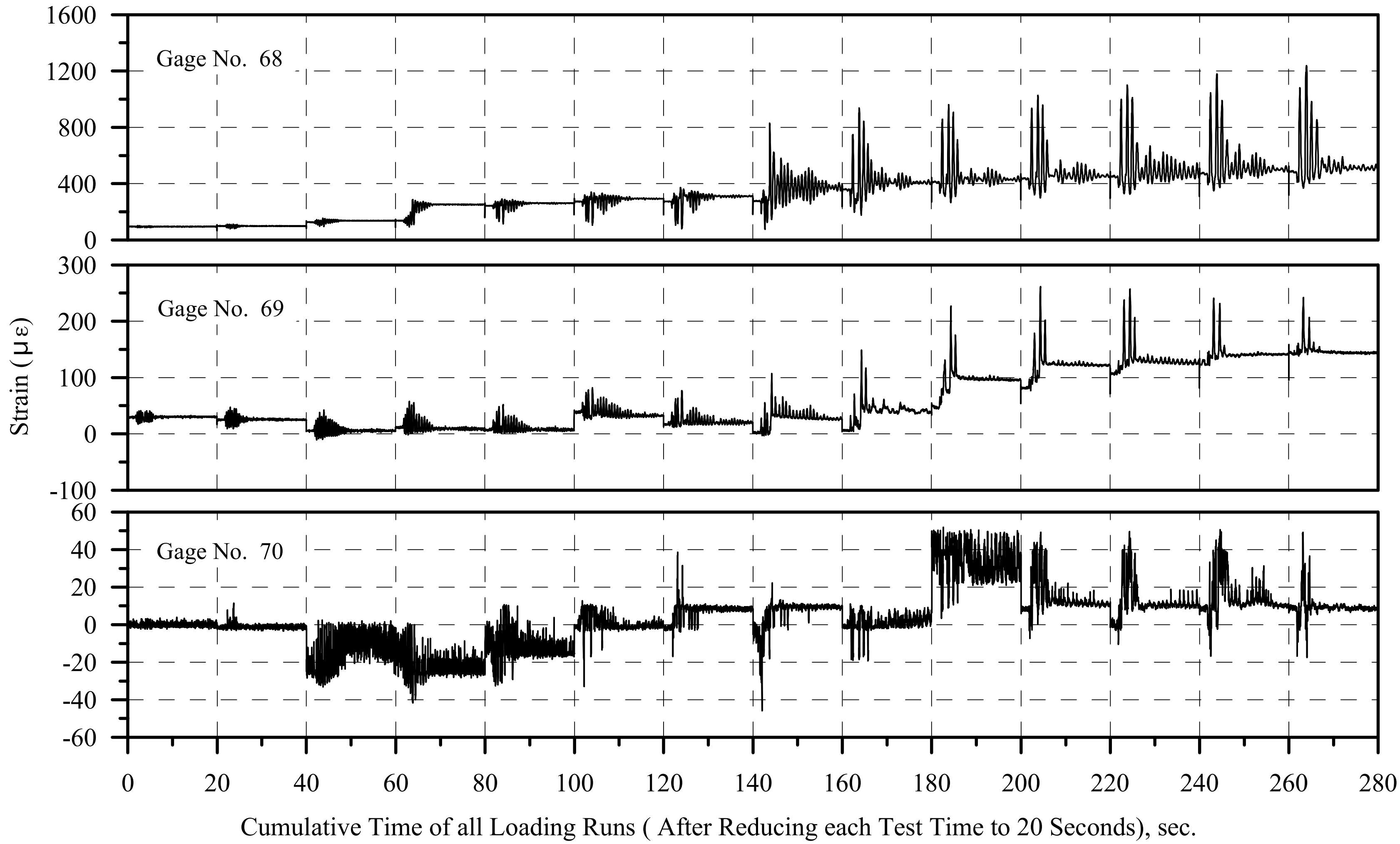

Fig. C-22: Strain History for Gages 68, 69 and 70 of Specimen B2CT

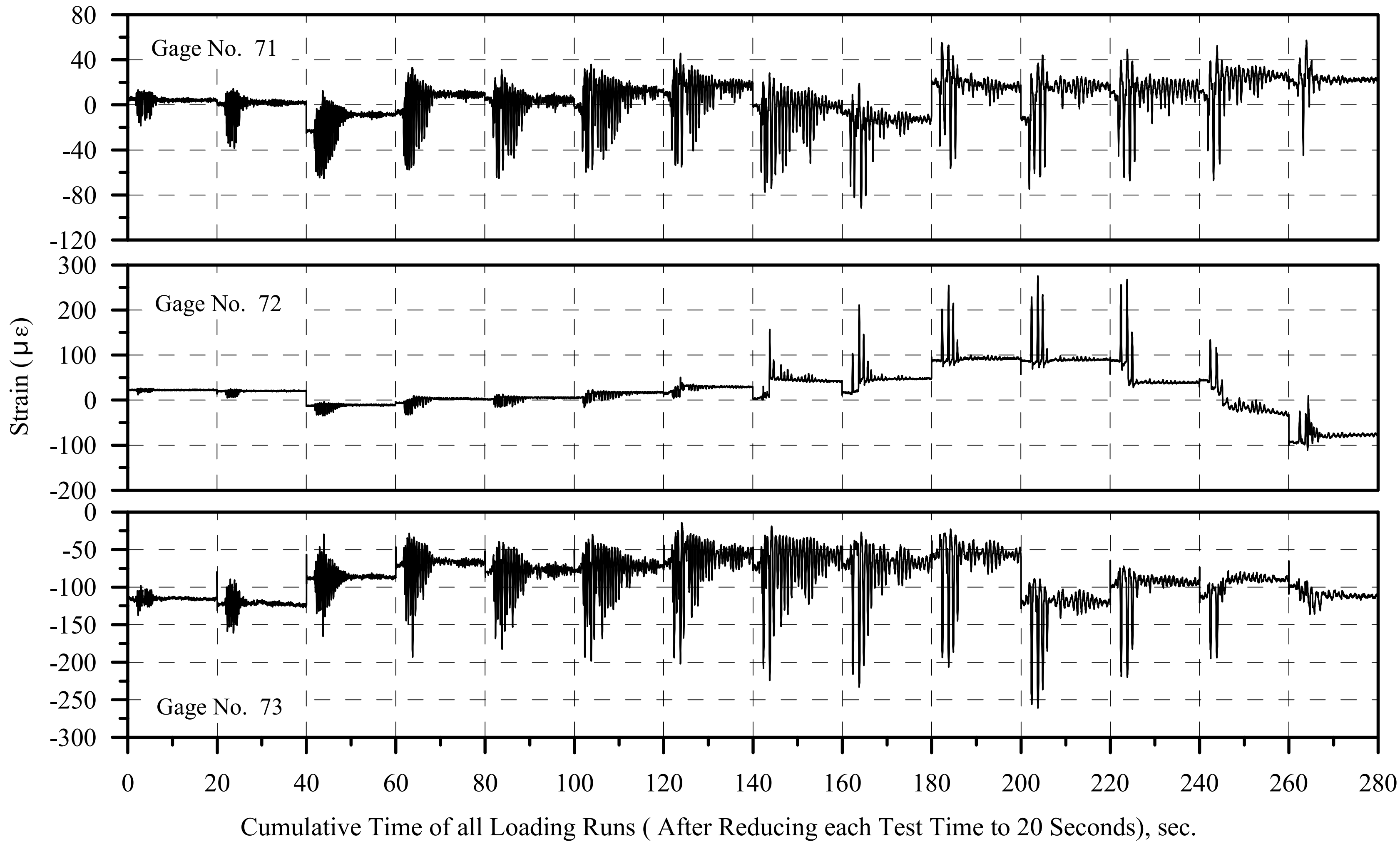

Fig. C-23: Strain History for Gages 71, 72 and 73 of Specimen B2CT

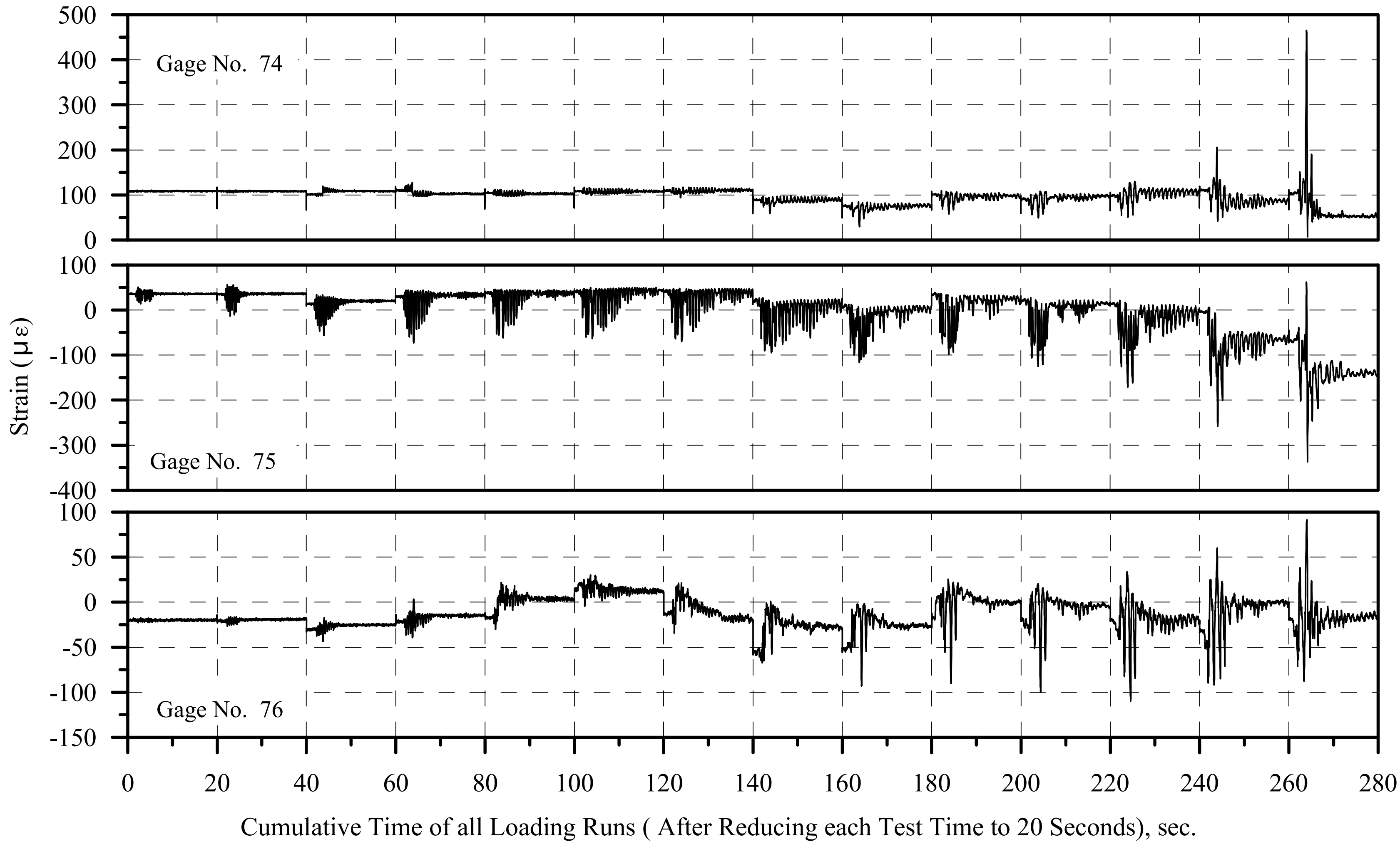

Fig. C-24: Strain History for Gages 74, 75 and 76 of Specimen B2CT

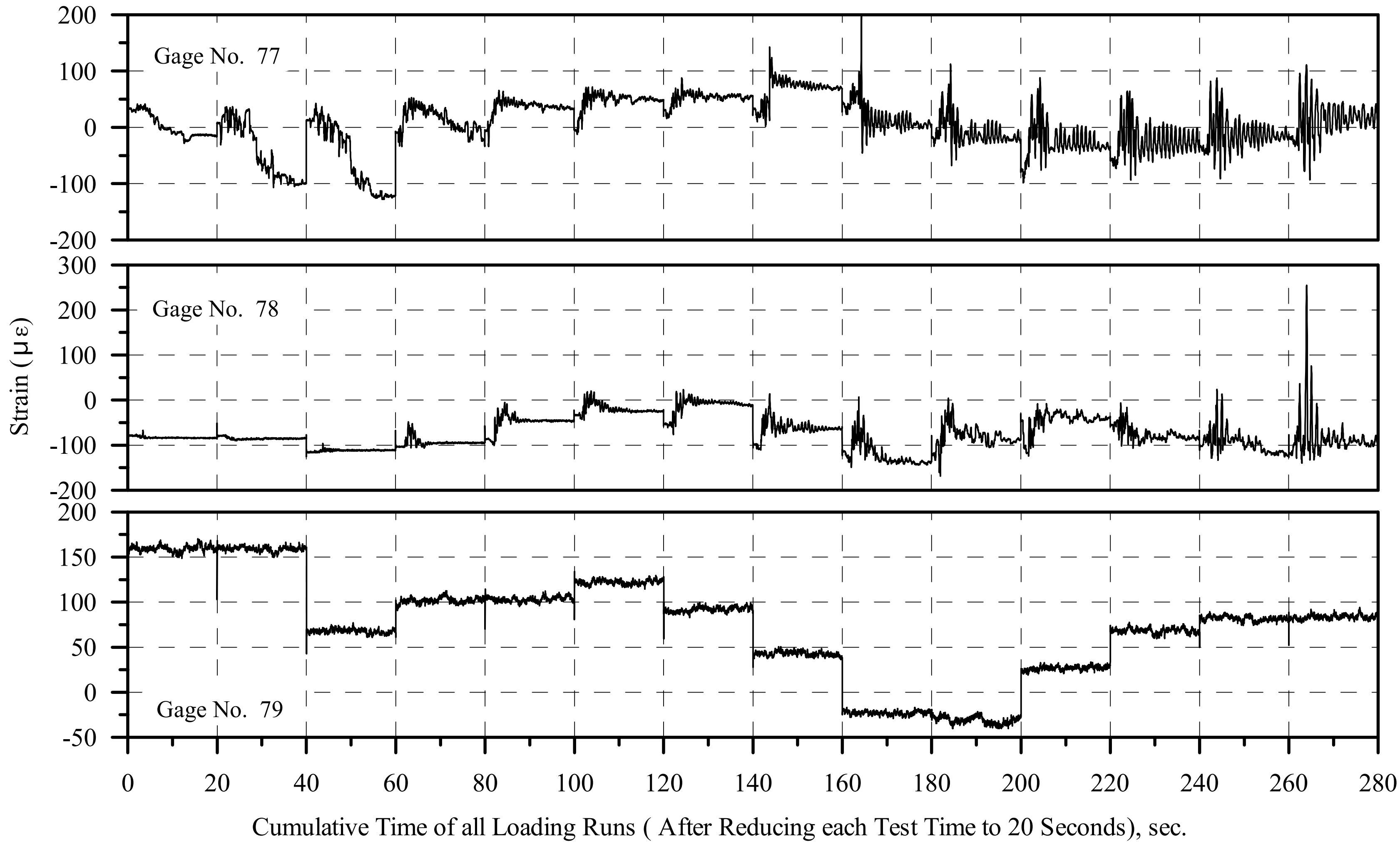

Fig. C-25: Strain History for Gages 77, 78 and 79 of Specimen B2CT

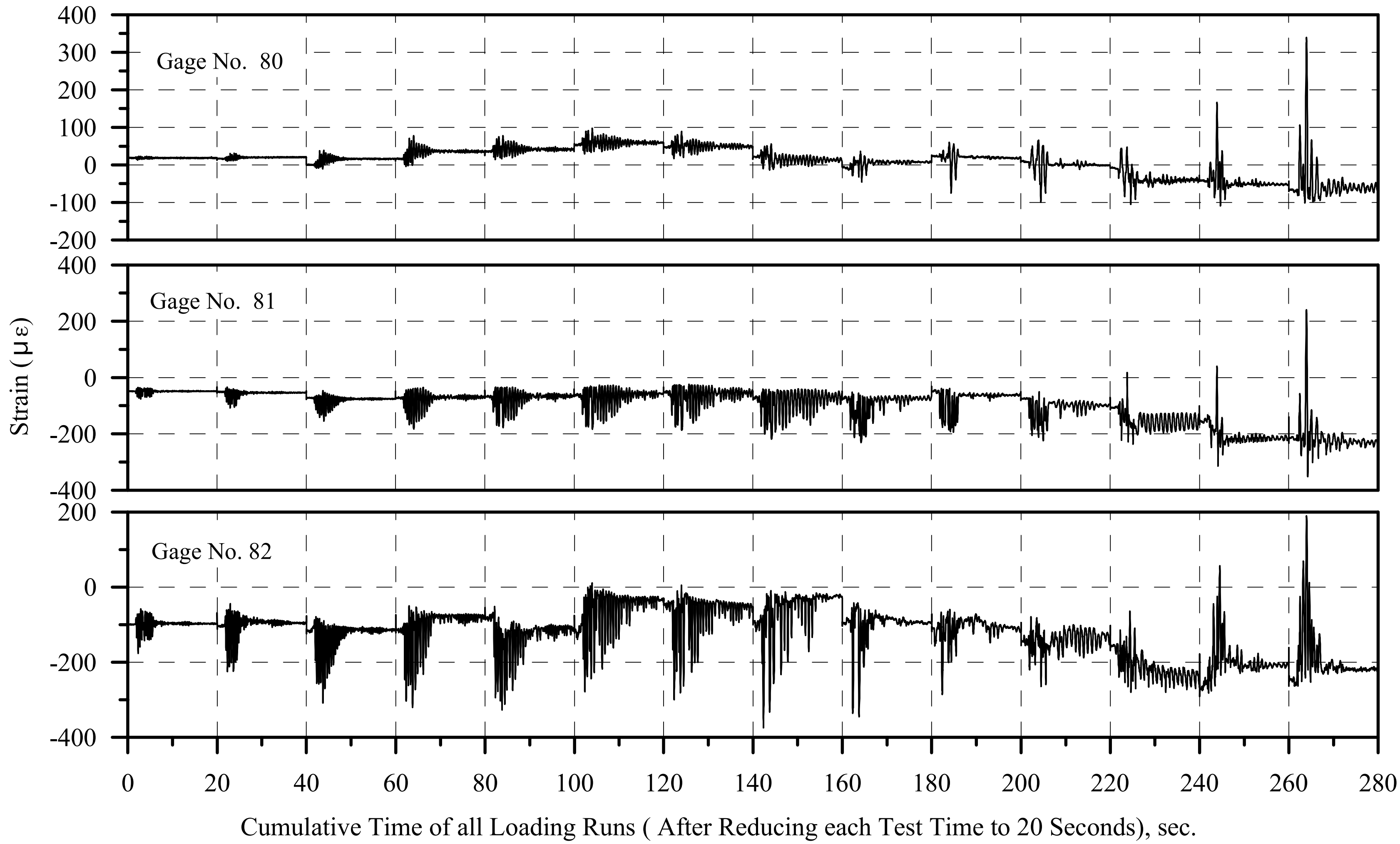

Fig. C-26: Strain History for Gages 80, 81 and 82 of Specimen B2CT

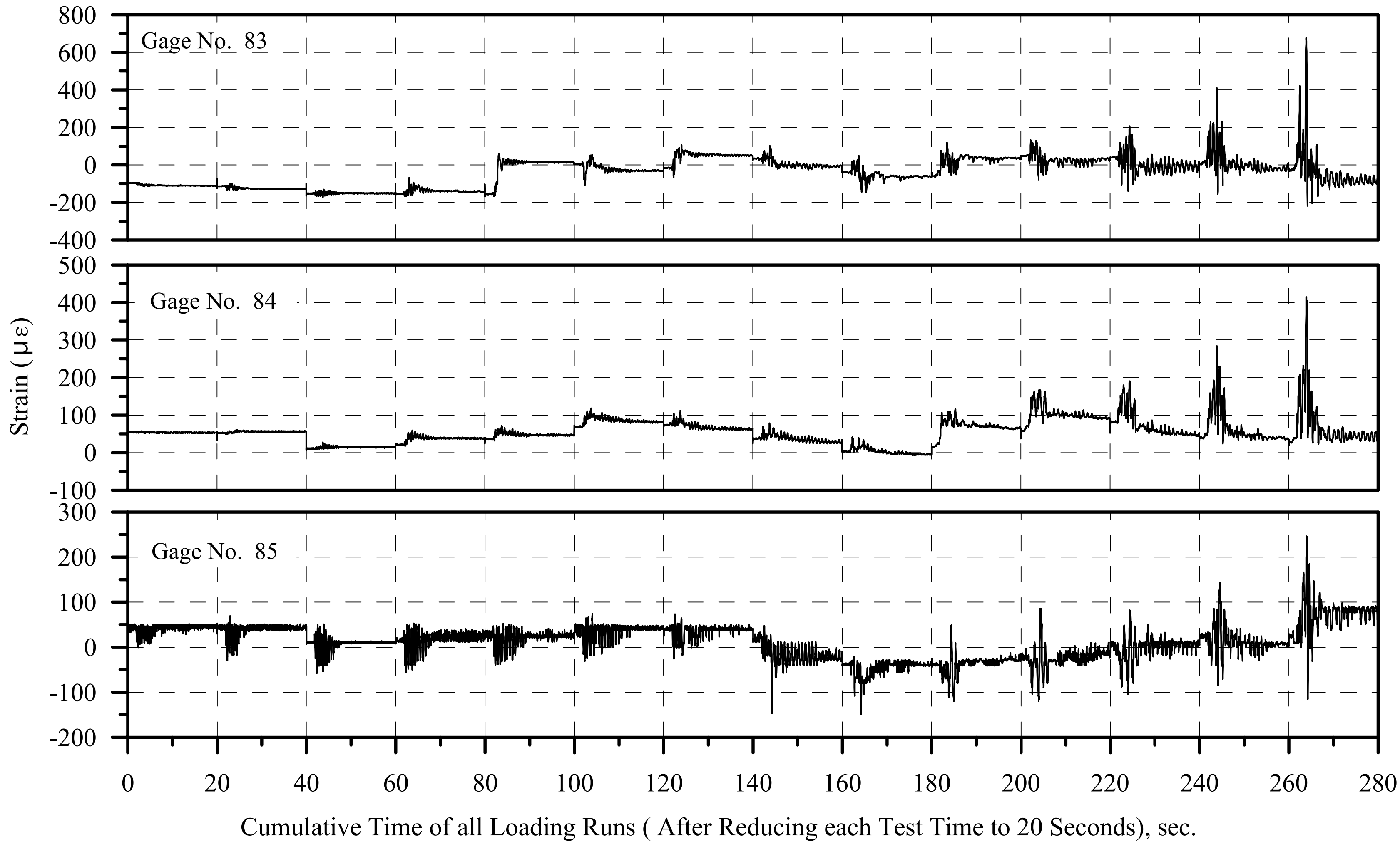

Fig. C-27: Strain History for Gages 83, 84 and 85 of Specimen B2CT

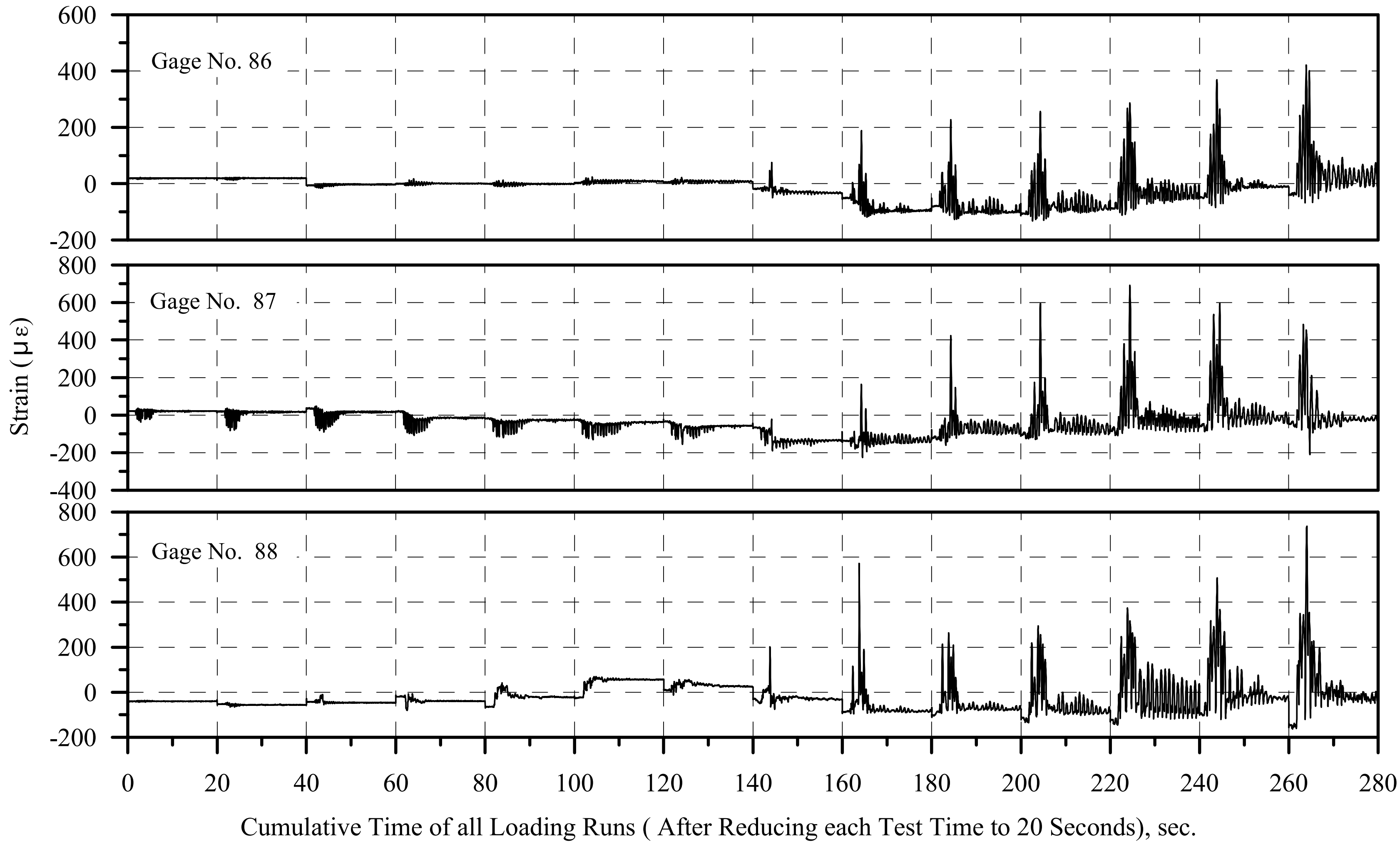

Fig. C-28: Strain History for Gages 86, 87 and 88 of Specimen B2CT

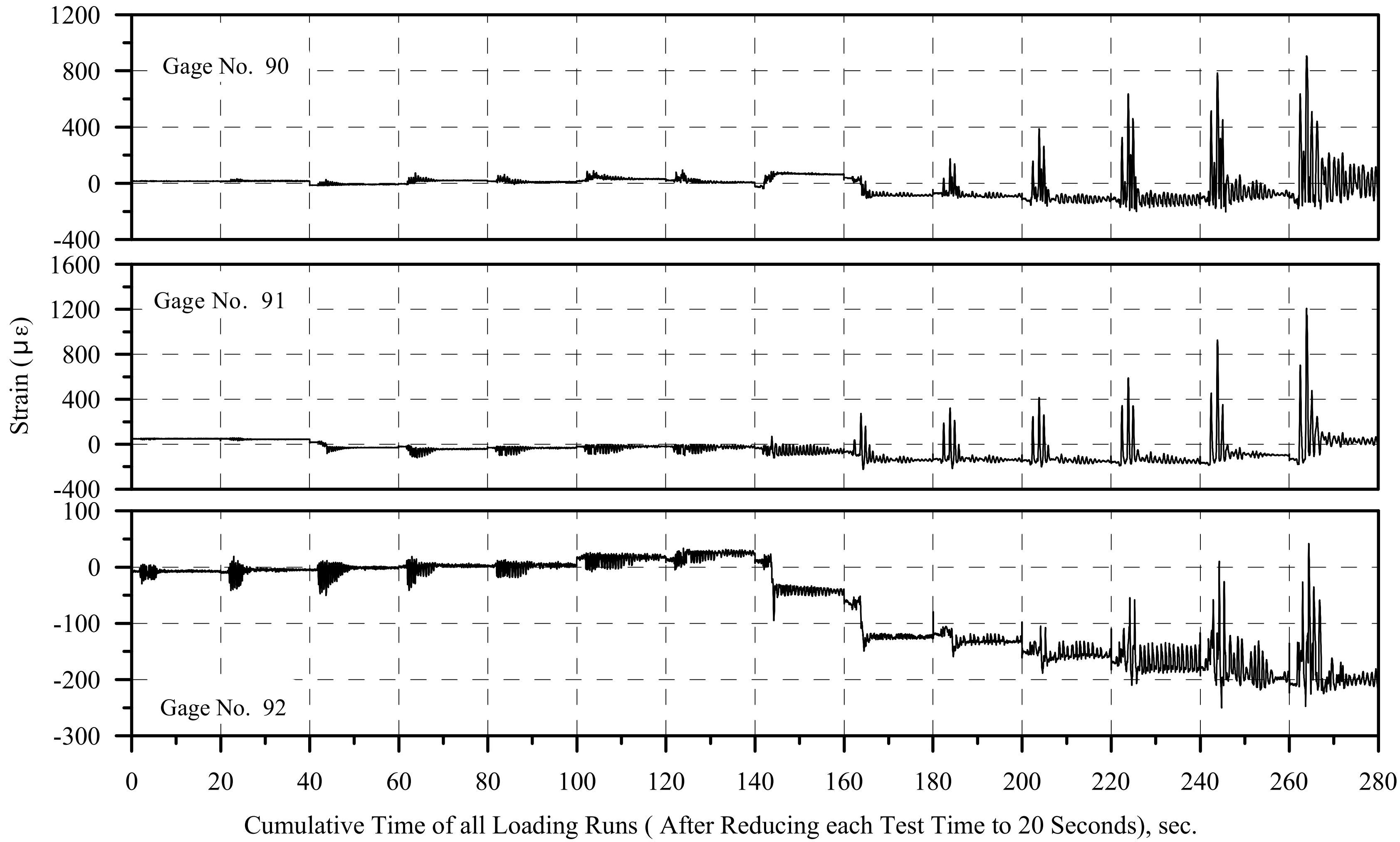

Fig. C-29: Strain History for Gages 90, 91 and 92 of Specimen B2CT

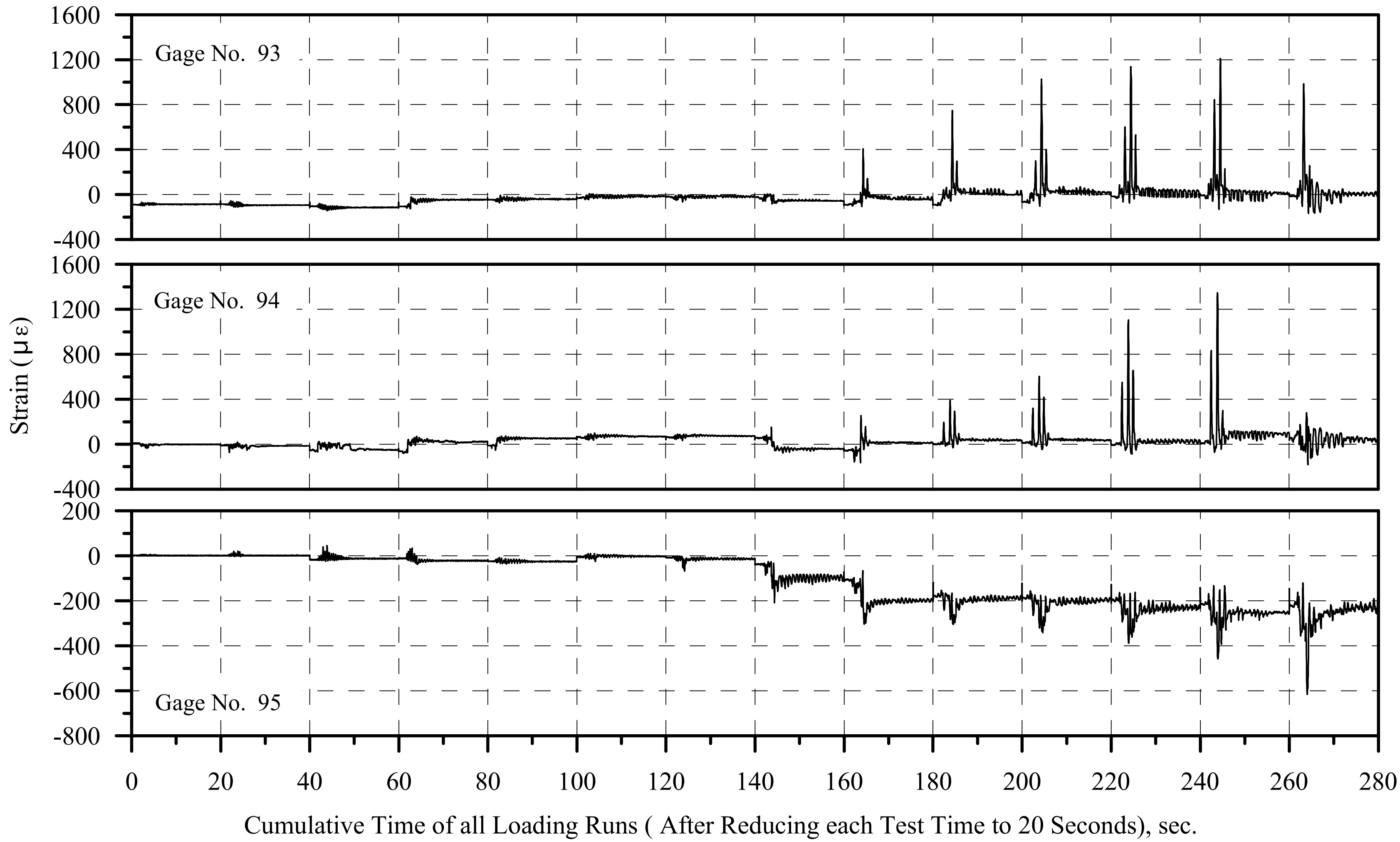

Fig. C-30: Strain History for Gages 93, 94 and 95 of Specimen B2CT

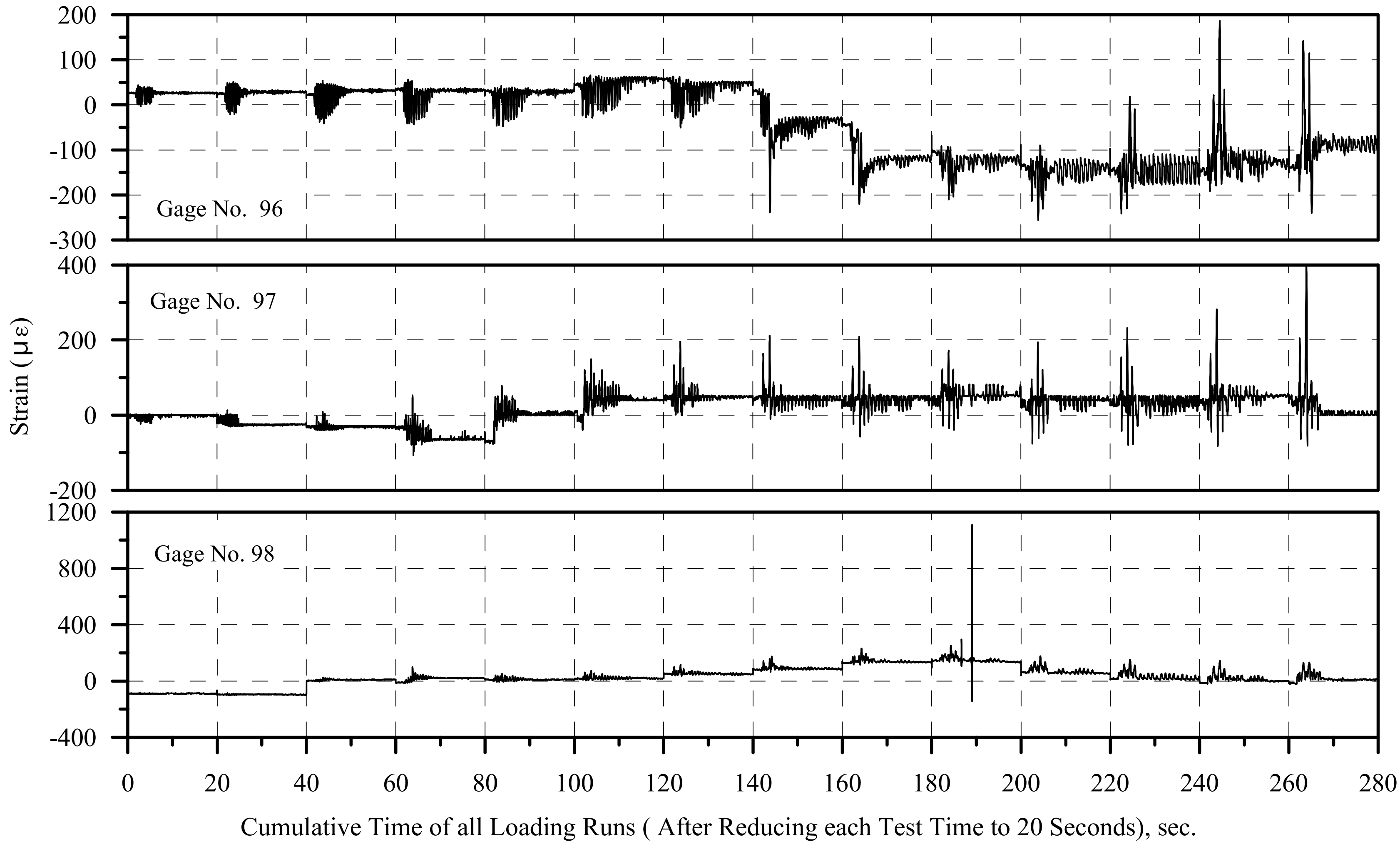

Fig. C-31: Strain History for Gages 96, 97 and 98 of Specimen B2CT

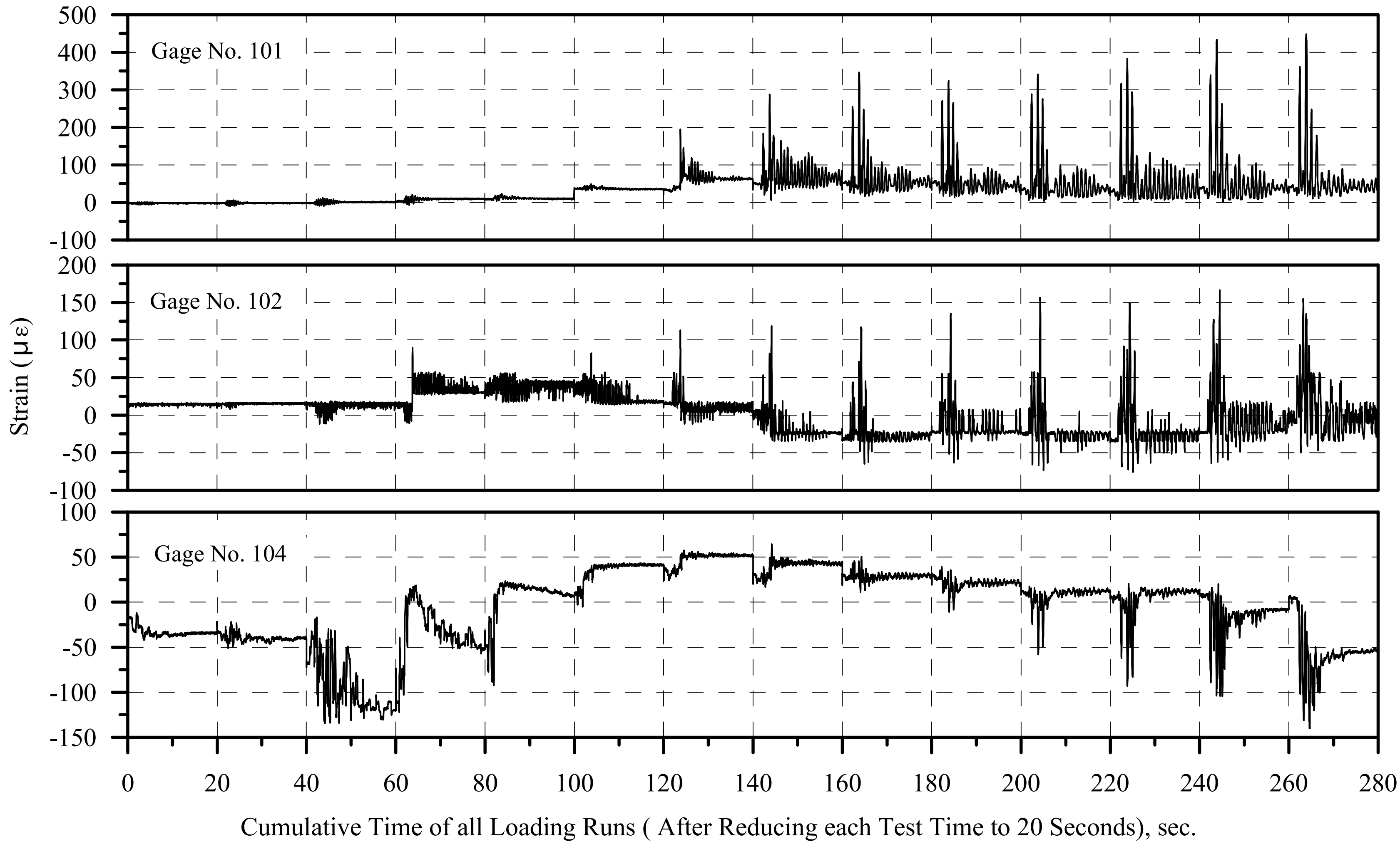

Fig. C-32: Strain History for Gages 101, 102 and 104 of Specimen B2CT

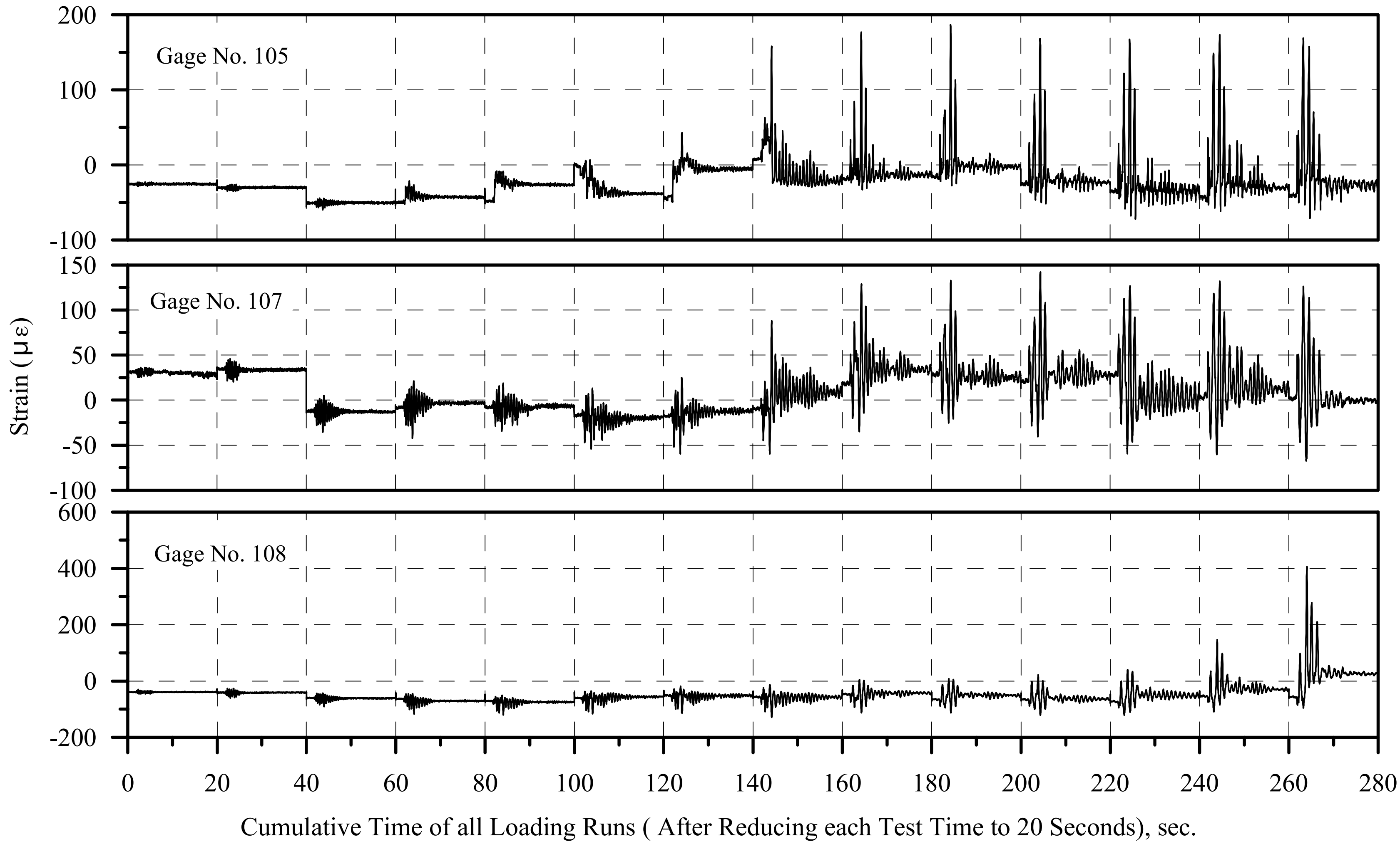

Fig. C-33: Strain History for Gages 105, 107 and 108 of Specimen B2CT

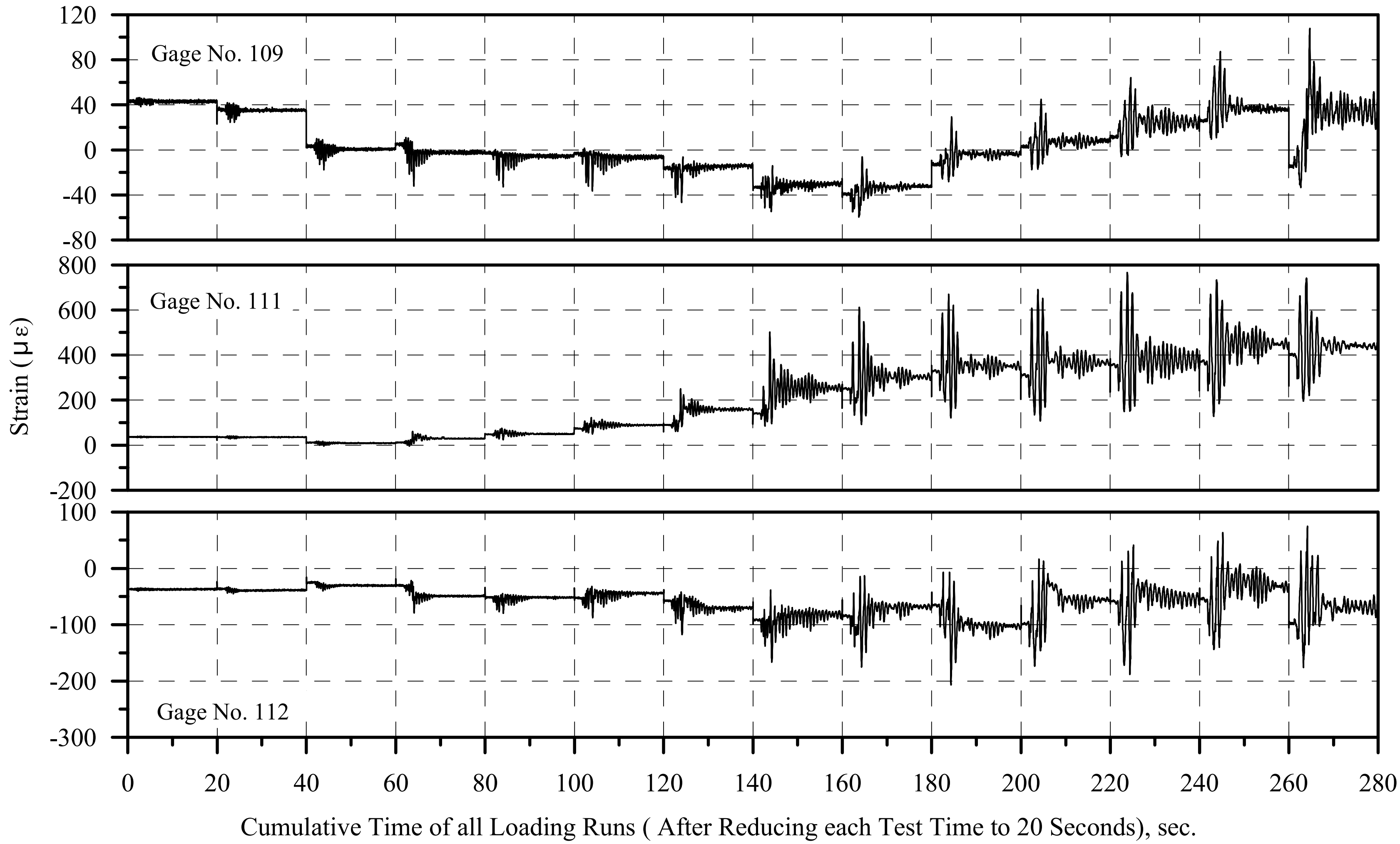

Fig. C-34: Strain History for Gages 109, 111 and 112 of Specimen B2CT

DISCLAIMER

❖ This document has been reproduced from the best copy furnished by the sponsoring agency.